WORKBOOK & PROGRAMME

NATO ADVANCED STUDY INSTITUTE

"NEW DIRECTIONS IN TERAHERTZ TECHNOLOGY"

Chateau de Bonas, Castera-Verduzan, France
June 30th- July 11th 1996

PREFACE

The Workbook contains copies of Viewgraphs kindly provided by Speakers before the meeting, together with Extended Abstracts and other materials.

The Edited Proceedings of this ASI will be published in due course by Kluwer as part of their NATO ASI Series.

We are most grateful to the following companies and organisations for their generous financial support and sponsorship of this meeting:

North Atlantic Treaty Organisation
European Research Office of the US Army
Engineering & Physical Science Research Council (UK)
National Science Foundation (USA)
Hughes Electronics
URSI
Daimler-Benz
The University of Leeds
The University of Nottingham

(List dated: June 8th 1996)

The Organisers also wish to add their thanks to the Management of the Chateau de Bonas, to all of the Speakers for their interest in this ASI and of course to all of the Participants for their attendance.

ORGANISING COMMITTEE

Co- Directors: T Itoh (UCLA) & E Kollberg (Chalmers)

J Bowen (Reading): *Workbook*
J M Chamberlain (Nottingham): *Secretary*
N Cronin (Bath): *Sessions Management*
J Leotin (Toulouse): *Local Arrangements*
R E Miles (Leeds): *Proceedings*
R D Pollard (Leeds): *Treasurer*

PROGRAMME

THEME #1: BACKGROUND AND INTRODUCTION

"Introduction to Solid State Terahertz Devices- (I&II)"
J M Chamberlain & R E Miles

"Mixers and Multipliers (I&II)"
N J Cronin

"Terahertz Detector Fundamentals"
J Leotin

"Terahertz Receiver Fundamentals"
G Beaudin

"Waveguide and Quasi Optical Measurements"
R D Pollard

THEME #2: DEVICE UPDATE

"Developments in Two and Three Terminal Active Devices"
C van Hoof

"Hot Electron Mixers and SIS Detectors"
E Kollberg

"Schottky Barrier Devices for THz Applications"
H-P Röser

"Device Physics of Intersubband Lasers"
P Harrison

"From Quantum Mechanics to s-parameters"
W S Truscott

POSTER#1

"Travelling Wave Detectors: A new Principle for Terahertz Operation"
H Sigg

"Materials Issues for New Devices"
D Lippens

"P-Ge and P-Si Lasers for Terahertz Applications"
T Wenckebach

THEME #3: INTEGRATION

"Integrated Waveguides and Mixers (I&II)"
C Mann

"Integration of Active Devices"
D Lippens

"Active Antenna Power Combining, Beam Control and 2-D Combining (I&II)"
T Itoh

"Grid Amplifiers"
D Rutledge

"System Characterisation Issues for Integration"
J Bowen

"Integrated Antennae (I&II)"
G M Rebeiz

THEME #4: APPLICATIONS

"Astronomy & Atmospheric Physics from Space"
T. de Graauw

"Terahertz Measurements from Satellites"
B Carli

"Spacecraft Applications of Terahertz Technology"
W J Hall

"Technical Issues of Terahertz Component Fabrication"
R J Wylde

"Likely Future Instrumentation Requirements at Terahertz Frequencies"
D Rytting

"Potential Applications of Terahertz Systems for Collision Avoidance and Related Areas"
H Brugger

"What Future for Wireless Telecommunications Beyond 60 GHz?"
D Wake

Panel Discussion
[R E Miles]

"Vector Measurements to 800 GHz"
P Goy

Presentation and Visit to MATRA Satellite Integration Facility, Toulouse.
(F Baudis and S Flamenbaum

THEME #5: LIGHTWAVE/TERAHERTZ INTERACTION

"Lightwave/Terahertz Interaction: An Overview of the Field (I&II)"
H R Fetterman

"Optical and Electrical Generation of Terahertz Pulses and Imaging Techniques (I& II)"
H Roskos

POSTER #2

"Multi Gigaghertz Optoelectronic Devices (I&II)"
C Ironside

CLOSING SESSION
Co-Directors

	0830 - 0945	0945 - 1100	COFFEE	1130 - 1245	LUNCH 1pm	1445 - 1600	TEA	1630 - 1745	DINNER 7pm	SUNDAY EVENING: INTRODUCTION FROM CO-DIRECTORS
MON JULY 1ST	Chamberlain [Theme #1]	Miles		Cronin (1)		Cronin (2)		Leotin		Reception
TUES JULY 2ND	Beaudin	Pollard (1)		Pollard (2)		Van Hoof [Theme #2]		Kollberg		Talk by Mme Simon
WED JULY 3RD	Roser	Harrison		Truscott		Poster #1		VISIT TO DISTILLERY		
THURS JULY 4TH	Sigg	Lippens (1)		Wylde	Photographer	Theme #3 Mann (1)		Mann (2)		
FRI JULY 5TH	Lippens (2)	Itoh (1)		Itoh (2)		Rutledge		Bowen		ASI Dinner
SAT JULY 6TH	Rebeiz (1)	Rebeiz (2)		de Graauw [Theme #4]		Carli		Hall		Jazz Concert
SUN JULY 7TH	OUTING TO CARCASSONNE									
MON JULY 8TH	Wenckebach	Rytting		Brugger		Wake		Panel Discussion [Miles]		Visit to Foie Gras Restaurant
TUES JULY 9TH	Goy 9.30 - 11.30		SCIENTIFIC VISIT TO MATRA							
WED JULY 10TH	Fetterman (1) Theme #5	Fetterman (2)		Roskos (1)		Roskos (2)		Poster #2		
THURS JULY 11TH	Ironside (1)	Ironside (2)		Closing: Directors						

Frequency Spectrum

	Microwave	Mmwave	Terahertz	Far Infrared	Optical
Frequency	10 GHz	100 GHz	1 THz	10 THz	100 THz
Wavelength (mm)	30	3	0.3	0.03	0.003
Wave Number (cm^{-1})	0.33	3.3	33	333	3333
Energy (eV)	4.135×10^{-5}	4.135×10^{-4}	4.135×10^{-3}	0.04135	0.4135
Energy (J)	6.625×10^{-24}	6.625×10^{-23}	6.625×10^{-22}	6.625×10^{-21}	6.625×10^{-20}
Temperature (K)	0.4797	4.797	47.97	479.7	4797

MONDAY JULY 1

INTRODUCTION TO SOLID STATE TERAHERTZ DEVICES

J M Chamberlain*, R E Miles#, C E Collins# & D P Steenson#

*Department of Physics, The University of Nottingham, Nottingham NG7 2RD, UK
#Department of Electronic and Electrical Engineering, The University of Leeds, Leeds LS2 9JT, UK

BACKGROUND: OPPORTUNITIES AND PROBLEMS.

PLAN OF TALK:

- **Background: Opportunities and Problems**
- **General Device Characteristics**
- **Fundamental Sources :** Gunns and IMPATTS; HEMTS and HBTs; DBRTDs; Josephson Devices; Intersubband devices.
- **Frequency Multiplied Sources:** Schottky diode; DBRTD; QBV.
- **Conclusions**

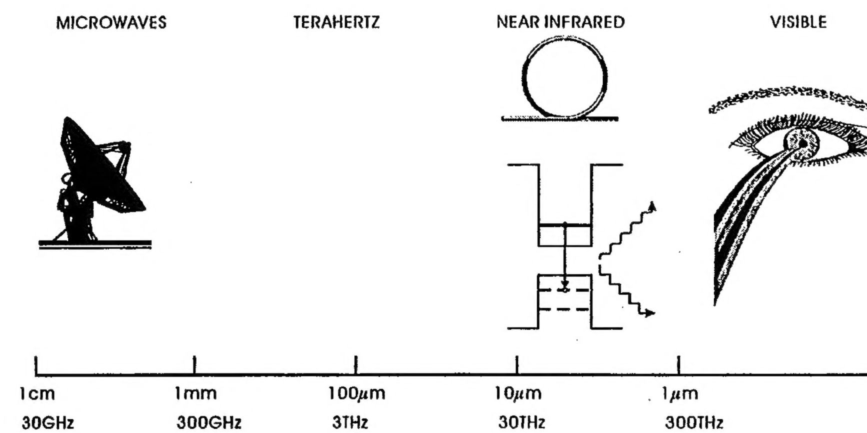

THE SPECTRUM

100 GHz - 3THz: "TRADITIONAL" APPLICATIONS

- Solid State Spectroscopy (useful $h\upsilon \approx$ few meV)
- Astronomy/Aeronomy
- Plasma Diagnostics

WIDE BANDWIDTH

Communications:

Global transmission of multimedia

LANs (with Optical Spine)

Digital Applications

WHAT OTHER APPLICATIONS?

RELEVANT PROPERTIES:

☺ **High frequency ⇒ Wide bandwidth**

☺ **Short wavelength ⇒ High resolution**

HIGH RESOLUTION

Radar - smaller antenna [$P_r \propto A^2/\lambda^2$] - short range in atmosphere.

Sensing - e.g. gases: chemically - specific absorption

Imaging

Medical Uses - non invasive, mobility aid

WHAT ARE THE <u>REAL</u> PROBLEMS?

- **Emphasis switches from detection to generation: lack of convenient, low cost, solid-state power source.**
- **Cost & difficulty of producing conventional waveguides & other components.**

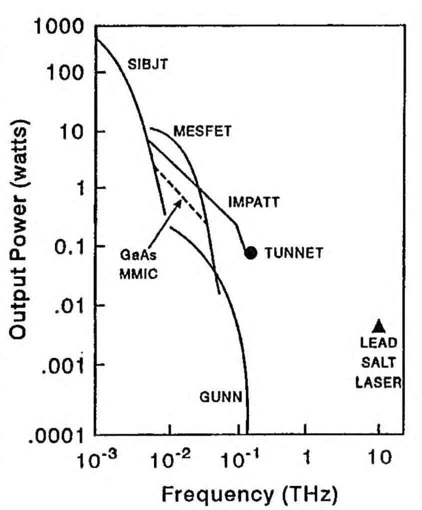

CONVENTIONAL (FUNDAMENTAL) SOLID STATE SOURCES (OMITTING DBRTD AND p-Ge LASER)

CONVENIENT SOURCES MUST BE INTEGRATED

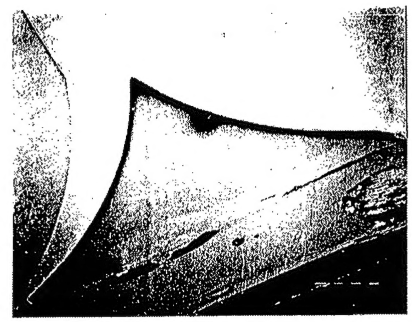

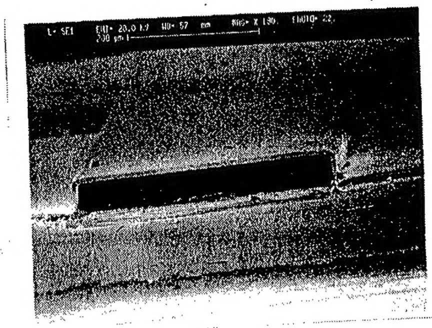

200 GHz Waveguide 600 GHz Waveguide

GENERAL DEVICE CHARACTERISTICS

ELECTRONIC SOURCES

Two types:-

- Transit time devices
  ("electronic devices" - e.g. FETs)

- Electron transition devices
  (e.g. diode lasers)

TERAHERTZ GENERATION

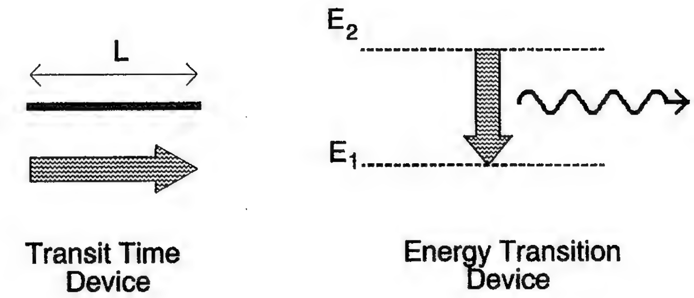

WHY TERAHERTZ GENERATION IS DIFFICULT

1) **Transit Time Devices:-**
For an f_T of 1 THz, device length < 0.01 μm
also power falls as $1/f^2$
⇒ quantum transport, DBRTD

2) **Lasers:-**
At 1 THz photon energy $hf \approx 4$ meV
thermal energy at room temp $kT \approx 25$ meV
⇒ separate energy levels in real and momentum space, intersubband laser

In Electronics - Two Kinds of Device

PASSIVE DEVICES	ACTIVE DEVICES
(Power Dissipated)	(Power Added)
☞ *Wave Guide* ☞ *Schottky Diode* ☞ *Quantum Varactor Diode* ☞ *Resonant Tunnelling Diode*	☞ *Gunn Diode* ☞ *Impatt Diode* ☞ *Resonant Tunnelling Diode* ☞ *HEMT (High Electron Mobility Transistor)* ☞ *HBT(Heterojunction Bipolar Transistor)* ☞ *Superconducting Josephson Junction*
Signal transmission Signal processing e.g. frequency conversion, mixing	Used to generate power i.e. sources

High Frequency Figures of Merit

CUT-OFF FREQUENCY f_T:-

(i) **Passive Device**
Frequency where function of the device becomes swamped by the parasitics

(ii) **Active Device**
Frequency where the short circuit current gain becomes < 1.

MAXIMUM FREQUENCY OF OSCILLATION f_{max}:-

Frequency where the power gain becomes < 1

CUT-OFF FREQUENCY

For a carrier velocity v and device length L then the limiting or cut-off frequency f_T is such that the phase change of the applied signal as an electron transits the device is small i.e.

$$2\pi f_T \tau = 2\pi L/v \leq 1$$

or

$$f_T \leq v/2\pi L$$

GENERAL CONSIDERATIONS

a) Transit Time Devices

Frequency of operation determined by the time τ taken for current carriers (usually electrons) to transit the device.

e.g. the drift region of a Gunn or Impatt

under the gate of a FET

across the base region of a bipolar transistor

For high frequency operation we need:-

short length devices
fast carriers - saturation velocity v_S

but

maximum voltage V_m across a device of length L is

$$V_m = E_B \times L$$

E_B is the breakdown field - depends on the material and the doping level.

Multiplying $V_m = E_B \times L$ and $f_T = v_S/2\pi L$

$$V_M f_T = v_S E_B/2\pi$$

The power P delivered to a load resistance R is given by

$$P = V_M^2/R$$

which can then be written as

$$P = 1/R(v_S E_B/2\pi f_T)^2$$

i.e. $$P \propto 1/f_T^2$$

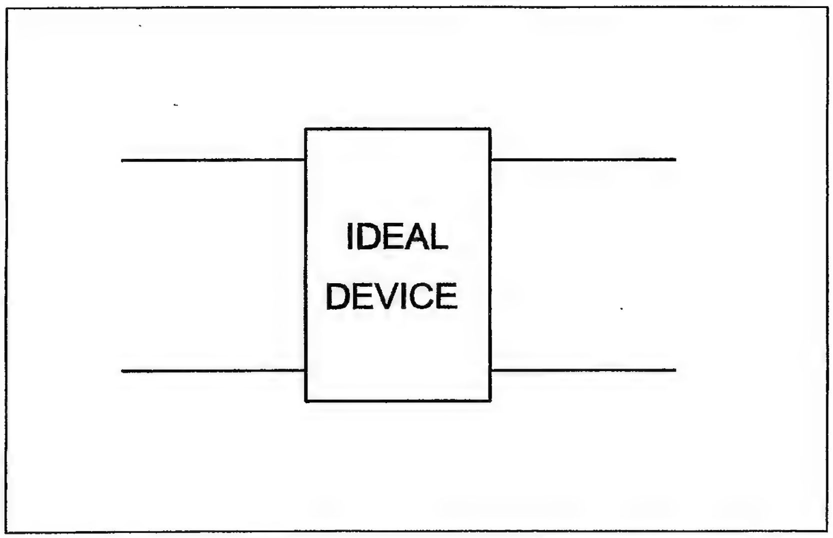

GENERAL CONSIDERATIONS (b)

- Devices are not "ideal"
- there are always parasitic elements
- these become particularly important at high frequencies

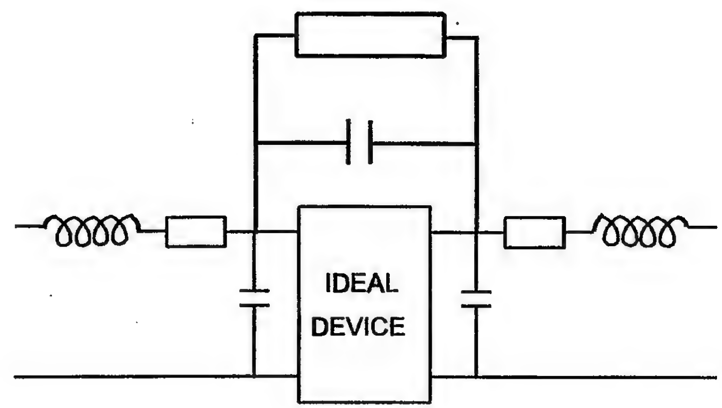

In Electronics - Two Kinds of Device

PASSIVE DEVICES	ACTIVE DEVICES
(Power Dissipated)	(Power Added)
☞ *Wave Guide* ☞ *Schottky Diode* ☞ *Quantum Varactor Diode* ☞ *Resonant Tunnelling Diode*	☞ *Gunn Diode* ☞ *Impatt Diode* ☞ *Resonant Tunnelling Diode* ☞ *HEMT (High Electron Mobility Transistor)* ☞ *HBT(Heterojunction Bipolar Transistor)* ☞ *Superconducting Josephson Junction*
Signal transmission Signal processing e.g. frequency conversion, mixing	Used to generate power i.e. sources

GUNN DIODES

- **Utilises the current-voltage characteristic of the 3-5 semiconductors.**
- **Useful millimetre wave source - particularly InP ~ 100 GHz.**
- **Frequency multiplication to THz range**

FUNDAMENTAL SOURCES - GUNN AND IMPATTS.

GUNN DIODES

Materials must exhibit the transferred electron effect

GaAs
InP
Si won't work

can be used as harmonic oscillators

NEGATIVE DIFFERENTIAL CONDUCTANCE I/V CHARACTERISTIC

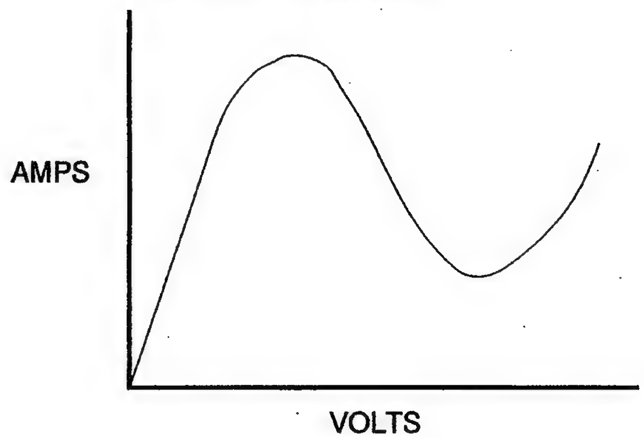

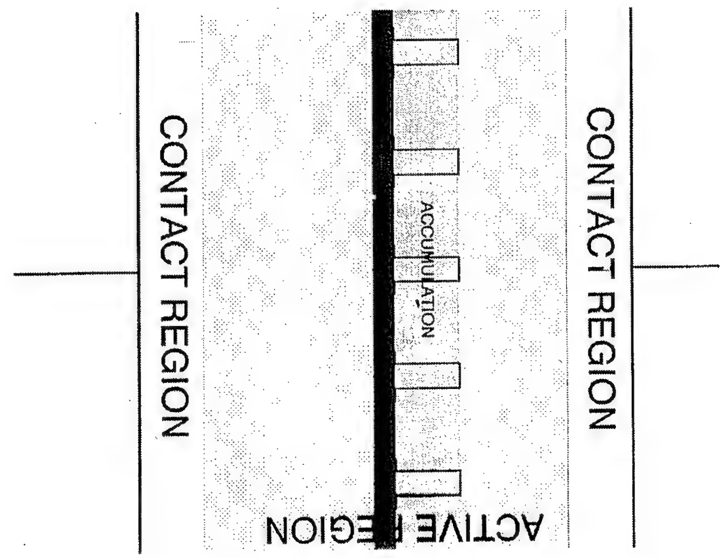

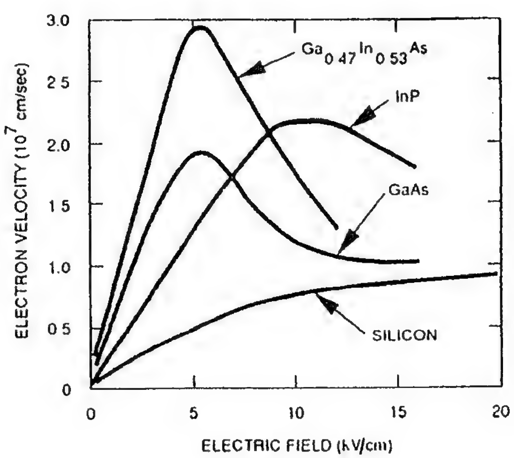

Velocity-Field characteristics of $Ga_{0.47}In_{0.53}As$, InP and Si.

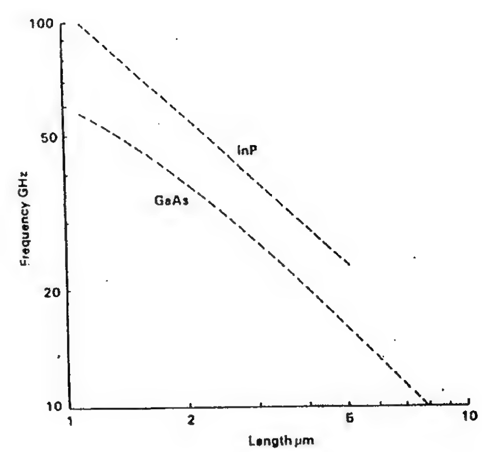

The frequency of optimum operation as a function of length for GaAs and InP TEOs

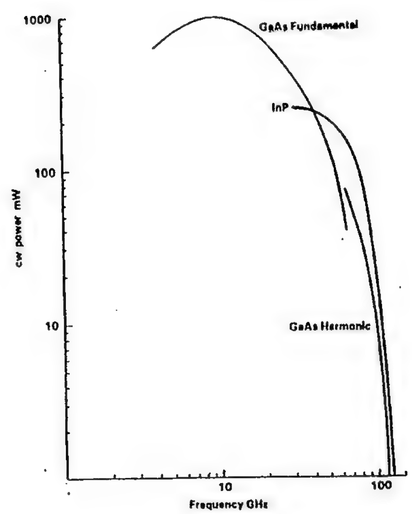

The CW power of TEOs

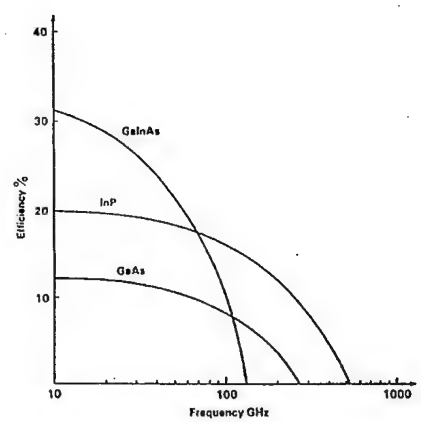

The predicted efficiency of TEOs

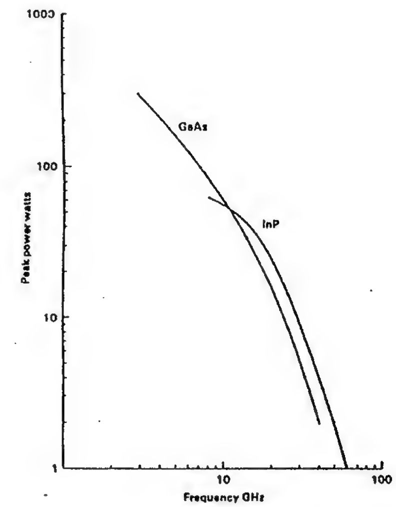

The pulsed power of TEOs

IMPATT (Impact Avalanche Transit Time) Diodes

Avalanche breakdown occurs in a high field region at one end during peak of applied voltage

Charge produced travels along a drift region to produce a current that is out of phase with the applied voltage

Result - negative resistance

Length of drift region determines the frequency

Can be made in Si and GaAs

IMPATT DIODE

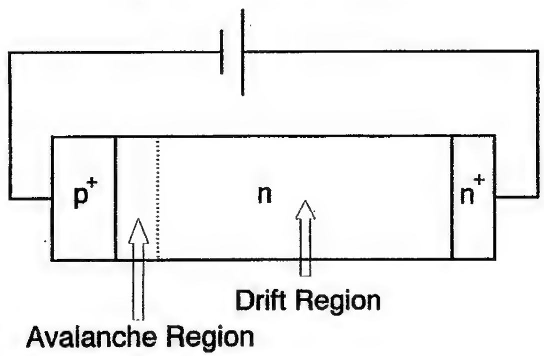

FUNDAMENTAL SOURCES - HEMTS AND HBTS

THE POWER OF IMPATT DIODES

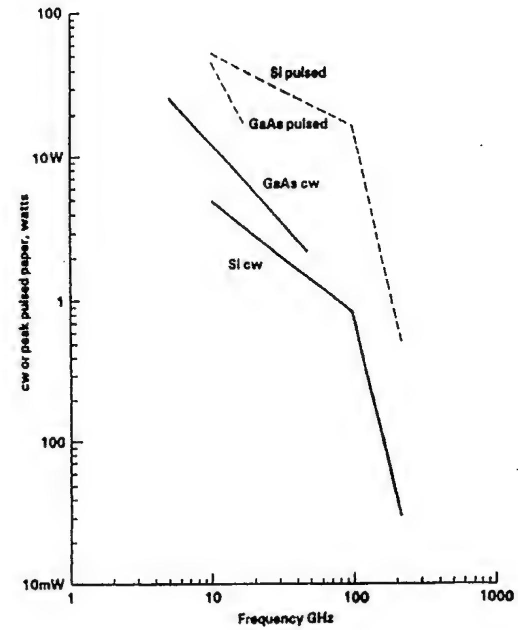

BASIC HEMT STRUCTURE

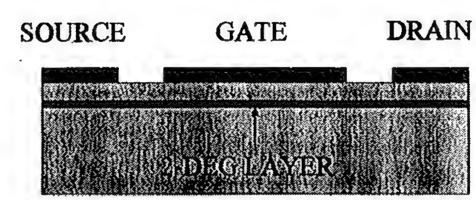

HEMT Conduction Band

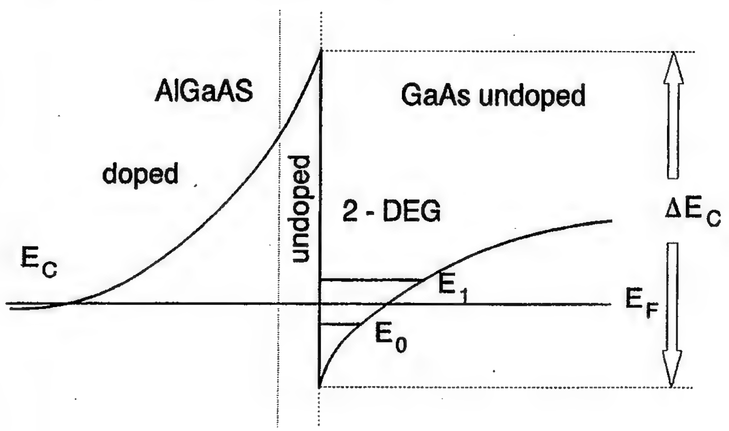

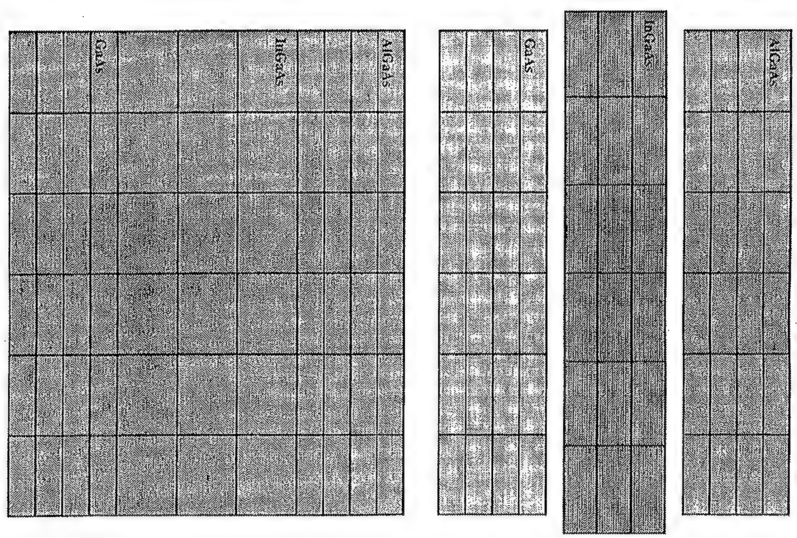

PHEMT CRYSTAL STRUCTURE

PSEUDOMORPHIC HEMTs

Superior transport properties and narrow band gap of InGaAs

Included as a non lattice matched 2-D electron channel.

GaAs based PHEMT InGaAs/AlGaAs narrow gap/wide gap

InP based PHEMT GaInAs/AlInAs narrow gap/wide gap

ADVANTAGES

- ☺ **Larger ΔE_C giving better carrier confinement**
- ☺ **Higher mobility - reduces parasitics**
- ☺ **Higher peak velocity - higher f_T and g_m**

HEMT Intrinsic Device

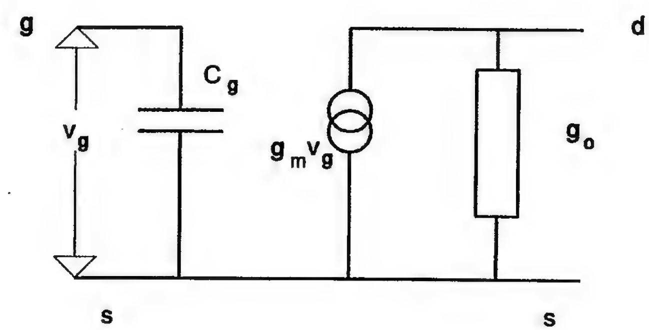

HEMT

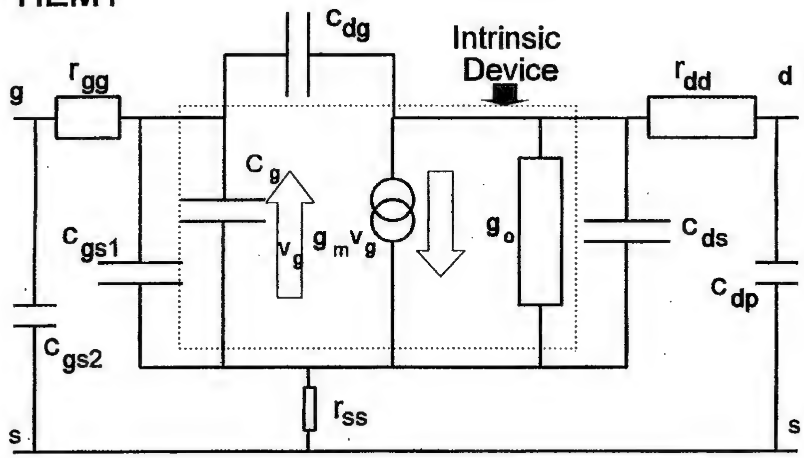

TYPICAL VALUES FOR PSEUDOMORPHIC HEMT EQUIVALENT CIRCUIT ELEMENTS

0.15 micron gate length **50 micron gate width**

g_m = **100 mS** c_g = **66 fF** c_{dg} = **7fF**

g_0 = **10 mS**

c_{21} = **100 fF (relates imaginary part of output current to input voltage)**

r_{ss} = **2 Ω** r_{gg} = **4 Ω**

f_T = **241 GHz** f_{MAX} **reduced from 537 GHz to 408 GHz by parasitics**

HEMT

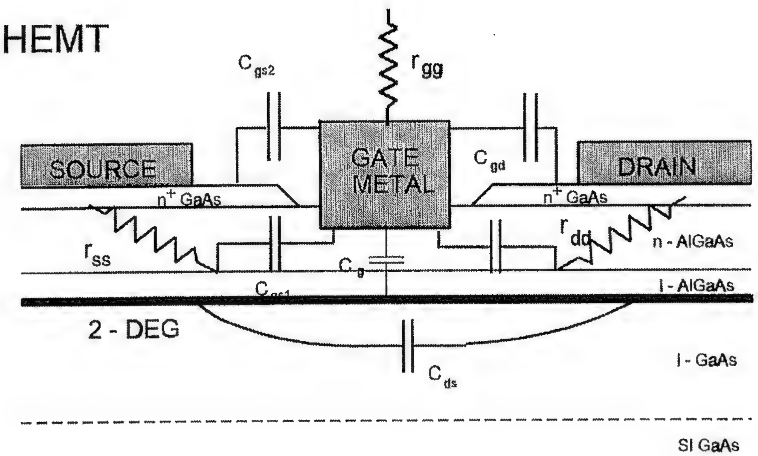

Dimensional Scaling in HEMTS

To maintain an acceptable geometry for the electric field under the gate and hence charge control in the channel

$$L_G \approx 5 L_C$$

i.e. an aspect ratio of 5

For 0.05 μm device, $L_C \approx$ 100Å

Can make the channel sensitive to surface processing.

Distributed Effects

As wavelengths become comparable to the lateral dimensions of the device distributed effects become important

e.g. In a HEMT the voltage can vary significantly across the gate WIDTH. This limits the finger size so devices must become multifingered

Heterojunction Energy Band Diagram

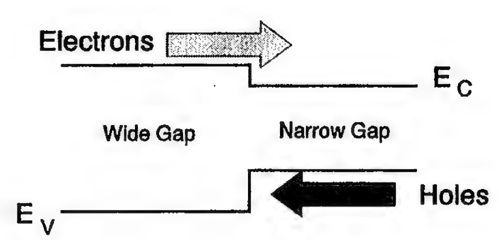

HEMT PERFORMANCE

- 0.05 micron InP based devices
- f_T ~ 300 - 350 GHz
- f_{MAX} ~ 255 GHz (*target 800 GHz*)
- 10 μW 155 GHz, 2 μW 213 GHz (Gate width = 10 micron)

npn HBT Energy Band Diagram

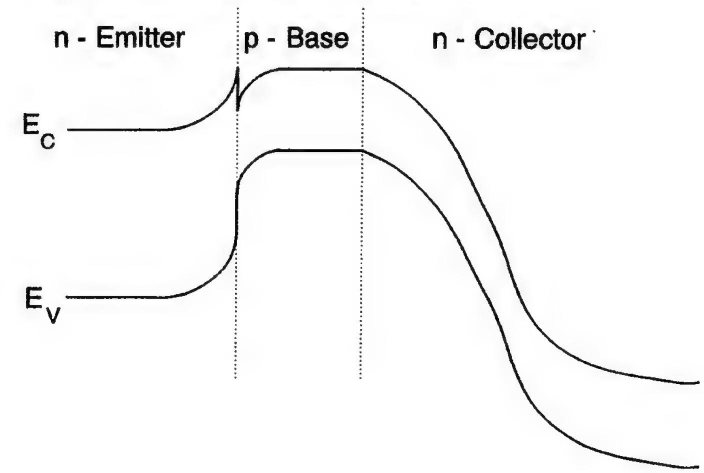

FUNDAMENTAL SOURCES

- DOUBLE BARRIER RESONANT TUNNEL DIODE (DBRTD)

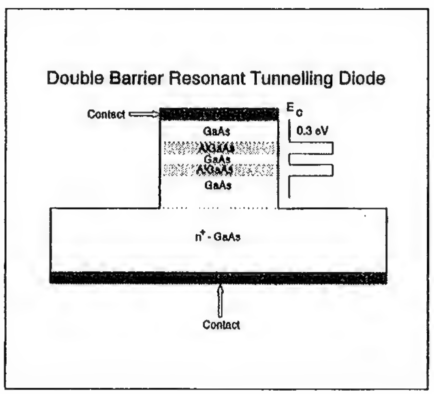

DBRTD

- "Fastest electronic device": operates to 712 GHz
- Realised in : GaAs/AlGaAs, InAs/AlSb ....
- Characteristics can be "tailored": mixer, multiplier etc
- Weak device, but power-combining and integration possible
- Operation frequency is <u>not</u> determined "geometrically"
- Building-block for other analogue and digital devices

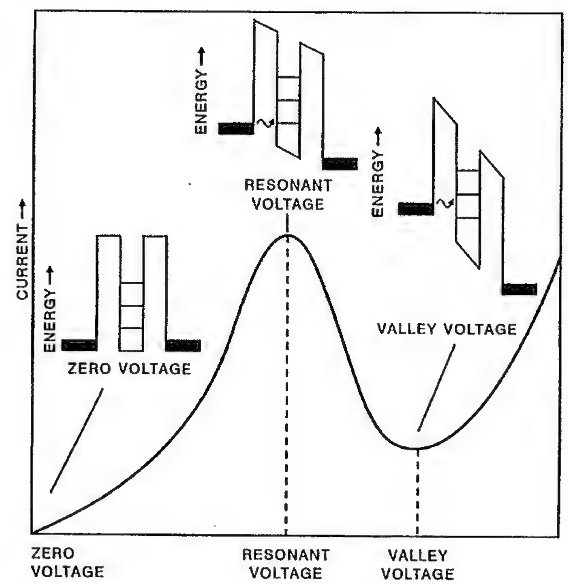

DBRTD PHYSICS - KEY POINTS (1)

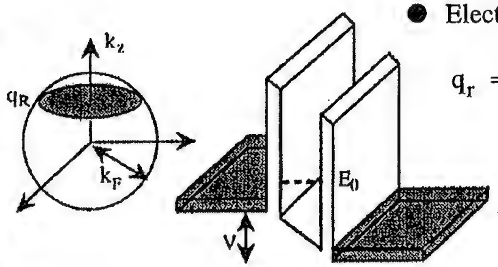

- Energy and momentum parallel to barrier are conserved
- Electrons in emitter have $k_z = q_r$;

$$q_r = \frac{1}{\hbar}\sqrt{\left[2m^*\ (E_o - E_c)\right]}$$

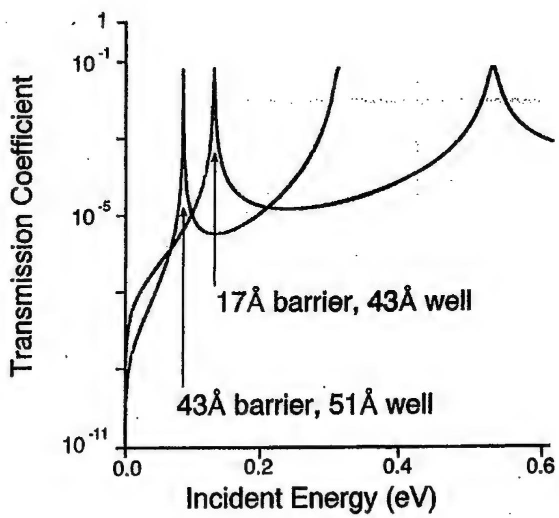

DBRTD PHYSICS - KEY POINTS (2)

- Global Coherent Tunnelling: electron phase coherence unbroken
- Transfer matrix calculation for transmission coefficient of single and double barrier
- Eventually obtain Breit-Wigner transmission

$$T_{tot} \propto \Gamma^2 / [\Gamma^2 + (E_z^2 - E_o^2)]$$

DBRTD PHYSICS - KEY POINTS (3)

- From T_{tot}, calculate device current

$$J = \int T_{tot}(E_z)\, S(E_z)\, dE_z$$

- $S(E_z)$ is *supply function*, involves: emitter and collector Fermi levels Temperature, m^* etc.
- Fold-in effects of electronic charge on potential profile.

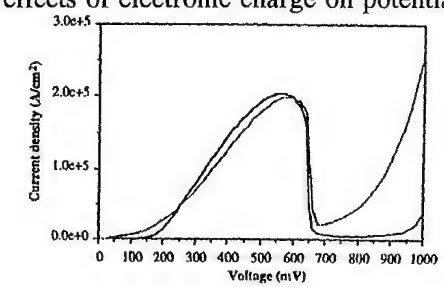

GROWTH BY MBE

- Molecular beam epitaxy is key technique
- Interface quality of supreme importance (3Å or less steps)
- Technique delivers required layer properties
- Reproduceability of devices (>5%) essential - limit to industrial application?

LAYER STRUCTURE FOR NU-366

0.4μm, GaAs (2^*10^{18})
17Å, GaAs (U.D.)
17Å, AlAs (U.D.)
43Å, GaAs (U.D.)
17Å, AlAs (U.D.)
17Å, GaAs (U.D.)
1500Å, GaAs (5^*10^{16})
2μm, GaAs (2^*10^{18})
GaAs (N^+)

DBRTD CHARACTERISTICS

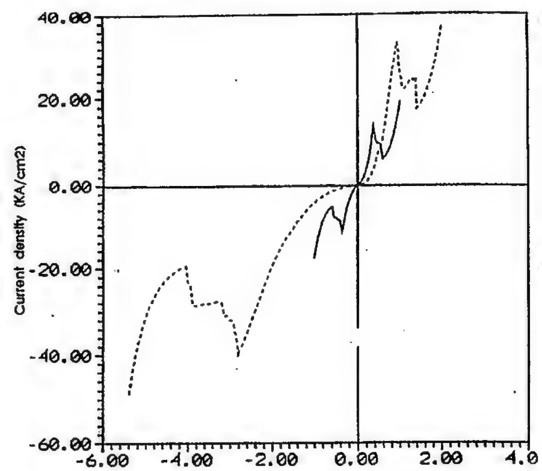

- *Anti symmetric*

  for harmonic multipliers (suppress even harmonics and subharmonic mixers ($f_{IF} = f_{sig} \pm 2f_{LO}$)
- *Asymmetric*

  for SOMS, Oscillators

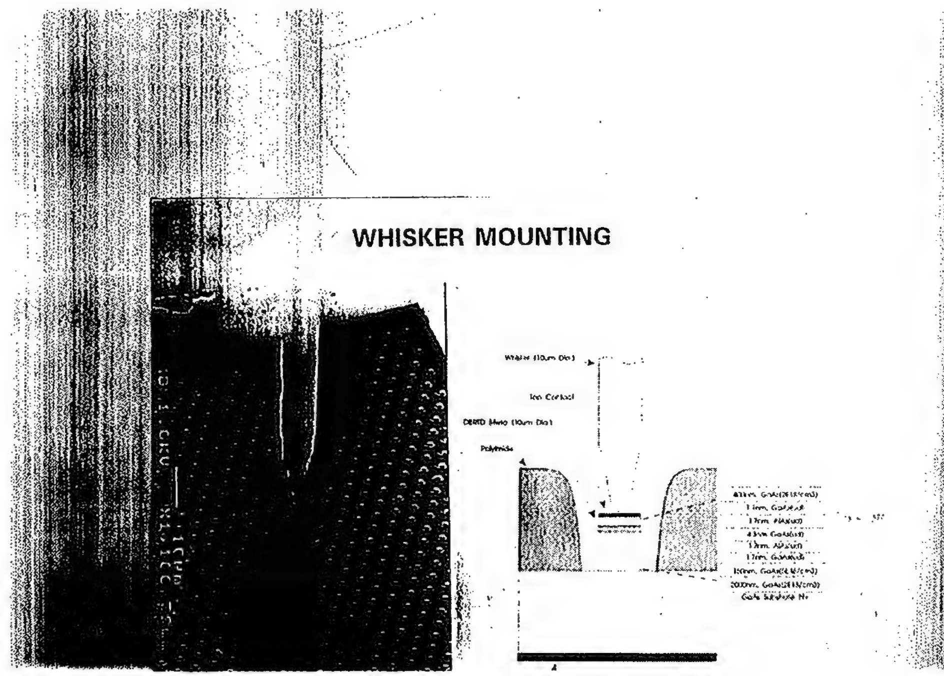

Output of a single 10um diameter whiskered device

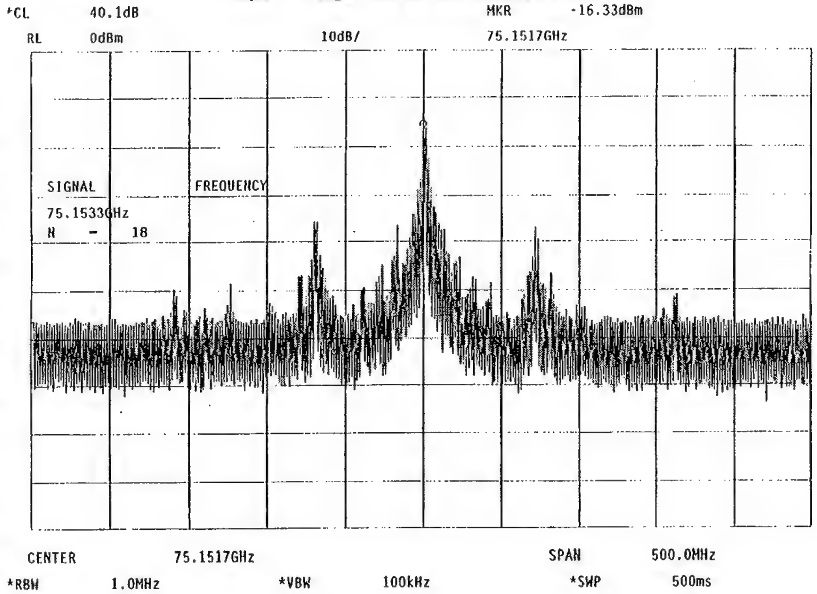

VIDEO OF FREE-SPACE TRANSMISSION

OSCILLATOR PERFORMANCE LANDMARKS

- 2GHz 20 mW GaInAs/AlAs (50% conversion)
- 90 GHz 60μw GaAs/AlAs
- 420 GHz 0.2μw GaAs/AlAs
- 712 GHz 0.3μw InAs/AlSb

POWER VERSUS FREQUENCY FOR DBRTD

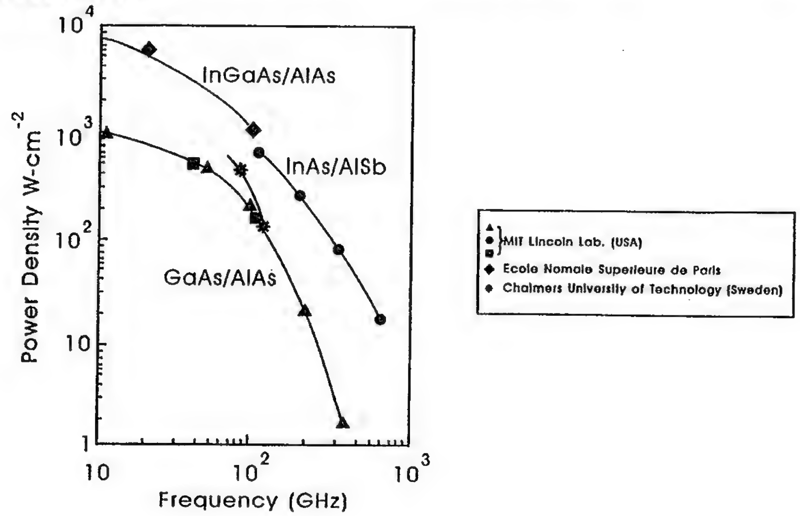

DBRTD FREQUENCY LIMITS

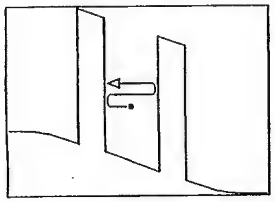

- Intrinsic lifetime $\tau_i = \hbar/\Gamma$ $\approx$ 100fs (10Thz)

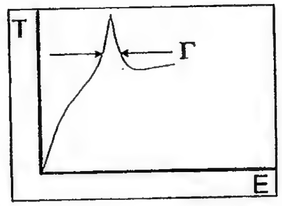

- Depletion region transit time, τ_d $= d/v \approx 10^{-7}/10^5 \approx$ 1ps (1THz)
- "RC" time, τ_{RC} $\approx C\sqrt{\{R.R_s\}}$ $\approx$ 2ps (0.5 THz)

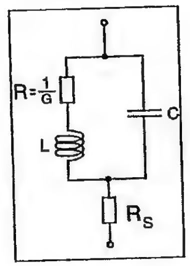

POWER FROM A DBRTD

- Sophisticated large-signal analysis possible
- Small signal approximation

$$P \approx \frac{3}{16}\,\Delta I.\Delta V$$

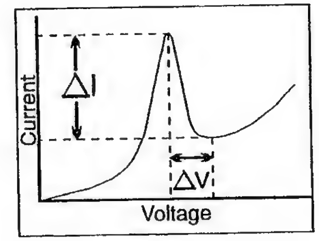

- Increase ΔV with depletion region before collector *(trade: C versus R_s)*
- Increase ΔI with thin barrier *(trade: heating problems)*

MORE POWER FROM A DBRTD (1)

- Individual design: thin barrier, correct depletion length, area, well-width

  [GaAs/AlAs: R_s <5Ω; C <100fF; J >10kAcm^{-2}; A <20 (μm)^2]

- Best material: contact resistance, peak/valley

  [GaInAs/AlAs; InAs/AlSb]

- New design concepts: Schottky collector DBRTD; triple barrier DBRTD; integrated DBRTD and FET

MORE POWER FROM A DBRTD (2)

- Enclosure in quasi-optic cavity (50μw @ 200 GHz: GaInAs/AlAs device: Brown, 1993)
- Series - (Boric-Lubecke, 1995) and Parallel - connected DBRTDs (Stephan, 1992); Synchronisation problems, perhaps RF excitation.
- Whisker and planar-mounted waveguide combining proof-of-principle demonstrated (Steenson, 1994: 12.6μw versus 2.6μw @ 120 GHz)

DBRTD POWER-COMBINING VIDEO

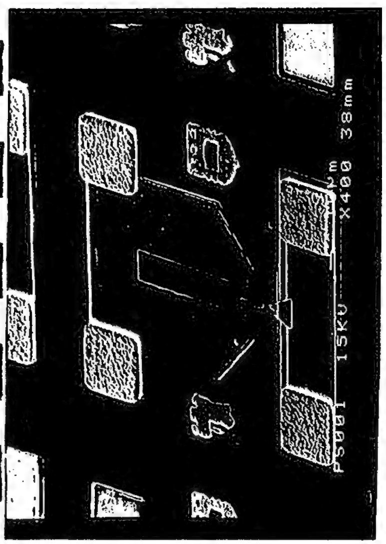

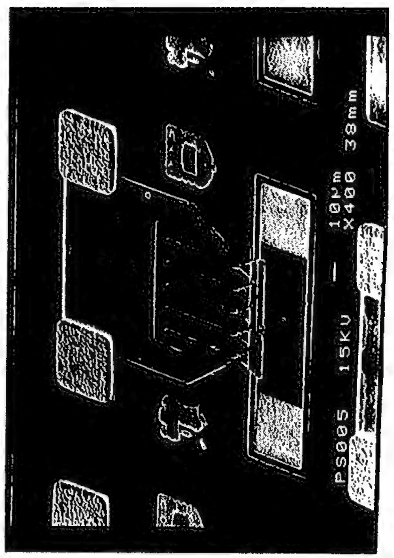

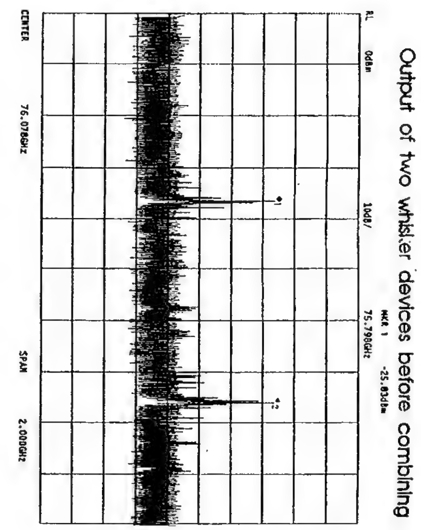

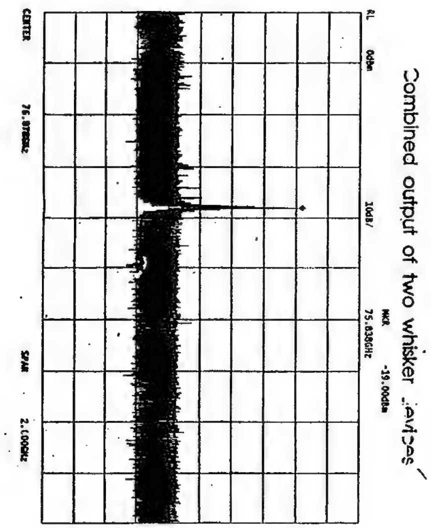

The Resonant Interband Tunnel Diode (RIT)

- RITs have been made of broken bandgap materials (InAs/GaSb), InGaAs/AlInAs double QWs in *pn* structure, GaAs/AlAs QW in *pn* structure....
- Large Peak-to-valley ratio exhibited (>100 at room temperature (Day et al., J Appl Phys., **73** 1993; InGaAs/AlInAs device) and high current densities ($>10^5$ Acm^{-2})
- Subtle differences between IV for RTD and RIT arising from different transport mechanisms.
- Much greater device capacitance (10x for similar size device)
- Device characterisation to 35 GHZ; no useful oscillation reported.

FUNDAMENTAL SOURCES INTERSUBBAND LASERS

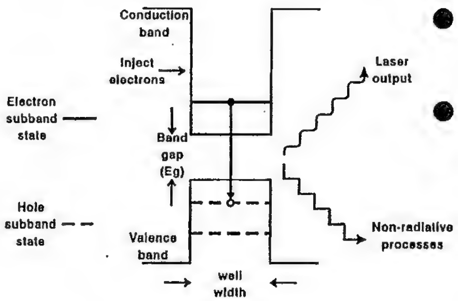

- Bipolar laser unsatisfactory at Terahertz (PbSnTe@10THz)
- Solution may be to use device relying on inter-subband emission:

  (a) hot hole p-Ge laser (Wenckebach)

  (b) Redesigned "Capasso" laser in III-V conductor band. (Harrison)

  (c) hole emission in III-V valence band

REDESIGNED "CAPASSO" LASER FOR TERAHERTZ?

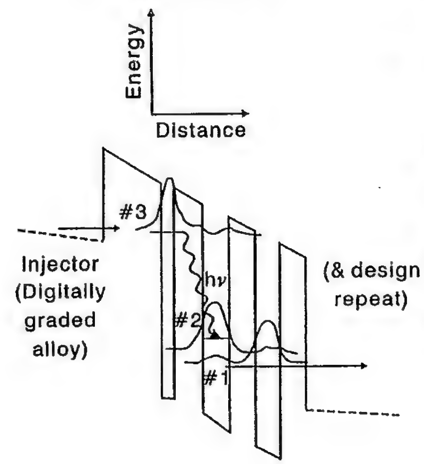

- Laser realised in well-controlled material system.
- Subtle well-width design to ensure inversion
- Bonus of $\hbar\omega < \hbar\omega_{LO}$
- More experimental information required

HOT HOLE P-Ge LASER

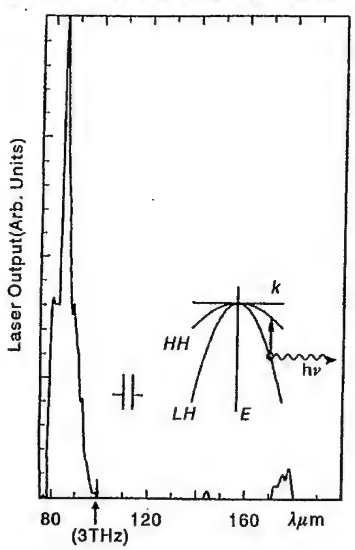

- Population inversion from different hole dynamics of light and heavy holes in crossed **E** and **B**.
- 10mW output at 5K with 100W pump.
- "Difficult" device; cryogenic operation.

THz HOT HOLE LASER IN P-GaAs/AlGaAs?

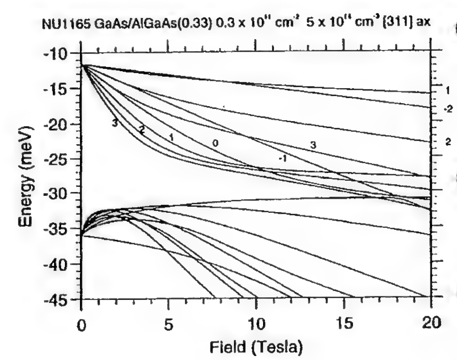

- Hole systems offer great flexibility - "any mass or τ you like"
- Parallel Landau levels implies high joint DOS
- Selection-rule breakdown assists output of energy.

FUNDAMENTAL SOURCES

Josephson Oscillators

- Superconducting/normal/superconducting junctions
- Resistively shunted junction, biased at voltage V, oscillates at:

$\nu = V/\Phi_0$: $\Phi_0 = h/2e$

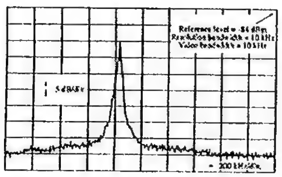

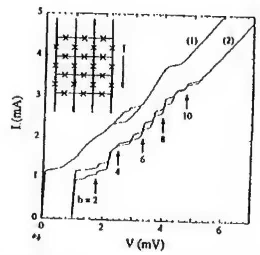

88 GHz output; 13KHz linewidth;
10x10 array of 4μm Nb/Al-AlO/Nb junctions at 4K

FREQUENCY-MULTIPLIED SOURCES - SCHOTTKY DIODES

Josephson Oscillators

- Phase locked array fabrication possible: power $\propto$ N; linewidth $\propto$ 1/N
- High T_c devices reported.
- *Performance figures:*
  Tens of μW at approx. 500GHz - dumped into on-chip resistor [Han, 1994]
  1μW at 110GHz from array - free space propagation [Martens et al, 1993]
  0.36μW at 190 GHz from array-free space propagation [Wengler 1995]
- Although ability to drive mixer has been demonstrated, more promising applications may be digital.

SCHOTTKY DIODE

- Traditional device for THz operation
- Barrier formed at metal/semiconductor function provides desired non-linear characteristic (I-V, C-V)
- Resistive or reactive multiplication possible
- For ideal resistive multiplier, $\eta = n^{-2}$; more complex statement for reactive multiplier; in practice mixed-mode operation
- η in reality dependent on embedding impedances, pump power, I-V and C-V characteristics
- Often run "back-to-back": antisymmetric I-V, symmetric C-V; odd harmonics only.

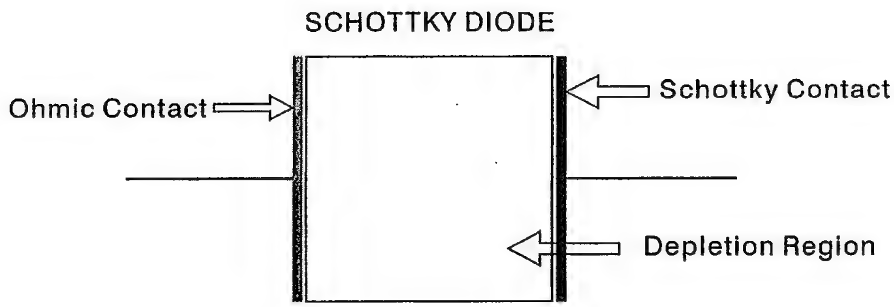

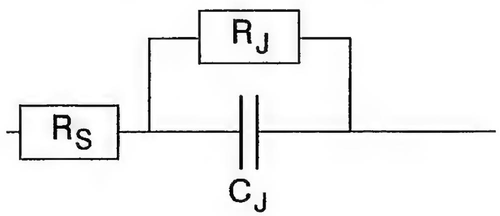

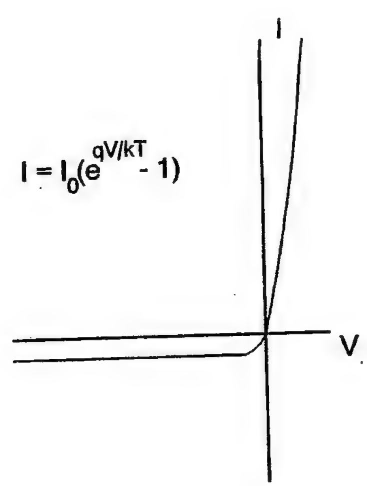

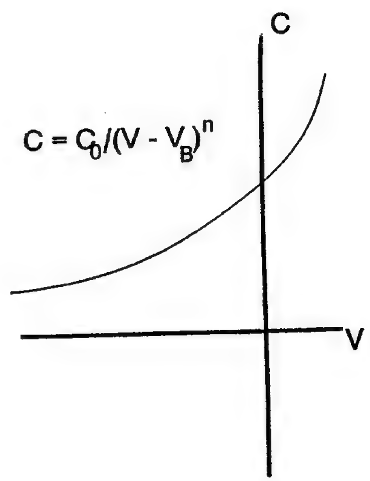

SCHOTTKY DIODE

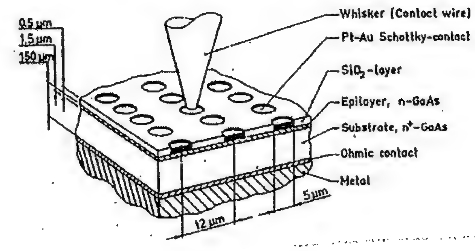

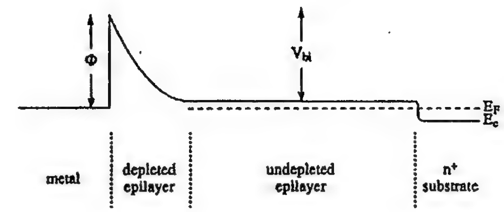

- Diameter ~ 5 μm
- Capacitance at zero bias ~ 20 fF
- DC series resistance ~ 10Ω
- Capacitance swing ~ 2-3
- Breakdown voltage ~ 15V
- Built-in voltage ~ 1V
- γ (doping profile parameter) ~ 0.4
- Depletion region width ~ 2-5 μm

SCHOTTKY DIODE AS NON-LINEAR DEVICE

$$I = I_o(e^{\frac{qV}{kT}} - 1) \quad = \quad 1 + \frac{qV}{kT} + \frac{1}{2!}\left(\frac{qV}{kT}\right)^2 \cdots \quad - 1$$

$$V = V_o \sin\omega t$$

V^2 terms will give 2nd harmonic ($2\omega t$)

V^3 terms will give 3rd harmonic ($3\omega t$)

PLANAR-SCHOTTKY MULTIPLIERS

- More robust than Whisker - contact
- Planar technology appropriate to integration
- Reduce finger-capacitance (size) and pad-pad capacitance with channels, etch-stop layer (lower ϵ) or substrate removal (flip-clip mounting)

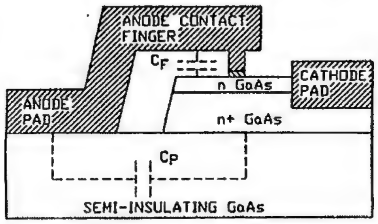

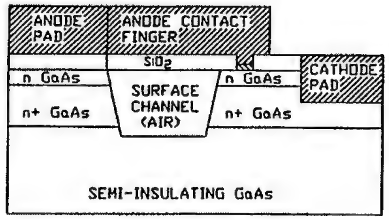

OPTIMISATION OF LAYER DESIGN FOR THz OPERATION (2)

- Idea of a "front" between depleted and undepleted regions
- "Front" speed limited by V_{sat} ($\sim 2 \times 10^5$ ms^{-1} in GaAs)
- Start with $t_{epi} \sim V_{sat} / 2f_{pump}$
- Try to maker $t_{epi} \approx W$ (depletion length) at most negative applied voltage
- Then choose doping density <u>just</u> to avoid breakdown (V_{Br})

  [$V_{Br} \propto (N_{epi})^{-3/4}$; $W \propto (V_{Bi} + V_{Br} / N)^{1/2}$]
- Then choose anode size to get capacitance right

e.g [$N_{epi} = 2.3 \times 10^{17}$ cm^{-3}; $t_{epi} = 0.24\ \mu m$; Diam $= 2.1\ \mu m$; $R_s = 8.5\Omega$; $C(o) = 3.9fF$]

OPTIMISATION OF LAYER-DESIGN FOR THz OPERATION (1)

At terahertz frequencies, new effects <u>may</u> be important:

(1) Similarity in size of anode radius, epilayer thickness, depletion thickness.

(2) Effects related to plasma resonances (in epilayer)

(3) Effects related to electron velocity saturation

NOTE: (1) leads to "edge" effects - new terms in equivalent circuit
(2) can be minimised with care
(3) probably represents limiting factor to performance.

SCHOTTKY MULTIPLIER PERFORMANCE FIGURES

<u>Doublers:</u> 160 GHz input; 4mW 320 GHz output; efficiency ~ 20% [Erickson 1990]

<u>Triplers:</u> 160 GHz input; 0.7mW 480 GHz output; efficiency ~ 5% [Erickson 1990]

<u>Planar device:</u> 220 GHz Tripler output of 0.7 mW; efficiency ~ 7% [Choudhury et al 1995]

<u>Record</u> (?):	250 μW at 800 GHz from tripler (3% efficient) [Crowe et al, 1996]

FREQUENCY - MULTIPLIED SOURCES
- QUANTUM BARRIER VARACTORS AND DBRTDs

THE QBV: A LITTLE DEVICE PHYSICS

- Aim is to produce good capacitance swing: analysis indicates best multiplication for $C_{max}/C_{min} \sim 2$-3
- Also aim to minimise R_s and keep device current low.
- Barrier width increase ☞ bigger C_{max}; wider depletion regions ☞ smaller C_{min}
- Barrier doping increases C_{max}, but may increase current.
- Material Choice Considerations- barrier height (thermionic current), breakdown voltages.

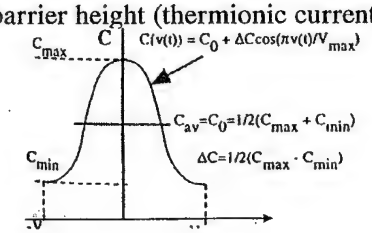

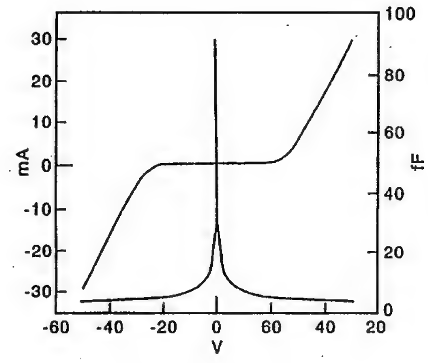

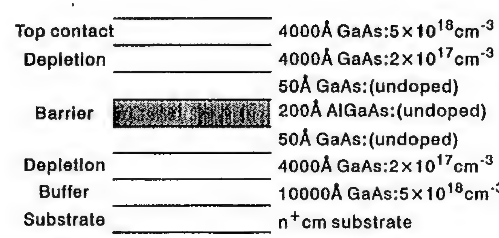

QBV

- Device with antisymmetric IV, symmetric CV
- Only odd harmonics generated: eg 5x, need only one idler.
- Device works with (AlGaAs) Barrier, prevents electrons passing.
- Depletion region at one side, voltage-dependent width ☞ CV
- Limiting factor to power-handling: avalanche breakdown.

THE STACKED QBV

- To obtain large cut-off frequency, need small C_{min} ~ small device, limited output power
- Concept of *stacked devices* to improve power handling and increase cut-off frequency.

eg Liu et al 1993: 3000 device array, 4x $20\mu m^2$, f_{co} =150GHz, output power of 1.25W at 99GHz

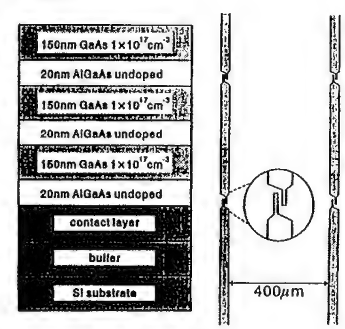

PERFORMANCE OF QUANTUM BARRIER VARACTOR DIODES (QBV)

FREQUENCY TRIPLING (x3)
≈ 1 mW AT 225 GHz, 5% conversion efficiency but down to 0.2% at 310 GHz (Rydberg et al 1990)

FREQUENCY QUINTUPLING (x5)
≈ 0.1 mW at 172 GHz, 0.78% conversion efficiency (Räisänen et al 1995)

☺ up to 20 mW and > 45% and 186 GHz *predicted* for "Stacked Heterostructure Varactors" in an optimised system.

CONCLUSIONS

QBVs As Multipliers

- Little activity now on this device: QBV (or VHV) probably better bet.
- Anti symmetric characteristics can be tailored for this application
- Most recent data appear to be for tripler at 257 GHz: efficiency ~ 1%, input power 30-40 mW (Chalmers Group)

TERAHERTZ SYSTEM REQUIREMENTS

For electronic systems we need:-

- **sources**
- **detectors**
- **multipliers**
- **mixers**
- **amplifiers**

SOURCES: Need ~ 1mW across the range
LO pump and free space transmission

HEMT: 800 GHz predicted but very low power.

DBRTD: lacking in power.

Inter-subband laser: could this save the day?

Gunns and multiplication. Best bet?

MULTIPLIERS:

QBV looks good
- especially stacked

DETECTORS:

Schottky Diodes - OK

Single and Double Barrier Diodes
Not yet proven but probably OK

MIXERS:

Schottky diodes

DBRTD

QBV

all with multiplied Gunn LO

AMPLIFIERS:

HEMTS up to 800 GHz?

DBRTD reflection amplifiers - low power?

INTER-SUBBAND LASER amplifiers?

Mixers and Multipliers

by

N J Cronin

School of Physics
University of Bath
UK

MICROWAVE MIXERS

BASIC PRINCIPLES

The function of a mixer is to reduce the frequency of a signal by beating (or mixing) it with a second locally generated signal from a Local Oscillator (L.O.).

Mixing takes place in a non-linear device — any non-linearity will do in principle e.g. consider a square law device. i.e. one in which

$$I = \alpha V^2$$

Suppose that we apply a voltage given by:–

$$V = \underbrace{V_s \cos(\omega_s t)}_{\text{Signal}} + \underbrace{V_{LO} \cos(\omega_{LO} t)}_{\text{Local Oscillator}}$$

The resulting current in the device is:–

$$I = \alpha \left(V_s \cos(\omega_s t) + V_{LO} \cos(\omega_{LO} t) \right)^2$$

expanding this expression gives:–

$$I = \alpha \Big\{ V_s^2 + V_{LO}^2 + V_s^2 \cos(2\omega_s t) + V_{LO}^2 \cos(2\omega_{LO} t) + 2 V_s V_{LO} \cos[(\omega_s + \omega_{LO})t] + 2 V_s V_{LO} \cos[(\omega_s - \omega_{LO})t] \Big\} / 2$$

NOTE: The non-linearity of the device has produced currents at frequencies other than the two driving frequencies ω_s and ω_{LO}.

In particular the frequency $\omega_s - \omega_{LO}$ is called the intermediate frequency (I.F.) It is this component which is usually considered to be the output from the mixer.

A basic heterodyne downconverter using the mixer would be :-

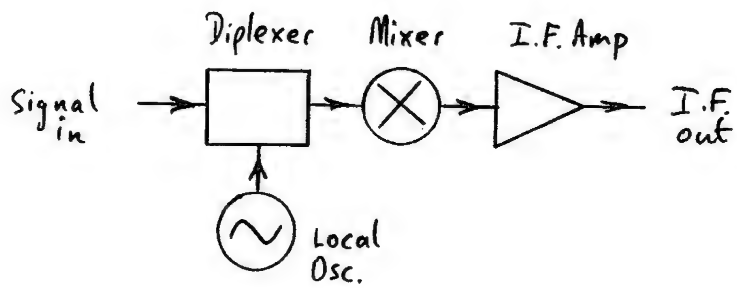

The diplexer is a device which overlays the signal and local oscillator before they enter the mixer. The I.F. amplifier amplifies only the I.F. rejecting all high frequency components such as $\cos(2\omega_s t)$ etc. as well as D.C. terms.

If the amplitude and phase of the L.O. are kept fixed then the I.F. output contains all the amplitude/phase information in the signal.

Mixer Noise Temperature and Conversion Loss

The two parameters used to characterise the performance of a mixer are the NOISE TEMPERATURE T_N and the CONVERSION LOSS L_o

If we consider a resistor at temperature T the available noise power per unit bandwidth at its terminals is given by :-

$$P_N = kT$$

Using this any component generating white noise can be assigned a temperature by dividing the noise power per unit bandwidth by Boltzmans Constant.

Consider now a noisy two-port device connected to a matched source and load :-

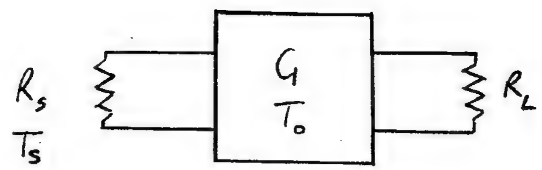

The noise per unit bandwidth delivered to the load R_L is the noise generated by R_s multiplied by the gain of the two port G plus the noise generated by the two port itself kT_o. Thus

$$P_L = k(GT_s + T_o)$$

The NOISE TEMPERATURE of the twoport is defined by reference to an equivalent NOISELESS two port :-

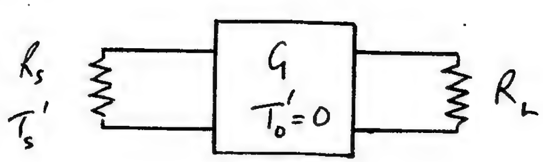

The power delivered to the load is now given by :-

$$P_L = kGT_s'$$

If this is the same as previously :-

$$GT_s' = GT_s + T_o$$

$$T_s' = T_s + \frac{T_o}{G}$$

The noise temperature of the two-port is defined as the increase in T_s required i.e.

$$T_N = \frac{T_o}{G} \qquad \text{——— (A)}$$

[Note: T_o may not be the physical temperature of the two port – it depends on the noise processes involved]

Noise Temperature of an Attenuator

If the two port is simply an attenuator then the total noise power into the load is given by $k[GT_s + T_{A_0}]$. However, an attenuator can be thought of as a network of resistors, which can be combined with R_s to give an equivalent resistance, still at temperature T_s (since there are no additional noise sources in an attenuator) Thus the power into the load is simply kT_s. Thus:-

$$kT_s = k[GT_s + T_{A_0}]$$

i.e.

$$T_{A_0} = T_s(1 - G)$$

From (A) above

$$T_{A_N} = \frac{T_{A_0}}{G}$$

Thus

$$T_{A_N} = T_s\left(\frac{1}{G} - 1\right)$$

or using $L = 1/G$ and $T_s = T$ in this case

$$T_{A_N} = T(L - 1)$$

e.g. at 290 K a 10 dB attenuator has a noise temperature given by $290(10 - 1) = \underline{\underline{2600\,K}}$

Returning to the simple mixer downconverter

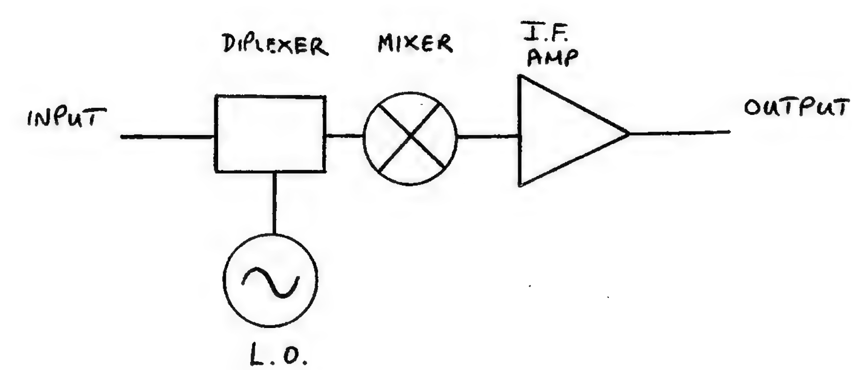

let f_{LO} = Local Oscillator frequency

f_{IF} = Centre frequency of the I.F. amp. passband

Δf = bandwidth of the I.F. amp.

There are two input bands which will produce beat frequencies with the L.O. which fall within the pass band of the I.F. Amplifier. These are called the signal and image sidebands

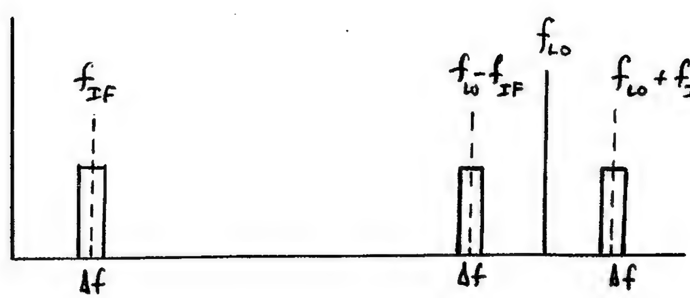

[which is the signal and which is the image depends on how the mixer is being used]

The fact that there are two input bands but only one output band complicates the definition of the noise temperature of this system — do we assign the noise generated in the mixer to one, or both, of the input sidebands?

Schematically :—

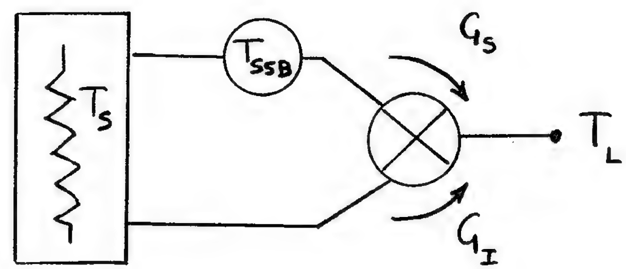

All mixer noise assigned to one side band

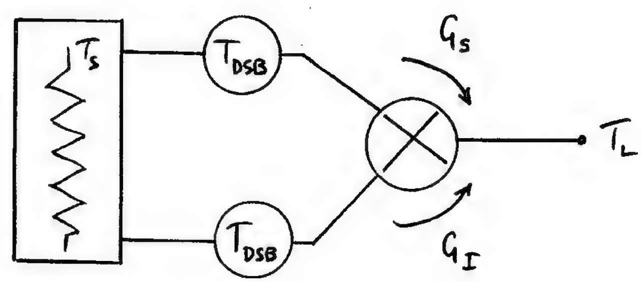

Mixer noise assigned to both sidebands

Clearly, since the actual noise generated by the mixer is the same in both cases, if $G_I = G_S$ then the double sideband mixer noise temperature is half the single sideband noise temperature.

In fact, most mixers exhibit loss rather than gain. This is called Conversion Loss and is given by

$$L_o = \frac{1}{G}$$

If we again consider a simple system:—

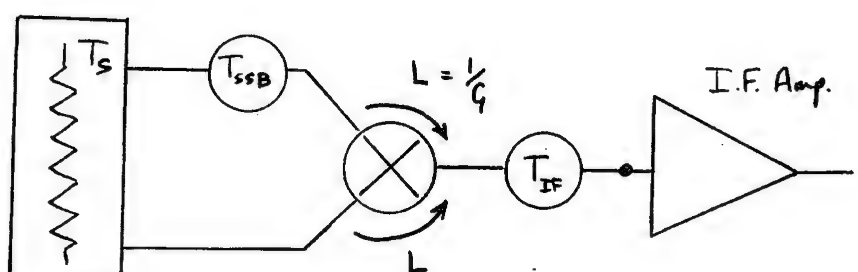

(using SSB Noise Temp.)

The noise power into the I.F. Amplifier is given by:—

$$P_N = k\left[(2T_S + T_{SSB})G + T_{I.F.}\right]$$

Subtracting the noise due to the source alone and dividing by Boltzmans Constant and the 'gain' of the mixer gives the single sideband noise temperature of the system:—

$$T_{sys,SSB} = \frac{k\left[(2T_s + T_{SSB})G + T_{IF}\right] - 2kT_sG}{kG}$$

or, in terms of the conversion loss:—

$$T_{sys,SSB} = T_{SSB} + L_o T_{I.F.}$$

Components following the I.F. amplifier have little effect since their noise contribution is divided by the large gain of the I.F. Amplifier

[Note, here I have included the loss of the diplexer in with that of the mixer — also I have assumed that there is no pre-amplifier between the source and the mixer — always the case at terahertz frequencies]

With these provisions we see that the system noise temperature is dominated by three factors :

- Mixer Noise Temperature
- Mixer Conversion Loss
- I.F. Amplifier Noise Temperature

QUESTION : Why is system noise temperature important.

Answer : Because it determines the minimum detectable power level in a given integration time.

In RADIOMETRY the signals are themselves noise and can be characterised by a temperature. The minimum detectable temperature by a system having noise temperature T_{sys} and bandwidth $\Delta\nu$ in an integration time τ is given by :-

$$T_{MIN} = \frac{T_{sys}}{\sqrt{\Delta\nu\,\tau}}$$ — The Radiometer Equation

i.e. if you double the system temperature it takes four times as long to get the same result.

DIODE MIXER THEORY

The analysis of a diode mixer proceeds in three phases:-

- The voltage and Current waveforms produced in the diode by the Local Oscillator are determined using non-linear circuit analysis
- Small signal analysis is then performed to obtain the mixer input and output impedances and the conversion loss.
- Down converted thermal and shot noise components produced in the diode are determined and the mixer noise temperature calculated.

Before proceeding we need to develop a few ideas concerning transmission lines and impedances:-

Transmission Lines

The parallel wire transmission line consists of two wires running parallel to each other with the spacing small compared to the wavelength.

If an oscillator is connected, as above, a wave will run along the line to the right.

If we now terminate the line in an impedance in general, there will be a reflected wave moving to the left:

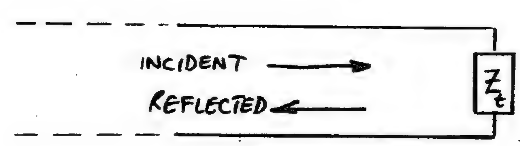

Every transmission line has a Characteristic Impedance, Z_o, if $Z_t = Z_o$ there is no reflected wave.

The transmission line is then said to be matched.

All prevailing conditions repeat every wavelength along the line. Thus if a line is an integer number of wavelength long the current, voltage and impedance are the same at both ends.

Thus, at a fixed frequency we can insert such a length of transmission line without any effect on a circuit.

As far as the termination is concerned the situation is :-

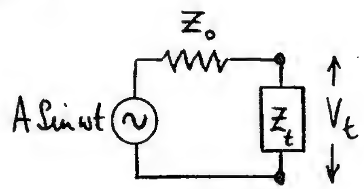

i.e. the transmission line looks like a source with output impedance Z_o

Note : if $Z_t = Z_o$ then $V_t = \dfrac{A \sin \omega t}{2}$

Thus, the voltage produced at the termination by a wave travelling to the right is half of that produced by the source.

Thus, if we know V_t and need an equivalent transmission line source we must use :-

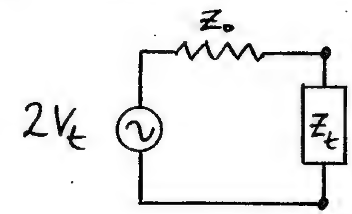

Equivalent circuit for the RIGHT travelling wave source

EMBEDDING IMPEDANCE

The operation of the mixer is dependant upon the electromagnetic environment in which the diode finds itself. For our purpose this is characterised by EMBEDDING IMPEDANCES.

These can be defined as follows:—

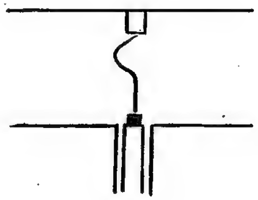

Actual Mixer

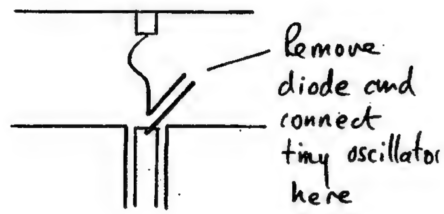

Imaginary Test set up

The tiny oscillator oscillates at the frequency of interest e.g. signal, L.O. etc.

The oscillator causes currents to flow into the terminals where the diode was located

If the applied voltage is $Ve^{j\omega t}$ and the resulting current is $Ie^{j\omega t}$, then the embedding impedance at frequency ω is:—

$$Z_e(\omega) = \frac{Ve^{j\omega t}}{Ie^{j\omega t}}$$

The value of $Z_e(\omega)$ depends upon the physical structure of the mixer e.g. whisker length, backshort position etc.

Embedding impedances may be determined by measurements on scale models, from equivalent circuit models or computer modelling of the electromagnetic fields (HFSS etc)

LARGE SIGNAL ANALYSIS

- determines the voltage and current waveforms produced at the diode by the Local Oscillator.

- A Harmonic Balance Technique

- Uses the Time Domain when considering the diode and the Frequency Domain when considering the embedding circuit.

Large Signal Equivalent Circuit :-

We need an equivalent circuit which represents the mixer at D.C, the local oscillator frequency and all of it's harmonics :-

D.C. :-

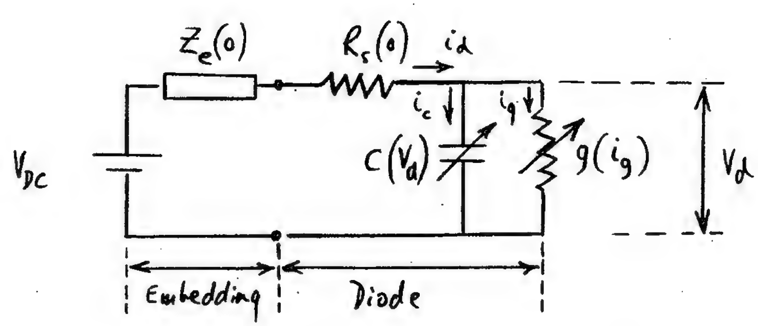

L.O. :-

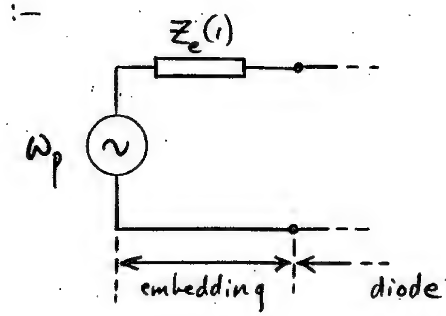

Harmonic $n\omega_p$:-

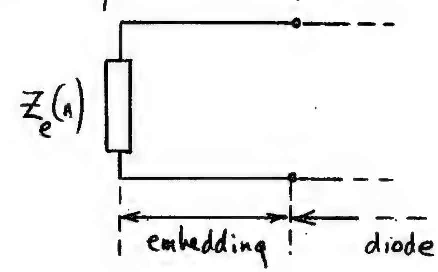

The first step is to express V_d and i_d as Fourier Series :-

1) $$v_d(t) = \sum_{n=0}^{\infty} V_{d_n} e^{jn\omega_p t}$$

2) $$i_d(t) = \sum_{n=0}^{\infty} I_{d_n} e^{jn\omega_p t}$$

From the equivalent circuits we can now derive the following constraints on V_{d_n} and I_{d_n} :-

3) $$\frac{V_{DC} - V_{d_0}}{I_{d_0}} = Z_e(0) + R_s(0) \qquad \text{D.C.}$$

4) $$\frac{V_{LO} - V_{d_1}}{I_{d_1}} = Z_e(1) + R_s(1) \qquad \text{L.O.}$$

5) $$\frac{-V_{d_n}}{I_{d_n}} = Z_e(n) + R_s(n) \qquad \text{Harmonic}$$

Once we have the correct solutions for $v_d(t)$ and $i_d(t)$ the Fourier components will satisfy these equations.

Multiple Reflections

In the method of Held and Kerr we now introduce an imaginary transmission line between the 'intrinsic' diode (diode

minus R_s - which is lumped in with the embedding network) and the embedding network.

This transmission line is an integer number of wavelength long at the L.O. frequency :-

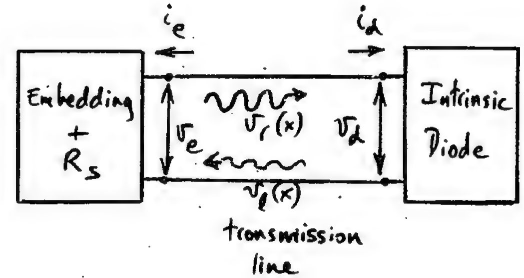

Let the characteristic impedance of this line be Z_0 (arbitrary)

In operation, at any instant, there will be waves, at all the harmonic frequencies, travelling in the left and right directions.

Because of the length of the line v_e and v_d should be equal at all the frequencies

The total voltage and current on the transmission line are given by:-

6) $$V(x) = V_r(x) + V_\ell(x)$$

7) $$i(x) = i_r(x) - i_\ell(x) = \frac{[V_r(x) - V_\ell(x)]}{Z_o}$$

Here x is a position coordinate along the line and the 'minus' comes from general transmission line theory.

Because the line is an integer number of wavelengths long

$$V(x=0) = V(x=\ell)$$

and $$i(x=0) = i(x=\ell)$$ (where ℓ = the length of the line)

We begin the calculation by assuming that at $t=0$ the diode is removed and replaced by a matched load Z_o which generates no reflected wave.

At $t=0$ the load is removed and replaced by the diode – we assume that the voltage on the diode is initially as it was with the load :-

D.C.

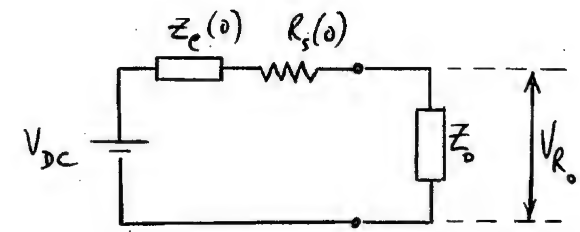

8) $$V_{R_o} = V_{DC} \frac{Z_o}{[Z_o + R_s(0) + Z_e(0)]}$$

L.O.

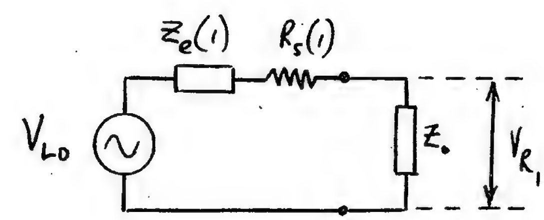

a) $$V_{R_1} = V_{LO} \frac{Z_0}{\left[Z_0 + R_s(1) + Z_e(1)\right]}$$

At $t=0$ these are the only voltages, therefore, the total voltage across the intrinsic diode is:—

$$v_d(t) = V_{R_0} + V_{R_1} e^{j\omega_p t}$$

After connection this voltage is applied across the diode by the transmission line, the equivalent circuit in the time domain is:—

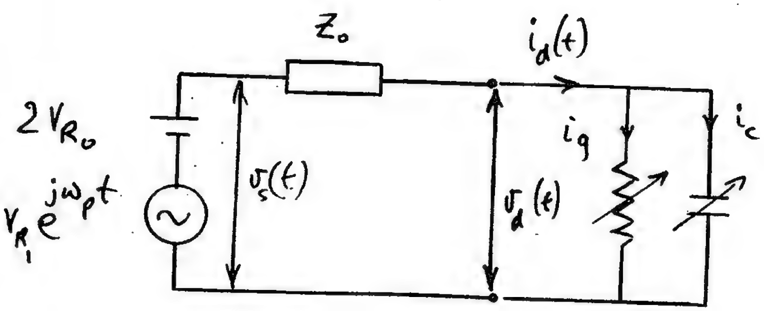

Note The factor of two described earlier

The state equation for this circuit is:—

$$C(t)\frac{dv_d}{dt} = \left[\frac{V_s - V_d}{Z_0} - i_g(t)\right] \quad (10$$

Using the diode characteristics this equation can be integrated numerically giving a first estimate of the diode voltage and current waveforms which will now include higher harmonics of the L.O. frequency.

These voltages now give rise to new left travelling waves on the transmission line. Solving (6) and (7) we can obtain the solutions for such waves from the currents and voltages at the end of the line:—

$$V_\ell(x=\ell) = \frac{v_d(t) - i_d(t)Z_0}{2} \quad (11$$

This can now be Fourier Analysed to yield an equivalent expression for each of the harmonics

12) $$V_{L_n} = \frac{V_{d_n} - I_{d_n} Z_0}{2} \qquad n = 0, 1, 2 \ldots$$

These waves now propagate to the LEFT where they encounter the corresponding Embedding Impedance in series with R_s. This results in reflections generating a new set of RIGHT travelling waves. The reflection coefficient ρ_n For each of the harmonics is given by:—

13) $$\rho_n = \frac{Z_e(n) + R_s(n) - Z_0}{Z_e(n) + R_s(n) + Z_0}$$

[$\rho_n = \dfrac{Z_t - Z_0}{Z_t + Z_0}$, Z_t = terminating impedance]

The new equivalent circuit for the time domain solution at the diode end now becomes:—

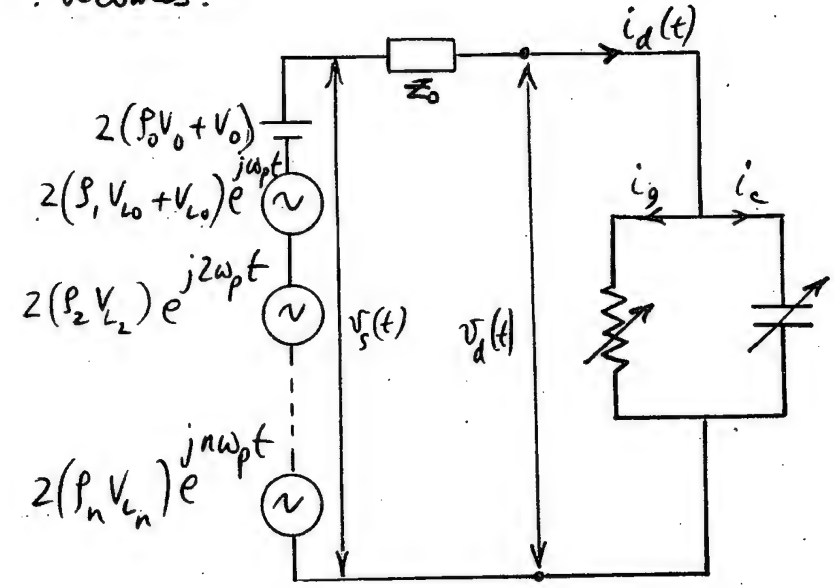

Equation (10) — the state equation can now be re-solved to give a new solution for $i_d(t)$ and $v_d(t)$

CONVERGENCE

The above procedure is repeated until equation (5) is satisfied for all the harmonic frequencies :–

$$-\frac{V_{d_n}}{I_{d_n}} = Z_e(n) + R(s) \qquad n > 1$$

and equation (4) is satisfied for the L.O. frequency :–

$$\frac{V_{LO} - V_{d_1}}{I_{d_1}} = Z_e(1) + R_s(1)$$

The current values of $v_d(t)$ and $i_d(t)$ are then taken to represent the true solution.

SMALL SIGNAL ANALYSIS

From the large signal analysis we have determined the current and voltage waveforms in the diode i.e. we now know $I_d(t)$ and $V_d(t)$:–

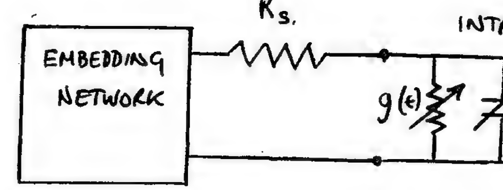

From the known characteristics of the S.B. diode

$$I_d = I_o\left[e^{\frac{qV_d}{\eta kT}} - 1\right]$$

The conductance $g = \dfrac{dI_d}{dV_d}$

$$= \frac{q}{\eta kT} e^{\frac{qV}{\eta kT}}$$

1)

$$\simeq \frac{q}{\eta kT} I(V_d)$$

Since V_d is a known function of time we can substitute into (1) and determine $g(t)$.

As we know that g must be periodic with the period of the L.O. pump we can express $g(t)$ as a complex Fourier series:-

$$g(t) = \sum_{n=-\infty}^{\infty} G_n e^{jn\omega_p t} \qquad (2$$

where, since $g(t)$ is real, $g_{-n} = g_n^*$

Similarly, from the known diode properties and the large signal analysis we can express the time varying diode capacitance as:-

$$C(t) = \sum_{n=-\infty}^{\infty} C_n e^{jn\omega_p t} \qquad (3$$

where $C_{-n} = C_n^*$

As far as the signal is concerned the pumped diode behaves as a linear component with time varying conductance and capacitance given by equations (2) and (3)

SMALL SIGNAL MIXING FREQUENCIES

When a signal is applied to a pumped diode currents and voltages are generated at many frequencies, illustrated below:-

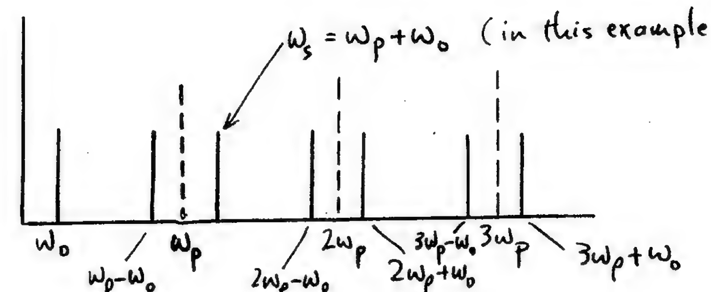

— Applied signal
— currents and voltages generated (as well as at ω_s)

The blue and red frequencies are called the small signal mixing frequencies. The pumped diode couples them all together

We can group these together as follows:-

I.F.	Upper Sidebands	Lower Sidebands
ω_0	$\omega_p + \omega_0$	$\omega_p - \omega_0$
	$2\omega_p + \omega_0$	$2\omega_p - \omega_0$
	$3\omega_p + \omega_0$	$3\omega_p - \omega_0$
	$\vdots$	
	$n\omega_p + \omega_0$	$n\omega_p - \omega_0$

In phasor notation, the upper sideband currents and voltages can be written as

4) $$I_n e^{j(n\omega_p + \omega_0)} \qquad n = 1 \cdots \infty$$

5) $$V_n e^{j(n\omega_p + \omega_0)} \qquad n = 1 \cdots \infty$$

The lower sideband frequencies are of the form

6) $$I_n e^{j(n\omega_p - \omega_0)} \qquad n = 1 \cdots \infty$$

7) $$V_n e^{j(n\omega_p - \omega_0)} \qquad n = 1 \cdots \infty$$

By examining these phasors in detail we can make a useful simplification. For example, consider equation (7). All voltages are actually REAL. Therefore when we write $V_n e^{j(n\omega_p - \omega_0)}$ we actually mean:-

$$Re\left\{ V_n e^{j(n\omega_p - \omega_0)} \right\}$$

V_n is a complex amplitude, therefore let

$$V_n = \tilde{V}_n e^{j\phi}$$

so that:-

$$Re\left\{ V_n e^{j(n\omega_p - \omega_0)} \right\} = Re\left\{ \tilde{V}_n e^{j\phi} e^{j(n\omega_p - \omega_0)} \right\}$$

$$= \tilde{V}_n \cos\left[n\omega_p - \omega_0 + \phi \right]$$

Using $\cos(-\theta) = \cos(\theta)$ we can re-write this as:-

$$\tilde{V}_n \cos\left[\omega_0 - n\omega_p - \phi \right]$$

This function can now be written as

$$Re\left\{ \tilde{V}_n e^{-j\phi} e^{j(\omega_0 - n\omega_p)} \right\}$$

or in phasor notation

$$V_n^* e^{j(\omega_0 - n\omega_p)}$$

If we now define the integers specifying the lower sidebands to be negative then equation (7) becomes

$$V_n^* e^{j(\omega_0 + n\omega_p)} \qquad n = -1, -2, \dots -\infty$$

The I.F. Frequency can be written as $V_0 e^{j\omega_0}$

hence now all of the sidebands fall into the series

$$V_n e^{j(\omega_0 + n\omega_p)} \qquad n = -\infty \dots -1, 0, 1, \dots \infty$$

Where for negative n V_n is the complex conjugate of the actual value.

Similarly the diode current can be written:-

$$I_n e^{j(\omega_0 + n\omega_p)} \qquad n = -\infty \dots -1, 0, 1, \dots \infty$$

With I_n complex conjugated for -ve integers.

The Conversion Admittance Matrix

The pumped diode can be thought of as a multi-port circuit with one pair of terminals for each of the mixing frequencies:-

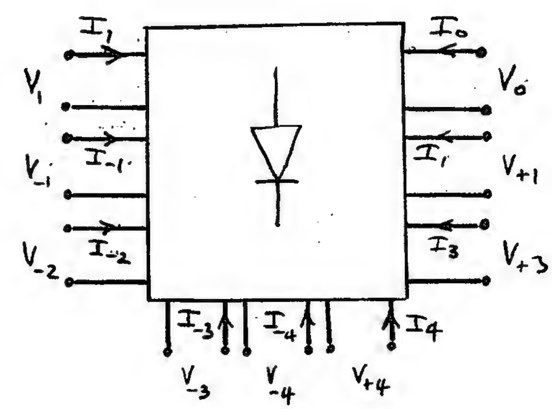

+ Many other ports

- Note — In practice we only need to consider a finite number of frequencies let this number be N.

The currents and voltages in the ports of the intrinsic diode can be represented as a MATRIX equation:—

$$\begin{bmatrix} I_N \\ I_{N-1} \\ \vdots \\ I_1 \\ I_0 \\ I_{-1}^* \\ \vdots \\ I_{-N+1}^* \\ I_{-N}^* \end{bmatrix} = \begin{bmatrix} & & & Y_{N0} & & & \\ & & & \vdots & & & \\ & & Y_{11} & Y_{10} & Y_{1-1} & & \\ Y_{0N} & \cdots & Y_{01} & Y_{00} & Y_{0-1} & \cdots & Y_{0-N} \\ & & Y_{-11} & Y_{-10} & Y_{-1-1} & & \\ & & & \vdots & & & \\ & & & Y_{-N0} & & & \end{bmatrix} \begin{bmatrix} V_N \\ V_{N-1} \\ \vdots \\ V_1 \\ V_0 \\ V_{-1}^* \\ \vdots \\ V_{-N+1}^* \\ V_{-N}^* \end{bmatrix}$$

So, if for example we were to short port N the current which would flow as the result of voltages applied to the other ports would be given by

$$I_N = Y_{NN} V_N + Y_{N,N-1} V_{N-1} + \cdots Y_{N0} V_0 + \cdots$$
$$\cdots Y_{N,-N+1} V_{-N+1}^* + Y_{N,-N} V_{-N}^*$$

The Matrix Y is called the CONVERSION ADMITTANCE MATRIX.

We can show that the components of Y are given by:—

$$Y_{mn} = G_{m-n} + j(\omega_0 + m\omega_p) C_{m-n}$$

Where G_{m-n} and C_{m-n} are the FOURIER COMPONENTS of the conductance and capacitance wave forms.

THE AUGMENTED NETWORK

The Y-matrix of the intrinsic diode is now AUGMENTED by connecting the spreading resistance, R_s, and the embedding network in parallel with the ports:-

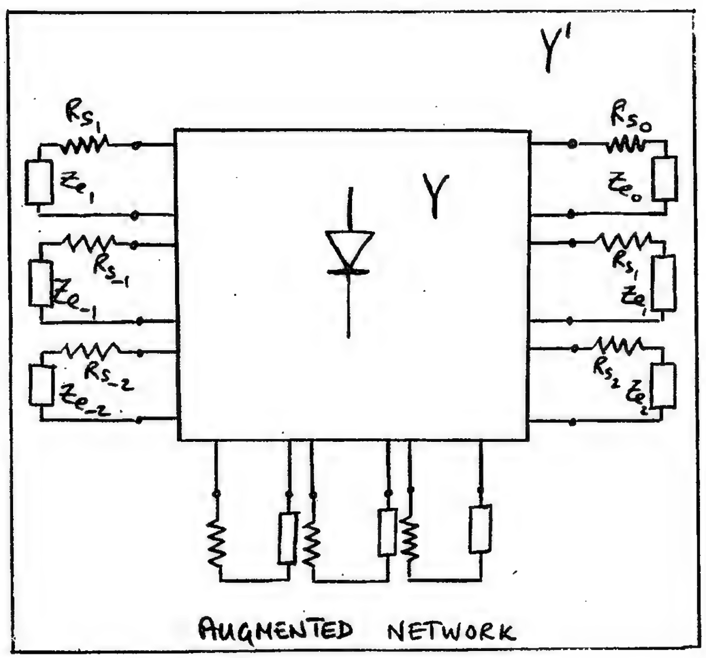

Note: the ports of the AUGMENTED network have remained as for the intrinsic diode.

e.g. consider port 1 :-

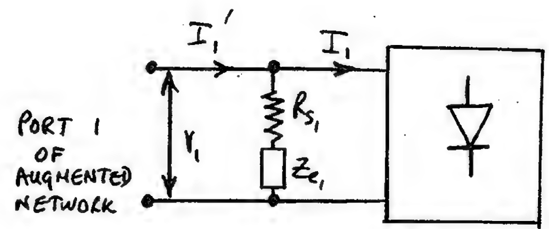

- R_{s_1} and Z_{e_1} are linear and do not add to the frequency conversion process. Therefore applying voltage V_1 to port 1 of the augmented network results in the same currents in all the other ports as generated by the intrinsic diode. Thus all the off diagonal elements of Y' are the same as Y

- From the definition of Y

$$I_1 = Y_{11} V_1$$

The current through R_{s_1} and Z_{e_1} is given by $\dfrac{V_1}{R_{s_1} + Z_{e_1}}$

Thus $$I_1' = Y_{11} V_1 + \frac{V_1}{R_{s_1} + Z_{e_1}}$$

i.e. $$I_1' = \left[Y_{11} + \frac{1}{R_{s_1} + Z_{e_1}}\right] V_1$$

hence $$Y_{11}' = Y_{11} + \frac{1}{R_{s_1} + Z_{e_1}}$$

In general, for the diagonal terms:–

$$Y_{nn}' = Y_{nn} + \left[R_{s_n} + Z_{e_1}\right]^{-1}$$

Determination of Conversion Loss

For the augmented network we have the matrix equation

$$\hat{I}' = Y' \hat{V} \qquad (8$$

where $$\hat{I}' = (I_N', I_{N-1}', \ldots I_1', I_0', I_{-1}'^{*} \ldots I_{-N}'^{*})^T$$

and $$\hat{V} = (V_N, V_{N-1}, \ldots V_1, V_0, V_{-1}^{*} \ldots V_{-N}^{*})^T$$

Inverting equation (8) gives

$$\hat{V} = Z' \hat{I} \qquad (9$$

where $Z' = [Y']^{-1}$ is the AUGMENTED CONVERSION IMPEDANCE MATRIX. From Z' we can determine the conversion loss.

If we assume that the signal is input to the mixer at frequency ω_1 $(\omega_p + \omega_0)$ and the I.F. is extracted at frequency ω_0 these are the only two ports of interest — the circuit is therefore effectively a two port:—

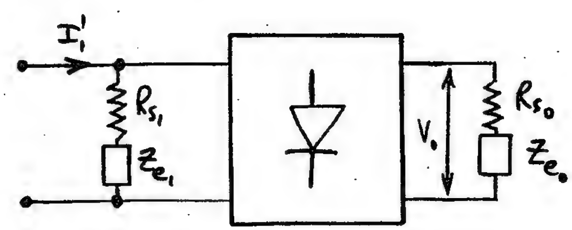

We excite the mixer by injecting a current into port 1 of the augmented network.
From equation (9) — assuming there are no inputs at other ports

$$V_0 = \hat{Z}_{10} I_1' \qquad (10)$$

The voltage which appears across Z_{e_0} — the actual I.F. load impedance is given by:–

$$V_{IF} = V_0 \frac{Z_{e_0}}{Z_{e_0} + R_{s_0}}$$

The current flowing through Z_{e_0} is given by:–

$$I_{IF} = \frac{V_0}{Z_{e_0} + R_{s_0}}$$

The time average power delivered to Z_{e_0} is given by:–

$$P_{del} = \frac{1}{2} \operatorname{Re}\left[V_{IF} I_{IF}^* \right]$$

Substituting

$$P_{del} = \frac{1}{2} \operatorname{Re}\left[V_0 \frac{Z_{e_0}}{(Z_{e_0} + R_{s_0})} \cdot \frac{V_0^*}{(Z_{e_0} + R_{s_0})^*} \right]$$

$$= \frac{1}{2} \frac{|V_0|^2}{|Z_{e_0} + R_{s_0}|^2} \operatorname{Re}(Z_{e_0})$$

Using equation (10) this becomes:–

$$P_{del} = \frac{1}{2} \frac{|\hat{Z}_{10}|^2 |I_1'|^2}{|Z_{e_0} + R_{s_0}|^2} \operatorname{Re}(Z_{e_0}) \qquad (11)$$

On the input side (Port 1) we can use Thevenins theorem to show that:–

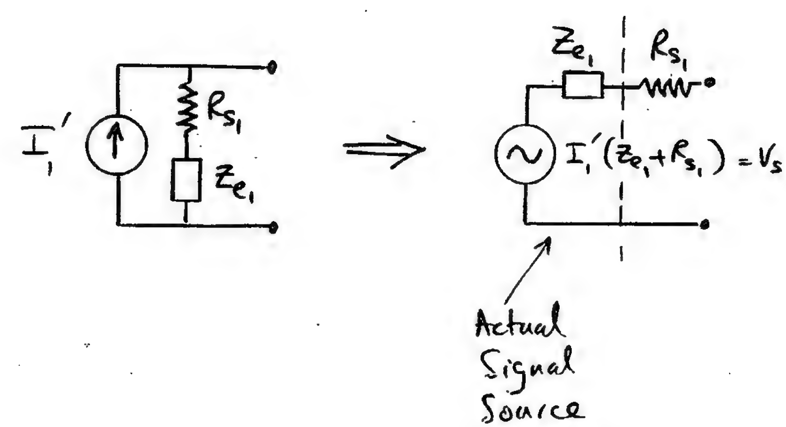

The power AVAILABLE from the actual signal source is that which it would deliver to a matched load :-

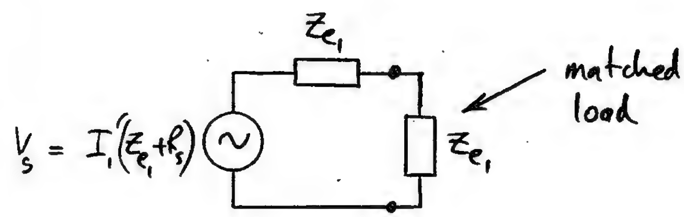

The voltage across the matched load is:-

$$V_{M.L.} = \frac{1}{2} V_s = \tfrac{1}{2} I_1'(Z_{e_1}+R_{s_1})$$

The current is given by:-

$$I_{ML} = \frac{V_s}{2Z_{e_1}} = \frac{I_1'(Z_{e_1}+R_s)}{2Z_{e_1}}$$

∴ Power delivered to the matched load is:-

$$P_{AV} = \frac{1}{2} Re\left[V_{ML} \cdot I_{ML}^{*} \right]$$

So that

$$P_{AV} = \frac{1}{2} Re\left[\frac{1}{2} I_1'(Z_{e_1}+R_s) \frac{I_1^{*}(Z_{e_1}+R_{s_1})^{*}}{2Z_{e_1}^{*}} \right]$$

$$P_{AV} = \frac{1}{8} |I_1|^2 \frac{|Z_{e_1}+R_s|^2}{Re[Z_{e_1}]} \qquad (12$$

The conversion loss is now defined to be the power available from the source divided by the power delivered to the I.F. load. Using 11) and 12) above, we now have the result :-

$$L = \frac{|Z_{e_1}+R_{s_1}|^2 \, |Z_{e_0}+R_{s_0}|^2}{4\,|\hat{Z}_{10}|^2 \, Re[Z_{e_0}] \, Re[Z_{e_1}]}$$

MIXER NOISE ANALYSIS

Sources of noise in a mixer are:-

- Thermal Noise in R_s
- Shot Noise in current through the diode junction
- lattice scattering noise
- Hot electron noise
- Thermal noise from resistive elements in the embedding network

Usually only the first two are considered to be significant.

The NOISE EQUIVALENT CIRCUIT in this case is:—

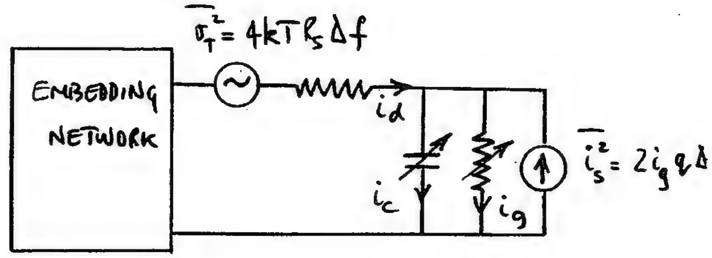

These noise components appear at all of the 'PORTS' of the AUGMENTED NETWORK. Some of this noise power is converted to the I.F. frequenc[y] where it contributes to the noise temperature of the mixer. Knowledge of the conversion impedance matrix $\hat{Z}'$ enables the noise temperature of the mixer to be calculated:-

$$T_{SSB} = \frac{\langle |\delta V_N|^2 \rangle \, |Z_{e_1} + R_{s_1}|^2}{4k\,\Delta f\, |\hat{Z}_{0,1}|^2 \, Re\left[Z_{e_1}\right]}$$

where $\langle |\delta V_N|^2 \rangle = \hat{Z}_0' \,(C_s + C_t)\, \hat{Z}_0'^{*T}$

$\hat{Z}_0'$ is the centre row of the Augmented Impedance conversion Matrix

C_s and C_t are matrices representing the correlation properties of the noise at the mixer output terminals.

C_s and C_t have been evaluated :-

$$C_{s_{mn}} = 2q\, I_{m-n}\, \Delta f$$

where I_{m-n} is the $(m-n)$th Fourier component of the diode conductance current (available from the large signal analysis)

$$C_{t_{mn}} = 0 \quad \text{for } m \neq n$$

$$= \frac{4kT R_{s_m} \Delta f}{|Z_{e_m} + R_{s_m}|^2} \quad \text{for } m = n \neq$$

$$= \frac{4kT R_{s_0} \Delta f}{|Z_{e_0} - R_{s_0}|^2} \quad \text{for } m = n = 0$$

FREQUENCY MULTIPLIERS

- Use the non-linearity of the S.B. diode to generate harmonics of a pump source — provide solid-state L.O. sources above about 100 GHz.

- Harmonic generation is possible through either the non-linear conductance or capacitance of the diode. However, modern multipliers almost always use the non-linear capacitance of the diode as the main harmonic generation mechanism.

- Diodes used in multipliers differ from those used in mixers — they are optimised to give the greatest capacitance variation possible. Such diodes are referred to as VARACTOR DIODES

- Varactor diodes are operated under REVERSE BIAS to give the best possible capacitance variation and limit the current – thereby increasing the power handling capability of the device.

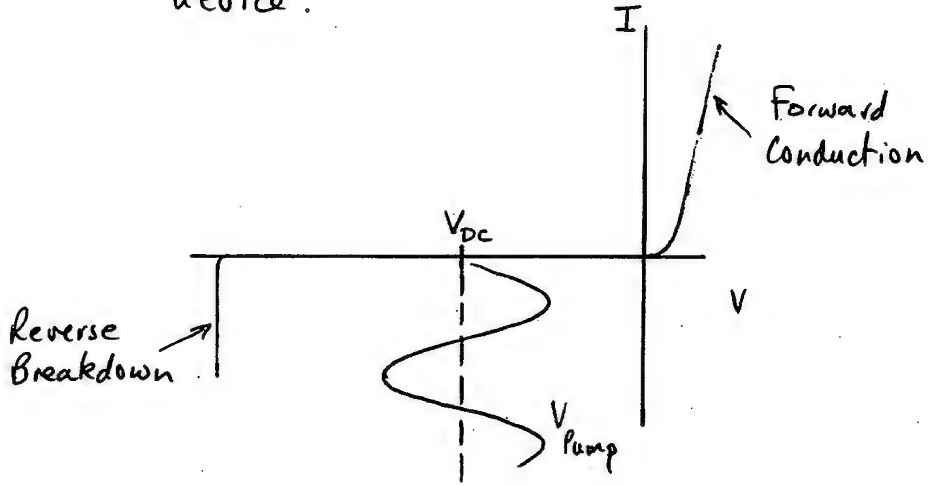

In the reverse bias region the depletion layer thickness varies with bias – giving the capacitance variation. The epi-layer thickness must be great enough to accomodate this variation – therefore VARACTOR diodes have thicker epi-layers than MIXER diodes

- It can be shown that a multiplier using a non-linear capacitance can have a conversion efficiency $\left(\frac{P_{HARMONIC}}{P_{PUMP}}\right)$ of at most $\frac{1}{n^2}$ where n is the harmonic number. Varactors have no such limitations – efficiencies of 100% are theoretically possible (but of course not practically achievable)

- To achieve the maximum efficiency at the third harmonic, for example, it may be necessary to allow significant current flow at the second harmonic into a low loss resonator. This is an example of an IDLER circuit.

- The Analysis of a frequency multiplier is – in principle the same as the LARGE SIGNAL analysis of a mixer.

FREQUENCY TRIPLER — SCHEMATIC

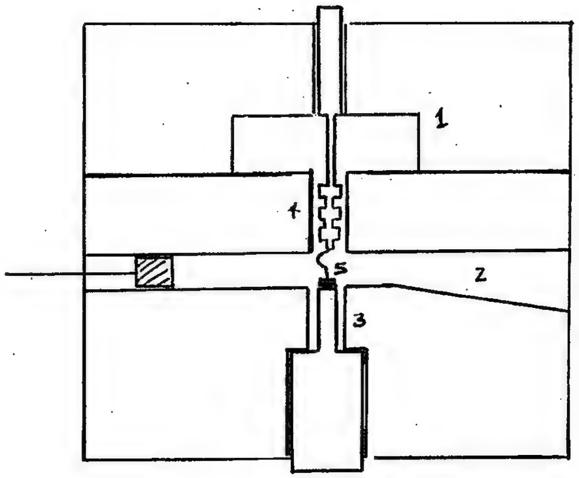

1 — pump waveguide

2 — 3rd harmonic output waveguide

3 — Coaxial resonator, the 2nd harmonic IDLER

4 — Filter to prevent 3rd harmonic loss to the pump waveguide

5 — The diode

6 — Moveable back short (also in pump waveguide — not shown)

MULTIPLIER ANALYSIS

The frequencies of interest in the multiplier are the pump frequencies ω_p and its harmonics $n\omega_p$. Once again we assume that we know the embedding impedances at all of these frequencies (up to a reasonable number of harmonics) and the diode conductance and capacitance characteristics.

One again we carry out the harmonic balance calculation to determine diode voltage, current, capacitance and conductance waveforms

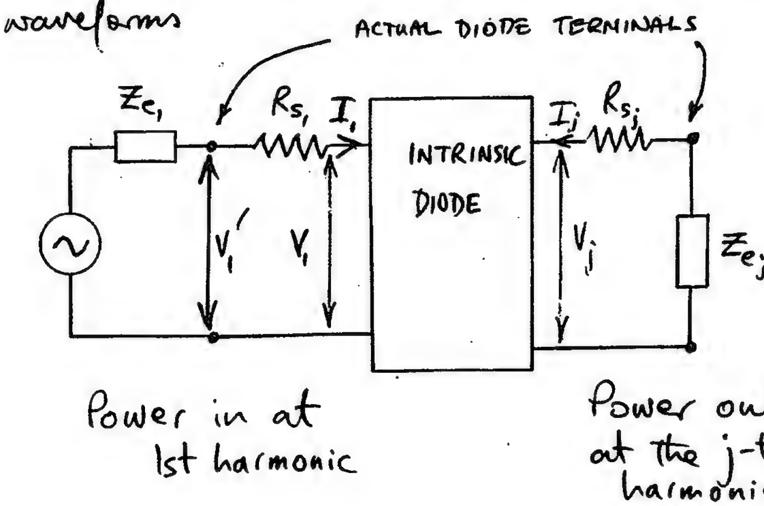

V_1, I_1, V_j and I_j are available from the harmonic balance calculation

The pump power 'absorbed' by the diode is given by :-

$$P_{abs} = \frac{1}{2} Re\left[V_1' I_1^* \right]$$

$$= \frac{1}{2} Re\left[\{ V_1 + I_1 R_{s_1} \} I_1^* \right]$$

The power 'delivered' to the load impedance Z_{e_j} is given by :-

$$P_{out} = \frac{1}{2} Re\left[I_j^* V_j \right]$$

$$= \frac{1}{2} Re\left[I_j^* I_j Z_{e_j} \right]$$

$$= \frac{1}{2} |I_j|^2 Re\left[Z_{e_j} \right]$$

The efficiency is therefore :-

$$\mathcal{E} = \frac{P_{out}}{P_{abs}} = \frac{|I_j|^2 Re\left[Z_{e_j} \right]}{Re\left[\{ V_1 + I_1 R_{s_1} \} I_1^* \right]}$$

TUESDAY JULY 2

FUNDAMENTALS OF RECEIVERS FOR TERAHERZ SYSTEMS
by
G. Beaudin and P.J. Encrenaz
Observatoire de Paris, DEMIRM,URA CNRS 336 - ENS PARIS
61 avenue de l'Observatoire - 75014 Paris - France

I - INTRODUCTION

The submillimeter wavelength spectral band, covering the frequency range 0.3 THz ($\lambda = 1$mm) to 3 THz ($\lambda = 0.1$ mm), represents one of the the least explored yet information rich segments of the electromagnetic spectrum. This frequency span encompasses all of the critical spectral emissions from the key molecules involved in atmospheric chemistry on Earth (and on the planets and comets). These include those molecular transitions which have been identified as crucial to our understanding and monitoring of the global ozone depletion problem. The submillimeter-wave regime also contains spectral line emissions which can further our understanding of interstellar chemistry, new star formation and galactic structures. Due to high atmospheric opacity (Fig. 1) both astrochemical and stratospheric observations in the submillimeter-wave spectral bands must be made from high altitude aircraft : Kuiper Airborne Observatory (KAO/NASA) and SOFIA ; balloons : PIROG (SSC), Programme National d'Astronomie Submillimétrique (PRONAOS/CNES) or satellites :

There are three funded space missions which will carry submillimeter wave radiometers : Submillimeter-Wave Astronomy Satellite (SWAS/NASA), ODIN (Swedish Space Centre, SSC) combining Astronomy and Aeronomy objectives, and Earth Observing System Microwave Limb Sounder (EOS-MLS/NASA) . Four other missions are in phase A/B study : the Submillimeter Observation of PRocesses in the Atmosphere Noteworthy for Ozone (MASTER-SOPRANO/ESA) for Aeronomy, ROSETTA for planetary and cometary observations, SAMBA-COBRAS for cosmology and the Far-Infrared Space Telescope (FIRST/ESA) for Astronomy .

SWAS has two radiometers at frequencies of 490 and 550 GHz ; ODIN has three radiometers, at 120, 480 and 550 GHz ; EOS-MLS is currently configured with radiometers at 210, 440 and 640 GHz and potential channels at 1.2 and 2.5 THz.

MASTER - SOPRANO is a project having two instruments on 200, 325 and 350 GHz ; and 500, 630 and 950 GHz frequency bands ; ...

FIRST is designed to have broad spectral coverage beginning at 500 GHz and going up to 1.2 THz.

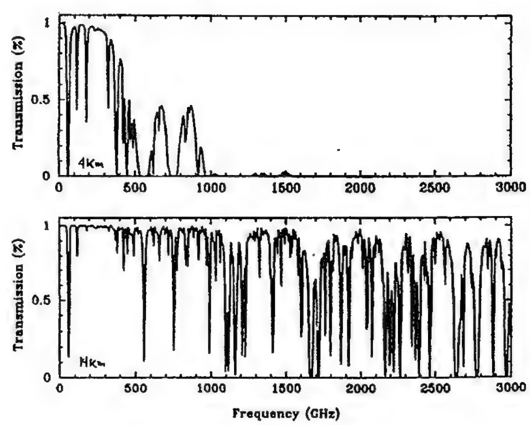

Figure 1 : Atmospheric transmission in the submillimetre and far-infrared from a very good high-altitude ground-based site (Mauna Kea at 4.1 km with 1 mm of precipitable water vapour) and from the altitude of an airborne observatory (e.g. KAO at 14 km altitude). The blocked regions are mostly caused by molecular absorption.

II - DETECTION TECHNIQUES FOR SUBMILLIMETER WAVES

There are two basic ways to analyse electromagnetic radiation at submillimetre and far-infrared wavelengths, either by (super-) heterodyne (coherent detection) or by direct (incoherent) detection techniques. This part of the spectrum lies between what traditionally can be regarded as the radio and infrared domains and the two techniques reflect this fact (fig.2) :

Direct and Heterodyne Detection Systems

In direct detection (fig. 3) the detectors respond to the signal photons themselves ; in heterodyne detection (fig. 4) the signal is converted to a lower convenient intermediate frequency (IF) by "mixing" with a generated stable monochromatic local oscillator (LO) signal before signal processing.

The fundamental difference between the two types of detection is the retention or destruction of the phase in the detected signal. The quantum mechanical uncertainty principle shows that heterodyne detection can never be more sensitive than direct detection, at least in principle. Fixing the phase causes a measurement uncertainty of order one photon in a heterodyne conversion process ; this is equivalent to imprecision introduced by a noise source. The lack of phase sensitivity in incoherent detection enables the direct detection of individual photons.

Since instruments based on direct detection respond to signal photons alone, spectroscopy must be done by separating individual frequency components in the incoming signal (fig. 3) before detection. With the exception of Fourier transform instruments, incoherent systems measure one frequency channel per detector, requiring some scanning of the predetection filter to obtain a spectrum. A typical heterodyne receiver consists of two seperate parts : a heterodyne mixer (the "front-end), which shifts a high frequency band of frequencies from one center frequency to a lower one without altering the spectral information within the band, and a separate ("backend") spectrometer which obtains the spectrum of the lower frequency band (fig. 4). Since the spectroscopy is performed at low frequencies, simple filters with modest resolution can be used. The backend spectrometers of heterodyne systems analyze the entire instantaneous receiver bandwidth, which in practical cases will cover the spectral line and baseline. The frequency multiplex advantage of the heterodyne backend can be offset by the simpler spectral or spatial multiplexing of incoherent array elements.

The choice of heterodyne or direct detection for a given application at submillimetre and far-infrared wavelengths is not always obvious, as it is in this range of the spectrum that the two methods both cross in sensitivity and become technologically possible. Tradeoffs, involving for instance observing frequency, spectral and spatial resolution and coverage, required sensitivity and detector availability, will determine whether Fourier transform, grating, Fabry-Pérot, or heterodyne instruments will be best suited to this figure :

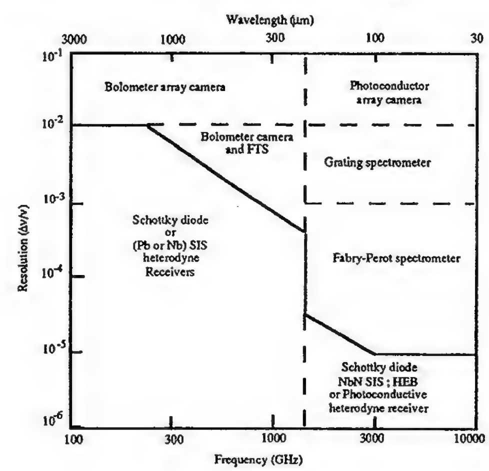

Figure 2 : There are two basic ways to analyze electromagnetic radiation at submillimetre and far-infrared wavelengths, either by (super-) heterodyne (coherent detection) or by direct (incoherent) detection techniques. This part of the spectrum lies between what tradionally can be regarded as the radio and infrared domains and the two techniques reflect this fact.

NATO : Advanced Study Institute new directions in Terahertz Technology, Toulouse, July 1996

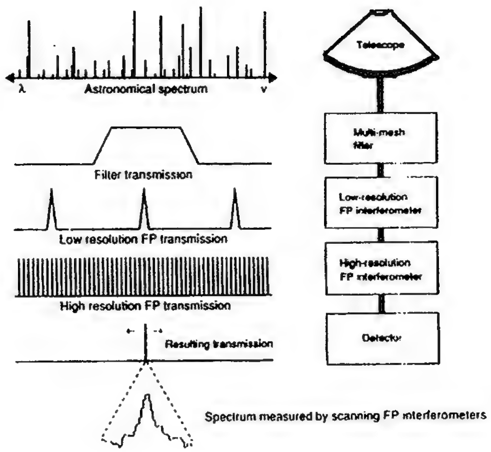

Figure 3 : Principle of direct detection system
The spectral bandwidth is reduced by a succession of filters and interferometers. Approximate wavelength selection is made by means of a bandpass filter isolating one Fabry-Pérot interferometer transmission fringe. By adding one additional interferometer at higher resolution (larger mesh spacing) a final higher resolution is achieved. the transmitted, very narrow bandpass, can be scanned in wavelength by tuning the two interferometers enabling the detectors to sample different parts of the spectrum.

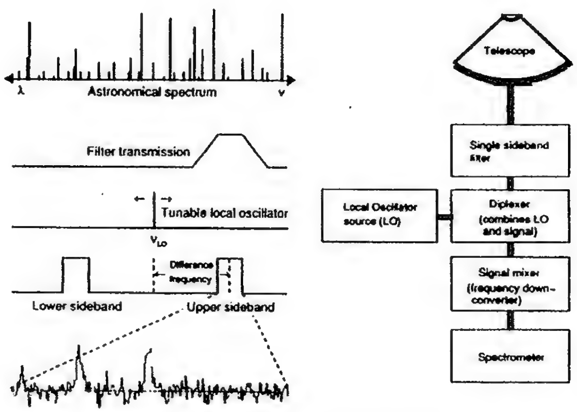

Figure 4 : Principle of heterodyne detection system
Downconversion of the received signal to an easier to process frequency is achieved by adding a tuneable line signal (local oscillator) to the received one and extract the different frequency. A filter can be used to select any of the two received sidebands. Signal merging is performed in a diplexer before feeding the signal to the mixer. After further amplification the downconverted signal can be analysed at the chosen frequency resolution in the backend spectrometer. This device samples simultaneously a very large number of frequency channels.

III - SUBMILLIMETER HETERODYNE TECHNOLOGIES

All of the missions requiring high sensitivity and high spectral resolution use the heterodyne detection technic (fig. 5). Such receivers generally consist of a low loss signal coupling structure (waveguide feed horn of planar antenna), a local source of RF power (local oscillator, L.O.) at a frequency very closed to that the observed signal, a frequency diplexer which efficiency couples the RF signal and LO into the low noise down converting (mixer) element (Schottky barrier diode or SIS superconducting tunnel junction), a low noise intermediate frequency (IF) usualy in the microwave band, and finally a high resolution spectrometer to separate out the spectral lines (filter banks, digital autocorrelators, surface acoustic-waves filters, acousto-optic spectrometers), are used.

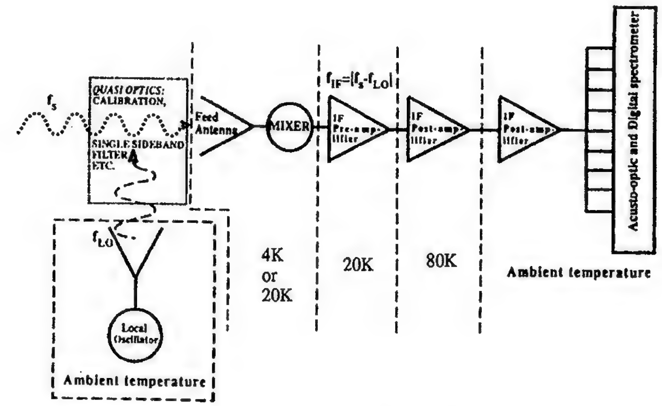

Figure 5 : Schematic outline of a heterodyne receiver
using common quasi-optics and spectrometers. Each channel have SIS mixers operating at 4 K, or Schottky mixers operating between 20 K and room temperature.

A - SUBMILLIMETER HETERODYNES MIXERS

Both Schottky diode and superconducting tunnel junction (Superconducting-Insulator-Superconducting = SIS) mixers could be used on the submillimeter heterodyne receivers. The Earth (or other planets) atmospheric research don't need a so high sensitivity, is the more often using Schottky diode mixers ; the astrophysic research needed the highest sensitivity, currently employ SIS mixers. Waveguide with horn and Quasi-optical mixer technologies are both employed up to 2.5THz. Arrays have been developped for astronomical focal imagery.

Submillimeter Schottky diode developments

For more than two decades the best uncooled heterodyne radiometers for use in the 100 GHz - 3 THz frequency range have been composed of waveguide or open structure mixers with whisker-contacted metal-semiconductor Schottky-barrier honeycomb diodes.
In order to reduce the assembly cost and improve the reliability and reproducibility of heterodyne receivers for the space missions throughout the millimeter and submillimeter wavelength bands, two major changes must be incorporated into current radiometer design. First, the whisker-contact honeycomb diode must be replaced by a more reliable, easier to handle, integrated structure similar to the beam-lead diodes now routinely used below 100 GHz. Second, for applications up to (or above) 600 GHz, the diode must be integrated with the remaining, physically larger, mixer circuitry to increase flexibility and simplify assembly. An added benefit to this latter approach is the potential of going one step further and replacing the last remaining mechanically fabricated component, the waveguide mount, with an all planar photolithographic structure scalable to frequencies well beyond a THz (JPL, SHP mixer at 650GHz). A major goal is to advance the state-of-the-art in millimeter-wave quasi-planar-diode technology to the point at which it can be used readily at frequencies as high as 2.5 THz.
The Schottky diode must be cooled to about 20-30 K for optimum performances, but works even at room temperature.

SIS Tunnel junctions developments

In the push to obtain ever higher sensitivity, shorter observation times and the use of smaller collecting surfaces, the submillimeter-wave astrophysics community has devoted much of their ressources towards the developpement of radiometer front-ends based on the refractory superconductors niobium nitride. At present, the most prevalent form of high frequency superconducting heterodyne receiver is the small area superconductor-insulator-superconductor Nb(SIS) tunnel junction which offers the potential of near quantum limited sensitivity throughout the millimeter-wave bands up to 700 GHz (fig. 6) and possibly at frequencies as high as 1.2-1.4 THz with normal metal tuning stubs circuits (Al). 2-3THz could be achievable in the near future by using SIS with NbN superconducting junctions or by using Hot Electron Bolometers heterodyne mixers. The SIS mixers must be physically cooled to temperatures well below the superconduction transition temperature, i.e. to 4 K for $Nb/Al_xO_y/Nb$ elements. However, the requirement for a liquid helium ambient environment poses a significant limitation for remote, long lifetime space operation.

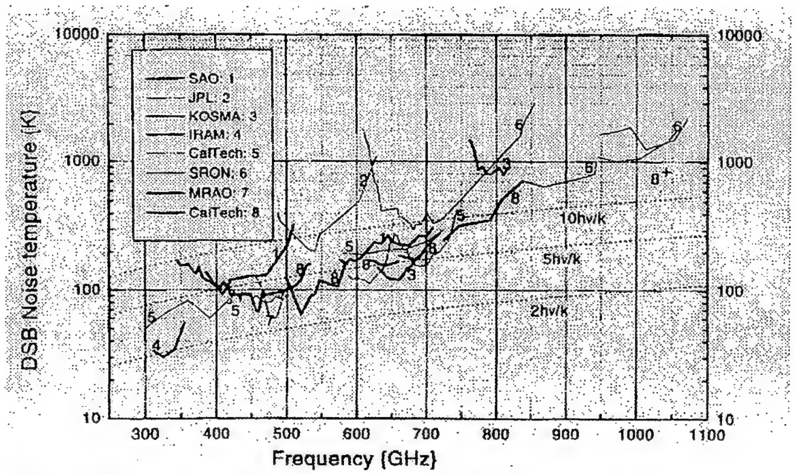

Thick lines represent fixed-tuned mixers. Compiled by SRON, March 19, 1996

Figure 6 : Heterodyne SIS receiver noise temperatures.
The currently best experimentally obtained receiver noise temperature (T_{rec}) vs frequency for SIS mixers.
It is estimated that T_{rec} for the 1 THz cooled Schottky receiver will be approximately 1000 K.

B - LOCAL OSCILLATOR GENERATION TECHNOLOGIES

The L.O. power needed for Schottky diodes or SIS junctions, is currently obtained by Gunn oscillators cascaded with frequency multipliers using whiskered varactor diodes (RPG, UVa...). This technology is able to provide enough power up to THz for Schottky and 1.5 THz for SIS mixers. New planars components are under development at JPL, U.Va, U.Michigan...).
HEMT oscillators, Quantum well oscillators are able to provide enough power up to 300-400 GHz ; long Josephson junctions and flux-flow oscillators arrays are also opportunities to drive the SIS mixers up to 600-700GHz.
CO_2 lasers pumping submillimeter masers are used as LO sources in the range 300 GHz - 3 THz, but they need too high electrical power consumption for space applications : Heterodyned lasers diodes technology is under investigation!

IV - SUBMILLIMETRE TECHNOLOGIES in the FIRST PROJECT

The Far InfraRed and Submillimetre Space Telescope (FIRST) is one of the four "Cornerstone" projects in the ESA Long-Term Programme for Space Science, "Horizon 2000". This mission is devoted to high troughput spectroscopy and photometry in the submillimetre and far-infrared wavelength range. FIRST is foreseen to have a 3m diameter radiatively cooled Cassegrain telescope equiped with a payload consisting of a multichannel, very high spectral resolution heterodyne receiver (table 1) and an imaging medium and spectrometer and photometer, covering the 85-900 µm wavelength band (table 2). FIRST will open up this virtually unexplored part of the spectrum which cannot be observed from the ground, and is only partially accessible from airborne platforms.
With its high throughput, low thermal background, extensive wavelength coverage, and high spatial and spectral resolution, FIRST will offer superb sensitivity for both photometry and spectroscopy. Its multiband instruments will give unprecedented information on the physics, chemistry and dynamics of interstellar, circumstellar, planetary and cometary gas and dust, resulting in a quantum step forward in the study of the cold universe. It will be the first multi-purpose submillimetre and far-infrared space observatory available to the world-wide astronomical community.

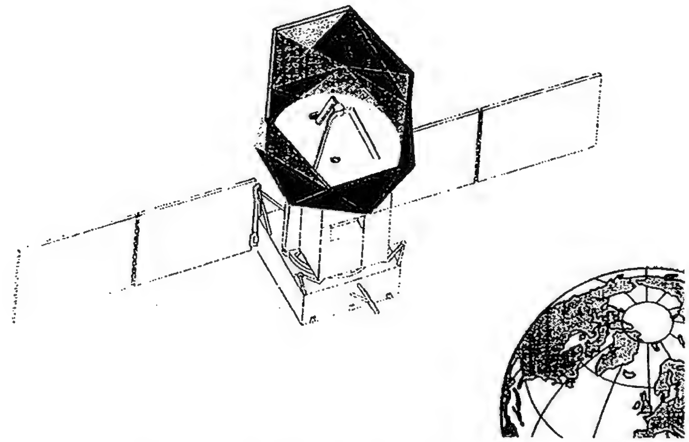

Figure 7 : The FIRST spacecraft in orbit (artist view)

Receiver band # / Mixer type	1 & 2 SIS	3 & 4 SIS	5 & 6 SIS	7 & 8 SIS	9 SIS
ν (GHz) / Beam FWHM	490 - 650 / 48 - 36	600 - 750 / 39 - 31	700 - 850 / 34 - 28	800 - 950 / 29 - 25	950-1200 / 25-20

Table 1 : FIRST MultiFrequency Heterodyne (MFH) receiver frequency bands

Wavelength range	85-210 µm	85-210 µm	210-300 µm	85-210 µm	210-280 µm	280-600 µm	600-900 µm
Filter bands	5	5	1	2	1	1	1
mode	hi-res.	med-res.	med-res.	photom.	photom.	photom.	photom.
Detector	photo-conductor	photo-conductor	short wavelength bolometer	photo-conductor	short wavelength bolometer	short + long wavelength bolometer	long wavelength bolometer

Table 2 : Modes of operation

V - CONCLUSION :

For most observations in the Earth's, planets and comets atmospheres, sensitivity is not nearly as critical an issue as it is for stellar astrophysics. A large number of key molecular transitions can be observed with the sensitivity available from current room-temperature of passively cooled semiconductor-diode radiometers. For the most part, the emphasis for millimeter and submillimeter-wave, Earth remote sensing applications has been on pushing to higher frequencies (up to 3 THz), increasing the instantaneous bandwidth, improving device reliability and reducing radiometer complexity and cost.

For astrophysic, very sensitive and very high spectral resolution heterodyne spectroscopy ($R_{max} \geq 10^6$) are requiered. SIS mixers in the 500 to 1200 GHz range and flexible backend spectrometers with more than 4 GHz instantaneous bandwidth will be used on the FIRST project. Significant progress is being made on both mixer performances and junctions reliability as well as cryocooler technology (Sterling closed cycle cryogenerator and JT stage, Pulsed Gaz Tube...). It seems no doubt that SIS heterodyne submillimetric receivers will fly in space sometime in the very near future ...

Acknowledgements : to the FIRST heterodyne payload team, with *ESTEC-ESA, (the Netherlands)*, as well as *JPL-Caltech, Pasadena (CA, USA)*, for their subtential participations to this paper and CNES, ESA, NASA for funding the submillimeter developments.

References :

This paper has been made from the listed articles on the following references ; using mainly the EOS-MLS and the FIRST ESA reports :

- *Microwave Remote Sensing, F.T. Ulaby et al. (1984), AR Tech House Inc.*
- *Infrared and Millimeter Waves vol 1-13 (1985), edited by Kenneth J. Button (MIT, USA), Academic Press Inc (London) LTD.*
- *RadioAstronomy, Kraus 2e edition (1986), Cygnus Quasar Books, Ohio (USA)*
- *Coherent detection at millimeter wavelengths and their applications, Nova science publications New York, Centre de physique des Houches, France, march 1990.*
- *Proceedings of the 29th Liege international colloquium held at the Institut d'Astrophysique, Liege, Belgium, july 90, ESA 8-10 rue Mario Nikis, 75738 Paris Cedex 15 - France.*
- *International Symposium of Space Terahertz Technology, JPL-NASA, Pasadena California, february 1991 ; University of Michigan, march 1992 ; UCLA, March april 1993, ; U. Michigan, may 1994 ; University of Virginia Charlottesville, March 1996.*
- *Radiométrie en ondes millimétriques au sol et dans l'espace ; G. Beaudin, D. Scouarnec, G. Thomas, IEEE workshop millimétrique, Carry le Rouet, novembre 1991.*
- *Etat de l'art en détection cohérente dans la domaine millimétrique et submillimétrique ; G. Beaudin, M. Gheudin, G. Thomas, P. Encrenaz, 2èmes Journées d'Etudes Micro-ondes et Espace, Toulouse 14-15 janvier 1992.*
- *ODIN, a swedish small satellite project for astronomical and atmospheric research, SSC reports 1992-1996.*
- *Earth Observing System Microwave Limb Sounder (EOS-MLS), P. Siegel et al, SPIE conf Proc 1874 - IRMMW engineering, may 1993.*
- *FIRST, far infrared and submm space telescope, G. Pilbratt et al, ESA phase A report, SCI 93 - 6 sept 1993.*
- *HET HIFI meeting reports SRON (and al) ; JPL-Caltech (and al), Dec. 95/Jan, May 96.*
- *MASTER - SOPRANO submillimetre observation of processes in the atmosphere noteworthy for ozone, ESA proposal, october 1993 and june 94.*

Millimetre Wave & Terahertz Waveguides & Measurements

Roger D. Pollard
Department of Electronic & Electrical Engineering
The University of Leeds
Leeds LS2 9JT, U.K.

Agenda

- Some fundamentals and useful definitions
- The problems with increasing frequency
- Reflectometry
  - six-ports and related technology
  - quasi-optical techniques
- Network analysis
  - down-converters for vector network analyzers
  - wafer probing
  - calibration issues
- Spectrum analysis

Review of Transmission Line Fundamentals

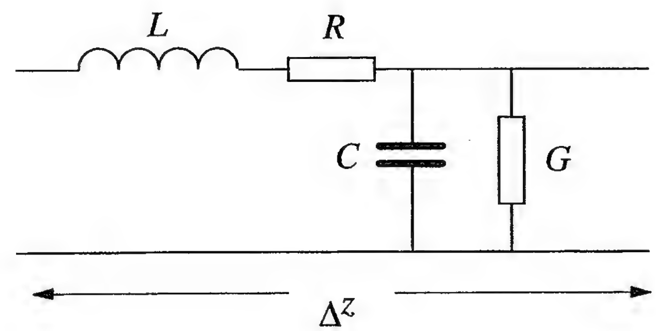

Transmission Line Fundamentals (2)

v and i are of the form $e^{j\omega t}$

$v(z) = K_0 e^{-\gamma z} + K_1 e^{+\gamma z}$

$\gamma = \sqrt{(R + j\omega L)(G + j\omega C)}$ propagation constant

$Z_0 = \sqrt{\dfrac{R + j\omega L}{G + j\omega C}}$ characteristic impedance

if $R = G = 0$ (lossless), $Z_0 = \sqrt{\dfrac{L}{C}}$

Transmission Line Fundamentals (3)

$$\gamma = \alpha + j\beta$$
$$= \sqrt{j\omega\mu(\sigma + j\omega\varepsilon)}$$

$$\alpha = \omega\sqrt{\frac{\mu\varepsilon}{2}\left(\sqrt{1+\frac{\sigma^2}{\omega^2\varepsilon^2}}-1\right)} \qquad \text{Np / m}$$

$$\beta = \omega\sqrt{\frac{\mu\varepsilon}{2}\left(\sqrt{1+\frac{\sigma^2}{\omega^2\varepsilon^2}}+1\right)} \qquad \text{rad / m}$$

Transmission Line Fundamentals (4)

- Conductor loss
  - skin effect

$$R_{dc} = \frac{\rho\ell}{A}$$
$$R_s = \frac{1}{\sigma\delta} = \sqrt{\frac{\pi f\mu}{\sigma}}$$
$$L_i = R_s / \omega$$
$$Z_s = R_s + j\omega L_i$$

- Dielectric loss (tan d)
  - modify with filling factor $\neq 1$
- Radiation loss
- Leakage loss
  - semiconductors

Transmission Line Fundamentals - Useful Definitions

Voltage $V = E_i + E_r$

Current $I = \dfrac{E_i + E_r}{Z_0}$

VSWR $\sigma = \dfrac{|E_i| + |E_r|}{|E_i| - |E_r|}$

Reflection Coefficient $\Gamma = \dfrac{E_r}{E_i} = \dfrac{Z_L - Z_0}{Z_L + Z_0}$ $\quad(\rho\angle\theta)$

$\rho = \dfrac{\sigma - 1}{\sigma + 1} \qquad \dfrac{Z_L}{Z_0} = z_L = \dfrac{1+\Gamma}{1-\Gamma}$

Coaxial Line

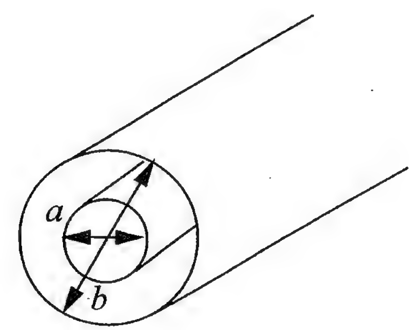

$b = 0.5$ mm
f < 170 GHz
$\alpha = 33$ dB/m

Rectangular Waveguides

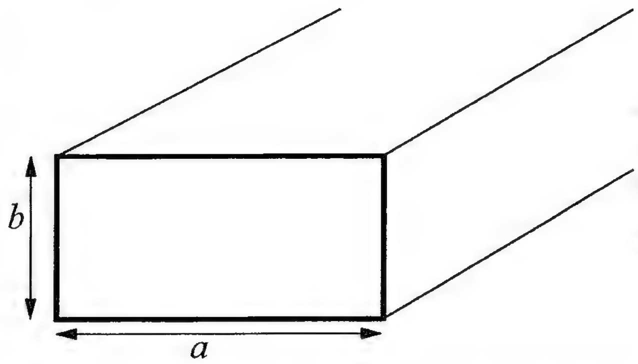

$a = 20$ mm
$b = 10$ mm
90-140 GHz
$\alpha = 3.6$ dB/m

Rectangular Dielectric Waveguide

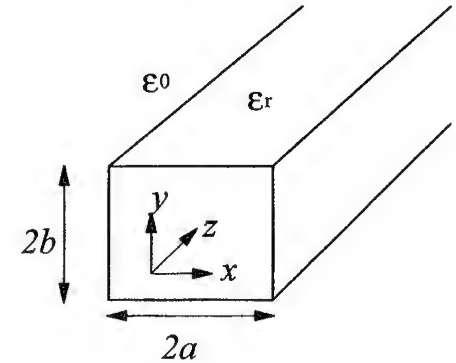

$a = 10$ mm
$b = 5$ mm
$\varepsilon = 2$
80-150 GHz
$\alpha = 1$ dB/m

Microstrip

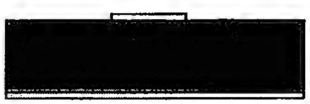

Coplanar

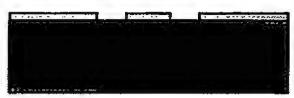

Slot Line

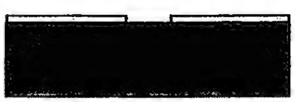

Fin Line

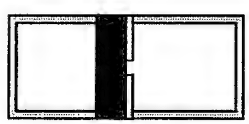

Some useful definitions

- Limits for operation of coaxial lines
  - waveguide modes
  - loss
  - tolerances and manufacturability

OD (mm)	ID (mm)	f max (GHz)	Loss at 1GHz (dB/m)
14	6.08	8.5	0.1
7	3.04	18	0.2
3.5	1.52	34	0.4
2.82	1.22	40	0.5
2.4	1.04	50	0.6
1.85	0.80	65	0.8
1	0.43	110	1.4

Some useful defintions (contd.)

- Waveguide specifications

Band	Frequency (GHz)	Waveguide EIA	ID (a x b) (mm)	Tolerance (μm)	Cutoff (GHz)	Attenuation (dB/m)*
K	18-26.5	WR-42	10.668 x 4.318	+5.1	14.047	0.35
Ka	26.5-40	WR-28	7.112 x 3.556	±3.81	21.081	0.5
Q	33-50	WR-22	5.690 x 2.845	±2.54	26.342	0.7
U	40-60	WR-19	4.775 x 2.388	±2.54	31.357	0.9
V	50-75	WR-15	3.759 x 1.880	±2.54	39.863	1.3
E	60-90	WR-12	3.099 x 1.549	±2.54	48.350	1.7
W	75-110	WR-10	2.540 x 1.270	±2.54	59.010	2.3
F	90-140	WR-8	2.032 x 1.016	±1.27	73.840	3.3
D	110-170	WR-6	1.651 x 0.8255	±1.27	90.840	4.6
G	140-220	WR-5	1.295 x 0.6477	±1.27	115.750	6.5
Y	170-260	WR-4	1.092 x 0.5461	±1.27	137.520	8.5
J	220-325	WR-3	0.8636 x 0.4318	±1.27	173.280	11.6

* at high frequency end of band (approx., Ag)

Quasi-optical systems

- Dielectric guides (fibres) work well for visible and near-visible - free-space very low loss and well-suited to millimetre applications.
- Ray optics, beams, lenses, etc. assume sizes which are thousands of wavelengths and transmitted via plane wave beams.
- Can make compact using GBM (Gaussian Beam Mode) - small beam size, phase-front curvature, etc.
- Fundamental mode has no cutoff frequency.

Use of Waveguides at Terahertz Frequencies

- Losses increase rapidly with frequency
- Fabrication difficulties, tolerances
  - problems of construction of components inside guide
- Surface resistance
  - can be up to 25% worse than theory
- Surface roughness
- Power handling

Gausssian Beams in Free Space

- Usual techniques of geometrical optics require components at least 100λ
- Issues of diffrcation, focussing collimation, etc.
- Gaussian beams
  - paraxial (cross-section small enough to be considered plane
  - *scalar* field distribution
  - minimum value at *beam-waist* (quasi-focus)
    - e.g. for λ=1mm, feed aperture ratio 10 beam waist approx 6 mm approx. 120 mm between 40mm lenses/mirrors
  - power losses <0.1 dB

Gaussian Beam Amplitude

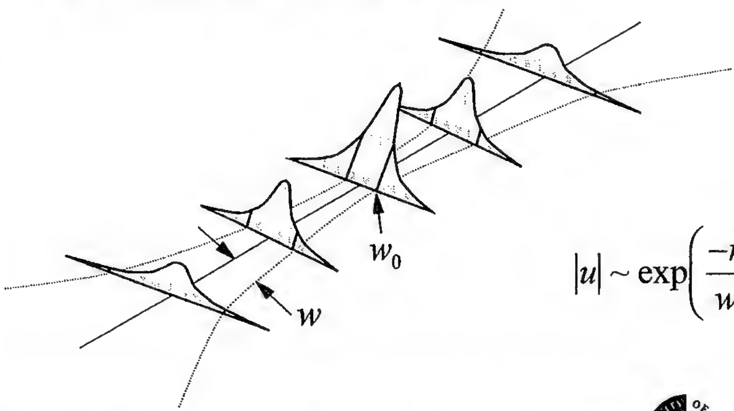

$$|u| \sim \exp\left(\frac{-r^2}{w^2}\right)$$

Parameters of Gaussian Beam

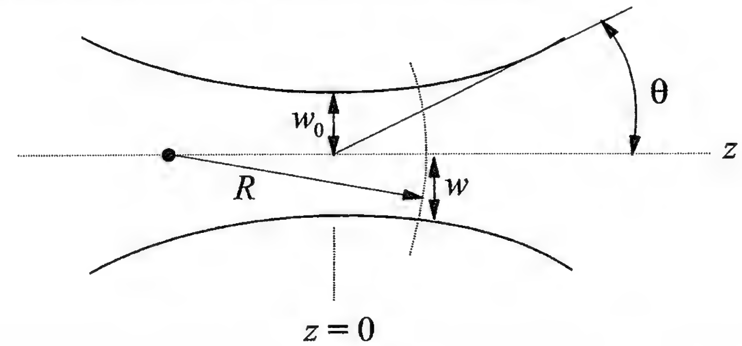

Field distribution in RDWG

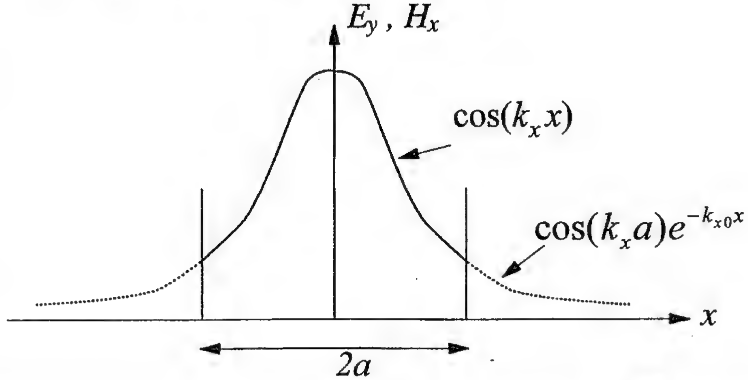

Gaussian Beam Mode Theory (1)

$\nabla^2\psi + k^2\psi = 0$ where $k = 2\pi/\lambda$

if we define

$\psi = u(x,y,z)\exp(-jkz)\exp(j\omega t)$

and assume $\dfrac{\partial^2 u}{\partial z^2} \to 0$

$$\frac{\partial^2 u}{\partial x^2} + \frac{\partial^2 u}{\partial y^2} - 2jk\frac{\partial u}{\partial z} = 0.$$

Gaussian Beam Mode Theory (2)

The fundamental mode solution is

$$u = \frac{w_0}{w}\exp\left(\frac{-r^2}{w^2}\right)\exp[-j(kz-\phi)]\exp\left(\frac{-jkr^2}{2R}\right)$$

where

$$w^2 = w_0^{\,2}\left[1+\left(\frac{\lambda z}{\pi w_0^{\,2}}\right)^2\right] \qquad R = z\left[1+\left(\frac{\pi w_0^{\,2}}{\lambda z}\right)^2\right]$$

$$\phi = \arctan\left(\frac{\lambda z}{\pi w_0^{\,2}}\right) \qquad r^2 = x^2 + y^2$$

for large values of $|z|$, $\theta = \dfrac{\lambda}{\pi w_0}$

Scattering Parameters

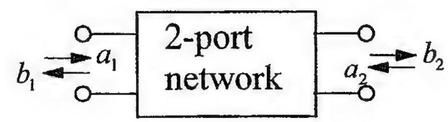

$$b_1 = S_{11}a_1 + S_{12}a_2$$
$$b_2 = S_{21}a_1 + S_{22}a_2$$
$$\begin{pmatrix} b_1 \\ b_2 \end{pmatrix} = \begin{pmatrix} S_{11} & S_{12} \\ S_{21} & S_{22} \end{pmatrix}\begin{pmatrix} a_1 \\ a_2 \end{pmatrix}$$

$S_{11} = \left.\dfrac{b_1}{a_1}\right|_{a_2=0}$ input reflection coefficient with output matched

$S_{21} = \left.\dfrac{b_2}{a_1}\right|_{a_2=0}$ forward transmission coefficient with output matched

Scattering Parameters

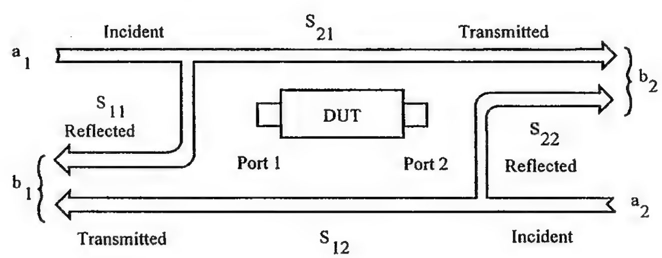

$$b_1 = S_{11}a_1 + S_{12}a_2$$
$$b_2 = S_{21}a_1 + S_{22}a_2$$

Basic measurement issues

- Sources
  - power
  - spurious
  - match
- Detectors
  - diodes
  - bolometers
- Downconverters
- Passive elements
  - connectors and flanges
  - calibration components

Network Analyzer

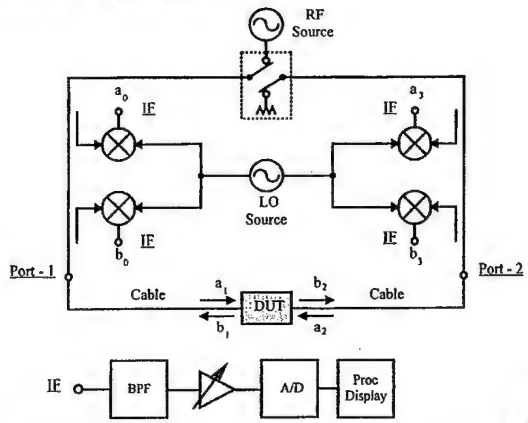

Time Domain Measurements

Calculated:

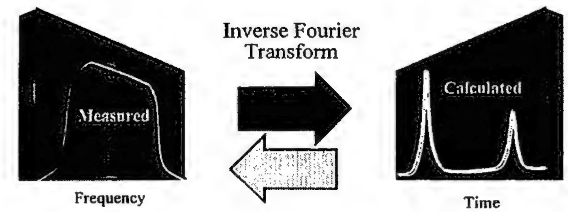

Network Analyzer Displays

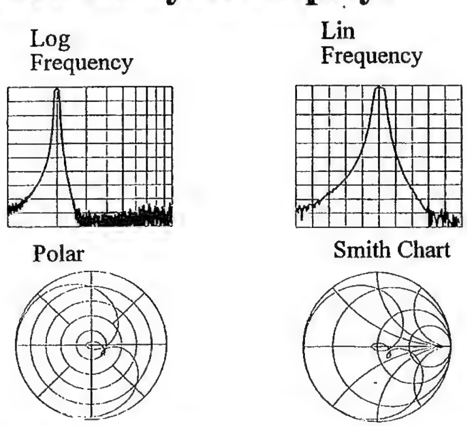

Time Domain Gating

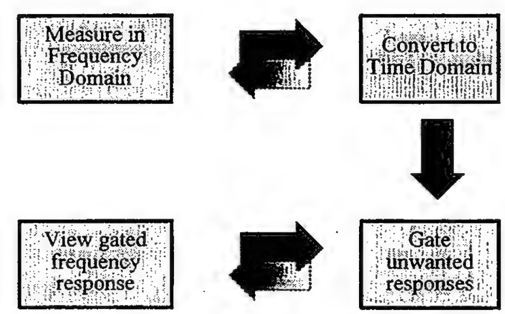

Time Domain Example Input/Output Launches

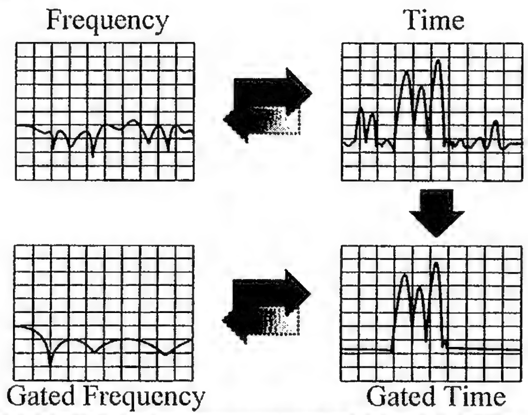

Six-port reflectometer

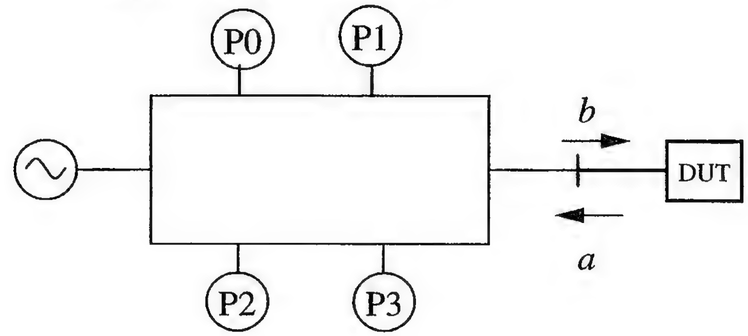

Reflectometers

- Dual-directional couplers - scalar detection
  - magnitude only
  - low cost
  - limited dynamic range
- Six-port and related techniques (vector)
  - dynamic range depends on detectors
  - lowest cost vector solution
  - slow
- Quasi-optical techniques
- Vector network analyzer range extenders

Six-port reflectometer

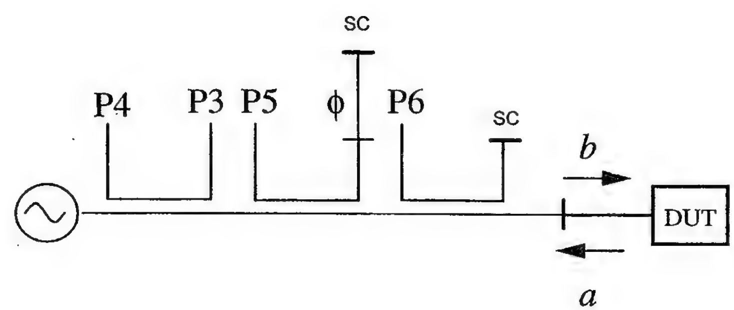

Multi-state reflectometer

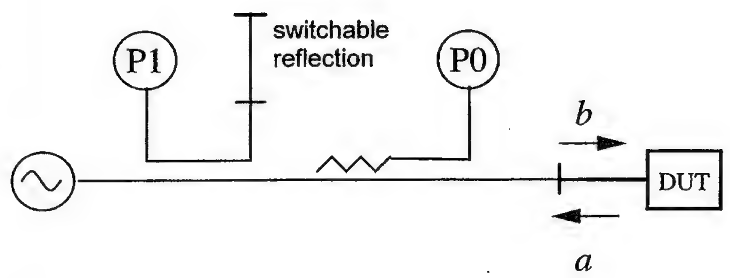

Vector network analyzer frequency extension

- Synthesizer + frequency multiplier as mm-wave source.
- Harmonic mixers allow use of 2-8 GHz L.O.
  - phase lock or synthesis ensures that IF is precisely 20 MHz required for receiver.
  - resolution and multiplication factor determine stimulus frequencies.
- Full two-port operation, error correction and time domain available.

Vector network analyzer frequency extension

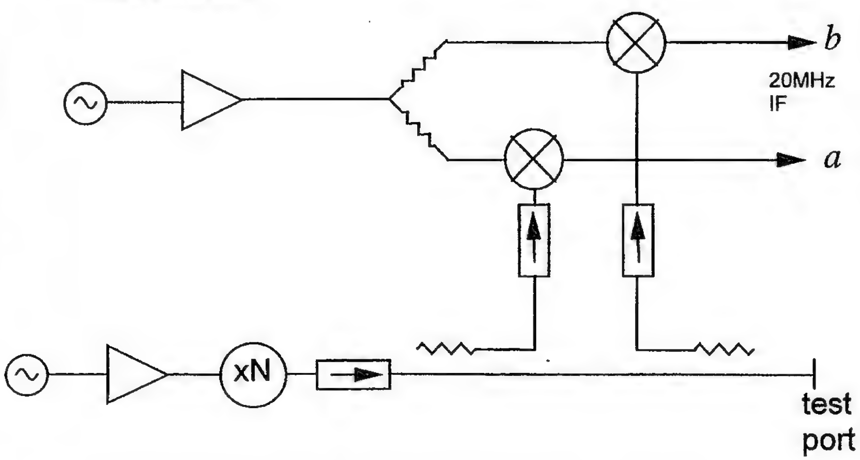

Quasi-optical reflectometer

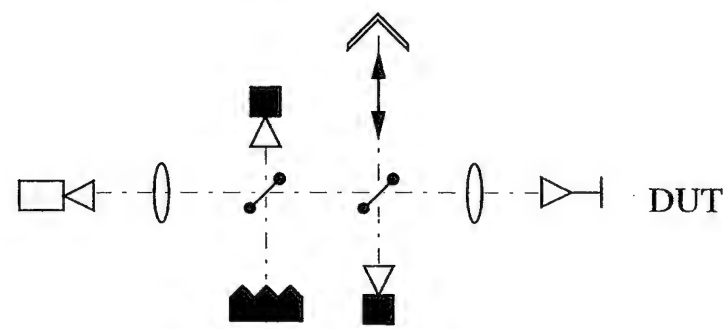

Quasi-optical reflectometer

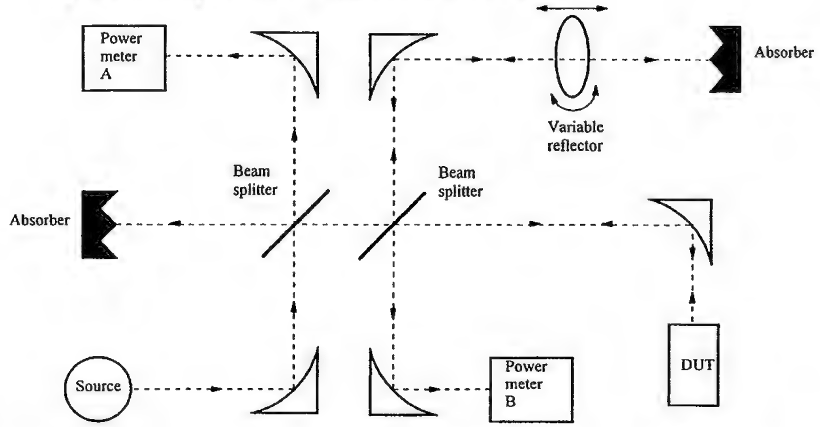

Accuracy Improvement

Cal Type	When to Use	Errors Removed
Uncorrected	* Transmission Measurement * Reflection Measurement Convenient but generally not accurate	None
Response (Normalization)	* Transmission Measurement * Reflection Measurement When highest accuracy not required	Tracking only (Frequency response)
S_{11} 1-Port	* Reflection Measurement Highest accuracy for 1-port devices	Directivity Port-1 Match Reflection Tracking
Full 2-Port	* Transmission Measurement * Reflection Measurement Highest accuracy for 2-port devices	Directivity Port-1 and Port-2 Match Refl & Trans Tracking Crosstalk

Measurement Errors

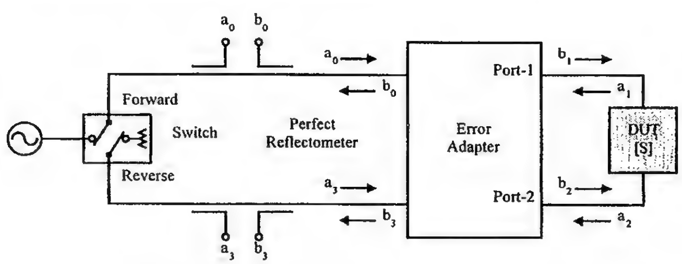

Microwave Errors (Forward)

Directivity	Port-2 Match
Port-1 Match	Transmission Tracking
Reflection Tracking	Crosstalk

Calibration Standards

Open	Thru
Short	Line
Load	Etc.

Accuracy Improvement

Calibration Removes Frequency & Response Mismatch Errors

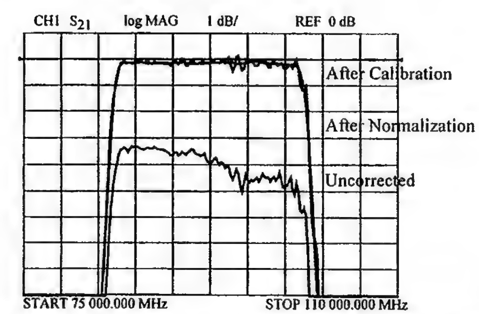

Error Correction Methods

TOSL	Thru (T) with known S-parameters [4 conditions]	3 known Reflects (OSL) on port-1 [3 conditions]	3 known Reflects (OSL) on port-2 [3 conditions]
TRL & LRL	Thru (T) or Line (L) with known S-parameters [4 conditions]	Unknown equal Reflect (R) on port-1 and port-2 [1 condition]	Line (L) with known S_{11} and S_{22} [2 conditions]
TRM & LRM	Thru (T) or Line (L) with known S-parameters [4 conditions]	Unknown equal Reflect (R) on port-1 and port-2 [1 condition]	Known Match (M) on port-1 and port-2 [2 conditions]
TXYZ & LXYZ	Thru (T) or Line (L) with known S-parameters [4 conditions]	3 known Reflects (XYZ) on port-1 or port-2 [3 conditions]	
UXYZ	Unknown Line (U) with $S_{12} = S_{21}$ [1 condition]	3 known Reflects (XYZ) on port-1 [3 conditions]	3 known Reflects (XYZ) on port-2 [3 conditions]

A Known Reference Impedance and a Port-1 to Port-2 Connection are Required
A Thru Measurement with Terminations on Port-1 and Port-2 is also Required for Leakage Calibration

Solution of equations (de-embedding)

Measured S - Parameters

$$\mathbf{S_m} = (\mathbf{T_1 S_A} + \mathbf{T_2})(\mathbf{T_3 S_A} + \mathbf{T_4})^{-1}$$

Actual DUT S - Parameters

$$\mathbf{S_A} = (\mathbf{T_1} - \mathbf{S_m T_3})^{-1}(\mathbf{S_m T_4} - \mathbf{T_2})$$

System equations (TOSL)

Actual and measured DUT

$$\begin{bmatrix} a_1 \\ a_2 \end{bmatrix} = \mathbf{S_A} \begin{bmatrix} b_1 \\ b_2 \end{bmatrix} \quad \begin{bmatrix} b_0 \\ b_3 \end{bmatrix} = \mathbf{S_M} \begin{bmatrix} a_0 \\ a_3 \end{bmatrix} \quad \mathbf{S_{A,m}} = \begin{bmatrix} S_{11A,m} & S_{12A,m} \\ S_{21A,m} & S_{22A,m} \end{bmatrix}$$

Error adaptor

$$\begin{bmatrix} b_0 \\ b_3 \\ a_0 \\ a_3 \end{bmatrix} = \mathbf{T} \begin{bmatrix} a_1 \\ a_2 \\ b_1 \\ b_2 \end{bmatrix} \quad \mathbf{T} \equiv \left[\begin{array}{c|c} T_1 & T_2 \\ \hline T_3 & T_4 \end{array}\right] = \left[\begin{array}{cc|cc} t_{00} & t_{03} & t_{01} & t_{02} \\ t_{30} & t_{33} & t_{31} & t_{32} \\ \hline t_{10} & t_{13} & t_{11} & t_{12} \\ t_{20} & t_{23} & t_{21} & t_{22} \end{array}\right]$$

Three 2-port ("TRL")Calibration

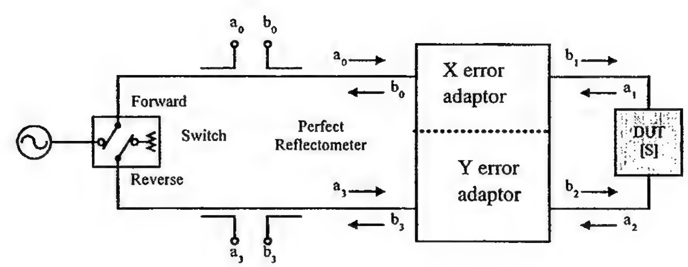

System equations (Three 2-ports, "TRL")

$\mathbf{M = X.A.Y}$ measured DUT

$\mathbf{M_1 = X.C_1.Y}$ measured 2 - port + cal. std 1

$\mathbf{M_2 = X.C_2.Y}$ measured 2 - port + cal. std 2

$\mathbf{M_3 = X.C_3.Y}$ measured 2 - port + cal. std 3

CPW Wafer Probing

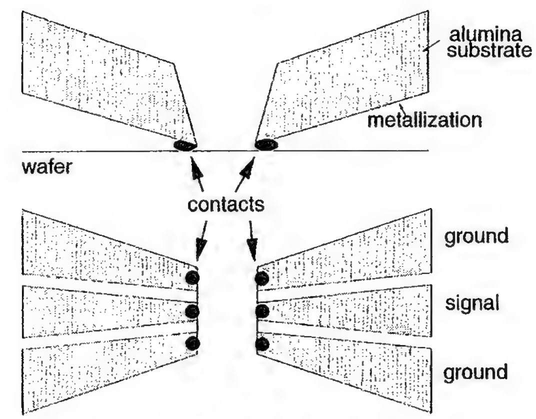

Calibration issues

- All the well-established cal. methods work at mm-wave.
- 1-port
  - Short, offset short, (sliding or offset) load
- 2-port
  - TRL (using precision waveguide shim)
- On-wafer
  - SOLT
  - LRL, LRM

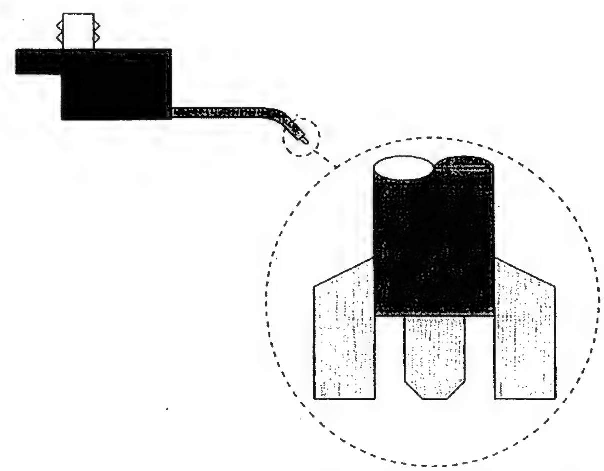

Spectrum Analyzer Frequency Extension by Harmonic Mixing

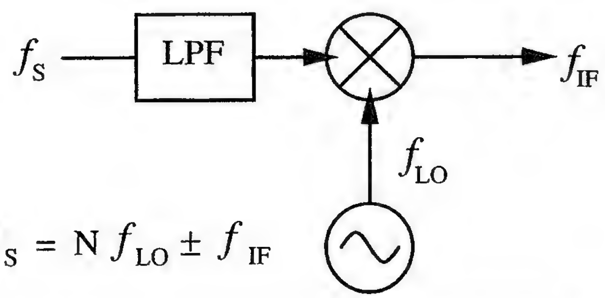

$$f_S = N f_{LO} \pm f_{IF}$$

Harmonic mixing tuning curves

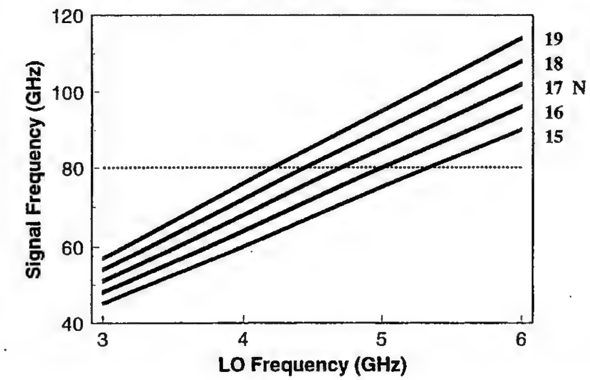

Harmonic mixing tuning curves

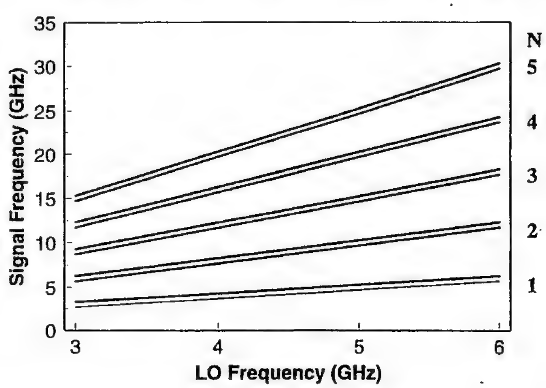

Signal Identification

- Preselection
  - usually impractical at mm-wave
- Image identification
  - change LO up and down by $2/n$ x IF.
  - response at higher LO = n- mixing mode
  - response at lower LO = n+ mixing mode
  - no response = incorrect value of n

Signal identification (contd.)

- Shift method
  - reduce second LO by m MHz
  - shift first LO by + or - m/n MHz
  - correct response at n- or n+ mixing mode when there is no frequency shift of displayed signal.
- Manual identification
  - set span wide enough to see response pair
  - responses separated by 2 x IF
  - if closer together, then higher harmonic number if further apart, then lower harmonic number

Conclusions

- Conventional transmission lines and components are difficult to manufacture and have high loss.
- Dielectric waveguide and quasi-optical techniques are recommended.
- Calibration and measurements successfully employ extensions of the same techniques developed at lower frequencies.

Recent developments in resonant tunneling components

Chris Van Hoof
IMEC, division MAP
Kapeldreef 75, B-3001 Leuven, Belgium
VANHOOFC@IMEC.BE

Overview of the lecture

1. Resonant tunneling transistors
- Definitions
- Growth and fabrication issues
- Characteristics

2. 3D integration of microwave sensors
- Passive components
- Active components
- Applications

3. Application of passive resonant tunneling components :
- A resonant tunneling pressure sensor

Resonant Tunneling Transistors (RTT)

C. Van Hoof
IMEC, division MAP
Kapeldreef 75, B-3001 Leuven, BELGIUM, vanhoofc@imec.be

Performance is the basic driving force causing downscaling of devices in micro-electronics. The minimal junction width is one of the fundamental downscaling limits for bipolar devices. This limit can be bypassed by replacing the junctions by tunneling barriers. The high tunneling speeds will move the frequency limitations.

However, also the minimally required width of the base layer (for reasons of resistivity) seems to be one of the fundamental limits. The preferred solution to overcome this limit is to use two-dimensional electron gasses as base layer because of their high mobility.

As soon as the first resonant tunneling devices were realized [1], one has tried to control the amount of tunneling carriers. In principle, every transistor in which resonant tunneling occurs could be called a resonant tunneling transistor, which then involves many devices [2]. In this workbook summary we consider a confined class of devices that can be studied as a group. We will only consider three terminal devices in which carriers tunnel resonantly from the emitter to the collector through a double (or multiple) barrier structure and in which a quantum well base layer is added in order to obtain control over the (electrical or optical) device output. Excluded from this overview are integrations of conventional transistors (HEMTs and MESFETs) and resonant tunneling devices. These will be addressed during the course.

1. *An overview of four classes of RTT's.*

We can classify all devices belonging to the area of resonant tunneling transistors in four groups according to their carrier nature and according to the position of the base quantum well. Considering the carrier nature, we can distinguish between unipolar and bipolar devices. A further classification is obtained by distinguishing between devices in which the quantum well, where confinement determines the tunneling current, forms the transistor base and others. In the latter case, an extra (modulation-doped) well is added to the structure. These four groups are summarized in table 1

	Unipolar devices	Bipolar devices
Base and tunneling quantum well are equal	Bound-State Resonant Tunneling Transistor	Bipolar Quantum well Resonant Tunneling Transistor
Base and tunneling quantum well are different	Resonant tunneling Hot Electron Transistor	Resonant Tunneling Light Emitting Transistor

Table 1. The classification of RTT

1.1. Unipolar device.

The Bound-State Resonant Tunneling Transistor (BSRTT) has been proposed first by Schulman *et al.* [3] and Haddad *et al.* [4]. The principle of operation of this device is described in figure 1

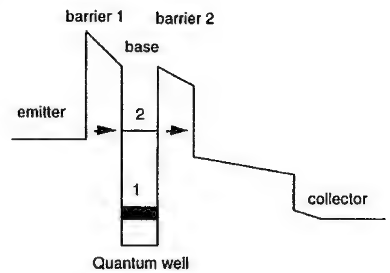

Figure 1 Principle of operation of the Bound-State Resonant Tunneling Transistor. The first energy level is strongly populated by confined electrons to obtain a good base conductivity. Changing the bias applied to this layer will change the band structure and in this way also the position of the second energy level. The second energy level is used for resonant tunneling from the emitter to the collector.

The base quantum well is made of a semiconductor with a lower bandgap than the emitter layer so that the first energy level is far below the conduction band of the emitter. Tunneling can only occur using the second energy level.

The second barrier consists of 2 parts: the first part is a small but high barrier to have a high tunneling rate through the second energy level combined with a good confinement of that energy level at any bias. The second part is an additional barrier to prevent tunneling escape from the first energy level. This additional barrier needs to be effective even under a high base-collector bias. We will discuss this device more in detail during the lecture.

1.2. Unipolar device with separated base quantum well.

The Room-Temperature Resonant-tunneling Hot-Electron Transistor (RT-RHET) evolved from a transistor with a wide base and no confinement [5, 6] to a device with a 10 nm base and hence confinement [7]. Initially, the wide base was used to obtain a low base resistance (figure 2).

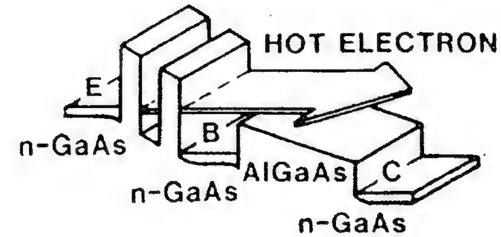

Figure 2 Principle of operation of the Resonant-tunneling Hot-Electron Transistor. The major part of the electrons that tunnel through the double barrier structure remains hot until they are above the base-collector separation barrier. The electrons that relax contribute to the base current. After reference [6]

To obtain a good room temperature operation, the base width was reduced from 60 nm to 10 nm [7]. In the case of a 10 nm wide base layer, this transistor corresponds to our definition of a Resonant Tunneling Transistor.

This device has been mentioned in 1991 by the Japanese Research and Development Association for future Electron Devices as the device that can realize a breakthrough in speed limitations [8].

A general band structure of a unipolar Resonant Tunneling Transistor with separated quantum wells is given in figure 3

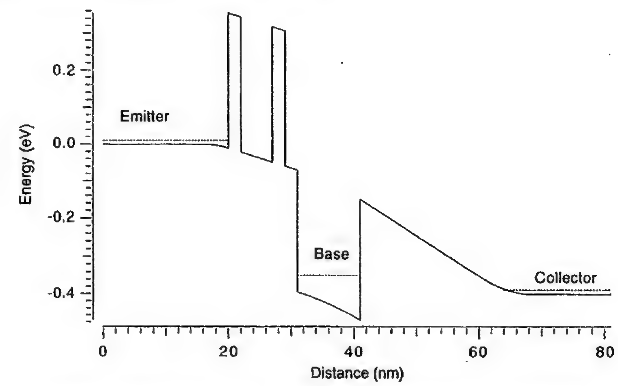

Figure 3 Band structure of the unipolar tunneling transistor with a separation between the tunneling quantum well and the base quantum well.

1.3. Bipolar Devices.

1. *The bipolar device proposed by Seabaugh.*

The bipolar alternative of the RTT has been proposed first by Ricco and

Solomon [9]. The first realization of this device, including the negative transconductance, has been reported by Seabaugh and Reed [10-12]. However, the operation of this device is still controversial [13].

It was realized using an n-type emitter and collector and a p-type double barrier tunneling structure, but also the inverse is conceptually feasible. A superlattice is added in both the emitter and the collector to restrict the tunneling in the quantum well to the second electron energy level. The base contact is realized by a p-implantation, providing the required isolation.

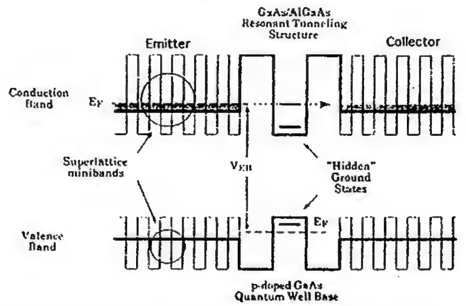

Figure 4 Schematic band diagram of the BiQuaRTT. After reference [11].

This device requires a high doping concentration in the base, which deteriorates the device characteristics. The multiple-quantum-well base equivalent of this structure has also been realized [14] and recently, clear negative differential resistance characteristics have been observed [15].

2. *The bipolar device proposed by Iogansen.*

Another bipolar device in which the base quantum well is used as the tunneling quantum well has been proposed recently by Iogansen [16]. A schematic band structure that also explains the principle of operation is given in figure 5. The electrons tunnel from the first electron state in the emitter quantum well to the collector using the second hole state in the base quantum well. The first hole state in the base quantum well is used to obtain a good base conductivity.

The difference with the devices in the previous section is twofold. It is an interband tunneling transistor and it is a triple-barrier device. It is bipolar because the emitter carriers are different from the base carriers. Nevertheless it also resembles strongly to the bound-state resonant tunneling transistor because the first energy level in the base is highly populated for a good base conduction combined with a second energy level used for tunneling. This means that almost all remarks that will be made further on enhanced base current due to intersubband relaxation in the Bound State Resonant Tunneling Transistor (BSRTT) also apply to this device.

Another major difference between the BiQuaRTT of Seabaugh and this device is that the base in this device can remain undoped. This will allow to obtain better characteristics.

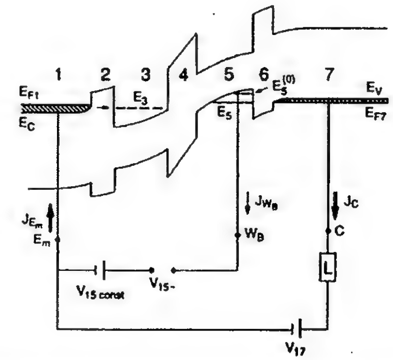

Figure 5 The interband resonant tunneling transistor by Iogansen. [16]

3 *Other possible interband devices.*

The triple barrier device proposed by Iogansen has both the advantages and disadvantages related to charging and alignment in triple barrier devices. In terms of advantages, it acts as a better energy filter and leads to sharper resonances. In terms of disadvantages, the large amount of charging screens the electric field across the quantum wells leading to large bistabilities in the I(V) characteristics. Another material system may be more advantageous for the interband resonant tunneling transistor. We propose the pseudomorphic $InAs/GaSb_{0.91}As_{0.09}$ and $GaSb/InAs_{0.91}Sb_{0.09}$ systems (see figure 6). In both cases we use AlSb as barrier material and for the p-type quantum well base layer we use the strained GaSb to confine the bound state. The asymmetry in the position of the additional bound state quantum well is introduced to diminish the tunneling escape from the quantum well although it can also have an important influence on the intersubband relaxation rate. For the $InAs_{0.91}Sb_{0.09}$ quantum well no strained quantum well is added because the band discontinuity in the conduction band is not big enough (see figure 1.1). The escape from the bound state is much lower in an interband device because interband tunneling occurs between two occupied states (with an opposite carrier), and the emitter has a low occupation at high energies.

The major difference between this device and the Bound State Resonant Tunneling Transistor is that a higher base ground-level population can be easily obtained. No doping is required. A high position of the Fermi level in the base is almost automatically obtained using a lowly doped emitter. The Fermi level in the base can be easily varied without causing a leakage current to the emitter or collector layer. The leverage factor of the base steering will be high without deteriorating the device performance.

The quantum well base contact could be made in a similar way as the BiQuaRTT, i.e. by an implantation. However, for these devices, it is not that evident. InAs, a material with n-type background has to be made p-type by ion implantation. GaSb, a material with p-type background has to be made n-type by ion implantation. Little is known yet about these issues. It is preferable to make the base contact using the self-

aligned base contact technology discussed further in the text. The surface pinning of InAs prevents the free base layer from being depleted. No highly resistive part in the base resistance is present, which allows high frequency operation.

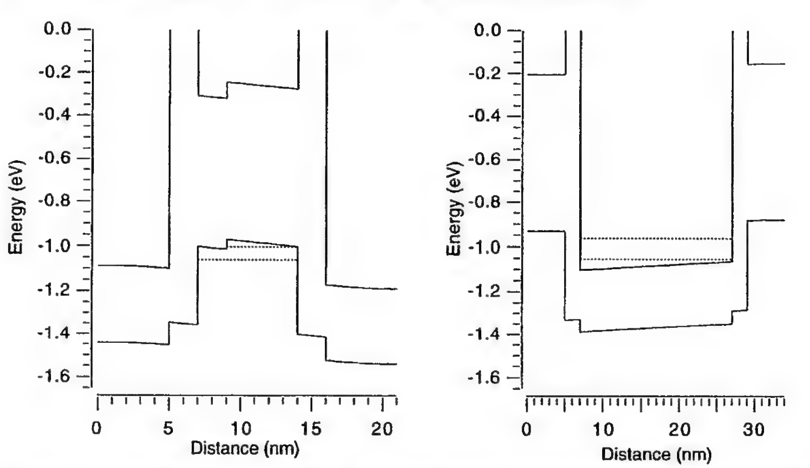

Figure 6 Suggestions for double-barrier interband resonant tunneling transistors in the InAs/GaSb$_{0.91}$As$_{0.09}$ (left) and GaSb/InAs$_{0.91}$Sb$_{0.09}$ (right) pseudomorphic systems.

The intersubband relaxation is as problematic in these devices as in all previously mentioned devices, but this is the only drawback of the proposed new device. However, type II heterostructures offer possibilities to prevent or reduce the optical phonon relaxation (which is the dominant relaxation) by a proper design of the in-plane dispersion relations. The last part of this overview will address this concept.

1.4. Bipolar devices with separated quantum well's .

The Resonant Tunneling Light Emitting Transistors (RTLET's) and the Barrier Base Bipolar Resonant Tunneling Transistors (BBBRTT's) both belong to the class of bipolar Resonant Tunneling Transistors with separated tunneling and base quantum wells.

1. *Resonant Tunneling Light Emitting Transistors (RTLET's).*

Due to the reduced density of states, electrons in a 2DEG need to reside on a higher energy (Pauli principle) which makes a 2DEG unable to screen an electric field completely [17, 18]. The RTLET design is based on this incomplete screening. A relatively lowly-populated base quantum well acts as a transparent base which allows us to maintain the emitter-collector tunneling characteristics, including the NDR feature and oscillation region. At the same time, we can use the quantum-well base layer to inject minority carriers into the tunneling structure [19]. Two types are possible: the npn-type and the pnp-type. Both types are discussed below.

1. **npn-type RTLET**

In the npn-type RTLET (see figure 7) electrons tunnel from the n-doped emitter to the n-doped collector through a double-barrier tunneling structure. The emitter-collector current-voltage characteristics are similar to the characteristics of an n-type double barrier tunneling structure, i.e. a region of oscillation or bistability. A quantum-well base layer is added behind the tunneling structure and is populated with holes (minority carriers).

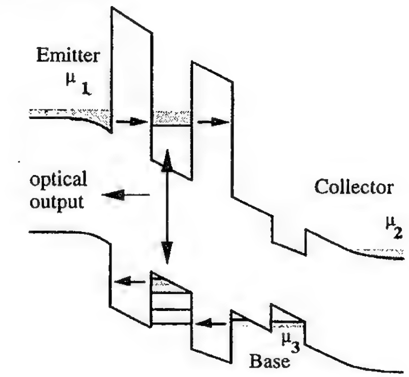

Figure 7 Schematic band diagram for the npn RTLET.

The base contact made on this quantum well layer allows the injection of minority carriers through the tunneling structure, without influencing the emitter-collector current-voltage characteristics. These injected carriers partly recombine in the tunneling quantum well which results in an optical output at the exciton wavelength. This optical output follows both independently the oscillation of the majority carriers and the applied changes in the injected base current. In this way an electro-optical heterodyne conversion could be obtained.

2. **pnp-type**

The operation of the pnp-type RTLET (see figure 8) is completely equivalent to the npn-type RTLET. The holes are the majority carriers and the electrons the injected minority carriers. The use of electrons as base carriers results in a higher base mobility and makes the technology to contact the base layer easier. However, the tunneling speed is lower for the holes (majority carriers) than for the electrons. This decreases the maximal operation frequency of this device.

This pnp-RTLET will be discussed during the lecture.

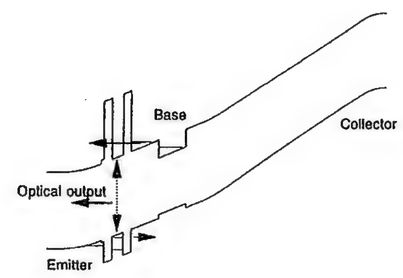

Figure 8 Schematic band diagram for the pnp RTLET.

2. *Barrier Base Bipolar Resonant Tunneling Transistors (BBBRTT)*

The possibility to grow materials with a staggered band alignment (see figure 1) allows the growth of a layer structure in which a quantum well in the valence band is a barrier in the conduction band (a) or vice versa (b). The base layers, populated with minority carriers can be in this case the barriers of the tunneling structure. The two possibilities that we suggest are shown schematically in figure 9. The classification above based on clearly separated quantum wells is, for this device not evident any more. Indeed, the wells are separated in energy and in space but the problem of e.g. carrier-carrier scattering during tunneling (resulting in a deterioration of the linewidth) is here also problematic and the spatial separation is not big enough to prevent indirect transitions.

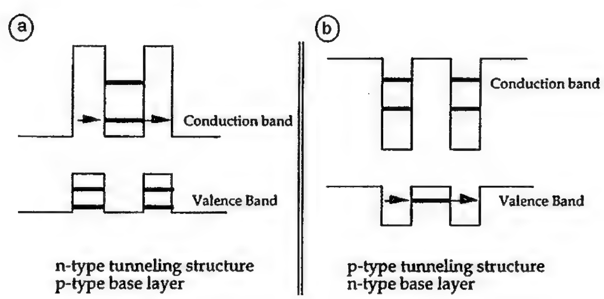

Figure 9 (a) Modulation of the resonant tunneling electron current due to hole quantum well base layers formed by the electron barriers and (b) the modulation of the resonant tunneling hole current due to electron quantum well base layers formed by the hole barriers .

Recently, Chow and Schulman have studied this layer structure (type a) as a diode [20] and observed huge intrinsic bistability due to large accumulation of holes

in the second barrier after bringing the barrier level above the Fermi level in the collector. We should be able to obtain these huge current changes by contacting the $Al_xGa_{1-x}Sb$ barrier layer. A contact technology by etching and regrowing, similar to the RTLET, is almost impossible on this layer because the rapid oxidation of both the Al and the Sb. But a good base contact could be obtained by a p-type implantation.

The GaSb/AlSb (1 nm)/ GaSb (4nm)/AlSb (1 nm)/ GaSb structure, which is rather similar to the structure of type b, gave a poor peak-to-valley ratio at 77K [21]. On the devices of type (b) the same base-contact technology could be used as developed in this thesis for the RTLET.

2. *The feasibility of the different options.*

2.1. Theoretical comparison.

- High intersubband relaxation.

In many Resonant Tunneling Transistors the second energy level in the quantum well is used for the tunneling from the emitter to the collector.

If this second energy level is separated from the first by more than the energy of an optical phonon (~36 meV), which is usually the case, intersubband relaxation will occur at a high rate [22, 23]. This will give rise to high emitter-base current and will reduce the amplification.

If the separation is smaller than the optical phonon energy, it becomes almost impossible to populate only the ground level via the contact layers. Moreover, the small energy separation does not allow the fabrication of an efficient additional barrier for the ground state. Also in this case we will have a high base current and a low amplification. The effects of intersubband relaxation will be discussed in more detail further in the text.

- High carrier-carrier scattering rate during tunneling.

The linewidth of the energy level is strongly dependent on the scattering rate [24]. This broadening of the energy level deteriorates the tunneling characteristics. This is especially the case for devices that use the tunneling quantum well as the base of the transistor (devices described in sections 2.1 and 2.3).

- High carrier-dopant scattering rate during tunneling.

The devices that use the tunneling quantum well as the base usually require a high doping in order to obtain a good base conductivity. This doping deteriorates the linewidth and the tunneling characteristics in a similar way as described above.

- Low leverage factor of the base steering.

All devices that have a quantum well base layer suffer from the fact that the leverage factor of the base steering is not unity. (see below). In contrast

with the two former topics, this handicap becomes more important when the charge in the base layer is smaller. This handicap applies to all four device types.

- High recombination rate in the tunneling quantum well.

  The presence of both electrons and holes will give rise to a large optical recombination rate, in all bipolar devices (devices described in sections 2.3 & 2.4). In the RTLET this is wanted because the optical output is the aim. In the BiQuaRTT, this recombination rate will give an increase in base current.

2.2. Technological comparison.

- Base-to-collector separation is difficult.

  In unipolar devices (devices described in sections 2.1 & 2.2) it is always difficult to foresee a good tunneling probability from the emitter via the base to the collector and to restrict in the same time the tunneling from the base to the collector for a much larger amount of carriers with a lower energy. In the bipolar devices, one can use the pn junction to separate the base from the collector.

- The realization of a good Ohmic contact on a 10 nm thick layer is not evident.

  In a traditional Ohmic metalization scheme, there is always a Schottky barrier present which is made very small by high semiconductor doping, penetrating in the semiconductor from the metal during the alloy process. This penetration is always a few nanometers, having spikes up to 80 nm. In the case of a contact on a quantum well, this is not allowable. This problem can be solved in several ways, using the PdGe technology, in which experiments indicate that no spiking occurs [25], using MBE-regrowth on the base contact or using an implantation in the case of a bipolar device.

- Surface pinning completely depletes the free base layer.

  A free base layer may result in a complete depletion of the base depending on the Fermi-level pinning. A remaining barrier of about 5 nm on top of the base quantum well is enough to stop the surface recombination rate and the remaining charge will be dependent on the band structure as determined by the pinning position [26].

- The wet etching down to the base layer (10 nm) must be done under strict control

  This problem does not occur for the bipolar devices where the contact is made by implantation.

3. *Conclusions.*

Resonant Tunneling Transistors have been proposed to overcome the scaling limits and speed restrictions of bipolar transistors. The limit of the minimal junction width can be overruled when junctions are replaced by tunneling barriers. The shorter devices allow to obtain a higher speed when the speed is restricted by the transit time through the device.

This overview summarized Resonant Tunneling Transistors with a two-dimensional electron gas as the base layer. Two major intrinsic problems have been reported to deteriorate the device performance, namely the low leverage factor of the base steering and the relaxation problems in the base layer.

The low leverage factor of the base steering is a repercussion of the Pauli principle: additional electrons in the base layer are forced to reside on higher energies. As a consequence, the changes in the Fermi-level do result in much smaller changes in band structure and the base contact does not obtain a good control over the tunneling current.

The influence of intersubband relaxation in a resonant tunneling transistor on the performance degradation is similar to the influence of the recombination in the base layer of a bipolar transistor. Both effects result in a additional base current and a reduction of the gain. However, the intersubband relaxation rate is some orders of magnitude larger than the recombination rate in the base layer of a bipolar transistor. The reduction of this intersubband relaxation is a major topic.

The technological problems to realize a good Ohmic contact on this two-dimensional base layer are also compared in the different devices.

4. *References.*

1. R. Tsu and L.Esaki, "Tunneling in a finite superlattice", *Appl. Phys. Lett.* **22** pp 562-564 (1973).
2. F. Capasso, S. Sen, A. F. Cho and D. L. Sivco, "Multiple negative transconductance and differential conductance in a bipolar transistor by sequential quenching of resonant tunneling", *Appl. Phys. Lett.* **53**(12) pp 1056-1058 (1988).

J. N. Schulman and M. Waldner, "Analysis of second level resonant tunneling diodes and transistors", *J. Appl. Phys.* **63**(8) pp 2859-2861 (1988).

4. G. I. Haddad, R. K. Mains, U. K. Reddy and J. R. East, "A proposed narrow-band-gap base transistor structure", *Superlattices and Microstructures* **5**(3) pp 437-441 (1989).
5. T. Mori, H. Ohnishi, K. Imamura, S. Muto and N. Yokoyama, "Resonant Tunneling hot-electron transistor with current gain of 5", *Appl. Phys. Lett.* **49**(26) pp 1779-1780 (1986).
6. N. Yokoyama, K. Imamura, H. Ohnishi, T. Mori, S. Muto and A. Shibatomi, "Resonant-Tunneling Hot Electron Transistor (RHET)", *Solid-State Electronics* **31**(3/4) pp 577-582 (1988).
7. A. C. Seabaugh, Y.-C. Kao, J. Randall, W. Frensley and A. Khatibzadeh, "Room

Temperature Hot Electron Transistors with InAs-Notched Resonant-Tunneling-Diode Injector", *Jpn. J. of Appl. Phys.* **30**(5) pp 921-925 (1991).

8. Activities of the Research and Development Association for future Electron Devices", *FED Journal* 1991 pp 44-60.
9. B. Ricco and P. M. Solomon, *IBM Tech. Dig. Bull.* **27** pp 3053 (1984).
10. A. C. Seabaugh, M. A. Reed, W. R. Frensley, J. N. Randall and R. J. Matyi, "Realization of Pseudomorphic and Superlattice Bipolar Resonant Tunneling Transistors", Proceedings of *IEDM*, Washingthon DC, 1988, 900-902.
11. M. A. Reed, W. R. Frensley, R. J. Matyi, J. N. Randall and A. C. Seabaugh, "Realization of a three-terminal resonant tunneling device: The bipolar quantum resonant tunneling transistor", *Appl. Phys. Lett.* **54**(11) pp 1034-1036 (1989).
12. A. C. Seabaugh, W. Frensley, J. Randall, M. A. Reed, D. L. Farrington and R. J. Matyi, *IEEE Trans. Electron Dev.* **36** pp 2328 (1989).

1 F. Capasso, "Is the Resonant Tunneling Transistor a Reality?", *Physics Today* (September) pp 132 (1990).

14. T. Waho, K. Maezawa and T. Mizutani, "Resonant Tunneling in a Novel Coupled Quantum well base Transistors", *Jpn. J. of Appl. Phys.* **30**(12A) pp L2018-L2020 (1991).
15. T. Waho, K. Maezawa and T. Mizutani, "Clear Negative Characteristics Observed in Coupled Quantum well base Resonant Tunneling Transistors", *IEEE Electron Device Lett.* **14**(4) pp 202-204 (1993).
16. L. V. Iogansen, V. V. Malov and J. M. Xu, "Time dependent theory of a double quantum well resonant interband tunnel transistor", *Semicond. Sci. Technol.* **8** pp 568-574 (1993).
17. S. Luryi, "Quantum capacitance devices", *Appl. Phys. Lett.* **52** pp 501-503 (1988).
18. S. Luryi, "Coherent versus incoherent resonant tunneling and implications for fast devices", *Superlattices and Microstructures* **5** pp 375-382 (1989).
19. J. Genoe, C. Van Hoof, K. Fobelets, R. Mertens and G. Borghs, "pnp resonant tunneling light emitting transistor", *Appl. Phys. Lett.* **61**(9) pp 1051-1053 (1992).
20. D. H. Chow and J. N. Schulman, "Intrinsic current bistability in InAs/AlGaSb resonant tunneling devices", *Appl. Phys. Lett.* **64**(1) pp 76-78 (1994).
21. R. Beresford, L. F. Luo and W. I. Wang, "Resonant tunneling of holes in AlSb/GaSb/AlSb double barrier heterostructures", *Appl. Phys. Lett.* **55**(7) pp 694-695 (1989).
22. T. P. E. Broekaert, *"Characterisation of InGaAlAs Resonant Tunneling Transistors "*, [PhD Thesis]. M.I.T., 1992.

2 T. P. E. Broekaert and C. G. Fonstad, "Quantum well intersubband relaxation in resonant tunneling diodes and transistors.", *J. Appl. Phys.* **72**(2) pp 746-753 (1992).

24. M. Büttiker, "Coherent and sequential tunneling in series barriers", *IBM J. Res. Develop.* **32** pp 63-75 (1988).
25. C. Van Hoof, J. Genoe, M. Van Hove, P. Jansen, M. Van Rossum and G. Borghs,

2. 3D integration of microwave sensors

The following slides give an overview of our work on 3D integration of microwave sensors. Passive and active components have been realized.

3D integration of microwave sensors

MCM-D

- Passive components

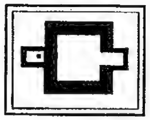

- Antenna

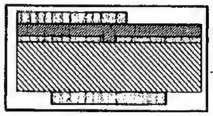

Active components

- Resonant tunneling diode

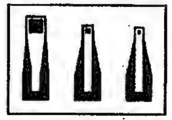

- HEMT

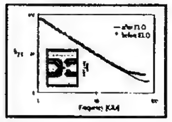

Epitaxial lift-off

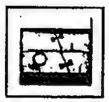

3D-integration of microwave sensors Aim

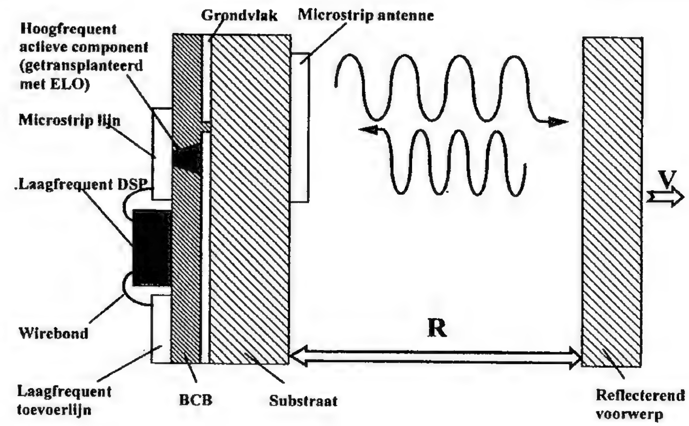

Passive components in MCM-D

Cross-section of MCM-D

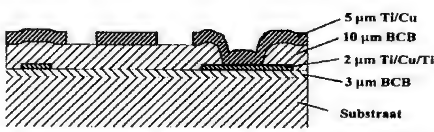

Planar capacitor

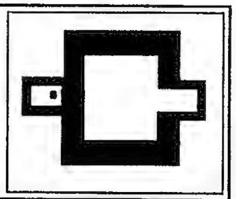

Spiral inductance

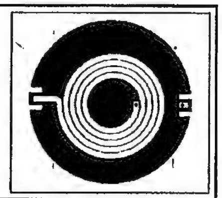

Example: Butterworth low-pass filter in MCM-D

Top-view

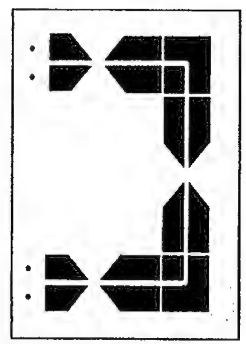

Transmission (measurements and simulation)

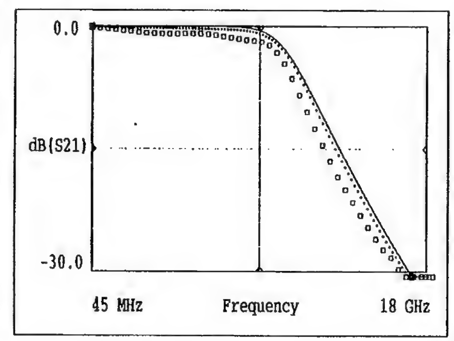

Realisation of integrated antenna in MCM-D

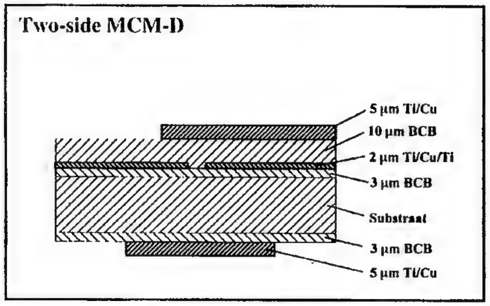

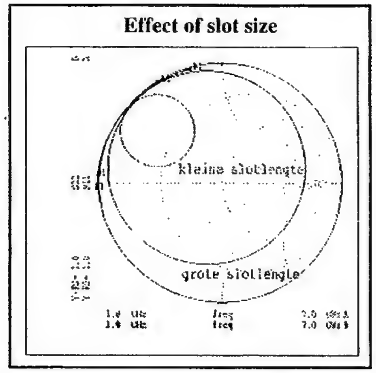

Active component:
Resonant Tunneling Diode

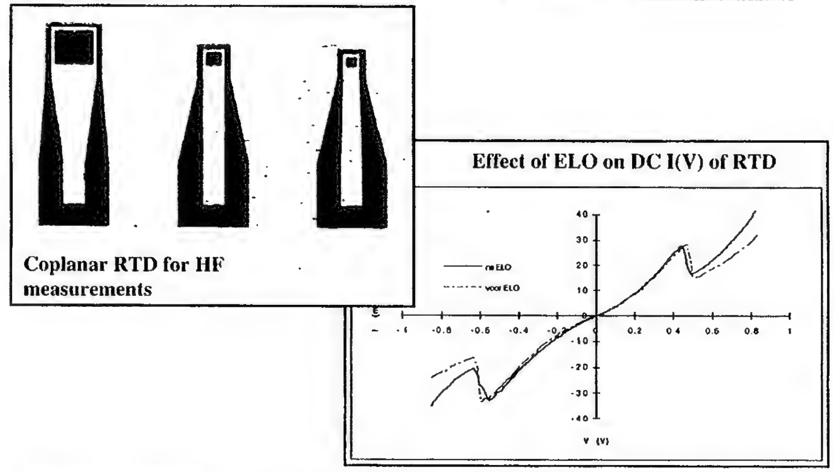

Active component:
High Electron Mobility Transistor

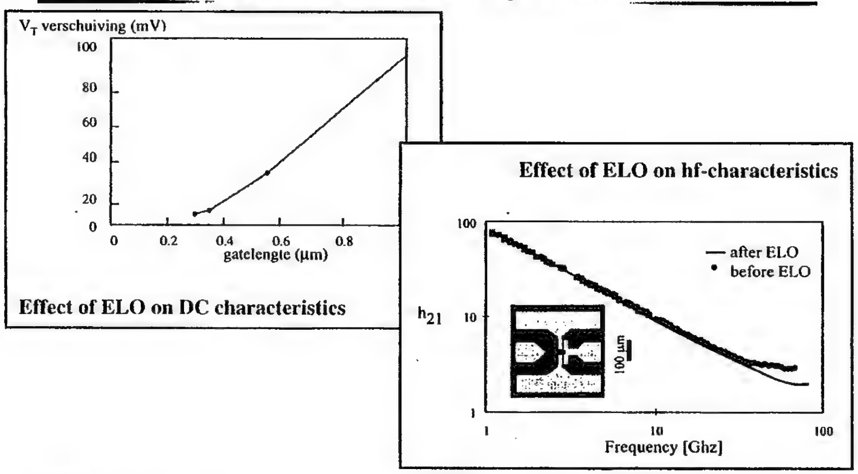

Epitaxial Lift-Off
Setup and Method

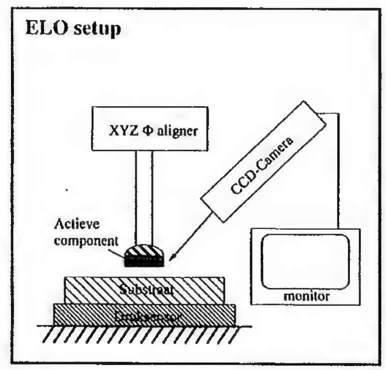

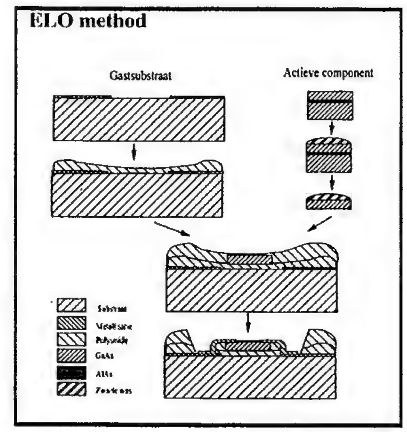

HOT ELECTRON MIXERS AND SIS-DETECTORS

BY

ERIK KOLLBERG

Chalmers University of Technology

Göteborg, SWEDEN

- The first electron distorts the lattice ≡ + and creates a trace of positive charge.
- The other electron is attracted by this positiv excess charge.

Cooper pairs are created — Bosons

The energy drops for the two electrons: a bandgap is created:

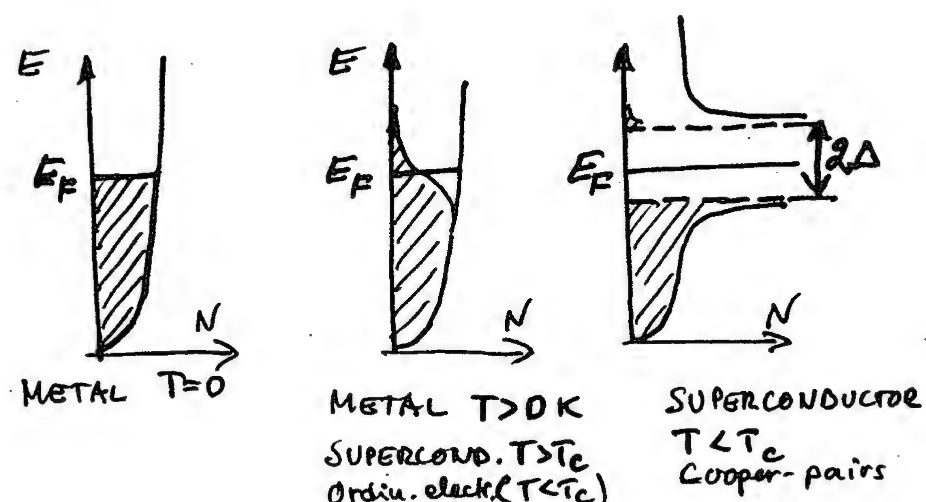

Timedependent Schrödinger equation:

$$i\hbar \frac{\partial \Psi}{\partial t} = \underbrace{-\frac{\hbar^2}{2m}\nabla^2 \Psi}_{\sim \text{kinetic energy}} + \underbrace{2eV\Psi}_{\sim \text{potential energy}}$$

$$\Psi(x,y,z) = \left[\rho(x,y,z)\right]^{1/2} e^{-i\Theta(x,y,z)}$$

SIS : **S**uperconductor - **I**nsulator - **S**upercond.

SIN : **S**uperconductor - **I**nsulator - **N**ormal metal

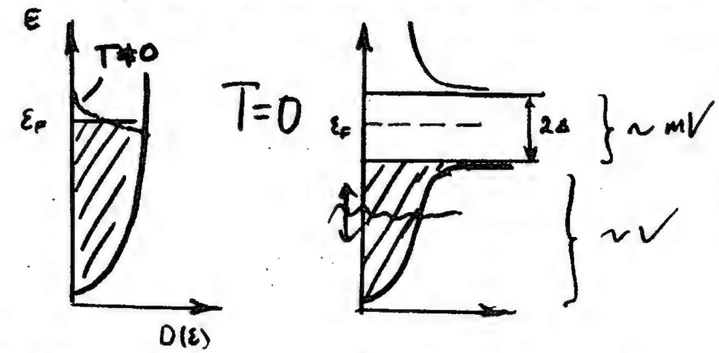

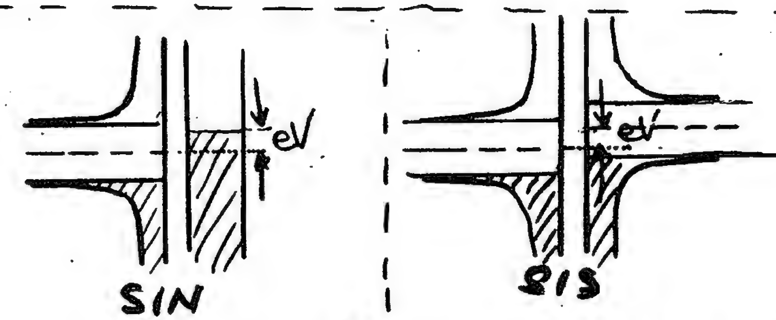

$$I = I_0 \int_{-\infty}^{\infty} D_1(\varepsilon) D_2(\varepsilon+eV)\left\{f_1(\varepsilon)\left(1-f_2(\varepsilon+eV)\right) - \left(1-f_1(\varepsilon)\right)f_2(\varepsilon+eV)\right\} d\varepsilon$$

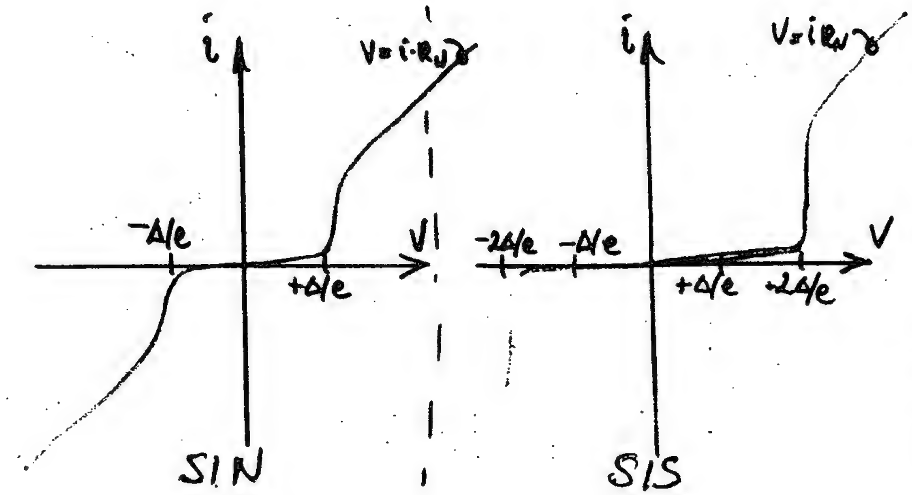

Planar Device on a substrate.

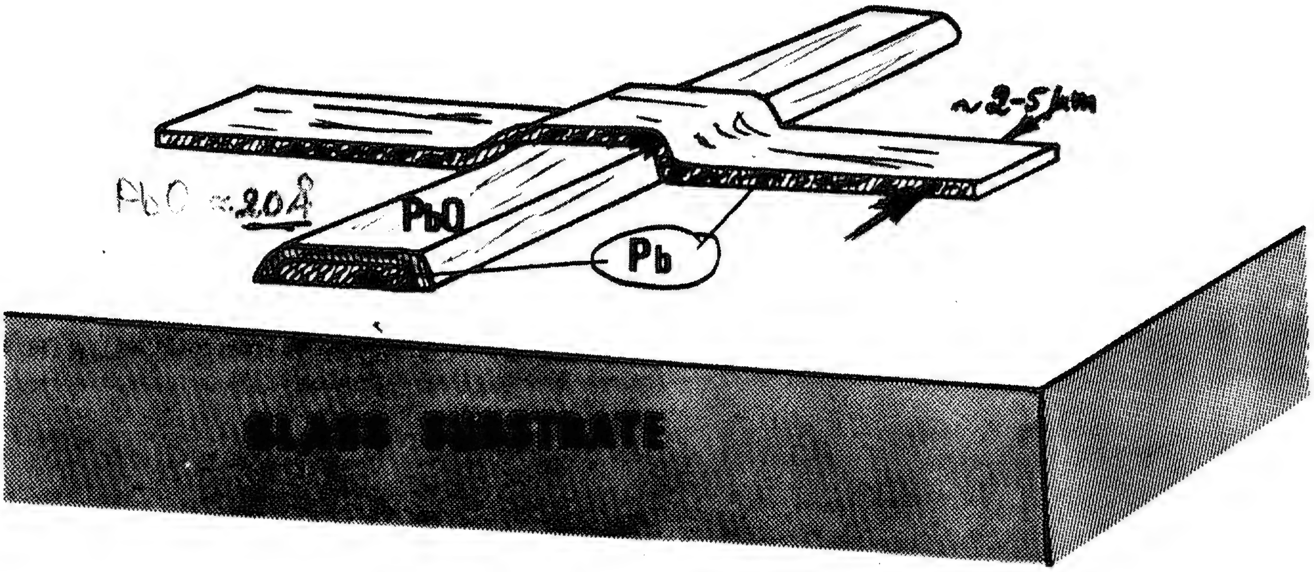

Tunneling of cooper pairs ≡ Josephson effect

— " — of electrons ≡ Quasiparticle tunnelling

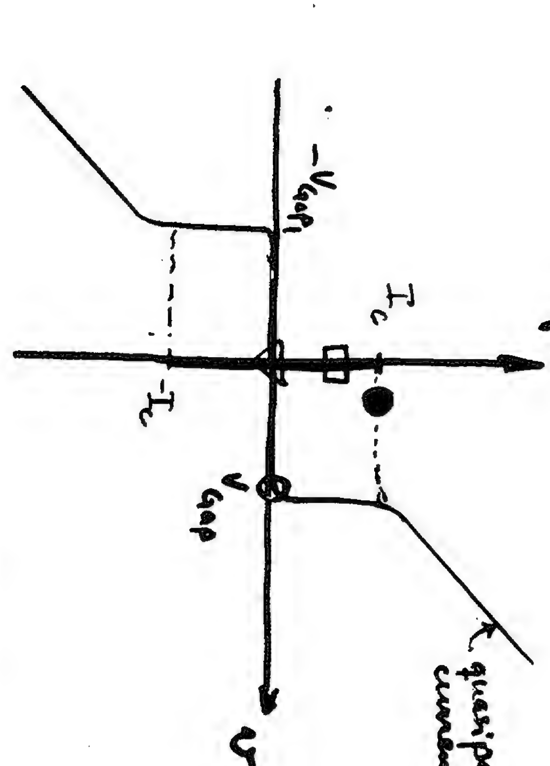

A. JOSEPHSON EFFECT ("parametric devices")

$$\frac{di_j}{dt} = v(t) \cdot L(v(t)) \qquad L(t) = \frac{2eI_c}{\hbar} \cos\left[\frac{2e}{\hbar}\int_0^t v(t)\,dt\right]$$

i. Parametric Amplifier (▽, □)

ii. Frequency Downconverter ≡ MIXER (●)

B. Quasiparticle mixer ("resistive mixer").

$$i(t) = v(t) \cdot g(t) \quad + \text{a "reactive current"}$$

Notice: Non-classical in the sense that quantum effects are essential.

EQUIVALENT CIRCUIT

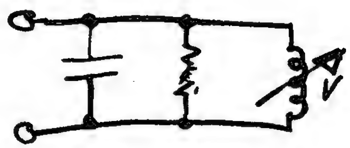

JOSEPHSON

$L(t)$

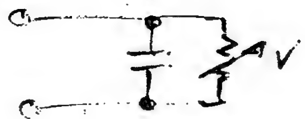

SIS

$R(t)$

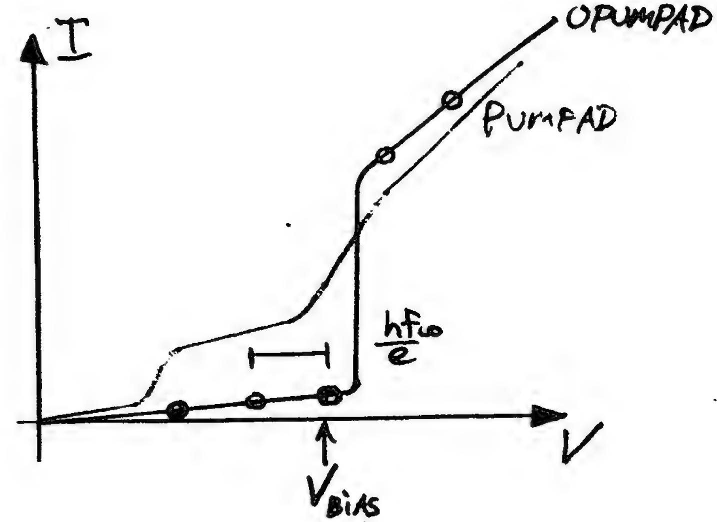

$$I_{LO} = \sum_{-\infty}^{\infty} J_n^2\left[\frac{eV_{LO}}{hf_{LO}}\right] I_{DC}\left[V_0 + \frac{nhf}{e}\right]$$

$T_0 \approx 2-4K$

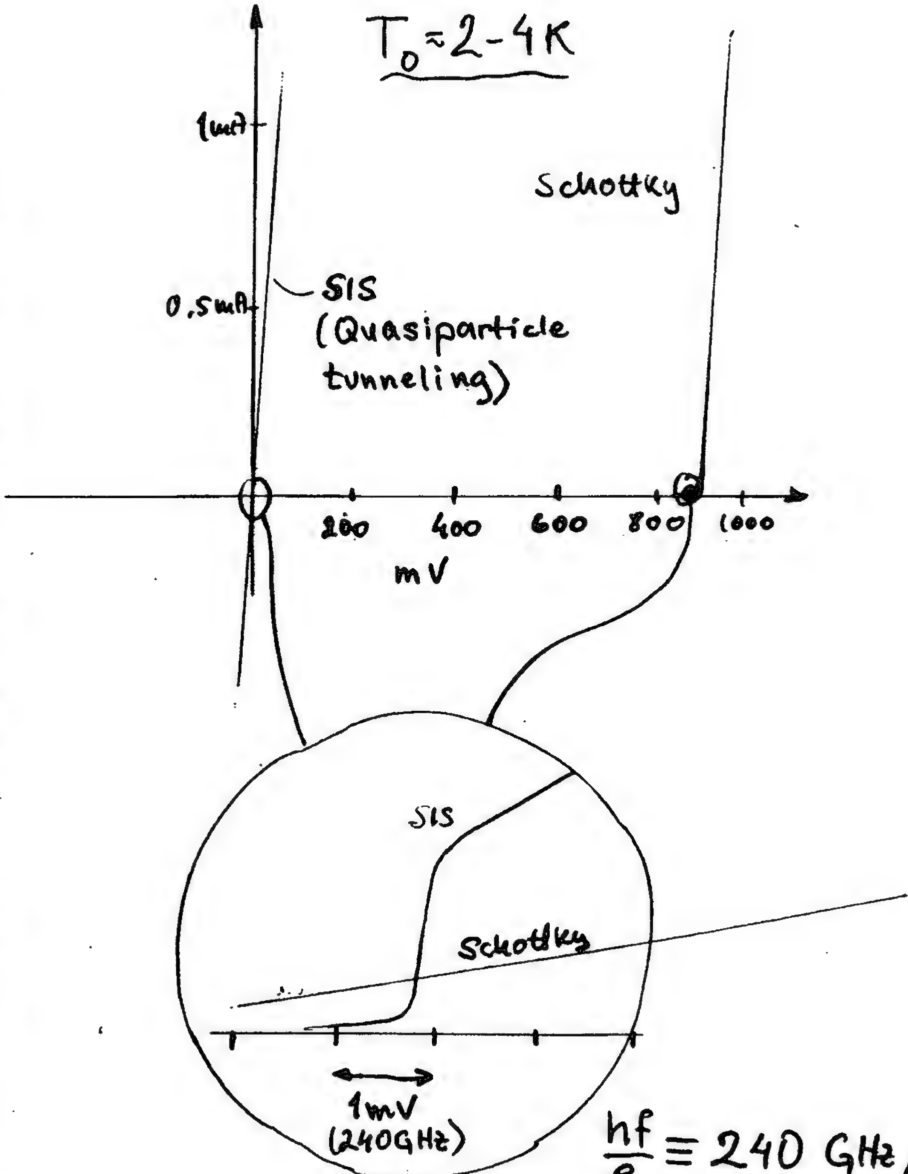

$$\frac{hf}{e} \equiv 240 \text{ GHz/mV}$$

Why low noise for SIS-mixer?

Shot noise:

$\delta i^2 = 2ei\Delta f$

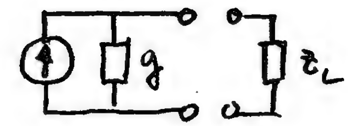

$$P_{noise} = \frac{\delta i^2}{4 \cdot g} = \frac{\delta i^2}{4 \cdot di/dv} = \frac{ei\Delta f}{2 \cdot di/dv} \equiv k T_{elec} \cdot \Delta f$$

$$\underline{T_{elec}} = \frac{e}{k} \cdot \frac{1}{2} \cdot \frac{i}{di/dv} = \frac{e}{k} \cdot \frac{1}{2} \cdot i \cdot r_{diff}$$

Noise of a Schottky diode:

* $T_{elec} \sim 40\frac{K}{2}$ (cooled)
* excess noise from series resistance

Noise of an SIS element:

* $T_{elec} \sim$ a few kelvin typically
* No series resistance.

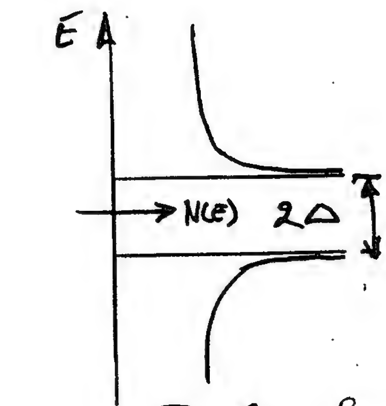

$f_{gap} = \frac{2\Delta}{h} \approx 3.52\, T_c$

	T_c K	f_{gap} GHz	2Δ mV
Pb	7.196	528	~2.5
PbBi	8.4	616	~3.4
Nb	9.25	678	~2.8
NbN	≲ 16	≲1173	~5.0

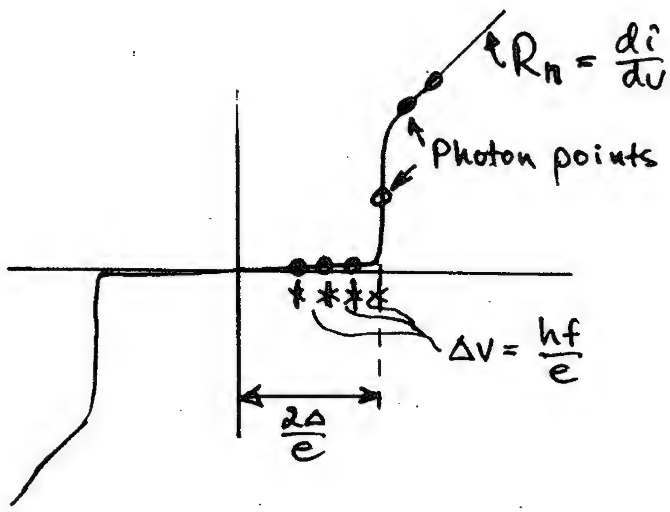

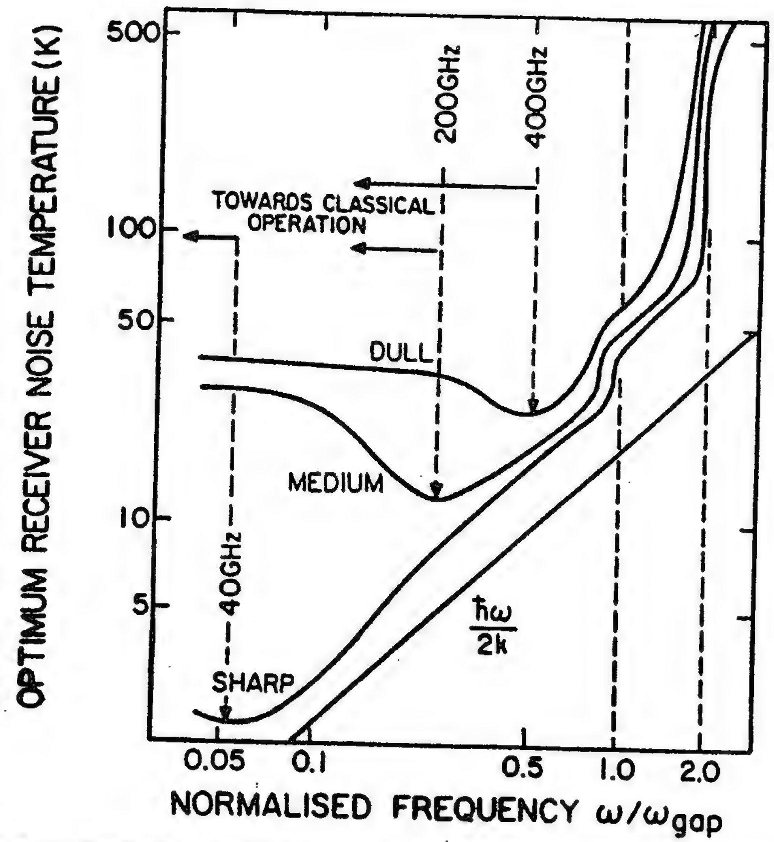

Figure 11. Predicted receiver noise temperature as a function of frequency for three synthetic I-V curves representative of a dull, medium and sharp SIS nonlinearity, after Feldman [21].

resistance and gap voltage and covered the entire range of junctions used for SIS mixing [21]. Figure 11 summarizes part of the data obtained for the three I-V curves differing only in their sharpness of the current rise at the gap voltage. At each frequency, the d.c. and LO voltages and the signal, or source, conductance were optimized. A double sideband mixer was assumed (i.e. LO and image conductances were set equal to the signal conductance, this is often the for a small IF) and all reactances were ignored (i.e. the junction capacitance was assumed to be tuned out by the millimetre-wave circuit). The load conductance was chosen to be $0.3/R_N$, which is close to the optimum value, and a gap voltage of 3mV and an IF noise temperature of 10K were chosen as typical values. From the data given in Figure 11,

(3)

Fabrication of SIS devices

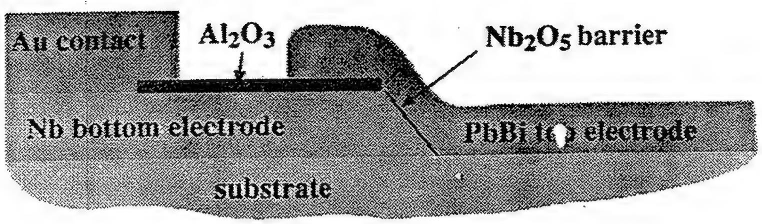

$Nb/Nb_2O_5/PbBi$ edge junction

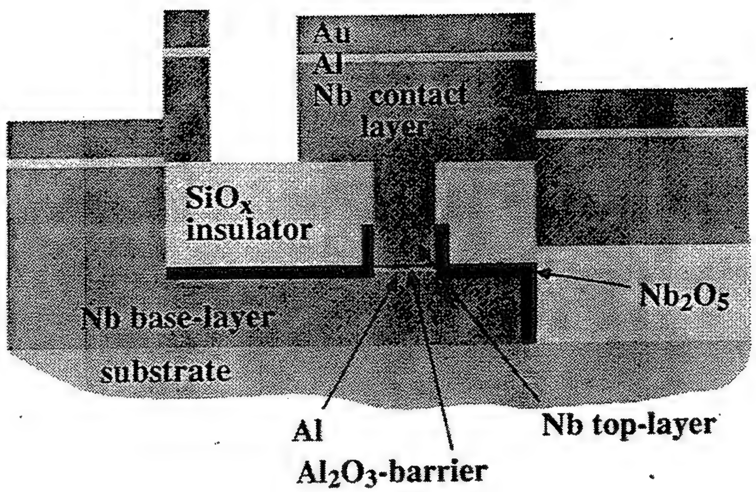

$Nb/Al\text{-}Al_2O_3/Nb$ trilayer junctions

DSB receiver noise temperature 330-350 GHz ≈ 100 K

Niobium edge junctions

$A = 0.2\ \mu m^2$; $C = 30$ fF

$\omega RC = 3.3$ @ 700 GHz

Nb – NbOx – PbBi

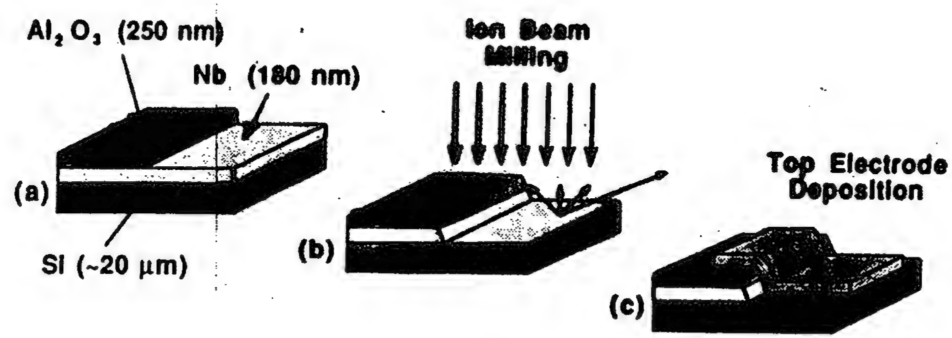

350GHz SIS mixer

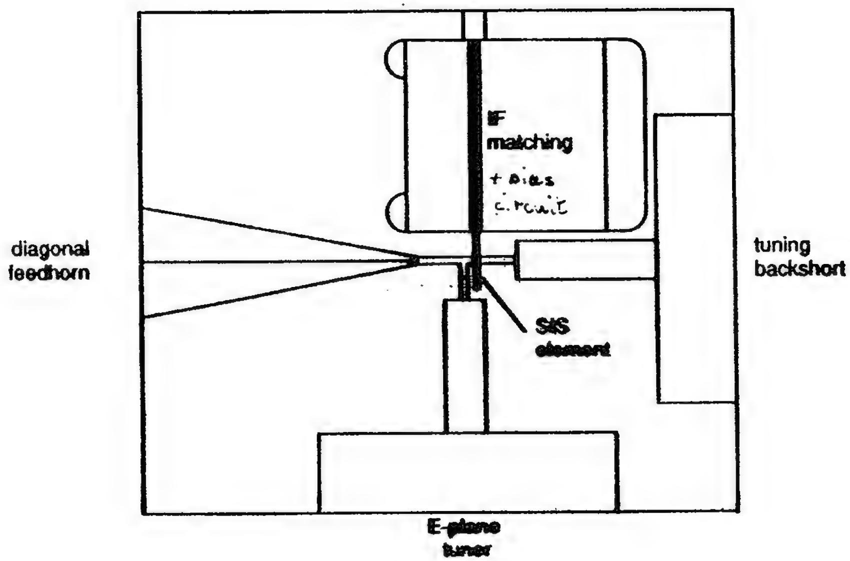

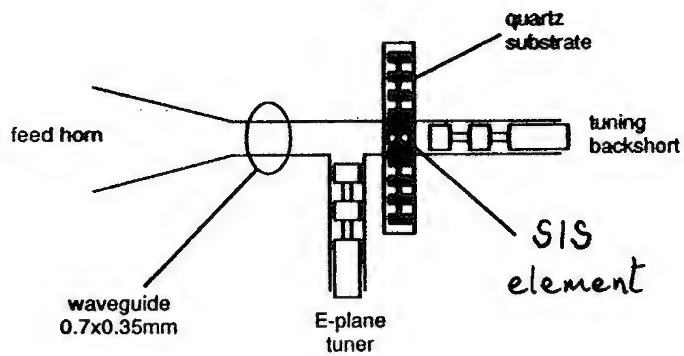

The Millimetre Wave Laboratory

500 GHz SIS mixer
Twin junction tuning circuit

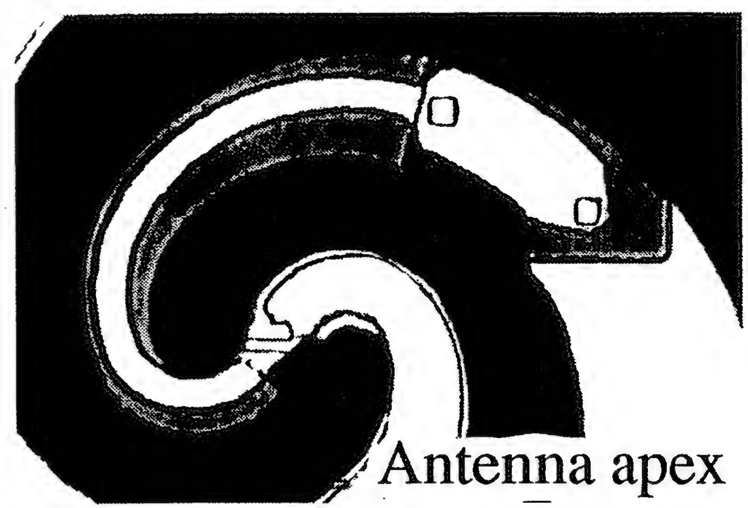

Chalmers University of Technology
Göteborg, Sweden

The Millimetre Wave Laboratory

Principle of twin junction tuning circuit

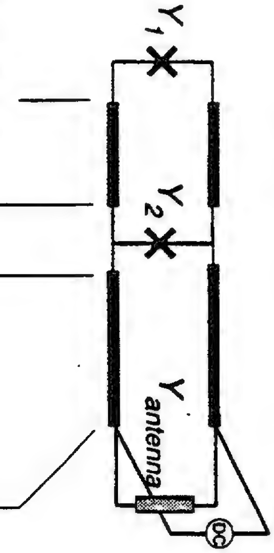

$Y_1 = A + jB$

$Y_2 = A + jB$

$Y_1^* = A - jB$

$Y_{comp.} = Y_1^* + Y_2 = (A - jB) + (A + jB) = 2A$

$Y_{comp.} \xrightarrow{\text{transformed to match}} Y_{antenna}$

Chalmers University of Technology
Gothenburg, Sweden

SJ 1994-05-26

The Millimetre Wave Laboratory

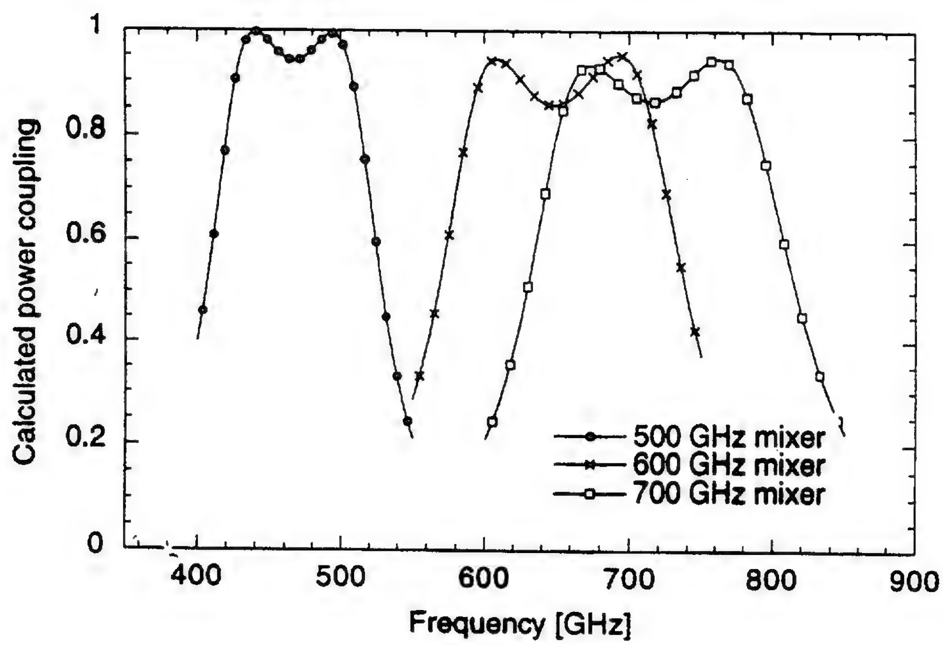

V.Yu.B. 95-03-14

Chalmers University of Technology

The Millimetre Wave Laboratory

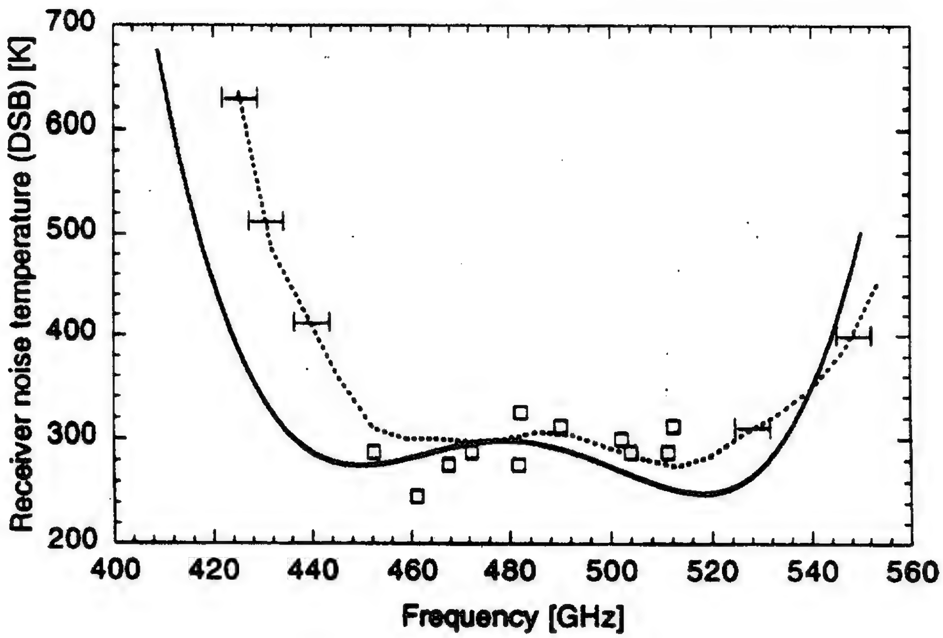

V.Yu.B. 95-03-15

Chalmers University of Technology
Gothenburg, Sweden

BLTSA on thin dielectric membrane

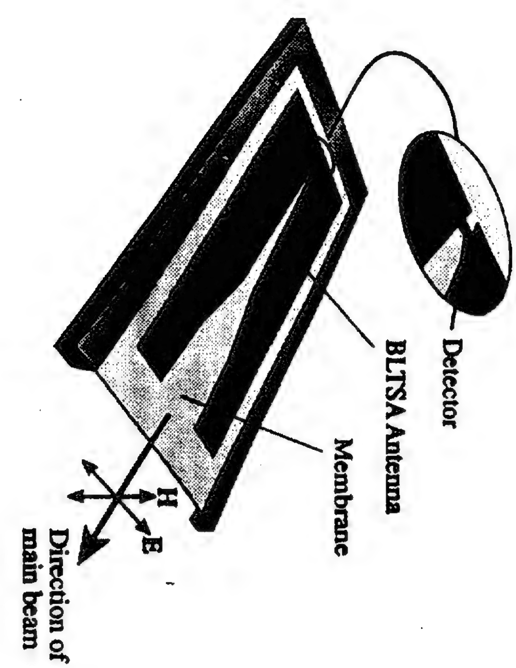

Cr/Au antenna structure on SiO_2/Si_3N_4 dielectric membrane thickness 1.7 µm

Antenna length L=6.7 λ_o

Opening width = 1.1 λ_o

Total width = 2.85 λ_o

Detector: room-temperature micro Bi bolometer

$w \times l = 5 \times 10$ µm

thickness ≈ 100 nm

resistance ≈ 100 Ω

The Millimetre Wave Laboratory

Principle of twin junction tuning circuit

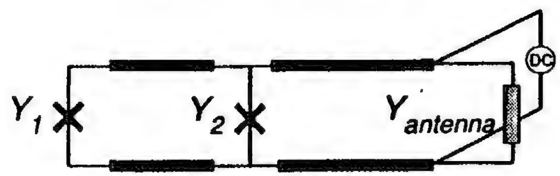

$Y_1 = A + jB$

$Y_2 = A + jB$

$Y_1^* = A - jB$

$Y_{comp.} = Y_1^* + Y_2 =$

$= (A - jB) + (A + jB) = 2A$

$Y_{comp.} \xrightarrow{\text{transformed to match}} Y_{antenna}$

The Millimetre Wave Laboratory

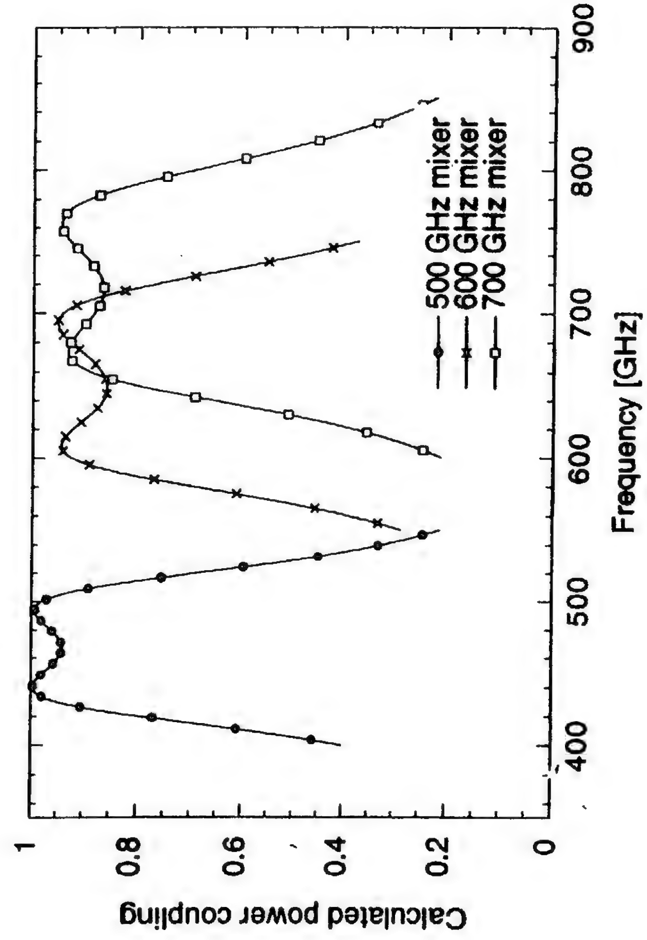

Measured antenna patterns at 350 and 800 GHz

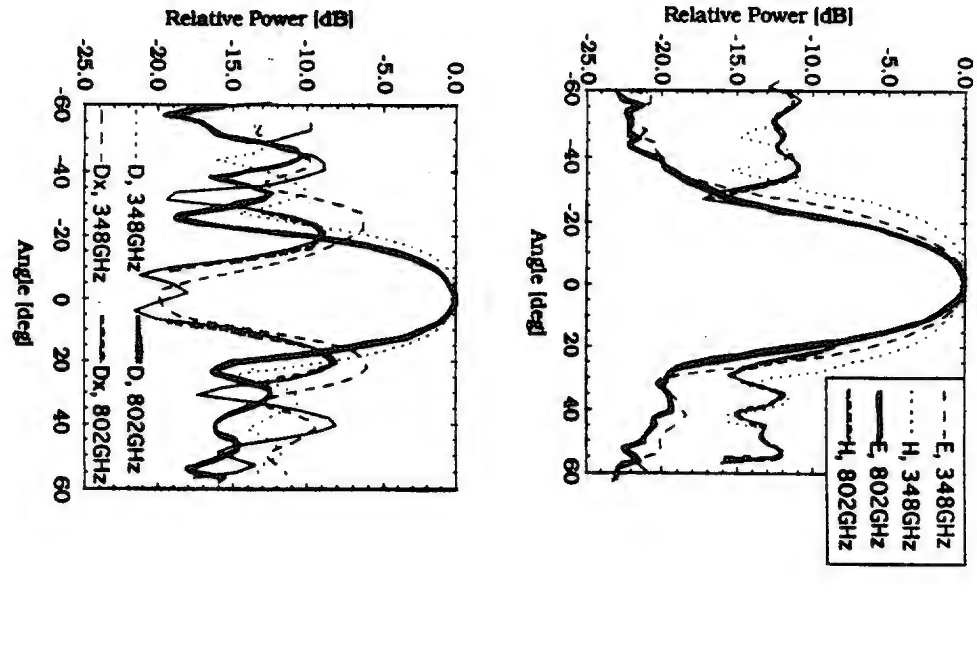

Directivity ≈ 13 dB

-10 dB Beam width ≈ 40°

Narrower and more circular beam at 800 GHz

Sensitivity of SIS Heterodyne Receivers above 300 GHz

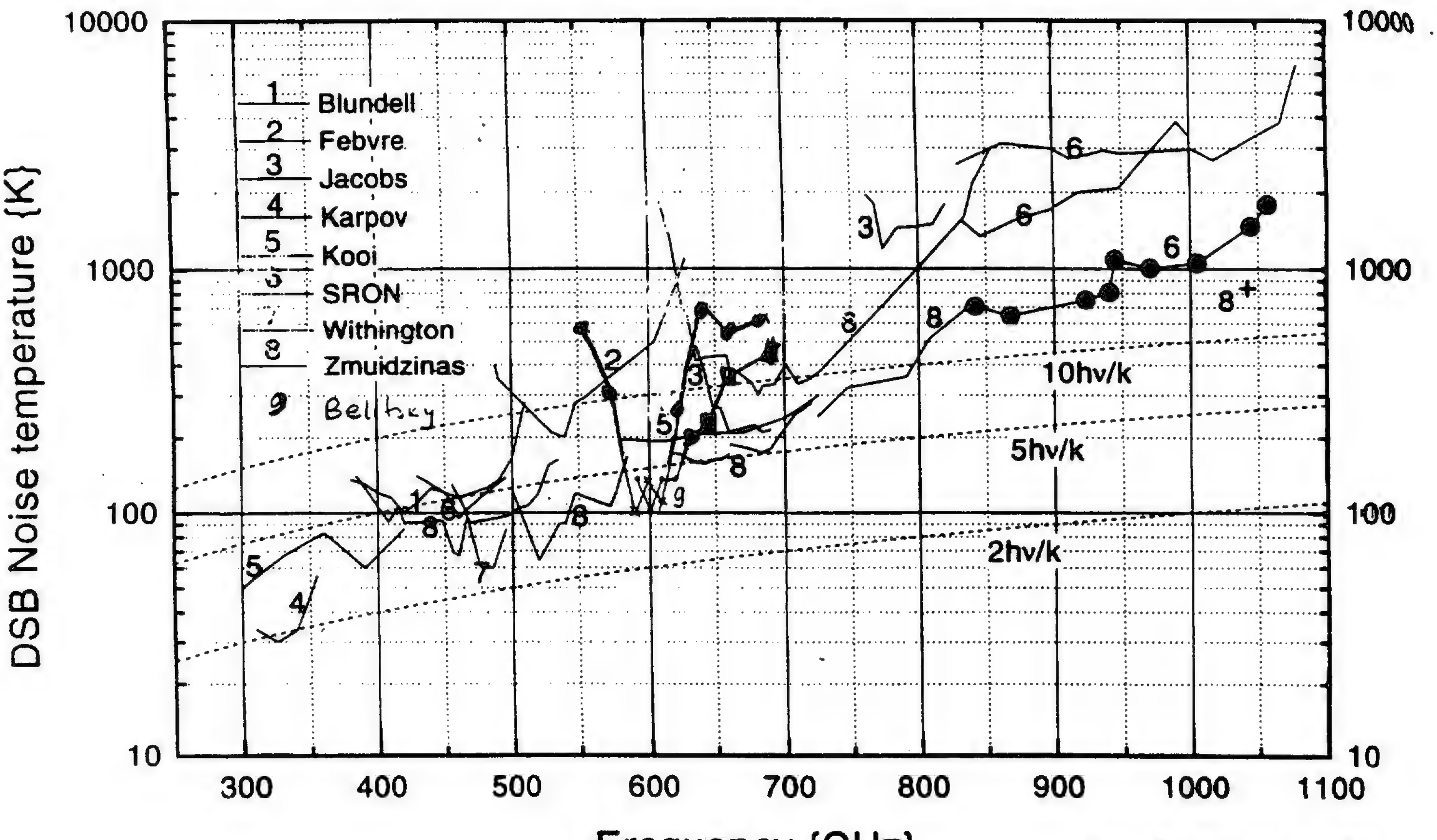

SRON, Nov 16, 1995.

The Millimetre Wave Laboratory

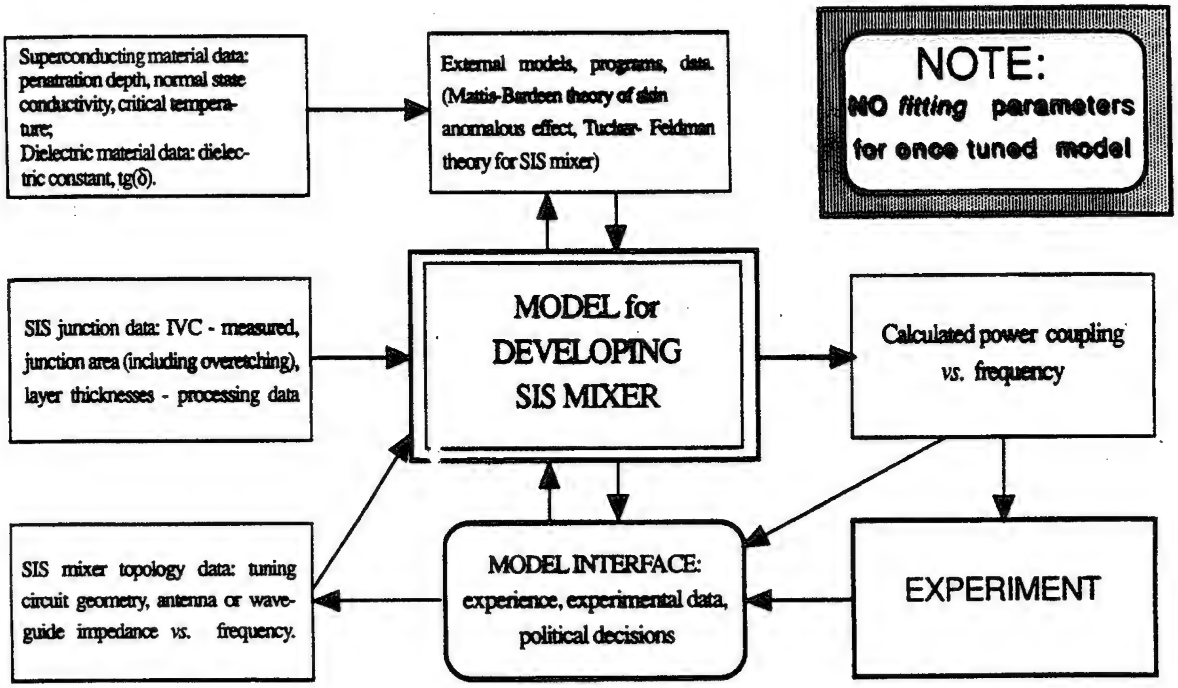

Victor Belitsky 95-08-31

Chalmers University of Technology
Gothenburg, Sweden

HOT ELECTRON MIXERS

OLD HISTORY

Very low noise

InSb-mixers have been used up to near *1 THz* successfully

Bolometric type of detector element;

allows for maximum *1-2 MHz* intermediate frequency only.

The hot electron bolometer mixer

Why ?

Frequency independent in the submillimeter range

High conversion efficiency

Low noise determined by temperature fluctuations

Easy integration with antennas etc

but

Relatively narrow IF bandwidth

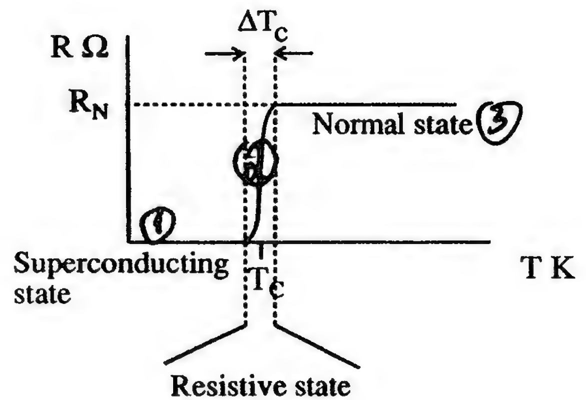

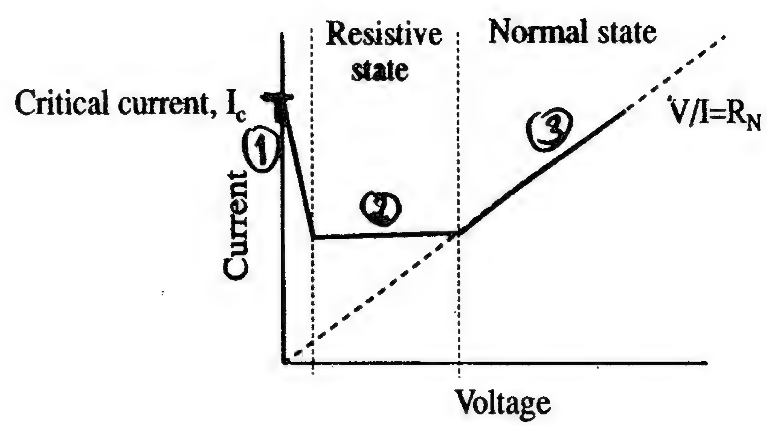

The three states of the bolometer

"PHONON-COOLED"

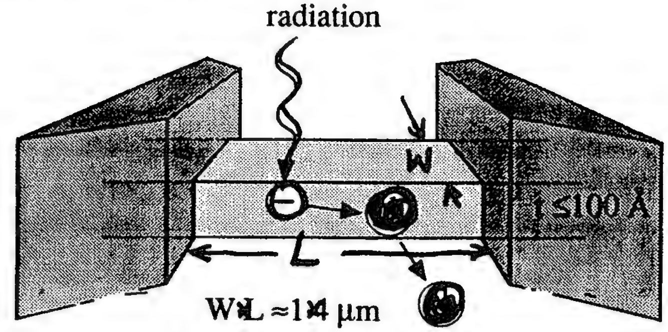

W·L ≈1·4 μm

Energy from hot electrons
to Nb lattice
to substrate lattice

energy relaxation time -> $f_{IF} \approx$ 100-2000 MHz

"DIFFUSION-COOLED"

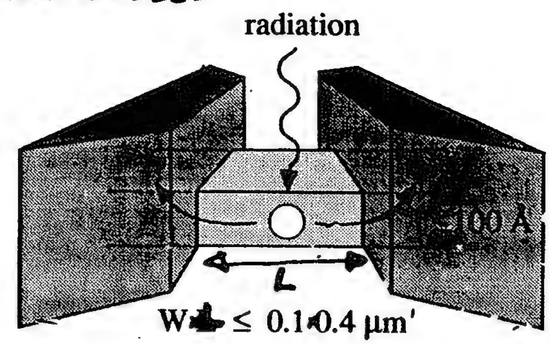

W·L ≤ 0.1·0.4 μm'

Energy is removed by
hot electron diffusion
to the thick contacts

$L < 2\sqrt{D \cdot \tau_{ee}}$

energy relaxation time -> $f_{IF} \approx$ 2-3 GHz

$$\text{Thermal response time} = \frac{\text{Thermal Capacitance}}{\text{Thermal Conductance}}$$

- RESISTANCE of a Hot Electron Device changes with *electron* temperature T_e, *lattice* temperature T_L is constant .

- T_e depends on the total absorbed power

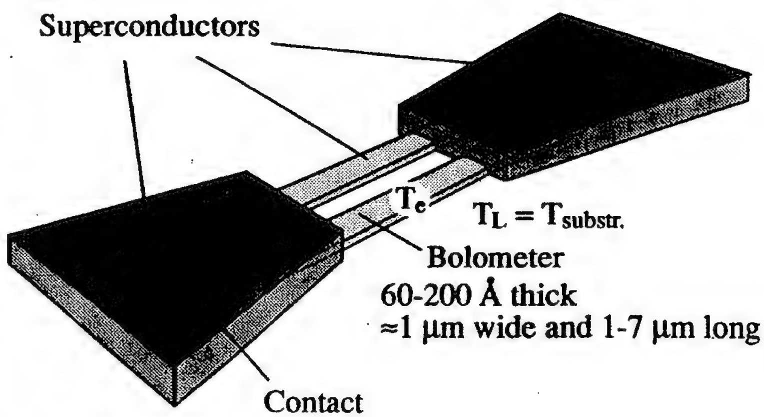

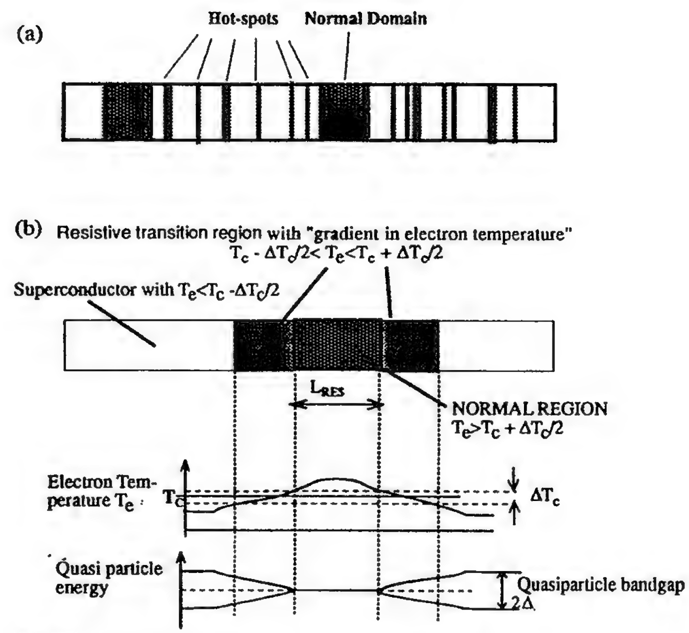

Different possible regions in the bolometer strip.

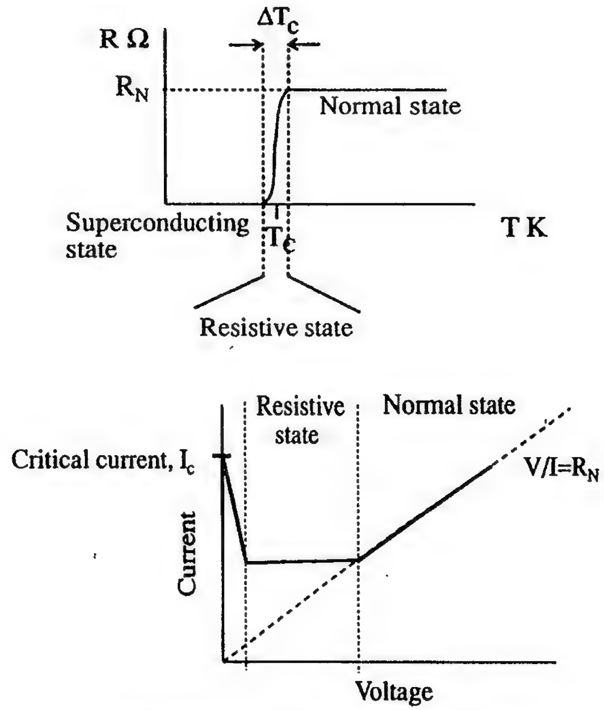

The three states of the bolometer

COMPARE I-V:

P_{LO} constant
Temperature varied

Temperature constant
Different P_{LO}

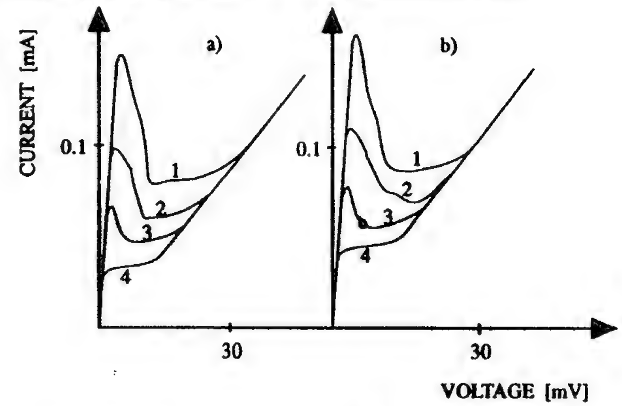

$T_1<T_2<T_3<T_4$ **$P_1<P_2<P_3<P_4$.**

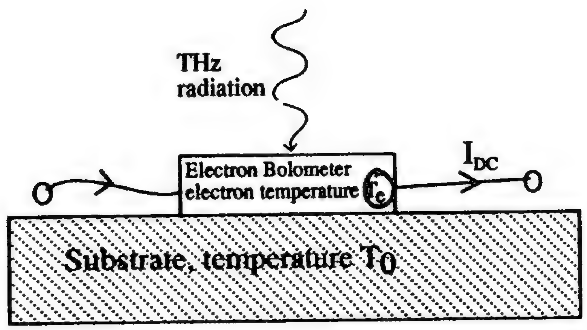

HOT ELECTRON DEVICES ARE "ENVELOPE DETECTORS"

Electron temp. T_e VARIES AT IF

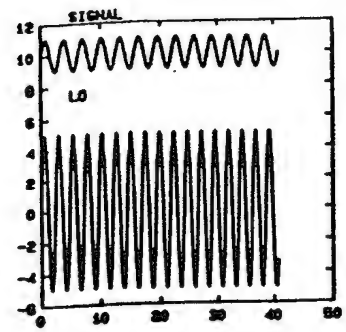

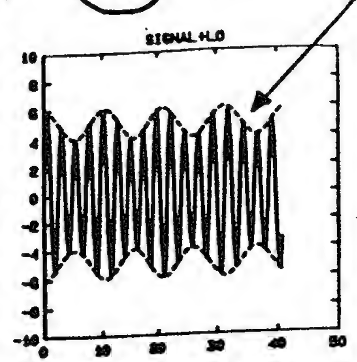

$$\boxed{P(t) = \frac{(V_S \cos \omega_S t + V_{LO} \cos \omega_{LO} t)^2}{R_B}}$$

DEVICE RESPONSE

TIME ~ τ_e (ENERGY RELAXATION TIME) — THUS DEVICE CURRENT DOES NOT FOLLOW DC I–V–CURVE — DEVICE RESISTANCE FOLLOWS THE ENVELOPE OF THE INSTANTANEOUS POWER

$\xrightarrow{I_D}$ R(P)

EQUIVALENT CIRCUIT OF HOT ELECTRON MIXER

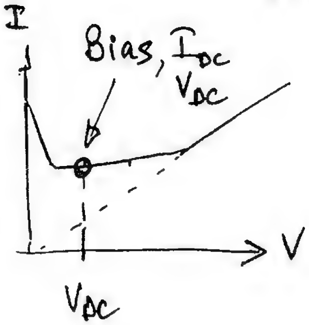

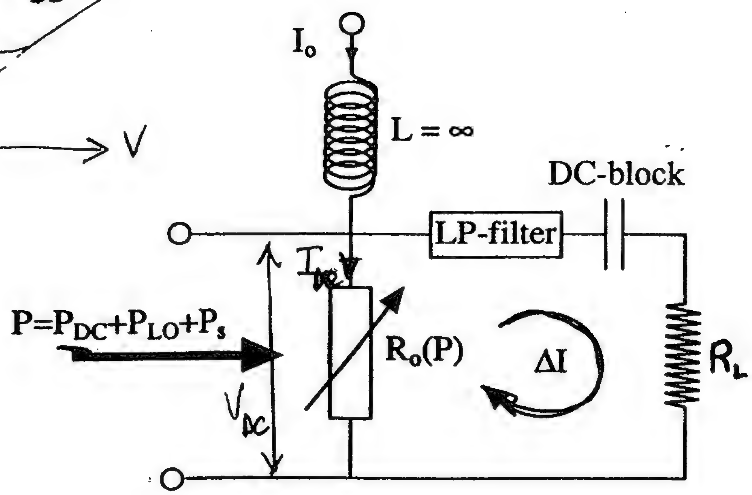

LP-filter:

- The electron response time is long compared to inverse signal frequency.
- Thus mixer performance is independent of signal frequency.

HE 5/9/94

InSb: Arams 1966

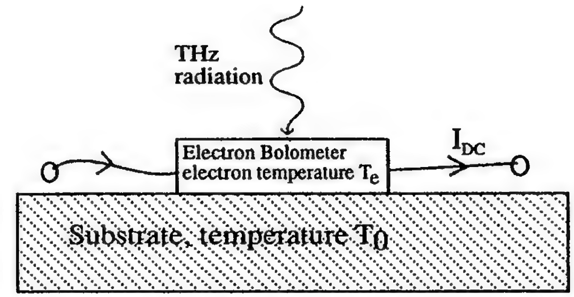

Schematic drawing of a hot-electron bolometer device.

$$P_{RF}(t) = \frac{1}{2R_{BO}}\left(V_{LO}\sin(\omega_{LO}t) + V_s\sin(\omega_s t)\right)^2$$

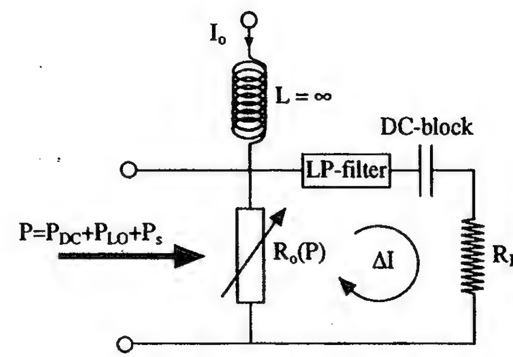

Equivalent circuit of bolometer with load.

Arams, 1966:

$$G = \frac{P_{IF}}{P_s} = 2C_o^2 \frac{P_{LO}P_{DC}}{(R_L+R_o)^2}\frac{R_L}{R_o}\left(1 - C_o\frac{P_{DC}}{R_o}\frac{R_L-R_o}{R_L+R_o}\right)^{-2}$$

$$C_o = \frac{dR_o}{dP}$$

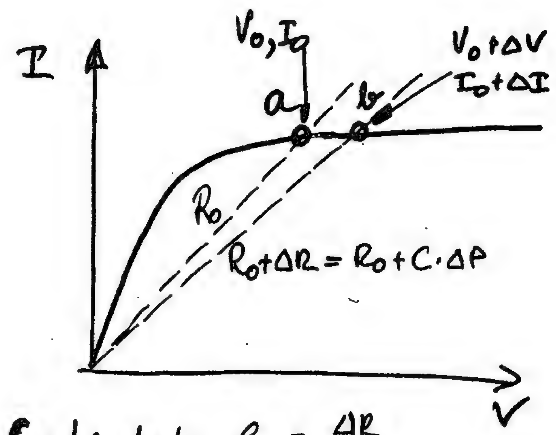

Calculate $C_o = \frac{\Delta R}{\Delta P}$

$$\Delta R = \frac{V_o + \Delta V}{I_o + \Delta I} - \frac{V_o}{I_o} \approx \frac{V_o}{I_o}\frac{\Delta I}{I_o}\left(\frac{\Delta V}{\Delta I}\frac{I_o}{V_o} - 1\right)$$

$$\Delta P = (V_o + \Delta V)(I_o + \Delta I) - V_o I_o \approx V_0 \Delta I\left(\frac{\Delta V}{\Delta I}\frac{I_o}{V_o} + 1\right)$$

$$C_O = \frac{dR}{dP} = \frac{1}{I_O^2}\frac{\frac{\Delta V}{\Delta I}\frac{I_O}{V_O} - 1}{\frac{\Delta V}{\Delta I}\frac{I_O}{V_O} + 1} = \frac{R_O}{P_{DC}}\frac{\left(\frac{dV}{dI}\right)_{DC} - R_O}{\left(\frac{dV}{dI}\right)_{DC} + R_O}$$

$$G = \frac{1}{2}\frac{P_{LO}}{P_{DC}}\frac{R_L}{R_o}\left(1 - \frac{R_o}{(dV/dI\ )_{DC}}\right)^2\left(1 + \frac{R_L}{(dV/dI\ )_{DC}}\right)^{-2}$$

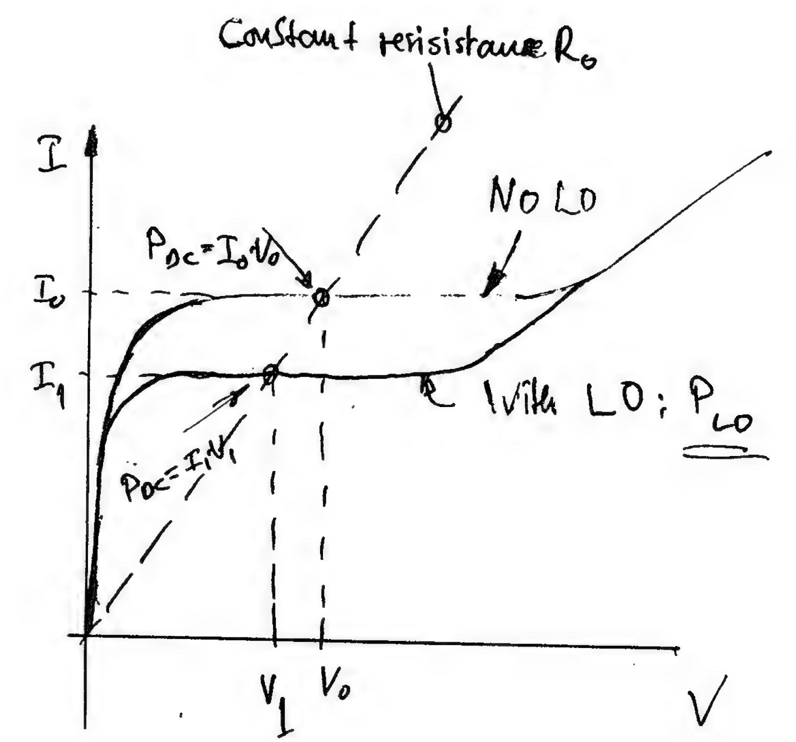

$P_o - P_1 = I_o V_o - I_1 \cdot V_1 = P_{LO}$

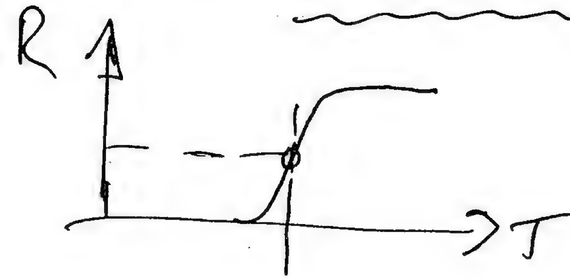

POSITIVE CONVERSION GAIN

With $\left(\frac{dV}{dI}\right)_{oo} < 0$ for the unpumped IV-curve

and

for certain values of $\frac{R_L}{R_o}$

Loss less than 6 dB
or even
Positive conversion gain.

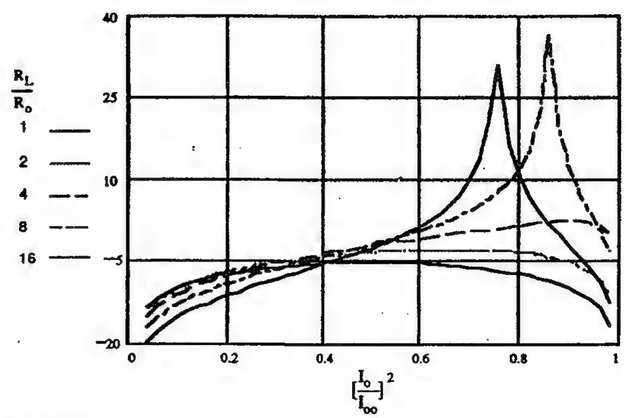

$\left(\frac{dV}{dI}\right)_{oo} = -5R_o$

WITH

$$G = 2C'^2 \left(\frac{I_o^2}{I_{oo}^2}\right)\left(1-\frac{I_o^2}{I_{oo}^2}\right)\frac{R_L}{R_o}\frac{1}{(R_L/R_o+1)^2}\frac{1}{\left(1-C'\frac{I_o^2}{I_{oo}^2}\frac{R_L/R_o-1}{R_L/R_o+1}\right)^2}$$

RF COUPLING

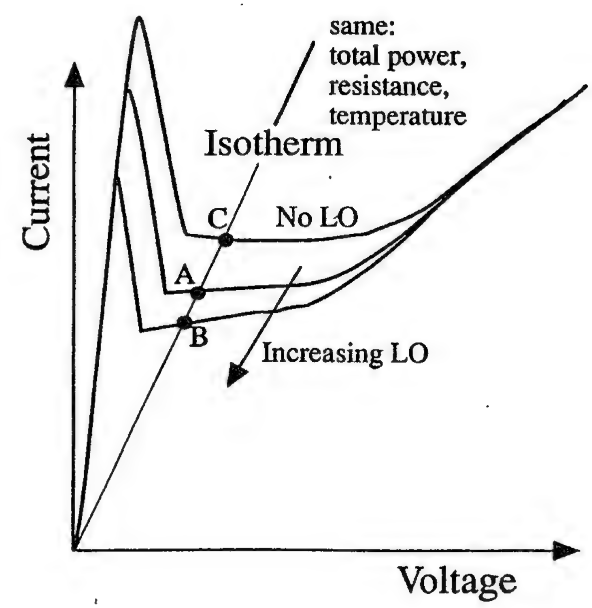

$$\alpha = \frac{P_{DC,A}-P_{DC,B}}{P_{LO,B}-P_{LO,A}}$$

$P_{LO,B}-P_{LO,A}$ = Difference in applied LO-power between curve A and B

CONVERSION VS BIAS

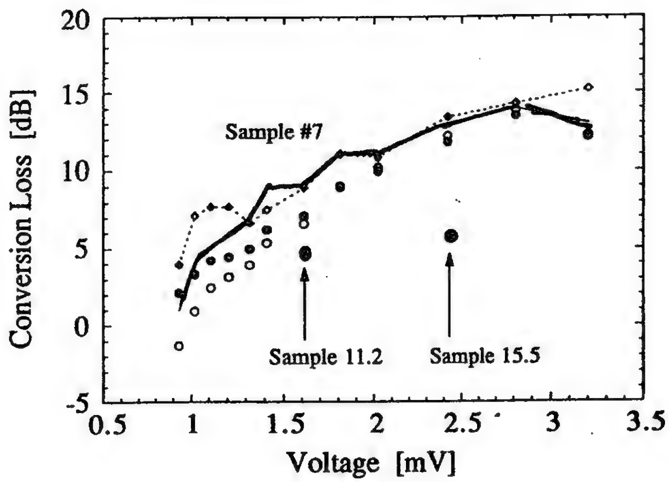

MEASURED LOSS: Solid line

CALCULATED LOSS:

From pumped curve: Dots

From unpumped curve:
Loss with calculated slope — Circles
Loss with measured slope — Diamonds

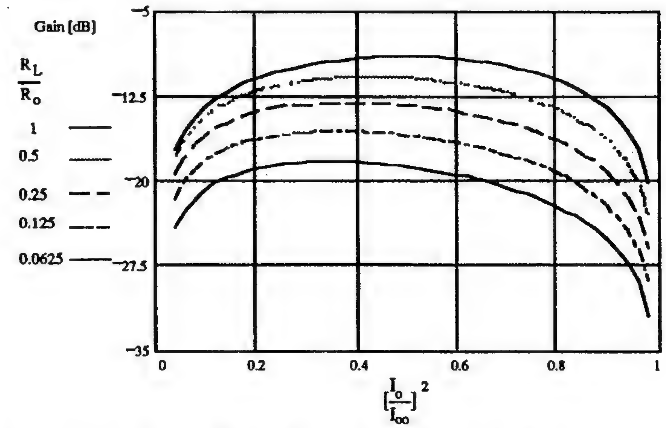

Conversion Gain vs. $P_{DC}/(P_{DC}+P_{LO})$ for different IF load resistances. $R_L<R_O$. The differential resistance for the unpumped curve: $dV/dI=\infty$, or $C_0 \cdot I_{00}^2=1$

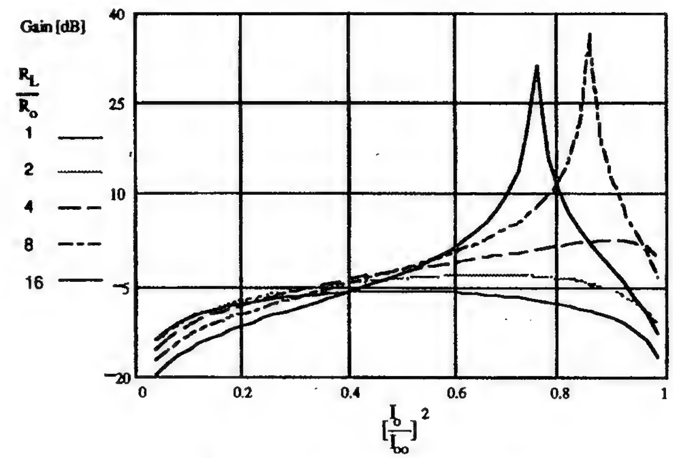

Conversion Gain vs. $P_{DC}/(P_{DC}+P_{LO})$ for different IF load resistances. $R_L>R_O$. The differential resistance for the unpumped curve is negative: $dV/dI=-5 \cdot R_0$, or $C_0 \cdot I_{00}^2=1.5$.

CONDITIONS FOR HOT-ELECTRON MIXING

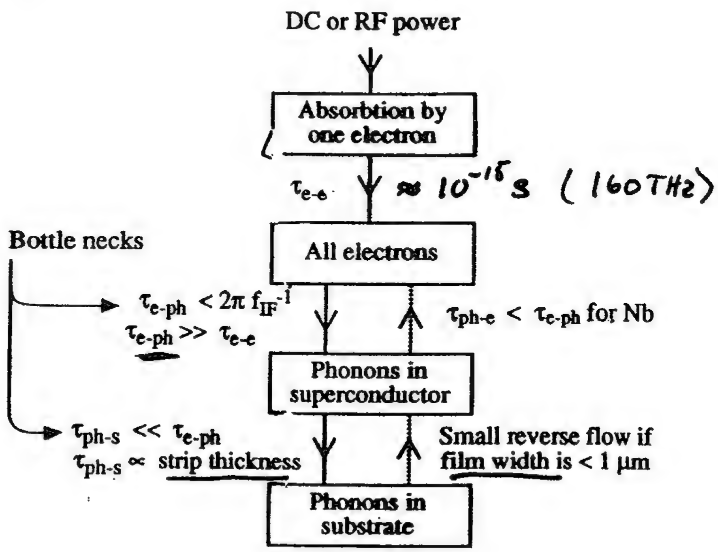

τ_{e-ph} is material dependent and limits the IF bandwidth.

$$f_{IF} < (2\pi\tau_{e-ph})^{-1}.$$

τ_{ph-s} is determined by the bolometer thickness. $t < 100$ Å

τ_{s-ph} is determined by the bolometer-substrate contact area.

RELAXATION PROPERTIES

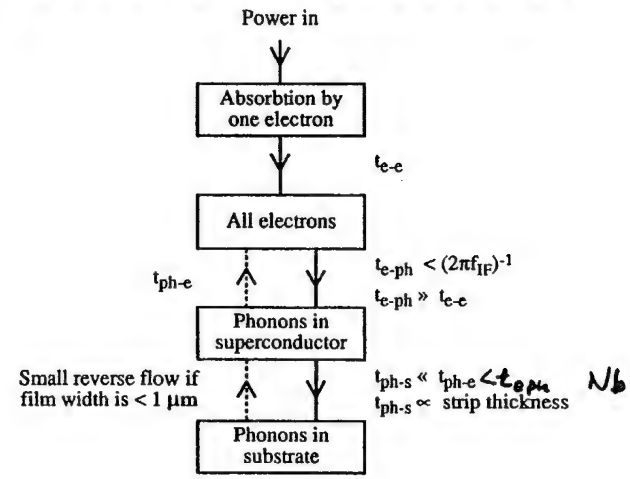

Predicted

Mate-rial	te-e [s]	te-ph [s]	IF [GHz]	Experi-mental
Nb	10^{-11}	3×10^{-10}	0.3	~ 0.1 GHz
NbN	$<10^{-11}$	10^{-11}	20	~5 GHz
HTSC	?	10^{-12}	100	?

CONVERSION GAIN AND IF IMPEDANCE VS INTERMEDIATE FREQUENCY

$$C_o = dR/dP = [dR/dT]\cdot[dT/dP]$$

Assuming

$dT/dP \sim 1/(1+j\omega\tau_e)$ and dR/dT = constant

$$C_o(\omega) = \frac{C_o(\omega=0)}{1+j\omega\tau_e}$$

Hence:

$$G = G(\omega=0)\cdot\frac{1}{1+\left(\omega\tau_{MIX}\right)^2}$$

where

$$\tau_{MIX} = \frac{\tau_e}{1-C_o I_o^2\cdot\dfrac{R_L-R_o}{R_L+R_o}}$$

and

$$Z(\omega) = R_o\left(1+\frac{2C_o I_o^2}{1-C_o I_o^2}\;\frac{1}{1+j\omega\tau_{imp}}\right)$$

where

$$\tau_{imp} = \frac{\tau_e}{1-C_o I_o^2}$$

IF BANDWIDTH

Nb

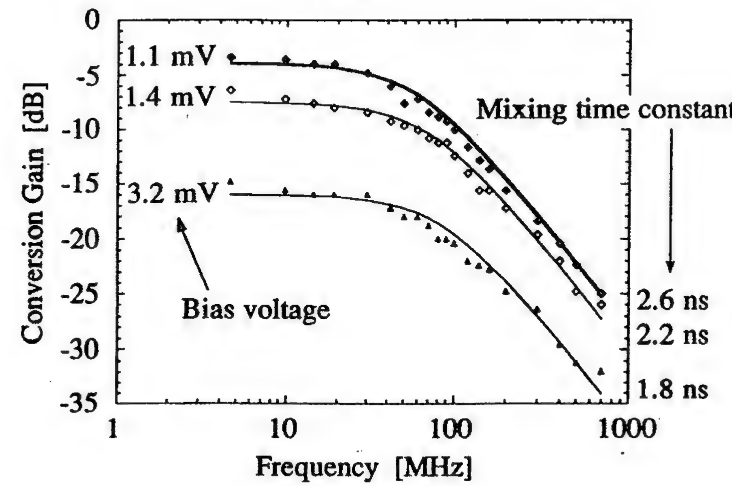

Bandwidth around 100 MHz increases slightly for larger bias

with $\tau_{mix} = \dfrac{\tau_e}{1+C_o I_o^2\dfrac{R_o-R_L}{R_o+R_L}}$ from IV curve, $R_o = \dfrac{V_o}{I_o}$

τ_{mix} is 2.6, 2.14 and 1.83 ns respectively

$\tau_e = 1.78$ ns

Nb

CONVERSION VS IF

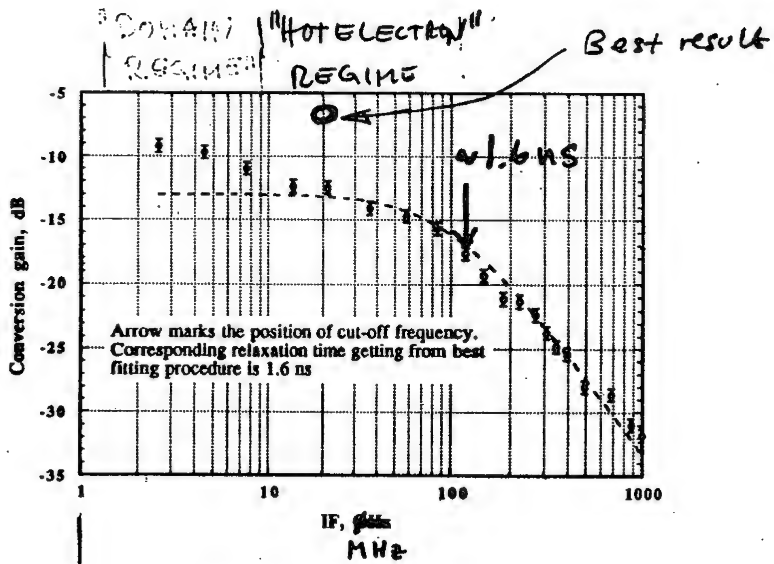

NbN : -3dB at ≈ 5 GHz

Using a complex load impedance viz. $R_L \rightarrow Z_L = R_L + jX_L$ we obtain for the frequency dependence of the conversion gain.

$$G = \frac{2\left(1-\frac{I_o^2}{I_{oo}^2}\right)\frac{\left(C_o I_o^2\right)^2}{\left(1-C_o I_o^2\right)^2} R_o \cdot R_L}{\left| R_L + (dV/dI)_{pumped} - \omega\tau_e \cdot \frac{X_L}{1-C_o I_o^2} + j\left[X_L + \omega\tau_e \cdot \frac{R_o + R_L}{1-C_o I_o^2}\right]\right|^2}$$

Hence it should be possible to improve the bandwidth somewhat by a proper design of the load circuit Z_L.

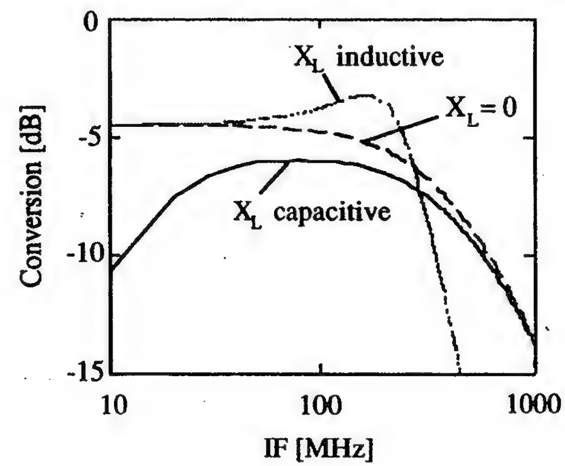

IF Bandwidth for different load reactances.

IMPEDANCE

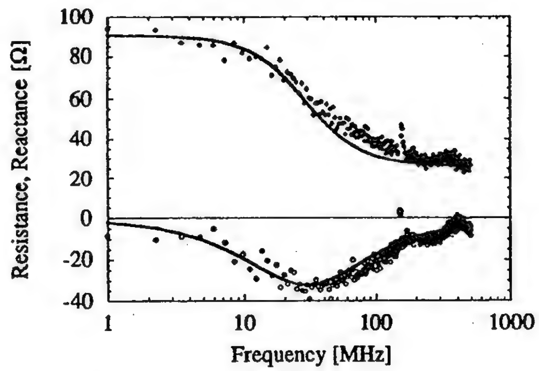

Dots measured IF impedance
Lines impedance of load

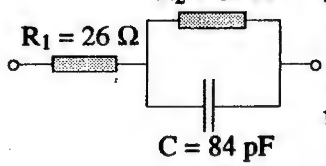

$$Z = R_d \frac{1+j\omega\tau}{1+j\omega\tau_{imp}}$$

where $\begin{cases} R_d = R_1 + R_2 \\ \tau_{imp} = R_2 C \end{cases}$

<u>Impedance time constant.</u>

Measured $\tau_{imp} = R_2C = 5.4$ ns.

From IV-curve $\tau_{imp} = \dfrac{\tau_e}{1-C_o I_o^2} = 5.1$ ns.

τ_e from mixer experiment

THEORETICAL

Assuming:

Temperature fluctuations $\Delta\theta \Rightarrow$

$\Rightarrow$ Resistance fluctuations $\Delta R \Rightarrow$

$\Rightarrow$ IF voltage fluctuations $\Delta V \approx I_{DC} \times \Delta R$

$\equiv$ IF-NOISE OUT FROM MXR

$$T_{IF,noise,out} = G \times \underline{T_{Mixer,FL}}$$

$$\boxed{T_{Mixer} = T_{noise,out}/G = \underline{T_{M,FL}}}$$

$$!!!!!!!!!!!!!\quad \underline{T_{M,FL}} = \frac{2\theta^2 c_e}{\tau_{e-ph} P_{LO}} \quad !!!!!!!!!!!!!$$

θ	**is the electron temperature**
c_e	**is the electron heat capacity**
$\tau_{e\text{-}ph}$	**is the electron-phonon relaxation time**
P_{LO}	**is the absorbed LO power.**

Transition

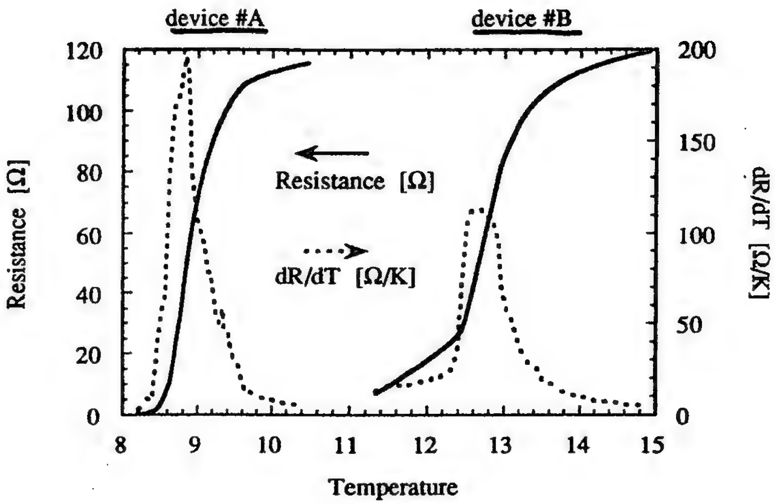

TABLE I

#	d [Å]	R_s 1) [Ω]	R_N 1) [Ω]	dR/dT [Ω/K]	T_c 2) [K]	T_c 3) [K]	ΔT_c [K]	I_c [μA]	I_{∞} [μA]
A	200	390	120	190	8.5	8.8	0.5	1900	600
B	100	500	150	110	11	12.6	1 4)	3150	1130

1) At room temperature
2) At onset of resistance
3) At maximum dR/dT
4) Excluding the foot structure below T_c.

IF Response

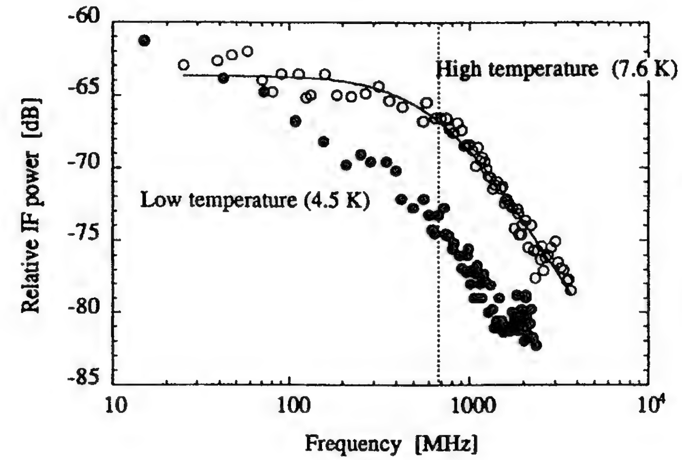

#A
$T_c = 8.5K$

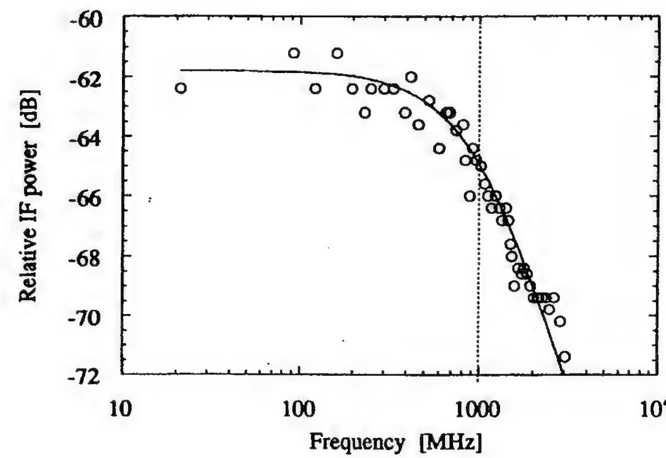

#B
$T_c = 11K$

$$Bandwidth^{-1} = 2\pi\tau_{mix} \propto \tau_{e-ph} \propto \theta^{-1.6} \approx T_c^{-1.6}$$

$$680\left(\frac{11}{8.5}\right)^{1.6} = 1020\ MHz$$

Double dipole antenna integrated NbN hot electron bolometer

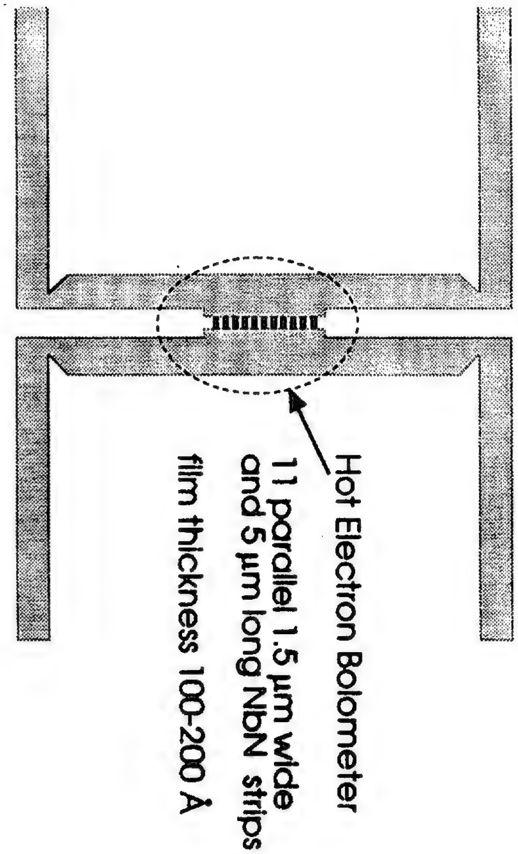

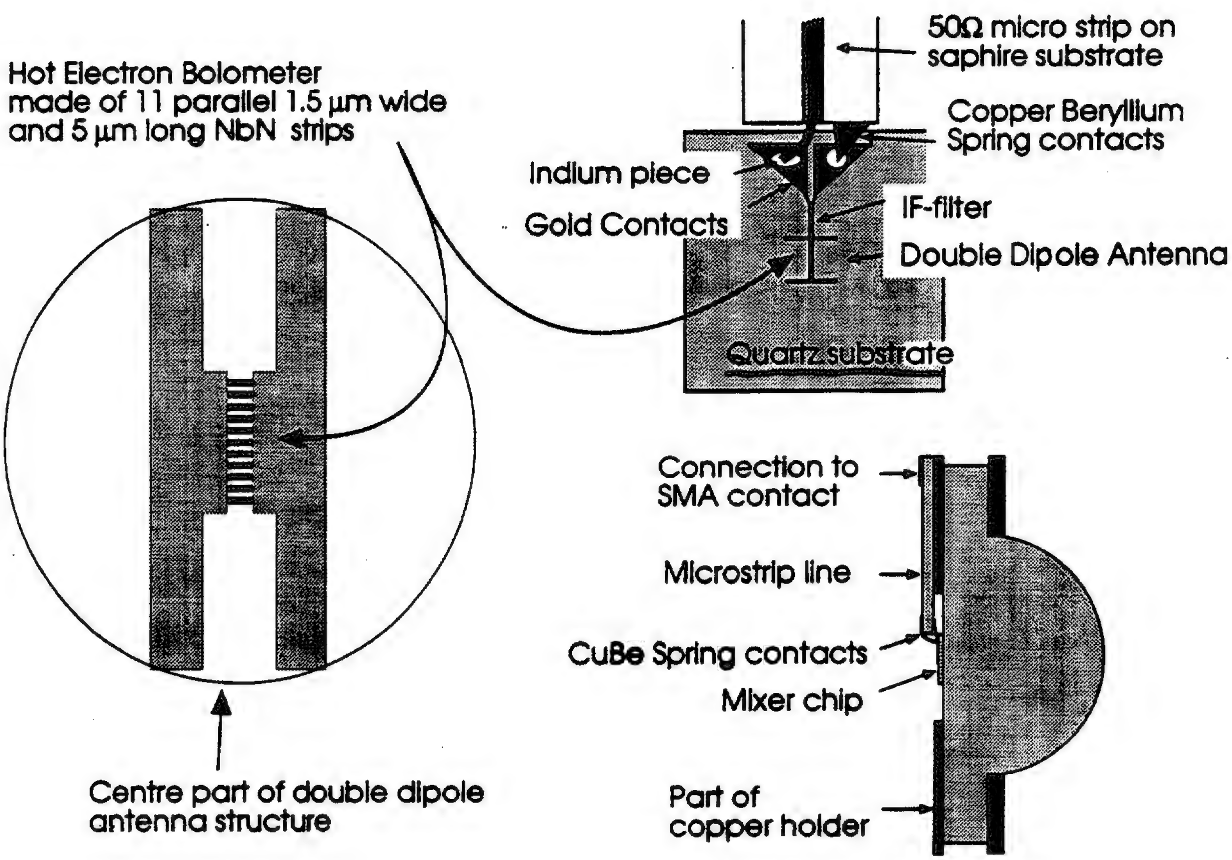

Output Noise   device #A

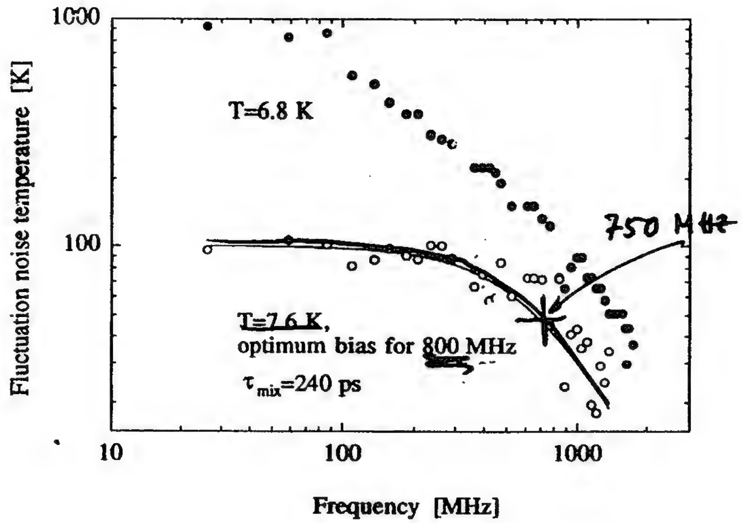

T_{FL} has the same roll-off frequency as the IF response

IMPROVEMENTS

Improved performance expected if:

1. **smaller ΔT_C**, larger dR/dT –> **larger C** and gain
2. **higher signal frequency** –> more uniform absorption along strip–> **larger C** and gain
3. Better film quality expected for films on **sapphire** or **silicon.**
4. Thinner superconductor

WEDNESDAY JULY 3

Deutsche Forschungsanstalt für Luft- und Raumfahrt e.V.

Schottky Barrier Devices for THz Applications

Prof. Dr. H.-P. Röser
DLR, Institute for Space Sensor Technology
Rudower Chaussee 5
12489 Berlin
Germany

NATO ASI New Directions in Terahertz Technology

German Aerospace Research Establishment
Institute of Space Sensor Technology

HIGH RESOLUTION HETERODYNE SPECTROSCOPY

Range:	600 GHz	- >	3,000 GHz
	500 μm	- <	100 μm
	20 cm^{-1}	- >	100 cm^{-1}
	2.5 meV	- >	12 meV

Resolution: $\nu/\Delta\nu \geq 10^6$

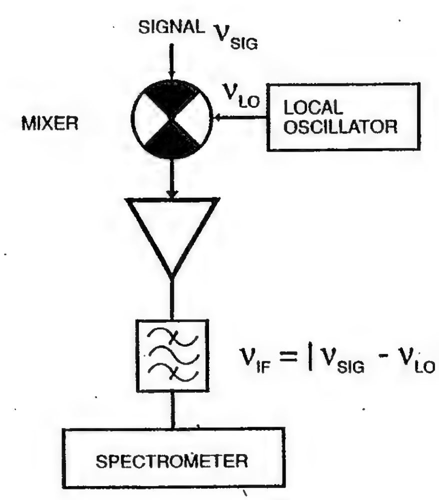

$\nu_{IF} = |\nu_{SIG} - \nu_{LO}| \approx$ GHz

HETERODYN - EMPFANG

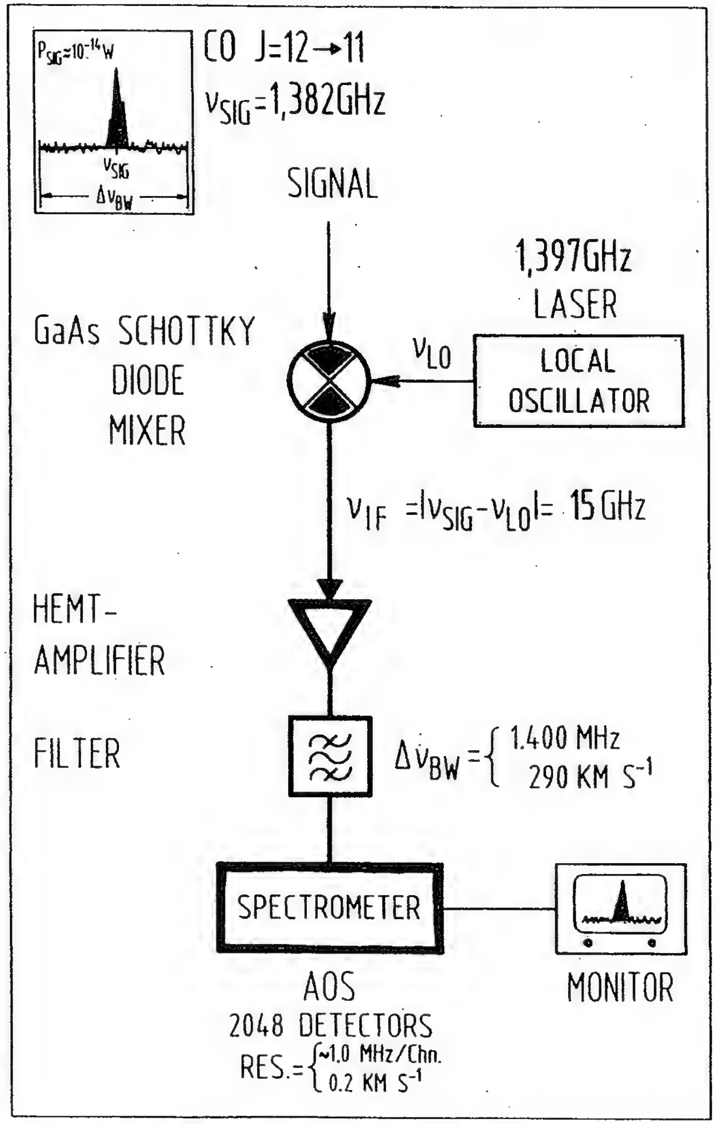

$\Delta\nu/\nu \approx 10^{-7}\ldots \rightarrow \Delta E \approx 10^{-9}$ eV

HETERODYNE DETECTION

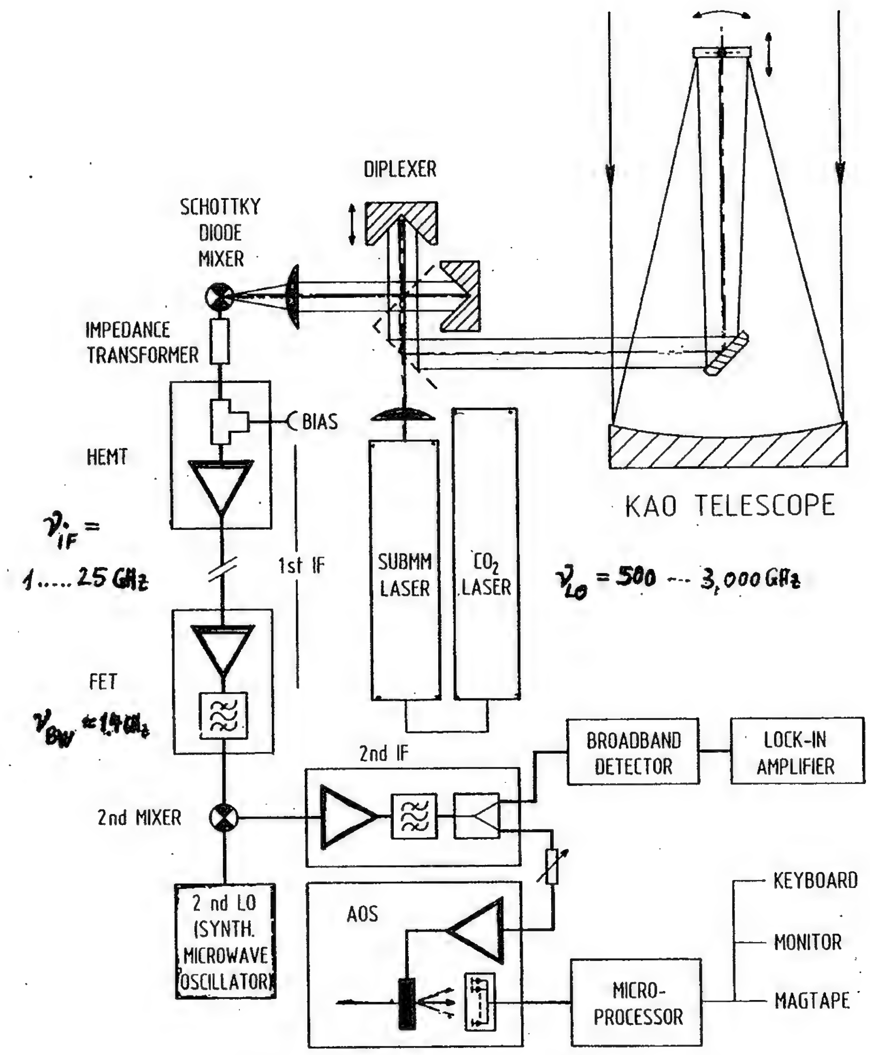

DETECTOR ARRAY 2.048 ELEMENTS

$\Delta\nu_{RES}$: 100 KHz / 1 MHz per Channel

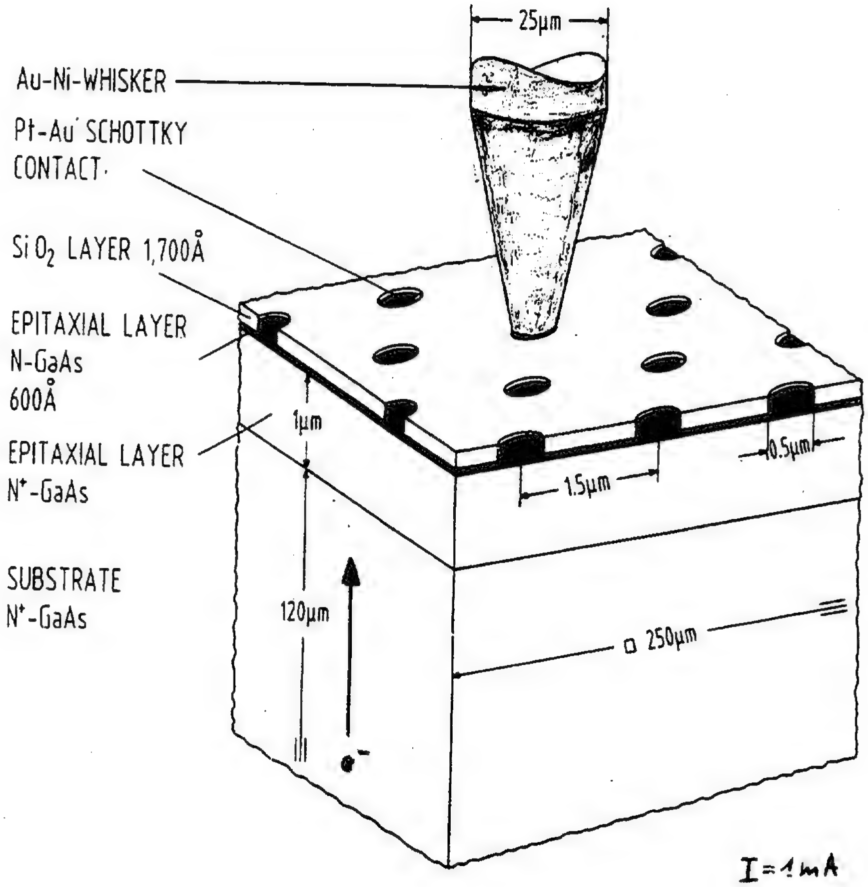

$\phi \geq 0.25\ \mu m$

$C_j \geq 0.25\ fF\ [10^-$

$R_s \approx 10\ \Omega$

$I = 1\ mA$

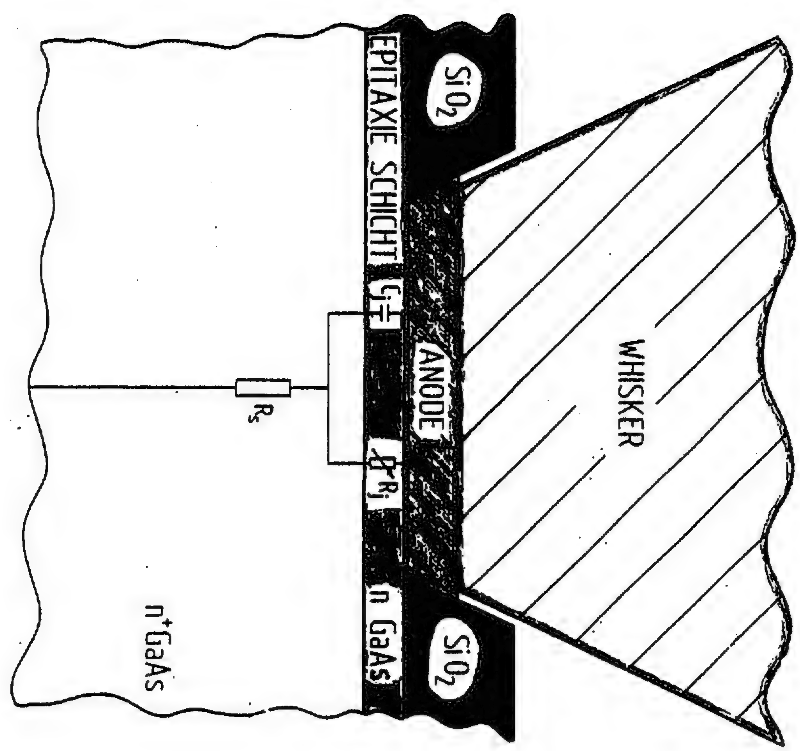

ANODE ϕ : 1 - 0.25 µm

C_j : $\geq 0.25 \times 10^{-15}$ F

R_s : $\approx 10\ \Omega$

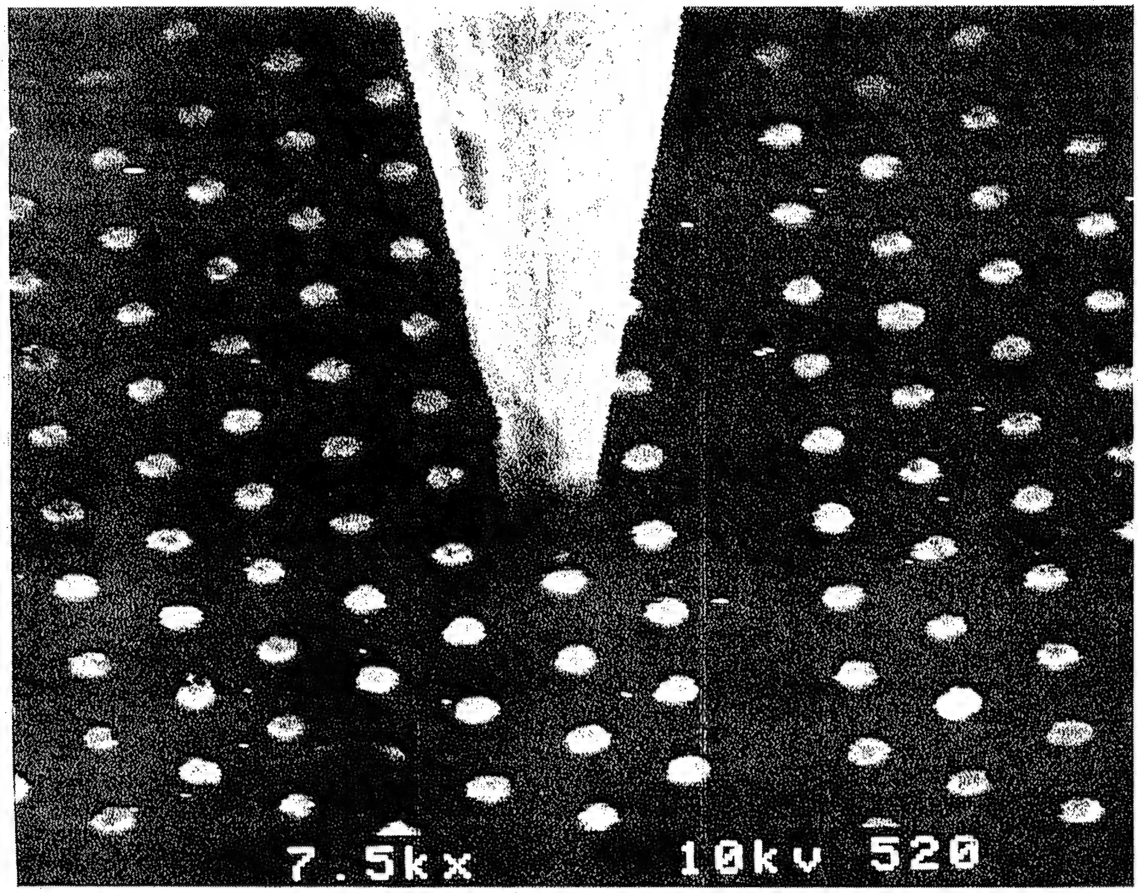
7.5kx 10kv 520

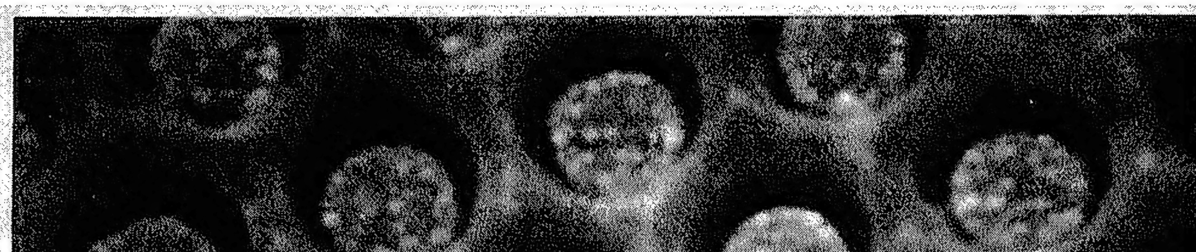
30.0Rx 10kv 068

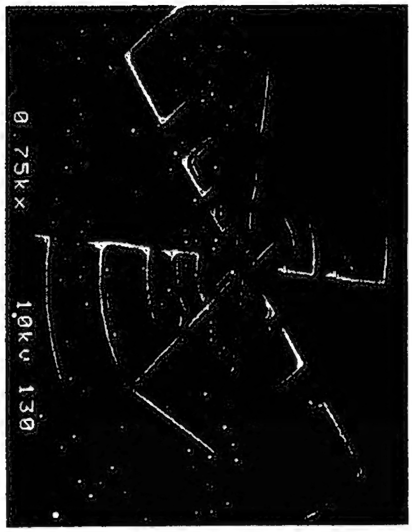

DIODE	J 118	1 I 7	1 I 12	1 T 15
ANODE DIAMETER [µm]	1.0	0.8	0.45	0.25
EPITAXIAL LAYER THICKNESS D_{epi} [Å]	1,000	1,000	600	~300
DEPLETION THICKNESS AT ZERO BIAS D_{depl} [Å]	~1,000	650	500	~300
EPITAXIAL LAYER DOPING $N_D \cdot 10^{17}$ [cm^{-3}]	1.0	3.0	4.5	10
CAPACITY AT ZERO BIAS C_{j0} [fF]	1.8	0.9	0.45	0.25
SERIES RESISTANCE R_S [Ω]	30	13	33	~20

$$\nu_{co} = \frac{1}{2\pi RC}$$

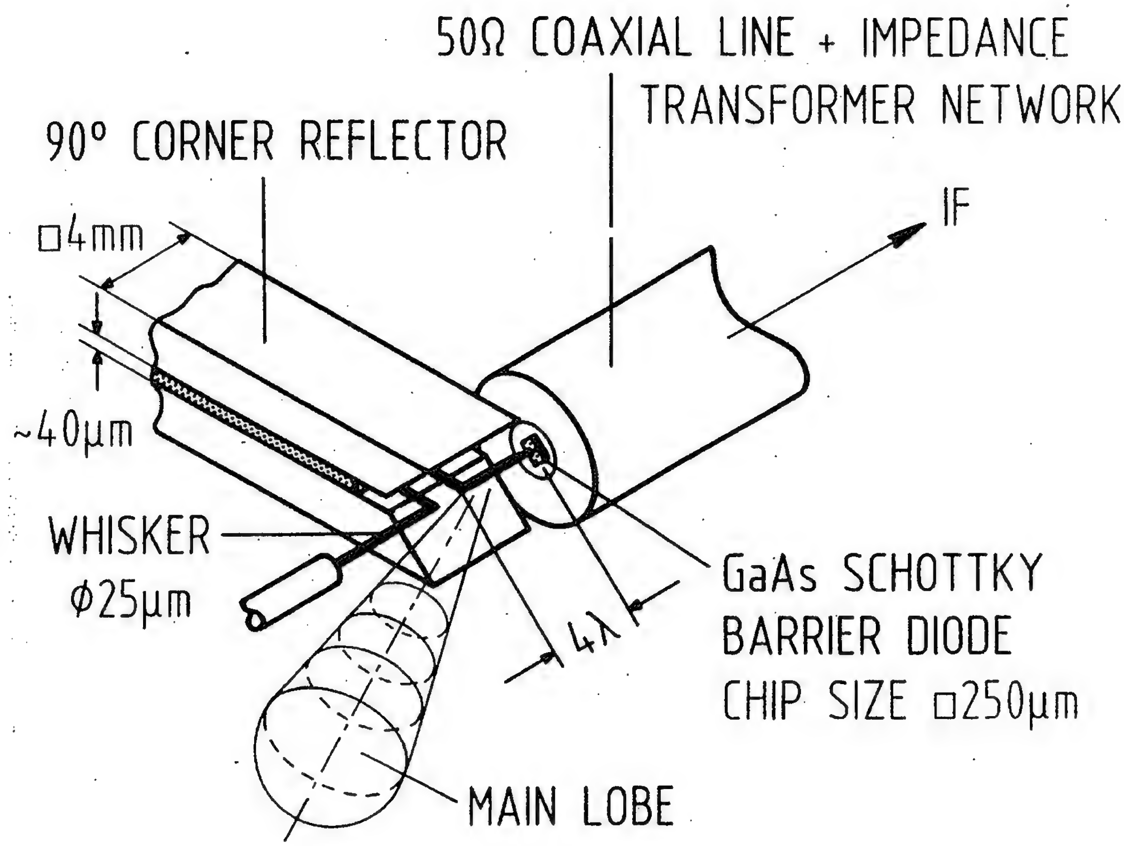

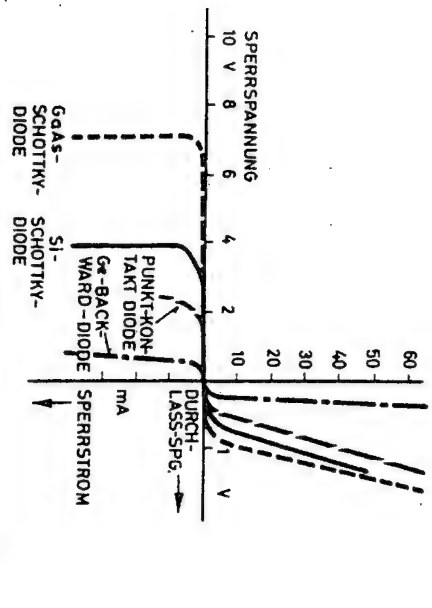

Kennlinien von Schottky- und Punktkontaktdioden

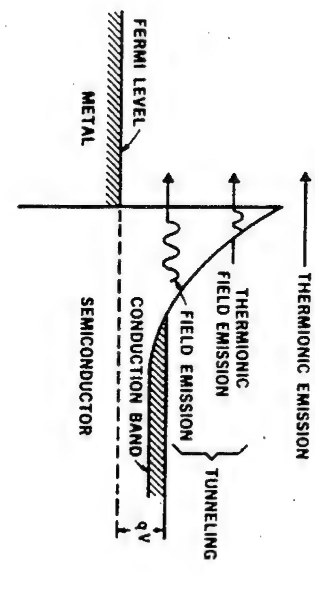

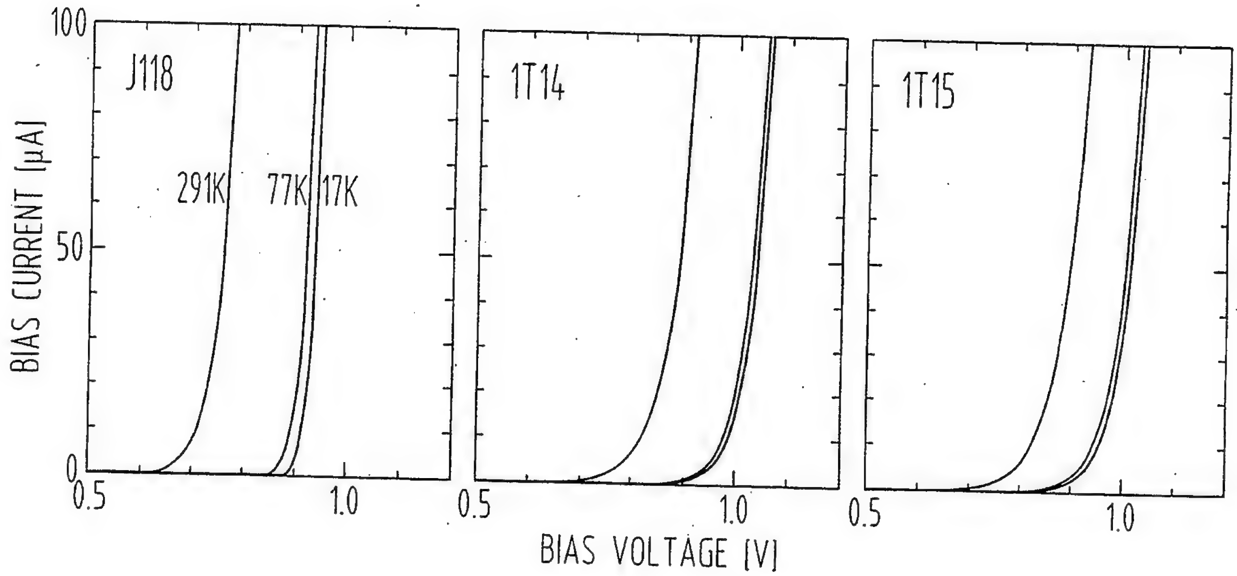
J118
1T14
1T15
291K
77K
17K
BIAS CURRENT [μA]
BIAS VOLTAGE [V]
100
50
0
0.5
1.0

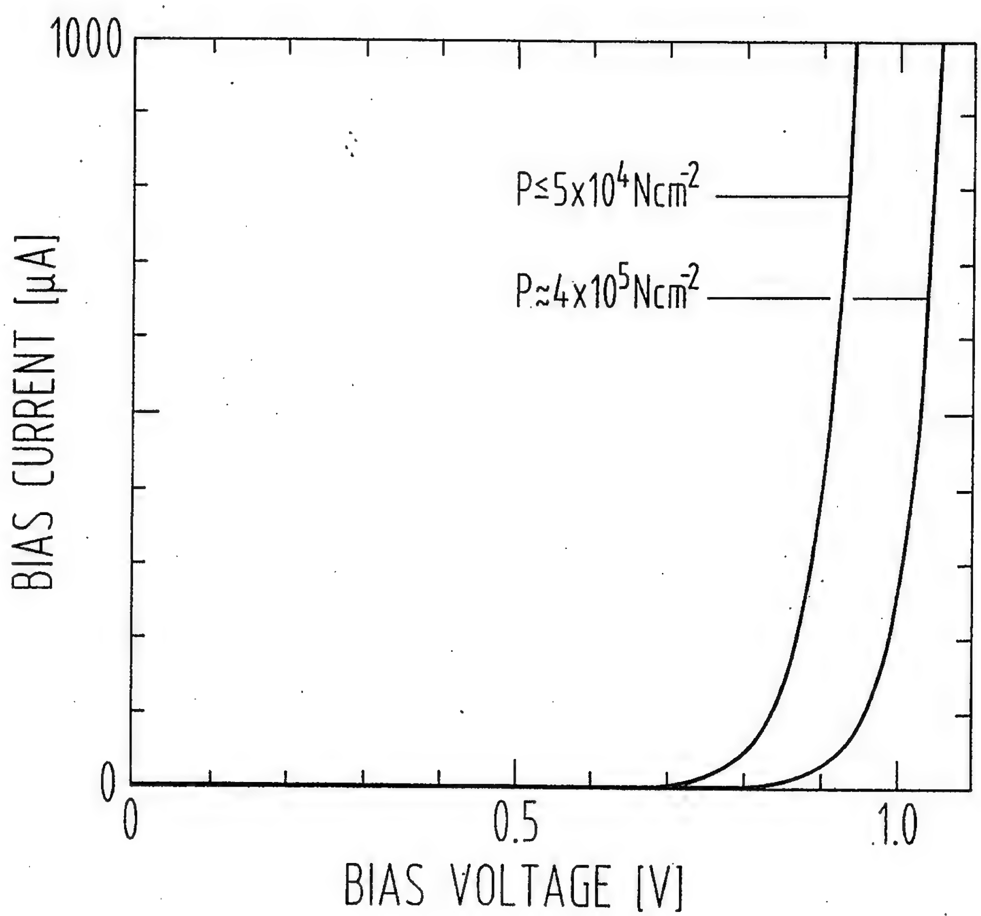
P≤5x10⁴Ncm⁻²
P≈4x10⁵Ncm⁻²
BIAS CURRENT [μA]
BIAS VOLTAGE [V]
1000
0
0.5
1.0

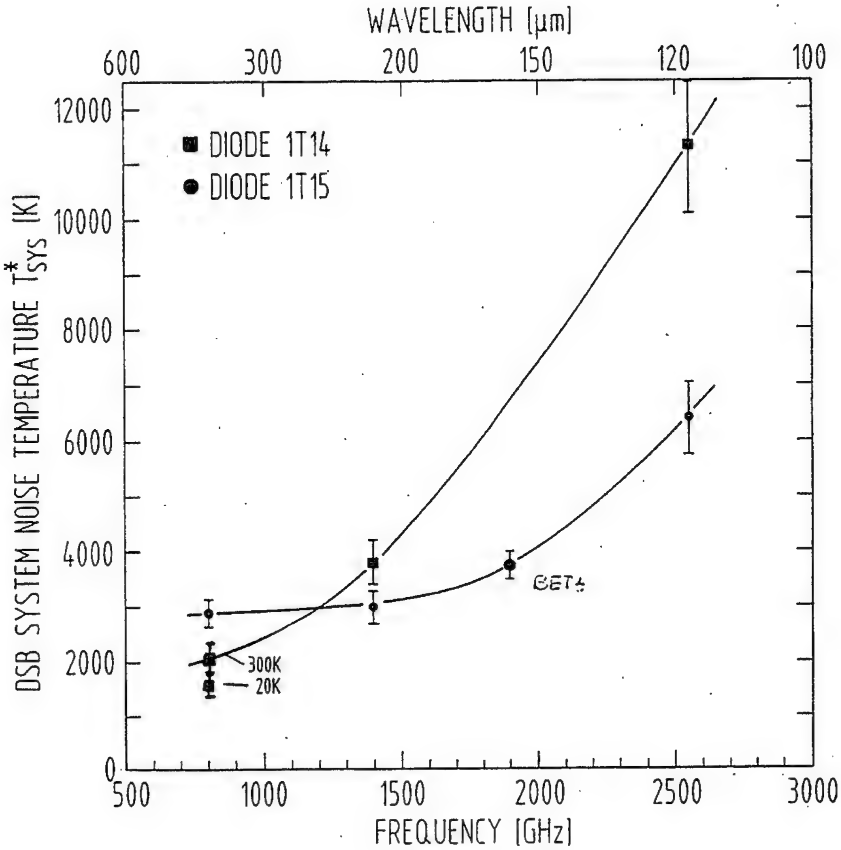
WAVELENGTH [µm]
600 300 200 150 120 100
DIODE 1T14
DIODE 1T15
DSB SYSTEM NOISE TEMPERATURE T^*_{SYS} [K]
12000 10000 8000 6000 4000 2000 0
300K
20K
FREQUENCY [GHz]
500 1000 1500 2000 2500 3000

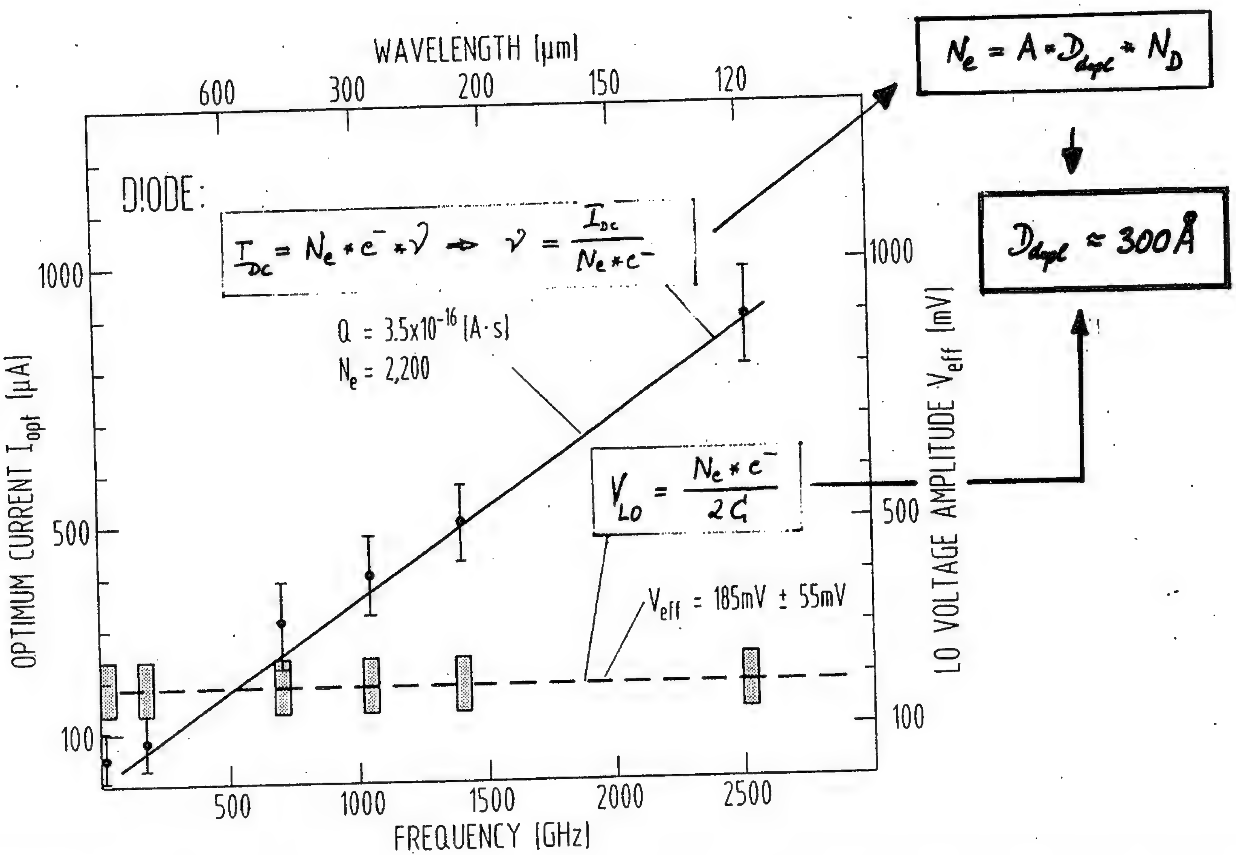
WAVELENGTH [µm]
600 300 200 150 120
DIODE:
$I_{DC} = N_e * e^- * \nu \Rightarrow \nu = \frac{I_{DC}}{N_e * e^-}$
$Q = 3.5 \times 10^{-16}$ [A·s]
$N_e = 2{,}200$
$V_{LO} = \frac{N_e * e^-}{2C_j}$
V_{eff} = 185mV ± 55mV
OPTIMUM CURRENT I_{opt} [µA]
1000 500 100
LO VOLTAGE AMPLITUDE V_{eff} [mV]
1000 500 100
FREQUENCY [GHz]
500 1000 1500 2000 2500
$N_e = A * D_{depl} * N_D$
$D_{depl} \approx 300$ Å

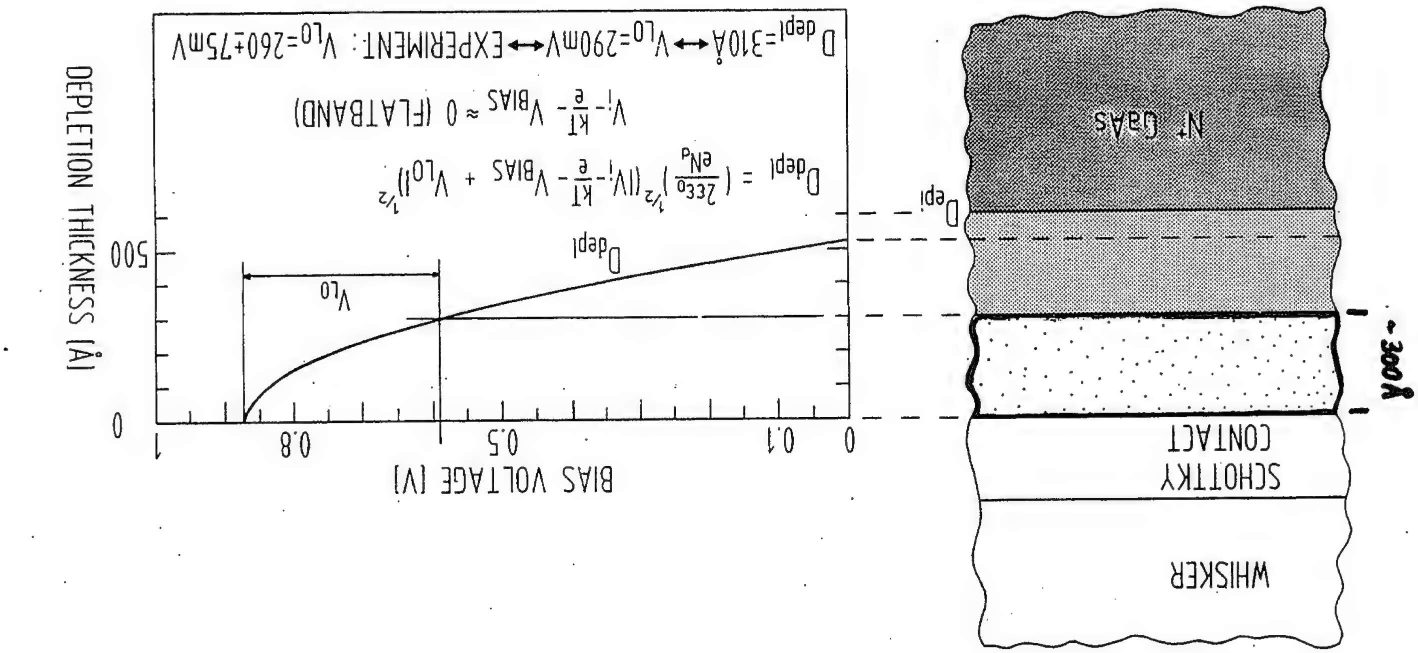

ELECTRON TRANSPORT IN MIXING VOLUME

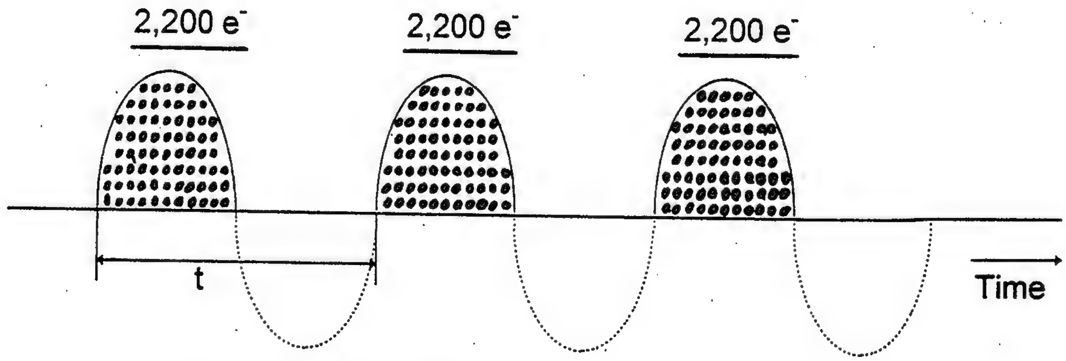

$t = 1/\nu_{LO} \approx 10^{-12} - 10^{-13}$ sec

$$I_{opt} = 500\,\mu A \equiv 1.6 * 10^{-19}\,C * 2{,}200 * 1.4 * 10^{12}\,Hz$$

$$= 3 * 10^{15}\,e/sec \equiv \underbrace{e^-} * \underbrace{N_e} * \underbrace{\nu}$$

DLR

Table 2

DIODE	J 118	1 I 7	1 I 12	1 T 15
EPITAXIAL LAYER DOPING $N_D \cdot [10^{17} \cdot cm^{-3}]$	1.0	3.0	4.5	10
ELECTRONS PER LASER CYCLE N_e	2,800	4,500	2,200	1,300
ACTIVE DEPLETION THICKNESS D_{depl}^* [Å]	320	270	260	208
RECTIFIED LO SIGNAL V_{LO} [mV]	70	160	260	380
MEAN FREE PATH L_{fp} [Å]	835	635	520	350
MOBILITY μ [$cm^2V^{-1}s^{-1}$]	4,900	3,600	3,200	2,100

GaAs Lattice constant: 5.6533Å

$D_{depl} < L_{fp}$!!

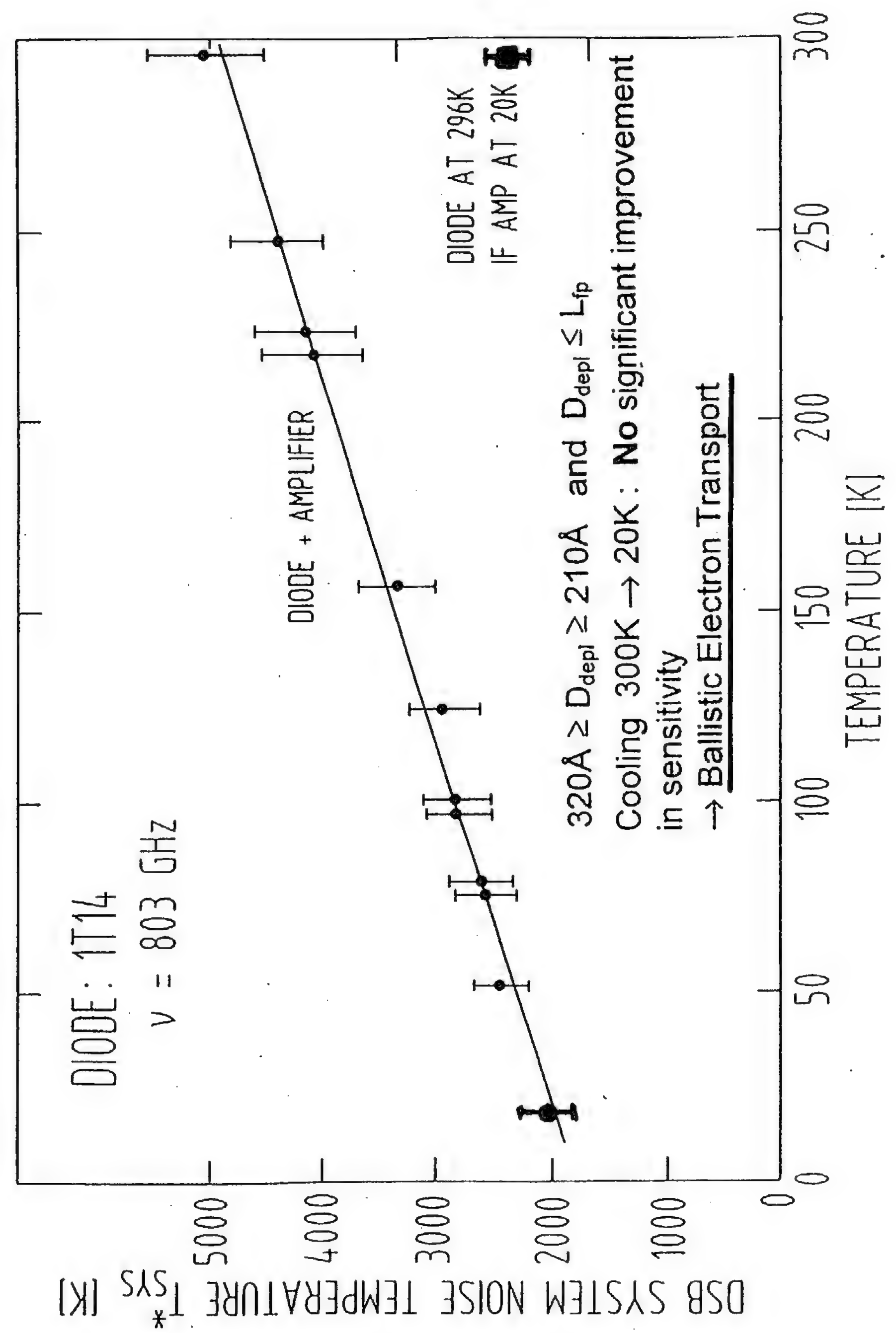

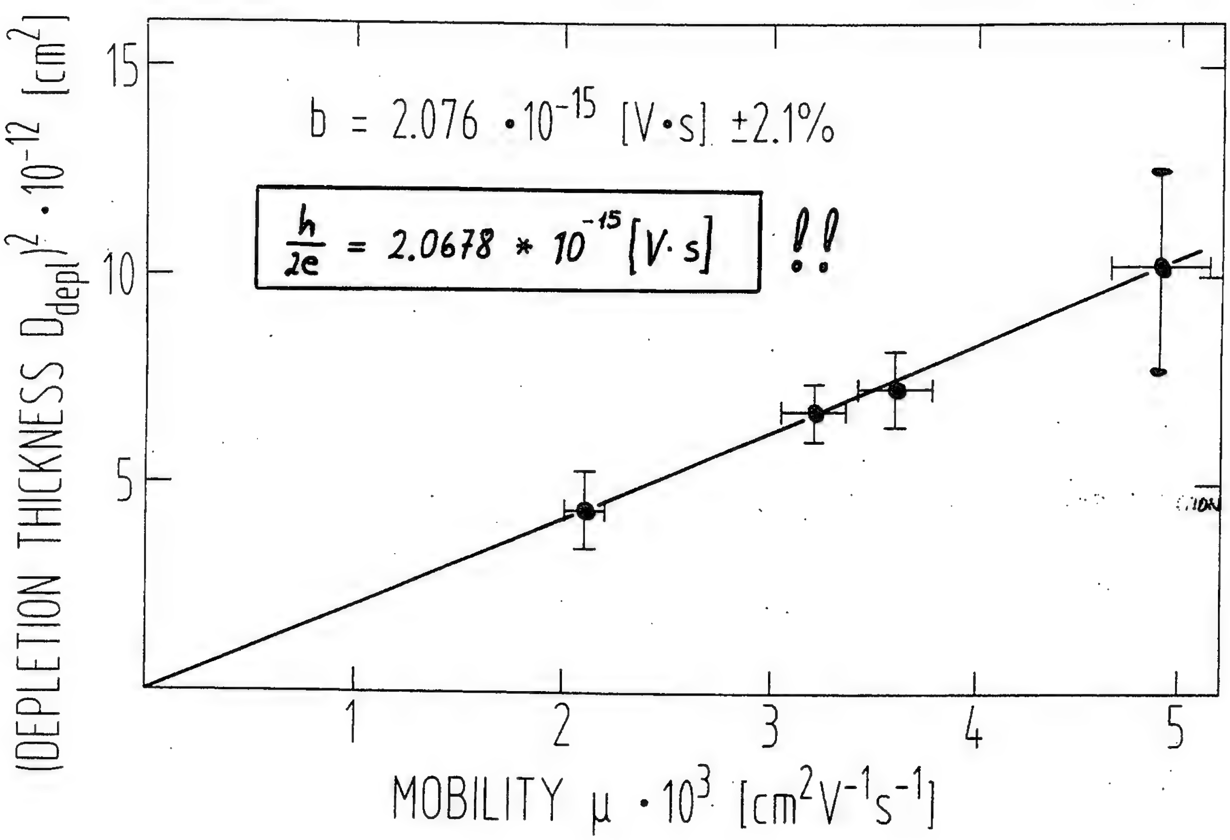
b = 2.076 ·10^-15 [V·s] ±2.1%
h/2e = 2.0678 * 10^-15 [V·s] !!
(DEPLETION THICKNESS D_depl)^2 ·10^-12 [cm^2]
MOBILITY μ ·10^3 [cm^2V^-1s^-1]

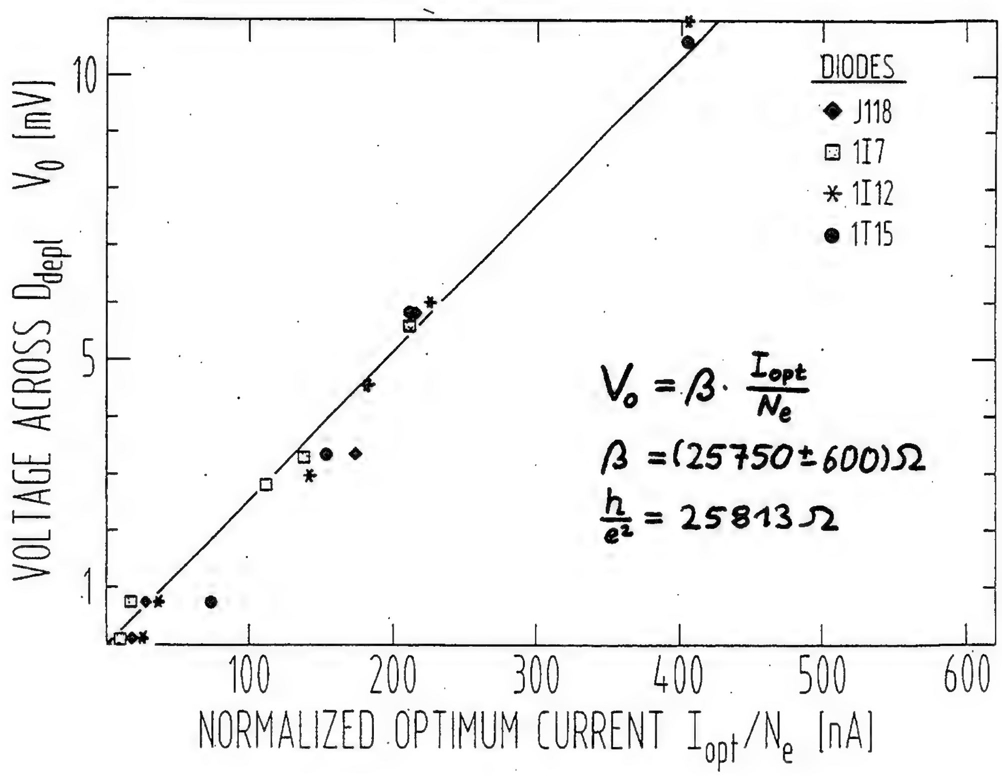
DIODES
J118
1I7
1I12
1T15
V_o = β · I_opt / N_e
β = (25750 ± 600) Ω
h/e^2 = 25813 Ω
VOLTAGE ACROSS D_depl V_0 [mV]
NORMALIZED OPTIMUM CURRENT I_opt/N_e [nA]

DLR

Device Physics of Intersubband Lasers

P. Harrison

Department of Electronic and Electrical Engineering,
University of Leeds,
LS2 9JT,
U.K.

e-mail: p.harrison@elec-eng.leeds.ac.uk
http://www.elec-eng.leeds.ac.uk/eenph/

1 Introduction

The two points I wish to make are

1. Intersubband transitions will be important in the future development of terahertz technology, and
2. In order to appreciate, and therefore exploit fully, the physics of intersubband transitions, a detailed theoretical approach needs to be employed.

2 Introduction to Lasers

2.1 Time reversal and stimulated emission

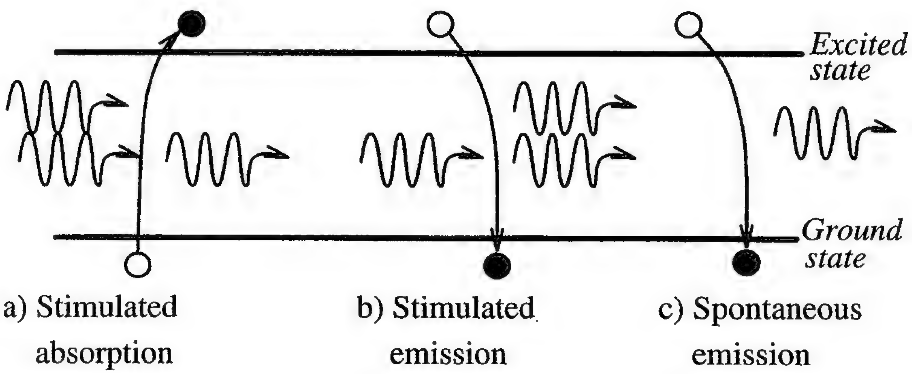

Figure 1: The three optical transitions within a laser

2.2 Population inversion and light amplification

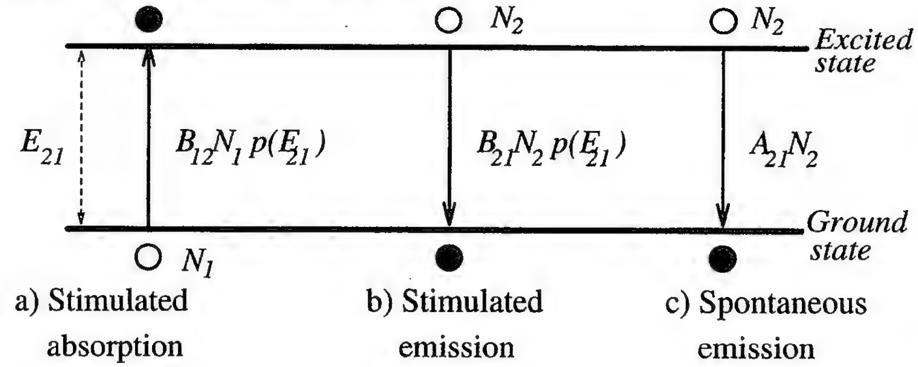

Figure 2: The three optical transitions within a laser

$$B_{21} = B_{12} \qquad \frac{A_{21}}{B_{21}} = \frac{n_R^3 E_{21}^2}{\pi^2 \hbar^3 c^3} \tag{1}$$

In order for amplification to occur the stimulated emissions must exceed the absorptions, given $B_{21} = B_{12}$ then

$$N_2 > N_1 \tag{2}$$

Population inversion is therefore a necessary condition, but it is not sufficient.

2.3 Cavities and coherence

- Cavity
- Spontaneous emission
- Optical feedback
- Stimulated emission
- Amplification
- Gain *(threshold condition)*
- Lasing

2.4 Calculation of Einstein coefficients

Using a *'time dependent perturbation'* approach, Mroziewicz (P36) gives

$$B_{12} = \frac{\pi e^2 \hbar}{m_0^2 \epsilon_0 n_R^2 E_{21}} \left|\langle \Psi_2^*(\mathbf{r})|\mathbf{p}|\Psi_1(\mathbf{r})\rangle\right|^2 \qquad (3)$$

A_{21} follows as above.

To proceed further requires knowledge of the *'state functions'* Ψ.

3 Quantum well physics—theory and computation

3.1 Assumptions and approximations

3.2 Effective mass approximation

$$\text{In vacuo} \quad E = \frac{\hbar^2 k^2}{2m_0} \qquad \text{in a crystal} \quad E = \frac{\hbar^2 k^2}{2m^*} \quad (4)$$

At relatively small wave vectors (k) it is also possible to make the further assumption that the effective mass m^* is constant, i.e. the crystal has parabolic bands.

3.3 Envelope function approximation

Representing the electron by a *'wave function'* Ψ then, Ψ must have the same period as the crystal

$$\Psi = \mathrm{e}^{i\mathbf{k}.\mathbf{r}}u(\mathbf{k},\mathbf{r}) \tag{5}$$

where the function u has the periodicity of the lattice and is known as a Bloch function, the plane wave component repeats at an integral number of lattice constants.

In the description of localized states the wave functions can be composed of a linear combination of the bulk states above and hence are written,

$$\Psi = \psi(\mathbf{r})u(\mathbf{r}) \tag{6}$$

where the sets of envelope functions ψ and Bloch functions u are both orthonormal.

Generally the properties of quantum wells can be expressed in terms of just the more readily calculated envelope function ψ, thus simplifying the problem considerably.

3.4 Form of the kinetic energy operator

The quantum mechanical linear momentum operator is given by

$$\mathbf{p}_z = -i\hbar\frac{\partial}{\partial z} \tag{7}$$

Generally is is accepted that the kinetic energy operator is given by

$$\mathcal{T} = \frac{1}{2}\mathbf{p}_z\frac{1}{m}\mathbf{p}_z \tag{8}$$

Recently, it has been demonstrated that, the correct operator should be

$$\mathcal{T} = \frac{1}{2}\frac{1}{\sqrt{m}}\mathbf{p}_z^2\frac{1}{\sqrt{m}} \tag{9}$$

For now we will avoid the issue by assuming that the effective mass is constant across the quantum well structures, this is a good approximation in GaAs/$\mathrm{Ga}_{1-x}\mathrm{Al}_x\mathrm{As}$ structures with low x.

3.5 Solution of one-dimensional quantum well potentials

Under the envelope function and effective mass approximation the Schrödinger equation is of the form

$$\left(-\frac{\hbar^2}{2m^*}\frac{\partial^2}{\partial z^2}+V(z)\right)\psi(z)=E\psi(z) \qquad (10)$$

The Transfer Matrix Technique:

$$\psi(z)=A\cos(kz)+B\sin(kz), \qquad E>V(z) \qquad (11)$$

$$\psi(z)=A\exp(\kappa z)+B\exp(-\kappa z), \qquad E<V(z) \qquad (12)$$

where

$$k=\sqrt{\frac{2m^*E}{\hbar^2}} \qquad \kappa=\sqrt{\frac{2m^*(V(z)-E)}{\hbar^2}} \qquad (13)$$

Recalling the standard boundary conditions $\psi(z)\longrightarrow 0$ as $z\longrightarrow\pm\infty$ then in the simplest structure, the single quantum well, the wavefunction is as below:

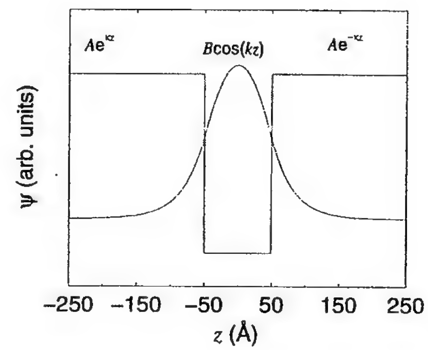

Figure 3: Transfer matrix solution

$$k\tan\left(\frac{ka}{2}\right)=\kappa, \qquad \text{where } a \text{ is the well width} \qquad (14)$$

3.6 Numerical solution of arbitrary potential

Using the standard finite difference expansion

$$\frac{d^2f}{dx^2} = \frac{f(x+\delta x) + f(x-\delta x) - 2f(x)}{(\delta x)^2} \tag{15}$$

then the Schrödinger equation can be rewritten as

$$\psi(z+\delta z) = \left(2(\delta z)^2 \frac{m^*}{\hbar^2}(V(z) - E) + 2\right)\psi(z) - \psi(z-\delta z) \tag{16}$$

and is now in the form of a 'shooting equation'.

This is solved by choosing the starting conditions of exponential growth in the left hand barrier and varying the energy E until the standard boundary conditions are satisfied, i.e.

$$\psi(z) \longrightarrow 0 \qquad \text{as} \qquad z \longrightarrow \infty \tag{17}$$

An example of the implentation of this numerical method is given below.

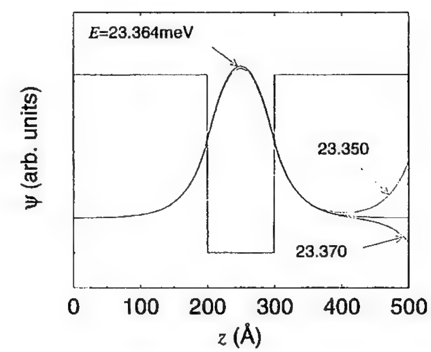

Figure 4: 'Shooted' wave function for energies around solution

3.7 In-plane solutions

The in-plane potential is zero and hence the solutions are plane waves and the total energy is

$$E + \frac{\hbar^2 k_{\|}}{2m^*} \tag{18}$$

4 Physics of interband devices

In a bipolar (electrons and holes) device, the quantum well has energy levels in both the conduction and valence bands. These are generally represented schematically as:

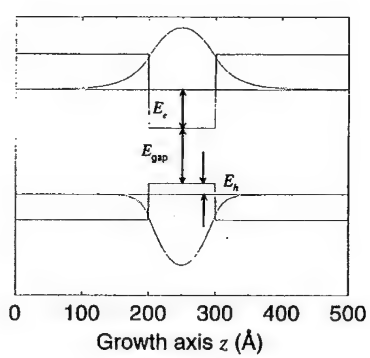

Figure 5: Interband recombination in quantum well structures

4.1 Interband recombination

$$h\nu = E_{\text{gap}} + E_e + E_h \tag{19}$$

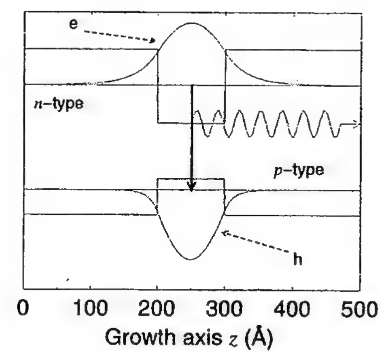

Figure 6: Interband recombination in quantum well structures

4.2 Effect of electric field F

The electric field necessary to produce current injection into the device tilts the conduction and valence band potential profiles, hence to model working devices it is necessary to account for this in the solution of the Schödinger equation.

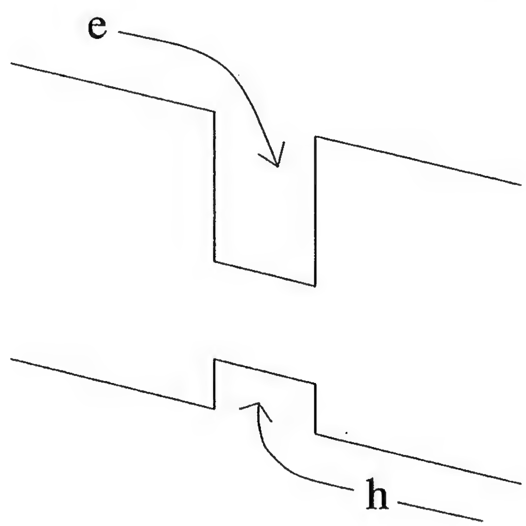

Figure 7: 'Tilting' of bands under an electric field

In principle the Transfer Matrix Technique can be implemented again, however the solutions are no longer linear combination of exponential and trignometric functions.

Making the substitution

$$y = \left(\frac{2m^*}{\hbar^2}\right)^{\frac{1}{3}} \left[\frac{(V(z) - E)}{(e|\mathbf{F}|)^{\frac{2}{3}}} - (e|\mathbf{F}|)^{\frac{1}{3}} z\right] \tag{20}$$

allows the Schrödinger equation to be expressed in the form

$$\frac{\partial^2 \psi}{\partial y^2} - y\psi = 0 \tag{21}$$

which has a general solution

$$\psi(y) = A\mathrm{Ai}(y) + B\mathrm{Bi}(y) \tag{22}$$

Alternatively the potential due to the electric field $(-e\mathbf{F}z)$ can be added to $V(z)$ in Eq. 16 and solved using the same program.

4.3 Interband transition rates and selection rules

Considering the electromagnetic field as a time dependent perturbation H'_{if} causing transitions between electronic energy levels, then the transition rate is given by Fermi's golden rule,

$$W_{i\to f} = \frac{2\pi}{\hbar}\left|H'_{if}\right|^2 \delta(E_i - E_f - \hbar\omega) \tag{23}$$

Using the envelope function formalism applied to quantum wells, i.e. $\boldsymbol{\Psi}(\mathbf{r}) = u(\mathrm{r})\psi(z)$,

$$H'_{if} = \frac{eA_0}{2m_0}\{\langle u_f|\hat{\mathbf{e}}.\mathbf{p}|u_i\rangle_{\text{cell}}\langle\psi_f|\psi_i\rangle + \langle u_f|u_i\rangle_{\text{cell}}\langle\psi_f|\hat{\mathbf{e}}.\mathbf{p}|\psi_i\rangle\} \tag{24}$$

where $\hat{\mathbf{e}}$ is the unit polarization vector and $\mathbf{p} = -i\hbar\nabla$ is the momentum operator.

In the case of interband transitions

$$\langle u_f|u_i\rangle_{\text{cell}} = \int_{\text{cell}} u_f(\mathbf{r})u_i(\mathbf{r})\ \ d\mathbf{r} = 0 \tag{25}$$

Therefore

$$\left|H'_{eh}\right|^2 = \left(\frac{eA_0}{2m_0}\right)^2 \left|\langle u_h|\hat{\mathbf{e}}.\mathbf{p}|u_e\rangle\right|^2 \left|\langle\psi_h|\psi_e\rangle\right|^2 \tag{26}$$

The last factor is known as the overlap integral between the envelope functions

$$\langle\psi_h|\psi_e\rangle = \int_{-\infty}^{+\infty}\psi_h(z)\psi_e(z)\ \ dz \tag{27}$$

and determines which optical transitions within the quantum well are allowed.

For symmetric quantum wells transitions are allowed between states of the same parity,

E1$\longrightarrow$H1
E2$\longrightarrow$H2
E3$\longrightarrow$H1
E1$\longrightarrow$H3

4.4 Interband lasers

- *p-n* junction
- heterostructure laser *(cladding by a higher band gap material produced efficiency gains by means of increased injected carrier and 'optical' confinement)*
- quantum well lasers *(separate confinement)*, higher efficiency and low threshold current

The dominant recombination method, i.e. the lasing mechanism, in all quantum well *diode* lasers is electron-hole plasma.

5 Quantum well subbands

5.1 Higher levels

As the *majority* of work to date has been on the physically simpler n-type systems, then for this introduction we will focus our attention on the conduction band:

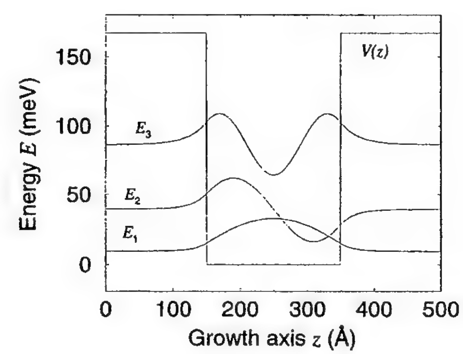

Figure 8: Ground and higher electron states in the conduction band of a quantum well

The higher energy solutions E_2, E_3, etc are called *'subbands'* as they originate from conduction band states of the bulk crystals.

5.2 Intersubband transitions

Recalling equation 24

$$H'_{if} = \frac{eA_0}{2m_0}\{\langle u_f|\hat{\mathbf{e}}.\mathbf{p}|u_i\rangle_{\text{cell}}\langle\psi_f|\psi_i\rangle + \langle u_f|u_i\rangle_{\text{cell}}\langle\psi_f|\hat{\mathbf{e}}.\mathbf{p}|\psi_i\rangle\} \tag{28}$$

but

$$\langle\psi_f|\psi_i\rangle = \int_{\text{all space}}\psi_f(\mathbf{r})\psi_i(\mathbf{r})\ d\mathbf{r} = 0 \tag{29}$$

Therefore

$$H'_{if} = \frac{eA_0}{2m_0}\langle u_f|u_i\rangle_{\text{cell}}\langle\psi_f|\hat{\mathbf{e}}.\mathbf{p}|\psi_i\rangle \tag{30}$$

Now ψ are functions of z only.

This implies that transitions are only allowed when there is a component of the polarization vector $\hat{\mathbf{e}}$ along the growth z-axis.

No intersubband absorption occurs for normal (along the growth z-axis) incident light.

5.3 Consequences of perpendicular polarization

The natural device geometry for optical detectors, and optically stimulated lasers would be based upon normal incidence excitation. However the Brewster angle geometry has had to be adopted.

There are however exceptions in the n-type system:

- anisotropic effective mass,
- spatial dependence of the effective mass and the band non-parabolicity

Emitting devices naturally produce polarized radiation which leaves the sample at the edges, this allows for fabrication into simple edge emitters.

5.4 Intersubband transitions selection rule

In a *symmetric* system, $\partial\psi/\partial z$ is of opposite parity to ψ, hence the factor

$$\langle\psi_f|\hat{\mathbf{e}}.\mathbf{p}|\psi_i\rangle = -i\hbar\hat{\mathbf{e}}_z\left\langle\psi_f\left|\frac{\partial\psi_i}{\partial z}\right.\right\rangle \tag{31}$$

becomes zero for ψ_i and ψ_f of the same symmetry parity, i.e. $\psi_i \longrightarrow \psi_f$ is forbidden.

Representing $|i-f|$ as Δn,

$$\Delta n = 1, 3, \ldots \tag{32}$$

This can be overcome by introducing an asymmetry into the system, either with the application of an electric field, or structurally.

6 Non-radiative mechanisms

6.1 Phonons

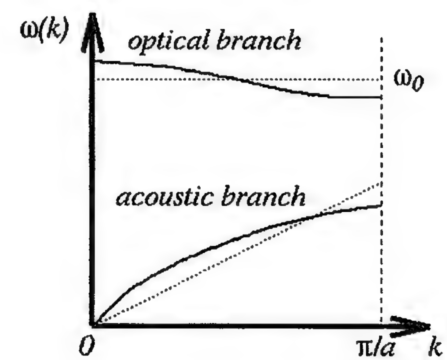

Figure 9: Acoustic ($\omega \propto k$) and optical (ω=constant) branches in a one-dimensional diatomic lattice

- Upper optical branch: $\lesssim$1 ps, 36 meV for GaAs, particularly important for intersubband events.
- Lower acoustic branch: $\gtrsim$100 ps, small momenta and energy, important for intrasubband relaxation of warm carriers

6.2 Competing mechanisms

In this example $E_{LO} < h\nu$. An electron initially in the 2nd subband can relax (lose in-plane momentum) by emitting both LO and acoustic (AC) phonons.

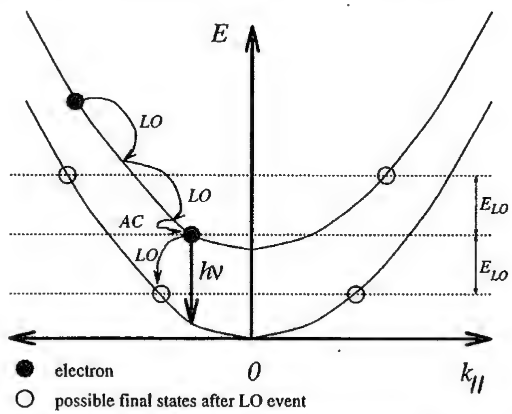

Figure 10: Acoustic phonon, LO phonon and optical scattering for a two conduction subband system

For optical emission the desired photon $h\nu$ emission must compete with the undesired intersubband LO phonon emission.

6.3 Calculation of phonon transition rates

Again using Fermi's Golden Rule, as in equation 23,

$$S(\mathbf{p},\mathbf{p}') = \frac{2\pi}{\hbar}|H_{_{\mathbf{p}'\mathbf{p}}}|^2\delta\left(E(\mathbf{p}') - E(\mathbf{p}) - \hbar\omega\right) \qquad (33)$$

Note the properties of the δ-function imply energy conservation.

The transition rate for Polar Optic phonon scattering with a 2D distribution of electrons is

$$S(\mathbf{p},\mathbf{p}') = \frac{\pi e^2\omega_0}{\epsilon_s\beta^2\Omega}\left(\frac{\epsilon_s}{\epsilon_\infty} - 1\right)\left(N_0 + \frac{1}{2} \mp \frac{1}{2}\right) \times$$

$$\delta\left(\mathbf{p}'_{\parallel} - \mathbf{p}_{\parallel} + \hbar\beta_{\parallel}\right)|G(\beta_z)|^2\delta\left(E(\mathbf{p}') - E(\mathbf{p}) - \hbar\omega\right) \qquad (34)$$

The '*scattering rate*' $\frac{1}{\tau}$ is obtained by summing the transition rate S over all possible final states.

Note that the scattering rates are often used in rate equation analysis employed to describe the carrier populations—see later.

7 Intersubband electroluminescence

If a population inversion isn't attained then the device can still give incoherent radiation, this is called electroluminescence.

First demonstrated by Helm at low temperatures and from a subband spacing below the optical phonon energy.

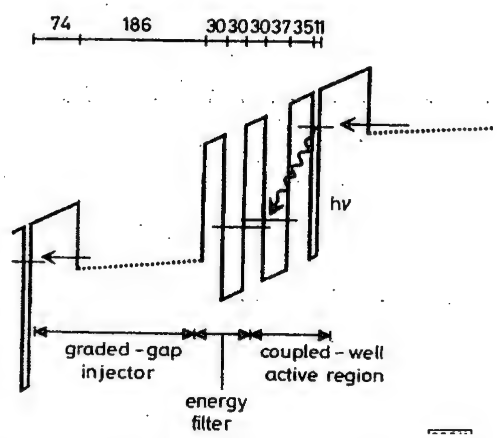

Figure 11: Band diagram of electroluminescent diode at 100 kV/cm

Faist *at al.*, Electronics Lett. **29** 2230 (1993), demonstrated the first electroluminescence in the mid-infrared (5μm), generated by a subband spacing greater than the LO phonon energy and at room temperature.

8 Infrared intersubband lasers

West, in September 1993, stated that although instantaneous spontaneous emission had been observed in a GaAs-AlGaAs quantum well, by Helm, to that date an intersubband infrared laser had not been developed.

Soon after, came the first report of such a laser, referred to as the *'Quantum Cascade Laser'*, Faist, Capasso, Sivco, Sirtori, Hutchinson and Cho, Science **264** 553 (1994). This gave a peak power of 8 mW at a wavelength of 4.2 μm (71 THz).

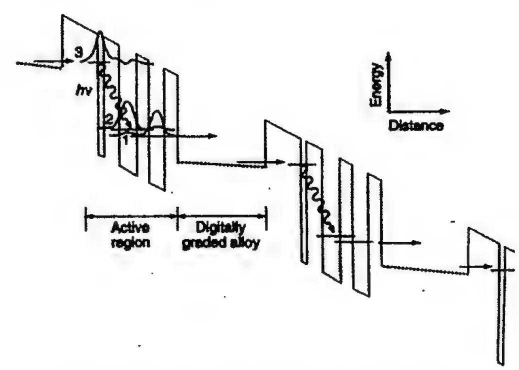

Figure 12: The *'Quantum Cascade Laser'*, Faist *et al.*

The lasing action was confirmed by the dramatic line narrowing above a certain current (the *'threshold current'*).

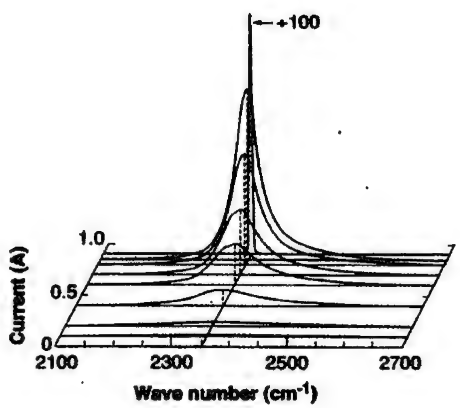

Figure 13: Emission spectrum of the quantum cascade laser at 10 K

As shown previously, the spontaneous emission and the laser radiation were polarized normal to the the layers.

For an early review of infrared intersubband lasers see Yang, Superlatt. Microstruct. **17** 77 (1995)

9 Vertical transition intersubband lasers

- less sensitive to interface roughness, impurity fluctuations,
- therefore exhibit a narrower gain spectrum and a lower threshold.

Faist *et al* Appl. Phys. Lett. **66** 538 (1995)

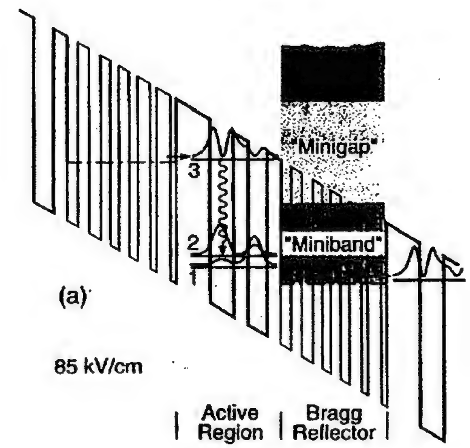

Figure 14: Vertical transition quantum cascade laser with Bragg confined excited state, Faist *et al.*

- $E_3 \longrightarrow E_2$ (271 meV$\sim$ 4.5μm) was 1.8 ps
- $E_2 \longrightarrow E_1$ (30 meV) 0.6 ps

This has led to pulsed operator up to 100 K, with a threshold current density of 3 kA/cm^2 and a slope efficiency of 300 mW/A.

10 Longest wavelength intersubband lasers—so far

Although intersubband light-emitting-diodes have been reported in the 8-13 μm wavelength region, Sirtori, Capasso, Faist, Sivco, Hutchinson, and Cho, *et al.* Appl. Phys. Lett. **66** 4 (1995), the longest wavelength intersubband *laser* to date is only 8.4 μm, also by Sirtori, *et al.*, Appl Phys. Lett. **66** 3243 (1995).

11 A dynamical advantage in moving to Terahertz

Quite simply the photon energy of terahertz frequencies is below that of the dominant loss mechanism, i.e. non-radiative LO phonon emission. Hence merely working at these frequencies eliminates the most detrimental physical loss.

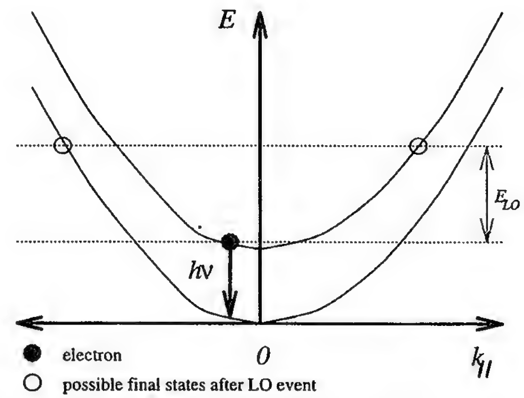

Figure 15: LO phonon emission forbidden near bottom of second subband when $E_2 - E_1 = h\nu < E_{LO}$

In GaAs the LO phonon energy is 36 meV which is equivalent to a photon frequency of 8.7 THz (34 μm).

12 Optically pumped 3-level terahertz *(far-infrared)* laser

As with any new laser, the simplest route to lasing is via optical stimulation rather than electrical injection.

Within this frequency range the most convenient optical pump is the 10.6μm CO_2 laser.

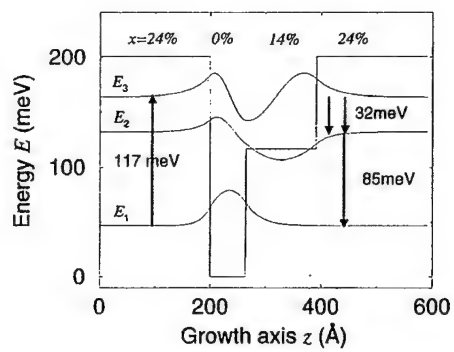

Figure 16: Optically pumped 3-level laser operating at ≈7.7 THz (32 meV, 39 μm)

The simplest device proposal is the asymmetric quantum well proposed by Berger, Semicond. Sci. Technol. **9** 1493 (1994), for the GaAs/$Ga_{1-x}Al_xAs$ system.

12.1 Structural tunability for access to other frequencies

Just varying the structural parameters of the step the design can be tailored across the Terahertz range as desired, whilst keeping the pump energy equal to the CO_2 laser line.

Step x (%)	Step width (Å)	$E_3 - E_1$(meV)	$E_3 - E_2$(meV)	$E_3 - E_2$(THz)
10	101	116.988	49.851	12.1*
11	105	117.321	45.708	11.1*
12	111	117.117	41.119	9.9*
13	118	117.154	36.504	8.8*
14	127	117.179	31.750	7.7
15	140	116.899	26.695	6.5
16	157	116.902	21.684	5.2
17	182	116.992	16.612	4.0
18	224	117.143	11.454	2.8

Table 1: Structural parameters of step in an asymmetric quantum well with a Terahertz $E_3 \longrightarrow E_2$ intersubband separation

Note the designs marked * have a spacing greater than the LO phonon energy of 36 meV, hence the dynamics of their operation will be considerably different from the others.

12.2 Optimization of optical properties

Berger proposed that the optimal band structure would occur for structural parmeters with which the product of the pump absorption efficiency and the lasing output efficiency was maximized.

Using

$$\langle \Psi_f|\mathbf{p}|\Psi_i\rangle = im\omega_{fi}\langle \Psi_f|z|\Psi_i\rangle \tag{35}$$

Then Berger's result can can be summarized as the structure with which

$$\delta^2 = \langle \psi_3|z|\psi_2\rangle\langle \psi_1|z|\psi_3\rangle \qquad \text{is maximum} \tag{36}$$

13 Rate equation analysis

Consider the lower laser level, level 2, of the optically pumped 3-level terahertz laser above.

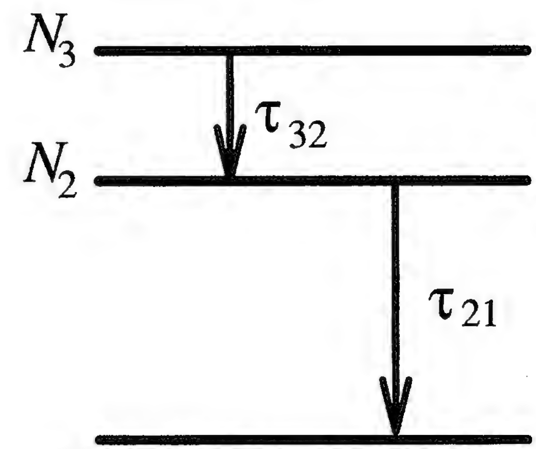

Figure 17: Rate equation analysis of population of 2nd level

$$\frac{dN_2}{dt} = +\frac{N_3}{\tau_{3\rightarrow 2}} - \frac{N_2}{\tau_{2\rightarrow 1}} \tag{37}$$

where the mean relaxation times τ are inversely proportional to the total scattering rates which include both radiative (optical) and non-radiative (phonon) mechanisms.

At equilibrium $\frac{dN_2}{dt} = 0$, for lasing $N_3 > N_2$ hence

$$\tau_{3\rightarrow 2} > \tau_{2\rightarrow 1} \tag{38}$$

14 Highest working temperature of an intersubband laser

To date is the **210 K** in *pulsed* mode, and **110 K** in *continuous wave* mode, of Sirtori *et al.* Appl. Phys. Lett. **68** 1745 (1996).

In the systems of interest here, the in-plane dispersions of the conduction subbands will be parallel, hence the broadening of the population in the upper state shouldn't have too much of a detrimental effect on the laser linewidth as the optical transitions are vertical (small momentum transfer) between the parallel bands.

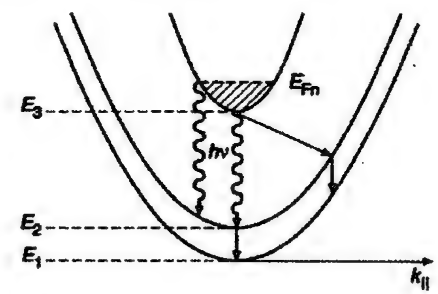

Figure 18: In-plane dispersion curves for conduction subbands, diagram from Faist, Science

This phenomena does not occur in interband recombination, since the conduction and valence bands have quite different parabolicities (effective masses).

15 Other materials

The LO phonon energy in GaAs is 36meV and this puts an upper limit of 8.7 THz on the devices.

Material	LO phonon energy (meV)	Maximum frequency (THz)
InAs	30	7
GaAs	36	8
AlSb	42	10
InP	43	10
AlAs	50	12
GaP	50	12

Table 2: LO phonon energies in selected III-V materials, Landolt and Bornstein, Vol 21

If room temperature operation proves difficult to achieve for frequencies below kT, then another avenue could be to restrict the frequency ν range to

$$kT < \nu < E_{LO}$$

which would retain the benefit of working below the LO phonon energy.

16 and finally...for completeness

An alternative technology is available for terahertz generation based on $LiNbO_3$ crystals pumped by a Nd:TAG laser, see for example, Kodo Kawase, Manabu Sato, Tetsuo Taniuchi, and Hiromasa Ito, Appl. Phys. Lett. **68** 2483 (1996).

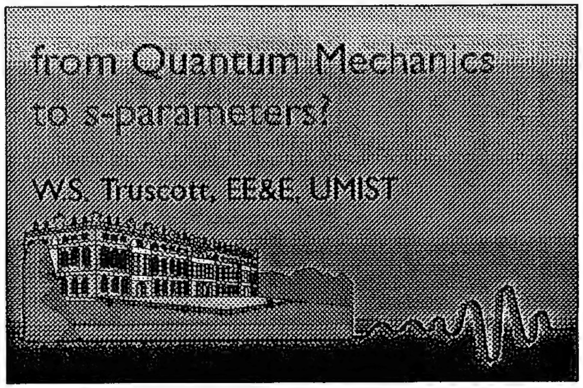

Overview

- Introductions
- Some semiconductor device physics
- When do we need quantum mechanics?
- Solutions to Schrödinger's equation in ac fields
- Consequences of solutions
- What can be calculated
- Self-consistency
- Summary and Conclusions

Acknowledgements

- UMIST research group
  - P.D. Buckle, M.A. Lynch, C-Y. Kuo
  - P. Dawson, M. Missous
- Colleagues
  - J. Lowell, K.E. Singer
- from an original idea by
  - M. Büttiker and R. Landauer

Aims of this lecture

- To discover when devices need to be described by quantum mechanics
- To outline the extent to which the electrical characteristics of devices can be calculated starting from quantum mechanics

The Art of Device Physics

- Choose best length and time scale to describe device operation

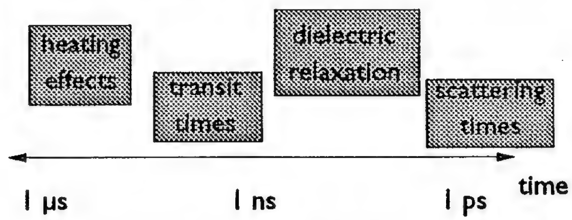

- Where do quantum effects lie?

What is Quantum Mechanics?

wavelength ⇔ momentum $\lambda = h/p$

⇕

frequency ⇔ energy $\nu = E/h$

for electrons in GaAs:

1 THz ⇔ 4 meV ⇔ 9 km/s (nm/ps) ⇔ 70 nm

Quantum Transition Devices

- Transitions between two electron states:
  - band-band - LEDs, LASERs, photodiodes
  - inter sub-band - quantum cascade laser, detectors
  - wavelengths 0.5 μm - 10 μm
- Only one photon per electron transition
  - Power to current ratio (W/A) $\propto 1/\lambda$
- Spontaneous emission (LEDs) requires:
  - charge motion ≅ half wavelength
  - for excitons in GaAs: 25 nm ≅ 80 nm

Quantum Transition Devices

- Stimulated emission (LASERs) requires:
  - optical (electromagnetic) waveguiding
  - active region at maximum field of guided wave
  - high n dielectric waveguiding structures ≅ 10 λ
- Terahertz LASERs would need:
  - stack of 10 - 100 transitions for good W/A ratio
  - high n dielectric waveguides 300 μm thick
  - active region 150 μm below top of guide
    - serious growth problems

Quantum Transition Devices

- Metal structures are a more compact alternative to dielectric waveguides
  - Antennas couple to free space e.m. radiation
  - Transmission lines, coaxial cables and metal waveguides are efficient carriers of e.m. radiation
  - These are characterised by impedances
    - $Z = \sqrt{L/C} = E/H$

What are s-parameters?

Structures with fixed impedance

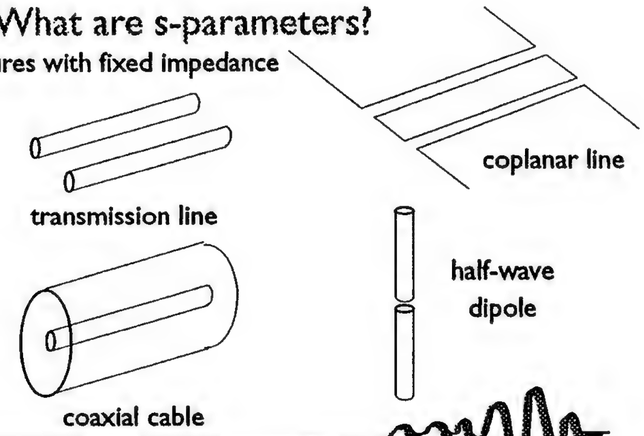

What are s-parameters?

- power ratios referred to a fixed impedance transmission line

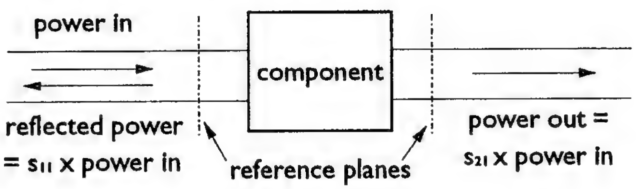

power reflected not dependent on distance
relative phases defined at reference planes

When are electronic devices quantum mechanical?

- Drift-Diffusion equation for electrons
  $J_n = - qD\partial n/\partial x + qn\mu E$
  - J_n current density
  - E electric field
  - D diffusivity
  - μ mobility
  - n density of carriers of charge q
- no inertia, no quantum mechanics, continuum
- rapid scattering ensures equilibrium velocities

When are electronic devices quantum mechanical?

- Scattering times
  - quantum effects require $\omega\tau \gg 1$
  - otherwise waves are always being "measured"
    - τ can be estimated from μ: $\mu = q\tau/m$
    - for $\mu = 1 m^2/Vs$ ($10{,}000\ cm^2/Vs$) in GaAs
    - $\tau = 0.35$ ps $f \gg 0.5$ THz
  - electron-phonon scattering strongly temperature dependent
  - onset frequency lower in cooled devices

When are electronic devices quantum mechanical?

- Ballistic carriers
  - with no scattering steady acceleration
    - $s = ut + \frac{1}{2}at^2 = ut + \frac{1}{2}qEt^2/m$
    - for GaAs

      $a = 3 \times 10^{19} m/s^2$ for $E = 10$ MV/m

      (30 $\mu m/ps^2$ for 10 mV/nm)
- but very fast optical phonon scattering occurs for

  $E > 36$ meV ($s = 4$ nm $t = 16$ fs)
- has inertia, discrete carriers
- no quantum mechanics

When are electronic devices quantum mechanical?

- Wave packets travel at group velocity $\partial\omega/\partial k$
  - for $\omega = E/\hbar = \hbar k^2/2m$
  - $v = \hbar k/m = p/m$ classical velocity
- Good description if wave packet stays together
  - low dispersion: $\Delta k/k$ or $\Delta E/E$ small, Δx large

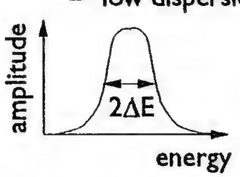

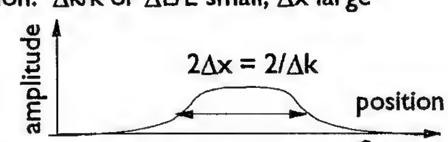

When are electronic devices quantum mechanical?

- If wave packet description is valid then carriers can be described by classical ballistics
- Quantum mechanics describes dispersion
  - wave packets broaden
  - "chirping"
  - Broadening in time t: $\Delta x = t\Delta v = d\Delta v/v$

    $\Delta x/d = \Delta v/v = \Delta k/k = 2\Delta E/E$
- Wave packets fail for: large $\Delta E/E$; long times; and for $k \neq \sqrt{2mE}/\hbar$

Time-dependent solutions to Schrödinger's equation

- Uniform potential modulation
  - adds uniform phase modulation to unchanged wavefunction
- $V(x,t) = V_0(x) + V_1\cos(\omega t)$
- $\Psi(x,t) = \Psi_0(x,t)\exp[-(iV_1/\omega\hbar)\sin(\omega t)]$

M. Buttiker and R. Landauer, PRL, **49**, 1740 (1982)

Time dependent solutions to Schrödinger's equation

- Uniform field modulation added to constant potential
  - Wave function oscillates as a classical particle
  - Space dependent phase modulation added
- $V(x,t) = V_0 - Fx\cos(\omega t)$
- $\Psi(x,t) = \Psi_0[x+F\cos(\omega t)/m\omega^2, t] \times \exp[(iFx/\omega\hbar)\sin(\omega t)]$
  - also small second order phase modulation

Time dependent solutions to Schrödinger's equation

- Uniform field modulation added to linear potential gradient
  - Wave function oscillates as a classical particle
  - Space dependent phase modulation added
  - Phase modulation dependent on F_0 and F_1
- $V(x,t) = V_0 - F_0x - F_1x\cos(\omega t)$
- $\Psi(x,t) = \Psi_0[x+F_1\cos(\omega t)/m\omega^2, t] \times \exp[(iF_1x/\omega\hbar + iF_0F_1/m\hbar\omega^3)\sin(\omega t)]$
  - also small second order phase modulation

Time dependent solutions to Schrödinger's equation

- Uniform field modulation added to parabolic potential
  - Wave function oscillates as a classical particle in same potential: effective field $G = F_1/(1-\omega_0^2/\omega^2)$
  - Space dependent phase modulation added
- $V(x,t) = \frac{1}{2}m\omega_0^2x^2 - F_1x\cos(\omega t)$
- $\Psi(x,t) = \Psi_0[x+G\cos(\omega t)/m\omega^2, t] \times \exp[(iGx/\omega\hbar)\sin(\omega t)]$
  - also small second order phase modulation

Linking exact solutions

- At a boundary between time-independent and time-dependent regions
  - Ψ and $\partial\Psi/\partial x$ must be continuous
- Match $A\exp\{ikx - iEt/\hbar\} + B\exp\{-ikx - iEt/\hbar\}$ with $[C\exp(i\kappa\xi) + D\exp(-i\kappa\xi)]\exp[-iEt/\hbar + (iFx/\omega\hbar)\sin(\omega t)]$
  - where $\xi = [x + (F/m\omega^2)\cos(\omega t)]$
- Expanding $\exp[i\alpha\cos(\omega t)]$ and $\exp[i\beta\sin(\omega t)]$ gives $[C\exp\{i\kappa x - iEt/\hbar\}\sum_{-\infty}^{\infty} i^n J_n(\kappa F/m\omega^2)\exp(in\omega t) +$
  $D\exp\{-i\kappa x - iEt/\hbar\}\sum_{-\infty}^{\infty} i^n J_n(-\kappa F/m\omega^2)\exp(in\omega t)]$
  $\times \sum_{-\infty}^{\infty} J_n(Fx/\omega\hbar)\exp(in\omega t)$

Linking exact solutions

- Match waves with same time dependence
- At Energy E
- From matching Ψ: $A + B = [C + D]\, J_0(\kappa F/m\omega^2)$
- From matching $\partial\Psi/\partial x$: $ik[A - B] =$
  $i\kappa[C - D]\, J_0(\kappa F/m\omega^2) + [C + D]\,\partial[J_0(Fx/\omega\hbar)]/\partial x$
  - these fix B/A, C/A and D/A [=0]

Linking exact solutions

- At Energy $E + n\hbar\omega$
- From matching Ψ: $B_n = \Sigma[C_m + D_m]\, J_{n-m}(\kappa_m F/m\omega^2)$
- From matching $\partial\Psi/\partial x$:
  $-ikB_n = \Sigma i^{n-m}\kappa_m[C_m - D_m]\, J_{n-m}(\kappa F/m\omega^2) +$
  $F/\omega\hbar[C_{n-1} - C_{n+1} + D_{n-1} - D_{n+1}]$
- In time-independent region additional waves are generated at all harmonics of ω with amplitudes determined by relevant Bessel functions

Linking exact solutions

Device structure with one time-dependent region and incident energy E

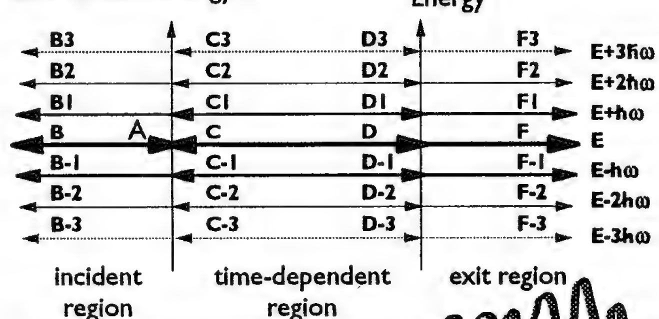

Exact solutions - line spectra

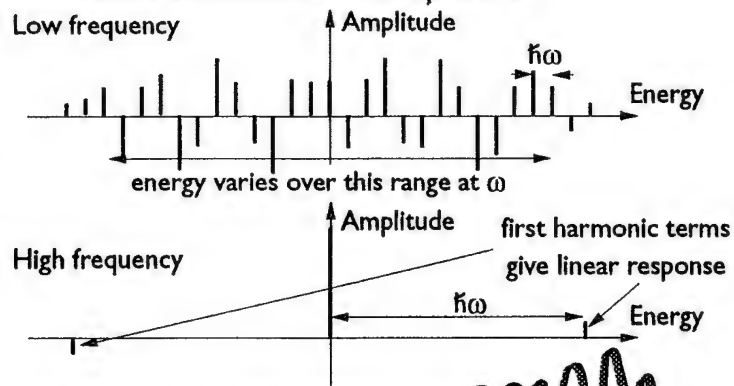

Is quantum mechanics needed?

- Quantum mechanical solutions are same as classical if $E \pm \hbar\omega$ can form a wave packet with E and system is linear with energy over $\pm \hbar\omega$
  - $\hbar\omega/E \ll 1$ and $k(E+\hbar\omega) = k(E) + \hbar\omega\partial k/\partial E$
- This will always fail at high enough frequencies
  - Quantum behaviour is possible in many Terahertz devices

Power spectra with scattering

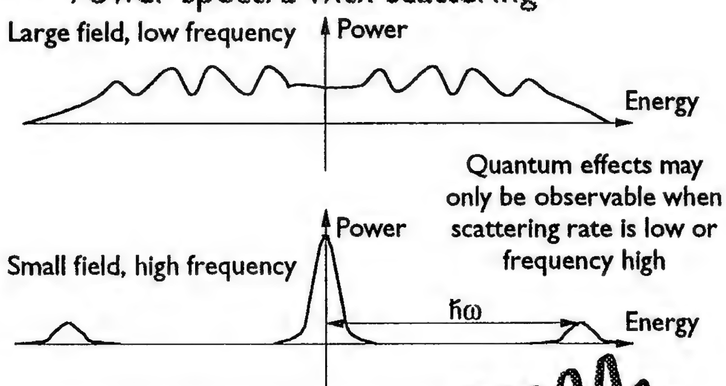

Calculation of current flow

- 1st order calculation
- Exit amplitude proportional to
  - $F + (F_1+F_{-1})\cos(\omega t) + i(F_1-F_{-1})\sin(\omega t)$
- Exit current proportional to
  - $F^*F + [F^*(F_1+F_{-1})+(F_1+F_{-1})^*F]\cos(\omega t) +$

    $i[F^*(F_1-F_{-1})-(F_1-F_{-1})^*F]\sin(\omega t)$

steady current

resistive current

capacitative current

Calculation of charge oscillation

- 1st order calculation of dipole moment variation
- $M = \int \Psi^* x \Psi \, dx$
- $M(\omega) = \int \Psi^* x \Psi(\omega) + \Psi(\omega)^* x \Psi \, dx =$
  $\int [C^* \exp(-i\kappa x) + D^* \exp(i\kappa x)] x \times$
  $[C_1 \exp(i\kappa_1 x - i\omega t) + C_{-1} \exp(i\kappa_{-1} x + i\omega t)$
  $+ D_1 \exp(-i\kappa_1 x - i\omega t) + D_{-1} \exp(-i\kappa_{-1} x + i\omega t)]$
  $+ cc \; dx$
- This may be interpreted in terms of polarisation currents

Effects of quantum mechanics:

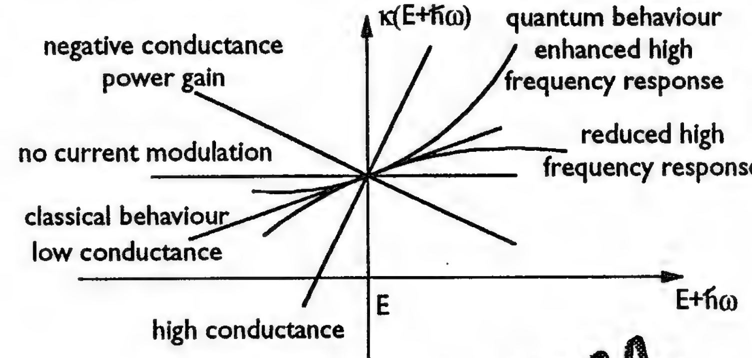

Quantum enhancement greatest with resonances

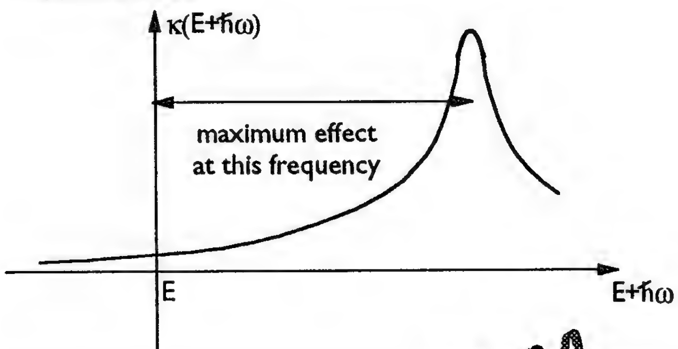

Phase shifts with resonances

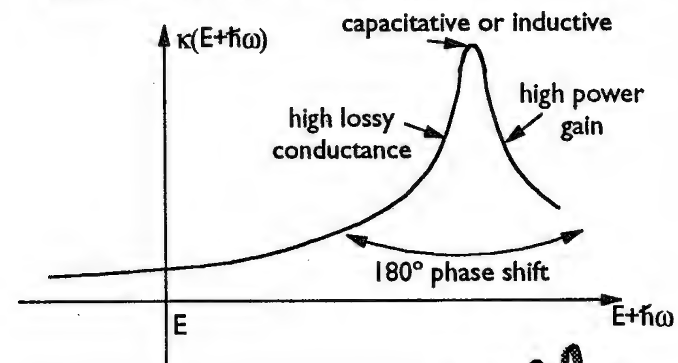

Maximising benefit from resonances

- Frequency of maximum gain depends on incident energy E
  - spread of incident energies should match resonance
  - use incident energy filter (another resonance)
- Effects scaled by dc current
  - High gain requires high current density
- Resonances above and below E can enhance both sidebands
  - use three resonances spaced by $\hbar\omega$

Self-consistency

- ac solutions
- $\varepsilon\partial E/\partial x = \rho(x) \propto \Psi^*(x)\Psi(x)$
- but $\chi(\omega) = \partial\rho(\omega)/\partial E(\omega)$ is non-local
- continuous variation of E:

  $\varepsilon E(x,\omega) = \varepsilon E(0,\omega) + \int \Psi^*(x,\omega)\Psi(x)+\Psi^*(x)\Psi(x,\omega)dx$

  can be approximated by a series of steps:

  $\varepsilon E_n(\omega) = \varepsilon E_{n-1}(\omega) + \int_n \Psi^*(x,\omega)\Psi(x)+\Psi^*(x)\Psi(x,\omega)dx$

Summary

- Quantum effects only observed when wave packet description fails
- Quantum effects give a frequency dependent response
- Quantum effects can enhance the response above its low frequency value over certain frequency ranges

Conclusions

- At terahertz frequencies semiconductor structures are likely to exhibit quantum effects particularly:
  - if cooled
  - if there are resonances
- s-parameters can be calculated for stuctures showing quantum effects
- But the requirement for self-consistency makes calculation of s-parameters very difficult if there are strong quantum resonances

THURSDAY JULY 4

Travelling Wave Detectors: A New Principle for Terahertz Operation

by

H Sigg

(No material available.)

Materials issues for new devices

D. Lippens

Institut d'Electronique et de Microélectronique du Nord
UMR CNRS 9929 Université des Sciences et Technologies de Lille
59652 Villeneuve d'Ascq Cedex, France

Chateau de Bonas, France
July 11, 1996

iemn Recherche Formation Transfert

Outline

Bulk materials
- Electronic structure
- Transport properties

Non stoichiometric materials
- Low temperature grown GaAs
- Related compounds

Doping issue
- n-type doping
- p-type doping

Heterostructure
- Single Heterojunction (type I and II)
- Material system grown on GaAs substrate
- InP-based materials

Quantum well and tunnelling heterostructures
- Modulation doped heterostructure
- Tunneling barrier
- resonant tunneling heterostructure (double barrier and superlattice)

ENERGY BAND STRUCTURE

Parameter		*AlP*	*AlAs*	*AlSb*	*GaP*	*GaAs*	*GaSb*	*InP*	*InAs*	*InSb*
Direct Energy Gap (eV)	$\Gamma_{15}-\Gamma_1$	3.62 (77K)	3.14	2.22	2.78	1.424	0.70	1.34	0.356	0.180
Indirect Energy Gap (eV)	$\Gamma_{15} \rightarrow X_1$	2.45	2.14^a	1.63^a	2.268^a	1.804	1.25 (10K)	2.04		
Temperature Dependence of Direct and Indirect Energy Gap (X 10^{-4} eV K^{-1})	dE_{d}/dT dE_{ind}/dT	−3.6	−5.2 −4.0	−3.5	−4.5 −5.2	−3.9 −2.4^b	−3.7	−2.9 −3.7^b	−3.5	−2.8
Pressure Dependence of Minimum Energy Gap (X 10^{-6} eV^{-1})	dE/dP			−1.5	−1.6	12.0	14.7	8.8	10.6	15.9
Indirect Energy Gap (eV)	$\Gamma_{15}-L_1$					1.81 (110K)	0.81	1.74		

(a) Minimum situated at the Δ axes near the boundary: $k = (0.903, 0, 0)$ for AlAs; $k = (0.95, 0, 0)$ for GaP.
(b) Temperature dependence of the energy separation between Γ and X minima.

ELECTRONIC STRUCTURE
(Bulk materials)

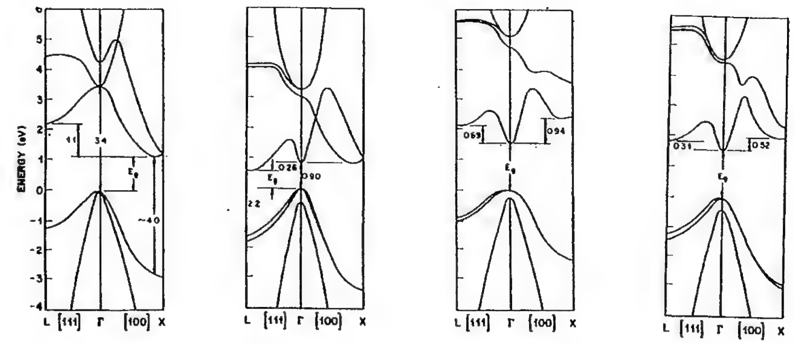

SILICON GERMANIUM INDIUM PHOSPHIDE GALLIUM ARSENIDE

BAND STRUCTURE

•Iso-energy curves for $Al_{0.45}Ga_{0.55}As$ (ΓXK)

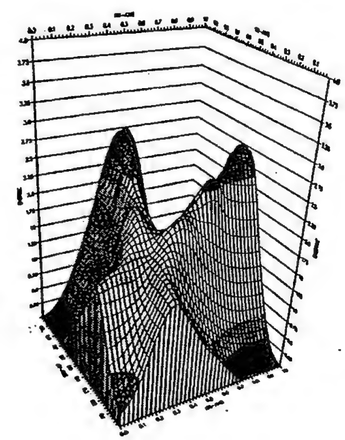

•Iso-energy for AlAs first conduction band

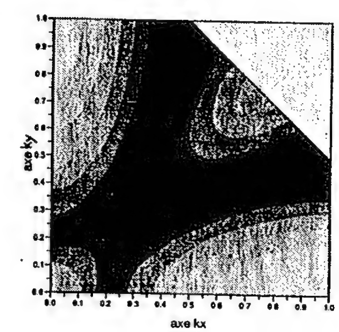

Illustration of the cross-over between Γ and X valley
Pseudopotential calculations

CARRIER VELOCITIES IN III-V COMPOUNDS

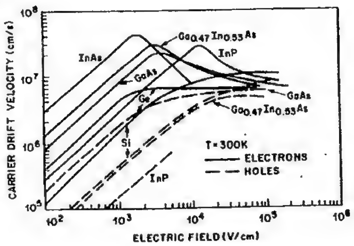

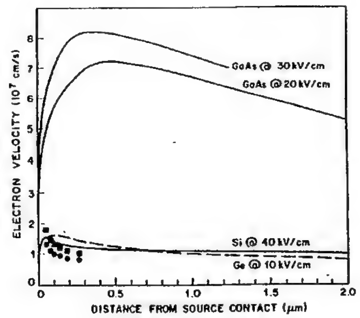

LOW FIELD MOBILITIES IN III-V COMPOUNDS

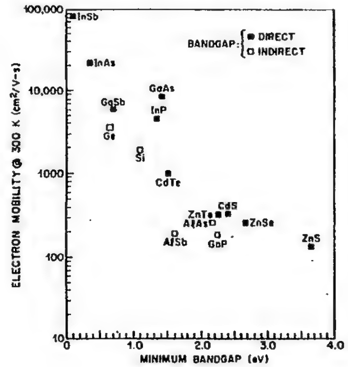

Electron mobilities

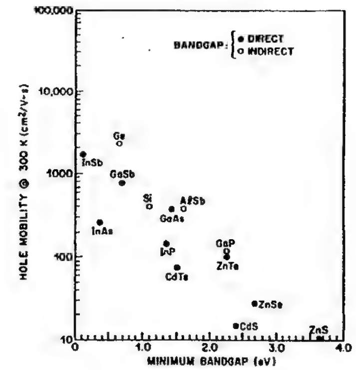

Hole mobilities

TRANSPORT PROPERTIES

Variation of electron mobility (cm^2/Vs) versus temperature

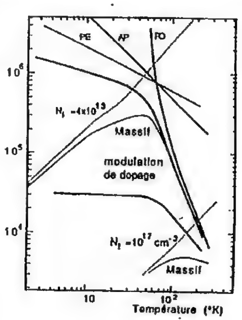

At room temperature
Mobility limited by optical phonon
At low temperature
Mobility limited by impurity scattering

Scattering probabilities in GaAs (10^{14} s^{-1})

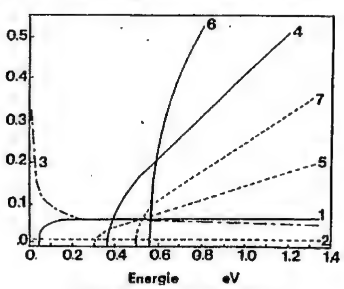

1. Polar optical phonon(emission)
2. Polar optical phonon (Absorption)
3. Impurity scattering
4. Intervalley scattering Γ-X (emission)
5. intervalley scattering Γ-X
6. Γ-L emission
7. Γ-L absorption

NON STATIONARY-TRANSPORT EFFECT

Velocity Overshoot : v= μ(E).F, (E electron energy, F: Electric field)
Unbalance between the local energy and the electric field

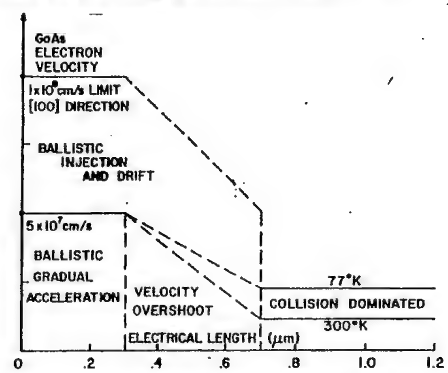

Maximum velocity limited by the band structure (v~ ∂E/∂k)
Hot electron injection for high velocity

IMPACT IONIZATION (I)

Energy conditions: E > 1.5 Eg
Creation of an electron hole pair

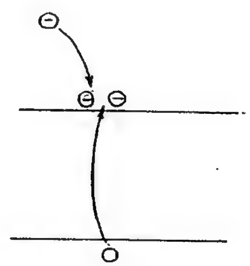

Impact ionization probability (cm^{-1})

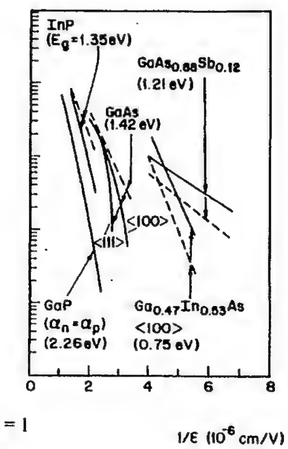

Avalanche condition: Multiplication coefficient →∞ ; $\int \alpha dx = 1$

IMPACT IONIZATION (II)

Order of magnitude of avalanche breakdown voltages (Vb)

Variation of Vb as a function of Doping concentrations for abrupt junctions
SM. Sze and G. Gibbons Appl. Phys. Lett. 8, 11(1966)

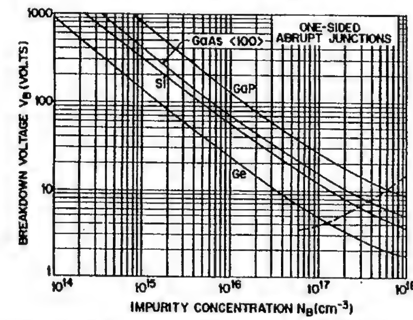

Approximate universal expression $Vb = 60\,(Eg/1.1)^{3/2}\,(Nb/10^{16})^{-3/4}$
Vb = 6V for $In_{0.53}Ga_{0.47}As$, 2V for InAs and Nb= $1x10^{17}$ cm^{-3}

NON STOCHIOMETRIC MATERIALS

Low-temperature growth of GaAs (200°C < Tgrowth <250°C)

Main advantage: Excess arsenic (typically 1%) by preserving the crystal quality

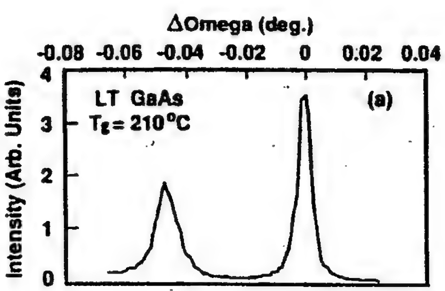

XR Diffraction
evidence of an increase in the lattice constant

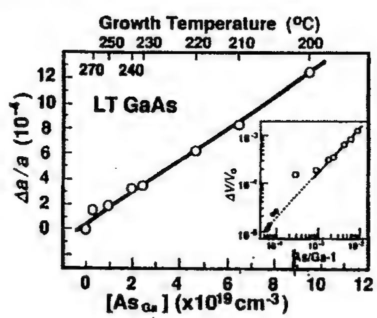

High concentration of As antisites (As_{Ga})

LOW TEMPERATURE GROWN GaAs

Short life time of photo-excited carriers

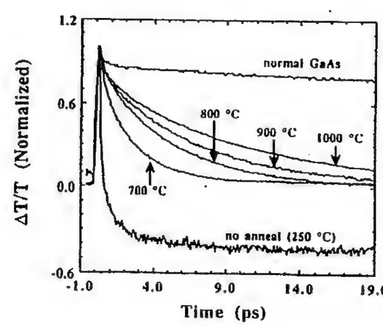

Due to the high concentration of defects, possibility of conduction by hopping process
Annealing of material: formation of As precipitates which act as micro Schottky's increasing the resistivity

APPLICATION IN ULTRA-FAST ELECTRONICS

Use of Photoconducting antenna and Electro-optic sampling

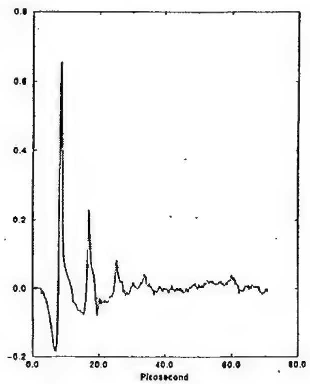

Subpicosecond terahertz pulse generation

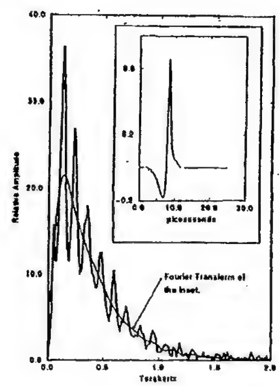

Fourier transform

HETEROJUNCTION

Basic Model
After Anderson Solid State Electronics, 5, 341, 1962

•Energy band Diagram for two isolated SC

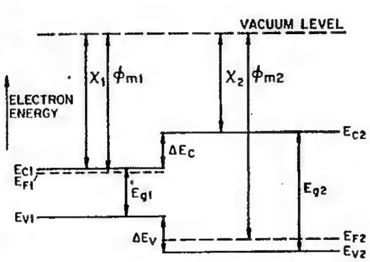

•Ideal aniso-type heterojunction

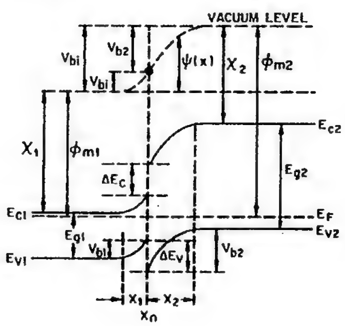

DOPING ISSUE

Measured ionization energies for various impurities in GaAs

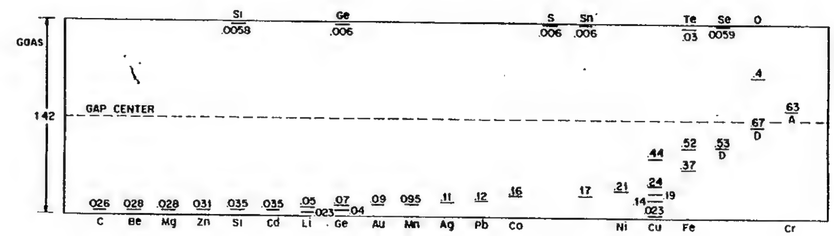

N-type doping : essentially Silicon

Typical doping level in GaAs : $2x10^{18} cm^{-3}$ for GaAs, $5x 10^{18} cm^{-3}$ for $In_{0.53} Ga_{0.47}$ As material

P-type doping :
Mg, Be, Zn
More recently systematic use of Be for low diffusion properties

POSSIBLE HETEROSTRUCTURE BAND ALIGNMENTS

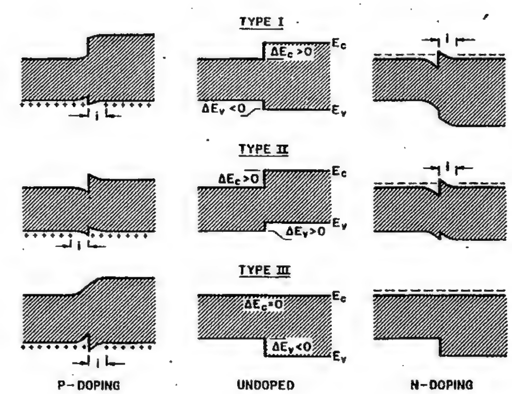

CHOICE OF A LAYERED STRUCTURE

Variation of the band gap as a function of lattice constant for III-V binary and alloy semiconductors

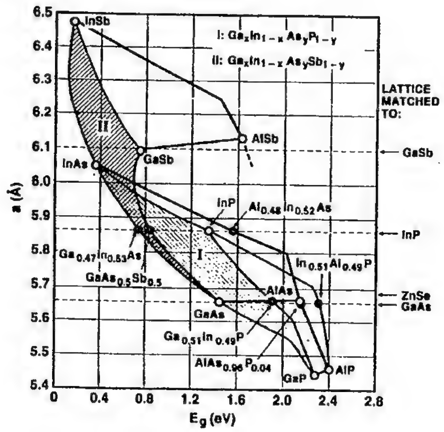

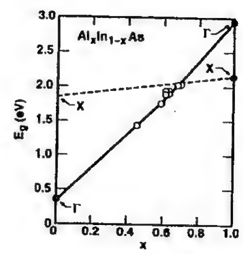

EIGENSTATES and DENSITY OF STATES

2 D confinement of electron or holes

Envelope wavefunction — dispersion along the k_x direction — 2D density of states

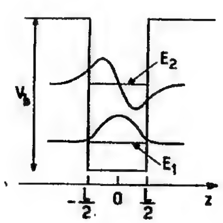

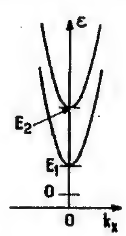

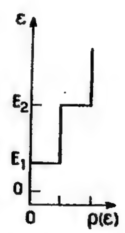

For a two-dimensional system, the density of states exhibits a stair-like evolution with

ELECTRONIC BAND PARAMETERS

AlxGa1-xAs Ternary alloys

	GaAs	AlAs	$Al_xGa_{1-x}As$
Band gap energy	1.42 Eg^Γ	2.16 Eg^x	$1.42 + 1.247x$ $(0 < x < 0.45)$
			$1.9 + 0.125x + 0.143x^2$
			$0.45 < x < 1$
Conduction band effective mass			
Γ valley	0.067	0.14	

Band gap discontinuity average values $\Delta Ec/\Delta Eg = 60:40$

AlInAs-GaInAs heterostructure

	InGaAs	AlInAs
Band gap energy	0.76	1.47
Effective mass	0.042	0.075
Conduction band offset	$\Delta Ec = 0.55$	

AlGaAs-GaInAs strained layers

	Lattice matched on InP $In_{0.53}Ga_{0.47}As$	AlAs
Band gap energy	0.76	3 Eg^Γ
Effective mass	0.042	0.14
Conduction band offset	$\Delta Ec = 1.2$ for the Γ-band	
	$\Delta Ec = 0.65$ for the X-band	

Energy in eV

SINGLE HETEROJUNCTION

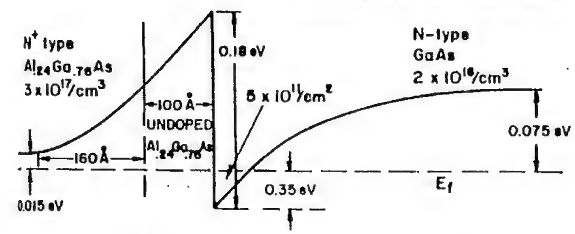

•Unbiased heterostructure

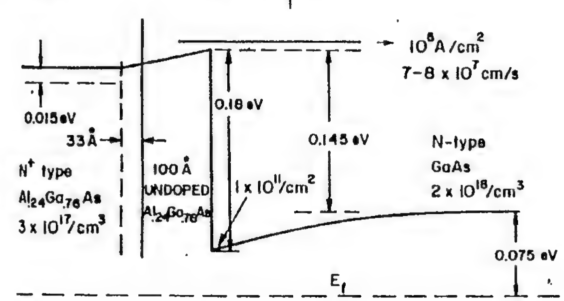

•Under bias

TUNNELING BARRIER

- Transmission of the electron wave function
- Quantum transmission probabilities

$T \sim e^{-2\alpha L_B}$

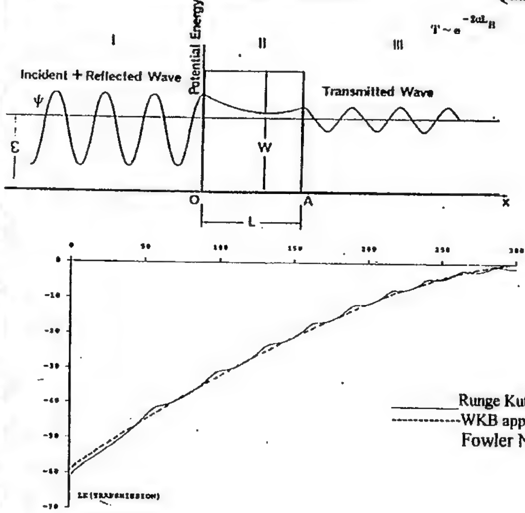

Runge Kutta numerical method
WKB approximation
Fowler Nordheim resonant tunneling effect

RESONANT TUNNELING HETEROSTRUCTURE

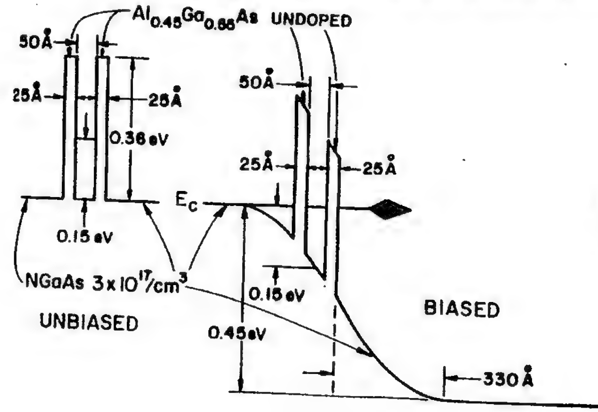

Resonant tunnel Emission of ballistic electrons

The double barrier heterostructure acts as an energy filter

DOUBLE BARRIER HETEROSTRUCTURE

(Resonance effect)

Constructive interference when the electron wavelength matches the well dimension

Quantum transmission probability (T)

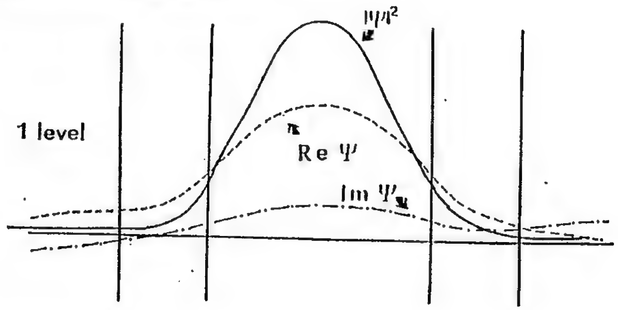

At resonance T#1 , $T \sim T_g T_d$ under off-resonance conditions
With T_g and T_d the transmission of the left and right barriers

SUPERLATTICE STRUCTURE

- Energy band diagram for undoped superlattice $GaAs/Al_{0.3}Ga_{0.7}As$ heterostructure

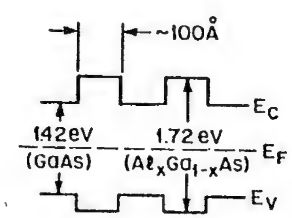

- For Modulation doped heterostructure *Dingle et al. Appl. Phys. Lett. 33, 665 (1978)*

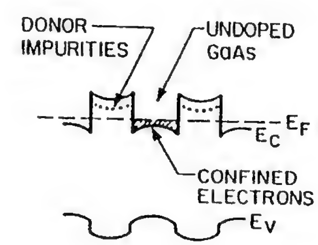

Real space transfer of electrons and band bending by space charge effect

MULTI-QUANTUM WELL (MQW) AND SUPERLATTICE (SL)

•Transition between MQW and SL

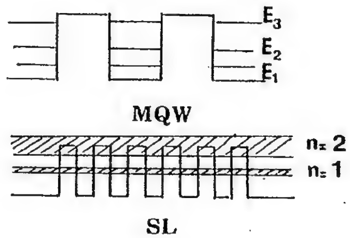

Envelope wave function approximation
G. Bastard Phys. Rev. B24(1981) 5693

•Calculated subband energies as a function of period d

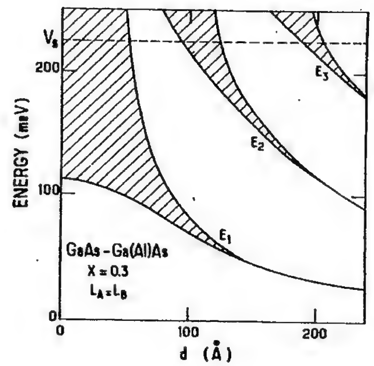

WAVEFUNCTIONS IN SUPERLATTICE

•Transmission probability versus energy

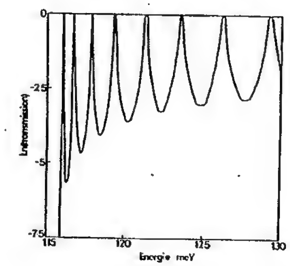

Miniband electron transport

•Eigenstates
At equilibrium

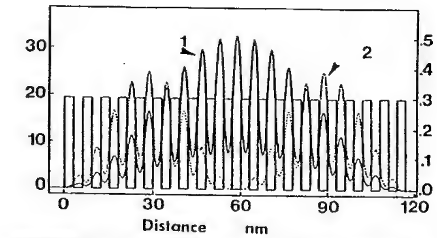

Eigenfunctions corresponding to the two first peaks in the transmission probability

Condition for localization F >ΔE/qd
ΔE: miniband width; d superlattice period

HETEROSTRUCTURE

As a general rule:

Good *Schottky* contact on *large band gap-undoped* material such as n⁻GaAs

Good *Ohmic* contact on *low gap-highly doped* semiconductor such as InGaAs with large Indium content

trade-off alleviated by the use of heterostructures

A crystalline Potential barrier permits:
•to confine the carriers by means of a quantum well on short scale → a room temperature operation

•to block the carriers in order to induce depleted zones with capacitance modulations (varactor effect)

•to fabricate high transmissivity tunneling barriers without the requirement of a high doping concentration

•to modify the density of states

However we have to distinguish between the intrinsic and extrinsic properties and some design rules are comparable to those of conventional devices

Transit time limited devices (Gunn diodes and superlattice diode with negative differential resistance effect)
RC time constant (Esaki-tunnel diode and Resonant tunneling diode)

FAMILY TREE OF HETEROJUNCTION DEVICES

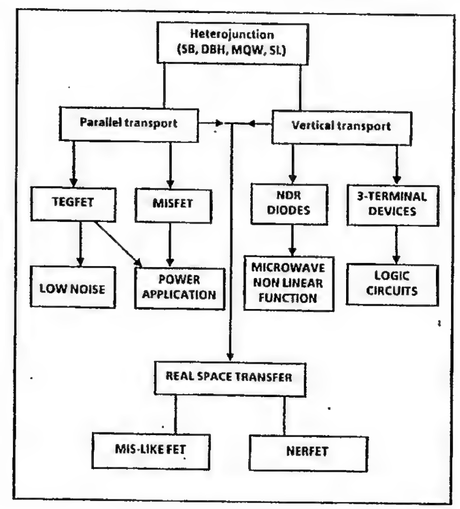

TEGFET:
Transverse Electron Gas Field Effect Transistor
NDR:
Negative Differential Resistance

MODULATION DOPED HETEROSTRUCTURE

Real space transfer between a large band gap highly doped region and a low band gap undoped region
Illustration of band bending resulting from charge accumulation

• AlGaAs/GaAs epilayer

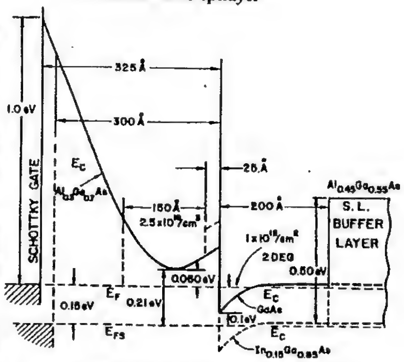

• AlInAs/GaInAs epilayer

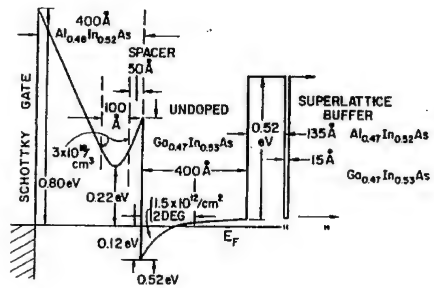

Self-consistent solution of the Schrödinger-Poisson equations

PSEUDOMORPHIC GROWTH

• Compressive strain

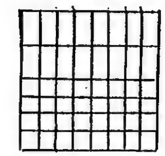

• tensile strain

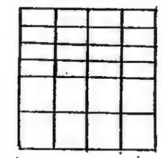

• edge dislocation

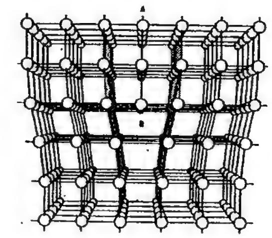

$In_xGa_{1-x}As$ on GaAs ($x<0.25$); $In_xGa_{1-x}As$ on InP ($x<0.53$)

$In_yGa_{1-y}As$ on InP ($y>0.53$)

CRITICAL LENGTH FOR STRAINED LAYER

• Critical length versus indium content

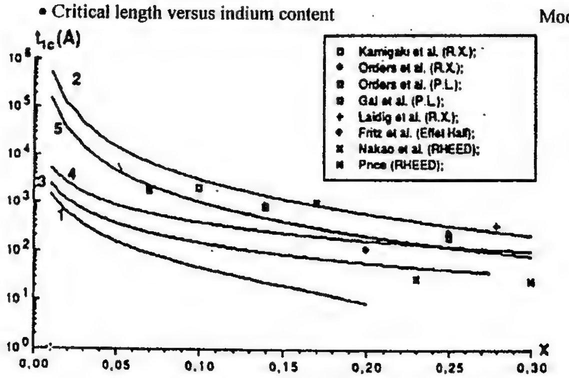

Models of:

1. Van der Merwe
2. People and Bean
3. Matthews
4. Van de Leur et al.
5. Marée et al.

Recently, the idea of compensated layers (tensile-compressive) has been used.
Also, the possibility to grow InAs islands self-organized on GaAs substrate for fabricating quantum dots was demonstrated

PSEUDOMORPHIC $In_{0.68}Ga_{0.32}As$/AlInAs TEGFET

• Growth parameter

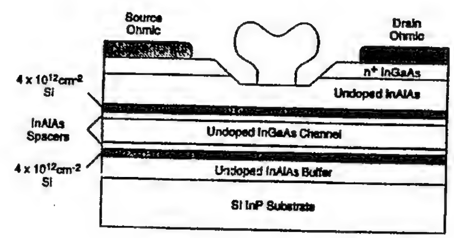

• Power and efficiency characteristics

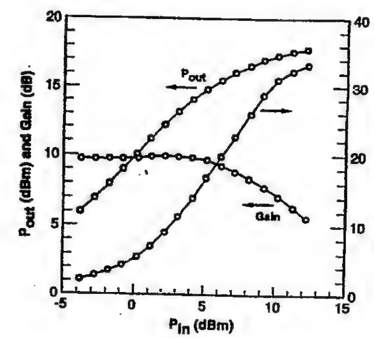

0.1 µm T-gate process, 200 µm gate width
Maximum frequency for oscillation fmax= 600 GHz, 58 mW at 94 GHz, F= 1.4 dB (Noise figure)
P.M. Smith IEEE EDL 5, 230 (1995)

InAs on GaAs

High Resolution Transmission Microscopy of a superlattice (InAs/GaAs heterostructure)

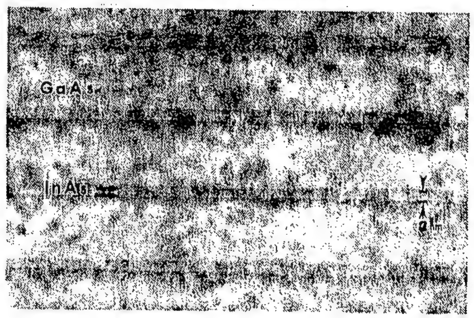

2D growth on very short scale to avoid the dislocation formation
possibility to use such epilayers for potential perturbations

iemn Recherche Formation Transfert

SINGLE AND DUAL
Heterostructure Barrier Varactor

• I - V curve at room temperature

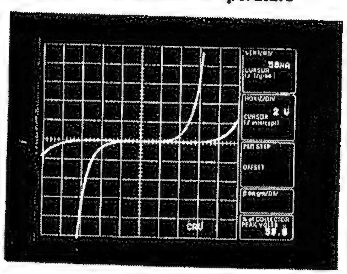

Ø = 38 µm
excellent symmetry
J < 10A / cm² at 6 V

• Modeling of I - V curves

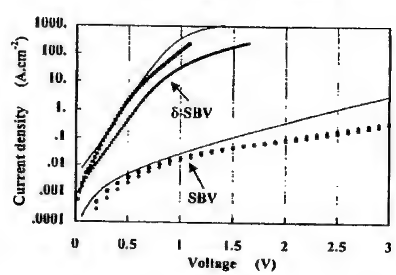

comparison between measured and calculated data

iemn Recherche Formation Transfert

STRAINED AlAs BLOCKING LAYER

• Epitaxy

InGaAs	5×10^{18} cm^{-3}	500nm
InGaAs	1×10^{17} cm^{-3}	300nm
InGaAs	Undoped	5nm
InAlAs	Undoped	5nm
AlAs	Undoped	3nm
InAlAs	Undoped	5nm
InGaAs	Undoped	5nm
InGaAs	1×10^{17} cm^{-3}	300nm
InGaAs	5×10^{18} cm^{-3}	500nm
InP Substrate		

x2 for DHBV's

growth sequence

accumulation layer

• conduction profile
AlInAs / AlAs / AlInAs
blocking layer

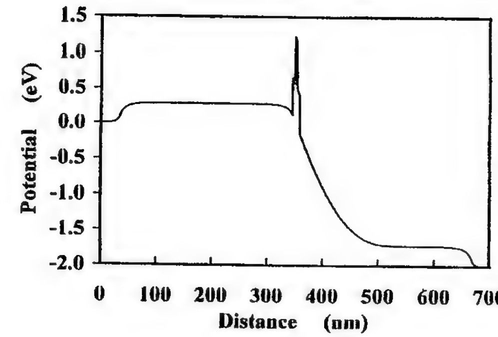

iemn Recherche Formation Transfert

CAPACITANCE - VOLTAGE CHARACTERISTICS
SHBV AND DHBV

• Experiment

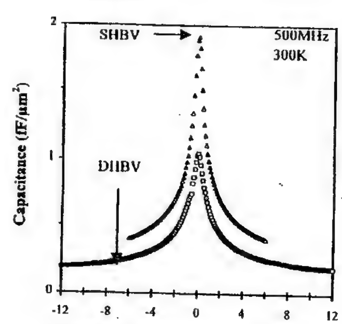

Ø = 38 µm

$\frac{C_0}{C_{sat}} = 6:1$ $C_o \sim 2^{fF} / \mu m^2$

• Modeling

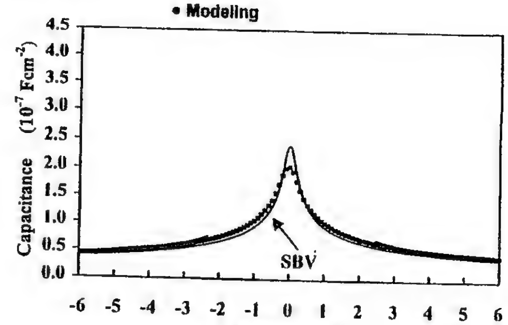

Comparison between measured

and calculated data

DOUBLE BARRIER HETEROSTRUCTURE
(DBH's)

Fabrication techniques **For high current structure L_b = 1.7nm**

InGaAs	5x10^{18} cm^{-3}	300nm
InGaAs	1x10^{18} cm^{-3}	50nm
InGaAs	Undoped	10nm
AlAs	Undoped	1.7nm
InGaAs	Undoped	5nm
AlAs	Undoped	1.7nm
InGaAs	Undoped	10nm
InGaAs	1x10^{17} cm^{-3}	300nm
InGaAs	5x0^{18} cm^{-3}	300nm
InP Substrate		

Gas Source MBE equipment
alloy composition and growth rates from RHEED intensity oscillations of
- **InP (on InP)**
- **GaAs and AlAs (on GaAs)**

Growth sequence

ANTIMONIDE MATERIAL SYSTEM

Band structure lineups for GaSb/AlSb/InAs:

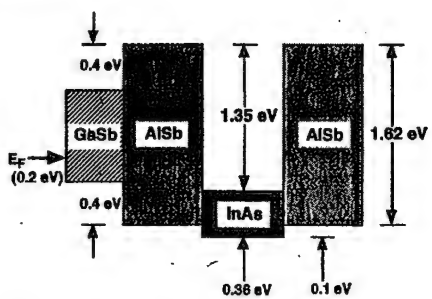

Potential advantages

High conduction band offset between InAs and AlSb (RTD's and TEGFET's)
low gap (high mobility, 33,000cm^2/Vs) InAs material for high speed applications
High peak and saturated velocity

In counterpart :

Low breakdown voltage unfavorable for power applications
no lattice matched SI substrate, immature technology

D - C CHARACTERISTICS

Typical current - voltage characteristics at room temperature (A = 4µm^2)

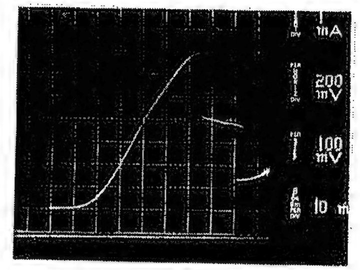

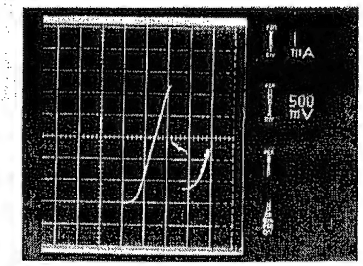

(a) J_p = 175 kA / cm^2
J_p / J_v = 5.5 : 1

(b) J_p = 135 kA / Ccm2
J_p / Jv = 9 : 1

E. Lheurette et al Electonics letters 1995, 31, pp 1508 - 1509

Département Hyperfréquences & Semiconducteurs

ANTIMONIDE TEGFET

Motivations: high carrier sheet carrier density
High velocity including overshoot for ultra short gate length
but low breakdown voltage

- epitaxial material

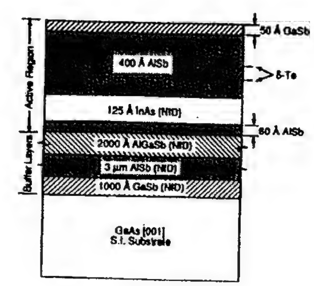

- Current-voltage characteristics

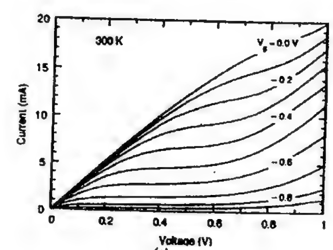

J. D. Werking et al. IEEE EDL, 13, 164(1992)

METAMORPHIC GROWTH

Sb-based material system grown on *GaAs* substrate (Resonant tunneling InAs/AlSb RTD's)
InAlAs/InGaAs on GaAs possibly Si in the future(high performance TEGFET's)

A buffer layer separates the substrate from the active layer so that the strain can be relaxed
Relaxation of strain, blocking of dislocations

•Example of buffer structure

52%In	InAlAs:Si	7500Å
growth pause		
52%In	InAlAs:UD	3000Å
graded 10-52%In	InAlAs:UD	5000Å
GaAs:UD buffer layer		1000Å
GaAs (Si) substrate		

•TEM for $In_{0.3}Ga_{0.7}As$ on GaAs with gradual transitions buffer $In_{0.15}Ga_{0.85}As$

J. R. Söderstrom et al. Appl. Phys. Lett. 58, 275(1991), E.R Brown IEEE EDL 41, 879(1992)
P.Win et al , D.E. Grider et al. T. Mishima et al., N. C. Tien et al.

METAMORPHIC RESONANT TUNNELING DIODES

•Typical I-V Characteristics (Jp>300kA/cm^2)

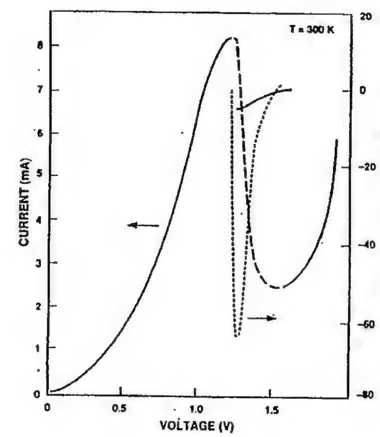

•output power versus frequency

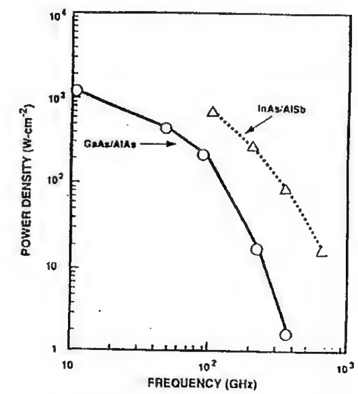

E. R. Brown et al. APL. 58, 2292(1991)

EPITAXIAL LIFT-OF TECHNIQUE

Basic idea:
Remove the active layer from the substrate by means of selective etching
and subsequent bonding on another substrate by van der Waals forces
E. Yablonovitch Appl. Phys. Lett. 51, 2222(1987)

2000Å cap	n-GaAs	n=4x10^{18} cm^{-3}
1500Å emitter	n-$Al_{0.3}GaAs$	n=5x10^{17} cm^{-3}
1000Å base	p-GaAs	p=5x10^{18} cm^{-3}
5000Å collector	GaAs	n=5x10^{16}cm^{-3}
8000Å subcollector	GaAs	n=4x10^{18}cm^{-3}
100 Å	AlAs	
1 μm	n$^+$ GaAs	
n$^+$ GaAs substrate		

Sample thickness μm	Temp. K	Carrier Conc. cm^{-2}		Change in carrier conc. %	Electron Mobility		Change in mobility %
		On-wafer	ELO		On-wafer	ELO	
0.44	290	9.4 x 10^{11}	8.7 x 10^{11}	-10.2	12960	18329	-20.3
	4	8.95 x 10^{11}	8.2 x 10^{11}	-9.1	79300	63965	-19.5
1.05	290	11.7 x 10^{11}	10.5 x 10^{11}	7.4	7328	5965	-18.6
	4	9.9 x 10^{11}	9 x 10^{11}	-8.4	47730	40467	-15.2

The epilayer can be processed before or after the bonding
This technique has to be distinguish from thinned wafers with bonding on low permittivity substrate

CONCLUSION

From the material point of view
•GaAs system : Mature technology, high performance Schottky's
Nonstoichiometric material (LTG GaAs) with ultra fast decay of photoexcited carriers

•InP-based materials: The frequency capability of InP-based material was demonstrated
with ultra high cut-off frequency for pseudomorphic TEGFET AlInAs/InGaAs
Pronounced Negative Differential Resistance effect at room temperature for RTD's

•Antimonide material system
record oscillation frequency with InAs/AlSb double barrier heterostructure
High sheet carrier density, high velocity TEGFET's
But immature technology, low breakdown voltage

From the structure point of view

Various heterostructures were tailored for improved performances
Single barrier varactors with AlAs blocking layers for varactor operation
Strained layer Double Barrier Heterostructure for high peak-to-valley ratio and High current density
Superlattice with transit time limitations
Planar doped TEGFET's with high current drivability

I would like to thank O. Vanbésien for his help in this overview

Technical Issues of Terahertz Component Fabrication

by

R J Wylde

Thomas Keating Ltd
Billingshurst
West Sussex
UK

In remote sensing of the atmosphere - from space and from the ground - in the development of Tokomak fusion reactors for 21st Century energy production and in probing the heavens, Terahertz technology can contribute to some of the `Grand Challenges' facing mankind at the end of the 20th Century.

This talk is about making things to deal with Terahertz radiation. And rather large things, on a terahertz reduced scale, rather than very small things (such as Schottky diodes). They will also be linear things, so they are not involved in the actual non-linear process of generating or detecting Terahertz radiation.It will not be a very exciting talk, in the context of others you will have and are about to hear at this conference. But it might be a useful one.

I will be talking about the manufacture, and before that, the design of a variety of Terahertz components. These will include

Beam forming and receiving components
Beam control components
Beam processing components
Beam absorbing components

Inevitably, most of these will be drawn from systems that I have been involved in, but I will try to cover as wide a range as possible.

Integrated Waveguides and Mixers

by

C Mann

Rutherford Appleton Laboratory
UK

(No material supplied.)

FRIDAY JULY 5

iemn Recherche Formation Transfert

New directions in terahertz technology

Integrated active devices

D. Lippens

Institut d'Electronique et de Microélectronique du Nord
UMR CNRS 9929 Université des Sciences et Technologies de Lille
59652 Villeneuve d'Ascq Cedex, France

Chateau de Bonas, France
July 11, 1996

iemn Recherche Formation Transfert

Outline

- Epitaxial growth and ion implantation
  - MBE and MOVPE techniques
  - Ion implantation
- Basic technological process
  - Ohmic contact
  - Schottky's contact
- Device isolation
  - Wet etching
  - Reactive Ion Etching (RIE)
- Integration techniques
  - dielectric cross over and planarization
  - Air-bridge interconnections
- High frequency devices
  - Schottky's diodes for mixer and harmonic multipliers
  - Low noise TEGFET's
  - Heterostructure devices

EPITAXIAL GROWTH

Molecular beam epitaxy techniques

Solid Source MBE (SSMBE)

Growth of: •GaAs-based materials
$Al_xGa_{1-x}As$ ($0<x<1$)
Typical growth temperature: 600°C for GaAs
700°C for AlAs
•InP-based compounds
$In_{0.53}Ga_{0.47}As$, $In_{0.52}Al_{0.48}As$ (T~530°C)
InP is used as a substrate

Gas Source MBE (GSMBE)

Growth of InP related compounds:

Binary and ternary Alloys $In_xGa_{1-x}As$ and $In_yAl_{1-y}As$
Quaternary GaInAsP
Type II Heterostructure (InP/InAlAs)

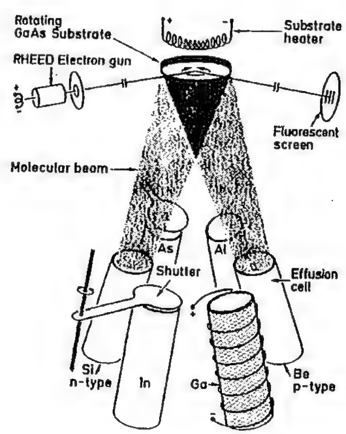

MOLECULAR BEAM EPITAXY

Schematic view of a GSMBE or MOMBE growth apparatus

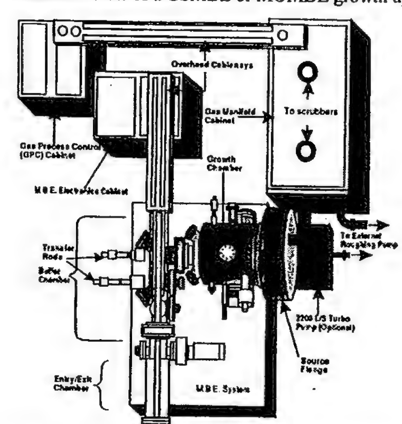

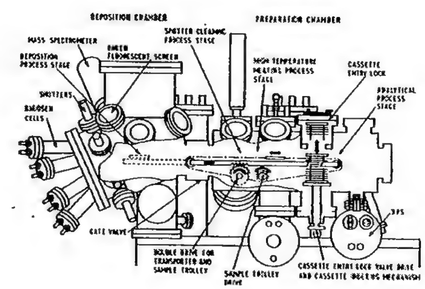

Several MBE systems can also be in series including surface analysis tools (ESCA and STM ...)

IN SITU ANALYSIS TECHNIQUE

Reflection High Energy Electron Diffraction (RHEED)

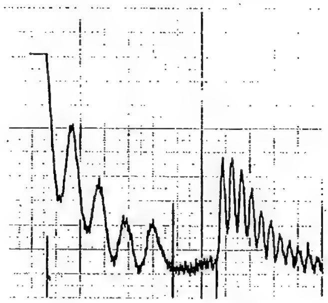

←AlAs→ interruption ←GaAs→

Growth interruption for limiting the interface roughness

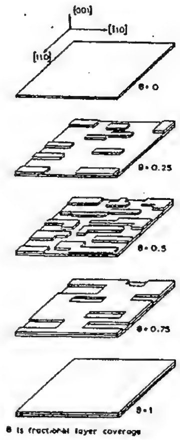

INTERFACE ROUGHNESS

Characterisation by High Resolution Transmission Electron Microscopy (HRTEM) and more recently by Scanning Tunnelling Microscopy (STM)

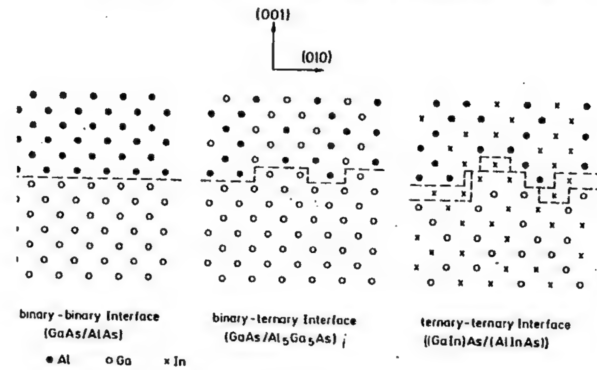

Differences between the direct and indirect Hetero-interfaces

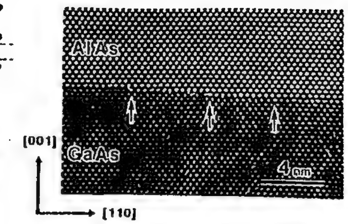

HRTEM of an AlAs/GaAs interface

METAL ORGANIC VAPOR PHASE EPITAXY
(MOVPE)

Principle of the MOVPE process in a cold wall reactor

Process precursors

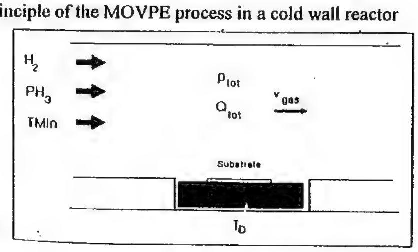

Element	*Precursor*	*Formula*	*Vapor Pressure @ 17°C*	*Melting Point*
Aluminum	Trimethyl Aluminum (TMAl)	$Al(C_2H_5)_3$	9.13 mbar dimeric	15.4°C
Gallium	Trimethyl Gallium (TMGa)	$Ga(C_2H_5)_3$	207.38 mbar monomeric	−15.8°C
Indium	Trimethyl Indium (TMIn)	$In(C_2H_5)_3$	1.76 mbar monomeric	88°C

Possibility to growth Phophorus-related compounds notably GaInP

ION IMPLANTATION

Principle: dopants are introduced into the semiconductor by ion implantation
Advantage: low cost and local doping

- Process conditions

First step: *implantation*

Typical energies: 30 to 400 kV

Doses 10^{12} to 10^{14} cm^{-2}
small angle (6 to 10°) for avoiding channeling

Second step: *Annealing*

in high temperature ovens
or flash lamps ; T~ 800-900°C

- Schematic of an ion implantation system

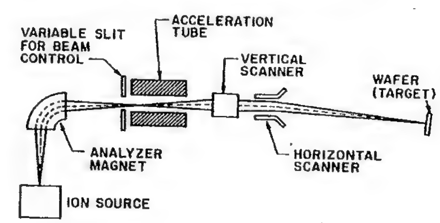

Illustration of ion channeling

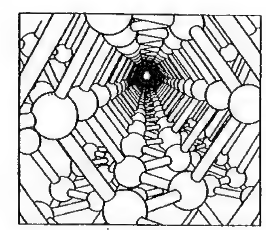

- Main implanted species
Silicon for n-type dopant
Beryllium for p-type dopant

LITHOGRAPHY TECHNIQUES

•Photolithography

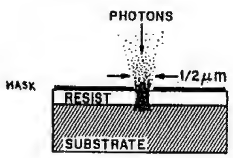

•Electron Beam Lithography

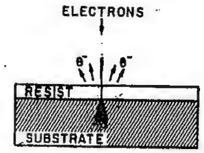

•X-RAY Lithography

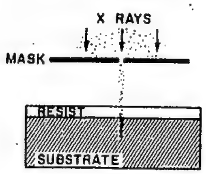

•Ion beam lithography

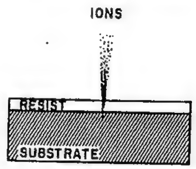

Photolithography for patterning on the micron scale; e-beam and X ray for nanostructures

BASIC RESIST PROCESSES

•Etch-process

•Lift-off technique

Uniform metal deposition

resist spinning

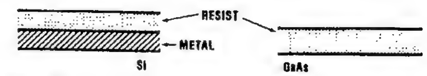

Patterning

undercut resist profile

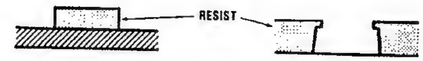

metal etching

evaporation

resist removed

Lift-off

LITHOGRAPHY TECHNIQUES (II)
(RESIST)

•Positive Resists
Spin coating

•Negative resists
spinning

Alignment and exposure

patterning

Revelation

Revelation

MULTILEVEL RESIST TECHNIQUE

•Tri-layer developed resist image
100nm T-gate

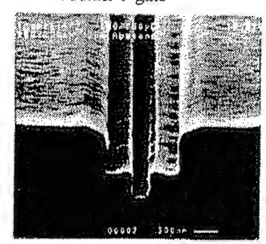

•Metallized gate formed by lift-off technique

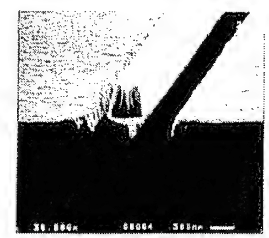

•Multilayered resist technique

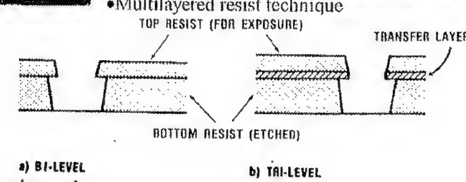

Photoresists or PMMA can be used

ELECTRON BEAM LITHOGRAPHY

E-beam writing of PMMA (Polymethylmethacrylate)
Electron dose between $2x10^{-7}$ and $8x10^{-7}$ C/cm^2
development using MIBK (Methylisobutylketone)

Thick resist writing

40kV 4µm Thick PMMA

100kV 10µm Thick PMMA

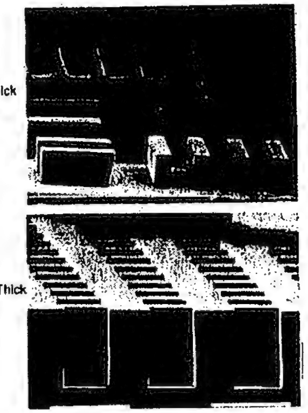

illustration of proximity effect

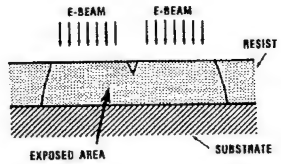

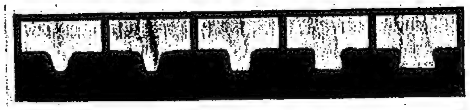

SEM views showing the resist profiles versus electron dose

ELECTRON BEAM LITHOGRAPHY

•Schematic of an electron beam machine

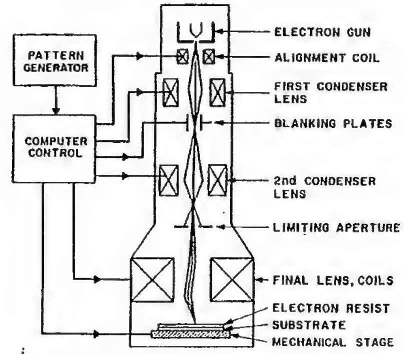

Electron energy between 20 and 100 kV
Beam current less than 50 nA
Spot size for high resolution ~10nm

•Electron beam pattern generator (High resolution)

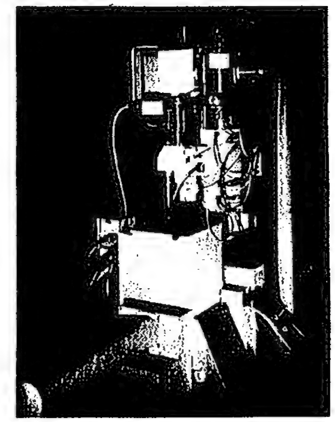

X-RAY DIFFRACTION

•Principle: Soft X-rays (0.2-1 nm)

The low wavelength makes diffraction nonexistent
In addition no backscattering or reflection from the substrate
Appropriate for exposure of very small lines in thick resist
Vertical walls

Penumbra effect arising from non collimated rays

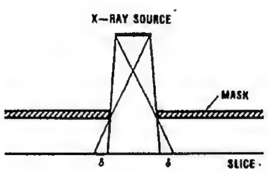

The optimum X-ray source is the synchrotron

•Schematic of an X-ray lithographic system

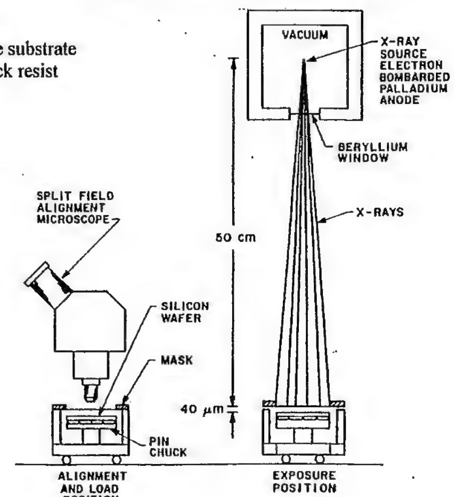

OHMIC CONTACTS

Principle of conduction
Thermionic emission (TE)

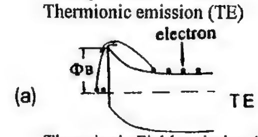

Thermionic Field emission (TFE)

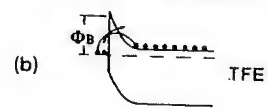

Field emisssion

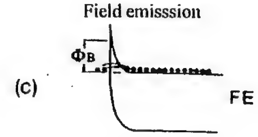

$J \sim Js \exp(-q\,\Phi_b/E_{00})$
with $E_{00} = q\hbar/2(Nd/\varepsilon\, m)^{1/2}$

Special techniques for contact improvement
Transition between large and low gap materials

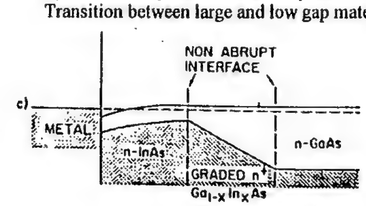

Band bending for metal on n-InAs on graded n^+ $In_xGa_{1-x}As/GaAs$
Planar doped epilayer

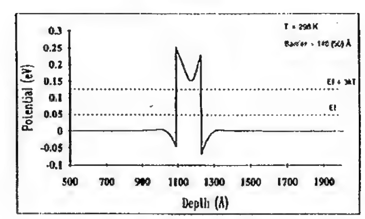

OHMIC CONTACT (II)

Metal system used to form Ohmic contacts on III-V

•n-type GaAs

Ag-In	75% Ag, 25% In; sinter 500° C
Ag-In-Ge	90% Ag, 5% In, 5% Ge; alloy 600° C
Ag-Sn	98% Ag, 2% Sn; alloy 550–650° C
	33% Ag, 67% Sn
Au-Ge	12% Ge (alloy); alloy 450° C
	Au overlayer
Au-Ge-Ni	12% Ge (alloy), Ni; alloy 480° C
Au-Ge-In	
Au-Si	alloy 425° C
Au-Sn	20% Sn; alloy 450° C
Au-SnNi-Au	alloy 300° C
Au-Te	10% Te; laser alloy
	2% Te; alloy 500° C
In	300° C melt
In-Al	alloy 320° C
In-Au	90% In; alloy 550° C
In-Ni	Ni plated to In
Pd-Ge	sinter 500° C two hours
Sn-Ni	Ni plated to Sn; alloyed
Sn-Sb	4% Sb; alloy 300–350° C

•p-type GaAs

Ag-In	25% In; alloy 500° C
Ag-In-Zn	80% Ag, 10% In, 10% Zn; alloy 600° C
Ag-Zn	90% Ag, 10% Zn; alloy 450° C
Au-Be	1% Be
Au-Zn	
In-Zn	(to semi-insulating GaAs)

Non alloyed ohmic contact on highly doped SC
Deep ohmic contact with subsequent annealing

Shallow ohmic contact :PdGe

WET ETCHING

•Background

Etching operation for semiconductor:

•by oxidising the surface

•by dissolving the oxide

•by removing some of the SC atoms

•Basic limiting mechanisms

etch rate controlled by:

•the rate at which reactant species reach the surface (diffusion limited or mass-transport-limited etching)
Diffusion coefficient ~10^{-9} m^2/s

•the rate of chemical reactions (reaction-rate-limited or kinetically limited etching)

•Anisotropy considerations

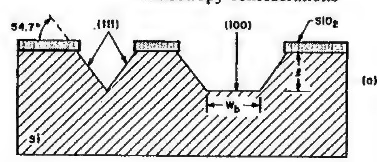

illustration of orientation dependent etching for Silicon (KOH etchant)

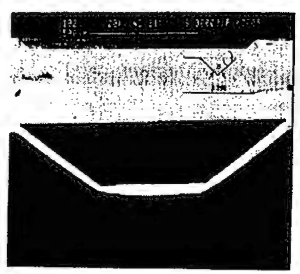

for GaAs (H_2SO_4 solution)

OHMIC CONTACT (III)

Characterisation techniques by Transmission Line Model (TLM)

•Basic pattern to measure the contact resistance

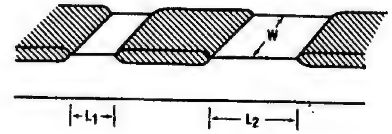

The resistance can be normalised to the contact area using the transfer length

Order of magnitude
On GaAs (Nd=$2x10^{18}$ cm^{-3}) Rc< $2x10^{-6}$ Ω cm^2

On $In_{0.53}Ga_{0.47}As$ (Nd=5x $10^{18}cm^{-3}$) Rc < $2x10^{-7}cm^2$
Rapid thermal annealing 430°C 30s

•Plot of measured resistance versus contact separation

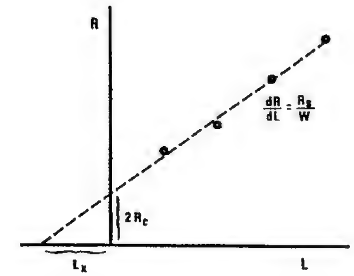

WET ETCHING

Principle: use of wet etchants to remove semiconductor, dielectric or metal

•Etch of III-V semiconductor

GaAs : $NH_4OH/H_2O_2/H_2O$
$H_2SO_4/H_2O_2/H_2O$

InP : HCl/H_2O

InGaAs $H_3PO_4/H_2O_2/H_2O$

Selective Semiconductor etchant

AlGaAs/GaAs: citric acid/H_2O

Basic mechanisms in wet chemical etching

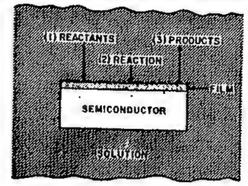

•Etchants for Metals

Gold: HCl/HNO_3 (3:1)
$KI/I_2/H_2O$ (4g:1g:40ml)

Titanium: HF/H_2O (1:9)

Platinium: $HNO_3/HCl/H_2O$ (1:7:8)

•Dielectrics

SiO_2: HF, BHF (Buffered HF)

Si_3N_4: HF, BHF, H_3PO_4

Al_2O_3: HF, BHF, H_3PO_4

HF: Hydrofluoric acid

DRY-ETCHING

Main goal : achieve etch anisotropy

•*Plasma etching*

The plasma generates reactive species
They serve to chemically etch material
Equipment : barrel $As=A_0$
More and less directionality
Pressure 0.1-5 torr

•*Reactive Ion Beam Etching(RIBE)*

Similar to RIE except that
The wafers are separated by an acceleration grid
ion energy > 1 KeV
Kinetically-Assisted physical etch

•*Reactive Ion Etching* (RIE)

K-A chemical etching
High directionality
Planar equipment with $A_0>As$
Low pressure 0.01-0.1 torr

•Ion milling

Pure mechanical process
Use of ions of inert gas
generated and collimated
$< 10^{-4}$ torr, Ion beam accelerator

As= area of electrode holding wafers
A_0= area of other electrode
KA: Kinetically assisted

DRY ETCHING

•Physical etching equipment

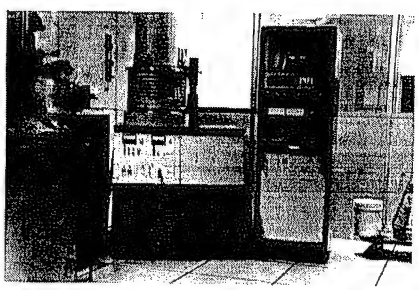

•Reactive Ion Etching apparatus

REACTIVE ION ETCHING
(RIE)

Schematic of a reactive plasma equipment

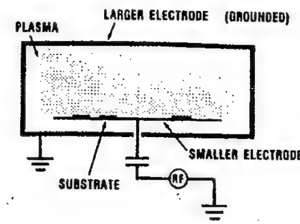

Use for:

mesa isolation with vertical walls
etching of via holes

gas species:
GaAs material : $CCl_4 + O_2$
InP-based material : CH_4/H_2

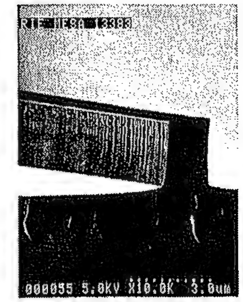

Illustration of a mesa etched
in an InP-based heterostructure
Pressure 50m torr, power density $0.4W/cm^2$
Bias voltage 340V

DIELECTRIC DEPOSITION

Silicon Nitride (Si_3N_4) used most in GaAs processing

Deposition by Plasma enhanced Chemical vapor deposition (PECVD)
Silane (SiH4) used for the Silicon source
Nitrogen (N2) or Amonina (NH3)used for the nitrogen source

Overall reactions:

$3SiH_4 + 4NH_3 \rightarrow Si_3N_4 + 12H_2$

$3SiH_4 + 2N_2 \rightarrow Si_3N_4 + 6H_2$

Properties of $Si_xN_yH_z$

Refractive index: 1.9-2.2
Dielectric constant: 6-9
Dielectric strength(V/cm): $6x10^6$
Bulk resistivity: $4-7x10^6$ Ω.cm
plasma etch rate CF_4/O_2: 50 nm/min
HF etch rate room temperature: 20-33 nm/min

Schematic of a PECVD system

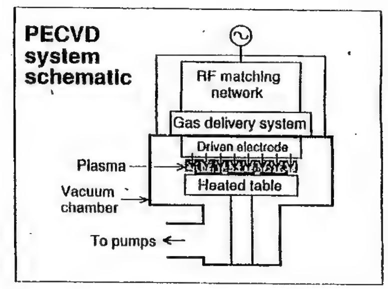

Dielectric cross over
for contacting planar integrated diodes

SCHOTTKY AND OHMIC CONTACT FORMATION

•Joule evaporator

Sample holder

quartz

Crucible

pump equipment

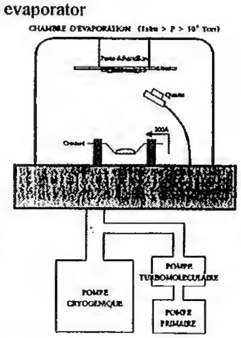

use of eutectic contact material (Au Ge)

Sequential ohmic contact with multi-crucible equipment

•Electron gun evaporator

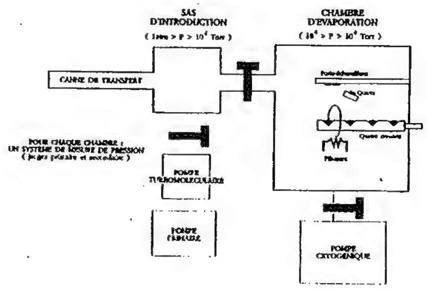

Cooled target

Possibility of Au/Ge sequential deposition
good adhesion
good electrical characteristics

ELECTROPLATING

Gold plating

•Process conditions

use of a gold cyanide complex
Plating bath usually near 60 °C
Control of pH
Current density typically 5mA/cm^2

Photoresist suitable for masking

Plating factor: plating area divided by total wafer area

a very thin layer of metal is applied to carry the current

•Use for
Thick strip lines for coplanar transmission lines
Free standing structures such as microswitchs
Air bridge interconnections

Heating element

temperature probe

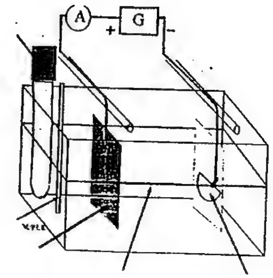

plated sample

Platinium anode   gold cyanide solution

Schematic of an electroplating system

Reaction: $M^{n+} + ne^{-} = M^{\circ}$ with M atoms of metals

BRIDGE INTERCONNECTIONS

Illustration of bridge formation

spinning of a first resist
and metal deposition (sputtering or evaporation)

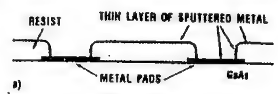

second resist coating

electroplating of gold

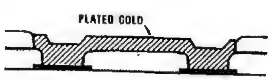

SEM of an evaporated airbridge

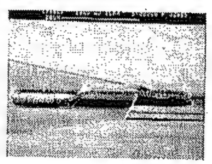

Completed bridge

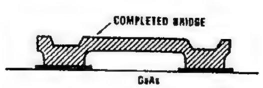

AIR-BRIDGE INTERCONNECTIONS ON NANOMETER SCALE

Direct writing by Electron beam lithography

•variation of the electron dose

•favorable backscattering on the metal pads

•Use of a P(MMA-MAA)/PMMA bilayer

Illustration of a micro air bridge fabricated by direct writing

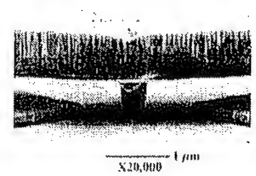

bi-layer developed resist image

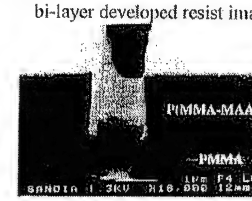

use for fabricating electron waveguides

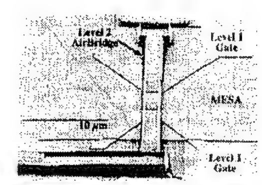

Starting from a high mobility 2D gas, electron waveguides can be formed assuming ballistic transport

FABRICATION TECHNIQUES FOR WAFER PROBING

- Simplified version for directly contacting the samples
- Planar Integration Techniques

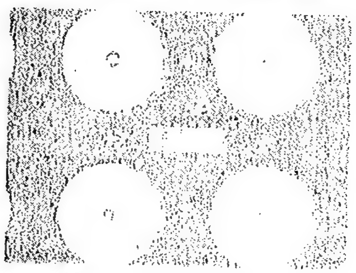

three photolithography masks

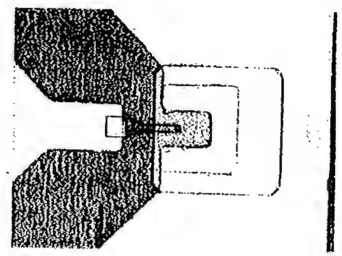

air - bridged devices

PLANAR TECHNOLOGY

Low parasitic integration technique

Air - bridged devices

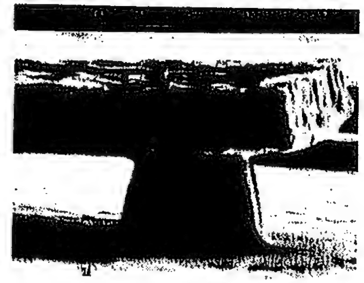

SEM of a 1 µm^2 diode

electron - beam lithography

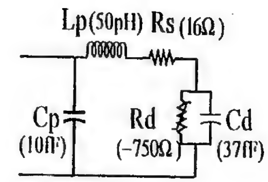

Equivalent - circuit model

Parasitic capacitance 10fF

inductance 50 pH

PLANAR INTEGRATION OF DIODES(I)

Surface channel diodes (Virginia University technology applied to InP-based material system)

Schottky's epilayer n/n+/S-I InP substrate

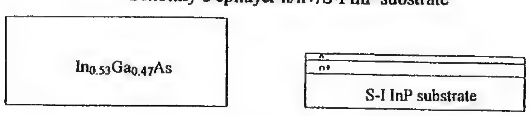

Deposit Silicon nitride film

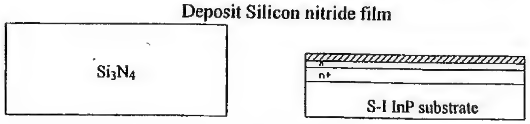

Form Ohmic contact

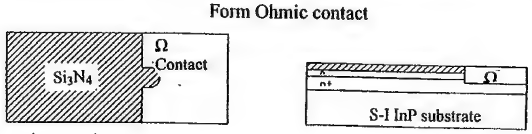

PLANAR INTEGRATION OF DIODES (II)

Form anode

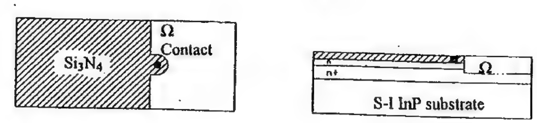

Form anode pad/finger

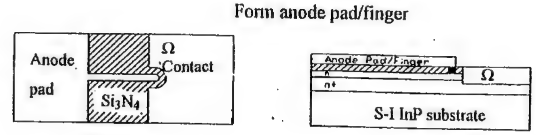

Etch surface channel

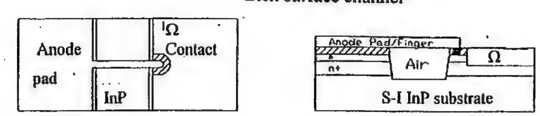

INP-BASED TEGFET (I)

Growth sequence of the epitaxial material

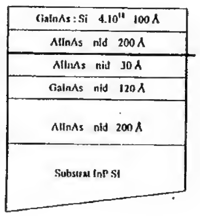

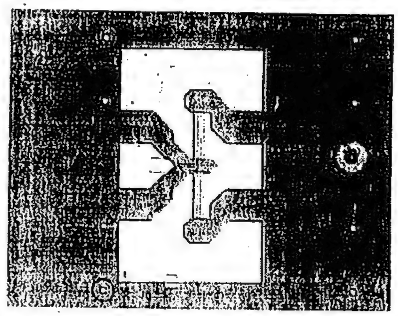

Highly doped cap layer for Ω contact formation
Undoped large gap InAlAs for Schottky contact formation
Planar doping for high sheet carrier density in the 2 D gas
buried AlInAs layer for better confinement

Growth by SSMBE or GSMBE

TECHNOLOGICAL STEPS

T-gate formation

Si3N4 deposition

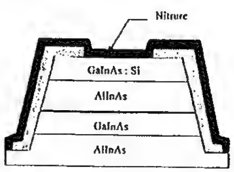

Opening of the Si_3N_4 film
CF4 plasma

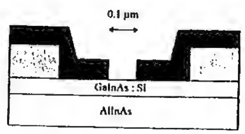

Positive resist deposition
e-beam patterning

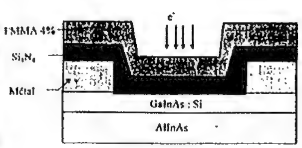

deposition of a bilayer
e-beam patterning

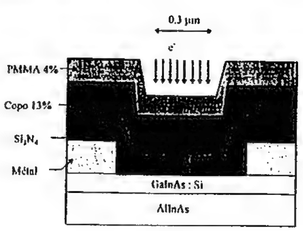

TECHNOLOGICAL STEPS

Ohmic contact formation

positive resist deposition

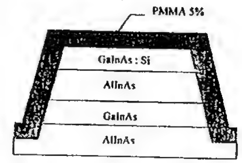

e beam patterning

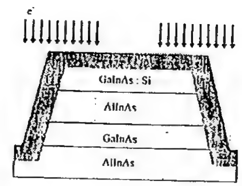

Ni/Ge/Au/Ni/Au deposition

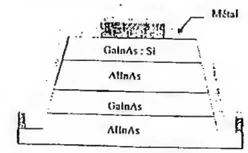

Lift-off and annealing

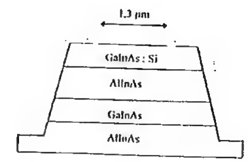

BACKSIDE PROCESSING

Wafer thinning

motivations: use of a flip-chip technology
thermal reason

lapping techniques

A slurry of water and grit is used between the wafer and a flat plate

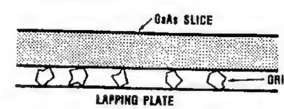

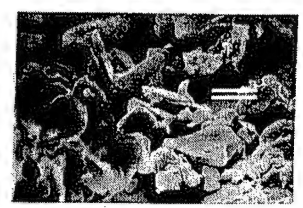

Deep etch-back for membrane formation

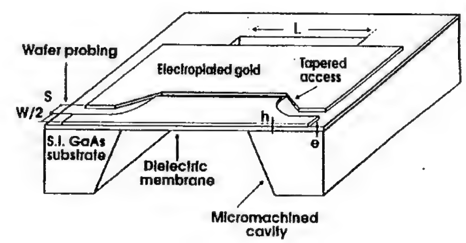

Deep etch using H_2SO_4:1/H_2O_2:8/H_2O:1solution

CONCLUSION

High quality epilayer with multiple heterostructures can now be fabricated using molecular beam epitaxy

For operation at millimeter and submillimeter wavelengths the devices are now patterned on the micron and submicron scale notably by e-beam writing

Good Ohmic and Schottky's contacts (ideality factor ~1 , low contact resistance) are fabricated with a high yield

Dry and wet etching are often combined in planar integration of the devices

Development of whiskerless contact technology by dielectric cross over or air-bridged devices

Successful fabrication of high performance devices notably of

- TEGFET with T-gate
- Planar Schottky diodes
- Single barrier and double barrier heterostructures

I would like to thank P. Mounaix for his help in this overview

ACTIVE ANTENNA POWER COMBINING, BEAM CONTROL AND 2-D COMBINING

by

Professor Tatsuo Itoh

Department of Electrical Engineering
University of California, Los Angeles
405 Hilgard Avenue,
Los Angeles, CA 90095, USA

SCOPE

- INTRODUCTION
- POWER COMBINING ARRAYS
  - GRID APPROACH
  - ARRAY TYPE
  - 2-DIMENSIONAL COMBINERS
  - SINGLE ELEMENTS
- BEAM-CONTROL
  - BEAM-SCANNING ARRAYS
  - BEAM SWITCHING ARRAYS
  - RETRODIRECTIVE ARRAYS
  - OTHERS
- CONCLUSION

INTRODUCTION

- Active devices at millimeter-wave frequencies have limited power
- In millimeter-wave spectrum, two-terminal devices deliver more RF power but with poor DC-RF efficiency
- Current technology has shown good progress in three-terminal devices
- There is a need to combine the power of many devices
- Transmission lines at these frequencies are lossy, resulting in poor power-combining efficiency
- To solve these problems, *ACTIVE ANTENNA* is sought
- An *ACTIVE ANTENNA* is one which integrates each active device directly to an antenna

INTRODUCTION (CONT'D)

- Each element radiates its power through its own antenna
- This class of active antenna is the *POWER-COMBINING ACTIVE ANTENNAS*
- Another class of active antenna is the *ACTIVE INTEGRATED ANTENNAS*
- *ACTIVE INTEGRATED ANTENNAS* integrate as many RF functions as possible at the antenna front-end
- This allows compact integration, monolithic fabrication, and low RF lossesand system noise

INTRODUCTION (CONT'D)

- *ACTIVE ANTENNAS* can be broadly categorized as follows :

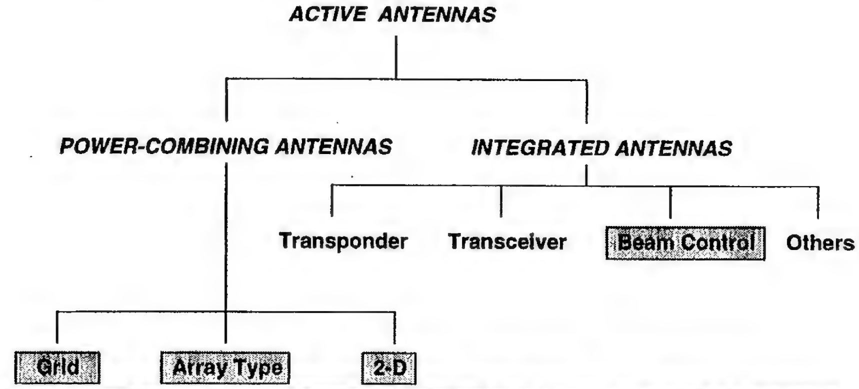

POWER COMBINING - GENERAL

- Power combining active antennas can be further classified as follows :

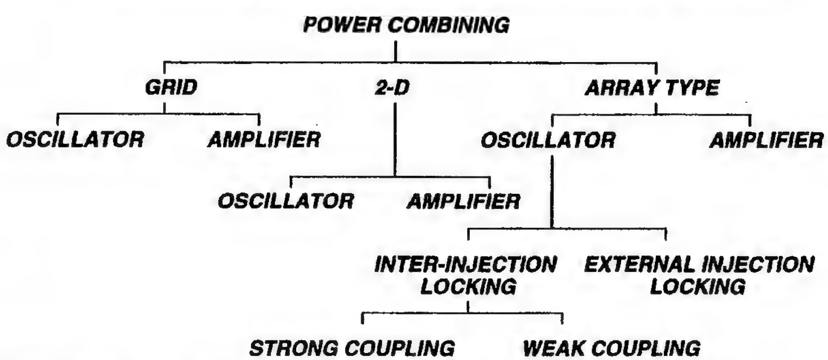

POWER COMBINING - GRID APPROACH

- Grid approach does not adopt the conventional antenna array design consideration
- Grid concept exploits periodicity in the array that is small compared to wavelength
- The grid can be considered as an active sheet in free-space capable of amplifying signals or generating negative resistance

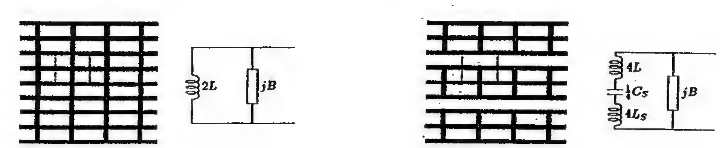

INDUCTIVE GRID

CAPACITIVE GRID

POWER COMBINING - GRID APPROACH (CONT'D)

- In an infinite grid, there is symmetry in the layout of the circuit. This allows electric and magnetic walls to be imposed when excited by a plane wave
- As such, analysis can be restricted to a waveguide cell in TEM mode
- Induced EMF is used to analyse the unit cell
- Leads of the active devices are treated as posts in a waveguide

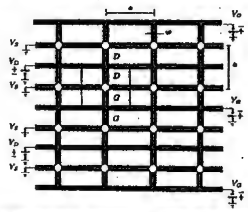

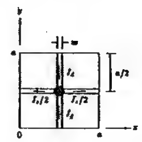

POWER COMBINING - GRID APPROACH (CONT'D)

- Currently, both amplifier and oscillator grids have been investigated
- In the amplifier grid, the unit cell consists of a differential pair FET or HBT
- Polarizers are placed on both sides of the grid as isolators
- Input and output signals have different polarization

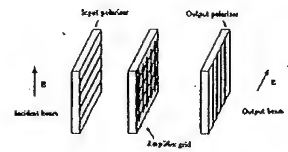

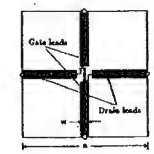

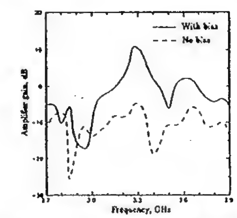

POWER COMBINING - GRID APPROACH (CONT'D)

- Oscillator grid is designed to operate in a Fabry-Perot cavity
- A mirror is placed about one wavelength behind the grid
- The grid locks to the cavity mode with the lowest diffraction loss per round trip

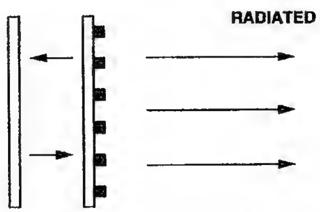

POWER COMBINING - GRID APPROACH (CONT'D)

- To increase the power generated, several grids are placed in parallel with dielectric spacers
- Interspacing between grids is experimentally determined
- Conducting plates are placed above and below to enforce TEM mode
- Four grids have been combined with 265 mW of delivered power

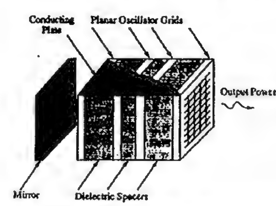

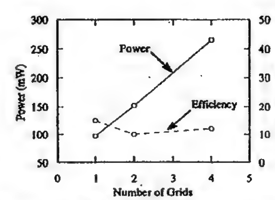

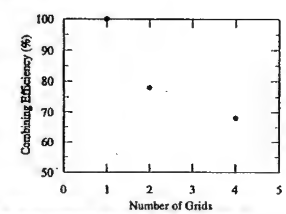

POWER COMBINING - GRID APPROACH (CONT'D)

- VCO grid incorporates a varactor grid behind the MESFET oscillator grid as the tuning element.
- Tuning bandwidth is about 10% with less than 2dB power change

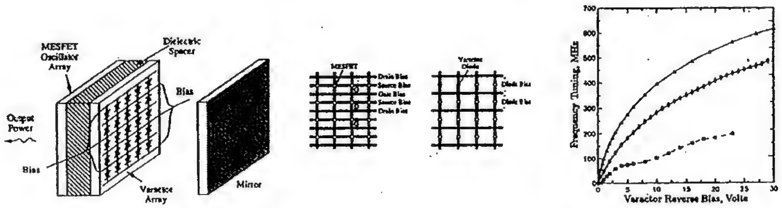

SQUARE	:	7X7 DIPOLE GRID
TRIANGLES	:	7X7 BOW-TIE GRID
DIAMONDS	:	4X6 BOW-TIE GRID

POWER COMBINING - ARRAY TYPE

- The array is designed using conventional antenna array theory
- Both amplifier and oscillator arrays have been investigated
- In amplifier array, an antenna each is connected to the input and output of the amplifier element
- Input and output antennas are of different polarization to reduce mutual coupling and prevent feedback for oscillation
- In oscillator, emphasis in active antenna is on how to ensure in-phase synchronisation of the individual elements

POWER COMBINING - ARRAY TYPE (CONT'D)

- In amplifier array, attempts have been made to broaden the bandwidth and incorporating more devices to an antenna
- To broaden the bandwidth, folded slot antennas have been used
- Folded slot antenna is relatively smaller and with wider bandwidth
- With CPW feed, the entire circuit is fabricated on a single layer

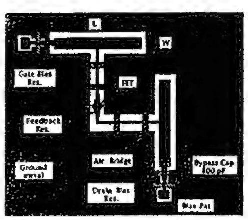

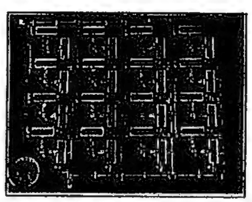

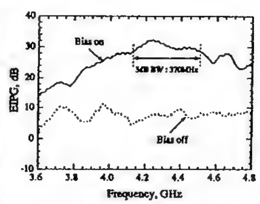

POWER COMBINING - ARRAY TYPE (CONT'D)

- Another attempt to broaden the bandwidth uses stacked patch
- Orthogonal modes in the stacked patch is used to isolate the input from the output

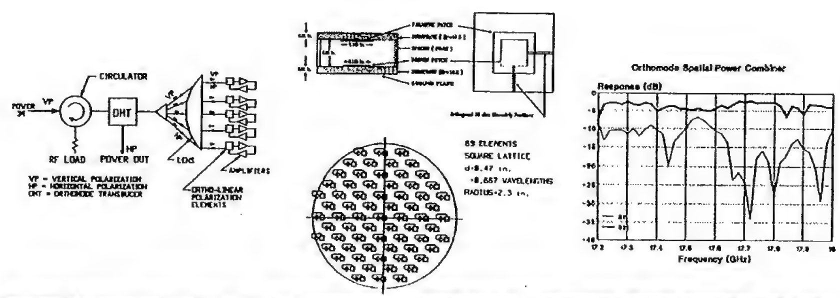

POWER COMBINING - ARRAY TYPE (CONT'D)

- To further isolate the input and output, patch antenna can be used
- The ground plane between the layers acts as a natural isolator
- The array is placed in the reactive field of the transmitting and receiving horns
- Hard horns are used to improve aperture efficiency

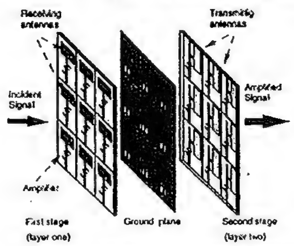

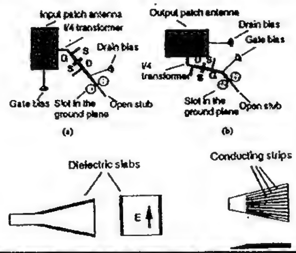

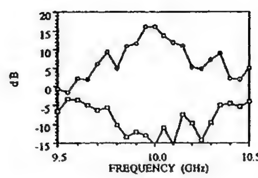

POWER COMBINING - ARRAY TYPE (CONT'D)

- To increase the power delivered by the array, more active devices can be incorporated into a single antenna

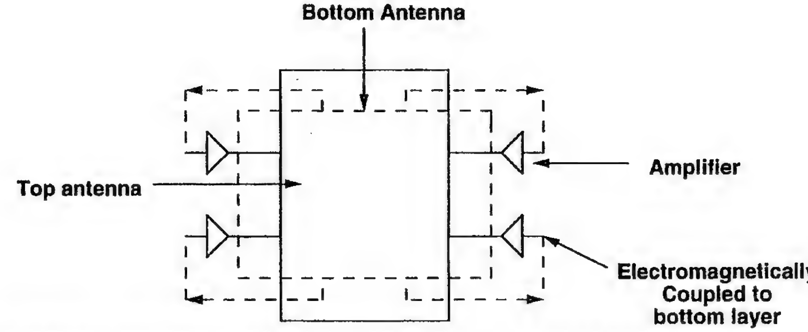

POWER COMBINING - ARRAY TYPE (CONT'D)

- To increase bandwidth and allow integration of many active devices, slot antenna is used
- Slot antenna has a wider bandwidth than patch antenna
- Power-combining circuit does not occupy space as natural microstrip-to-slotline transition is used.

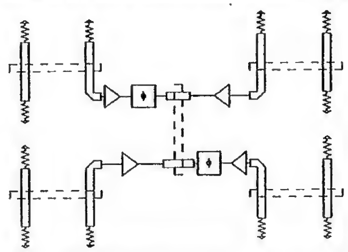

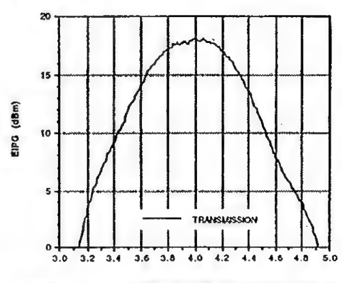

POWER COMBINING - ARRAY TYPE (CONT'D)

- As mentioned before, emphasis in oscillator arrays is how to synchronize the phase of each individual element
- Stephan has proposed INTER-INJECTION LOCKING
- Elements are mutually coupled (weakly or strongly)
- The system is then solved using differential equations of the amplitude and phase dynamics
- Weak coupling includes that of free-space between neighboring elements or lossy transmission lines
- Strong coupling includes direct connection of transmission lines or dielectric resonator coupling

POWER COMBINING - ARRAY TYPE (CONT'D)

- Here, the coupling network is the free-space coupling between elements
- Only coupling between adjacent elements is considered
- For a particular coupling phase, the interaction of the elements will result in broadside radiation

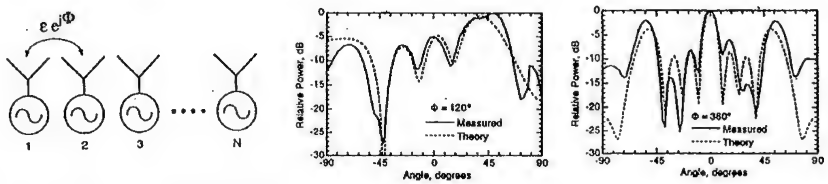

POWER COMBINING - ARRAY TYPE (CONT'D)

- The analysis of strongly coupled oscillator is very involved
- To simplify the analysis, broadband coupling is assumed
- This is equivalent to a lossy transmission line

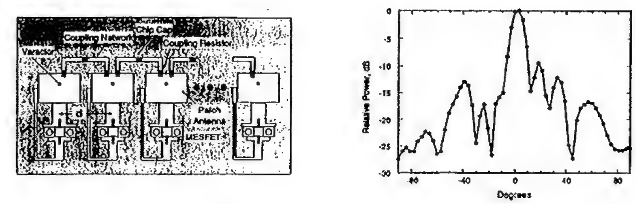

POWER COMBINING - ARRAY TYPE (CONT'D)

- To account for strongly coupled oscillators, mode analysis is used
- Using AVERAGE POTENTIAL THEORY, the dominant and stable mode that provides in-phase oscillation is found

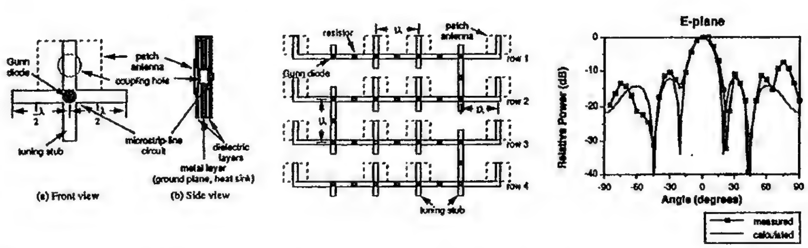

POWER COMBINING - ARRAY TYPE (CONT'D)

- By setting the interspacing to be half-wavelength at fundamental frequency, the second harmonic can be conditioned to radiate effectively
- Radiation of the fundamental signal is kept minimal as the phase relationship as a cancellation effect

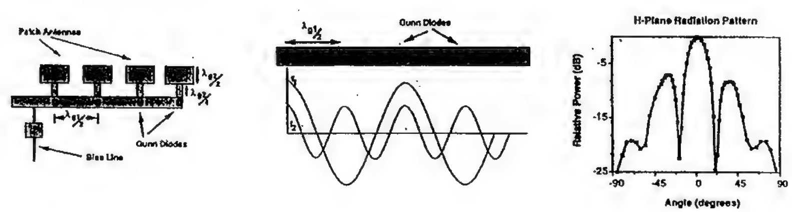

POWER COMBINING - ARRAY TYPE (CONT'D)

- To improve the phase noise of the array, injection locking is used
- Here, dielectric resonator is used as the coupling element
- The resonator is frequency-selective, thus there is no need to stabilize the dominant mode
- Phase noise of system is improved as the resonator is used
- This approach is also useful in receiver design

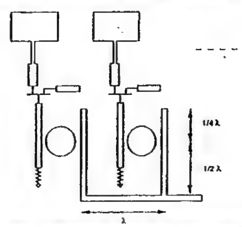

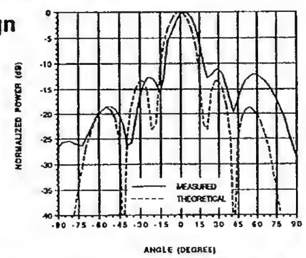

POWER COMBINING - ARRAY TYPE (CONT'D)

- To synchronise the oscillation, injection locking can be used
- Injected signal is divided in several stages to inject-lock the elements
- Through Kurokawa's analysis, the elements will be locked in-phase if the free-running frequencies of all elements are the same

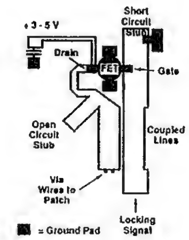

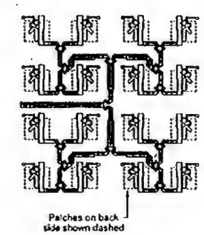

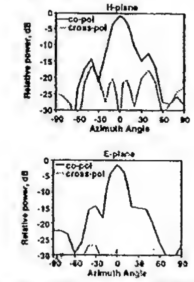

POWER COMBINING - ARRAY TYPE (CONT'D)

- Here, the system is treated as an entire system with one resonator This approach is the EXTENDED RESONANCE
- To achieve synchronization, the inter-connecting transmission line must be able to transform the reactance at one node to another node for cancellation of the reactance
- Then, oscillation will build up at the desired frequency

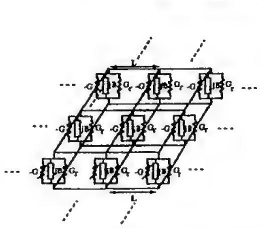

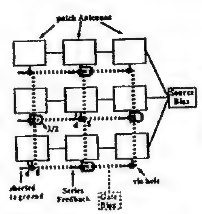

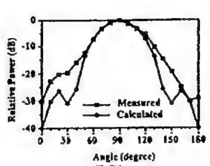

E Plane

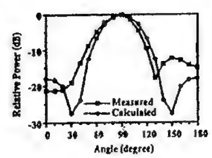

H Plane

POWER COMBINING - SINGLE ELEMENTS

- Although emphasis is placed on arrays, it must be noted that research in single element can lead to array implementation
- Also, quasi-optical array can be implemented using waveguides
- Short section of waveguide serves as isolator between cells and heat sinking structures.
- Enable single cell to be tested

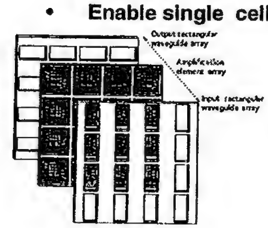

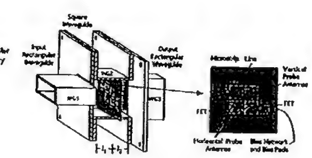

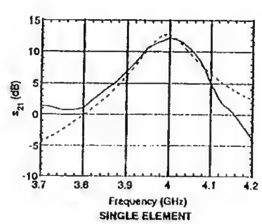

POWER COMBINING - 2-DIMENSIONAL COMBINING

- Two-dimensional arrays are now arousing research interests
- Suggested by J. W. Mink et al, hybrid dielectric slab beam waveguide can be used for transmission of signals
- 2-D arrays allow monolithic fabrication
- 2-D is not restricted by the real-estate and DC bias circuitry can be easily incorporated
- Lenses are planar, and alignment of array and lenses does not require mounting structures
- Heat-sinking and support can be provided by the slab waveguide
- Measurement is easy as it behaves like a connectorized component

POWER COMBINING - 2-DIMENSIONAL COMBINING (CONT'D)

- Here, an oscillator combiner was designed
- Coupling between oscillators is achieved using the curved reflector
- Oscillator is designed not to excite surface-of-slab to ground-plane resonance
- Vivaldi antenna is used to decouple the forward and backward waves
- TE modes, ie E field parallel to ground plane, are excited
- Through experiment, the placement of the oscillators is determined to ensure repeatable oscillation at the desired frequency

POWER COMBINING - 2-DIMENSIONAL COMBINING (CONT'D)

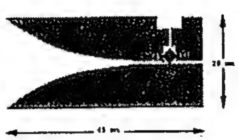

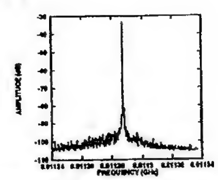

4 oscillators with injection-locking

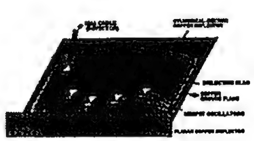

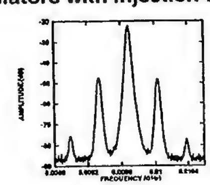

With 350 KHz FM modulation

POWER COMBINING - 2-DIMENSIONAL COMBINING (CONT'D)

- Similarly, an amplifier combiner was designed
- Several configurations of the amplifier placement were investigated
- Amplifier gain is the ratio of output power with and without bias
- Two groups of bias are measured
- Field strength is function of frequency and postion, hence different configuration has different power gain
- Placement of amplifier is experimentally determined to prevent oscillation and provide highest gain
- Since the amplifiers are not placed symmetrically, the amplification gain is not symmetrical

POWER COMBINING - 2-DIMENSIONAL COMBINING (CONT'D)

- The configurations and their gains are as follows :

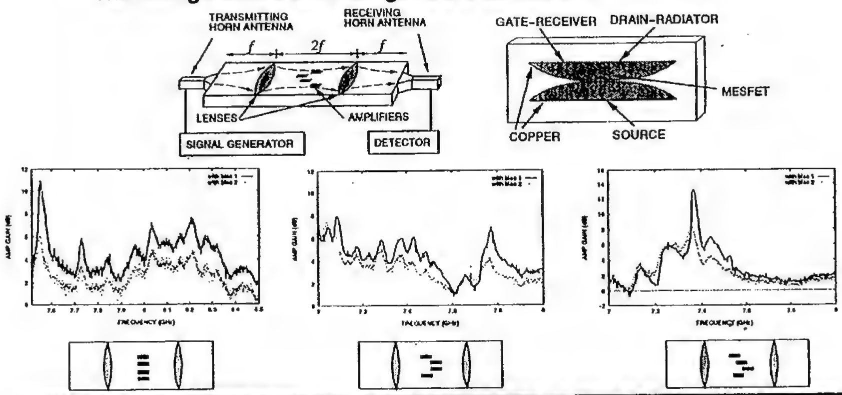

POWER COMBINING - 2-DIMENSIONAL COMBINING (CONT'D)

- To reduce beammode perturbation, scattering losses and reflection of the amplifier, amplifier cells are located on the ground plane

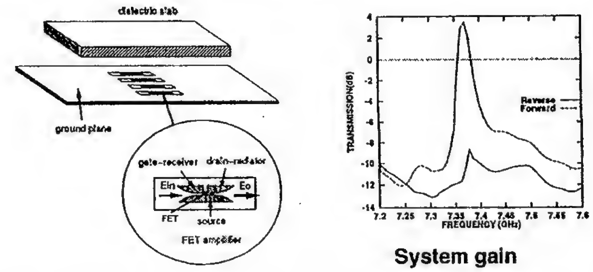

System gain

POWER COMBINING - 2-DIMENSIONAL COMBINING (CONT'D)

- Although low loss, the TE mode is difficult to excite cleanly
- Here, Yagi-Uda is used to excite the dominant mode with E field normal to the slab ground plane
- Microstrip delay lines are used to focus the guided waves
- Thickness of slab is chosen as such that center frequency is 90% of cut-off frequency of the 2nd order TM mode, thus maximizing coupling into DSWB

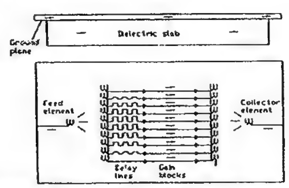

POWER COMBINING - 2-DIMENSIONAL COMBINING (CONT'D)

- Measured results of the 10-element combiner are as follows :

Total measured loss (minimum)	6.7 dB
Yagi-Uda slot array antenna losses (measured) Input return loss = 10 dB Mismatch loss = 0.46 dB Front-to-back ratio = 10 dB Back lobe loss = 0.41 dB Total antenna element loss 4(0.46 + 0.41) = 3.5 dB	-3.5 dB
Microstrip line losses (0.2 dB/in) (measured)	-1.6 dB
Deduced losses (spillover, radiation, and mutual coupling)	1.6 dB

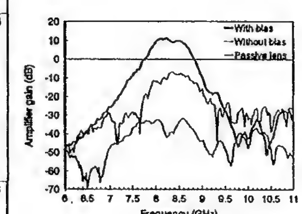

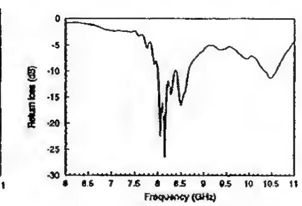

BEAM-CONTROL - INTRODUCTION

- To allow monolithic integration, phase control in active antenna must be achieved electronically
- Thus, ferrite-based phase shifter is not favored at all
- Various beam-controlled arrays are as follows :

BEAM-CONTROL

- *BEAM-SCANNING*
  - *END ELEMENTS*
  - *UNILATERAL INJECTION LOCKING*
  - *MULTIPLIERS*
  - *PHASE-LOCKED LOOP*
- *BEAM-SWITCHING*
  - *MODE-LOCKED*
  - *INJECTION LOCKING*
  - *OPTICAL*
- *RETRODIRECTIVE*
- *OTHERS*

BEAM-CONTROL - BEAM SCANNING

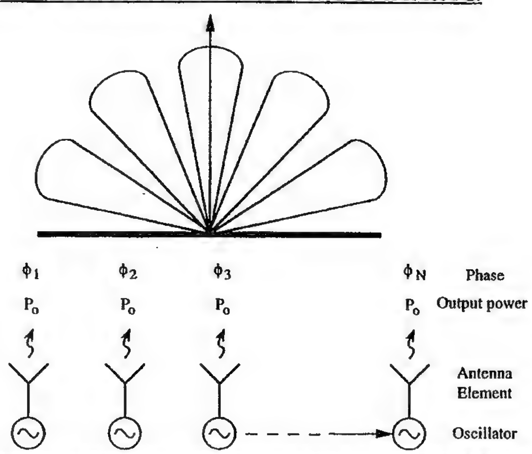

BEAM-CONTROL - BEAM SCANNING (CONT'D)

- Through coupled-oscillator theory, there is a phase progression in the array when the end elements are detuned in frequency
- The amount of phase shift is proportional to the amount of frequency detuning
- The array still operates at a single frequency with over 180° of phase tuning

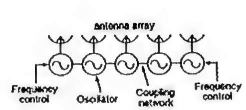

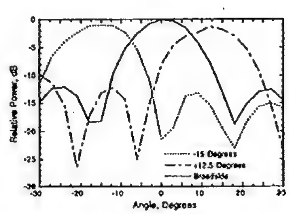

BEAM-CONTROL - BEAM SCANNING (CONT'D)

- To extend the previous concept, a multiplier is connected at each output of the oscillator before the antenna
- Intuitively, a 2X multiplier will double the phase difference in the oscillator
- This increases the scan range

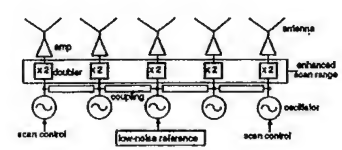

BEAM-CONTROL - BEAM-SCANNING (CONT'D)

- UNILATERAL INJECTION LOCKING

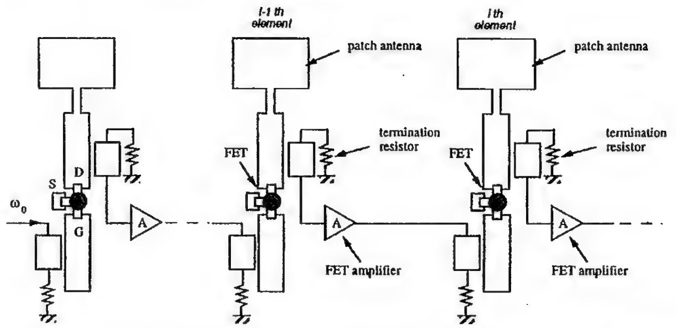

BEAM-CONTROL - BEAM-SCANNING (CONT'D)

- Another form of phase control is to use phase-locked loop
- When within locking range, there is a phase difference between the locking and oscillating signals
- It is this phase difference that is used for beam-scanning

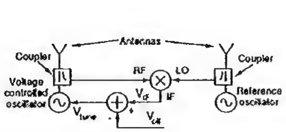

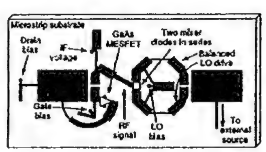

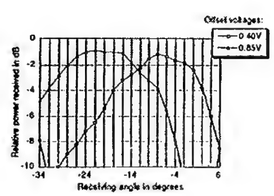

BEAM-CONTROL - BEAM-SCANNING (CONT'D)

- UNILATERAL INJECTION LOCKING

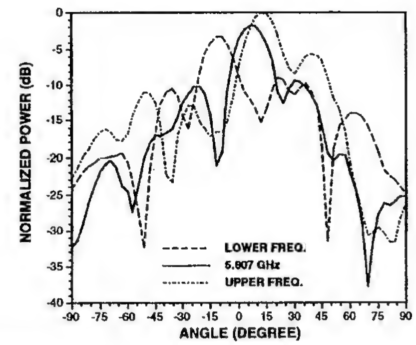

BEAM-CONTROL - BEAM-SCANNING (CONT'D)

- Grid approach has also demonstrated its capability in beam-scanning
- Diode grid has been implemented as phase shifter
- Fixed beam diffraction of 30^{o} has been reported by replacing the diode in the grid with gaps of varying sizes

BEAM-CONTROL - BEAM-SWITCHING

- Beam switching is used in radar application to extract target information, e.g. range and direction
- Conventional design uses bulky phase shifters to handle the high power transmission

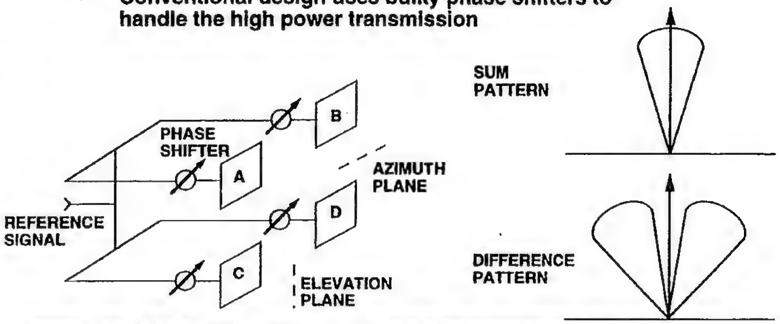

BEAM-CONTROL - BEAM-SWITCHING (CONT'D)

- By using different modes in the strongly-coupled oscillators, different patterns can be generated
- When a resistor is connected between two elements using transmission lines, the stable mode is the in-phase mode
- When the elements are connected with through transmission lines, the stable mode is the out-of-phase mode

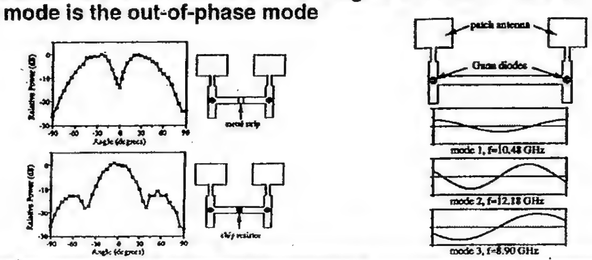

BEAM-CONTROL - BEAM-SWITCHING (CONT'D)

- To furhter extend this concept with electronic tuning, an active device is connected between elements to switch between low or high impedances
- A FET is used here. The impedances are controlled by the V_{gs}

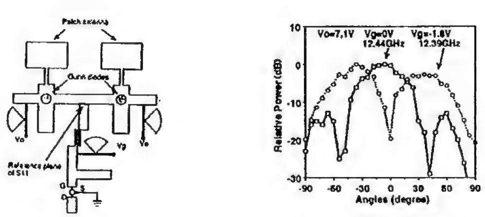

BEAM-CONTROL - BEAM-SWITCHING (CONT'D)

- To increase the degree of freedom for tuning, optical interaction is used
- Here, the photovoltaic and photoconductive effects are exploited
- By optical illumination, the FET characteristics are controlled to derive the necessary impedances

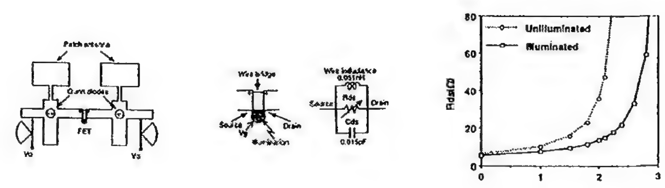

BEAM-CONTROL - BEAM-SWITCHING (CONT'D)

- Injection locking is used here
- Phase control is discretized (90^o,-90^o,0^o)

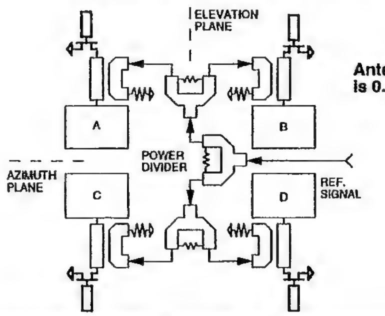

Antenna spacing is 0.7 λ_o

BEAM-CONTROL - BEAM-SWITCHING (CONT'D)

- Unilateral injection-locking array

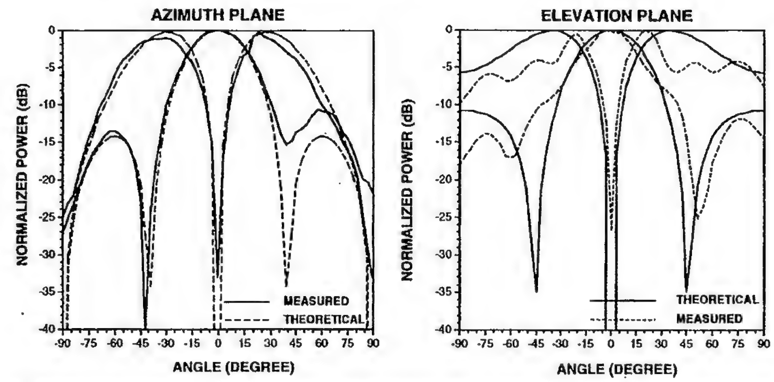

BEAM-CONTROL - RETRODIRECTIVE ARRAY

- Incident beams are reflected back to the source without prior knowledge of the source location
- Retrodirectivity is not destroyed by conformally mounting or partially blocking the array
- Use in communications/RFID transponder applications

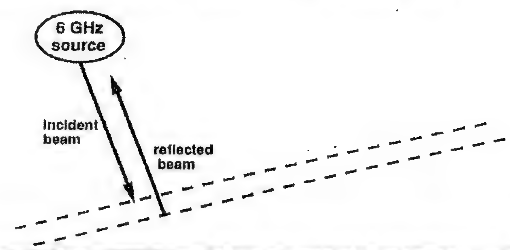

BEAM-CONTROL - RETRODIRECTIVE ARRAY (CONT'D)

- Phase conjugation via the heterodyne method

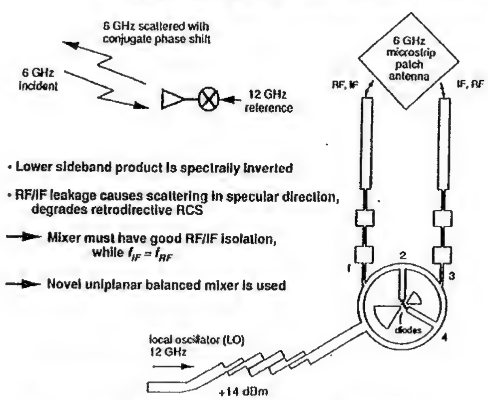

- Lower sideband product is spectrally inverted
- RF/IF leakage causes scattering in specular direction, degrades retrodirective RCS

→ Mixer must have good RF/IF isolation, while $f_{IF} = f_{RF}$

→ Novel uniplanar balanced mixer is used

(no antenna; LO freq. = 2 x RF freq.)

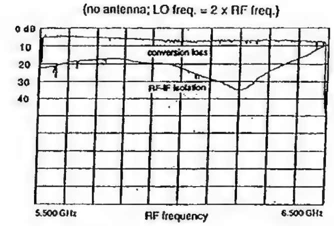

- 5 - 7 dB conversion loss
- 35 dB max RF-IF isolation

BEAM-CONTROL - RETRODIRECTIVE ARRAY (CONT'D)

- **Equivalent circuit**

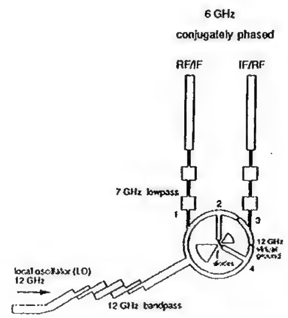

LO equivalent circuit

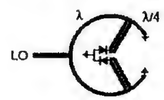

- ports 1,3 open at 12 GHz
- diode LO voltages are in phase

RF/IF equivalent circuit

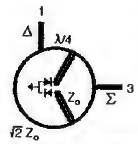

- LO port is open at 6 GHz
- 12 GHz pumped diode conductance waveforms are antiphased:

RF at Σ yields Δ IF product
RF at Δ yields Σ IF product

→ *RF-IF port isolation is high*

UNIVERSITY OF CALIFORNIA, LOS ANGELES

BEAM-CONTROL - RETRODIRECTIVE ARRAY (CONT'D)

- **A 8X1 linear array**

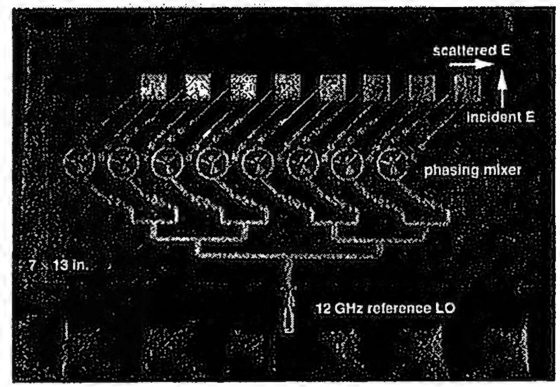

UNIVERSITY OF CALIFORNIA, LOS ANGELES

BEAM-CONTROL - RETRODIRECTIVE ARRAY (CONT'D)

- **Measured Bistatic RCS of the linear array**

source at 0° source at -20° source at +45°

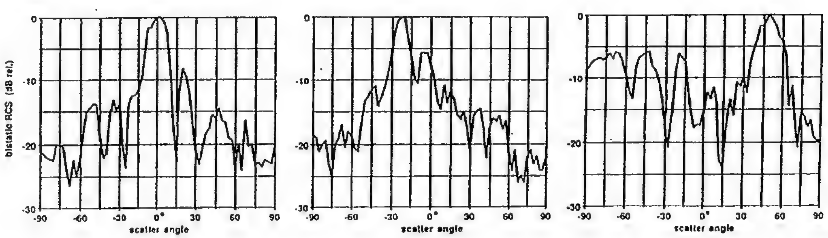

LO: 12.460 GHz, +20 dBm total
RF incident: 6.215 GHz
IF scattered: 6.245 GHz

cross-polarized response

UNIVERSITY OF CALIFORNIA, LOS ANGELES

BEAM-CONTROL - RETRODIRECTIVE ARRAY (CONT'D)

- **A 4X4 planar array with reference element**

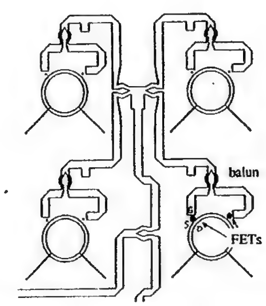

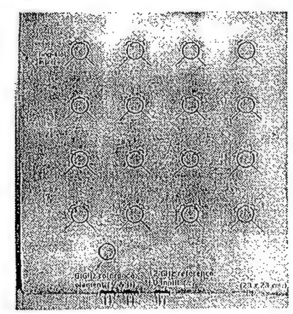

UNIVERSITY OF CALIFORNIA, LOS ANGELES

BEAM-CONTROL - RETRODIRECTIVE ARRAY (CONT'D)

- Measured RCS of planar array

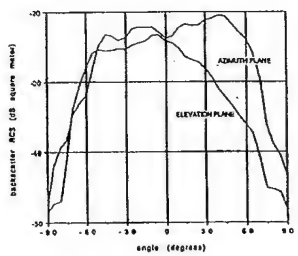

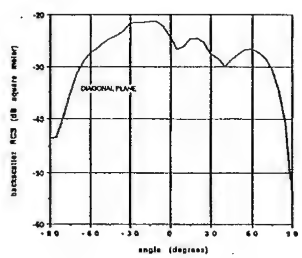

BEAM-CONTROL - OTHERS

- It is worth mentioning that another form of beam-control is the polarization-agile active antennas
- Currently, reported works are single element
- By turning 'on' the appropriate active devices in an antenna, linearly and circularly polarized beams can be synthesized

CONCLUSION

- A review of power-combining, beam control and 2-dimensional power combining arrays have been made
- It must be noted that single element, when properly considered, can lead to arrays
- There is a need to merge rigorous electromagnetic simulation with nonlinear analysis for active antenna
- This will account for all forms of coupling between elements
- Nonlinear analysis can then predict the amplitude and phase dynamics needed in active phased arrays

GRID AMPLIFIERS

David Rutledge, Caltech

Ph.D. thesis of Jeff Liu (Rockwell)

Prepared for NATO ASI, Chateau de Bonas,
July 1–11, 1996

Caltech

Monolithic Grid Amplifiers

Gain Model
Stability Model
Hybrid HBT Grid Amplifiers

Monolithic
HBT Grid Amplifier

Approaches
to
High-Power Millimeter-wave Amplifiers

Caltech

Gain and Stability Model for HBT Grid Amplifiers

- Introduction to Grid Amplifiers
- Gain Model
- Construction and Measurements
- Stability Model

Caltech

A Grid Amplifier

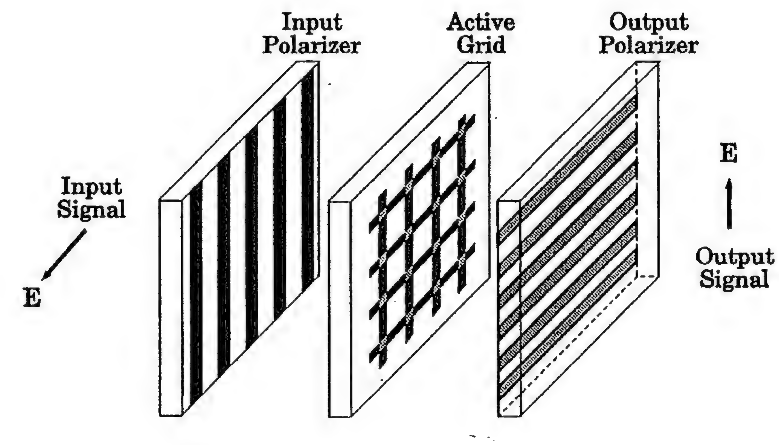

- Quasi-Optical Amplifier (Spatial Power-Combinig Amplifier)
  - No conduction loss associated with the feed networks
- Power Capability
  - Power proportional to the number of the unit cells
  - Produce a high-power beam using many low-power transistors

A Unit Cell

- Input & Output Leads
- Active Device
- Bias Lines

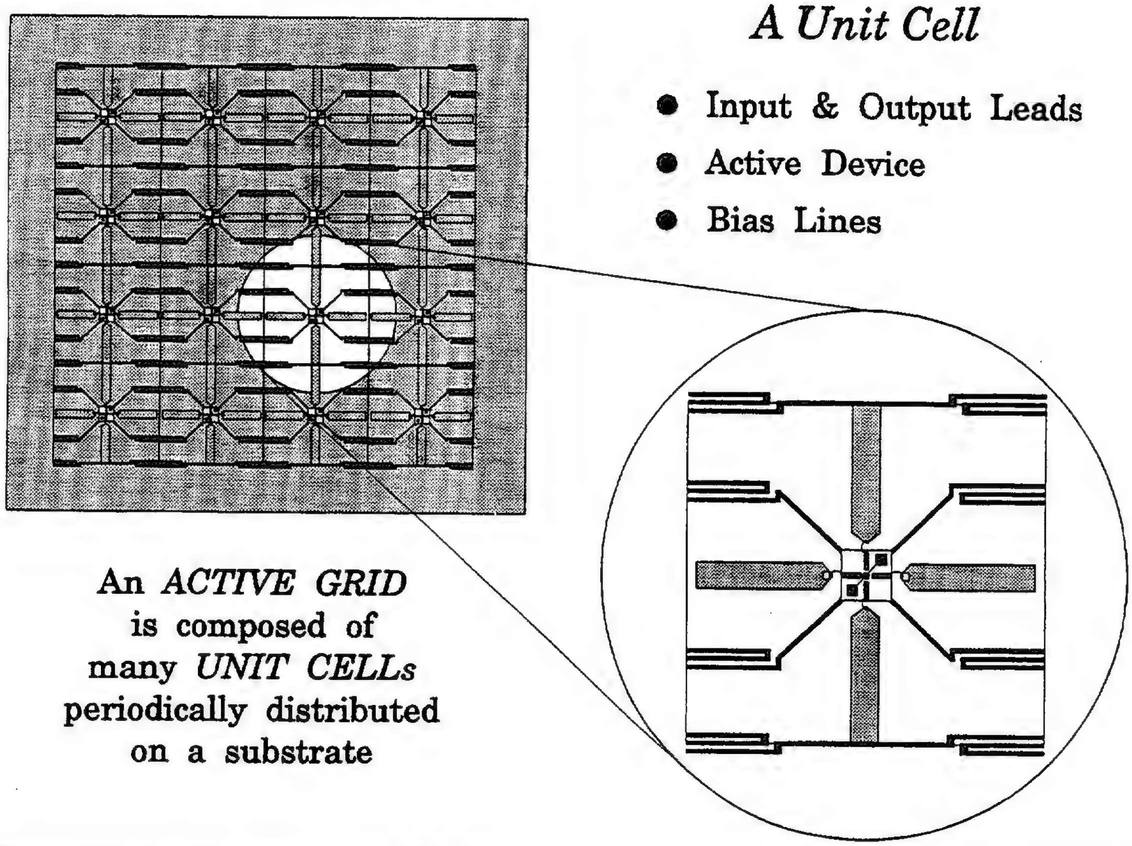

An *ACTIVE GRID* is composed of many *UNIT CELLs* periodically distributed on a substrate

Unit Cell

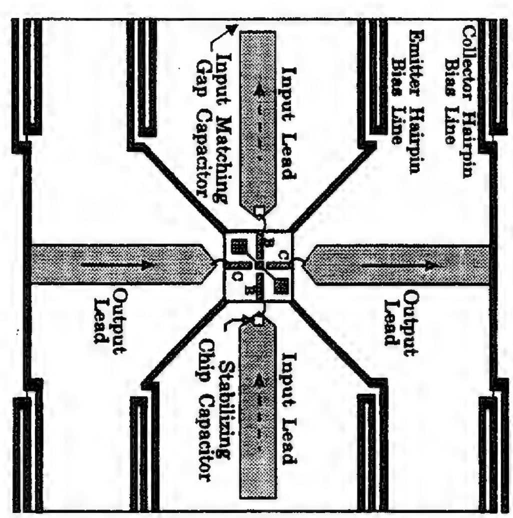

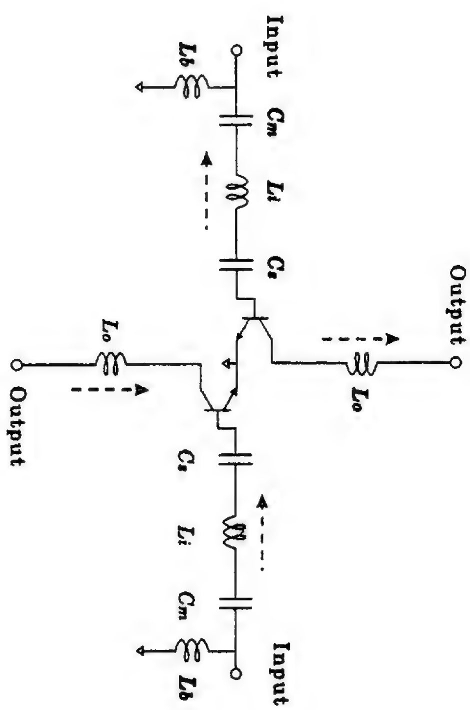

Caltech

HBT Grid-Amplifier Gain Model

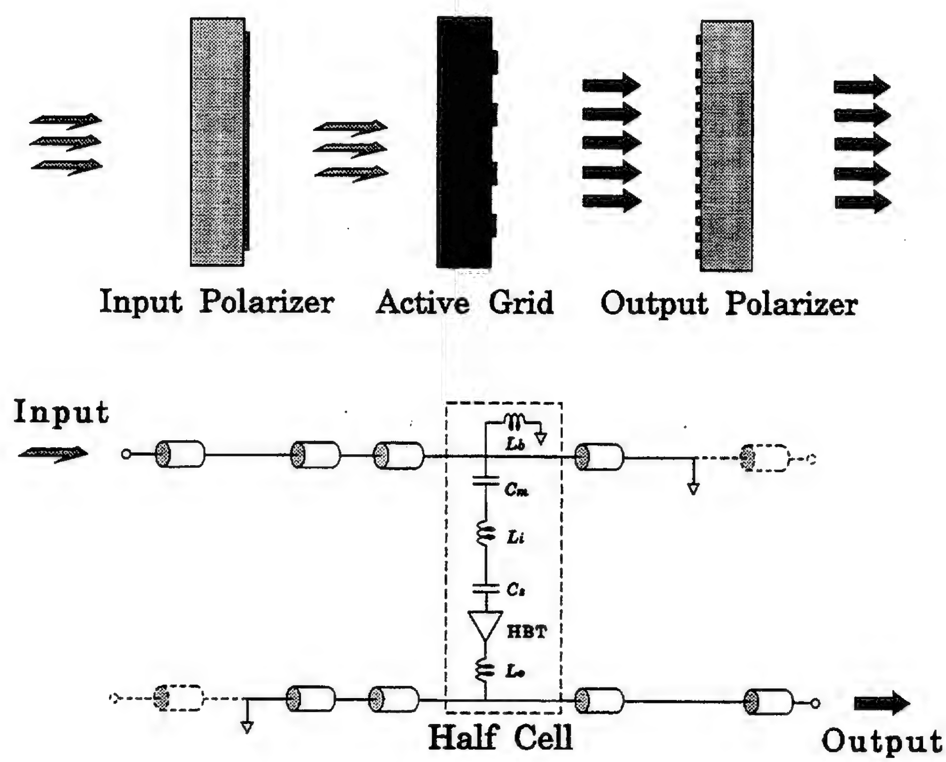

Caltech

Hairpin Bias Line

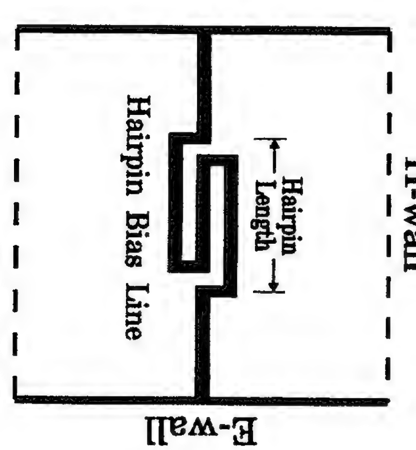

Equivalent Circuit

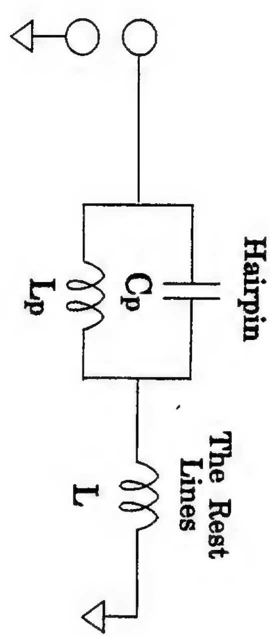

Caltech

Hairpin Line Reactance Response

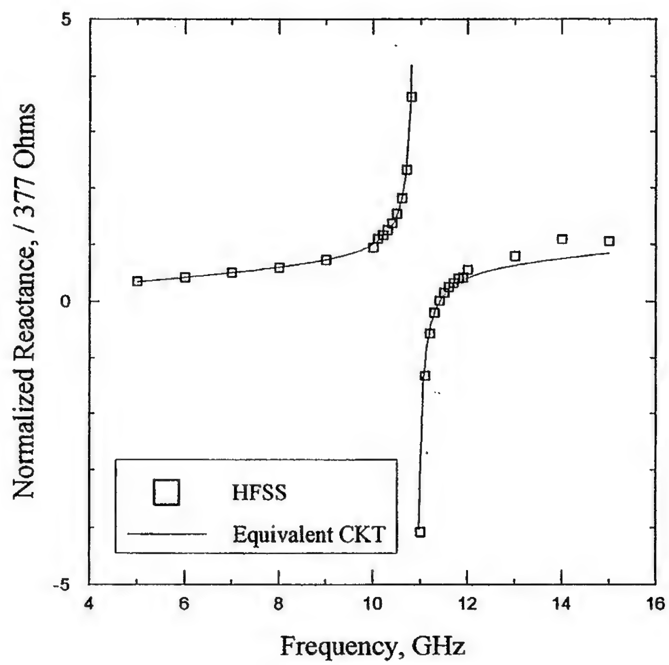

Hairpin Length: 2.1 mm
fp: 10.9 GHz
fs: 11.4 GHz

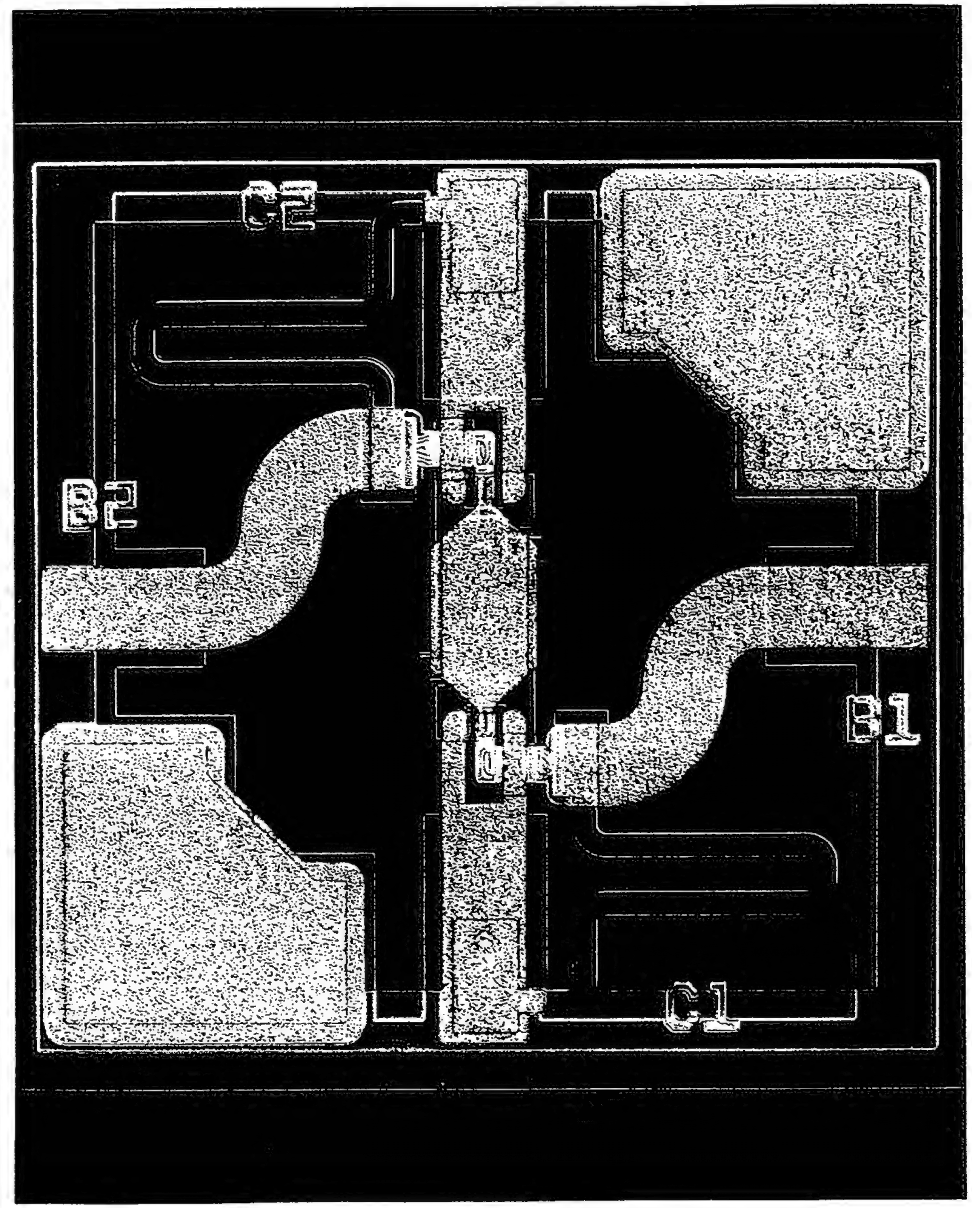

Caltech

10-GHz Hybrid HBT Grid Amplifier Unit Cell

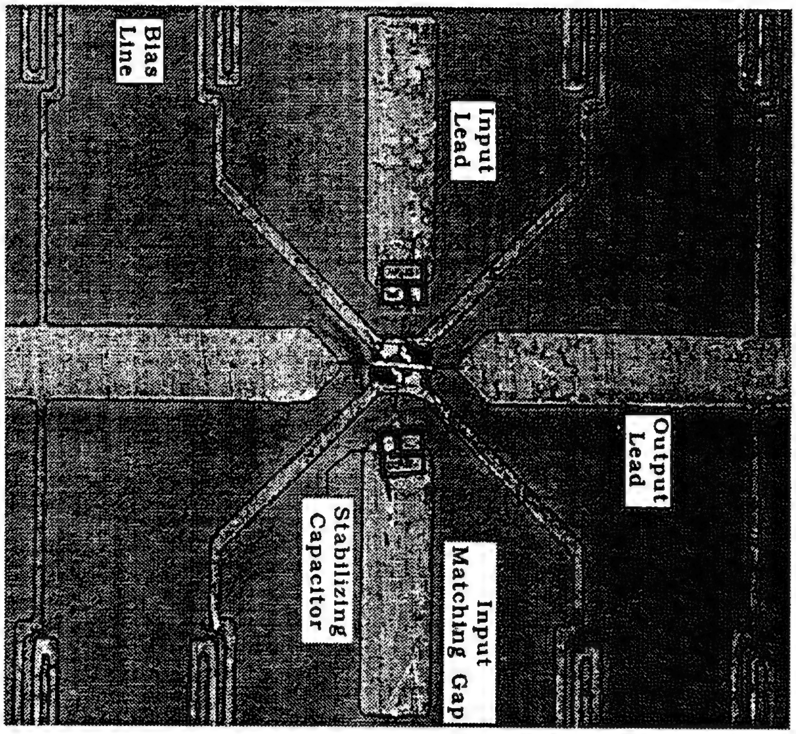

Cell Period: 8 mm
Lead Width: 0.8 mm
Input Matching Gap: 0.2 mm

Caltech

10-GHz HBT Grid Amplifier

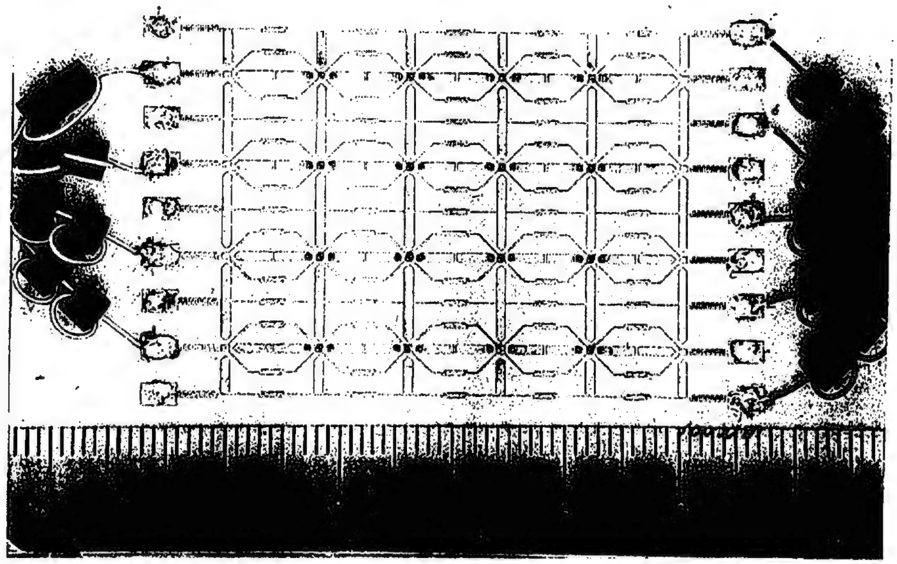

Gmax: 11dB , BW: 350 MHz (3.5%)

Caltech

Assembled 10-GHz Grid Amplifier

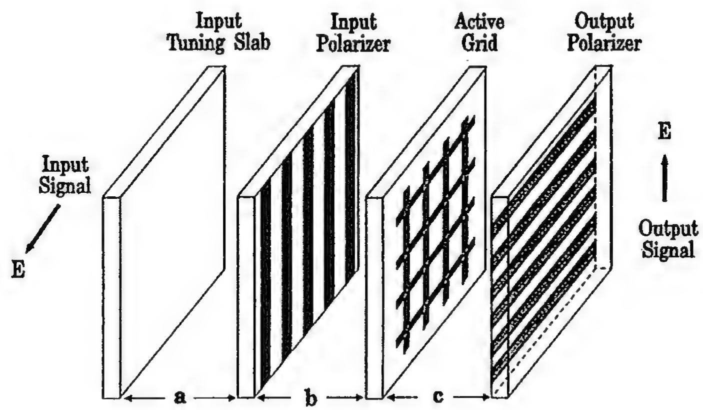

Tuning Procedure:

- ❒ Changing air spacings: a, b , and c
- ❒ Optimize the gain at 10-GHz

Layer	ϵ_r	Dimension (mm)	Elec. Length (° @10 GHz)
Substrate	10.8	1.27	50
Polarizer	2.2	3.18	57
Tuning Slab	10.2	2.54	97
Air Spacing a	1	4.8	58
Air Spacing b	1	19	228
Air Spacing c	1	26	312

Caltech

Tuning Grid Amplifier

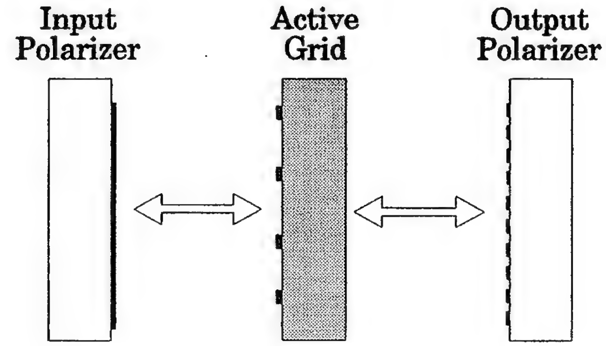

Equivalent Circuit

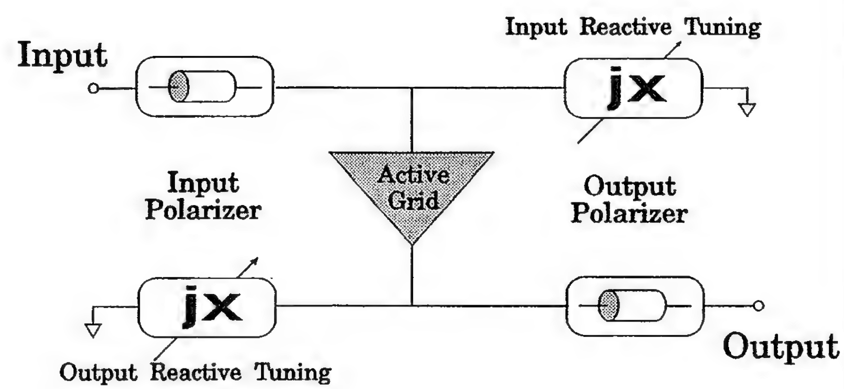

Caltech

10-GHz HBT Grid Amplifier Tuning Curve

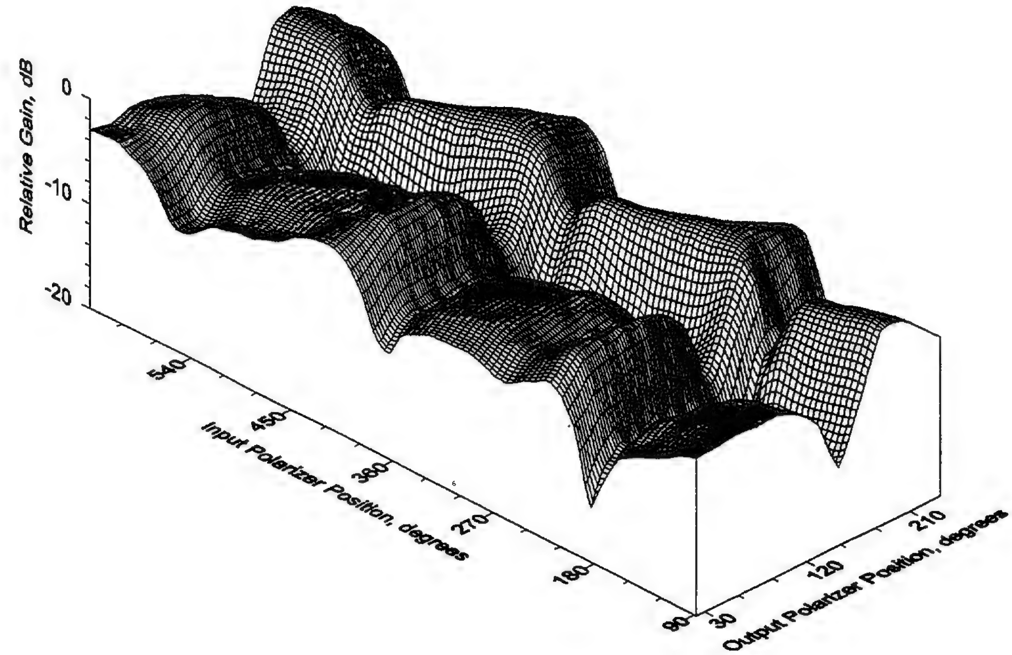

Caltech

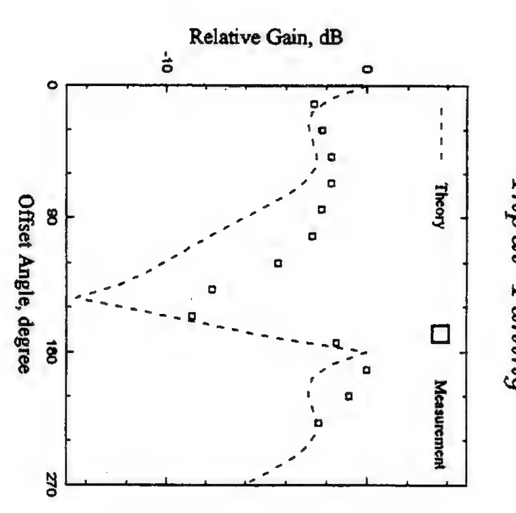

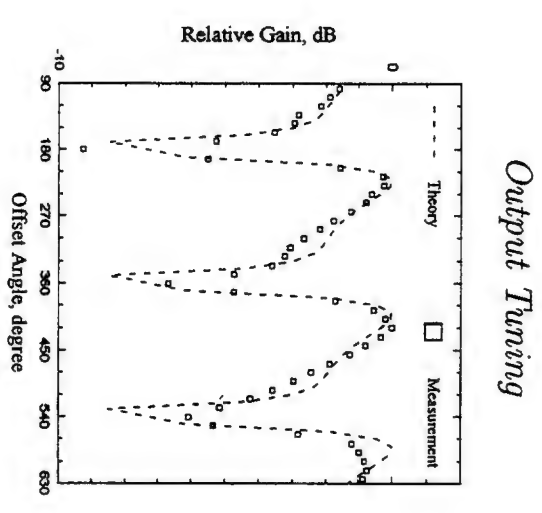

Caltech

10-GHz Hybrid HBT Grid Amplifier
with 0.18-pF Stabilizing Capacitors

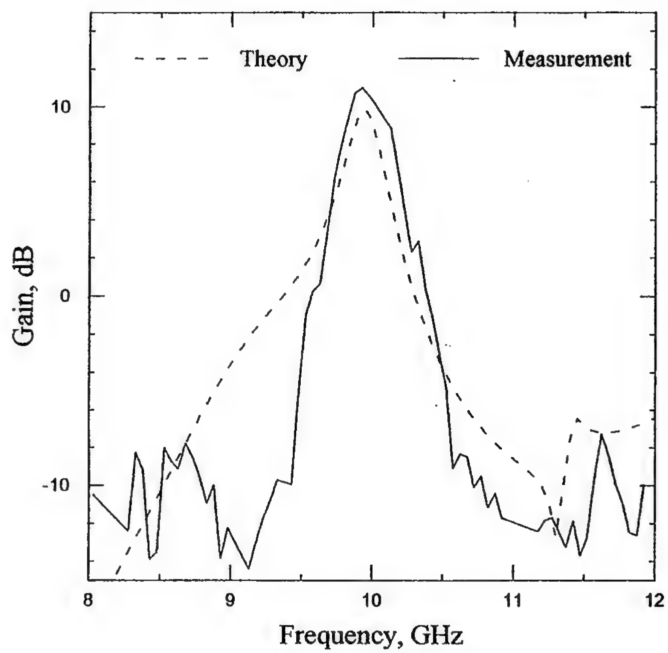

Gain: 11 dB @ 9.9 GHz
BW: 350 MHz (3.5%)

Caltech

Common-Mode Oscillation

Oscillating at 7.8 GHz @ 2mA/transistor

☐

Sensitive to the unit cell

☐

Not sensitive to the polarizer positions

☐

The greatest power density is
in the plane of the grid

Caltech

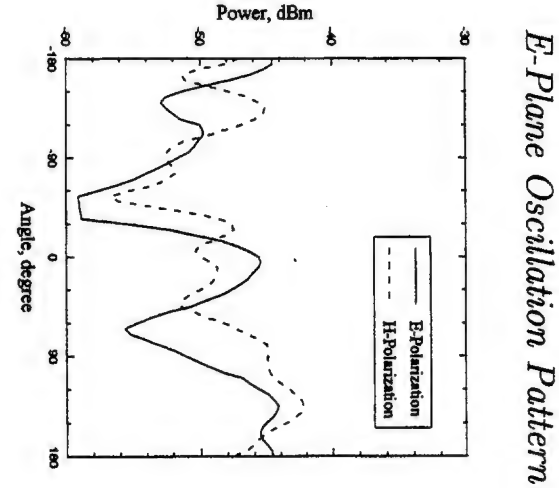

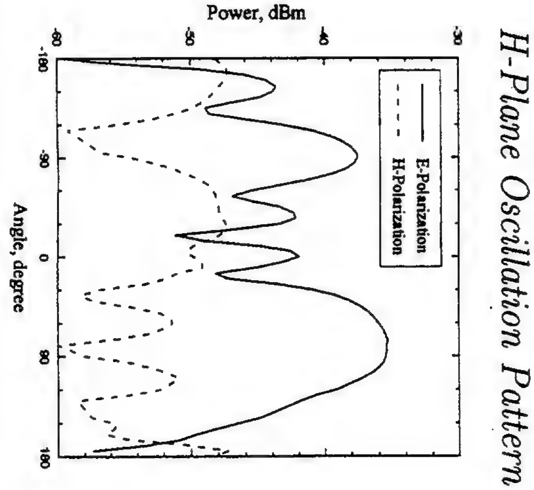

Caltech

R5E
10 GHz Grid Amplifier
Oscillation Frequency : 7.8 GHz
Azimuth Pattern

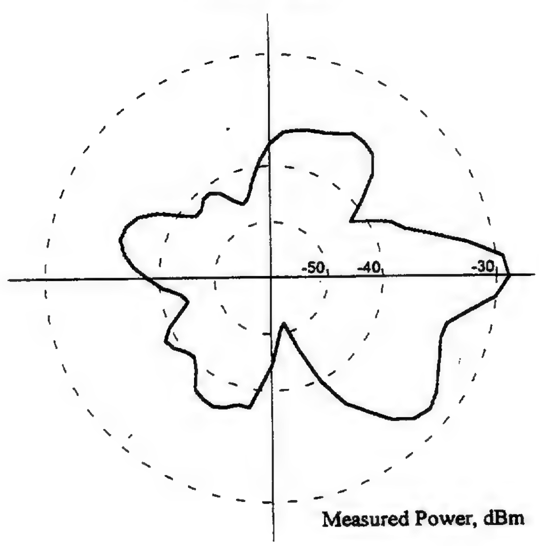

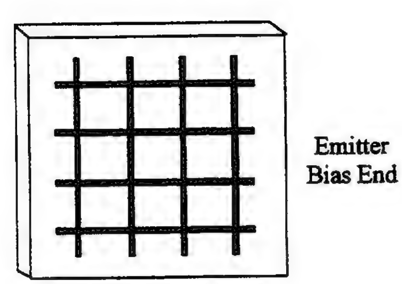

Caltech

Quarter Cell

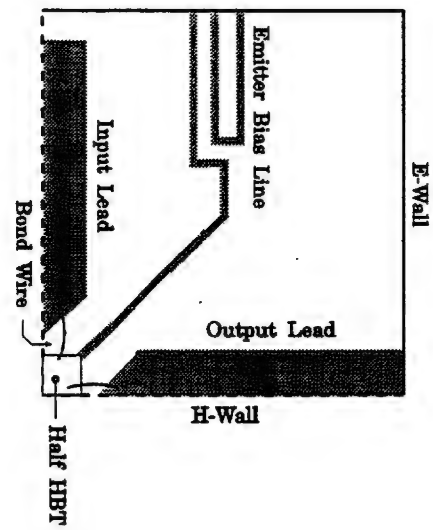

Equivalent Circuit

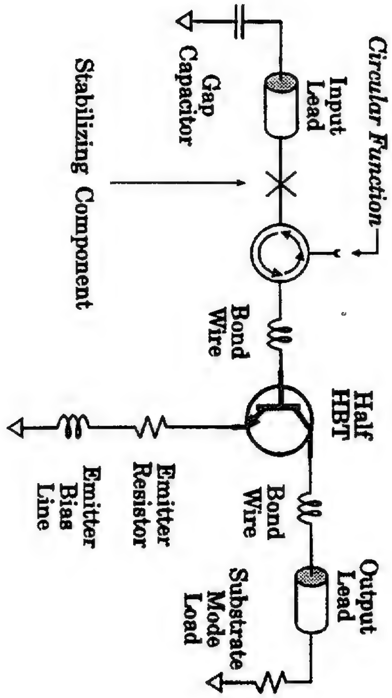

Caltech

Stability Analysis
@ Stabilizing Capacitors

Circular Function

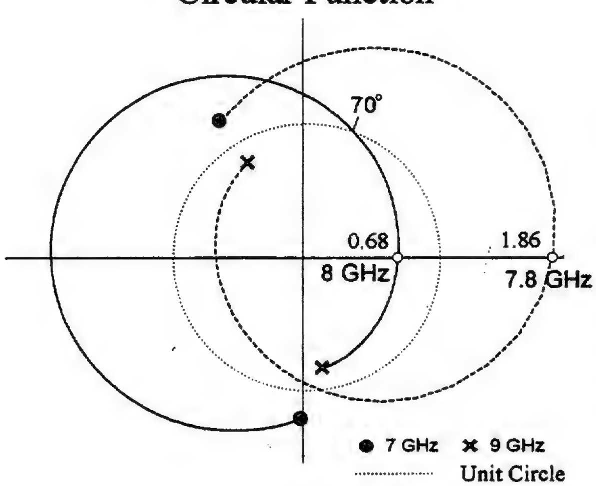

---------- Without Stabilizing Capacitor

Unstable,
Potentially Oscillating @ 7.8 GHz

———— With Stabilizing Capacitor, 0.1 pF

Stable with
Gain margin: 3.4 dB
Phase margin: 70 degrees

Caltech

Stabilizing the Grid Amplifier

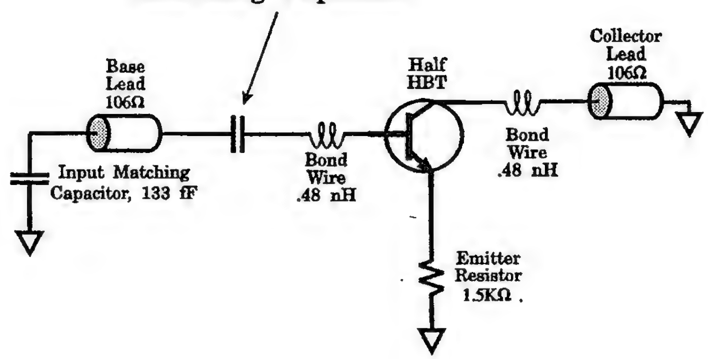

Positive Phase Shift of Circular Function

Caltech

Closeup of Unit-Cell Center

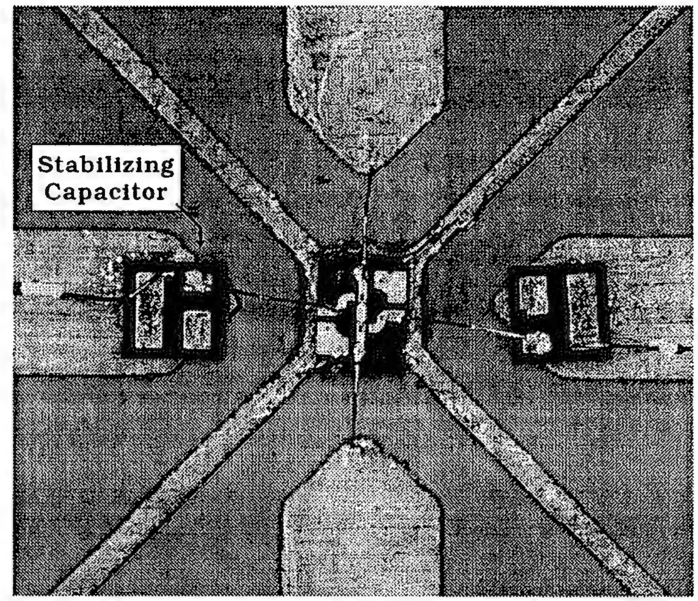

Smaller Capacitance

⇩

Higher Stability

Caltech

10 GHz Grid Amplifier
with 0.1 pF Stabilizing Capacitors

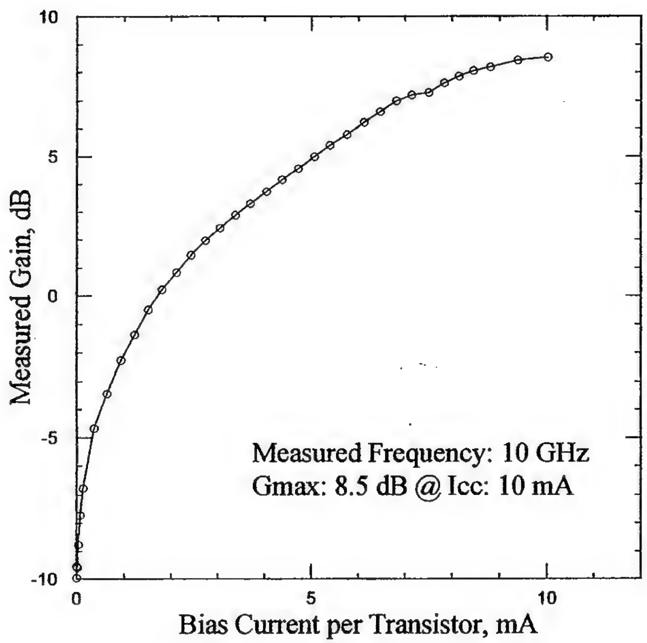

No Oscillation Observed

Caltech

Summary of Hybrid HBT Grid Amplifiers

Gain Model
and
Comparison of Theory and Measurement

□

Stability Model
for
Common-Mode Oscillation

□

Stable Grid Amplifier

⬇

40-GHz Monolithic HBT Grid Amplifier
Bias Current: 16 mA/transistor

G_{max}: 5 dB @ 40 GHz
P_{max}: 670 mW @ 40 GHz

Caltech

Monolithic HBT Grid Amplifier

Cheh-Ming Jeff Liu, David Rutledge
Michael DeLisio
Caltech

Emilio Sovero, Wu Jing Ho
Aiden Higgins
Rockwell Science Center

- ❐ Unit Cell and Models
- ❐ Gain Measurements
- ❐ Tuning Curves and Radiation Patterns
- ❐ Power Measurements
- ❐ Tiling

Caltech

Rockwell HBT Transistor

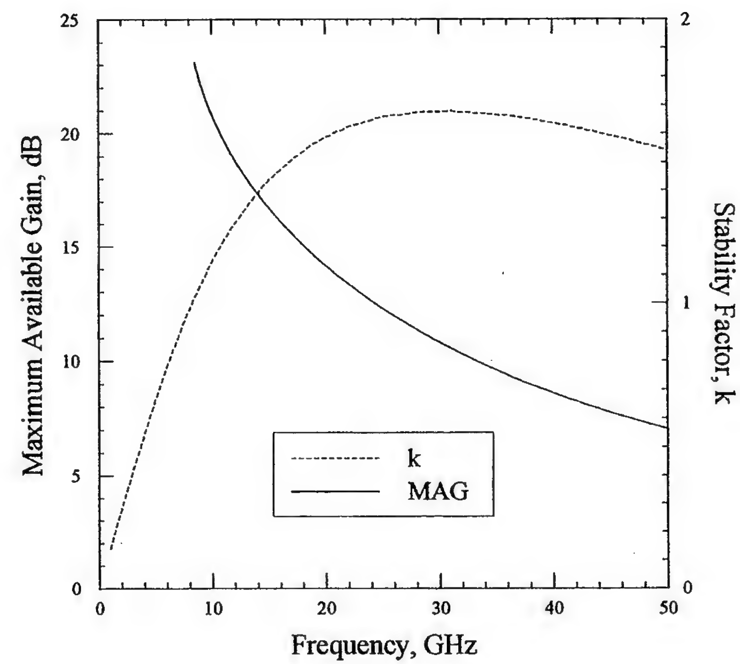

@ 40 GHz
MAG: 9 dB ; k: 1.6

Caltech

40-GHz Monolithic Grid-Amplifier Unit Cell

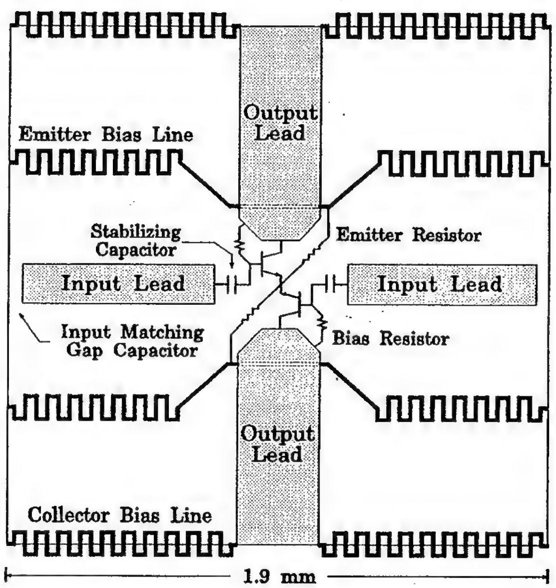

Unit-Cell Period: 1.9 mm
Input-Lead Width: 120 um
Output-Lead Width: 296 um
Input-Matching-Cap. Gap: 30 um

Caltech

Rockwell HBT Transistor Optimal Transistor Impedance

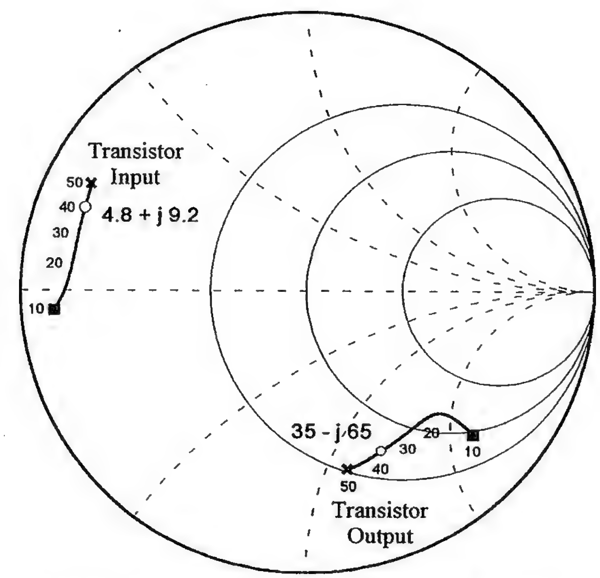

× 50 GHz ○ 40 GHz ■ 10 GHz

@40 GHz, MAG: 9 dB

Caltech

Gain Model for Monolithic Grid Amplifier

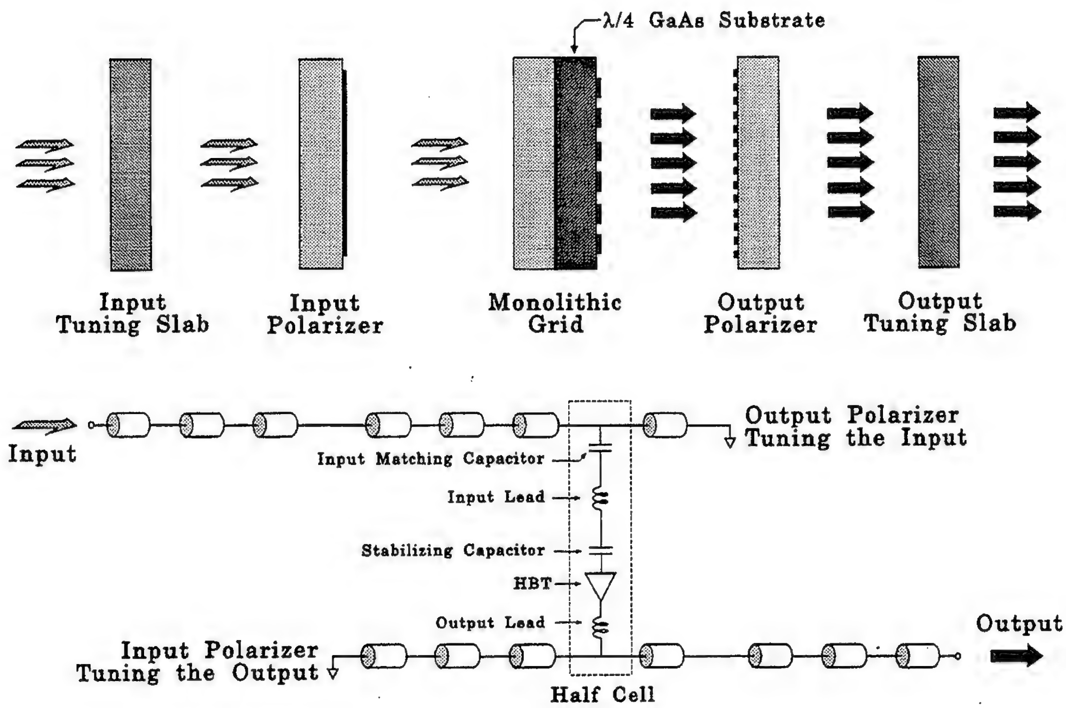

Caltech

Monolithic HBT Grid Amplifier
Stability Model for Common-Mode Oscillation

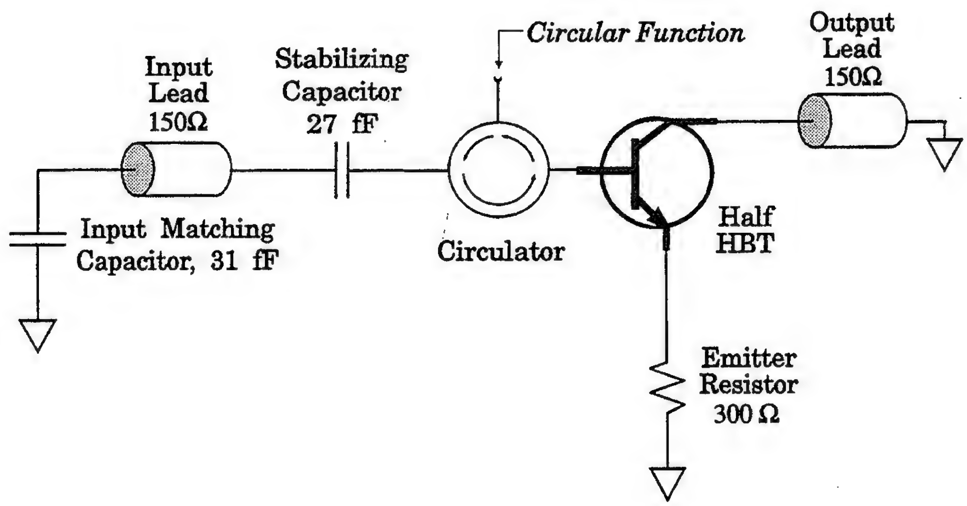

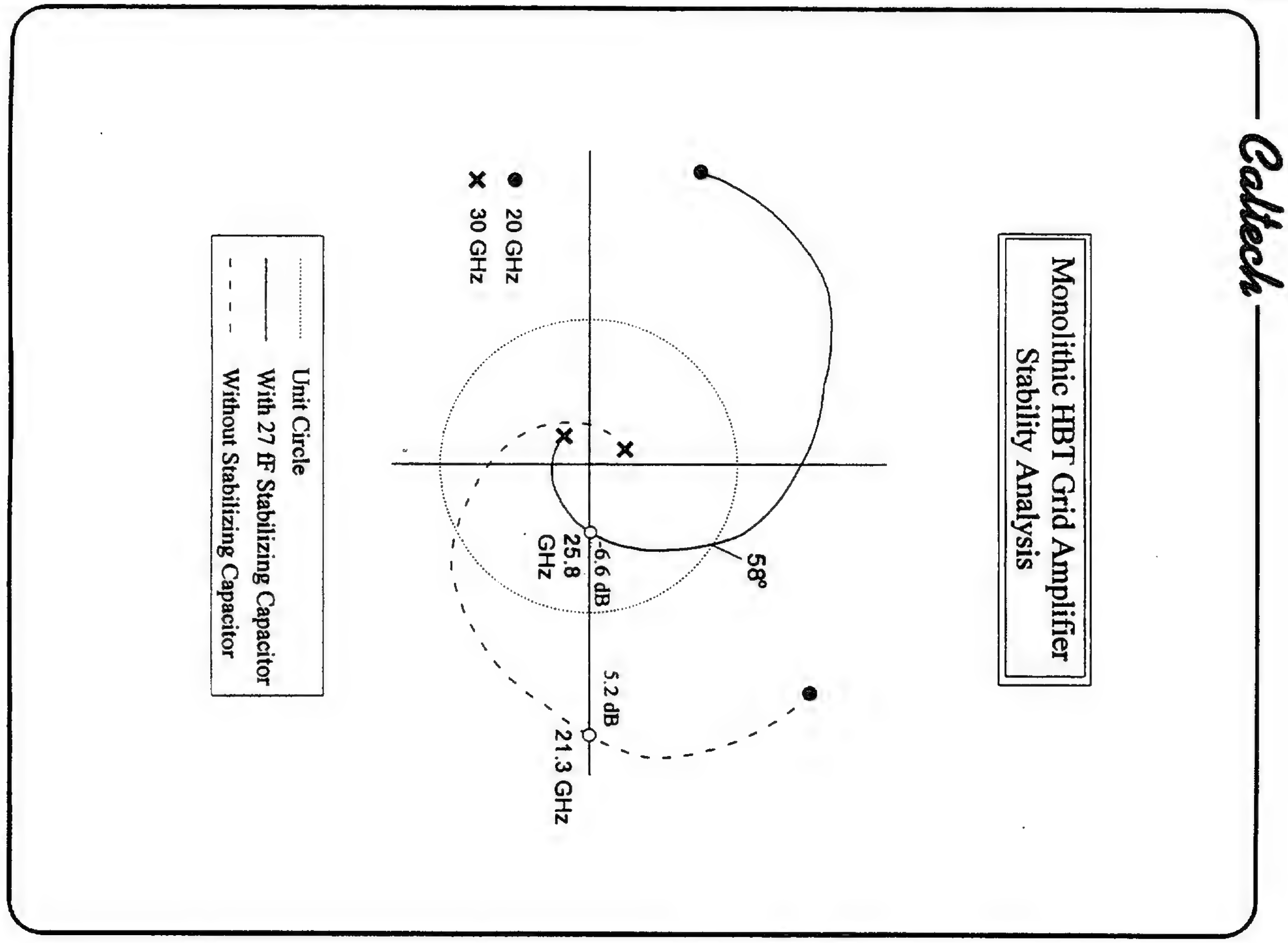

Monolithic Grid Amplifier

SCP.0816A.041395

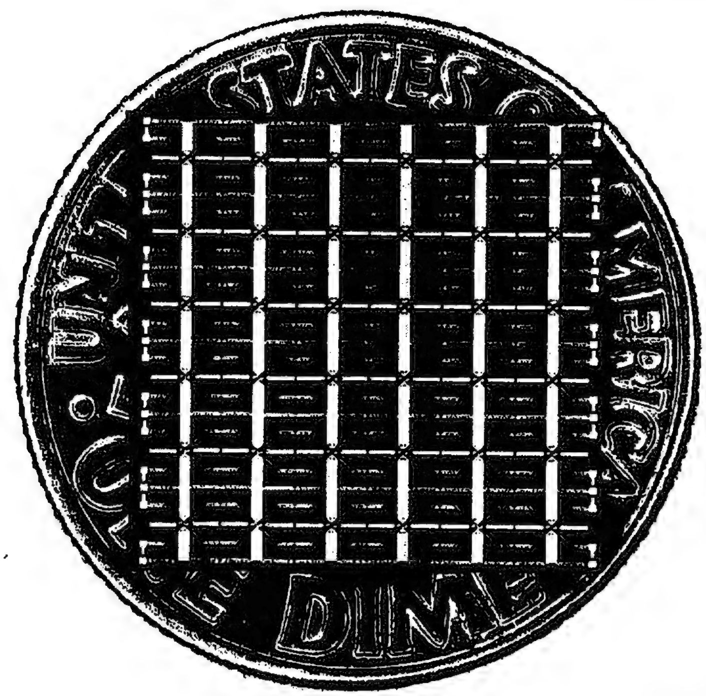

Rockwell

Science Center

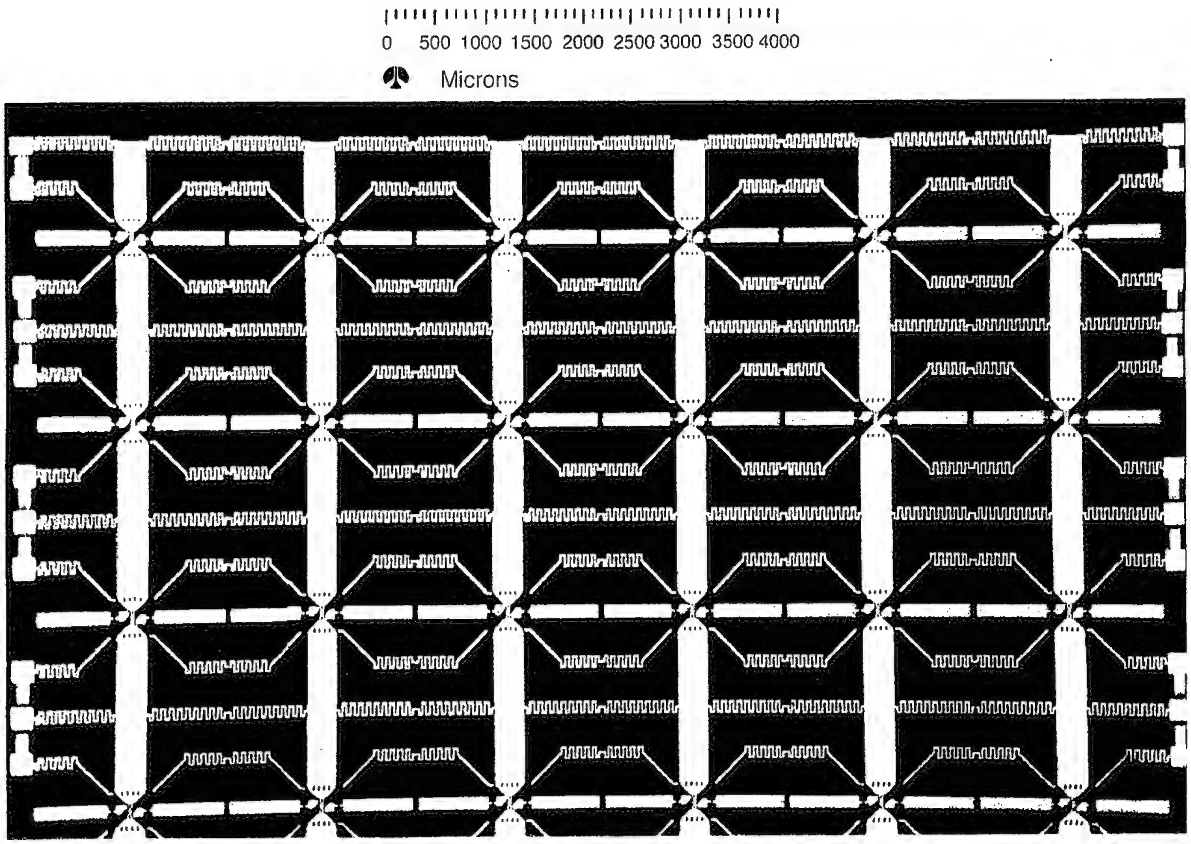

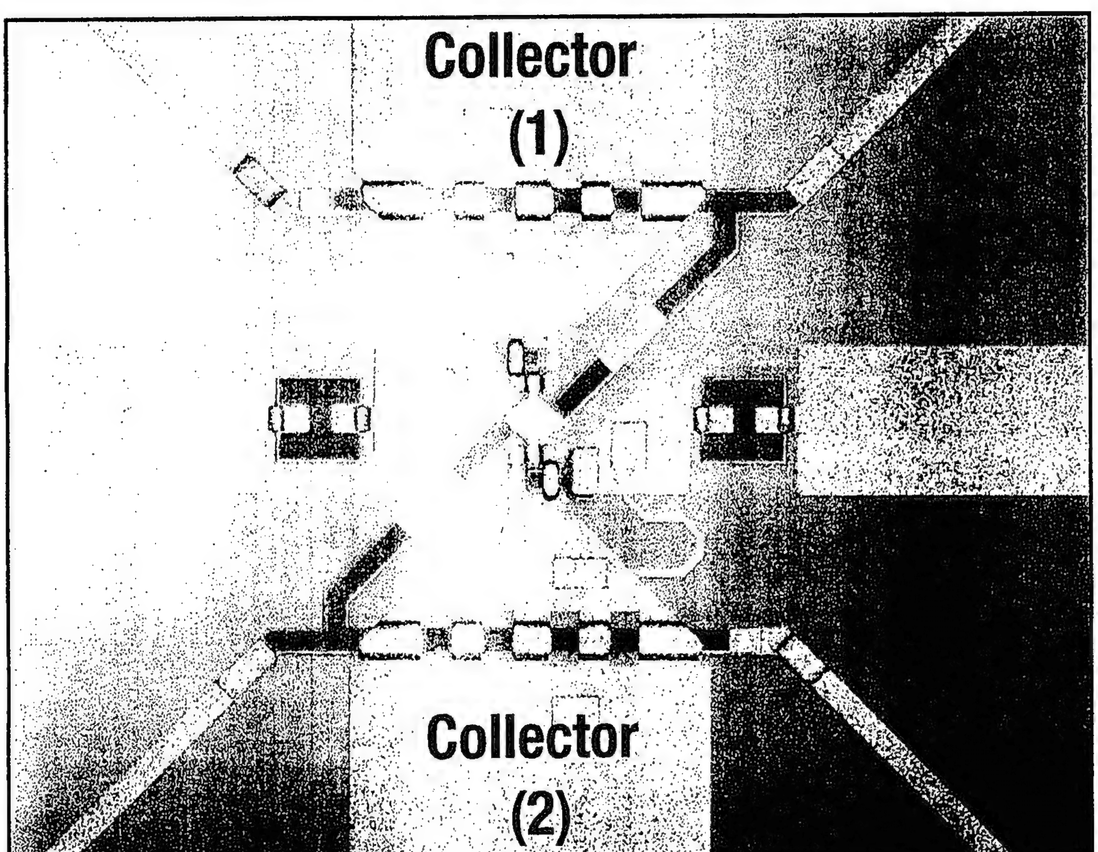

SCP.0882A.060795

Rockwell

Caltech

40-GHz Monolithic HBT Grid Amplifier

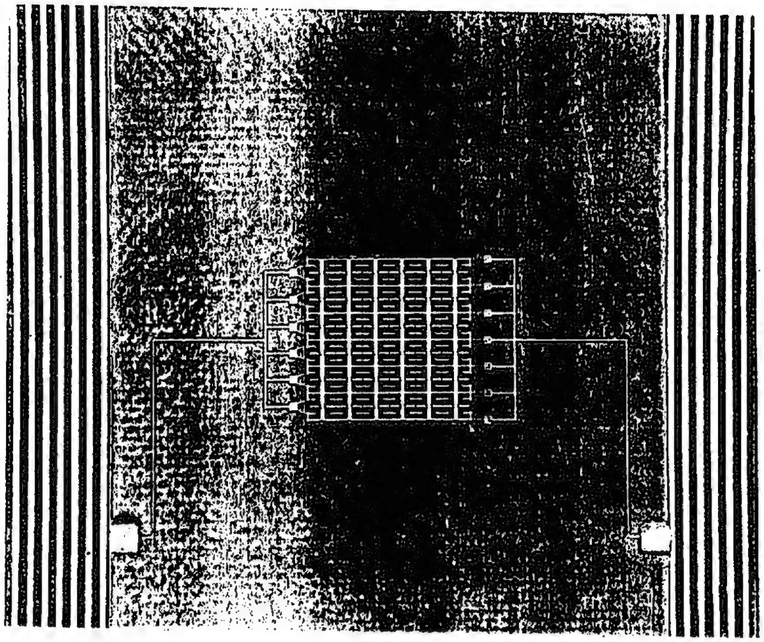

Gmax: 5dB , BW: 1.8 GHz (4.5%)

Caltech

Monolithic HBT Grid Amplifier DC Characteristic Curve

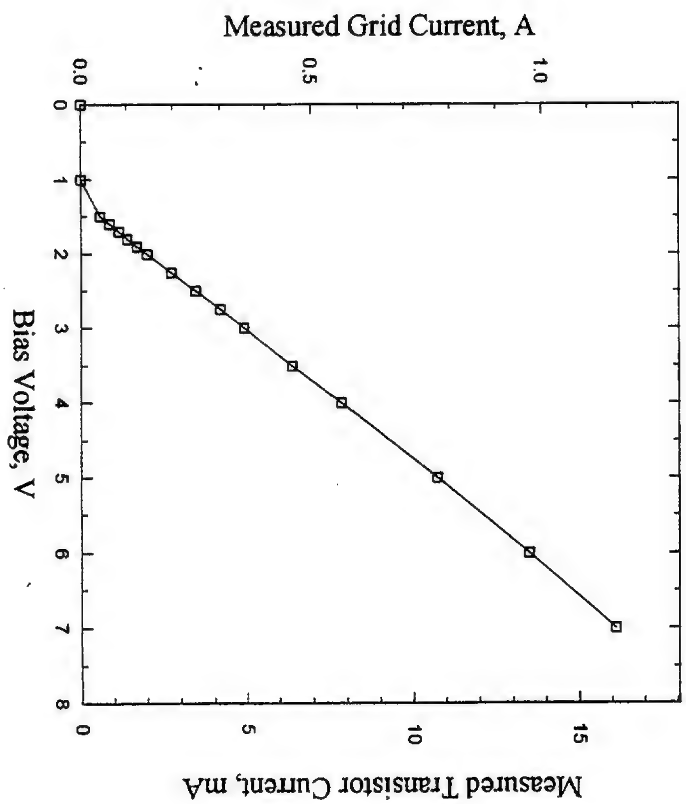

Caltech

Monolithic HBT Grid Amplifier
Gain Response

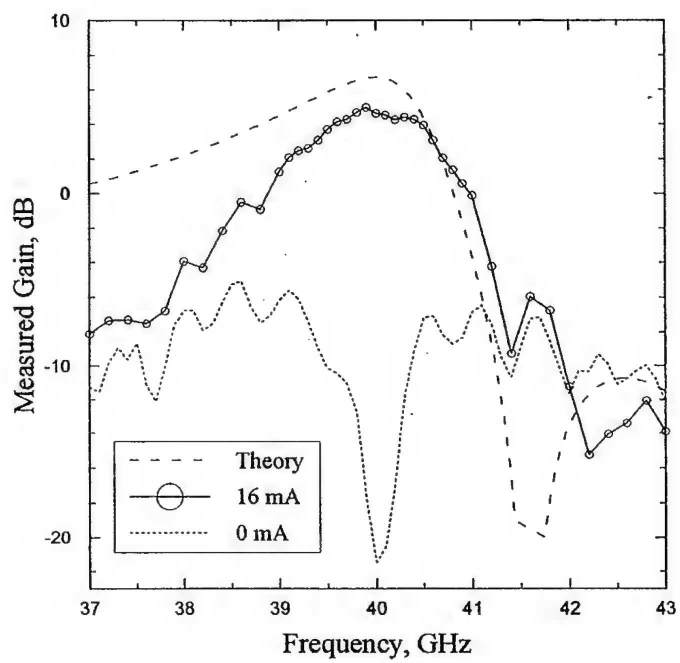

Gmax: 5 dB @ 40 GHz
BW: 1.8 GHz (4.5%)
Pmax: 670 mW @ 2.5 dB gain

Caltech

Monolithic HBT Grid Amplifier
Theoretical Gain Drop vs Surface Resistance

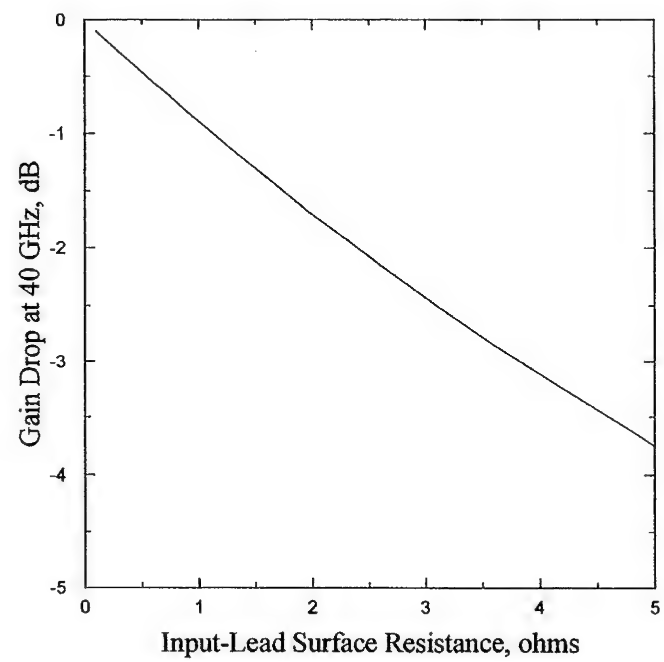

Rs: 0.5 ohms => 0.5 dB drop

Caltech

Monolithic HBT Grid Amplifier
Gain versus Bias Current

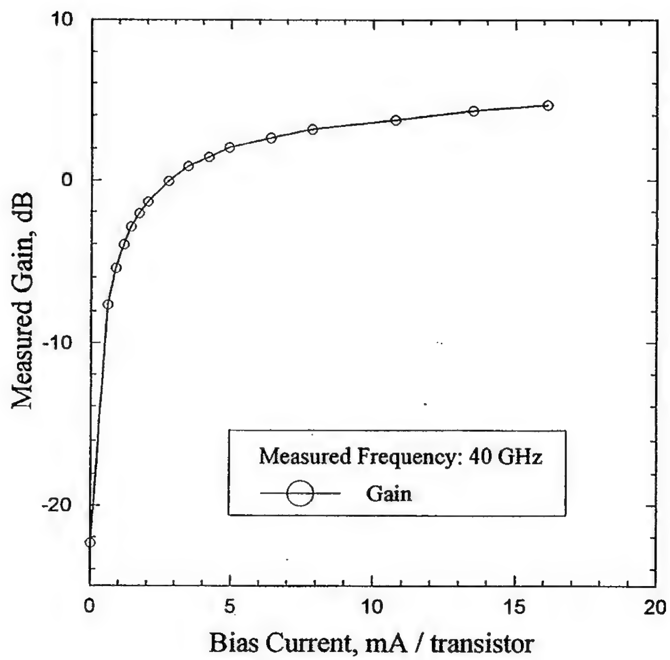

Gmax: 5 dB @ 16mA
On-Off Ratio: 27 dB

Caltech

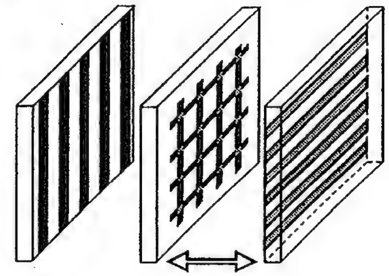

Monolithic HBT Grid Amplifier
Tuning the Input

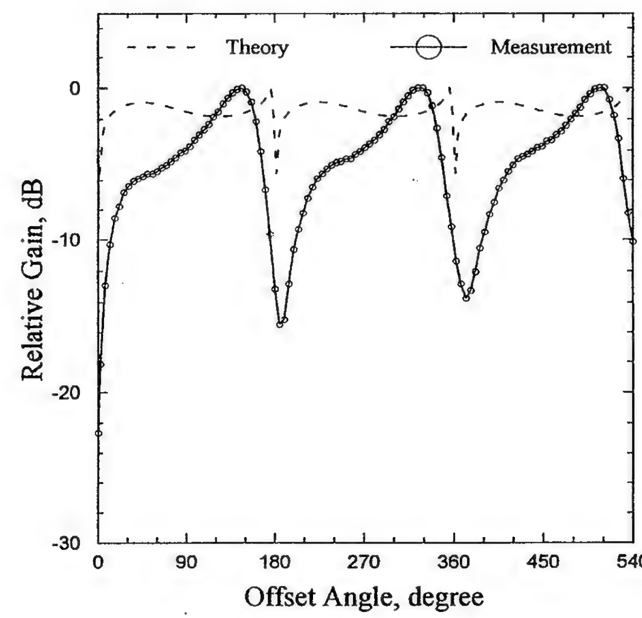

Caltech

Monolithic HBT Grid Amplifier Input Pattern Comparison (Input Tuning)

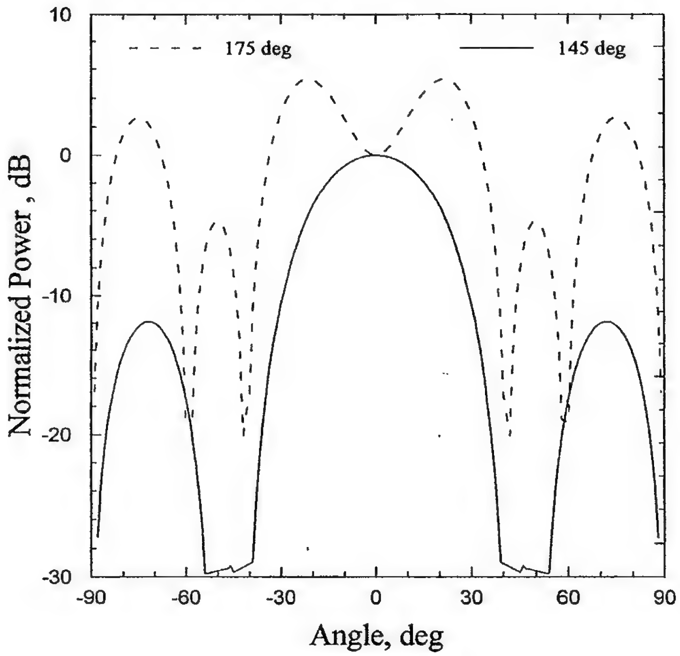

Aperture Efficiency:
145 deg: 0.34 dB
175 deg: -8.66 dB

Caltech

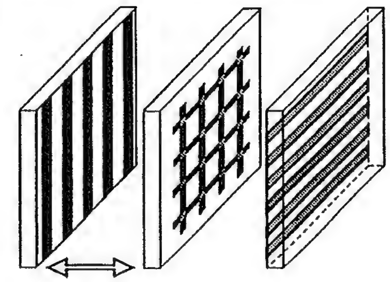

Monolithic HBT Grid Amplifier Tuning the Output

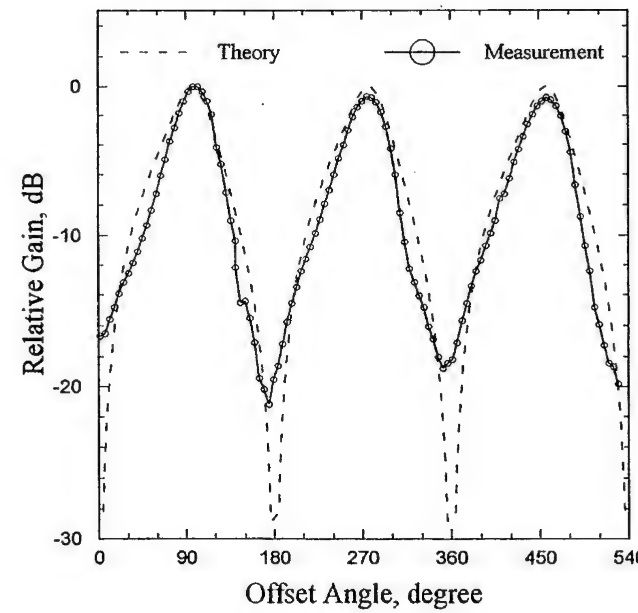

Caltech

Monolithic HBT Grid Amplifier
Output H-Plane Pattern

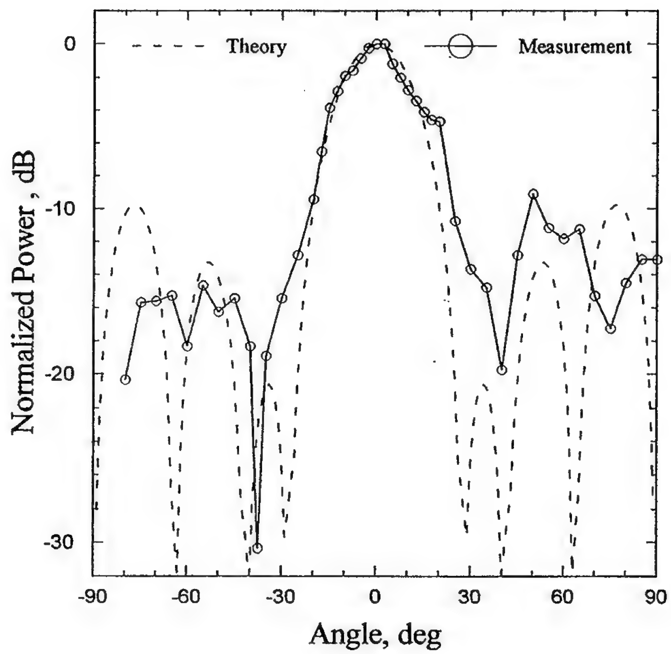

Caltech

Monolithic HBT Grid Amplifier
Input E-Plane Pattern

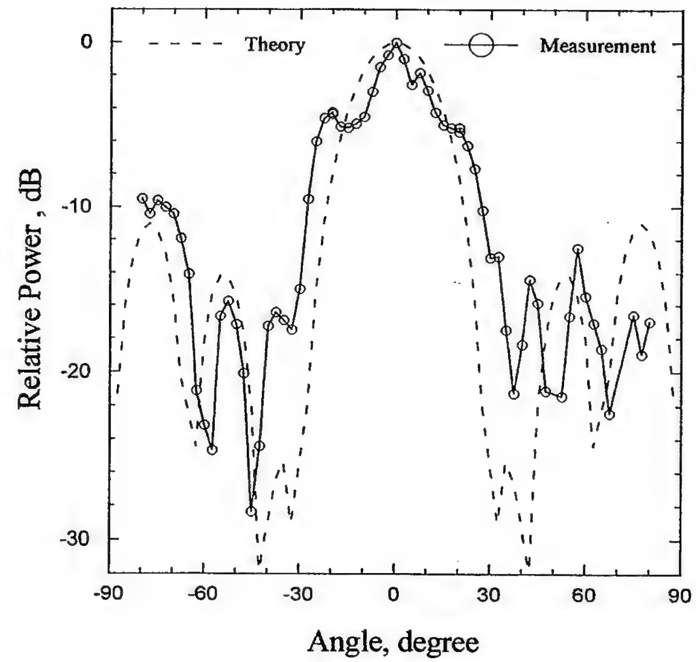

Caltech

GPIB Setup for Calibration Measurements

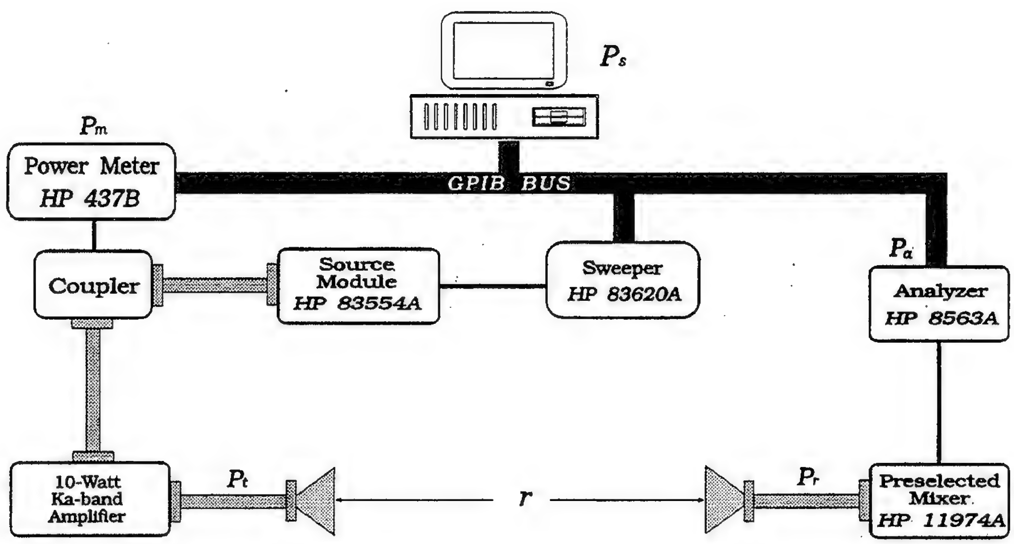

Caltech

GPIB Setup for Power Gain Measurements

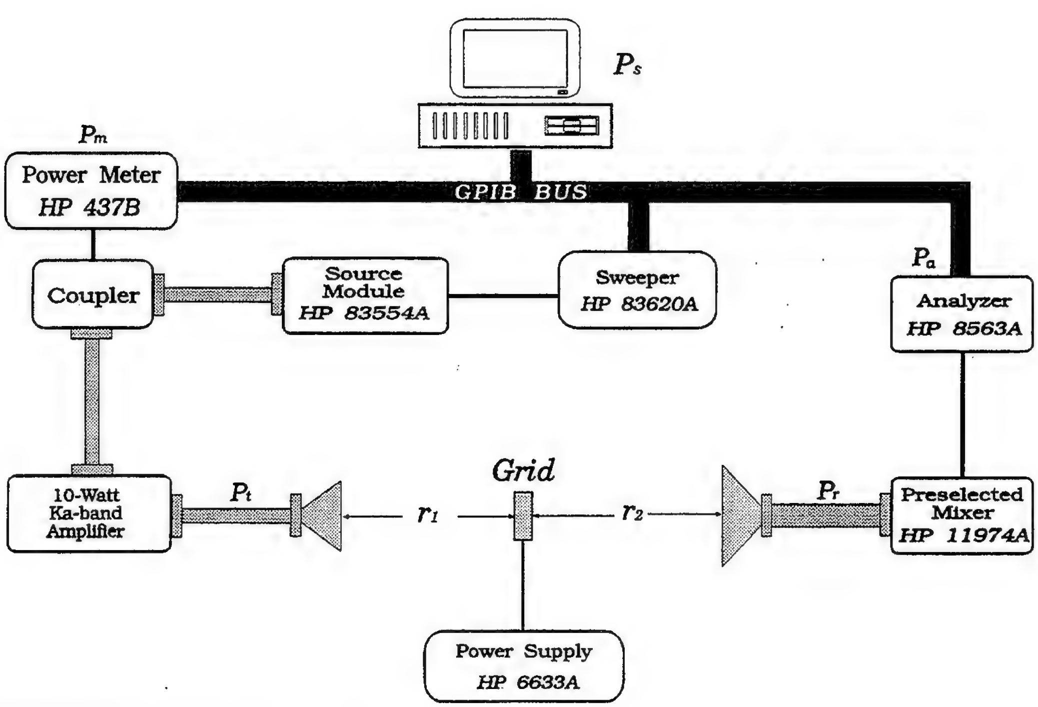

Caltech

Monolithic HBT Grid Amplifier
Output Power vs. Input Power

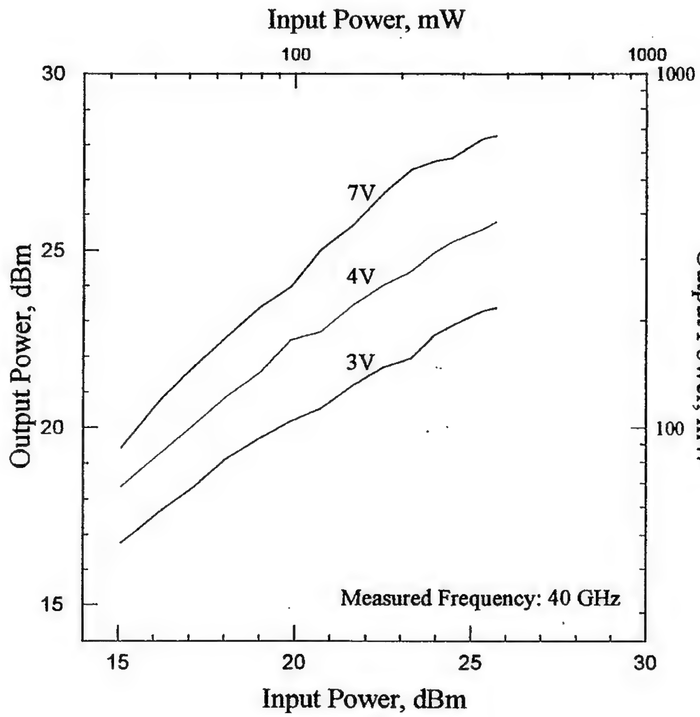

Max. Output Power: 670 mW

Caltech

Monolithic HBT Grid Amplifier
Gain vs Input Power

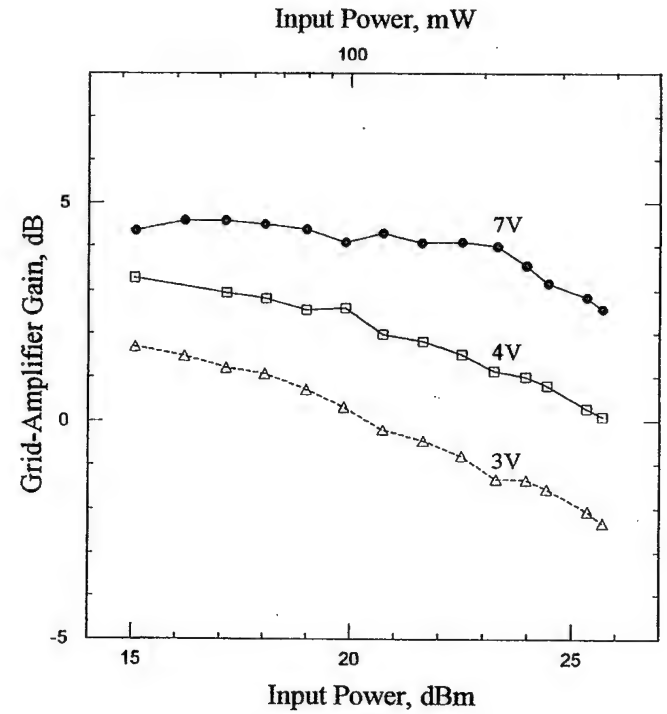

Pmax: 670 mW @ Gain: 2.5 dB

Caltech

Monolithic Grid Amplifier
Power-Added Efficiency vs. Input Power

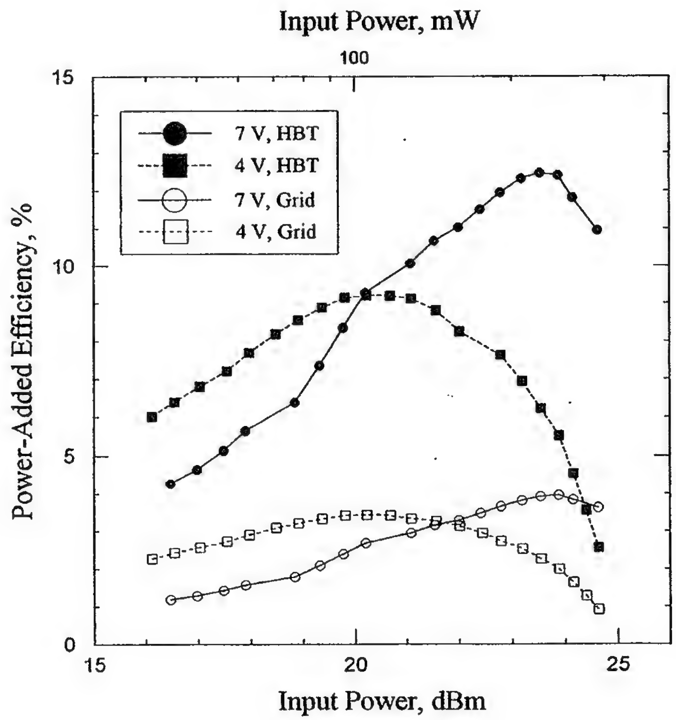

Max. Efficiency:
4% for Grid
12.5% for HBT

Caltech

Monolithic HBT Grid Amplifier
Power-Added Efficiency vs. Output Power

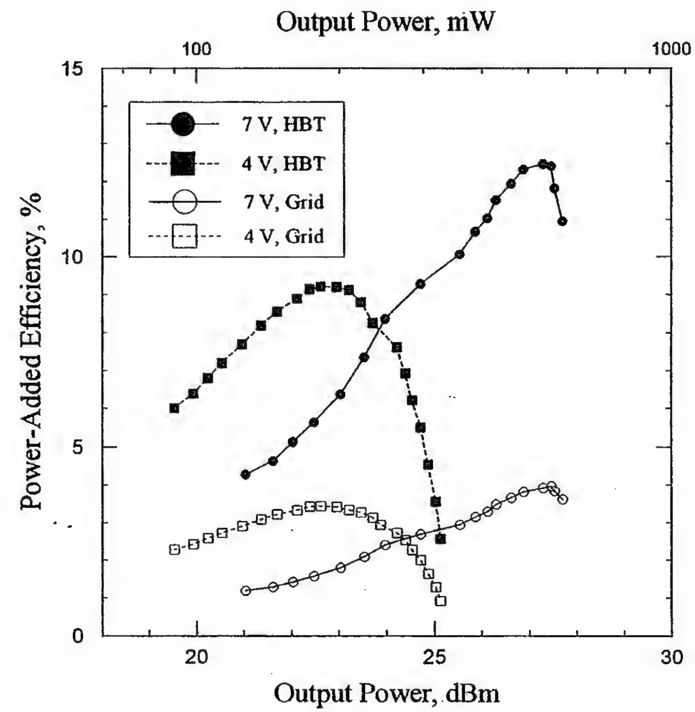

Max. Efficiency:
4% for Grid
12.5% for HBT

Caltech

Monolithic HBT Grid Amplifier
Output Power vs. Bias

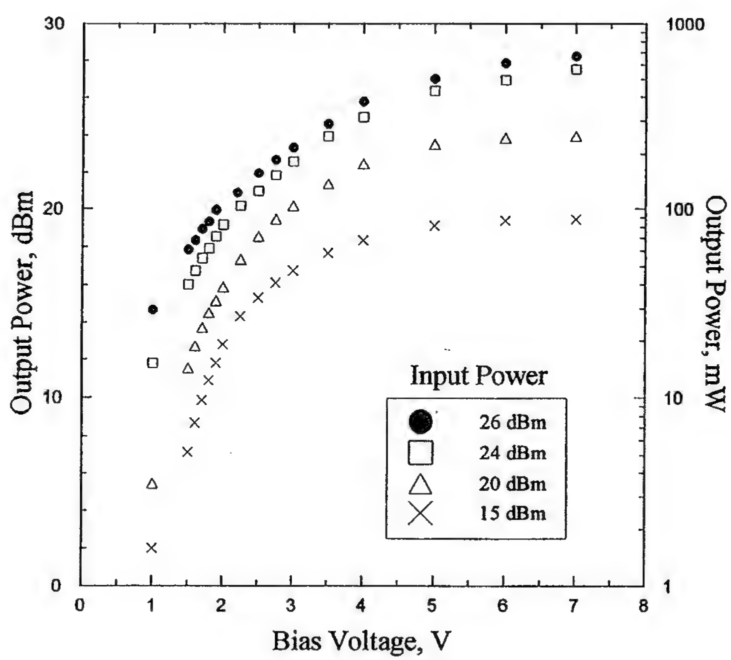

Pmax: 670 mW

Caltech

Monolithic HBT Grid Amplifier
Power Gain vs. Bias

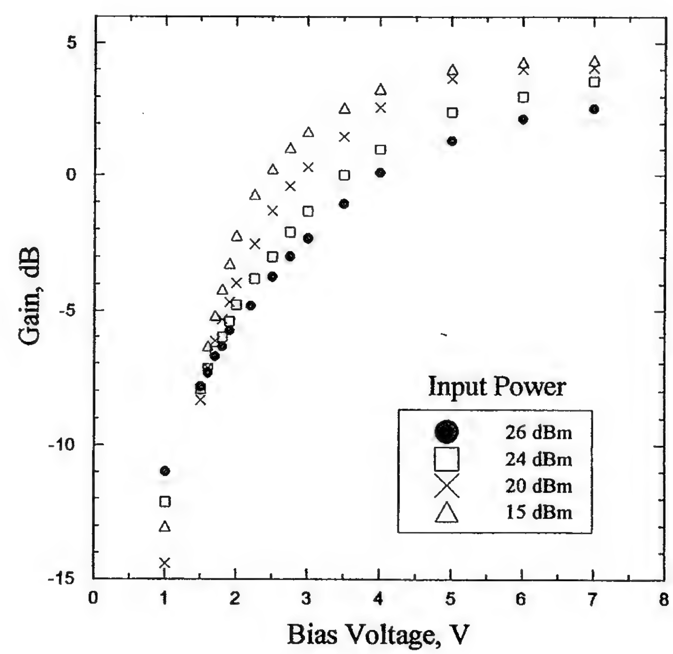

Gain: 2.5 dB @ Pmax: 670 mW

Caltech

45° Polarizer

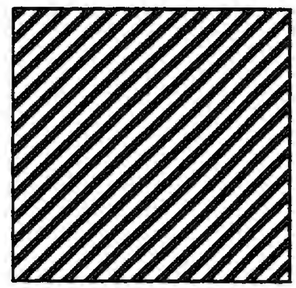

Signal Flow of Decomposition

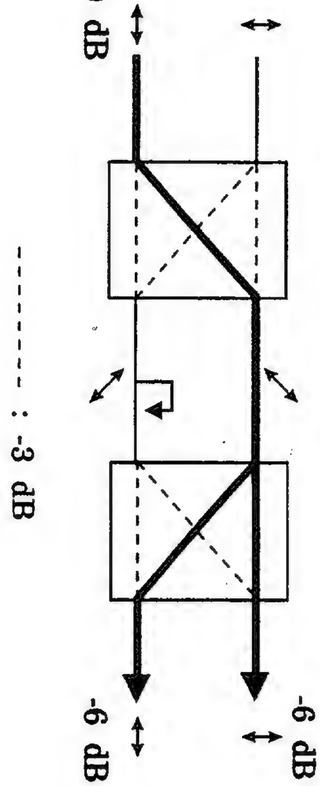

Gains for the 45° polarizer in both polarizations are: -6 dB

Caltech

45°-Polarizers

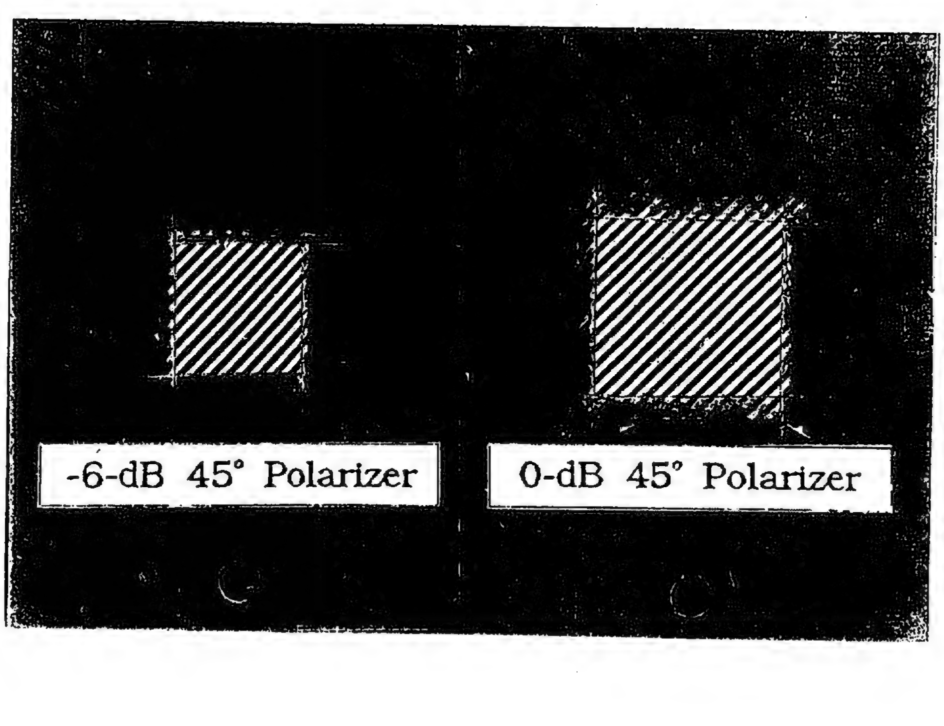

Caltech

Before Power Measurements

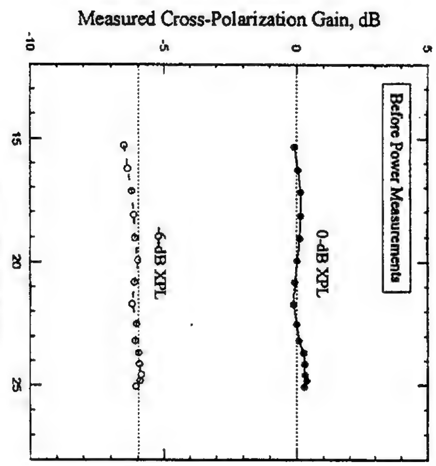

After Power Measurements

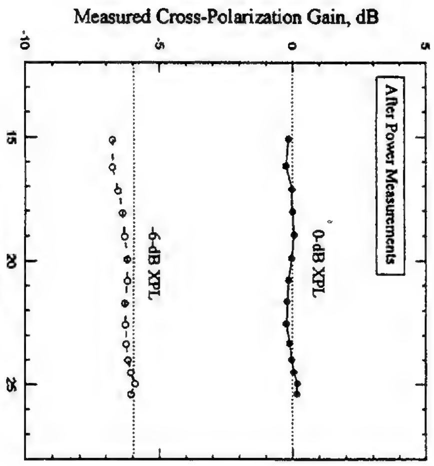

Caltech

Tiled Monolithic HBT Grid Amplifiers

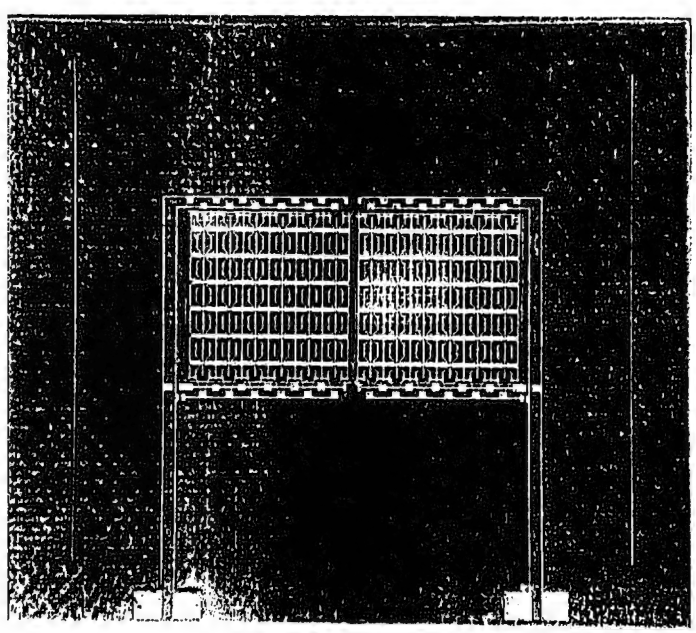

Caltech

Monolithic HBT Grid Amplifier
Tiled Grids, Gain Response

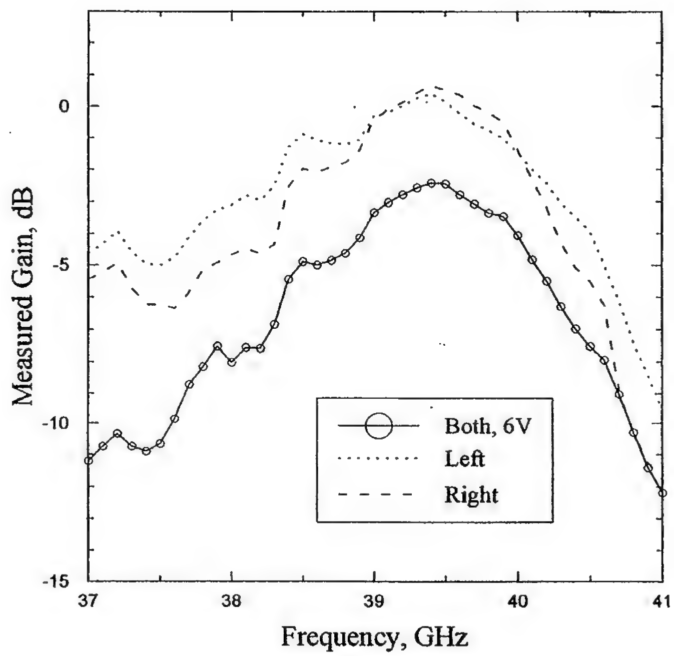

Caltech

Monolithic HBT Grid Amplifier
Input H-Plane Pattern

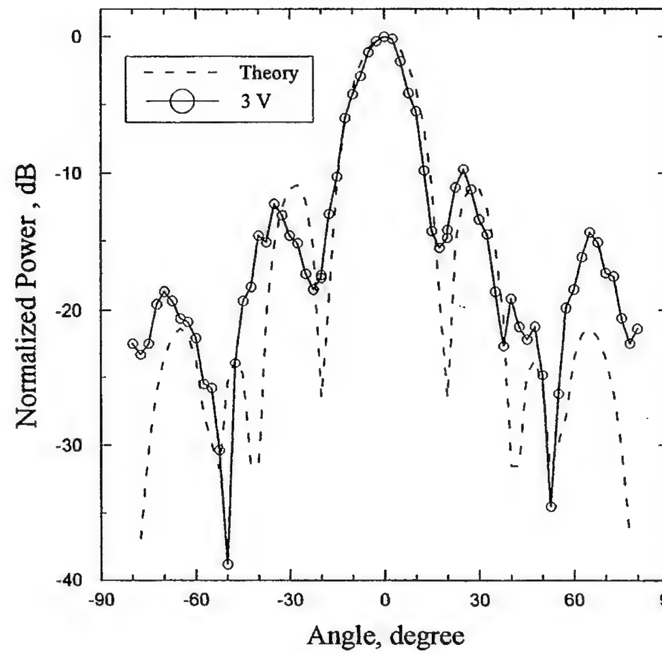

Caltech

Monolithic HBT Grid Amplifier
Input H-Plane Pattern

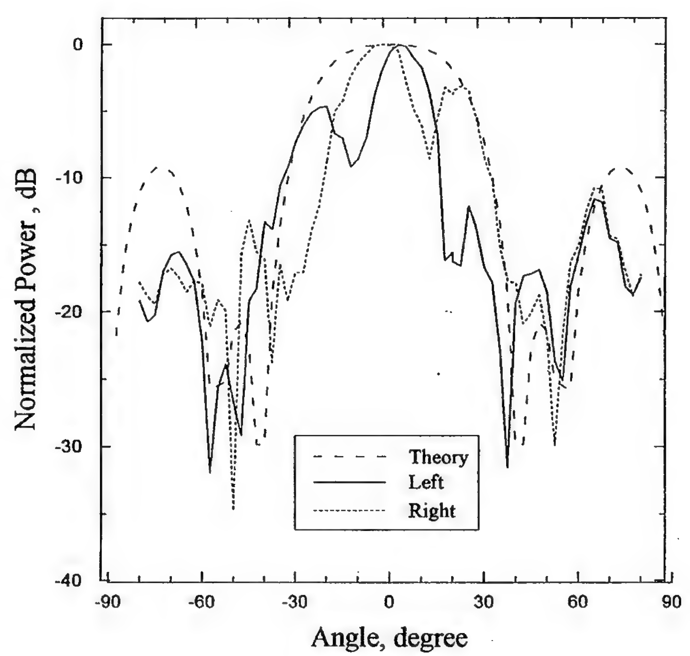

Caltech

Monolithic HBT Grid Amplifier
Output E-Plane Pattern

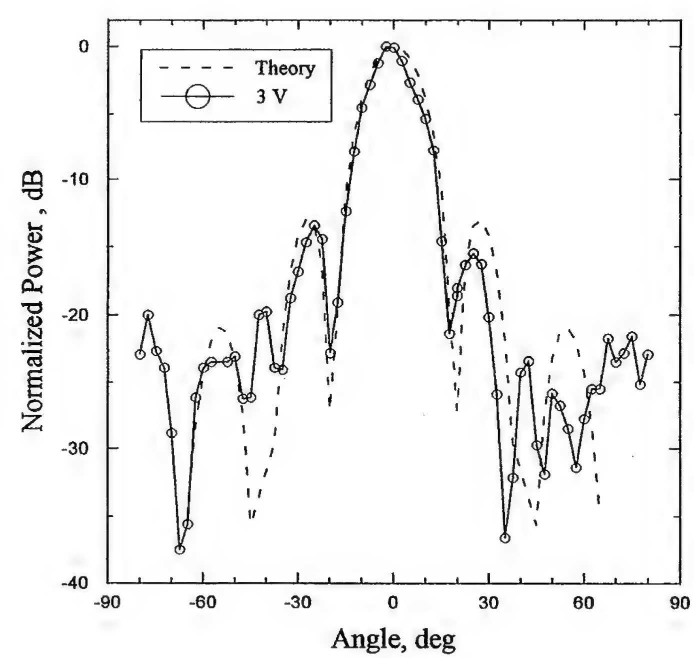

Caltech

Monolithic HBT Grid Amplifier
Output E-Plane Pattern

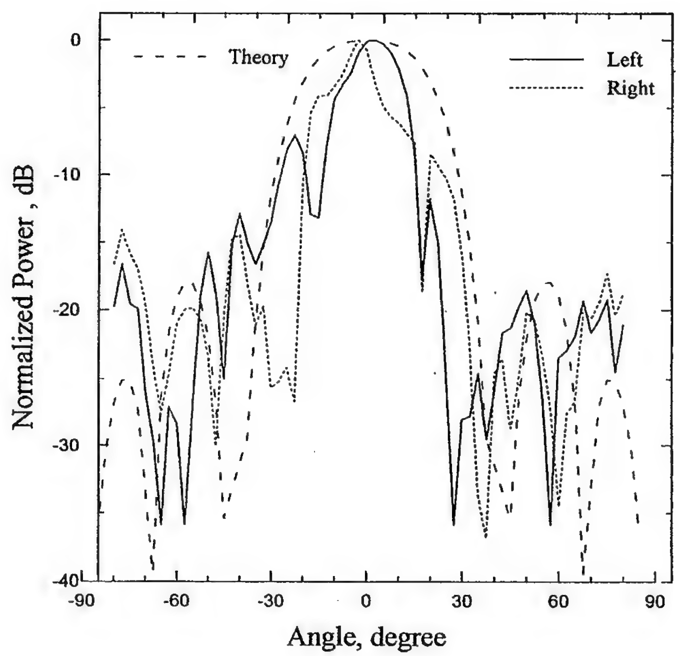

Caltech

Summary of Monolithic HBT Grid Amplifier

Gain Measurement

G_{max}: *5dB @ 40GHz*

3-dB Bandwidth: *1.8GHz ; 4.5%*

□

Power Measurement

Maximum Output Power: *670mW*

Maximum Power-Added Efficiency: *4%*

Caltech

Comparison of 3 HBT Grid Amplifiers

Design Frequency, GHz	10	16	40
Max. Gain, dB	11	6	5
Period, mm	8	4	1.9
Input Lead, mm	0.8	0.4	0.12
Output Lead, mm	0.8	0.5	0.3
Relative Size			

Caltech

3 HBT Grid Amplifiers

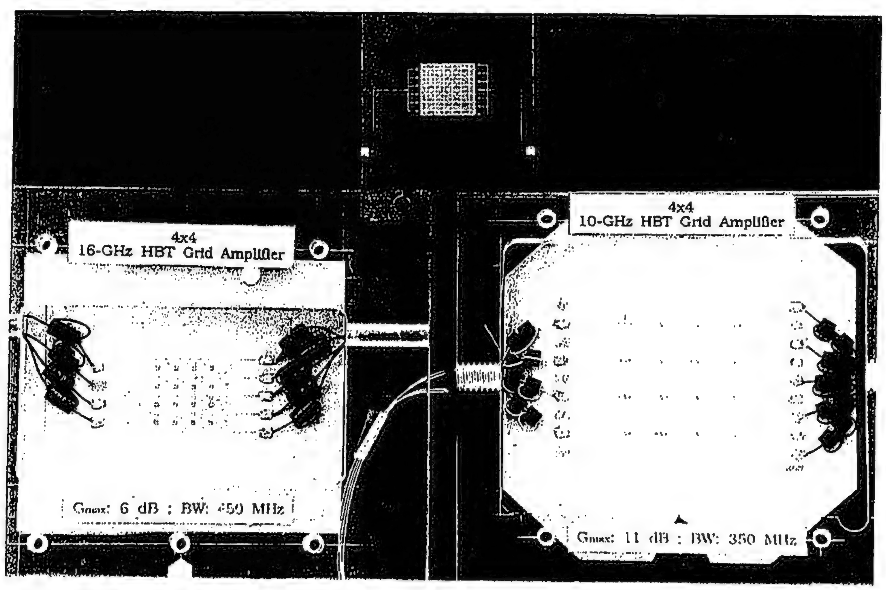

Caltech

Approaches to High-Power Grid Amplifier

6x6 HBT Grid 670 mW

⬇

- ❐ Improving Power Capability
  - Samller unit cell
  - High-Power & High-gain pHEMT
- ❐ Tiling technology
- ❐ Improving thermal performance
  - Reduce resistive loss of bias network
  - Thermal carrier, Diamond

⬇

16x16 pHEMT Grid with 20 W

Caltech

Thermal Analysis for 20-W 16x16 Grid

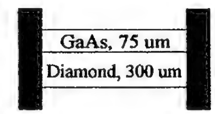

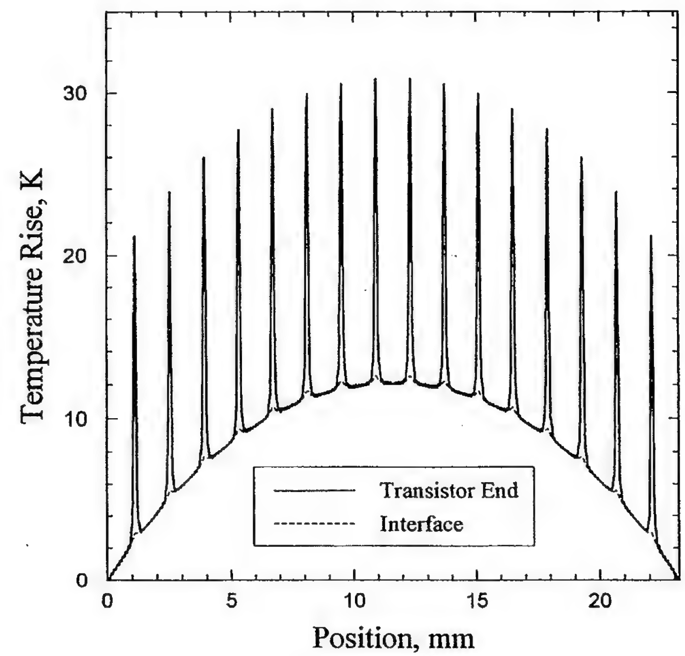

Thermal Analysis
for
20-W 16x16 Grid

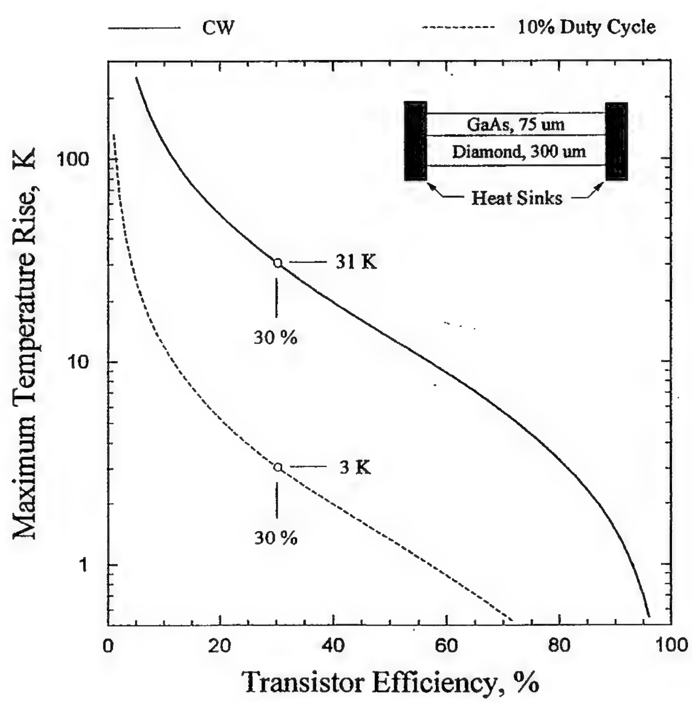

Thermal Analysis
for
20-W 16x16 Grid

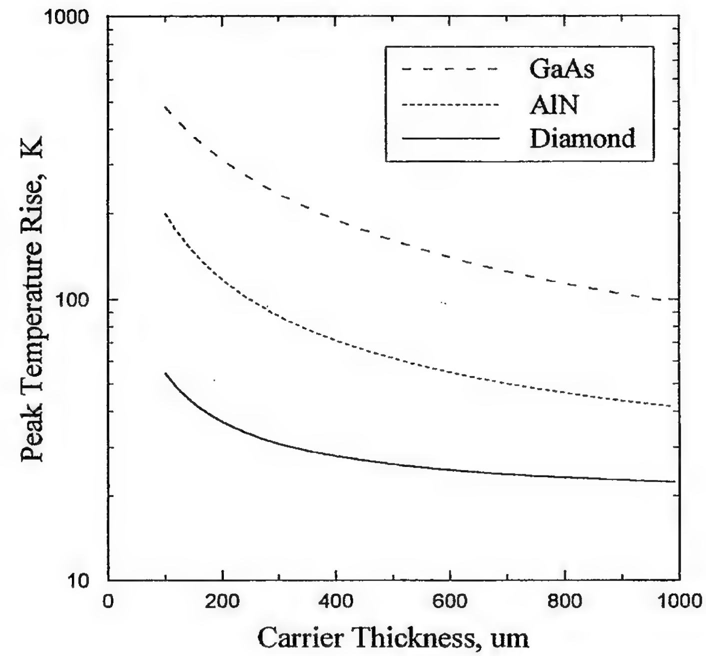

Caltech

A Cascade 20-W Power Amplifier System

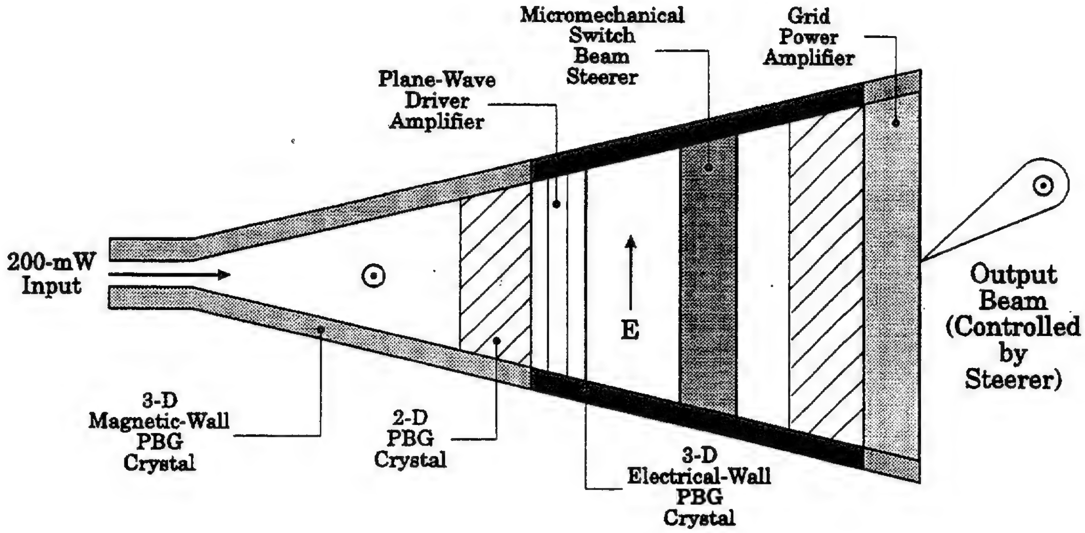

System Characterisation Issues for Integration

by

J W Bowen

Terahertz Technology Group

Department of Cybernetics
The University of Reading
Berks., UK

Parameters of interest:

- **System performance**
- **S-parameters of active and passive devices**
- **Mixer, detector and source characterisation**
- **Antenna patterns**
- **Dielectric constants of materials**

Measuring instruments are either:

- **Waveguide-based, or**
- **Quasi-optical**

Active techniques may be classified as:

- **Narrow-band, using coherent sources**
- **Wide-band, using noise sources**
- **Time domain, using pulsed sources**

The Interface Problem

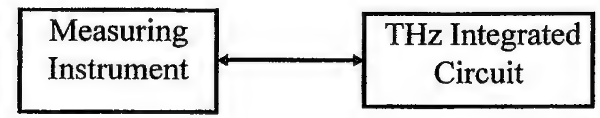

We need some means of coupling power between the integrated circuit to be tested and the measuring instrument.

Problems:

- **The waveguiding in the measurement instrument and the integrated circuit under test will be based on different technolgies and fabrication techniques.**

- **It is often impossible to monolithically fabricate a flange on the integrated circuit that allows direct connection to the measuring instrument.**

Solutions:

- **Butting waveguides end-to-end: Needs accurately machined end surfaces and requires very accurate alignment.**
- **Dielectric coupling: Works well for full-height rectangular waveguide at the lower frequencies. Does not work for reduced height waveguides and there may be mechanical and loss problems as the frequency is increased.**
- **Quasi-optical coupling via a monolithically integrated antenna: Appears to be the best solution --- avoids physical contact to delicate integrated structures.**

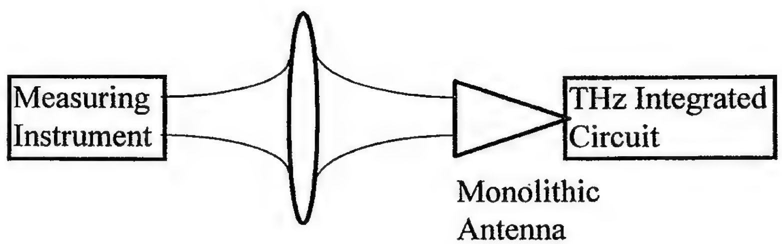

Beam-mode Decomposition

An arbitrary field in the $z = z_s$ plane can be written as a superposition of orthonormal basis functions:

$$u(x,y;z_s) = \sum_{m,n} C_{mn} u_{mn}(x,y;z_s)$$

It is advantageous to choose Hermite-Gaussian or Laguerre-Gaussian functions as the basis functions.

The Hermite-Gaussian function of order $m,\ n$ is

$$\begin{aligned} u_{mn}(x,y,z) = {} & \left(2^{m+n-1}\pi m!n!\right)^{-1/2}\frac{1}{w} \\ & \cdot H_m\left(\sqrt{2}\frac{x}{w}\right)\cdot H_n\left(\sqrt{2}\frac{y}{w}\right) \\ & \cdot \exp-\frac{x^2+y^2}{w^2}\cdot\exp-ik\frac{x^2+y^2}{2R} \\ & \cdot \exp i(m+n+1)\Theta \end{aligned}$$

The arbitrary real constants w, R and Θ can be freely chosen to give, for example, a good fit to the field with the minimum number of Hermite-Gaussian functions.

It can be shown that the field in any constant - z cross-section of an arbitrary paraxial beam, arising from the field in the source-plane $z = z_s$ can similarly be described by a superposition of Hermite-Gaussian functions and, further, that the propagating field can be considered to be a superposition of beam-modes.

$$u(x,y,z) = \sum_{m,n} C_{mn} u_{mn}(x,y,z)$$

The beam-modes $u_{mn}(x,y,z)$ take the form of the Hermite-Gaussian function above but *w*, *R* and Θ vary with *z* (the propagation direction) as:

$$w^2 = w_0^2 + \{2(z-z_0)/kw_0\}^2$$

$$R = (z-z_0) + \{kw_0^2/2\}^2 \Big/ (z-z_0)$$

$$\Theta = \tan^{-1}\left\{\frac{kw^2}{2R}\right\} + \Theta_0$$

$$= \sin^{-1}\left(1 + \left\{\frac{kw^2}{2R}\right\}^{-2}\right)^{-1/2} + \Theta_0$$

***w* describes the width of the beam, which takes a minimum value w_0 at the beam-waist located at $z = z_0$.**

***R* describes the radius of curvature of the spherical wave-front.**

Θ governs the phase-slippage between successive modes relative to an on-axis plane-wave.

It is a property of complete orthonormal sets of functions that the coefficients C_{mn} in the superposition that describes the arbitrary field $u_A(x,y;z_s)$ in the plane $z = z_s$ can be determined from the integral

$$C_{mn} = \iint_{z_s} u_{mn}^*(x,y;z_s) \cdot u_A(x,y;z_s)\,dx\,dy$$

Thus, for an antenna with a theoretically calculable field in a near-field plane, usually an aperture, this field can be decomposed into Hermite-Gaussian functions by evaluation of the above integral.

The launched beam will be a superposition of beam-modes described by the same C_{mn}.

The values of *w*, *R* and Θ can be chosen for maximum simplicity and computational economy.

For example, in the case of a corrugated feed-horn (Wylde, Proc. IEE, vol. 131, pt.H, no.4, pp. 258-262, 1984) the field at the horn aperture has a spherical wave-front with a radius of curvature equal to the length of the horn. Thus, simplicity dictates that we should set *R* equal to its length and Θ equal to zero.

By iteration, Wylde determined the value of *w* which maximised the coefficient of the fundamental of the set of functions and thus the power carried by the fundamental beam-mode (98% of the total, with $w = 0.6435$ x aperture radius).

If R and w at any point in a beam are known it is possible to determine the location and size of the beam-waist, which is the same for all modes in a superposition.

The far-field of an antenna is related to its near-field by Fourier transformation.

The Fourier transform of a Hermite-Gaussian function is, itself a Hermite-Gaussian function.

Therefore, if the amplitude and phase far-field patterns of an antenna are known, it is possible to carry out a beam-mode decomposition in a similar manner to in the near-field.

Beam-mode Coupling

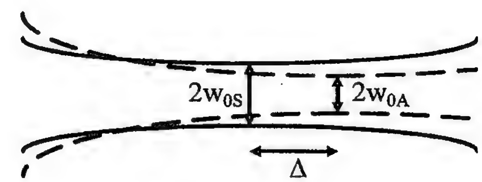

Relative amplitude and phase of the signal coupled from beam S to beam A is given by the coupling or overlap integral between the fields of the two beams, $u_S(x,y,z)$ and $u_A(x,y,z)$, over any constant z plane through the beams, c.

$$\langle u_A | u_S \rangle = \iint_c u_A^*(x,y,z) \cdot u_S(x,y,z)\, dx\, dy$$

The result is independent of the plane of integration.

If u_A and u_S represent two co-axial fundamental beam-modes the amplitude coupling integral becomes

$$\left|\langle u_A | u_S \rangle\right| = \left(k\overline{\overline{w_0}}\right)^2 \left\{ \left(k^2 \overline{w_0^2}\right)^2 + (k\Delta)^2 \right\}^{-1/2}$$

$\overline{\overline{w_0}}$ **is the geometrical mean of w_{0A} and w_{0S}**

$\overline{w_0^2}$ **is the mean of w_{0A}^2 and w_{0B}^2**

Similar expressions exist for laterally and rotationally displaced fundamental beam-modes.

More general expressions which quantify the coupling between beam-modes of different orders are given in H. Kogelnik, Proc. of the Symposium on Quasi-optics, New York, 1964, Microwave Research Institute Symposia Series, vol.14, pp. 333-349, Polytechnic Press, 1964.

The ideal situation would be to have perfect coupling between the test beam and that launched by the antenna on the integrated circuit under test.

Even so, it is likely that there will be some reflection at the antenna and calibration procedures will have to be gone through to de-embed device parameters.

System Characterisation Issues for Integration

Astigmatism Correction

Possibilities:

1. A train of two cylindrical lenses acting orthogonally on the E and H planes.

2. A single non-axially symmetric lens.

3. An off-axis spherical mirror.

1 and 3 give an elliptical rather than circular output beam-waist for all but a special-case ratio of astigmatic difference and output beam-waist size.

2 is the most difficult to manufacture.

3 gives lower throughput losses and freedom from interference effects.

Department of Cybernetics
The University of Reading

Astigmatism correction using a spherical mirror

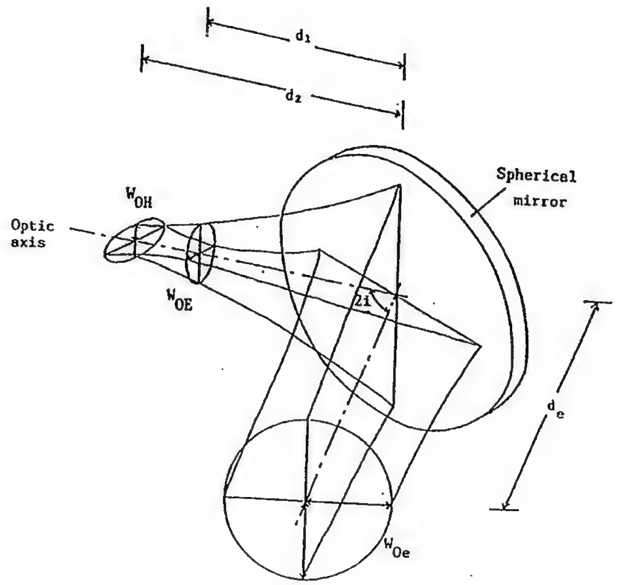

Elapsed phase lens design for astigmatism correction

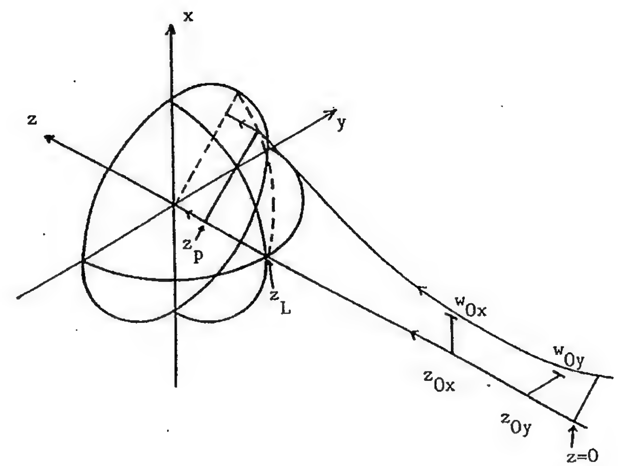

Zoom Optics

Single lens

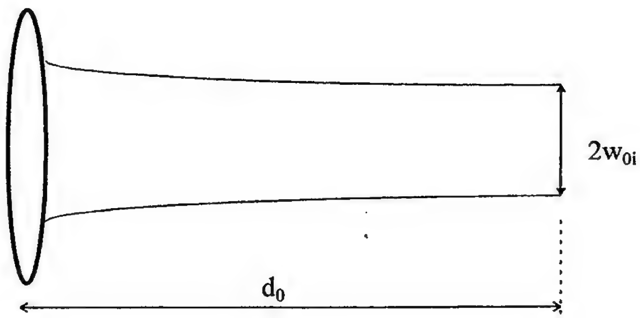

With added zoom system

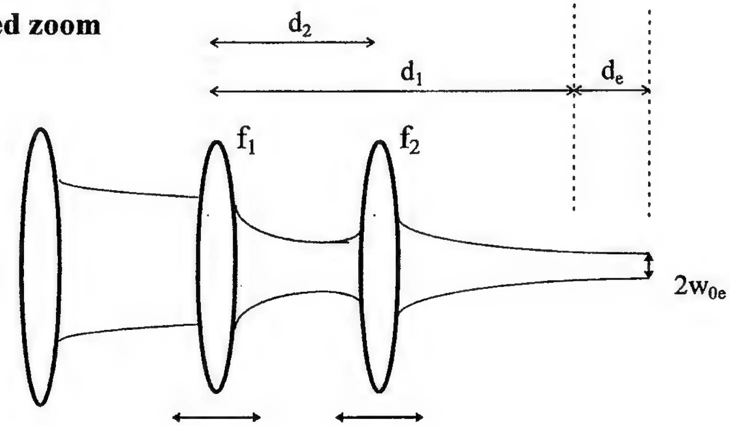

Contours of d_e (mm)

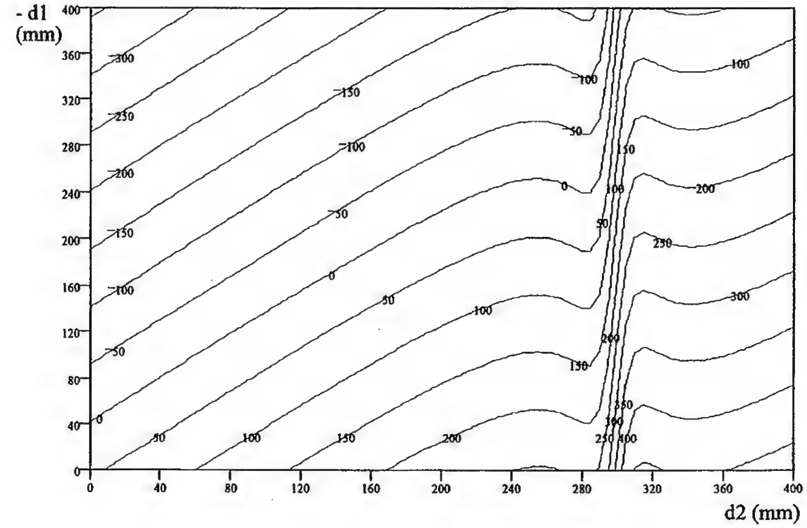

Contours of w_{0e} (mm)

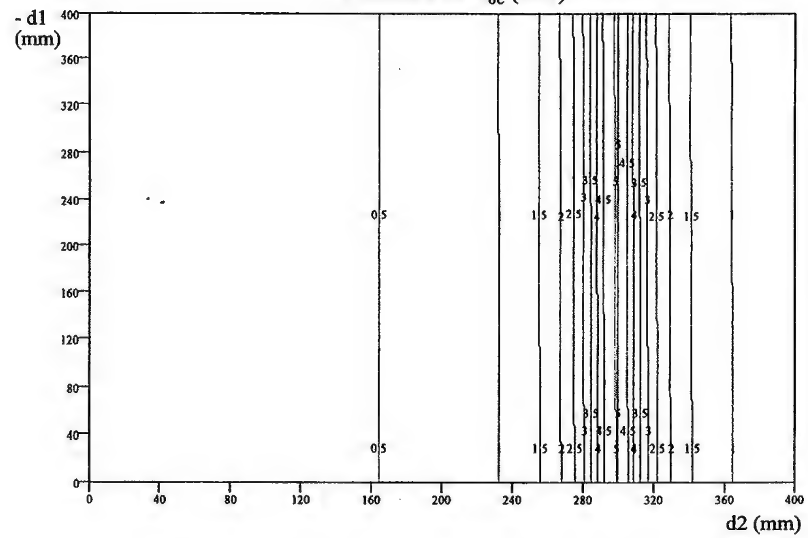

$f_1 = 250$ mm, $f_2 = 50$ mm, $w_{0i} = 25.2$ mm, frequency = 700 GHz

TINTIN Quasi-optical Spectrometer/Transmissometer/Reflectometer

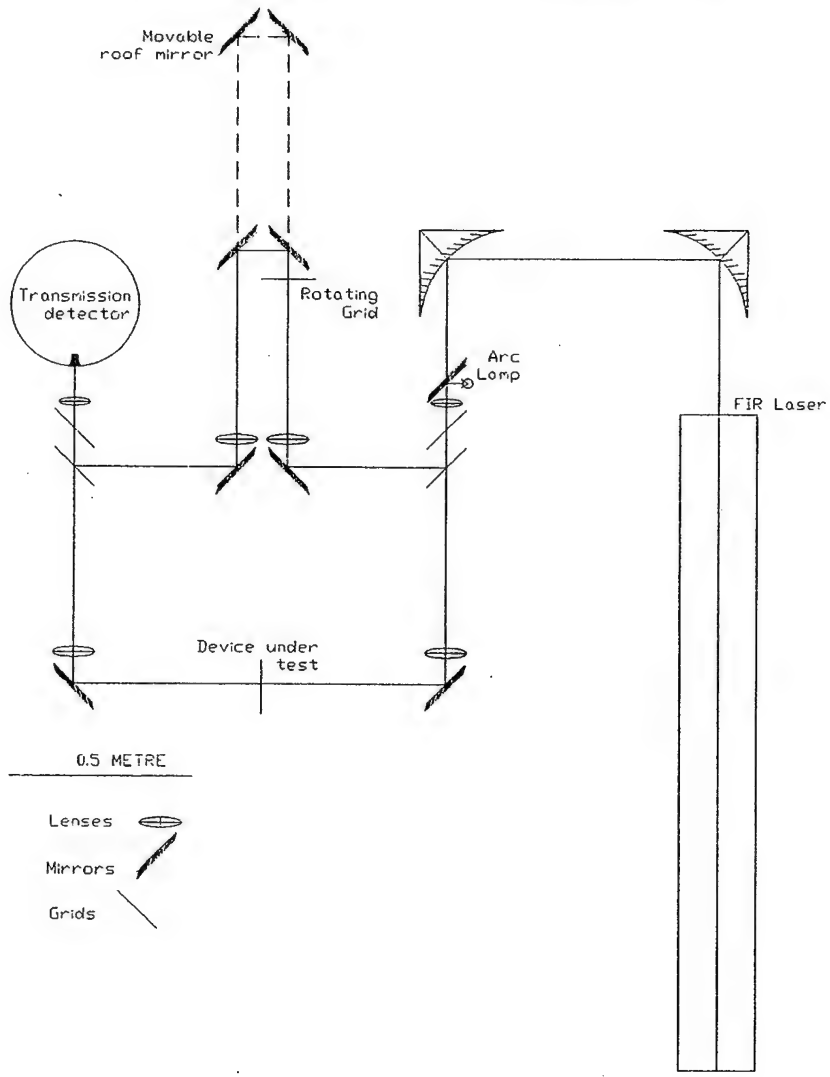

Department of Cybernetics
The University of Reading

TINTIN Quasi-optical Spectrometer/Reflectometer

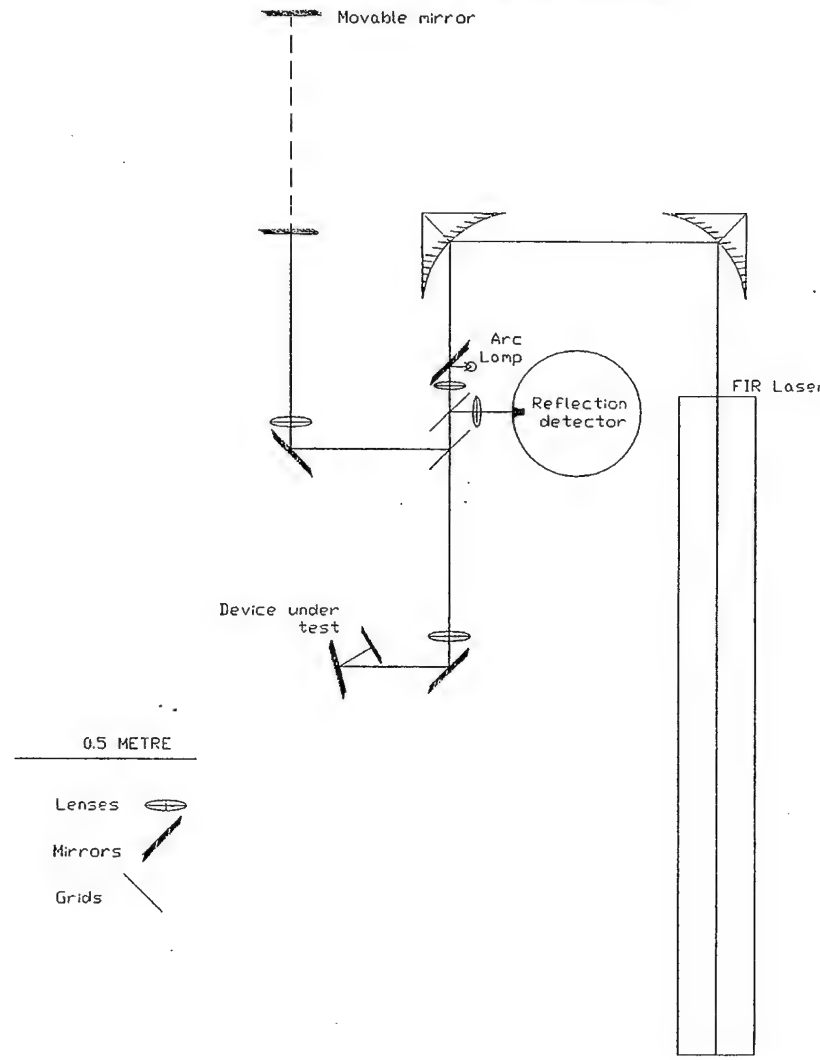

Department of Cybernetics
The University of Reading

SATURDAY JULY 6

Integrated Antennas

by

G M Rebeiz

(No material available.)

TeraHertz Astronomy from Space

Thijs de Graauw
Space Research Organisation of the Netherlands(SRON)
Groningen, The Netherlands.
e-mail: thijsdg@sron.rug.nl

Introduction:

The FarInfrared/SubMm/TeraHz range is the last part of the electromagnetic spectrum to be explored in astronomy. Sofar only parts of this range have been studied, either with a small(60cm) telescope from space or with a larger ground-based telescope(2m-15m) in only narrow atmospheric windows, or not at all. Till today there have been two all-sky survey/explorer space missions: The InfraRed Astronomical Satellite(IRAS) and the Cosmic Background Explorer(COBE). Both made full maps of the entire sky. IRAS covered the IR range from 12- 100 microns, COBE extended further, down to the mm range. IRAS with an angular resolution of a few arcminutes, COBE with a resolution of several degrees. The third (F)IR mision is the Infrared Space Observatory(ISO). It covers the 2.5 to 240 micron region with photometers, spectrometers and a near/mid IR camera. Its spatial resolution is given by the diffraction limit of the 60 cm telescope. Since November 1996 ISO is in orbit and produces detailed maps and spectra of selected regions in the IR sky previously mapped by IRAS. It is the first IR space observatory that can make full spectra over the entire wavelength range and thus explores a new dimension of the IR universe.

THz Astronomy from Space

There are now two new major ESA missions planned for the FIR-MM region. These are the Cosmic Background Radiation Anisotropy Satellite(COBRAS) in combination with the Satellite for Measurement of Background Anisotropies(SAMBA), the so-called COBRAS/SAMBA mission, and the FarInfrared and Submm Space Telescope(FIRST).
COBRAS/SAMBA with a 1.5m diameter telescope, will make a full sky survey in about 9 bands between 30 and 900 GHz, with an angular resolution of about 10 arcminutes and a very high precision which is needed for the assessment of the anisotropy of the cosmic background. In order to do this in an accurate way the foreground components of the Galaxy and the contributions of the nearby and distant galaxies have to be subtracted. This, as a sideproduct, will produce detailed maps of the foreground components and therefore extremely interesting data will become available to a wide astronomical community.
FIRST with a 3m diameter telescope excels in the following three areas.
A) It will make very sensitive and very high resolution wideband heterodyne spectroscopy in the 490-1200 GHz of submm lines of important light molecules that have not been detected in interstellar space. The spectral survey will result in a high quality analysis of the chemical composition, physical conditions and dynamics of interstellar, protostellar and

circumstellar clouds, planetary atmospheres and cometary comae.
B) The most important FIR cooling lines can be studied in heavily obscured star-formation regions in our Galaxy, nearby galaxies and in galaxies in the early universe.
C) With a 10-20 arcsec resolution spectrophotometric imaging will be possible at very high sensitivity in the 750-1500 GHz range. FIRST, thus, will be capable to detect very faint condensations in molecular clouds, signatures of dust cocoons of protostars.

The two missions, COBRAS/SAMBA and FIRST are very complementary in respect to their science objectives.

THz Technology for Space

The technology used in these two missions have a large commonality. First of all the direct detection instruments are probably going to use the same bolometers. The radioreceivers however will have very different technology. COBRAS' receivers are based on HEMT amplifiers as their upper frequency is only 125 GHz. FIRST's heterodyne packge will cover 490-1200 GHz. The requirements on the FIRST heterodyne instrument are therefore more challenging. Because of the sensitivity performance of SIS technology FIRST will use these 4K cooled receivers. The back-end spectrometer section is more demanding than the ones used at ground-based radio observatories. An overview of the preferred characteristics of a spectrometer for FIRST is given in the table.

Presentation

In the presentation an overview will be given of the main scientific goals in present astronomy. From this the requirements on the instrumentation will be derived. The development status of the instrumentation and its components will be discussed. An overview of the present sensitivities of Submm mixers will be given. See figures. The most critical items in the development of space qualified receivers (Local Oscillators) will be discussed. Also results of experiments to establish the space environment compatibility of the key technologies will be reported.

Table 1: Specification of the IF/Spectrometer for a planar receiver for Astronomy.

Specification	Galactic Sources				Extra Galactic Sources			
	Astro km/sec	400 GHz	1500 GHz	2000 GHz	Astro km/sec	400 GHz	1500 GHz	2000 GHz
Instantaneous bandwidth	100	130 MHz	500 MHz	650 MHz	1000	1.3 GHz	5 GHz	6.5 GHz
Spectral Resolution	.1	130 KHz	500 KHz	650 KHz	10	13 MHz	50 MHz	65 MHz
Number of Channels		1000	1000	1000		100	100	100

Sensitivity of SIS Heterodyne Receivers above 300 GHz.

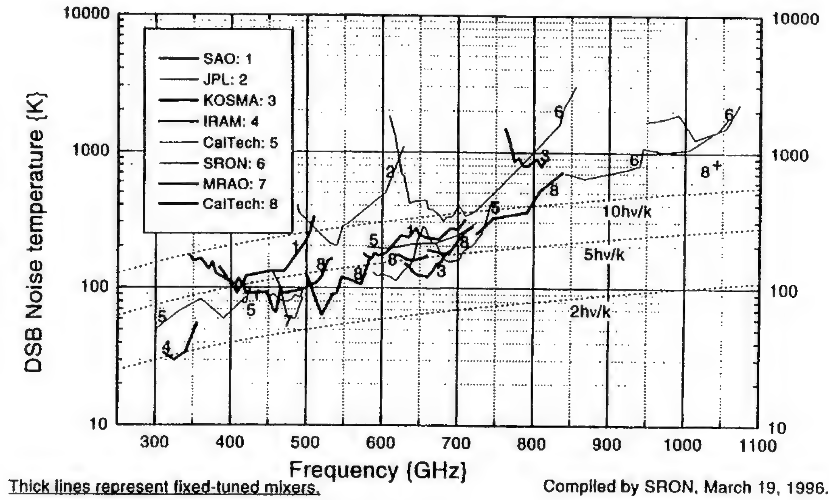

Thick lines represent fixed-tuned mixers. Compiled by SRON, March 19, 1996.

Sensitivity of SIS, HEB and Schottky Heterodyne Receivers.

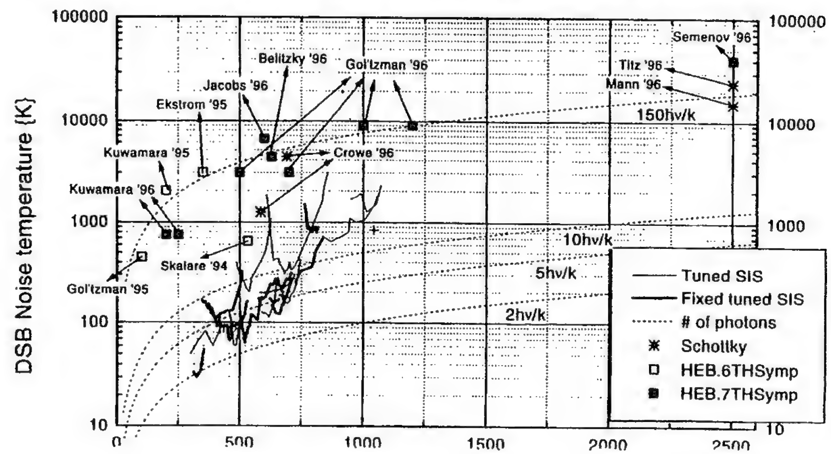

Terahertz Measurements from Satellites

by

B Carli

(No material available.)

Abstract of Paper for

NATO ASI- " **New Directions in Terahertz Technology**"

(July 1-11, 1996, Chateau de Bonas, Toulouse)

SPACECRAFT APPLICATIONS OF TERAHERTZ TECHNOLOGY

W.J.Hall*

* Matra Marconi Space, Bristol, UK.

The Terahertz bands offer exciting opportunities for the remote sensing from space of atmospheric consistuents with great importance for the planning of industrial and commercial activities. To exploit these opportunities requires the development of new sensor devices combining robustness with decreased dimensions and many developments of integrated receiver and antenna components are now in progress.

The paper will survey the range of studies and technology developments aimed at remote sensing applications in the milimetre, submillimtere and terahertz frequency bands. The emphasis will be on the critical technology needs and on meeting both the performance and spacecraft interface requirements.

The range of technologies described will cover components from antenna to intermediate frequency outputs with some comments on the data analysis equipments in the instrument back end. The heritage in millimetric instruments will be treated to explain the common and novel features of Terahertz applications.

Particular emphasis will be given to the newer integrated technologies and the developments now in progress and foreseen will be summarised in the context of their application to spacecraft instruments being planned for applications such as the sensing of atmospheric processes relevant to the ozone cycle.

Outlines of Terahertz instrument programmes and design studies will be included.

AUTHOR FOR CORRESPONDENCE:

W.J.Hall,

Head of R.F. Instruments & Technology

Directorate of Science & Radar Observation

FPC 320

PO Box 16, Filton, Bristol, BS12 7Y, England

Fax: + 44 117 936 6819

Tel : +44 117 936 3561

P.2/4

21 MAR '96 09:37 MMS SPACE SYSTEMS

MONDAY JULY 8

p-Ge and p-Si Lasers for Terahertz Applications

by

T Wenckebach

TU Delft
The Netherlands

Abstract

- the p-Ge IVB laser is based on a population inversion (PI) between the light hole and heavy hole band.
- the PI is achieved by applying strong crossed electric and magnetic fields at helium temperature.
- a Monte Carlo simulation is used to investigate the small signal gain dependency on the non-orthogonality of **E** and **B** fields.
- by tuning the **E** and **B** fields a few degrees from orthogonality the small signal gain is significantly decreased.
- this is due to the acceleration of the light holes out of the passive region in **k**-space below the optical phonon energy, where the PI exists.
- the feasibility of achieving active mode-locking in an IVB hot hole laser by using this idea for gain modulation is discussed. It turns out, that very short far infrared pulses of 10-100 ps may be obtainable in this way.
- some first experimental results are presented. Under certain conditions lasing can be stopped by applying an RF field at small additional contacts along the magnetic field direction. However, when the RF frequency is made equal to half the axial mode spacing, the lasing reappears.

Dependency on orthogonality E and B fields

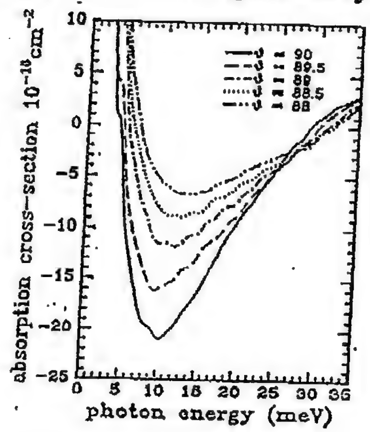

Figure 5: a) Small signal gain for different angles between **E** and **B**. $\mathbf{B} = 1.3\mathrm{T}[\bar{1}10]$; $\mathbf{E} = 2\mathrm{kVcm}^{-1}[00\bar{1}]$; $N_I = 1.3 \cdot 10^{14}\mathrm{cm}^{-3}$, $p_0 = 7 \cdot 10^{13}\mathrm{cm}^{-3}$; $T = 10K$; $\mathbf{e}_\nu \parallel \mathbf{E} \times \mathbf{B}$.

Conclusion: a few degrees non-orthogonality destroys population inversion completely, but *WHY*?

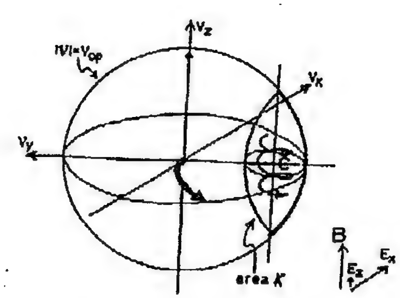

Figure 6: The spindle-shaped (in spherical approximation) accumulation region in velocity space. The holes are accelerated by the additional electric field $\parallel$ **B** and escape from the accumulation region along the helical orbits drawn. Thus the PI diminishes (see Fig. 2) and the small signal gain drops.

Possibility of an actively mode-locked p-Ge IVB laser

- we use this effect to achieve an actively mode-locked IVB laser by gain modulation
- This is done by applying an additional RF field parallel to the magnetic field with a frequency equal to cavity roundtrip frequency ($\approx$ 500 MHz)

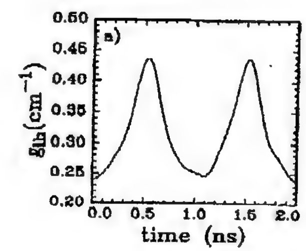

Figure 7: a) Small-signal gain g_{th} for far-infrared radiation ($h\nu = 12$meV, $\mathbf{e}_\nu \parallel \mathbf{B}$) in the modulated part of the *p*-Ge crystal due to the direct IVB transition during one (cosine) period of the RF field, as calculated from the Monte Carlo simulation. $\mathbf{E} = 2\mathrm{kVcm}^{-1} \parallel [111]$ and $\mathbf{B} = 1.3\mathrm{T} \parallel [0\bar{1}1]$, $T = 10$K, $E^0_{\mathrm{RF}} = 40\mathrm{Vcm}^{-1}$, $N_I = 2 \times 10^{14}\mathrm{cm}^{-3}$. g_{th} is modulated considerably at the second harmonic of the RF frequency $f_m = 500$ MHz but is more 'peaked': at least the first 8 Fourier coefficients have to be sampled to represent g_{th}.

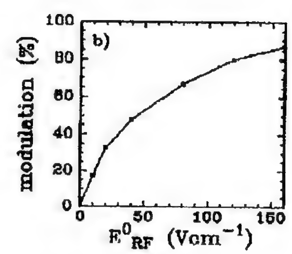

Figure 8: peak-to-peak gain modulation depth versus amplitude E^0_{RF} of the RF field.

Conclusions:

- a relatively small RF field already yields 30-50 % peak-to-peak gain modulation.
- from the linewidth $\Delta f \approx 3$ THz of the IVB transition, we can estimate the steady state pulsewidth:
  - if inhomogeneously broadened: $\tau_{p,ss} \approx 0.2$ ps.
  - if homogeneously broadened: $\tau_{p,ss} \approx 9$ ps.
- from saturation studies of the IVB transition [1], it is concluded that:
  - the passive material is inhomogenously broadened, with $\delta\nu_{\mathrm{inh}} \approx 200\mathrm{cm}^{-1}$ and $\delta\nu_{\mathrm{hom}} \approx 7\mathrm{cm}^{-1}$
  - the active material (i.e. lasing, with strong $\mathbf{E} \perp \mathbf{B}$ fields applied) is homogeneously broadened, due to:
    * transit-time broadening [1]
    * a small non-orthogonality of $\mathbf{E}$ and $\mathbf{B}$ [2]
- assuming a stable laser operation of $10^3 - 10^4$ roundtrips before laser saturation, we may still expect very short far infrared pulses of about 10 to 100 ps.

Experimental Results

- sample is mounted in Voigt configuration (long axis perpendicular to $\mathbf{B}$).
- crystallographic orientations: $\mathbf{E} \parallel [1\bar{1}0], \mathbf{B} \parallel [11\bar{2}]$.
- an external cavity is constructed by pressing a capacitive mesh ($g = 30\mu m, 2a = 1\mu m$ on a Si substrate) and a flat copper mirror (separated by a thin Teflon film) directly to the laser crystal.

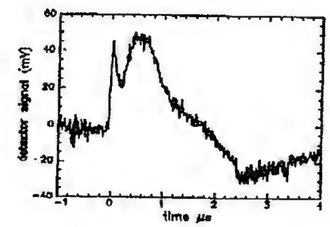

Figure 9: characteristic signal on Schottky diode, $\tau = 2.5\mu s$, $V = 800$V, $B = 0.9$T.

- the pulselength is limited to approximately 5 μs, due to heating of the sample.
- emission area:

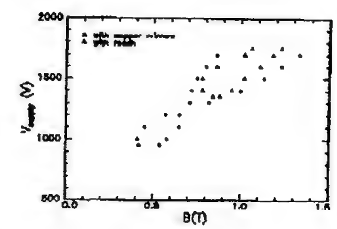

Figure 10: range of electric and magnetic field, where the crystal is lasing.

Application of an additional RF field

- at one side of the laser crystal, small (1×10 mm) additional electrical contacts have been made for the application of the RF field || **B**.
- the resistance between the additional contacts at RF frequency 100 MHz is approximately 1Ω (no magnetoresistance !).
- thus an impedance matching circuit has been designed to couple the RF power from a $50\Omega, 100W$, $200 - 500MHz$ amplifier into the laser crystal.
- by applying the RF field continuously, lasing is stopped at an RF power of only a few watts.
- for a gated RF pulse of a few hundred microseconds the behaviour is identical, even if the RF burst is applied before or after the high voltage pulse. Thus this small signal gain decrease is due to additional sample heating. However, it allows us to measure the frequency dependence of the impedance matching circuit.
- for a gated RF pulse of only a few microseconds during the laser emission, there is no significant decrease of laser intensity, even at maximum RF power.

However, if :

- the sample electrodes are tilted approximately 2 degrees with respect to the magnetic field axis (z-axis), such that $E_z = E_z^0 + E_z^\omega$. As a consequence the small signal gain has been decreased and is modulated strongly at the RF frequency (so no longer at the second harmonic !!).

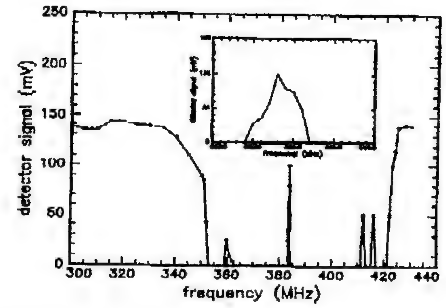

Figure 11: detector signal on Schottky diode ($\tau = 2.5\mu s$, $V = 800V$, $B = 0.9T$) as a function of the RF frequency; the estimated RF power dissipated in the laser crystal is approximately 60W. Lasing is prohibited by the RF field between 355 and 420 MHz, but reappears when the RF frequency is tuned to approximately 384 MHz (see inset). It is noted that the lasing around 360 MHz and 417 MHz is very unstable and is therefore ascribed to small additional resonances close to the resonance borders of the impedance matching circuit.

- Estimated cavity roundtrip frequency (or longitudinal mode spacing):

$$\nu_{RT} = c/2L' \approx 765\text{MHz}$$

with $L' = n_{Ge} * L_{cryst} + n_{Si} * d_{mesh} + n_{Teflon} * d_{Teflon}$.

- THUS: there is a clear resonance at half the cavity roundtrip frequency !!
- HOWEVER: we did not observe a corresponding modulation of laser intensity, when monitoring the laser pulse on a (400 MHz bandwidth) digital oscilloscope.

However, if :

- the sample is tilted approximately 2^o with respect to the **B** axis, such that $E_z = E_z^0 + E_z^\omega$. Thus the gain is smaller and modulated at the RF frequency.
- The small signal gain is almost constant up to 4^o, sample tilt contrary to theoretical expectations !!
- This is probably due to doping inhomogeneity, which causes an average non-orthogonality of **E** & **B** of a few degrees

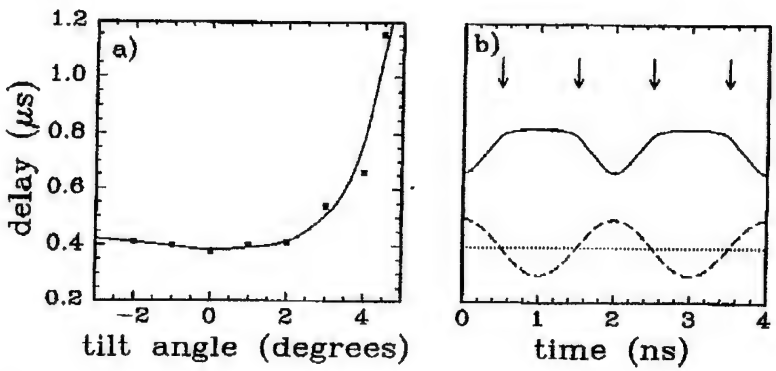

Figure 12: a) Delay of laser output pulse from the beginning of the HV pulse versus sample tilt angle. b) gain-modulation scheme for the tilted sample: the solid line shows the response of the small-signal gain to a strong 500MHz RF field along **B** (dashed line), as expected from a). The arrows indicate when a pulse travelling through the resonator at a cavity roundtrip frequency of 1GHz has to pass the modulator in order to be selectively amplified.

- The small signal gain is constant up to 4^o, contrary to theoretical expectations !!
- This is probably due to doping inhomogeneity (possibly enhanced by space-charge effects ?!), which cause an average non-orthogonality of **E** & **B** of a few degrees

Conclusions

- the application of an RF field along the magnetic field direction has a significant effect on the lasing behaviour of a p-Ge hot hole laser.
- this is due to acceleration of light holes out of the accumulation region below the optical phonon energy in **k** space.
- the additional sample heating effect is made relatively small by gating the RF burst up to a few μs.
- we observed a reappearance of laser emission, when an RF field is applied at HALF the cavity roundtrip frequency. This is observed only if the sample is tilted a few degrees.
- this can be understood from the behaviour of small signal gain, averaged over the laser crystal, as a function of sample tilt.
- The observed effect is a very strong indication for mode locking. Further investigations are necessary to demonstrate it in the time- and frequency domain.

Likely Future Instrumentation Requirements at Terahertz Frequencies

by

D Rytting

(No Material supplied.)

Potential Applications of Terahertz Systems for Collision Avoidance and Related Areas

by

H Brugger

(No Material supplied.)

What Future for Wireless Telecommunications Beyond 60 GHz?

by

D Wake

(No Material supplied.)

TUESDAY JULY 9

Nato Advanced Study Institute

New Directions in Terahertz Technology

Château de Bonas, near Toulouse, France

July 9th, 1996, 9.30-11.30

VECTOR MEASUREMENTS FROM 8 TO 800 GHz

Philippe Goy, Michel Gross,

AB MILLIMETRE,
52 rue Lhomond,
75005 Paris, France,
tel: 33 1 47 07 71 00
fax: 33 1 47 07 70 71

and

Laboratoire Kastler-Brossel,
Département de Physique de l'ENS
24 rue Lhomond,
75231 Paris Cedex 05, France,
tel: 33 1 44 32 34 18
fax:43 35 00 76.

Abstract

Part I. Presentation of the basic principles and evolution, over a period of about ten years, of a Millimeter Vector Network Analyzer.

Part II. Antenna measurements, where the phase information appears to be very useful, illustrate one of the first applications of the MVNA.

Part III. Fast and accurate dielectric characterizations are performed by various methods involving phase measurements.

Illustrations of MVNA use will be presented on the Analyzer itself, in action.

Fig.I.1.

All Millimeter Waves analyzers produce the Millimeter Waves frequencies Fmm by frequency multiplication, in a Schottky diode Harmonic Generator HG, from a centimeter source at the frequency F1.

$$Fmm = F1 \times N1 \quad \text{(N1 integer)} \qquad (I.1.)$$

Detection is firstly operated by harmonic mixing, the Schottky diode Harmonic Mixer HM being powered from a 2nd centimeter source at the frequency F2 (Fig.I.1). Finally a heterodyne receiver works at the frequency Fif (in the MHz range) such as:

$$Fif = | Fmm - N2\,F2 | \quad \text{(N2 integer)} \qquad (I.2.)$$

$$Fif = | F1 \times N1 - F2 \times N2 |. \qquad (I.3.)$$

Before 1989, AB Millimètre produced a **Scalar** Analyzer in which F1 and F2 were produced by 8-18 GHz sweepers, the 2nd sweeper being maintained at a constant distant frequency from F1, via a PLL control:

$$F2 = F1 - f. \qquad (I.4.)$$

The offset frequency f was chosen close to 3 MHz, and the heterodyne receiver was a 0.1-30 MHz traffic radio-receiver. The tuning of this receiver, at frequencies close tó 3 MHz x N, permitted to select the harmonics N such as:

$$N = N1 = N2 \qquad (I.5.)$$

$$Fif = N \times f. \qquad (I.6.)$$

Fig.I.2.

The **Scalar** Analyzer, shown Fig.I.2 at an exhibition in 1988, was including the short waves radio receiver (at top left). Called MSNA, it could use very simple, compact and mobile millimeter heads (at the bottom left of the picture). The large dynamic range available made the MSNA a good tool for applications such as antenna measurements.

Fig.I.3.

In 1989, the **Scalar** heterodyne receiver was replaced by a **Vector** one, and the Analyzer became a Vector Analyzer, called MVNA-8-350. The basic configuration of the MSNA is used also for the MVNA (Fig.I.3). From the I.1-6 above equations, one can deduce the phase Φ relationship:

$$\Phi if = | N1 \times \Phi 1 - N2 \times \Phi 2 |. \qquad (I.7.)$$

Since the 2nd sweeper is phase-locked onto the 1st, the noise components of the phases $\Phi 1$ & $\Phi 2$ of the two sources are the same:

$$\Phi 1 = \Phi 2, \qquad (I.8.)$$

and since the harmonic orders N1 & N2 have the same value, the detected phase (Eq.I.7.) Φif represents nothing but the DUT phase. There is no need for a parallel detection chain, which appears to be necessary in all previous millimeter vector analyzers, for supplying the phase reference onto the vector receiver. This new and very simple principle (1989) has been patented (EEC, USA, Japan). Due to it, millimeter heads remain the same, compact and light, as for the scalar analyzer. In particular, transmission measurements do not need any directional coupler (which hardly exist in the submillimeter).

Fig.I.4.

In the diagram Fig.I.4 is shown the maximum possible working frequency of successive analyzers MSNAs & MVNAs. Improvements have been done by reducing the noise, and also by increasing the microwave powers, by improving Schottky multiplication efficiency. It is also possible to associate a millimeter Gunn source at the required frequency. This is called ESA-0 (External Source Association nr0) when the Gunn is used directly, and ESA-1 (External Source Association nt1) when the Gunn feeds a Multi-Harmonic Harmonic Generator (Schottky diode multiplier). The use of a millimeter source (a Gunn around 100 GHz), instead of the 1st centimeter sweeper, produces a larger power at a given submillimeter frequency, since the harmonic rank N, necessary to reach this frequecy by multiplication, can be smaller. Similarly, a reduction of the noise is obtained from the use of a 2nd Gunn of the detection side as Local Oscillator of the Schottky Harmonic Mixer (called ESA-2), instead of the 2nd centimeter sweeper.

Fig.I.5.

In Fig.I.5 is shown the typical dynamic range of the MVNA-8-350, without or with extensions ESAs. ESA-1-95 means a Gunn centered at 95 GHz, ESA-1-110, centered at 110 GHz.

Fig.I.6.

Fig.I.6 shows the very schematic diagram of the MVNA, with the orders of magnitude of the powers along the source/detection chain. The values at the center (where the observed dynamic range S/N is of the order of 120 dB) correspond to 50-70 GHz, without ESA, and to ca 400 GHz, with ESA-1 & ESA-2, as well.

Fig.I.7.

Fig.I.7 is a table giving all relevant parameters concerning the diagram of Fig.I.6, and explaining the dynamic range observed Fig.I.5.

Fig.I.8.

The Schottky diode of the Multiplier M in the ESA-1 extension is a non-linear device. Controlling the feeding millimeter power by a calibrated attenuator K (Fig.I.8) permits to control the power emitted from this Multiplier.

Fig.I.9.

The MVNA-8-350's very large dynamic range and good linearity will permit to calibrate the Output/Input power law. This could be very interesting for the understanding of the frequency multiplication efficiency. Moreover, the sensitivity of the heterodyne receiver permits to observe good signals even for low-efficiency multipliers, far below the nanowatt level. In Fig.I.9 are shown the observed output signals, for harmonics 2 to 7, at the frequencies 220 to 770 GHz generated from the Multiplier M of the extension ESA-1-110. The absolute maximum powers (attenuator at 0 dB) of harmonics 2-5 have beeen measured on a bolometric probe: 3.7, 1.6, 0.92, 0.15 mW, respectively. Then harmonic two M=2 is detected by the Harmonic Mixer HM-D. Harmonics three M=3 and above are measured by using the extension ESA-2-110 as a detector. Close to the maximum incident power (0 dB at the input Attenuator knob), the slope of each curve in Fig.I.9 indicates the possible gain which could be obtained from a more powerful 110 GHz input (we have around 20 mW). For harmonics 3-5, the slope is close to one. One dB gain in Gunn gives about one dB more microwave after mutiplication. For harmonic two (M as a doubler), the dependence is very low, around 0.2, so that a Gunn increase of 1 dB leads to a 220 GHz power increased by about 0.2 dB only. After desaturation of the Schottky Multplier, which occurs between 15 and 20 dB at the attenuator, the Output/Input power law presents a slope which is just the harmonic order M, for M=2, 3, and 4. Harmonic M=5 presents a 4.72 slope, M=6 a slope 4.57, M=7 a slope 5.17. The deviation of the experimental points from linear extrapolation of the M=3 curve below the 40 dB position of the attenuator most probably comes from the unaccurate attenuator calibration at >40 dB values. With a recalibrated attenuator, or, preferably, with two calibrated attenuators in series, used in their "good" range (below 40 dB), one can have a set (220, 330, 440, 550, 660... GHz) of controlled small powers (eventually below the pW, disks at Fig.I.9, bottom), which could be used in sensitive receiver tests.

Fig.I.10.

The front panel of the microwave part of the first version of the Vector Analyzer MVNA-8-350-1 (Fig.I.10) is exactly similar to the one of the Scalar Analyzer MSNA (Fig.I.2): there is one output for the source side, and one output for the detection side. Each of the HG and HM millimeter heads can be biased, or self-biased ("short" switch position). The current, applied or due to the rectified centimeter microwave, appears in the galavanometers (full scale 25 mA).

Fig.I.11.

The front panel of the second version of the MVNA, model MVNA-8-350-2 produced since 1995, is shown in Fig.I.11, and is to be compared to the previous model Fig.I.10. MVNA-8-350-2 vector receiver is a dual-channel one. Two Harmonic Mixers, HM1 & HM2, can work in parallel. This possibility is very useful for measuring transmission-reflexion at the same time, or for measuring antennas, and then compensate any phase or amplitude drift on a long base by ratioing the signal obtained onto the tested antenna by a signal from a control antenna.

Fig.I.12.

As an exemple of the use of MVNA-8-350-2, Fig.I.12 shows the compensation of phase drift over three hours at 96 GHz.

Fig.I.13.

The model MVNA-8-350-2 can be used in a dual-millimeter frequency configuration. The only restriction is that the two frequencies Fmm1 & Fmm2 must be harmonics N1 & N2 (integers) of the same centimeter frequency Fcm (with 8<Fcm<18.75 GHz) from the MVNA sweeper. The centimeter power of this sweeper, split in a 3 dB coupler, generates Fmm1 = Fcm x N1 in HG1, and Fmm2 = Fcm x N2 in HG2. The two channels of the receiver are tuned on the different Fif from HM1 & HM2. In the example shown Fig.I.13 top, at the upper frequency of the sweep, one has Fcm = 12 GHz. The millimeter frequencies are Fmm1 = 36 GHz, and Fmm2 = 96 GHz, with N1 = 3 and N2 = 8. These harmonics were chosen in order to obtain the main frequencies of interest on the battle field, around 35 and 95 GHz. The obtained dynamic range (Fig.I.13 top) is not as good as it could be in standard working conditions, since the second harmonic, N2 = 8, is larger than the value N = 6 which is the best choice for 96 GHz generation.
Fig.I.13 bottom shows that the two detected different millimeter frequencies are quite independent (there is no crosstalk), when their power levels are modified via attenuators.

Fig.I.14.

The microwave front panel of the model MVNA-8-350-4 (Fig.I.14), created in 1996 for 4-S Parameters measurements, is similar to the model MVNA-8-350-2 (Fig.I.11), plus two outputs: "Source 1" (for HG1) and "Source 2" (for HG2). The HG centimeter sweeper is sent alternatively to HG1 and HG2.

Fig.I.15.

A MVNA-8-350-4 is installed at ENSTBr Telecom-Bretagne, Brest University, Prof. S. Toutain (Fig.I.15).

Fig.I.16.

The detail of the millimeter heads used in the Ka band (26.5-40 GHz) at ENSTBr is shown on Fig.I.16. From left to right, the millimeter heads are: HG1, HM2, HM1, HG2. When HG1 is powered, HM1 gives S21 and HM2 gives S11. When HG2 is powered, HM1 gives S22, and HM2 gives S12.

Fig.I.17.

In the millimeter, and especially in the submillimeter waves domain, most of the measurements do not involve a complete calibration of the error terms, which is possible only with the full reverse analyzer such as MVNA-8-350-4. With a single source-single detection configuration, complete calibration is possible for reflexion (S11 and S22 are measured in two steps). Transmission calibration (S21 & S12) is obtained by looking at the signal through an attenuator. This calibration is, most of the time, good enough. However, it is not perfect (at the typical +/-0.2 dB level), especially for low insertion, where the complete calibration must be used, if possible. Fig.I.17 shows 4S-Parameter measurements with the W-band WR-10 setup in a 90-100 GHz sweep, through a WR-15, 4-inch (101.6 mm) long waveguide. This waveguide presents a small insertion loss. The mismatches at its two ends create an interference pattern, like in a Fabry-Pérot resonator.
S11 (reflexion from port 1) is shown at top left onto the Smith chart.
S12 (transmission from port 2 to port 1) is shown at top right, linear scale.
S21 (transmission from port 1 to port 2) is shown at bottom left, polar plot.
S22 (reflexion from port 2) is shown at bottom right, log (dB) scale.

Fig.I.18.

The heterodyne vector receiver operates several downconversions of the detected millimeter signal. The last frequency has been chosen ca 500 Hz, allowing a low noise level and a good dynamic range, like the 99+/-10 dB observed in the 72-112 GHz interval, Fig.I.18, top. Such a frequency does not permit fast sweeps, and the 500 points sweep lasts for typically 30 s. A new version (1996) of the receiver downconverts the signal to ca 10 kHz. Then measurements can be about ten times faster (500 points obtained in 3 s), with, naturally, a decreased dynamic range: 89+/-10 dB in the 72-112 interval, Fig.I.18, bottom. The fast receiver can recover the best dynamic range, by slowing down the sweep, and averaging.

Fig.I.19.

For testing the fast receiver in the most difficult case, one observes a high-Q (Q = 160,000) Fabry-Pérot cavity by transmission. The width of resonances is of the order of 0.6 MHz. The first sweep, Fig.I.19, top, is made in 60 s with ten thousands points, which means 0.15 MHz steps, so that the resonances cannot be missed. The second sweep, Fig.I.19, bottom, is obtained in 3 s, with 500 points. The detected signal is quite satisfactory.
Let us remark that in the fast sweep, resonance details are shown despite the fact that the steps, now 3 MHz, are larger than the cavity width. Contrary to the other millimeter vector analyzers, MVNA-8-350 uses sweepers, not synthesizers, so that all frequencies are really emitted during a sweep.

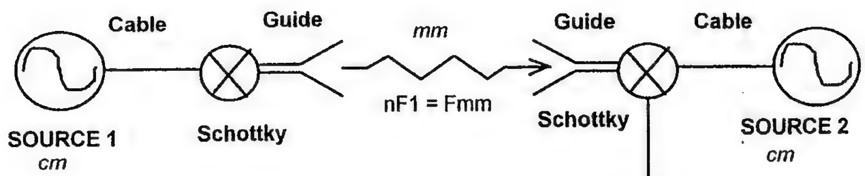

$$Fif = | Fmm - pF2 |$$
$$Fif = | nF1 - pF2 |$$

$$\left.\begin{array}{l} F2 = F1 - f \\ n = p \end{array}\right\} Fif = nf$$

- 1985, PLL F2/ F1
  SCALAR ANALYZER
  (with short wave radio)

Fig. I.1.

MM('88)
MILITARY MICROWAVES 88
CONFERENCE-EXHIBITION
Wembley Conference Centre · London 5 · 6 · 7 · July 1988
Organised by Microwave Exhibitions and Publishers Limited

MM '88 RETURNS TO WEMBLEY
– Europe's largest microwave event of its kind

EXHIBITION PRODUCT REVIEW

MILLIMETRIC FREQUENCIES

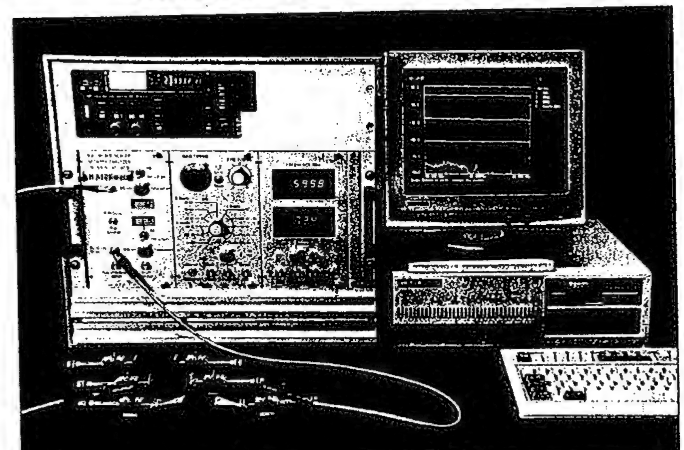

The 16–250 GHz analyser by AB Millimetre.

Fig.1.2

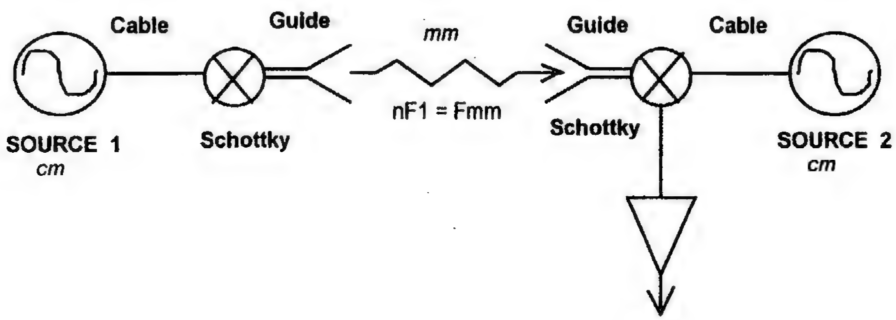

Fif= | Fmm - pF2 |

Φ if=|Φmm - p Φ2|

Fif= | nF1 - pF2 |

Φ if=|n Φ 1 - pΦ 2|

$$\left.\begin{array}{l} F2= F1-f \\ n = p \end{array}\right\} Fif = nf$$

Φ2=Φ1

Φ if=0

- 1985, PLL F2/ F1
  SCALAR ANALYZER
  (with short wave radio)
- 1989, VECTOR ANALYZER
  CNRS- ENS
  (with ABmm Vector Receiver)

Fig. I. 3

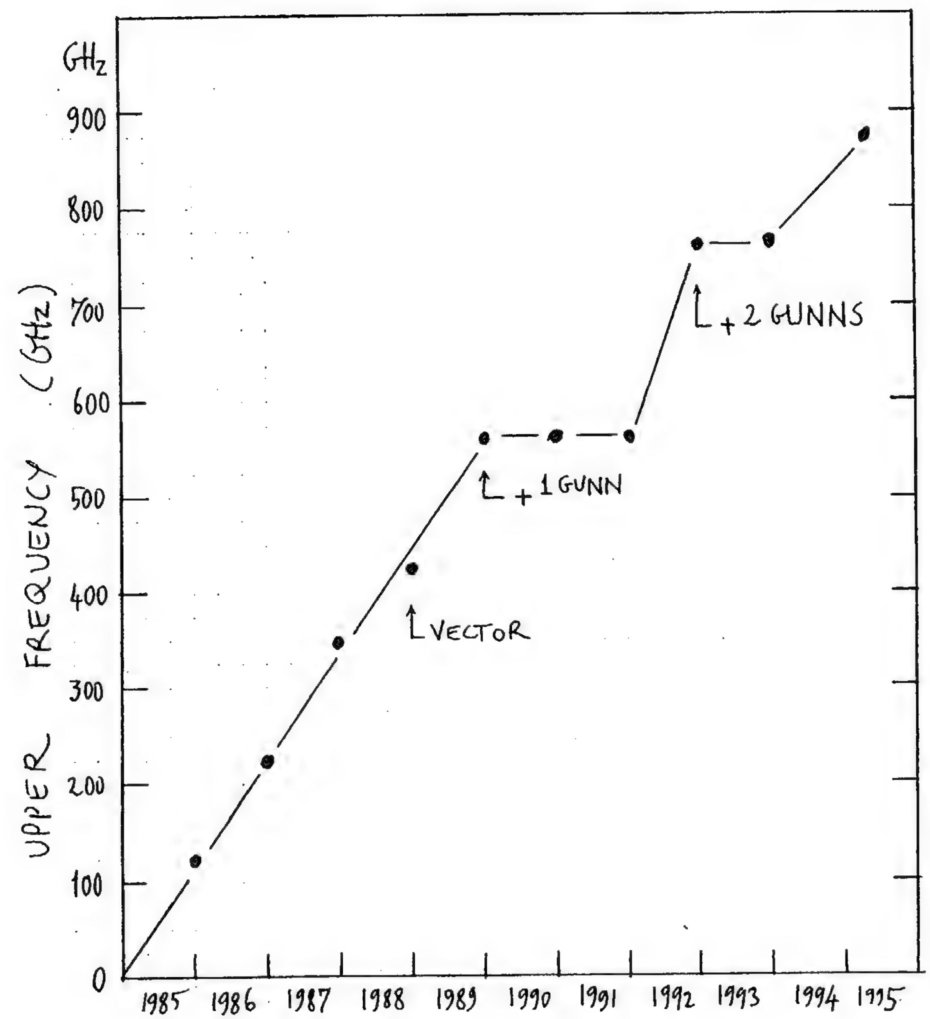

Fig. I. 4.

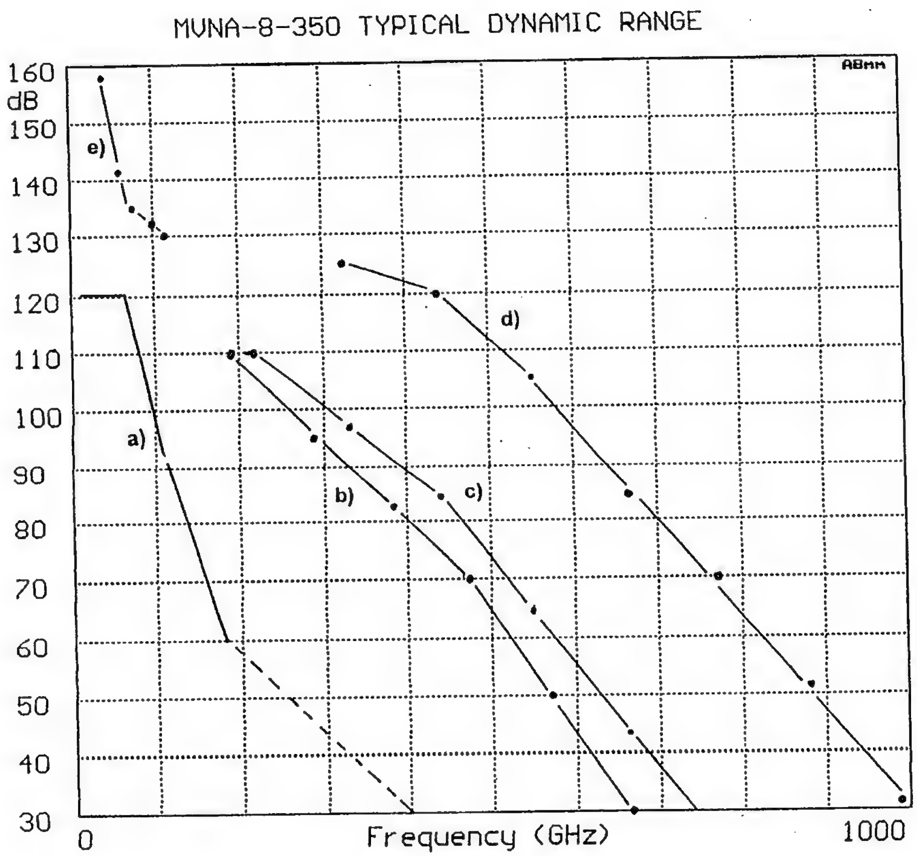

a) MVNA-8-350 alone,

b) with ESA-1-95 extension,

c) with ESA-1-110 extension,

d) with ESA-1-110 + ESA-2-110 extensions,

e) with different ESA-0 extensions.

Fig. 1.5.

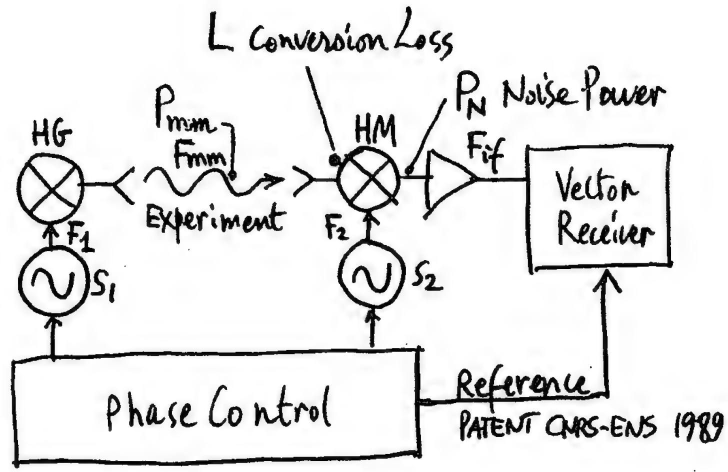

$$\boxed{S/N\,(dB) = P_{mm}\,(dB_m) - L\,(dB) - P_N\,(dB_m)}$$

$P_{mm} = 0\,dB_m$ (1 mW)
$L = 30\,dB$
$P_N = -150\,dB_m$ (10^{-18} W) at 20 pts/s
$\Rightarrow S/N = 120\,dB$

- MVNA-8-350 alone : S_1 & S_2 = 8–18 GHz sweepers
- with ESA-1 : S_1 = mm Gunn
- with ESA-1 & ESA-2 : S_1 & S_2 = mm Gunns

Fig. 1.6.

FREQUENCY GHz	M MULTIPLICATION OF THE GUNN FREQUENCY	POWER FROM ESA-1-95 dBm	POWER FROM ESA-1-110 dBm	POWER FROM 95-SEXTUPLER dBm	HM-D CONVERSION LOSS dB	ESA-2-95 SHM CONV-ERSION LOSS dB	ESA-1-95 SOURCE/ HM-D. DETECTOR DYNAMIC RANGE dB	ESA-1-110 SOURCE/ HMD DETECTOR DYNAMIC RANGE dB	ESA-1-95 SOURCE/ ESA-2-95 DETECTOR DYNAMIC RANGE dB	ESA-1-110 SOURCE/ ESA-2-95 DETECTOR DYNAMIC RANGE dB	SEXTUPLER SOURCE/ ESA-2-95 DETECTOR DYNAMIC RANGE dB	ESA-1-110 SOURCE/ ESA-2-110 DETECTOR DYNAMIC RANGE dB	ESA-2-110 CONVERSION LOSS dB
95	1	15			30		135					*	*
110	1		16										
190	2	8			48		110						
220	2		5.7		46			110					
285	3	0			55	29	95		120				
330	3		2		51			97				125	27
380	4	-3			64	39	83		104				
440	4		0.2		65			85				120	30
475	5	-10			70	42	70		91				
550	5		-7.4		77			66				106	37
570	6	-24		-4	76	45	50		80		110		
665	6		-26		81			43				84	40
665	7	-38			82	48	30		66	75			
764	7		-37		88			25				70	43
764	8	-57		-24	88	51			45	62	75		
864	8		-48									52	50
864	9					54				50			
950	10			-52?		57?					41		
990	9		-65									31	54

ESA OPTIONS. RELEVANT PARAMETERS.

* RESULTS IN THESE COLUMNS HAVE BEEN MEASURED AT NHMFL TALLAHASSEE IN DECEMBER 1995, PROF. L.C. BRUNEL.

Fig. 1.7.

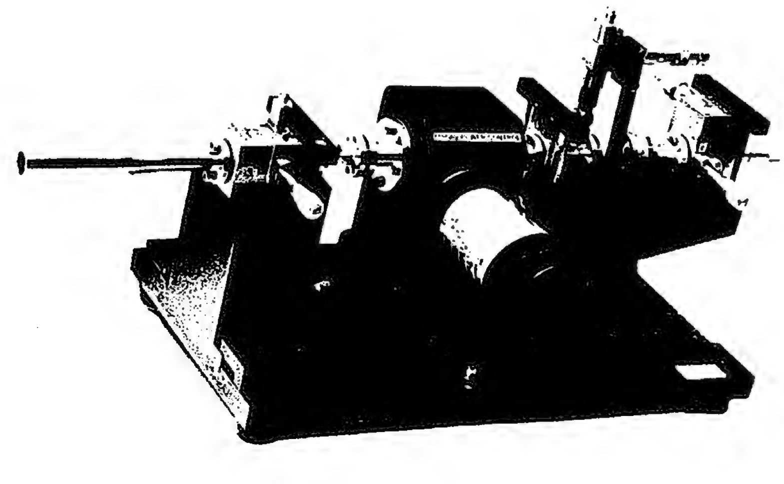

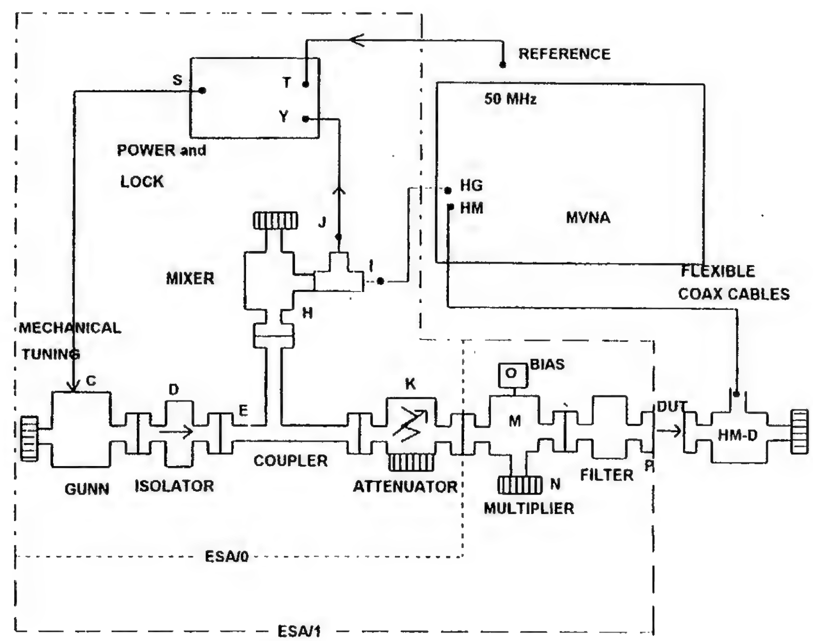

Fig. 1.8.

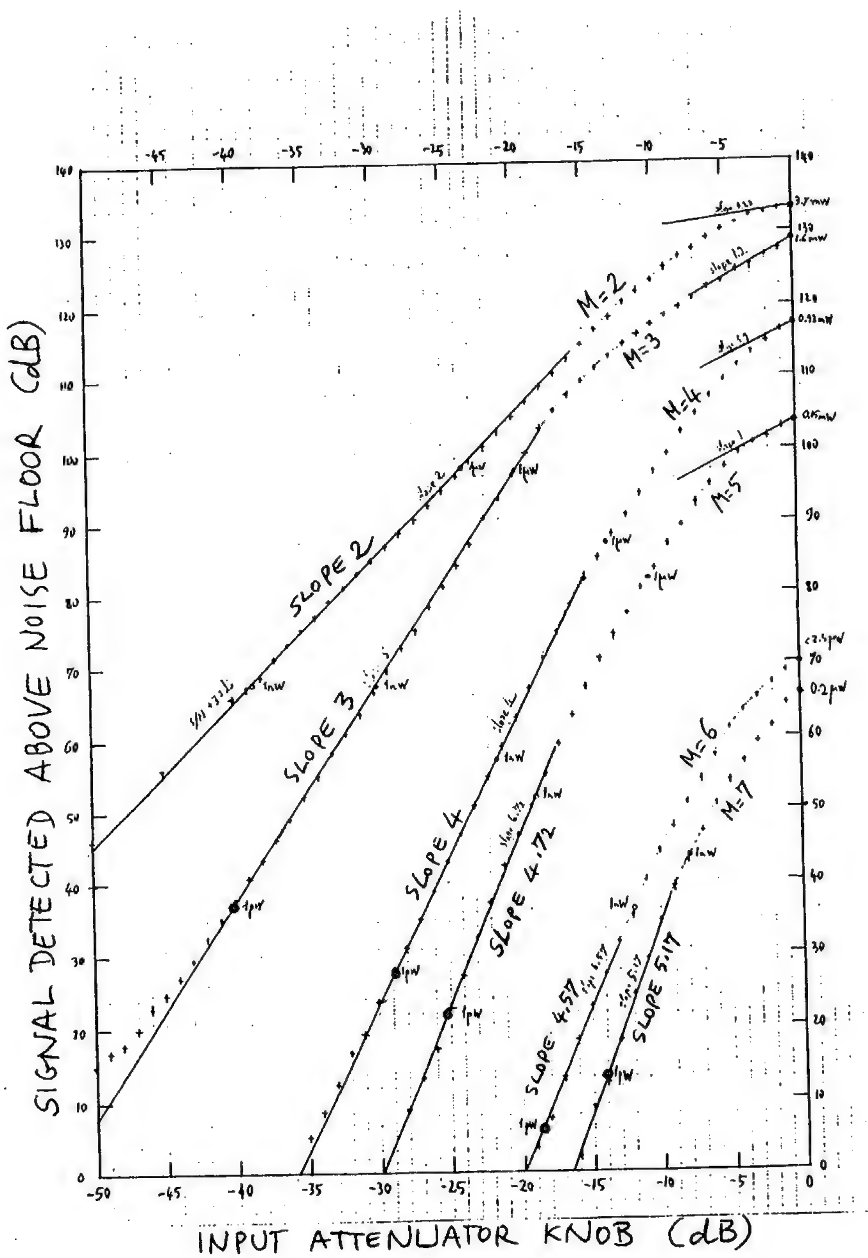

Fig. 1.9.

Fig. 1.10.

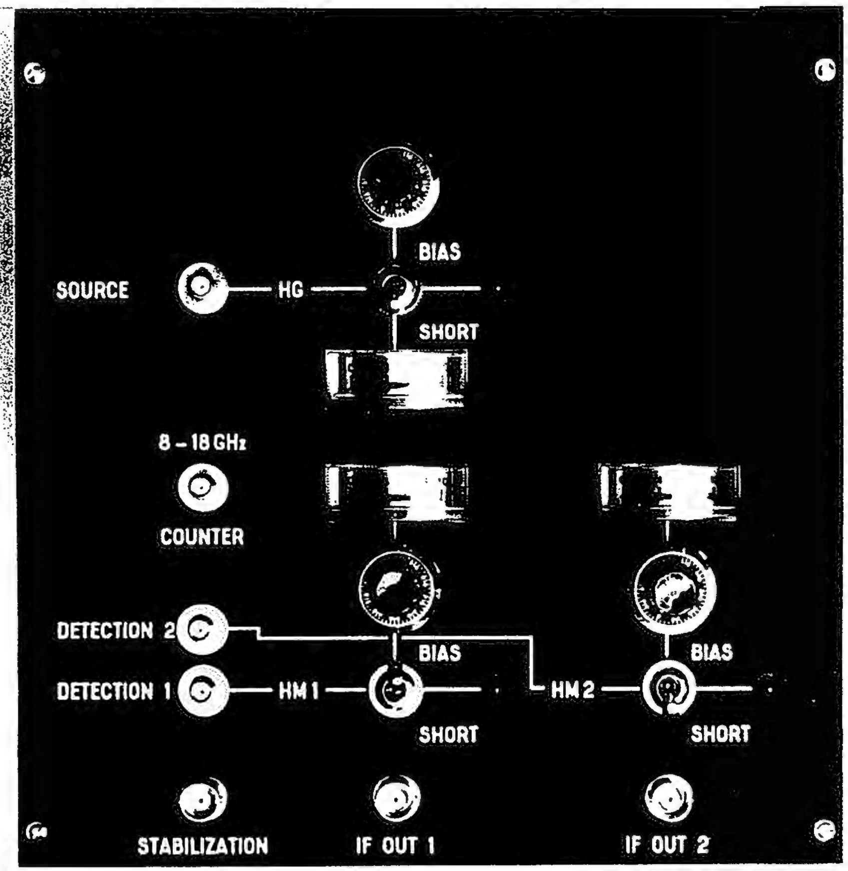

Fig. I. 11.

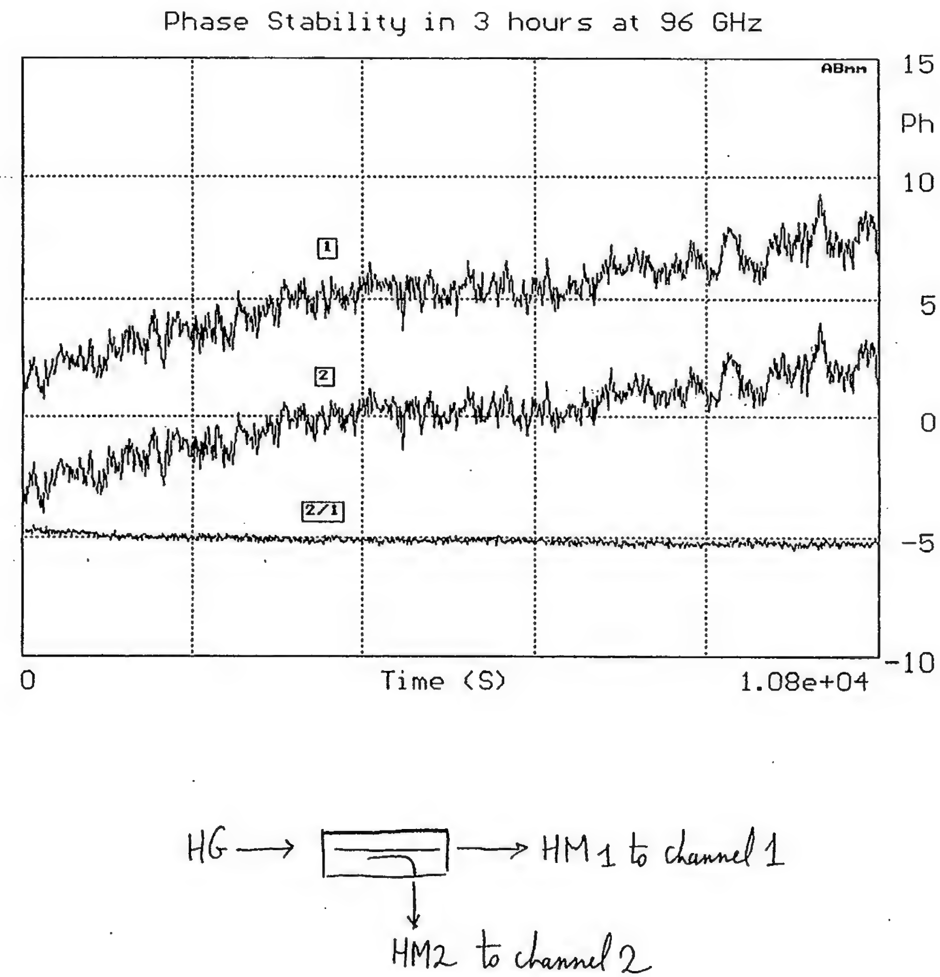

Fig. 1. 12.

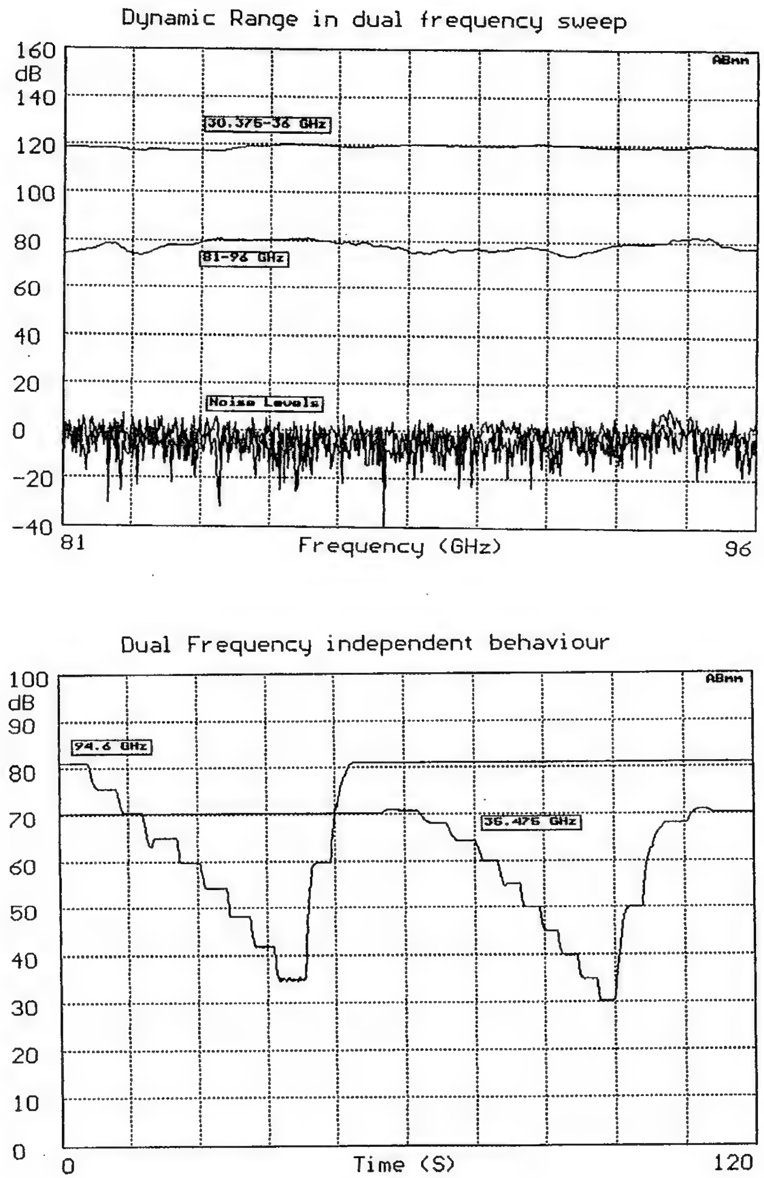

Fig. 1.13.

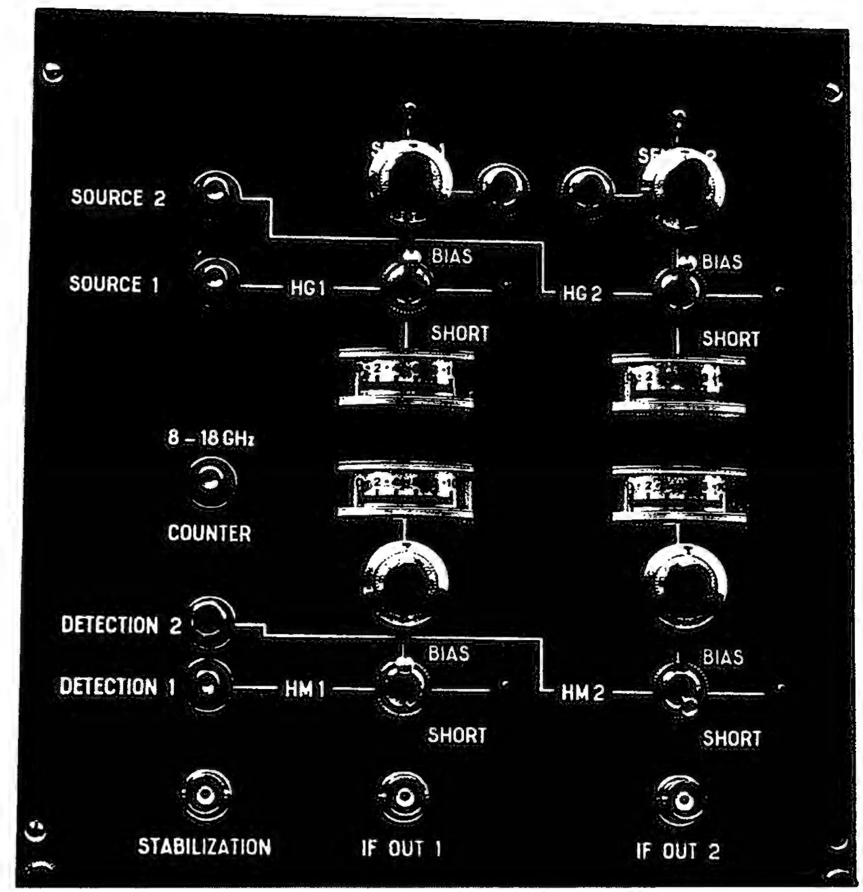

Fig. 1.14.

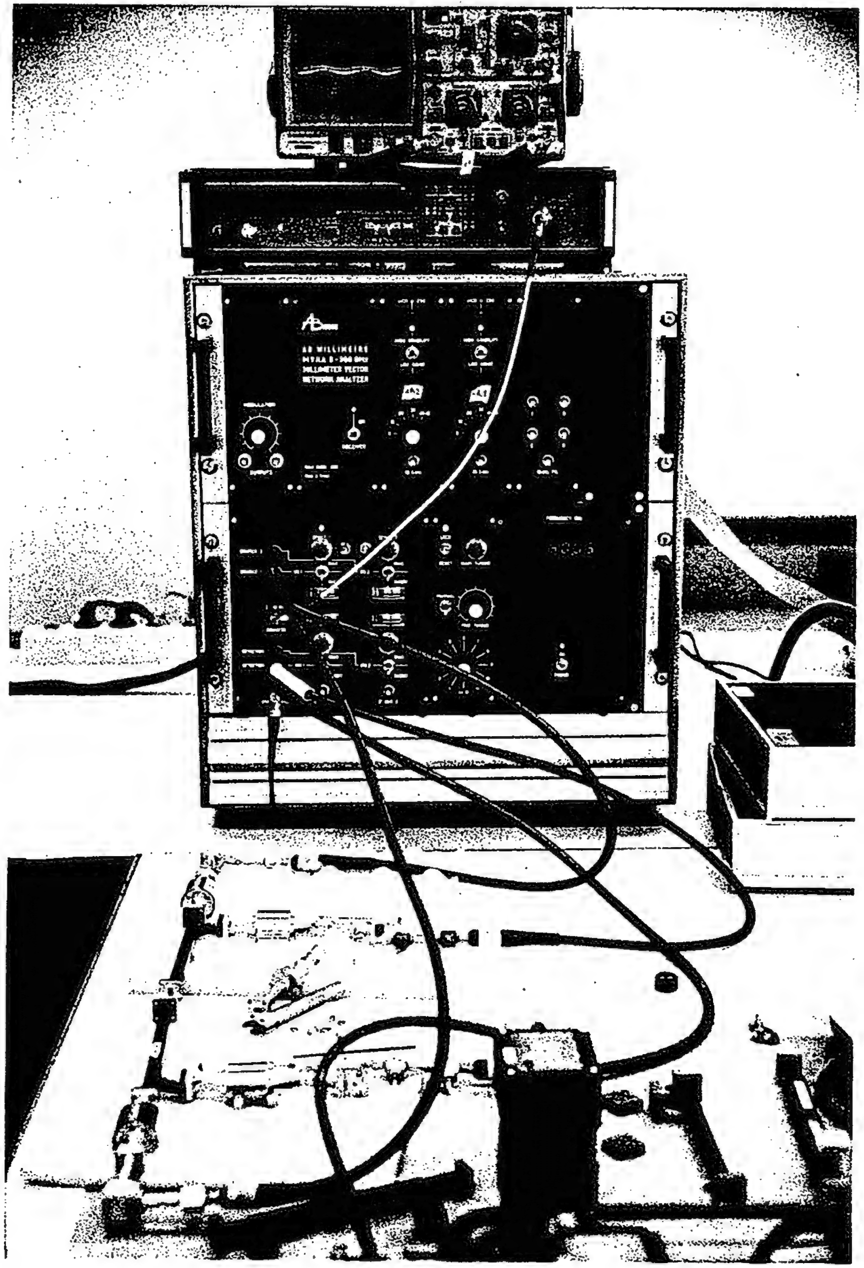

Fig. 1.15

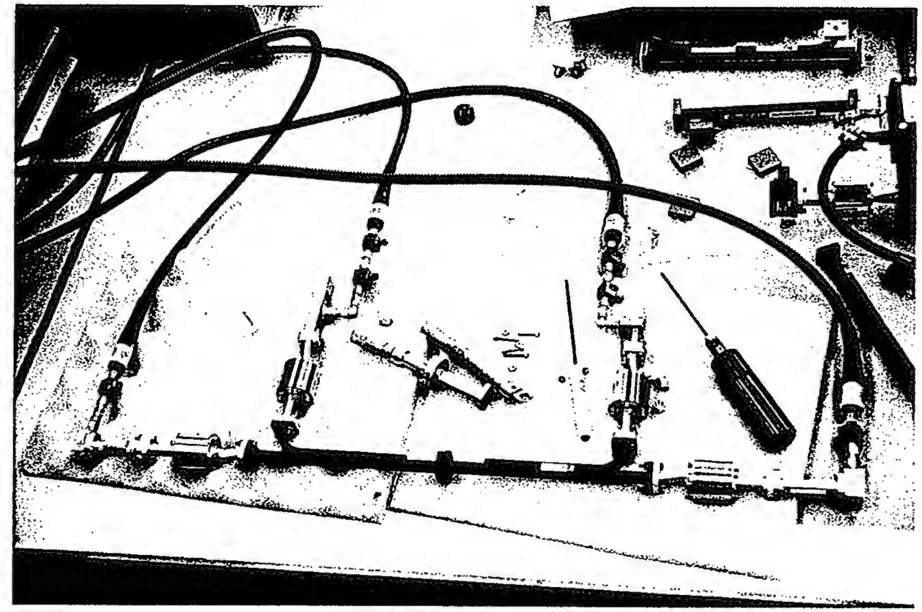

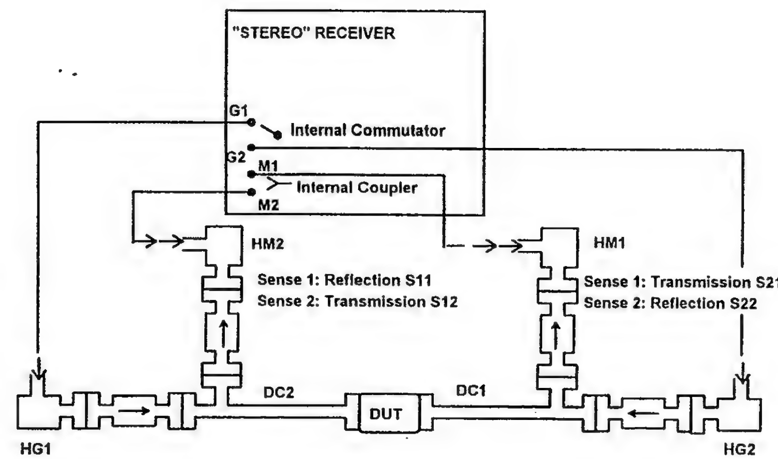

Fig. 1.16.

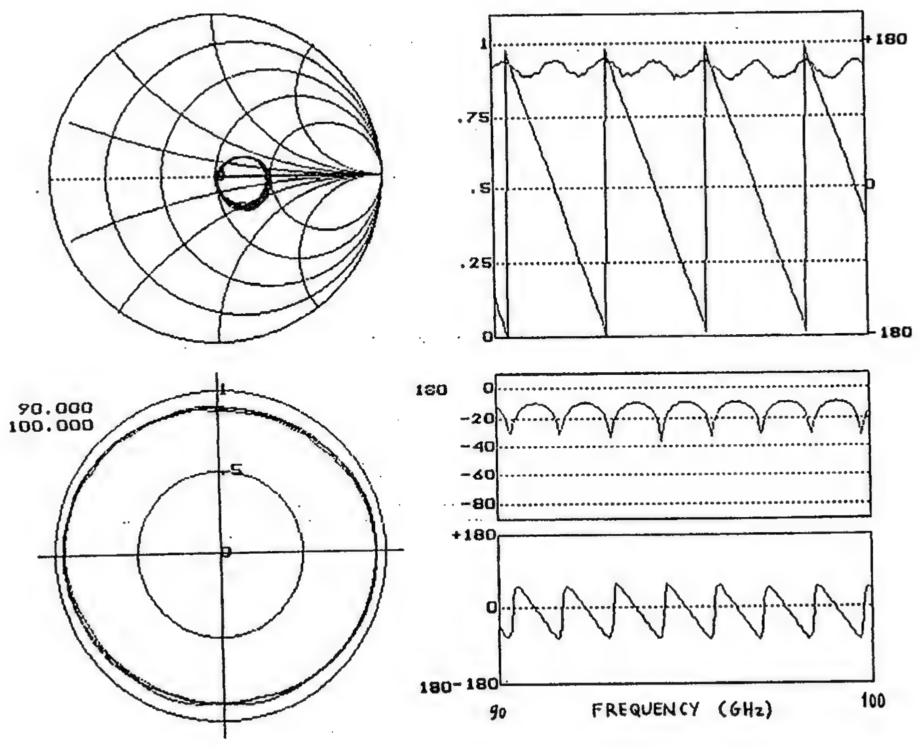

Fig. 1.17

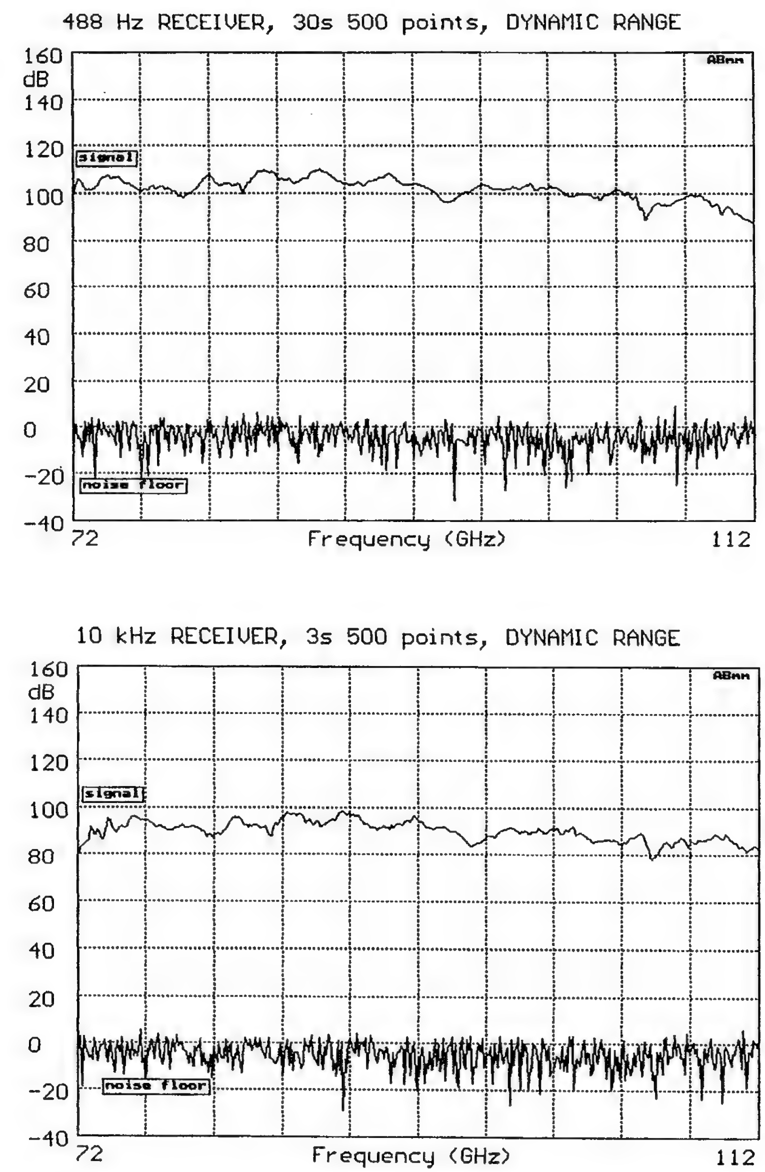

Fig. 1.18.

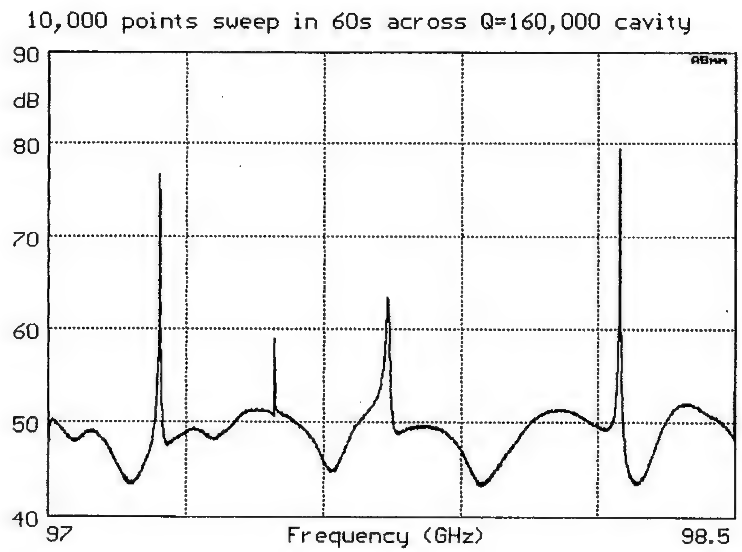

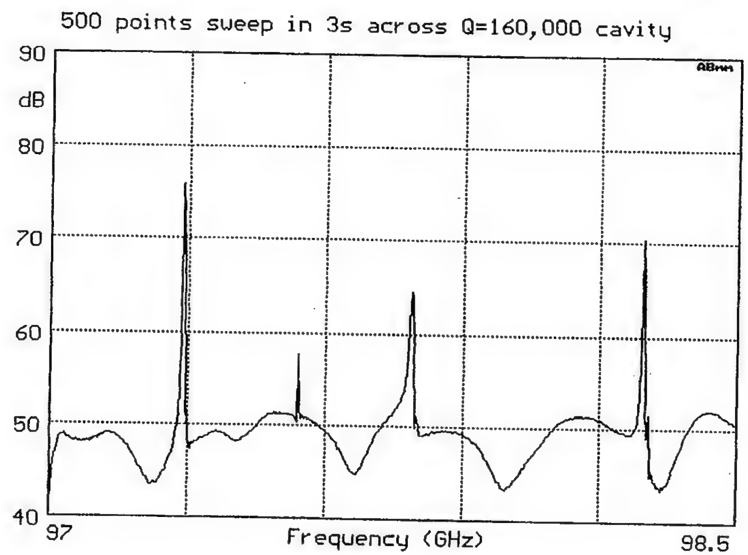

Fig. 1.19.

Fig.II.1.

The size of the millimeter components can be small. In Fig.II.1 are shown, from top to bottom, four W-band (75-110 GHz, WR-10) components: a scalar horn, a Potter horn, an attenuator, a lens-horn antenna; at bottom is an E-band (60-90 GHz, WR-12) standard gain pyramidal horn. Vertical ruler is in cm. With such small items connected to the small MVNA millimeter heads, measuring antennas can be a favourite and easy use of the MVNA. Moreover, the large available dynamic range permits fast and accurate measurements.

Fig.II.2.

A typical antenna measurement setup is shown in Fig.II.2. On the left is the standing HG-D source for 143 GHz. On the right is the Micro-Controle Co rotating table which permits the azimuth angle variation through a step-by-step motor drive controlled by the standard MVNA software. The antenna under test at 143 GHz is attached to this table, and the flexibility of the HM-D coax cable (at right) allows +/-90° angular sweeps.

Fig.II.3.

With the scalar analyzer MSNA, good amplitude antenna pattern could be obtained with a very simple setup like in Fig.II.2, where the step-by-step motor was replaced by a synchronous motor making 1 turn/minute, i.e. -90°/+90° in 30 seconds. Fig.II.3. shows an exemple of such a scalar measurement observed at 50 GHz on a conical horn from Thomson-CSF.

Fig.II.4.

Scalar horns around 95 GHz (Fig.II.4, top) and 230 GHz (Fig.II.4, bottom) have been designed and produced by the Labo DEMIRM, Radioastronomy group of Paris-Meudon-ENS (M. Gheudin, G. Beaudin). The quality of the antenna pattern, measured with the MSNA, is extremely good, especially for the 95 GHz horn, where secondary lobes (if any!) appear to be below -45 dB (Fig.II.4., top).

Fig.II.5.

The 230 GHz scalar horn of Fig.II.4, bottom, has been measured in more comfortable conditions, as shown in Fig.II.5, with the MVNA and an extension ESA-1.

Fig.II.6.

A Gaussian optics lens-antenna at 60 GHz, is made from a scalar horn feeding a dielectric lens of large aperture (around 10 cm). The aperture of the horn is at the focus of the lens. The antenna pattern as delivered by the factory (Fig.II.6., top) is not as good as the true antenna pattern as observed with the MSNA (Fig.II.6, bottom).

Fig.II.7.

With the same principle of a lens-horn antenna, a small 333 GHz Potter horn feeds a 35mm diameter teflon lens realized at DEMIRM (J-C Pernot). One can compare the E and H-planes antenna patterns of the horn alone, or associated with the lens. There is a dramatic narrowing of the beam, and a gain, along the axis, of the order of 17 dB (Fig.II.7, top). The dynamic range of the measurement is over 70 dB in the measurement conditions, as shown in Fig.II.7, bottom.

Fig.II.8.

The measurements which have been described above (Figs.II.3-7) are interesting. However none of them uses the phase information.
Now let us consider measurements which are not possible without observing the phase.
On a pair of smilar WR-10 Potter horns designed to work around 95 GHz, a vector measurement in a 70-110 GHz sweep gives a return below -22 dB (Fig.II.8, top and middle). The **Fourier transform FT** of these returns, gives similar responses for the two in the **time domain** (Fig.II.8, bottom).

Fig.II.9.

The time domain can be viewed as a **length domain**, the speed of light in the propagating medium being the scale coefficient. Thus the FT of return signals will give the positions of the mismatches as peaks. A non-destructive inside view of any propagating component, including antennas of course, can be realized. For a simpler visualization, the FT diagram can be represented at the geometrical scale of the component. Fig.II.9, top, shows such a FT signal obtained from a 70-110 GHz return signal from a Potter horn. The main mismatch is occuring at about half-distance of its total length, where is the excitation of the two circular modes, after the long rectangular-circular transition. Fig.II.9, bottom, shows the same for a scalar horn, where the excitation of the circular mode is operated closer from the input flange.

Fig.II.10.

A conical horn can have a very low return (below -30 dB from 86 to 110 GHz for a WR-10 horn, see Fig.II.10, top). The association of a Fresnel lens attached to the horn aperture increases the return (which is around -20 dB from 86 to 110 GHz, see Fig.II.10, middle). The FT time (or distance) display permits to understand precisely the effects of the parasitic reflexions due to the lens. In Fig.II.10, bottom, the plane input surface (hidden) of the lens creates a mismatch which is 12 dB above the mismatch of the aperture of the horn without lens. The curved output surface of the lens (made from Fresnel steps) creates a mismatch which is 5 dB below that of the plane surface.

Fig.II.11.

Far from the emitting antenna, the wave can be viewed as spherical, coming from a point called **phase center**. The precise determination of the phase center is crucial in all alignments and optimizations for obtaining the best Gaussian beams. Indirect measurements, from scalar measurements, are long and not unambiguous, contrary to direct vector measurements. For this reason and for the rich FT possibilities in antenna characterization, **vector measurements are very much to be preferred to scalar measurements**. The phase center search setup comprises, among others, a lateral adjustment and a longitudinal adjustment (Fig.II.11.). For fulfilling the far field conditions, the distance L between the source of typical aperture D, and the detection of the same aperture, must be:

$$L > 2D^2/\lambda. \qquad \text{(II.1.)}$$

Due to the large number of wavelength λ contained in the distance L, a small change in frequency may induce a very large change in the detected phase. For this reason, the antenna measurements will preferably be operated at a synthesized frequency (stabilization obtained from the EIP 575 (or 578) frequency counter-stabilizer). Moreover, one can compensate for the large phase versus frequency dependence by adding distance in the coax cable going to the HM. About 1m of our centimeter coax cables compensates for 1.2m millimeter waves propagation in air. For that reason the MVNA must stand on the HG source side, and the long cable must be connected to the HM detector on the measured antenna side.

Fig.II.12.

The phase center search, operated with the appropriate setup (Fig.II.11), consists in finding firstly the "optical" plane of symmetry of the antenna (which can be different from the "geometrical" plane of symmetry). As soon as the rotation axis does not belong to the optical plane of symmetry, there is a global move, towards or backwards, of the measured antenna aperture versus the far emitting antenna. Therefore the phase increases, or decreases, with rotation. This symmetry determination is very sensitive on the phase, and not at all on the amplitude. Such a phase center search is operated in Fig.II.12, at 285 GHz in the H-plane, by 0.2 mm lateral steps of a conical horn (from DEMIRM). The axis of rotation belongs to the plane of optical symmetry when the phase variation is horizontal around the zero azimuthal angle.

Fig.II.13.

The second step of the phase center search is operated in varying the longitudinal position of the antenna (Fig.II.11). Similarly to the same operation with the lateral position, but less sensitive (1 mm steps instead of 0.2 mm, respectively), one obtains the phase center position when the phase change with azimuth angle is flat, the curvature being up or down for the tested antenna too far, or too close (Fig.II.13, same conditions and same conical horn as in Fig.II.12).

Fig.II.14.

When measuring an antenna pattern versus azimuth angle, the Gaussian beam signature consists in observing a flat phase dependence, and a parabola for the amplitude when shown in log units (dB). Scalar horns (corrugated) are, most of the time, broad band devices. The Company Farran Ltd developped such a scalar horn for a meteorology satellite, where water vapour is to be characterized at the 183 GHz H_2O line, and also around the line, by +/-8 GHz. Final tests were operated at AB Millimètre, where a disaster occured at the upper frequency 191 GHz. On Fig.II.14, one sees a good Gaussian profile at 175 & 183 GHz. The 191 GHz profile is not Gaussian: the phase is not flat, and the amplitude has not a parabolic shape. This horn was rejected.

Fig.II.15.

A good scalar horn gives very similar antenna patterns at all polarizations (E & H-planes). The only parameter changing with frequency is the beam width, which is narrowing with frequency, according to diffraction laws. Fig.II.15 shows the second scalar horn after redesign, from Farran Ltd. This horn, excellent, was accepted.

Fig.II.16.

The measured phase profile of a non-Gaussian antenna can be used to design a dielectric lens, in view to correct the emitted phase curvature and to obtain a Gaussian profile. A conical horn antenna made by Thomson CSF Co (Fig.II.16, top) presents a beam which is not Gaussian: the amplitude is not a parabola (Fig.II.16, middle), and the phase is not flat (Fig.II.16, bottom). The lens profile reproduces the phase pattern around the axis. When the lens is attached to the horn aperture, the emitted phase is flat around the axis: the emitted beam is Gaussian (the amplitude has a parabolic shape), and the amplitude gain on the axis is 10 dB.

Fig.II.17.

Antenna measurements are very demanding in dynamic range. Submillimeter waves measurements will be performed with the help of extension ESA. The setup for a 380 GHz antenna pattern characterization, including an ESA-1 source (Fig.II.17) is quite similar, on the detection side, to the one used for 143 GHz measurement (Fig.II.2).

Fig.II.18.

In the submillimeter domain, Potter horns are much easier to build than scalar horns, since they do not require corrugations which are more and more difficult to machine with increasing frequencies (i.e. decreasing wavelength, i.e. demanding smaller and smaller corrugations). They are much more restricted in band than the scalar horns. When used, within a few percents, at the frequency for which they have been designed, they can present very low sidelobes and a good E and H-planes symmetry. Fig.II.18 shows the angular antenna pattern of a 380 GHz Potter horn made from Peter Zimmermann RPG, measured in the setup described Fig.II.17.

Fig.II.19.

Potter (also called dual-mode) horns create a beam which is the combination of two beams with opposite phase curvature. In the vicinity of the axis, the phase of the resulting beam is not flat, but stationary. This explains the low side lobes position. However, the beam is not exactly Gaussian. In Fig.II.19 is shown the detail of the H-plane antenna patern of the 380 GHz Potter horn of Fig.II.18. The amplitude does not show a parabolic profile. The opposite curvatures of the two modes are visible. The phase repeatability, of the order of 3 degrees, could be attributed to a mechanical repeatability of 6 micrometers.

Fig.II.20.

Millimeter waves correspond to small wavelength, allowing reduced size antennas which fit into missiles. Monopulse antennas are used for radar search and trak of targets. In such an antenna, one combines, by sum and difference, two beams. The sum gives a maximum on the axis, with a Gaussian shape and a flat phase dependence around the axis. The difference gives two beams apart from the axis, about zero amplitude on the axis, with a phase jump of 180°. Fig.II.20 shows amplitude (top) and phase (bottom) measured, in less than 30 seconds without any data averaging, on a very good monopulse antenna at 94 GHz.

Fig.II.21.

The antenna measurement facility at Matra Marconi Space, Toulouse, France, is equipped with MVNA-8-350 since 1991. A great number of vector antenna charaterizations could be operated in the millimeter range. Due to very accurate determinations, especially on the phase center, the necessary room for final geometry adjustments at the telescope focus could be reduced by an order of magnitude, which is very interesting in view of satellite radiometers. In Fig.II.21, top, is shown the measured MVNA+ESA signal amplitude stability during 15 hours, when temperature of the laboratory drops for about 2.5 °C, Fig.II.21, bottom.

Fig.II.22.

A telescope antenna has a single focus. However it is quite possible to use the same telescope for combined observations at different frequencies and polarizations, using beam splitters, dichroic filters, grid polarizers, etc. Such systems are particularly useful for increasing the efficiency of expensive satellite missions. The number of different frequencies can be as large as five (Matra-Marconi Space, in progress). In Fig.II.22 is shown the schematic diagram of a four-frequency telescope platform. The four frequencies: 63, 118, 184 and 205 GHz, are related to the molecular species to be observed: O_2, H_2O and O_3. The reversed (from detector to source) optical path at 205 GHz (O_3 frequency) is: the scalar horn, a parabolic mirror, a polarizer, an elliptic mirror, the dichroic filter d1, the dichroic filter d0.

FIG.II.23.

The phase center precise determination is particularly necessary when the cylindric symmetry of the antenna is broken. This is the case for a scalar horn fed through a dichroic filter, due to the refraction of the incident beam across the filter finite thickness (see Fig.II.23).

Fig.II.24.

The angular vector antenna pattern observed from the scalar horn-dichroic mirror system can be extremely good, as soon as the rotation is operated around the true phase center. Fig.II.24, communicated by Matra-Marconi Space, shows such a nearly perfect Gaussian beam observed at 62.5 GHz on the E and H-planes of the horn-dichroic mirror of Fig.II.23. Circles and triangles are for the amplitude, in dB, of E and H-planes, respectively. Crosses and X are the phase, in degrees, for E and H-planes, respectively.

Fig.II.25.

The copolar and crosspolar diagrams are obtained by data treatment after "azimuth" acquisition (horizontal rotation of the tested antenna) operated at different "roll" (roulis) angles (the tested antenna is rotated along its own axis), for a vertical polarization of the emitted wave at first, then for an horizontal polarization of the emitted wave. A perfect Gaussian beam gives, naturally, circles for a given intensity in the copolar diagram. Fig.II.25, communicated by Matra-Marconi Space, shows such a very good copolar diagram, obtained on the horn-dichroic filter of Fig.II.23 at 62.5 GHz. From the center at 0 dB and going to any external direction, one finds the circles at the levels -5, -10, -15, -20, -25 and -30 dB.

Fig.II.26.

In Fig.II.26, communicated by Matra-Marconi Space, is shown the crosspolar diagram obtained at 62.5 GHz from the scalar horn-dichroic mirror of Fig.II.23. The comparison with Fig.II.25 leads to the good maximum crosspolar/copolar ration at -26.5 dB.

Fig.II.27.

The very complicated 205 GHz optical path described in Fig.II.22 gives a reasonably good antenna pattern, as measured in Fig.II.27 at Matra-Marconi Space. Same symbols as in Fig.II.24.

Fig.II.28.

The copolar diagram of a non-perfectly Gaussian beam deviates from circles. In Fig.II.28, communicated from Matra-Marconi Space, is shown the copolar diagram of the 205 GHz channel of Fig.II.22. From the center at 0 dB, one finds the curves at -5, -10, -15, -20, -25 and -30 dB, respectively.

Fig.II.29.

The crosspolar diagram corresponding to the copolar diagram of Fig.II.28 is shown in Fig.II.29, from Matra-Marconi Space. The comparison of the two gives still a good maximum for the ratio crosspolar/copolar at -25 dB.

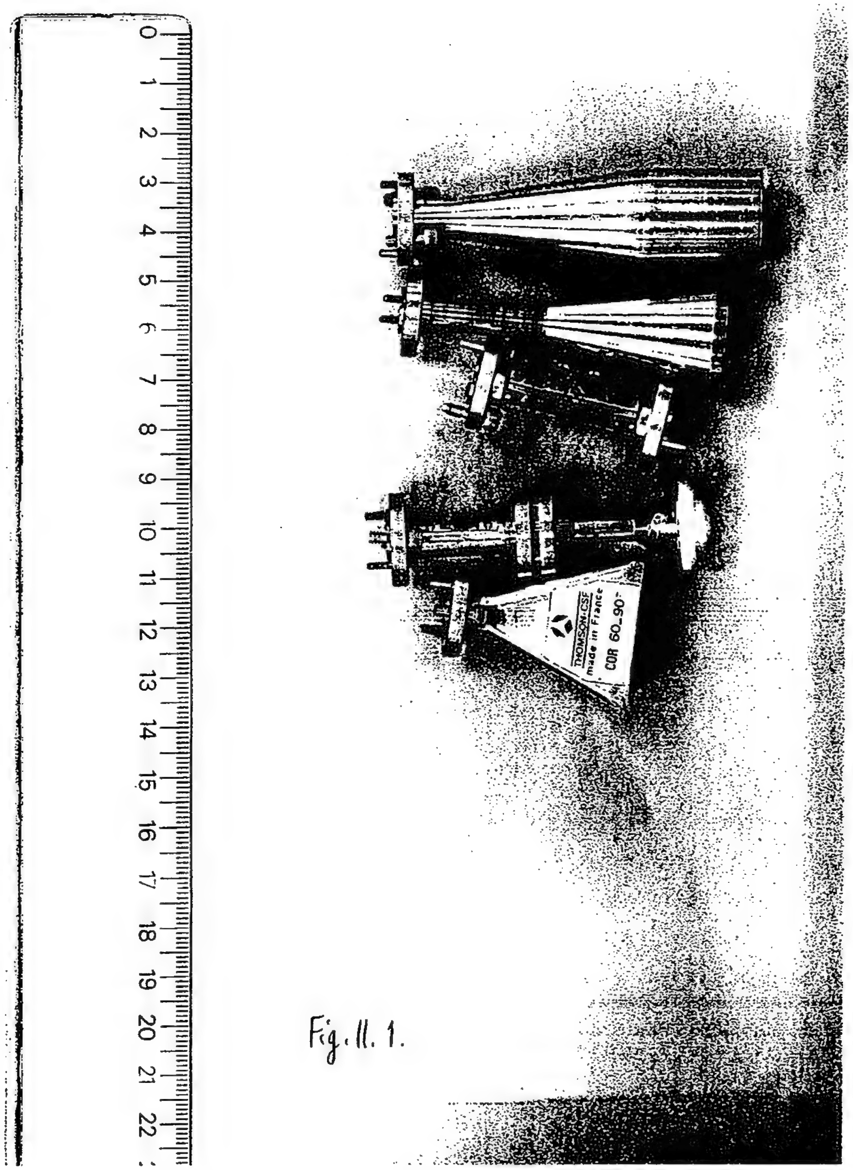

Fig. II. 1.

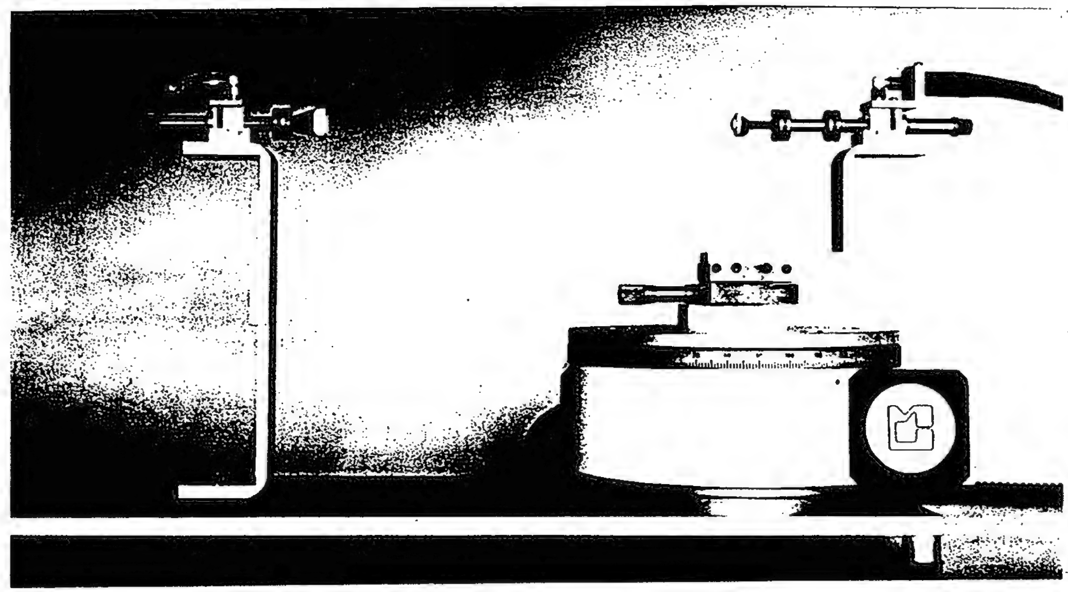

Fig. II.2.

CIRCULAR CONICAL
HORN ANTENNA

(Actual size)

circular

transition

rect.

WR-15

H (top) and E (bottom) planes antenna patterns observed at 50 GHz.
A -90°/+90° trace is obtained in 30 seconds. Each pattern has been measured twice. Notice the perfect reproducibility.
The noise level is at -86 dB below the on-axis signal.

6 Sept 1988. AB MILLIMETRE

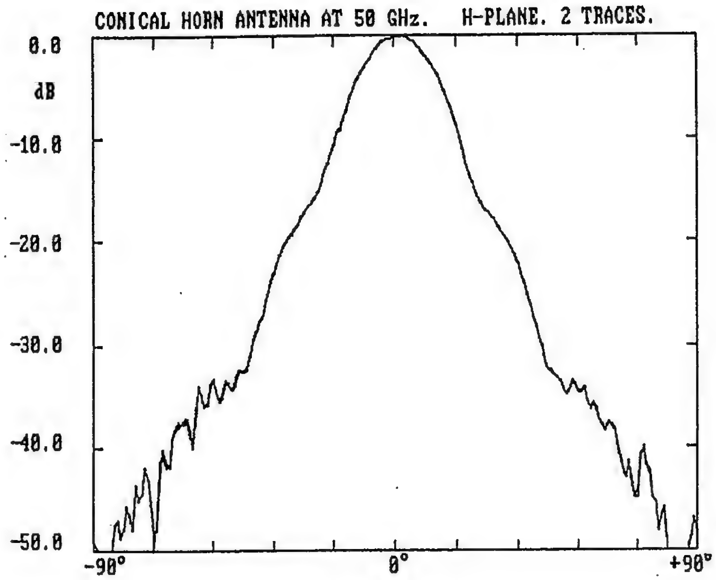

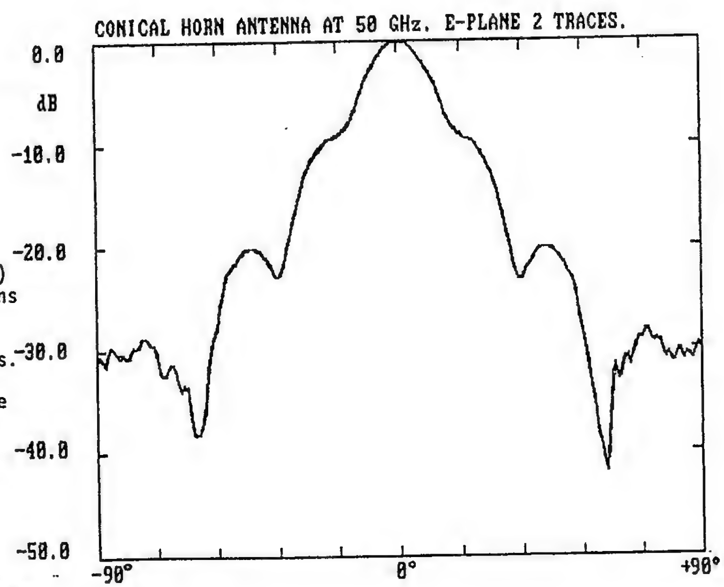

Fig. 11.3.

SCALAR HORN
ANTENNAS

(Actual size)

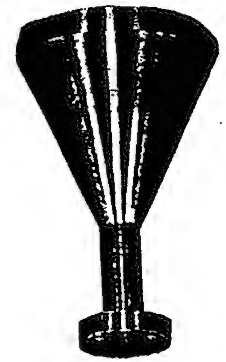

WR-10

This corrugated horn antenna (above) has extremely low side lobes (top figure).

(Actual size)

WR-4

This corrugated horn antenna (above) has a purely Gaussian pattern in both H and E planes, to -20dB (bottom figure).

6 Sept 1988. AB MILLIMETRE

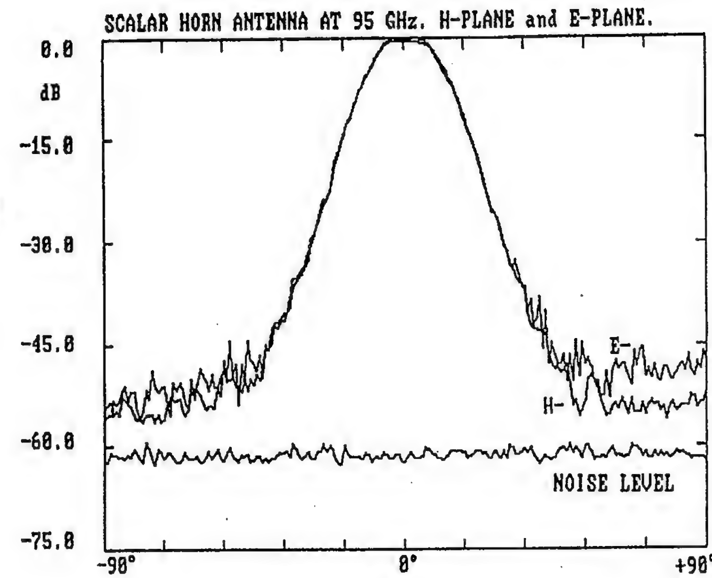

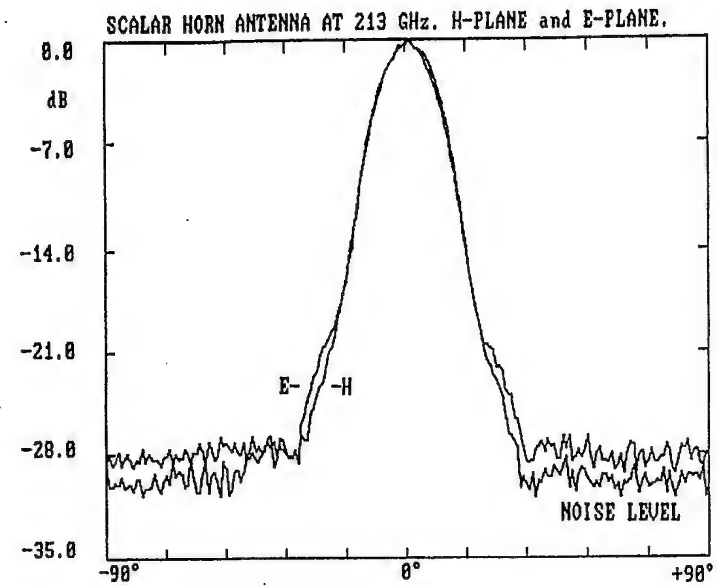

Fig. 11.4.

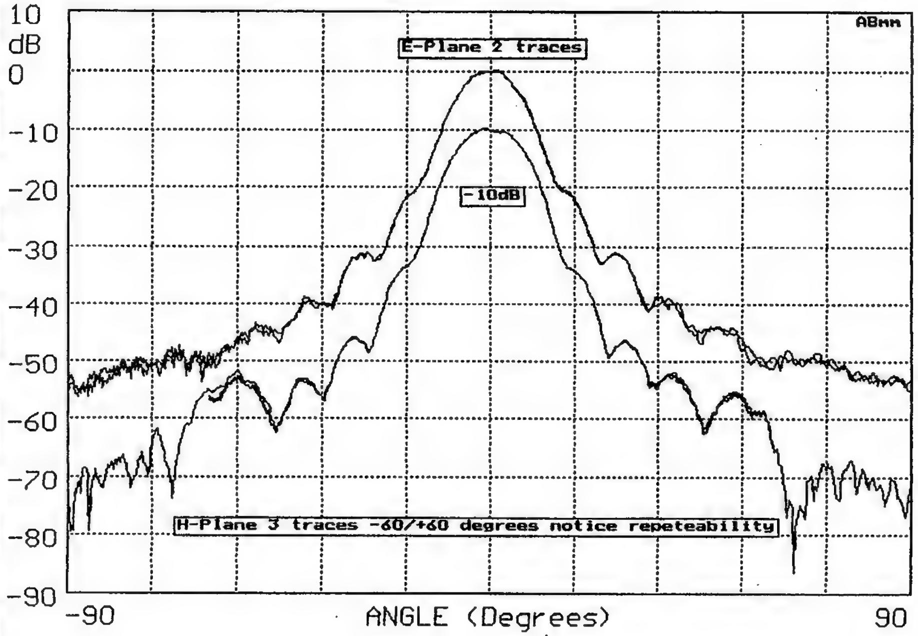

Fig. 11.5.

AB MILLIMETRE MSNA OFFERS THE EASIEST
AND MOST ACCURATE
WAY OF MEASURING ANTENNA PATTERNS

H-Plane rectilinear plots of a Gaussian Optics Lens Antenna at 60 GHz.
Horizontally : Azimuth in Degrees.
Vertically : relative Power in dB.

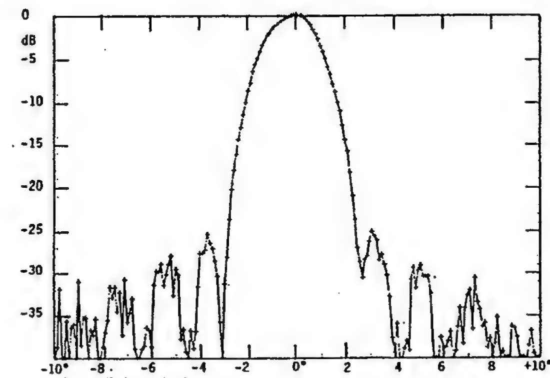

Top :
As provided by the Factory.

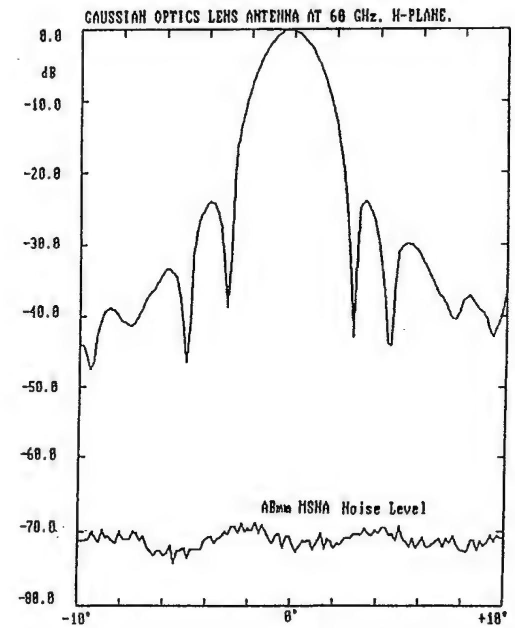

Bottom :
As done in 20 seconds with **AB MILLIMETRE MSNA.**

6 Sept. 1988.
AB MILLIMETRE

Fig. 11.6.

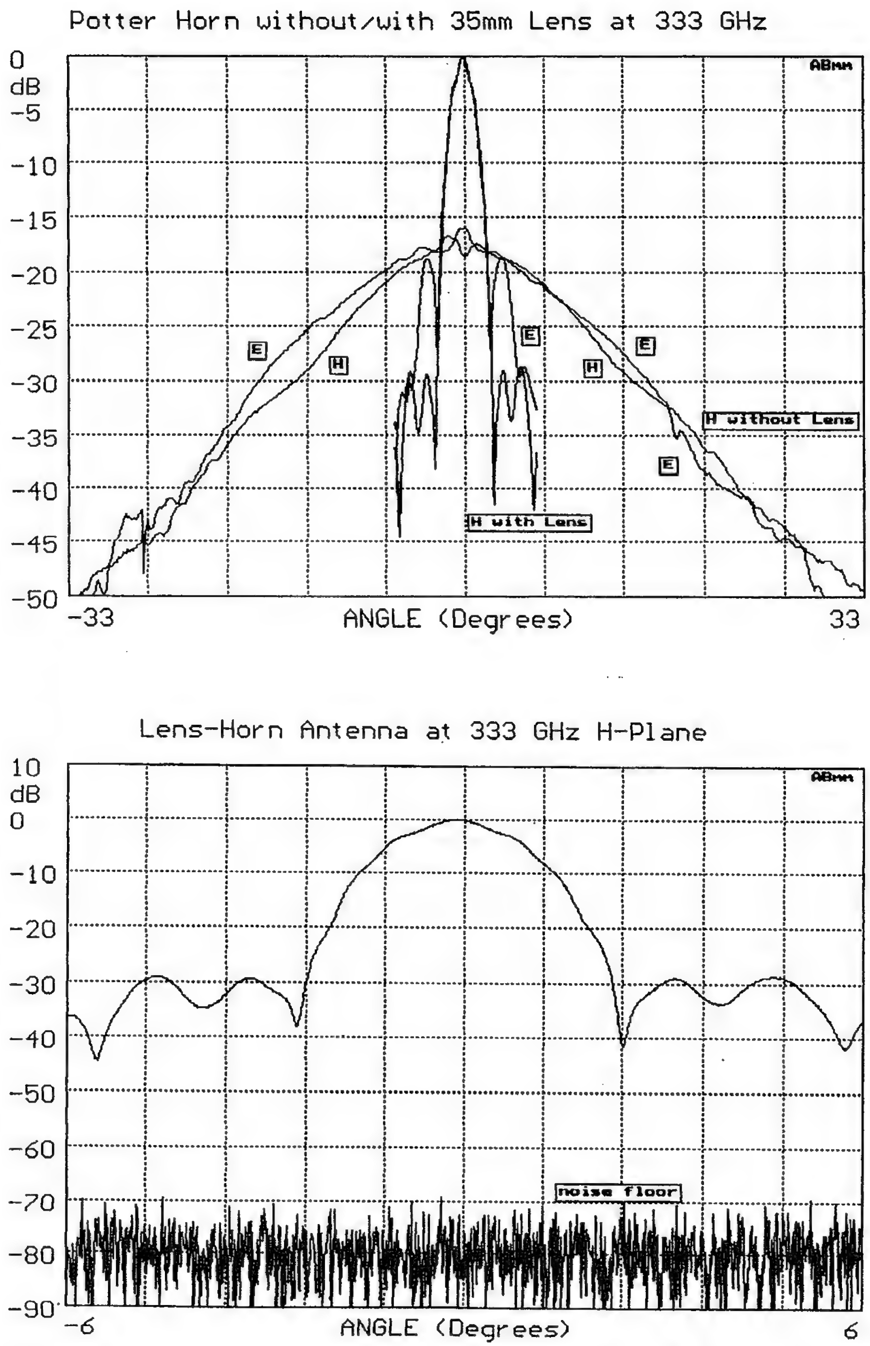

Fig. 11.7

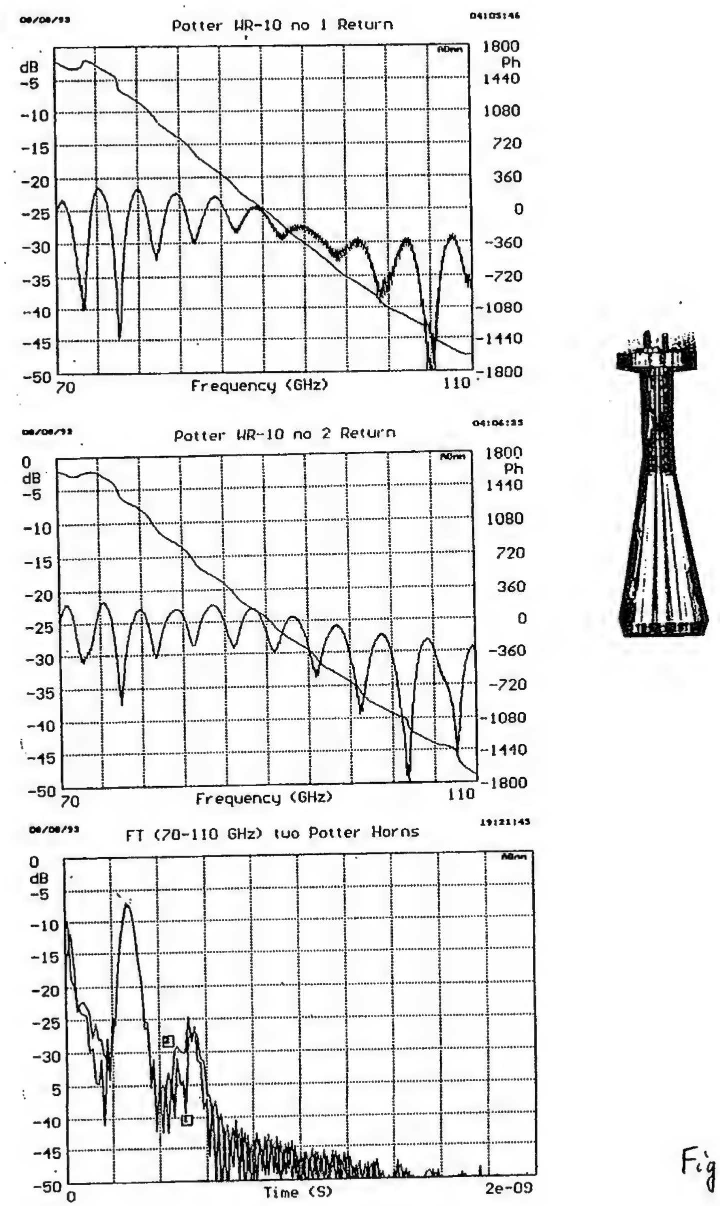

Fig. 11.8.

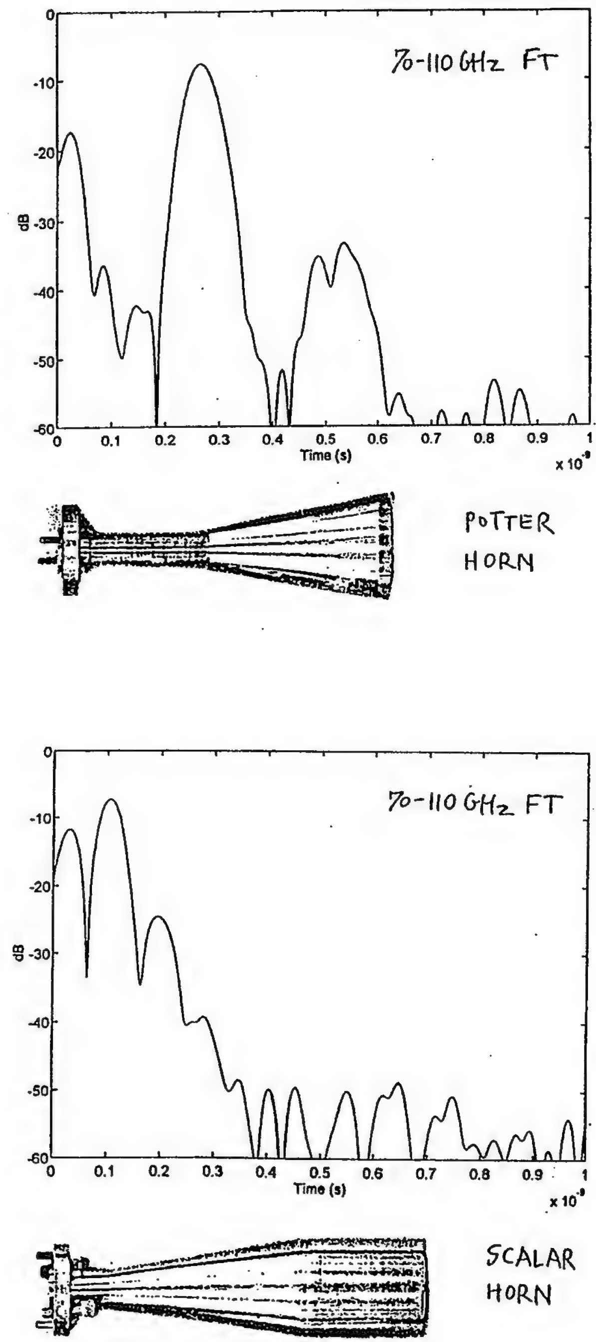

Fig. 11.9.

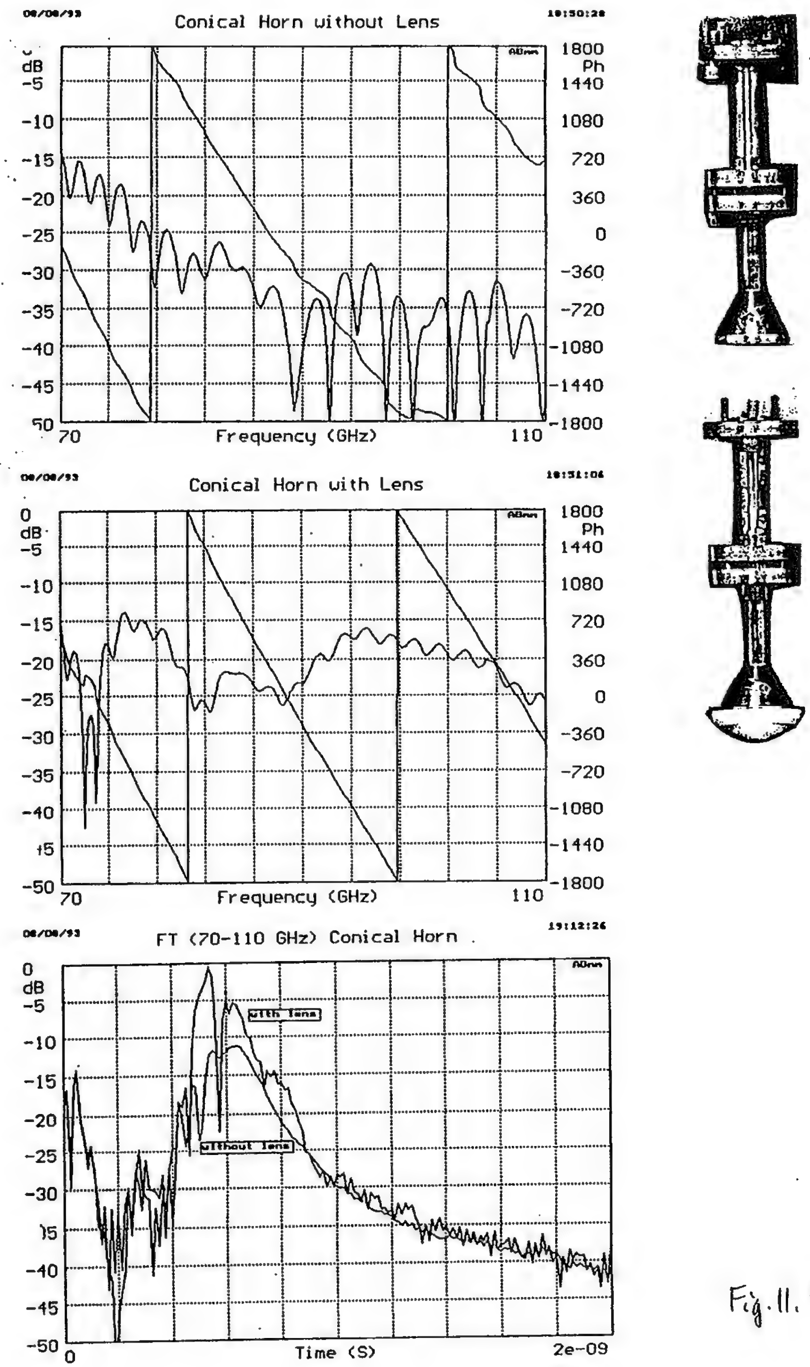

Fig. 11.10.

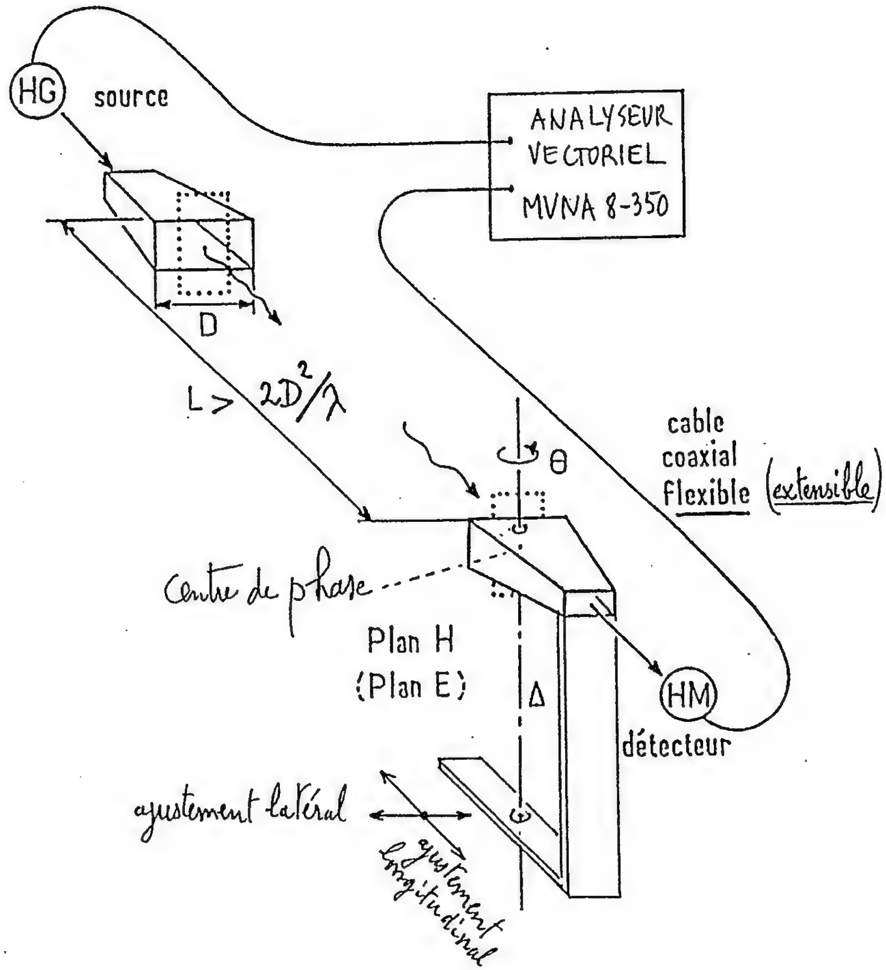

Fig. 11.11.

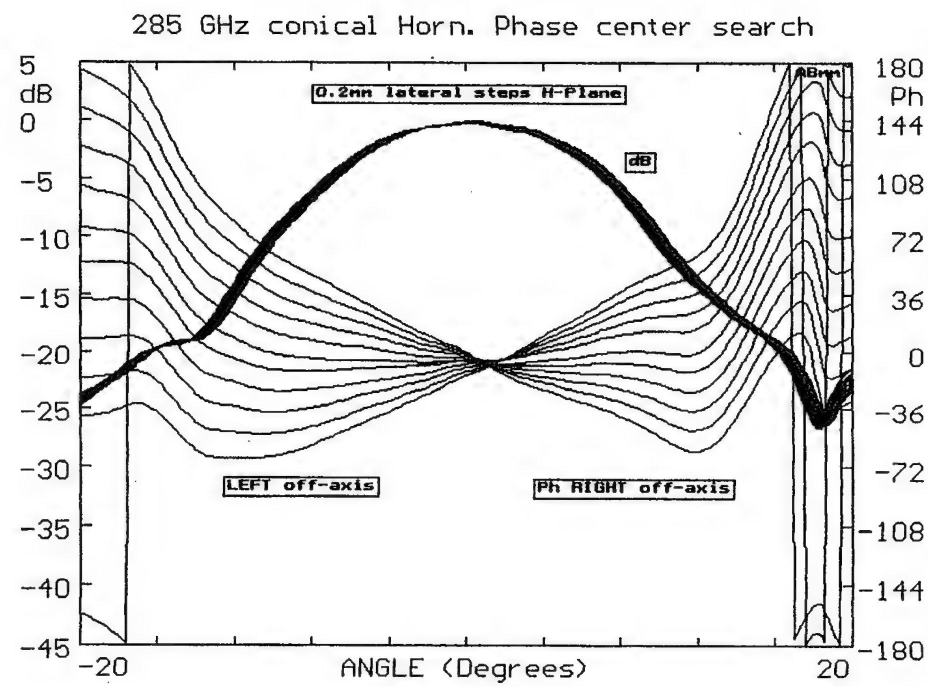

Fig. 11.12.

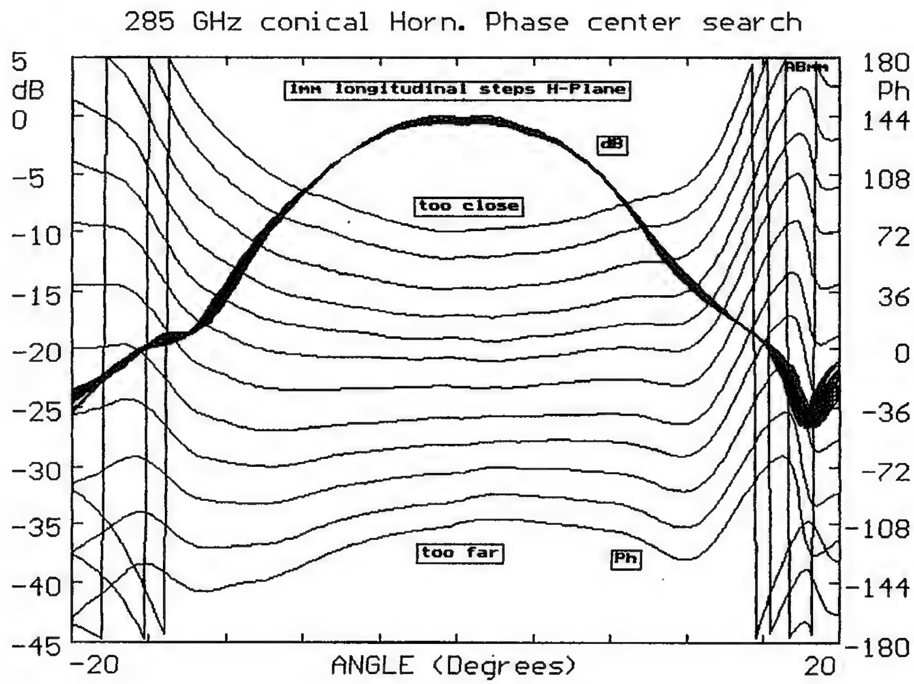

Fig. 11.13.

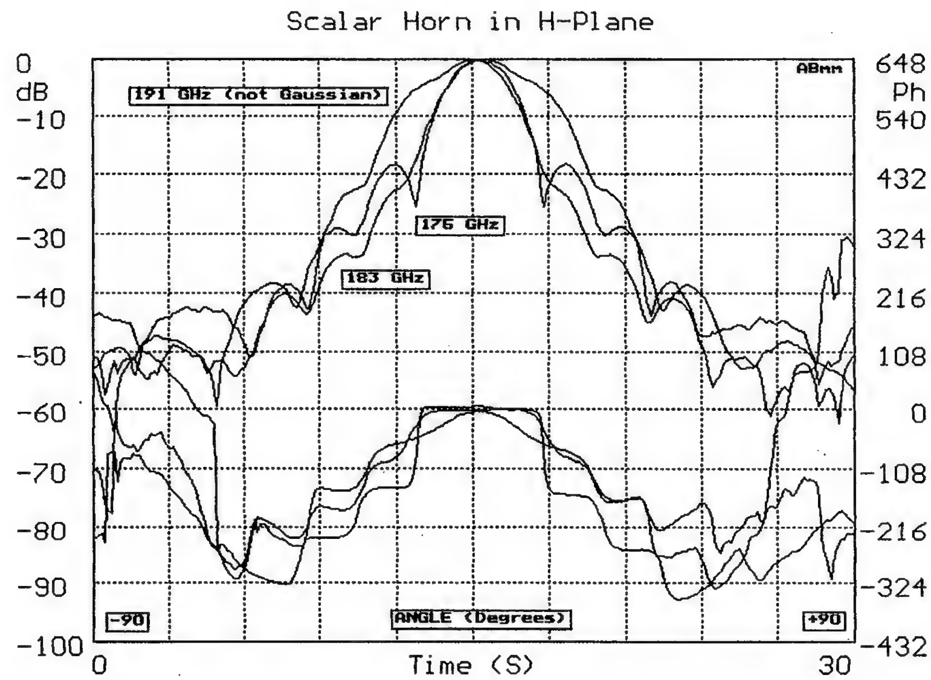

Fig. 11.14.

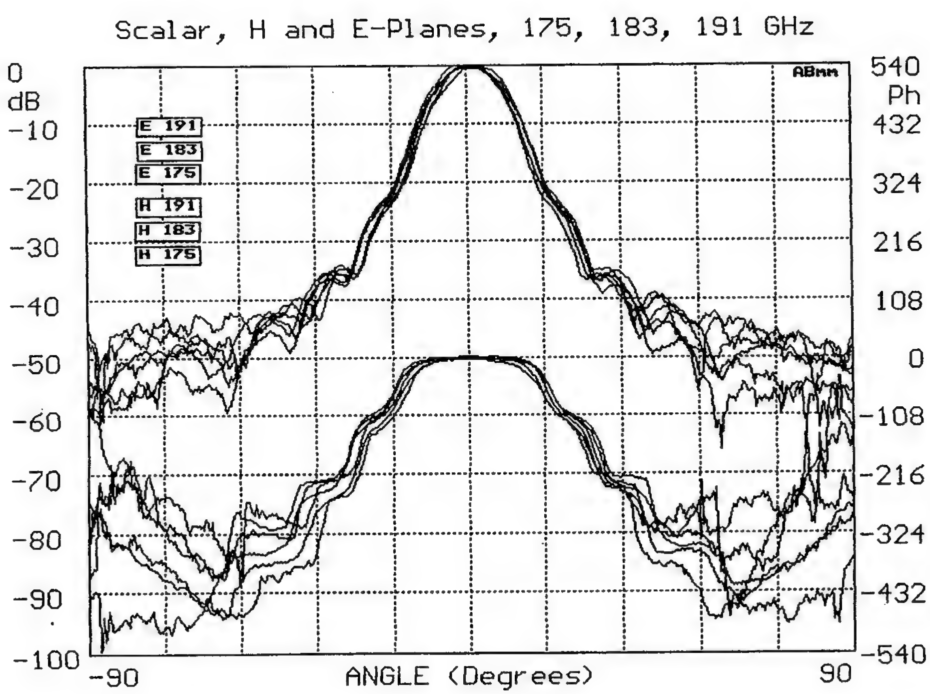

Fig. 11.15.

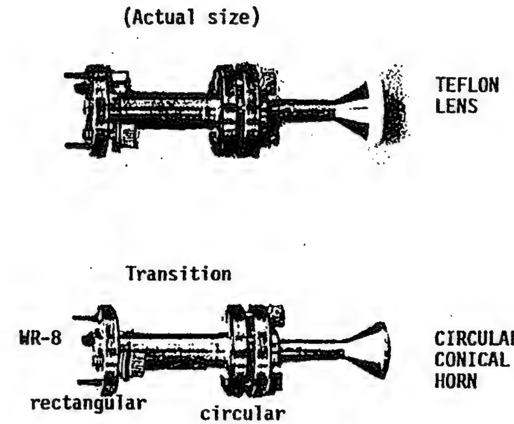

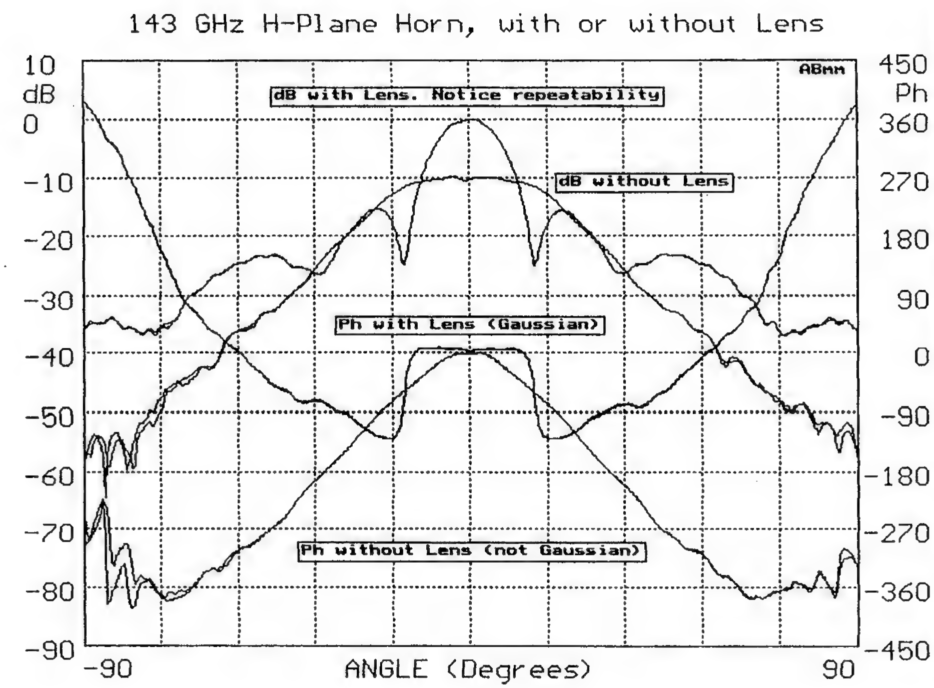

Fig. 11.16.

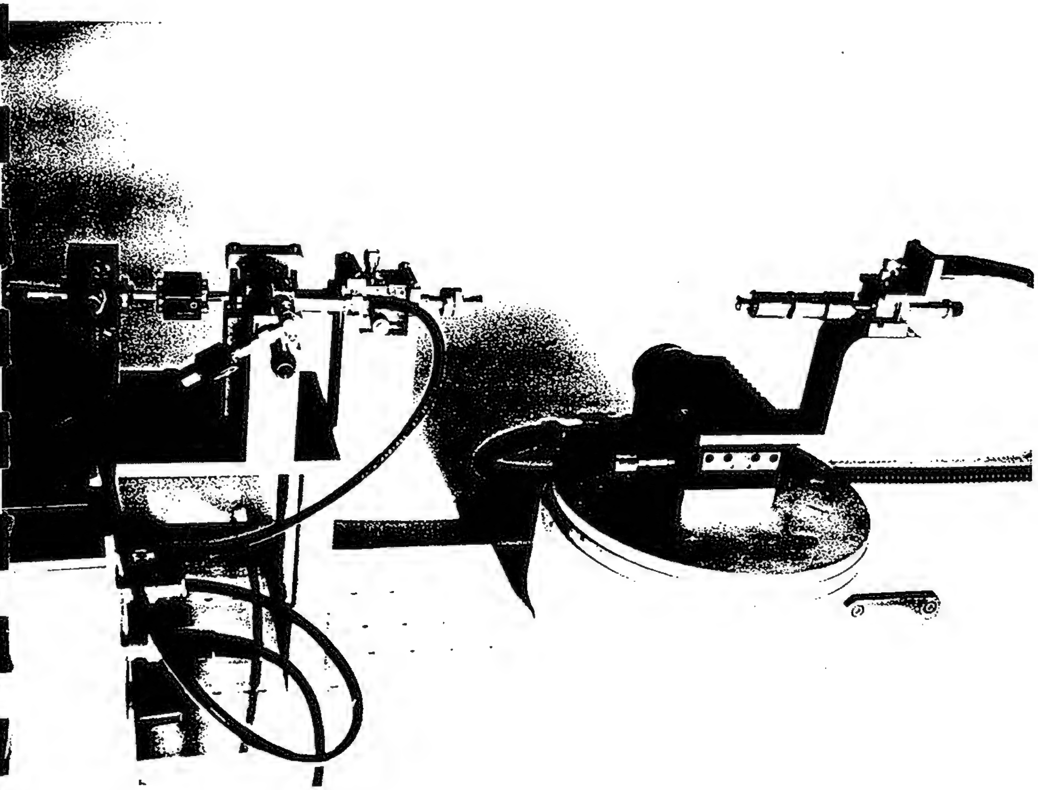

Fig. 11. 17.

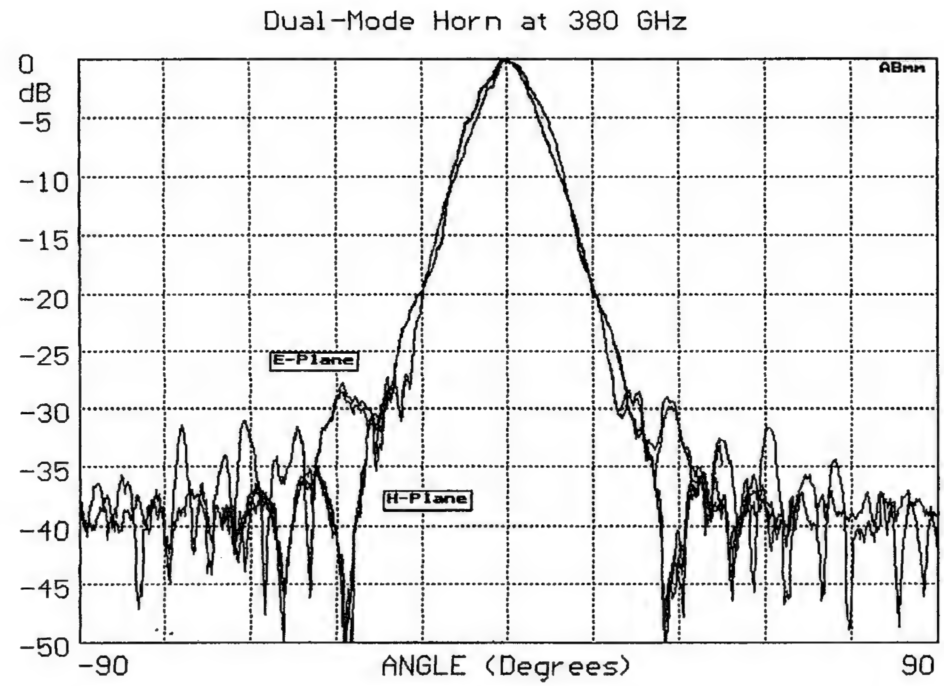

Fig. 11. 18.

380 GHz Dual Mode Horn H-Plane

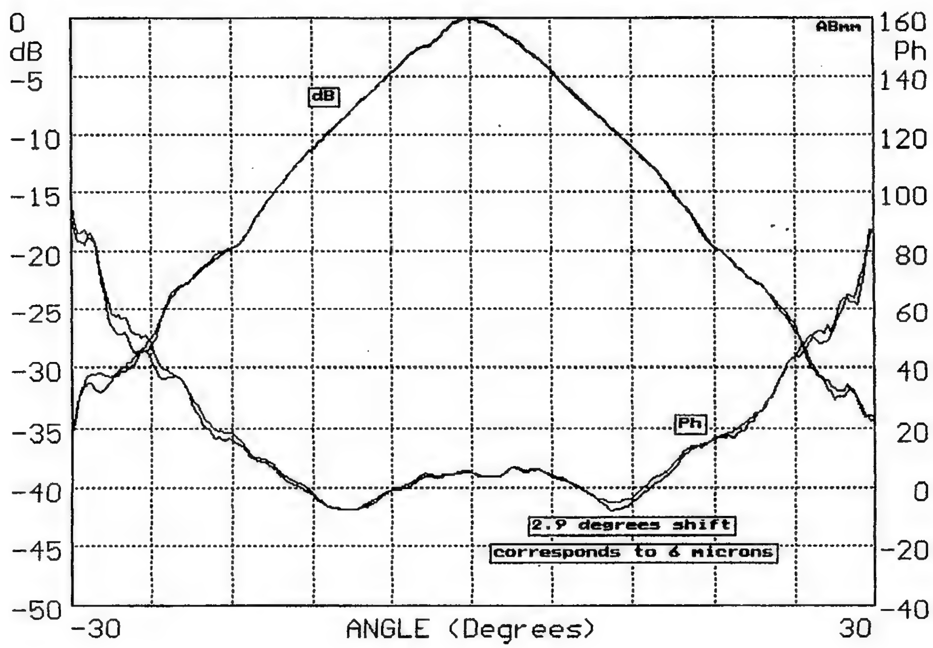

Fig. 11.19.

Monopulse Antenna, channels sum & difference

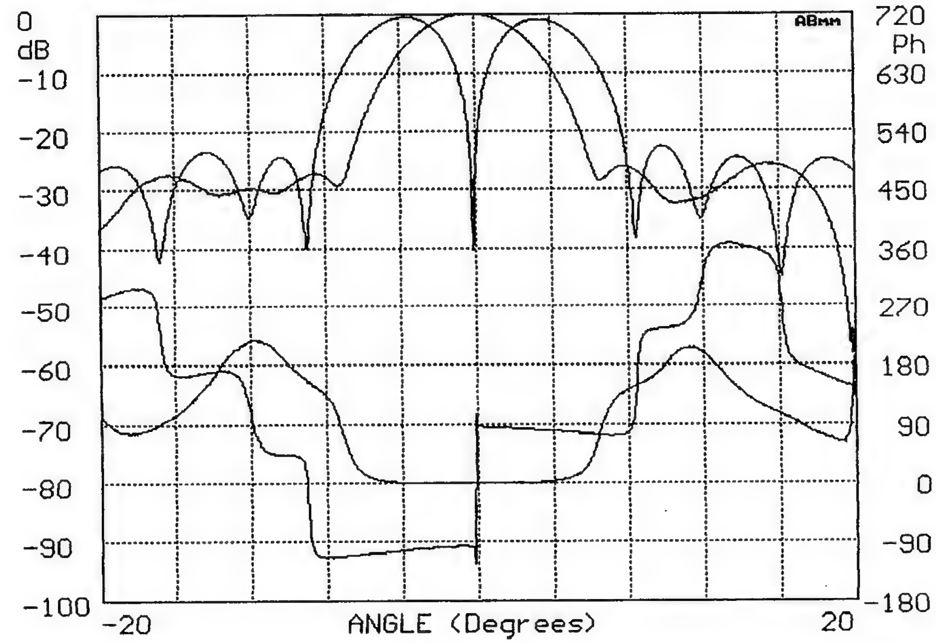

Fig. 11.20.

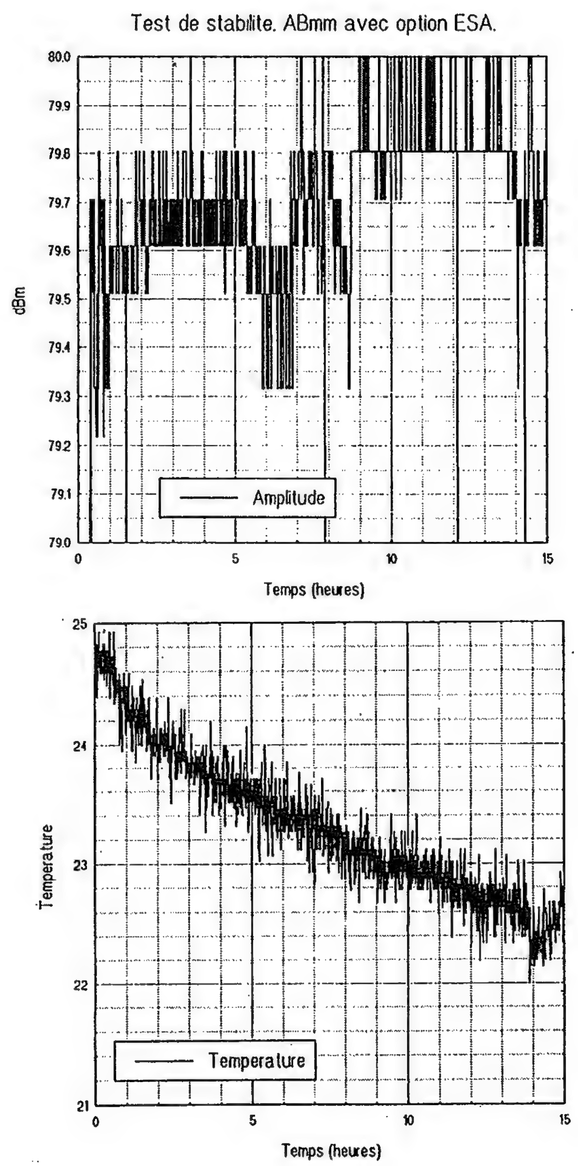

Fig. II.21.

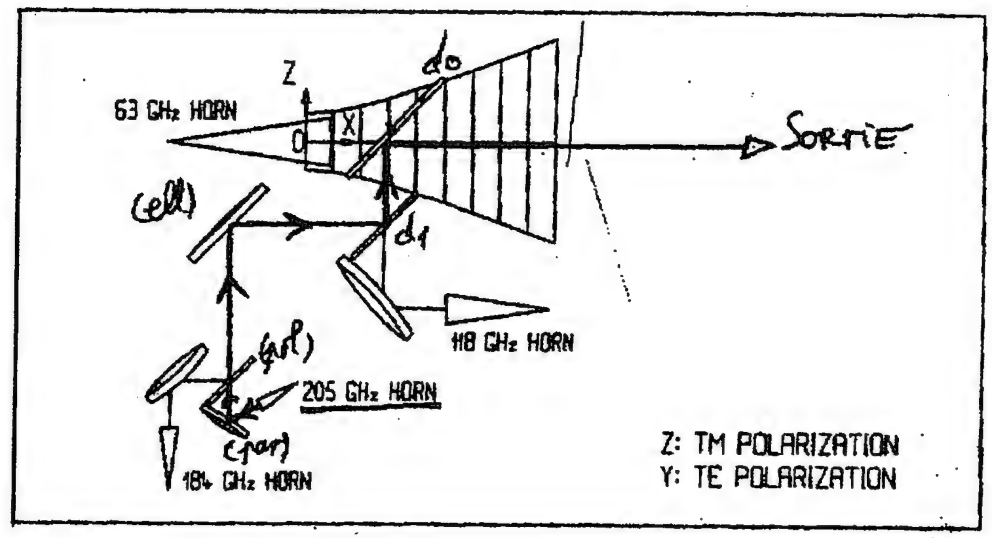

Fig. II.22.

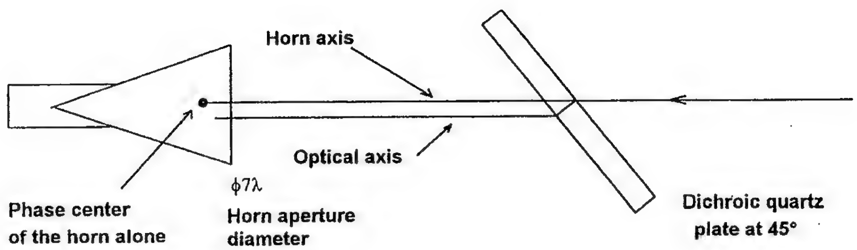

Fig. 11. 23.

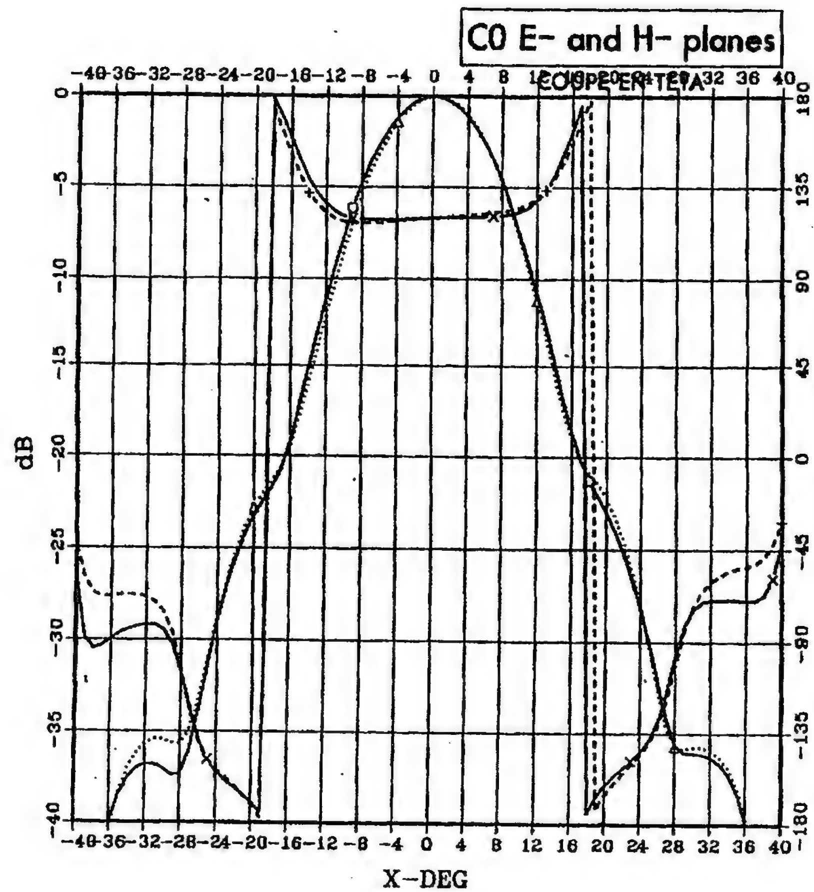

Fig. 11. 24.

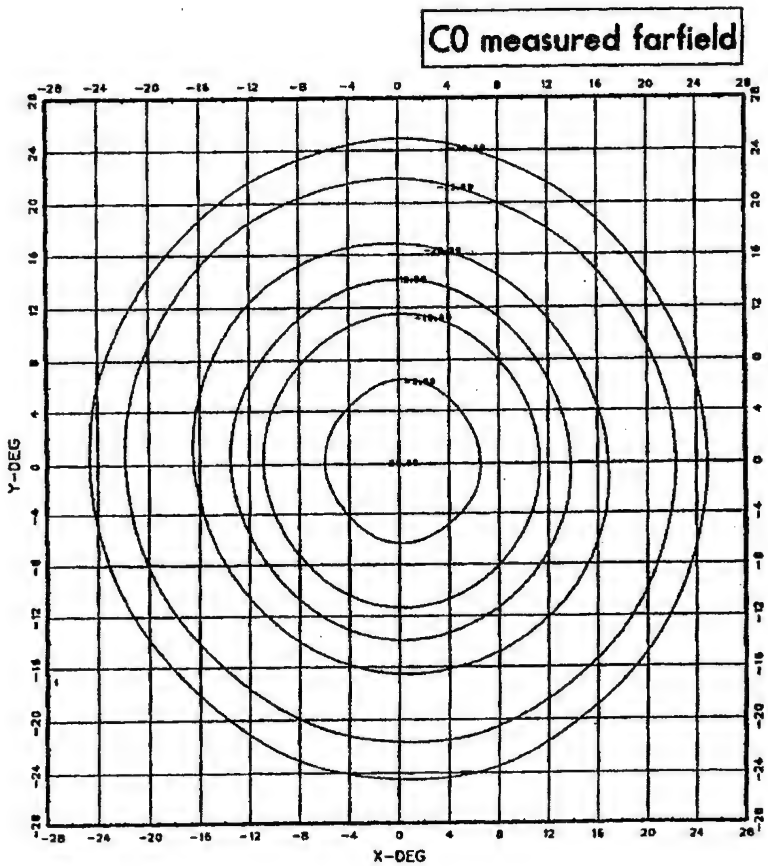

Fig. 11.25.

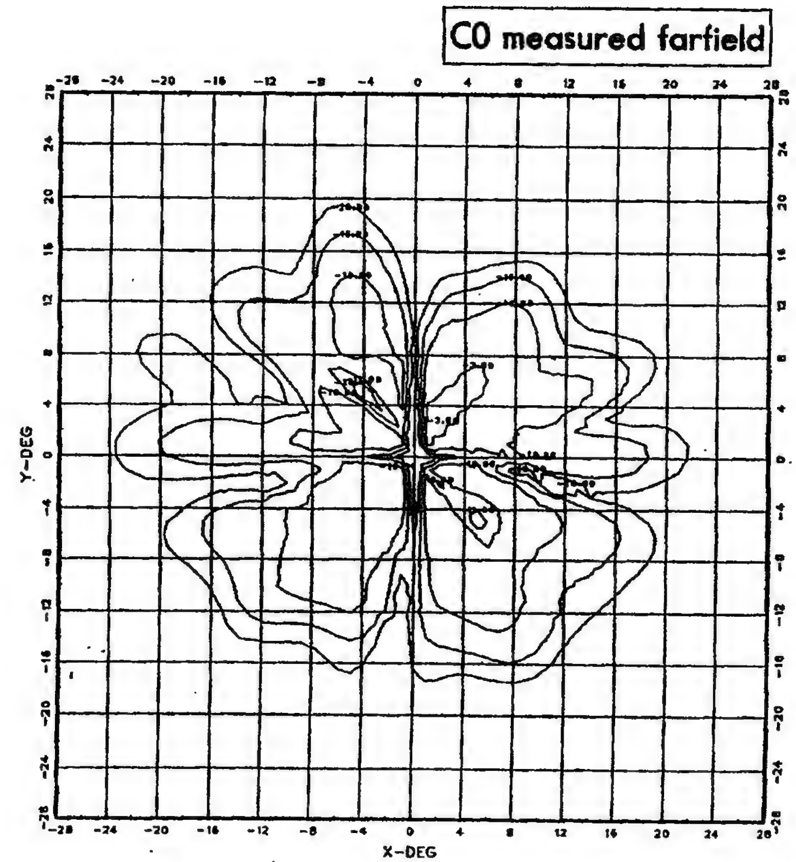

Fig. 11.26.

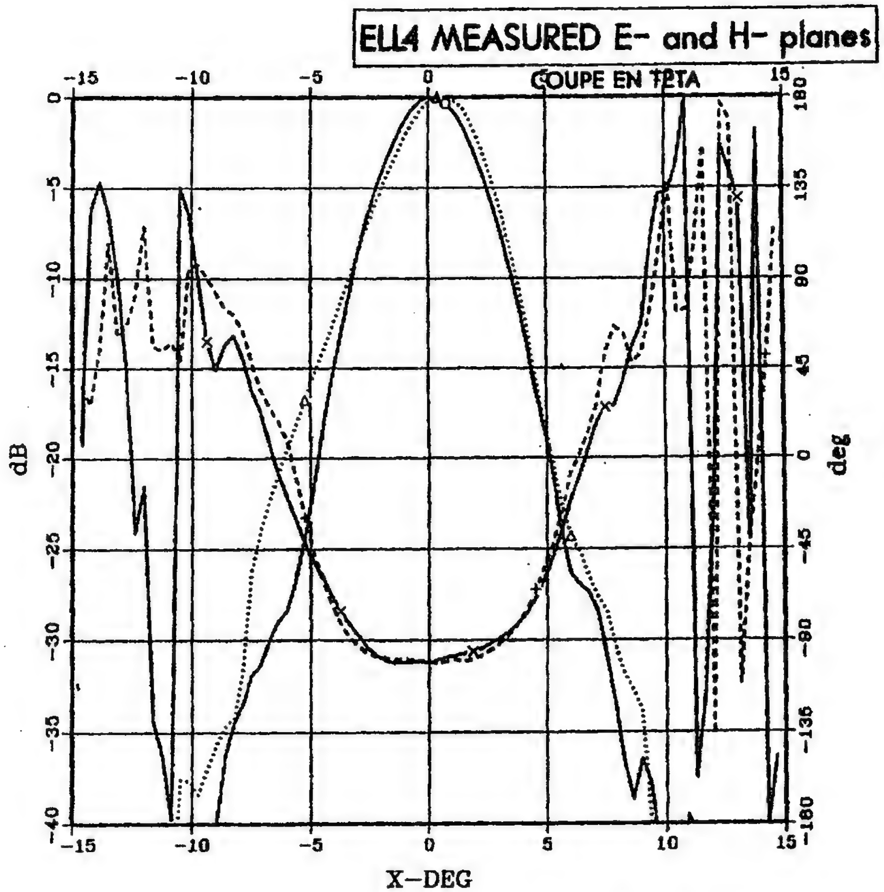

Fig. 11. 27.

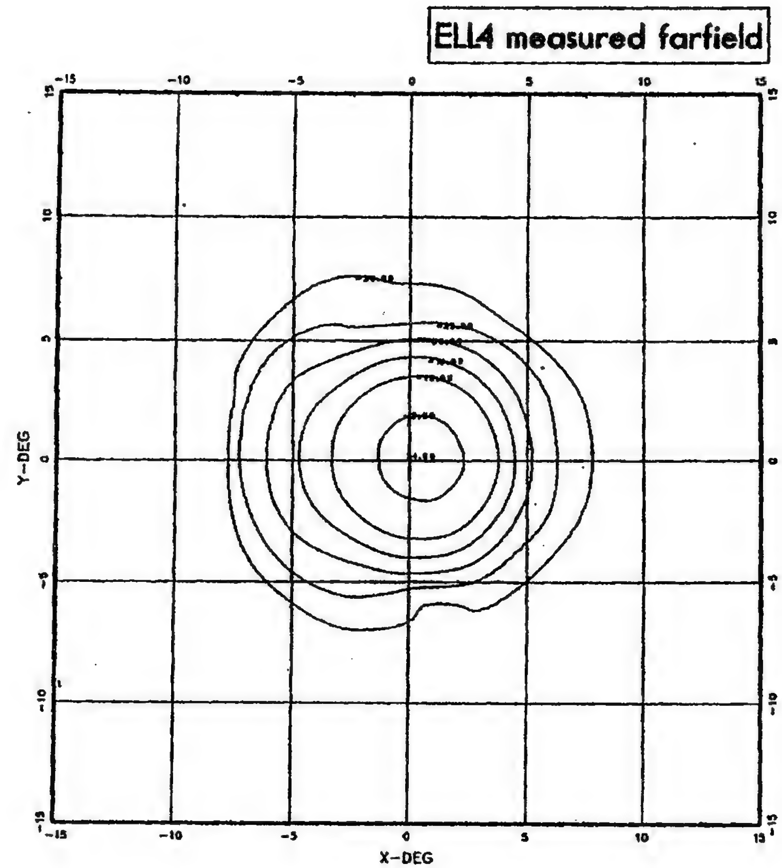

Fig. 11. 28.

ELL4 measured farfield

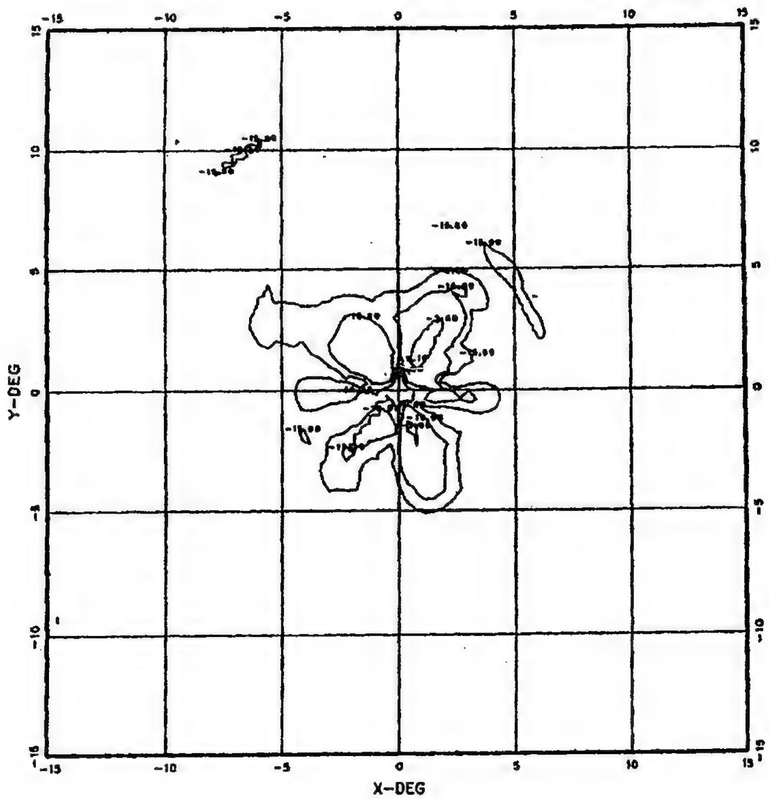

Fig. II. 29.

Fig.III.1.

With the vector analyzer MVNA 8-350, the transmission between the two horns (or two horns refocussed by two, or four, lenses) is firstly calibrated. Then one introduces the sample between the horns, and measures the change in amplitude and phase. For dielectric materials, and when eliminating the standing waves effects, the change in phase can give the permittivity ε', and the change in amplitude the loss tangent $\tan\delta$.

The change in phase $\Delta\phi$ (in degrees) due to the introduction of the slab of thickness e and refractive index n, instead of the same thickness of air of refractive index close to 1, can be predicted, with an integer number of turns k:

$$(n-1)e/\lambda = (\Delta\phi/360) + k \qquad \text{(III.1.)}$$

the refractive index n is related to the permittivity ε' by the law:

$$\varepsilon' = n^2 \qquad \text{(III.2.)}$$

When the dielectric material is relatively lossy (practically loss tangent $\tan\delta > 0.001$), measurement of the $\tan\delta$ is extracted from the observed decay of transmission α (in dB/cm), through the formula:

$$\tan\delta = 1.1\ \alpha(\text{dB/cm})/nF(\text{GHz}) \qquad \text{(III.3.)}$$

Fig.III.1, top, shows a rectangular plot, bottom a polar plot, with the amplitude in dB as the radius, and the detected phase as the angle, when introducing a bevelled Plexiglas sample between horns at 186 GHz. Both variations (amplitude drop in dB, phase) are linear with the actual thickness of Plexiglas, explaining the observed spiral shape. There is 13 phase turns (k=13, $\Delta\phi$=0), and the drop is 6 dB for 35 mm, so that one obtains the good values of permittivity ε'=2.59, and loss $\tan\delta$=0.006.

Fig.III.2.

Most of the samples to be measured have a simple plane-parallel shape, and the observed phase rotation does not give the integer number of turns. Then, several frequency points, or a frequency sweep, can give a complete determination of phase variation. The measurement in Fig.III.2. is performed with two rather poor quality E-Band (60-90 GHz) pyramidal horns facing each other. After a first frequency sweep to take the intrumental response, a 20mm thick fused quartz Tokamak window has been introduced at a given position between the horns. Then, the position of this sample has been changed before a second measurement. The superimposed two traces in Fig.6 show mostly the standing waves between the sample and the horns, which look like noise, but which are quite reproducible. (Measurement realized at Cadarache - Tore-Supra reactor, thanks to G. Berger-By and M. Paume).

Fig.III.3.

Fig.III.3, top, presents the Fourier Transform FT of the transmitted signal with the dielectric sample in the 1st position of Fig.II.2, and Fig.III.3, bottom, the FT of the 2nd position.

Fig.III.4.

In Fig.III.4, top, are simply superimposed the FT signals (of Fig.III.3) corresponding to the two sample positions. The first two peaks are not changed: they correspond to the time necessary for the wave to cross the sample. In Fig.III.4, bottom, are superimposed these signals, after having moved the second versus the first by an offset corresponding to the change in position of the sample, between the two recordings of Fig.III.2. The peaks due to the reflexions between the sample and the fixed obstacles, such as the horns, are now superimposed. The FT filtering will be operated by cutting these contributions.

Fig.III.5.

Fig.II.5. is the same as Fig.III.2, after filtering the spurious standing waves effects on the Fourier transform as indicated above. One clearly sees the ondulations due to standing waves inside the sample. The phase evolution gives $\varepsilon'=3.802$, and the loss is very small since the transmission maxima cannot be distinguished from 0dB (measurements in quasi-optical open cavity give $\tan\delta=0.0004$). Since the quartz slab sample is a low-loss material with a rather high permittivity, its acts as a Fabry-Pérot resonator, showing oscillations in amplitude with a period ΔF, according to the law:

$$\Delta F = c/2ne \qquad \text{(III.4.)}$$

The oscillations period (Eq.4) gives an approximate value of ε'. However it is the observed phase variation which gives the most accurate ε' determination (by Eqs.1-2).

Fig.III.6.

Standing waves problems and FT filtering solutions can also be observed in reflexion measurements. In Fig.III.6, top, is shown the signal amplitude reflected from a sapphire (dielectric constants $\varepsilon'=9.40$, $\tan\delta<0.001$) slab 9.97 mm thick, before and after filtering. Fig.III.6, bottom, is the polar plot, where the filtered signal is shifted by 180° for clarity.

Fig.III.7.

Transmission and reflexion amplitudes observed at the same time are varying in opposite directions, like it is observed with a 9.97 mm thick sapphire sample in Fig.III.7 (top: in dB, bottom: linear). The observed transmission minima correspond to maxima in reflection, with a maximum reflection amplitude coefficient r such as:

$$r = (\varepsilon'-1)/(\varepsilon'+1) \qquad \text{(III.5.)}$$

($r=0.8=-1.86$ dB for $\varepsilon'=9.40$ in sapphire). The corresponding minimum amplitude transmission coefficient t can be deduced from conservation power law:

$$r^2 + t^2 = 1 \qquad \text{(III.6.)}$$

($t=0.6=-4.59$ dB for sapphire).

Fig.III.8.

Fig.III.8. shows the polar plot of Fig.III.7. Reflexion signal describes a big circle R (due to full interference between multiple reflections). Transmission signal T decribes a cycloid. This clover-shape curve is the vector sum of the unity circle (transmission through the optical thickness ne of the sample slab without noticeable loss) with the transmission interference resonance circle, which is also shown (small circle "T-lin Ph" at right, obtained by substracting the linear variation of the phase in T).

Fig.III.9.

Transmission signal is enough for characterizing dielectric materials. Fig.III.9 shows the transmitted signal of Fig.III.7, with the actual phase "Ph" (declining trace), and the deviation of the actual phase from linear decrease ("Ph-Linear" trace around zero degree, corresponding to the small circle "T-lin Ph" in Fig.III.8). The actual phase exactly coincides with the purely linear variation, at the frequencies Fk where the transmission is maximum:

$$Fk = kc/2ne \qquad k \text{ integer} \qquad \text{(III.7.)}$$

or at the frequencies Fk' where it is minimum:

$$Fk' = (2k'+1)c/4ne \qquad k' \text{ integer} \qquad \text{(III.8.)}$$

The best frequencies for obtaining the permittivity ε' from the simple linear phase variation will be at the frequencies Fk and Fk'. The best frequencies for the loss are only at the values Fk (where the there is no standing waves inside the sample), the values at Fk' being the worst, due to maximum standing waves effects across the sample.

Fig.III.10.

By the single path transmission technique between horns as described above, materials which are not too much transparent will be easy to characterize. Fig.III.10 shows the transmitted signals observed through 5.06, 9.91, 19.96 mm thick PVC polymer samples (PolyVinylChloride, $\varepsilon'=2.825$, $\tan\delta=0.01$).

Fig.III.11.

With a 20.95 mm thick epoxy sample (Araldite) which is rather lossy, the standing waves oscillations are damped, so that the dielectric determination is fast and accurate (Fig.III.11, transmission and reflexion, top rectangular plot, bottom polar plot. One obtains from the measured transmitted Phase variation $\varepsilon'=2.90$, and from the amplitude drop $\tan\delta=0.02$).

Fig.III.12.

Most of our transmission measurements in the 70-100 GHz interval have been realized with a two-lens setup, the distance between the lenses being 200 mm, each lens having 100 mm focus. The source scalar horn aperture is placed at 200 mm from the first lens, the aperture of the detector horn at 200 mm after the second lens. After calibration of the instrument, the sample is inserted at mid-distance between the lenses. This setup is not free from standing waves effects, as it can be seen from data obtained at the European Microwave Conference, 5-8th September 1994. Fig.III.12, top, shows observed transmission, without filtering, through 9.97 mm sapphire (compare to Fig.III.8) and through 20.95 mm Araldite (compare to Fig.III.11, bottom). A substantial reduction of these standing waves is obtained when inserting attenuators between the horns and the lenses (Fig.III.12, bottom), total attenuation 30 dB.

Fig.III.13.

As observed above in a frequency sweep, standing waves give pig's tail shapes to the data. Periodic variation with position may also be seen at a fixed frequency, when moving the sample. The standing waves effects will be minimized at the frequencies according to Eq.III.7. Thus, a longitudinal move of the sample along the common axis xx' of the lenses would not induce any change to the measurement. On the contrary, standing waves effects are maximized at fixed frequencies according to Eq.III.8. A series of measurements have been performed, with the two-lens setup equipped with two attenuators (as in Fig.III.12, bottom) onto four dielectric samples moved along the xx' axis: Plexiglas thickness 3 mm, Araldite 20.95 mm, Teflon 10 mm, Sapphire 1.91 mm. For each sample, two frequencies have been used, the "best" (Eq.III.7) and the "worst" (Eq.III.8). Results are shown on Fig.III.13, where the "best" frequencies ("g" is for GHz) give small dots and accurate measurements, and "worst" frequencies give ellipses.

Fig.III.14.

The lenses of the 70-110 GHz setup do not have any surface treatment. They can be used at any frequency. Thus, the two-lenses setup can be used at submillimeter wavelengths. Scalar W-band horns are replaced by Potter horns, for instance at 475 GHz. Standing waves effects are observed at the 475 GHz fixed frequency, and can be damped by the attenuators. On Fig.III.14 are shown the observed signals versus the position of a 1.91 mm thick sapphire sample along the xx' axis. Top: amplitude in dB, bottom, polar plane, where 10V means amplitude unity. Without any attenuator ("no"), the standing wave pattern ("banana shape") results in the sum of the standing wave on the source Submillimeter Harmonic Generator "shg" side (large circle), and on the detector Submillimeter Harmonic Mixer "shm" side (large ellipse). Single side standing waves effects are also observed separately, each one with an attenuator on the opposite side. With the two attenuators ("2"), the measurement is reduced to a single point, Fig.III.14, bottom, or an horizontal line, Fig.III.14, top.

Fig.III.15.

Standing waves spirals are observed with the two-lens setup, used in a 474.5-475.5 GHz frequency sweep without attenuator (Fig.III.15). Good measurements are obtained with attenuators, on sapphire (9.95 mm in a, 1.91 mm in b), Araldite (0.93 mm in c), Teflon (10 mm in d), Plexiglas (3 mm in e).

Fig.III.16.

The Gunn extensions of the analyzer do not allow computer controlled large frequency sweeps, since the electronic tunability of the Gunns is of the order of +/- 100 MHz. A large submillimeter sweep, like 469-479 GHz, will be made in several steps, mechanically retuning the Gunns between steps. At such high frequencies, the losses into sapphire are large enough to be measured from simple transmission experiments, $\tan\delta=0.0008$. Damping of the standing waves by attenuators is quite necessary. As shown in Fig.III.16, large spiral (sweep versus frequency) and an ellipse (sweep versus position, at fixed 473 GHz) are visible when no attenuator is used. With the attenuators, the clover-shape curve is obtained. The losses into sapphire are large enough to be measured from this simple transmission experiment, $\tan\delta=0.0008$ at 475 GHz.

Fig.III.17.

The transmission through samples can be summarized by the polar plot of the results. In Fig.III.17, the dots, or lines (when the sample is thick enough) are given for 13 samples observed with the two-lens, two-attenuator setup, in a 283.55-284.15 GHz sweep.

Fig.III.18.

The Fig.III.18 shows results similar as in Fig.III.17, with a 473.4-474.4 GHz sweep.

Fig.III.19.

The Fig.III.20 shows results obtained in a 567.3-568.3 GHz sweep. Even with two attenuators, the standing waves are not completely damped, and the measurement accuracy is diminished.

Fig.III.20.

Measurements on polymers like araldite, plexiglas, nylon, in the millimeter and submillimeter, show practically constant values of ε' and $\tan\delta$ in the interval 18-190 GHz. Then, in the 190-760 GHz interval, are observed (see Fig.III.17-19) a very strong dependence of loss (which increases) and a slight dependence of permittivity (which decreases) on the frequency. In Fig.III.20 are shown the damping and the phase change (taken here upwards for clarity) of the microwave across a 10.95 mm thick sample of nylon The absorption strongly deviates from the extrapolation of its values observed in a 70-110 GHz sweep, for which the loss is $\tan\delta=0.0145$. It is only above 400 GHz that the phase rotation significantly deviates from the extrapolation from its values observed in the 70-110 GHz range, where one observes a constant permittivity $\varepsilon'=3.066$.

Fig.III.21.

Instead of avoiding the standing waves effects, one can characterize low-loss ($\tan\delta$ <0.01) dielectric materials in controlled standing waves devices such as the open Fabry-Pérot cavity. Then, there are many back-and-forth crossings of the microwave through the sample, and perturbation effects, like absorption, are enhanced. In Fig.III.21 are shown the resonances observed by transmission in such a cavity tuned close to 478.5 GHz, empty (top left), or loaded with a 10 mm thick Teflon sample (bottom center). The resonance fits give $\varepsilon'=2.064$ from the change in resonance position, and $\tan\delta=0.001$ from the broadening.

Fig.III.22.

A whispering gallery mode can be excited into a resonant structure (a sphere, a cylinder, etc.) via the evanescent wave emitted from a total reflexion prism. A prism with a right angle at the summit, and 45° at the other angles, cannot be made from teflon, where $n=\sqrt{\varepsilon'}=\sqrt{2.06}=1.44$, since the total reflexion angle $i = \arcsin(1/n) = 44°$ will be too close to 45°. On the contrary, Plexiglas, with $\varepsilon'=2.60$, will give $i=38°$, which is fine. A very elegant way of obtaining the loss of a dielectric will be to measure the intrinsic quality factor Qo of a cavity entirely made from this dielectric, such as a whispering gallery mode cavity. One has simply:

$$\tan\delta = 1/Q_o.$$

Fig.III.22, top, shows the amplitude transmitted through the total reflexion prism, when varying the coupling to a cylindrical Rexolite slab (i.e. simply varying the distance from the prism side to the cylinder side). The critical coupling position corresponds to a big amplitude dip. On Fig.III.22, bottom, the corresponding phase variations split into two families: undercoupled, and overcoupled, with a brutal phase step at the critical coupling. These measurements have been performed during the "Hyper '92" exhibition, Paris, January 1992.

Fig.III.23.

The polar plot of the resonances shown in Fig.III.22 is extremely clear: the critical coupling trace contains the origin. Overcoupled resonances are circles with the origin inside, and undercoupled outside. The measured quality factor Q increases with decreasing the coupling (there is less and less coupling loss). The outermost circle corresponds to the intrinsic quality factor Qo=830, leading to the rexolite loss value $\tan\delta=0.0012$, exactly similar to the loss measured in a cavity..

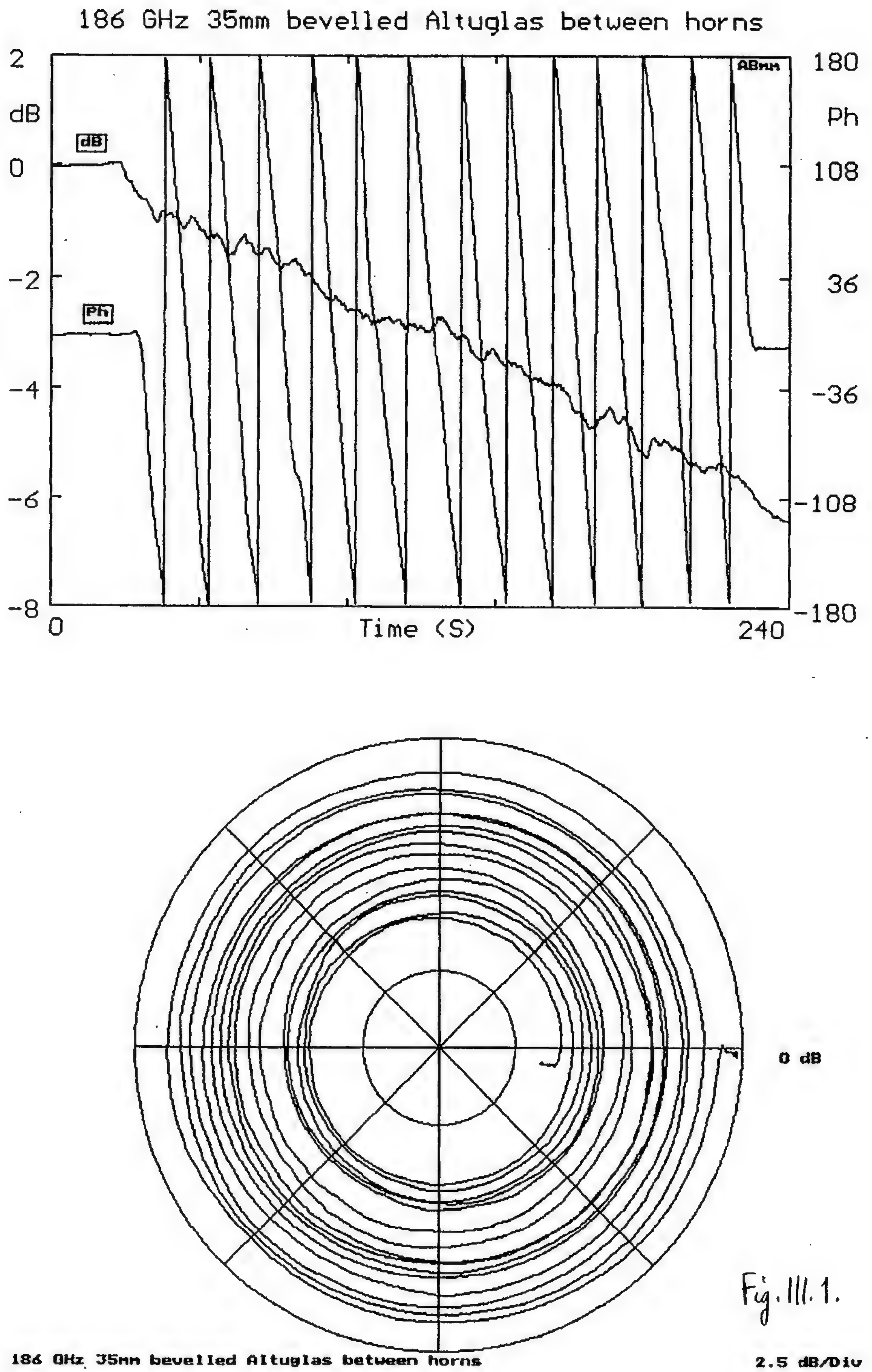

Fig. III.1.

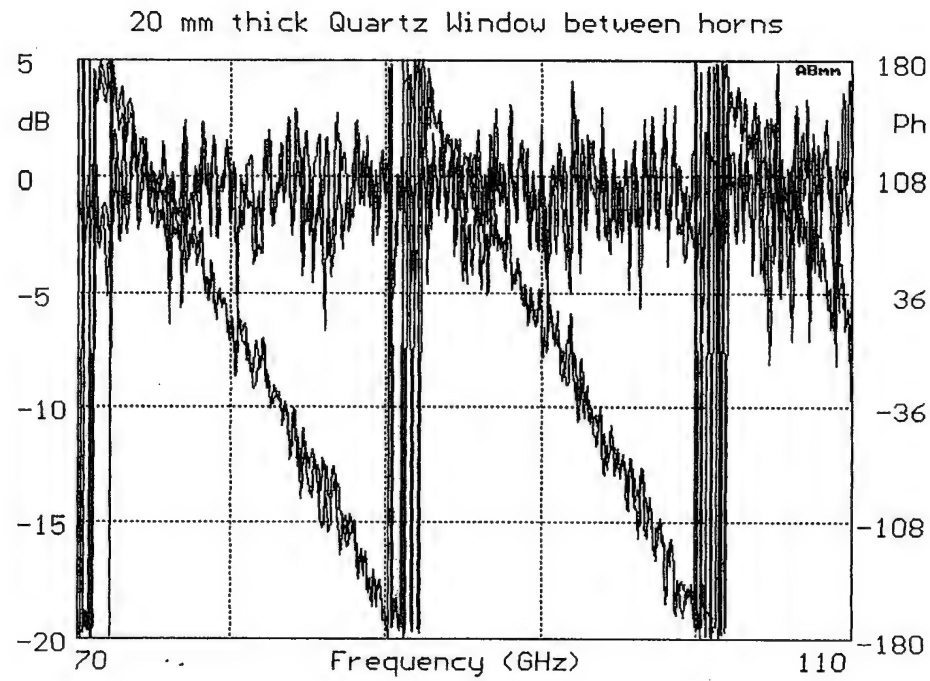

Fig. III.2.

2e exemple : La TF apporte une compréhension complète du comportement d'un montage en transmission

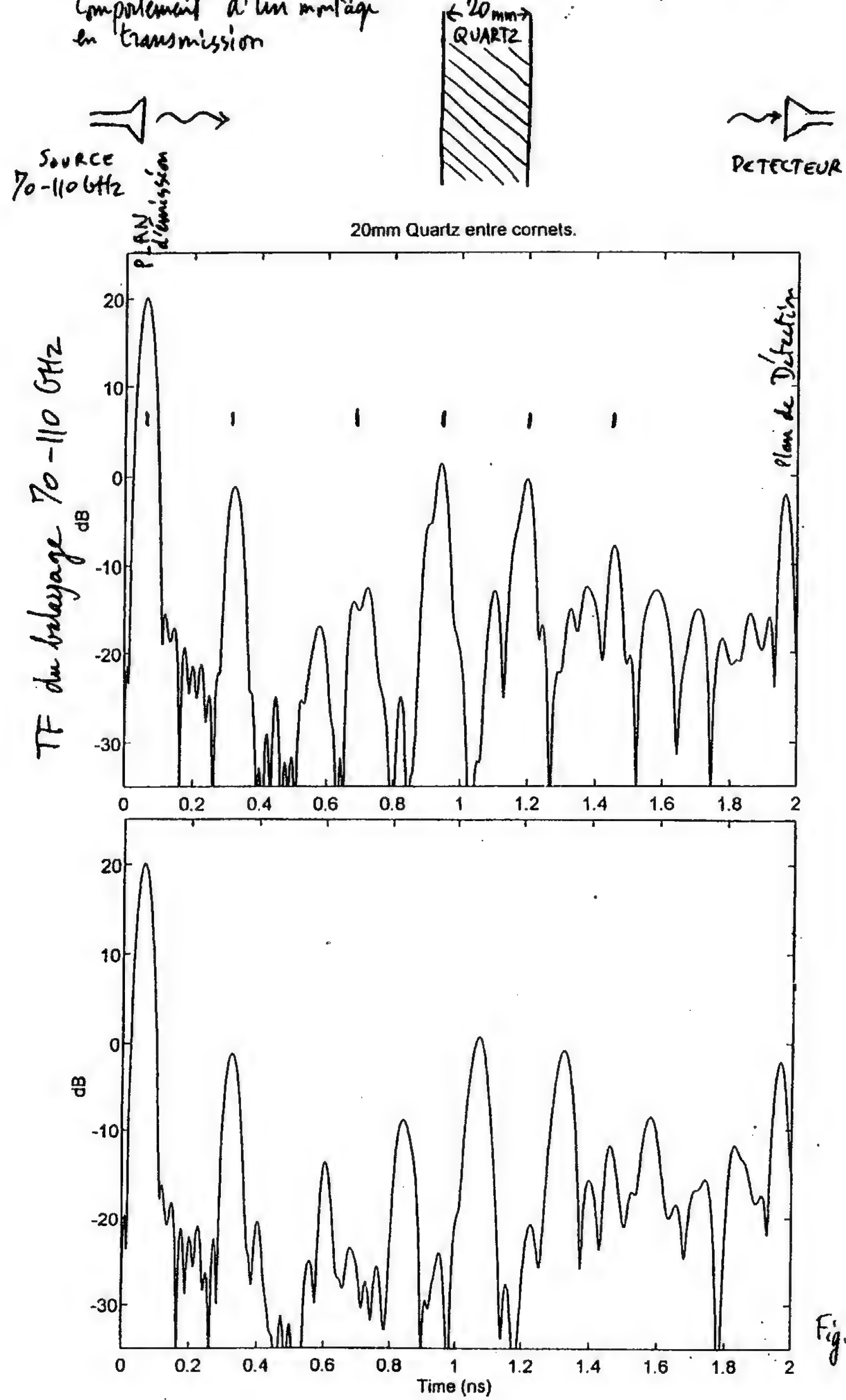

Fig. III.3.

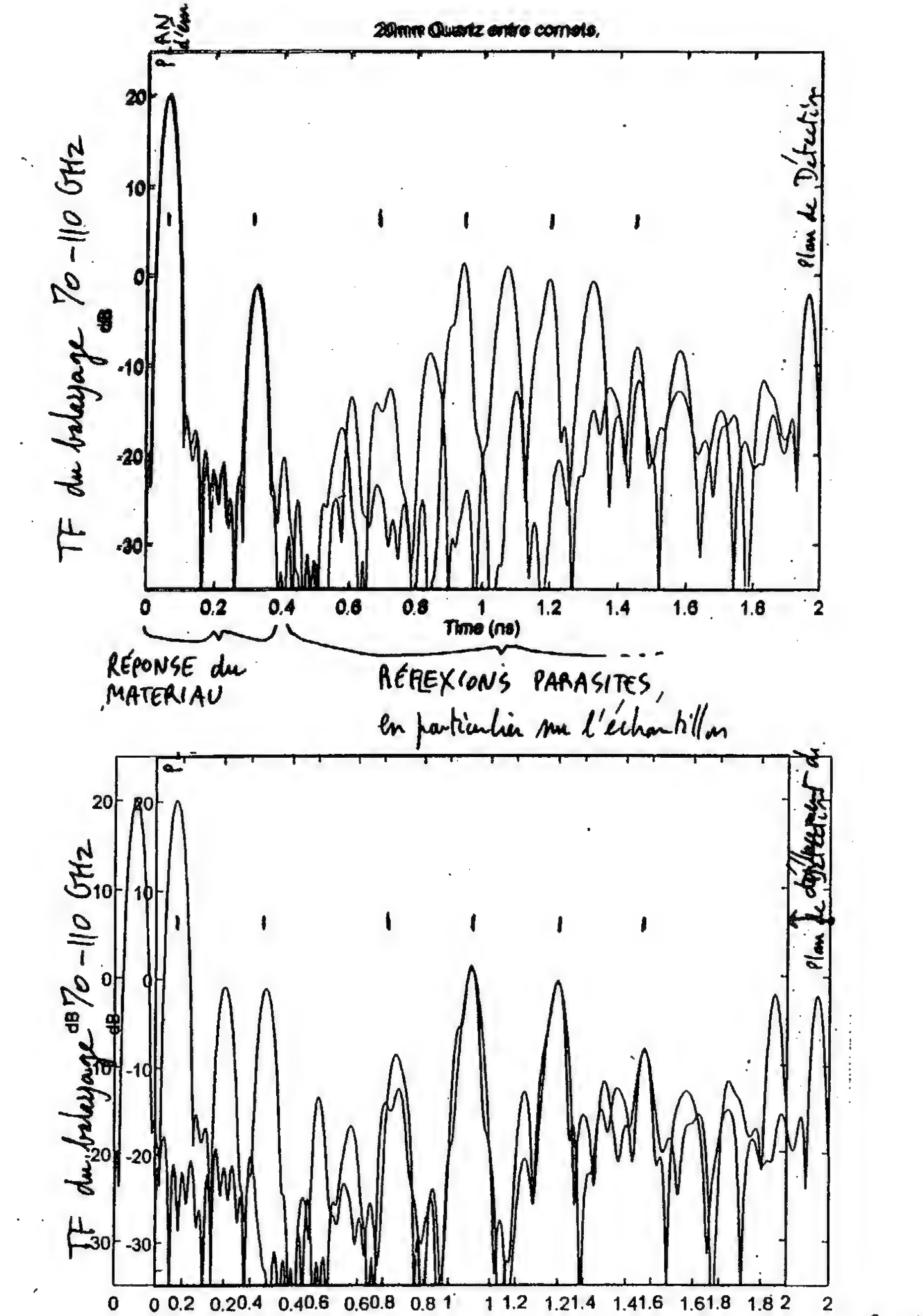

Fig. III.4

20 mm thick Quartz Window after FT Filtering

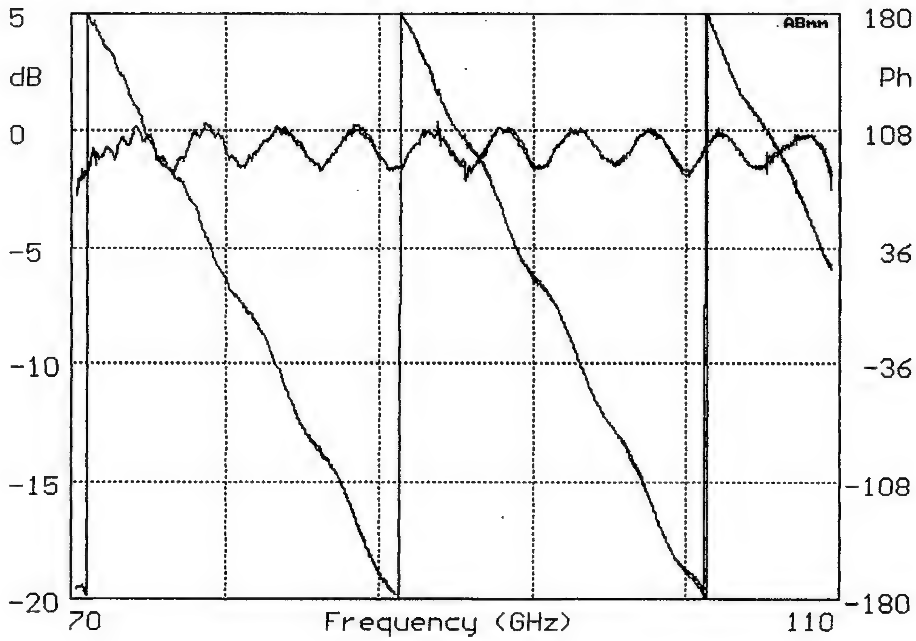

Fig. III.5.

REFLEXION FROM 9.97 mm SAPPHIRE with/out filtering

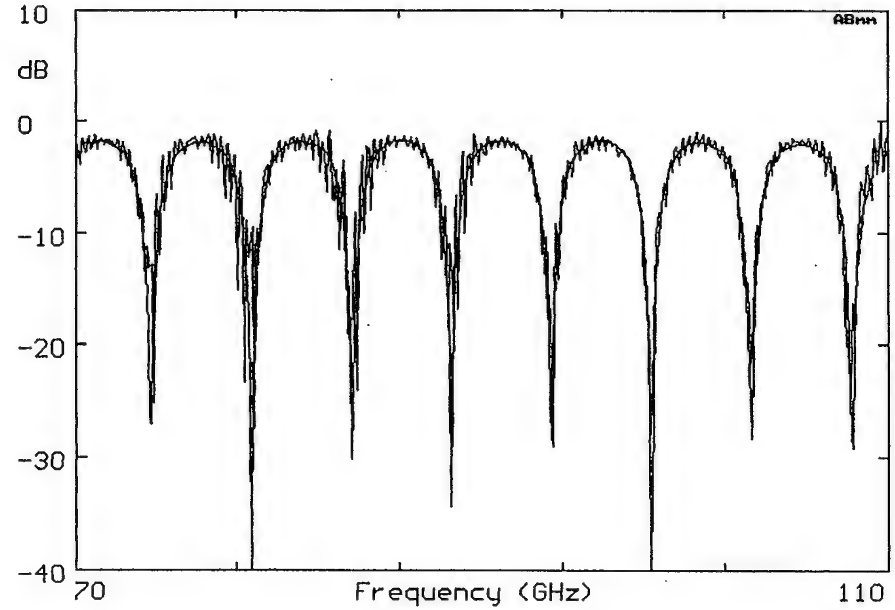

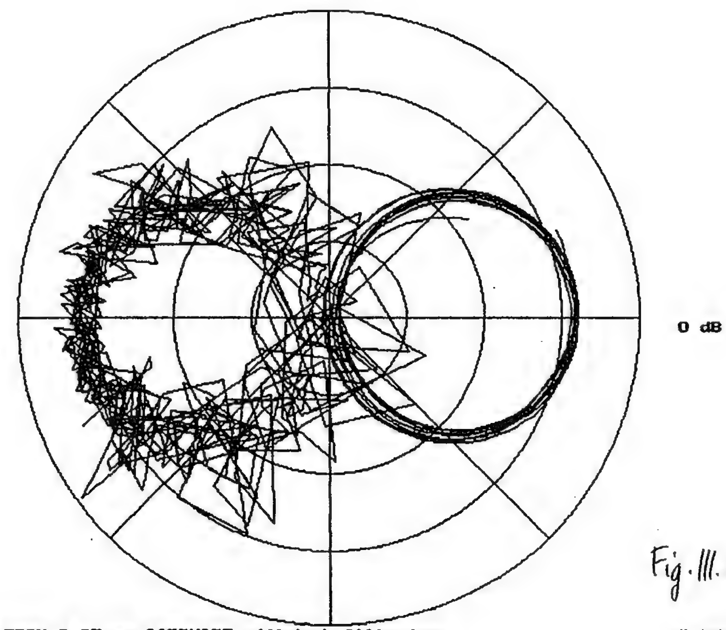

REFLEXION FROM 9.97 mm SAPPHIRE with/out filtering

0.25/Div

Fig. III.6.

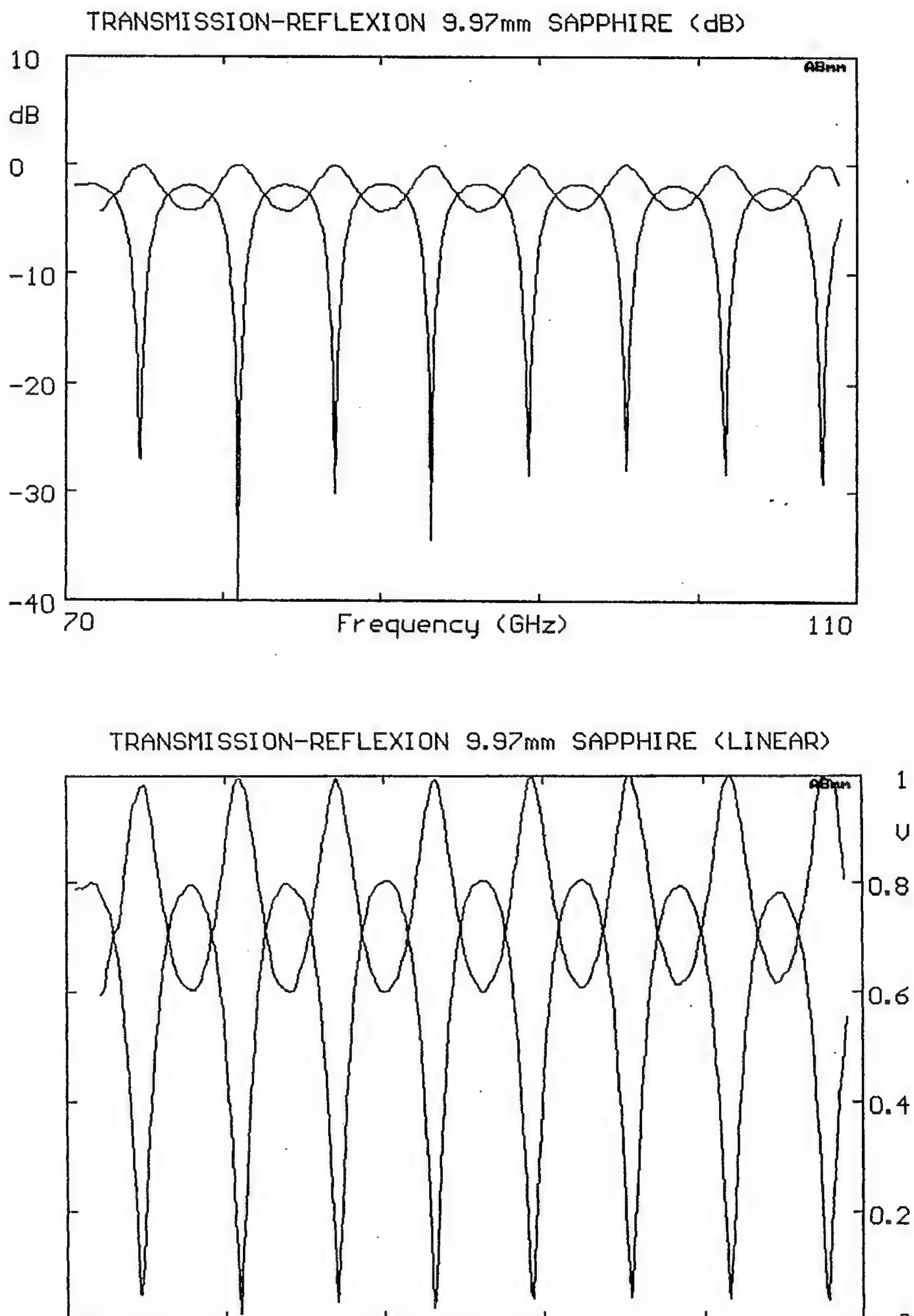

Fig. III. 7.

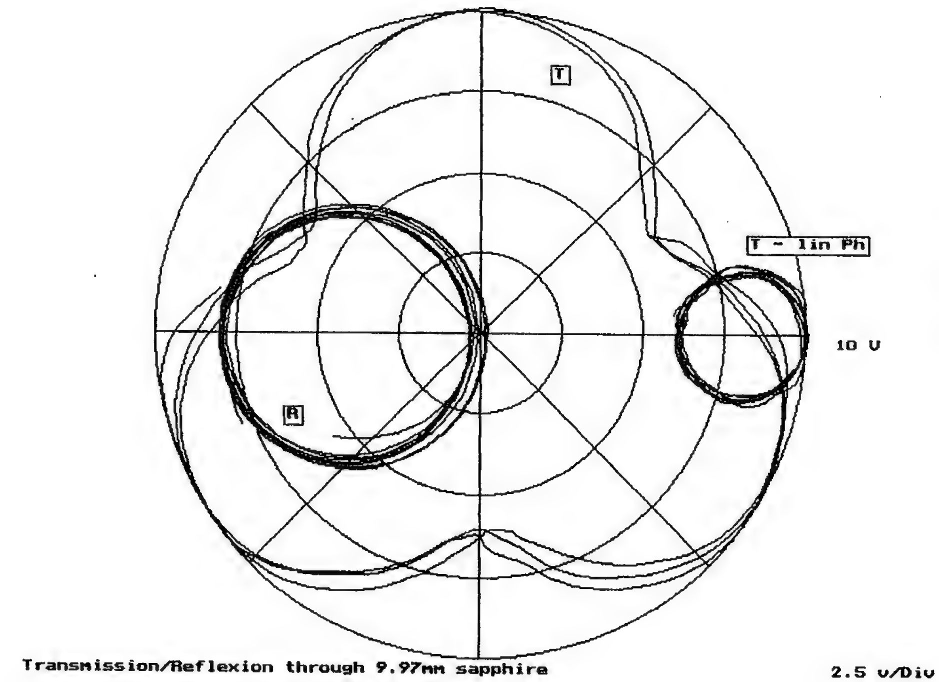

Fig. III. 8.

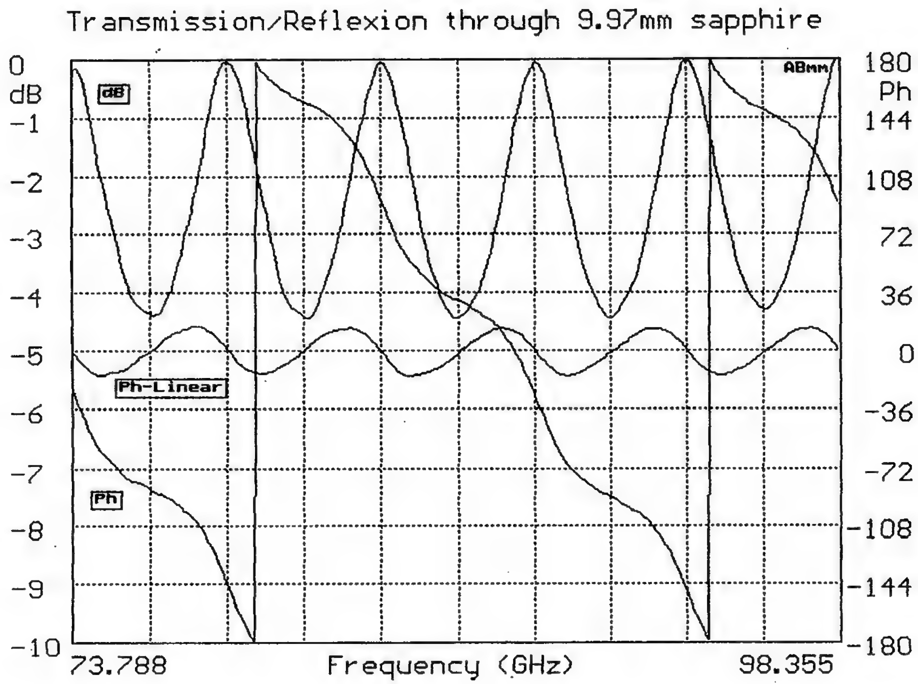

Fig. III.9.

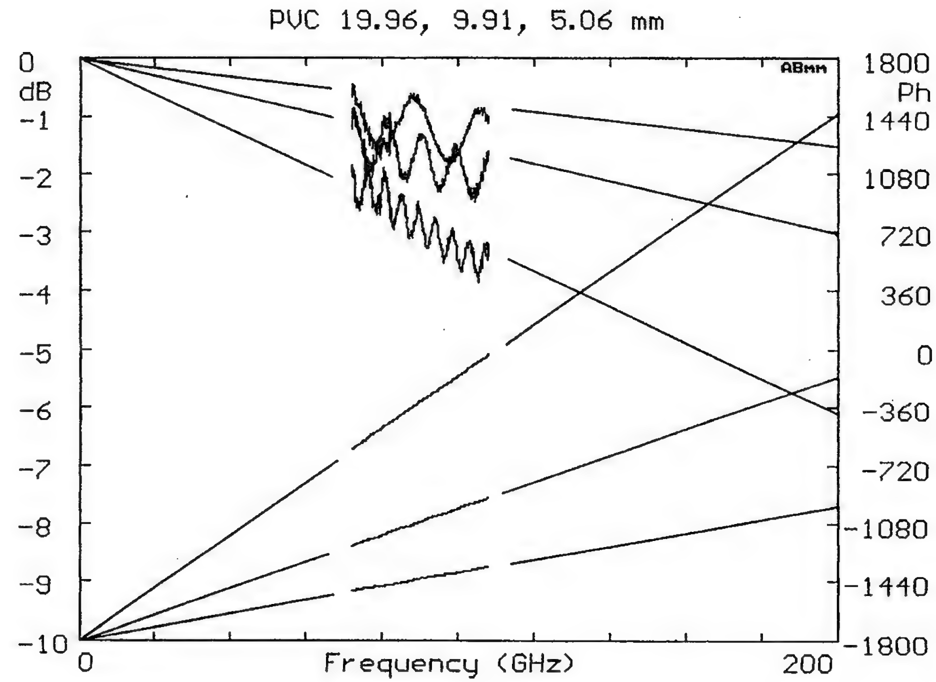

Fig. III.10.

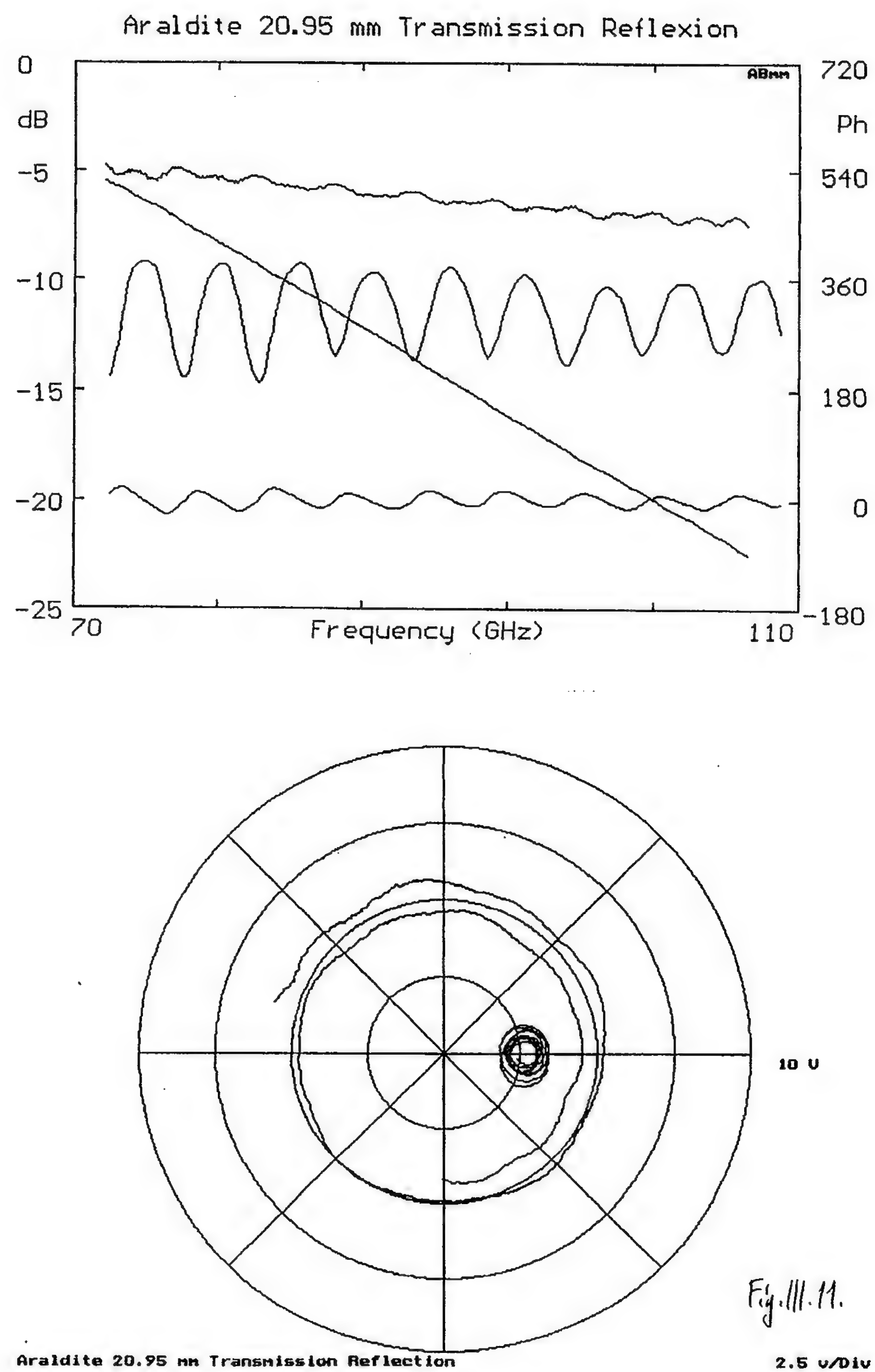

Fig. III. 11.

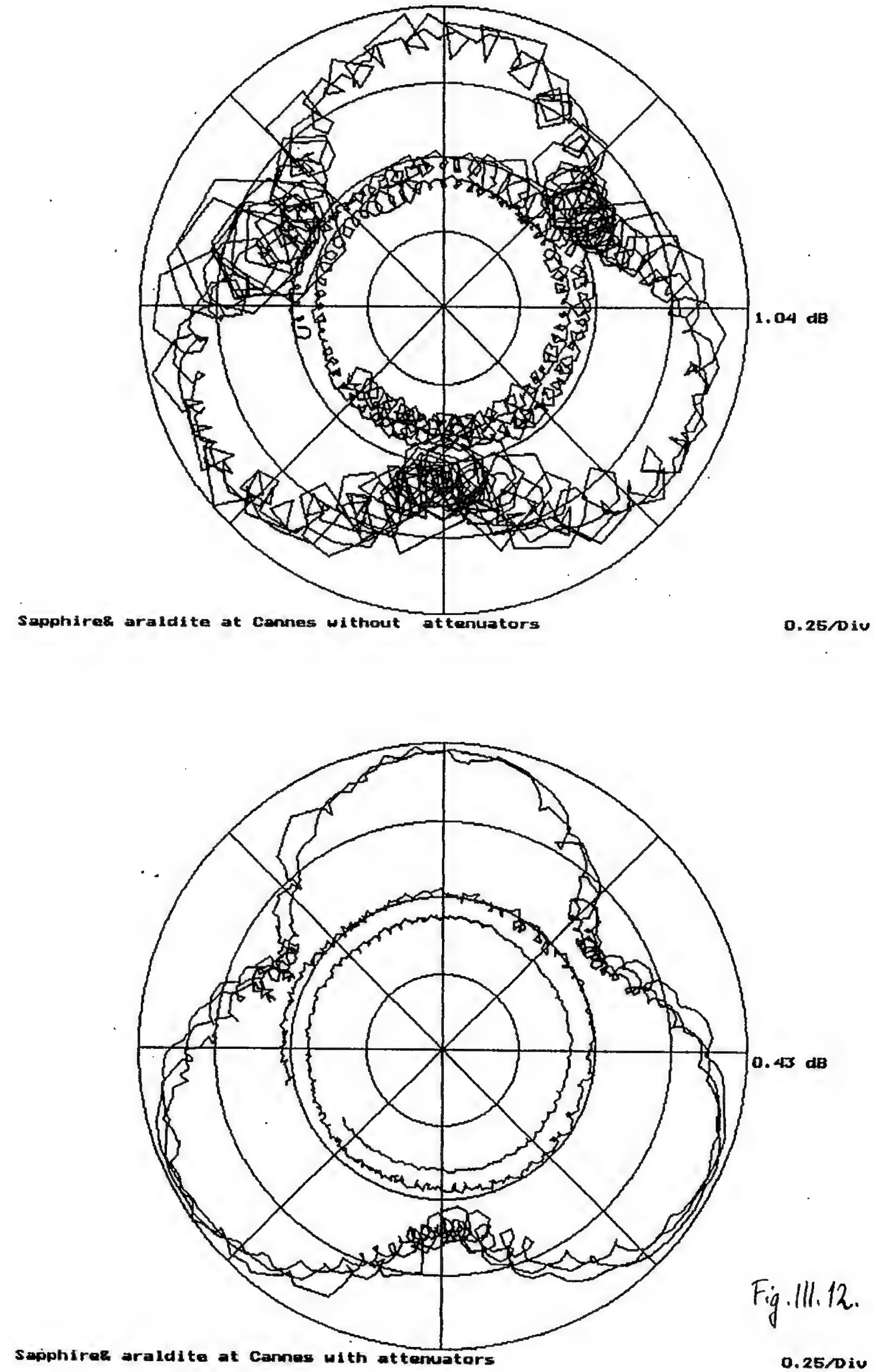

Fig. III. 12.

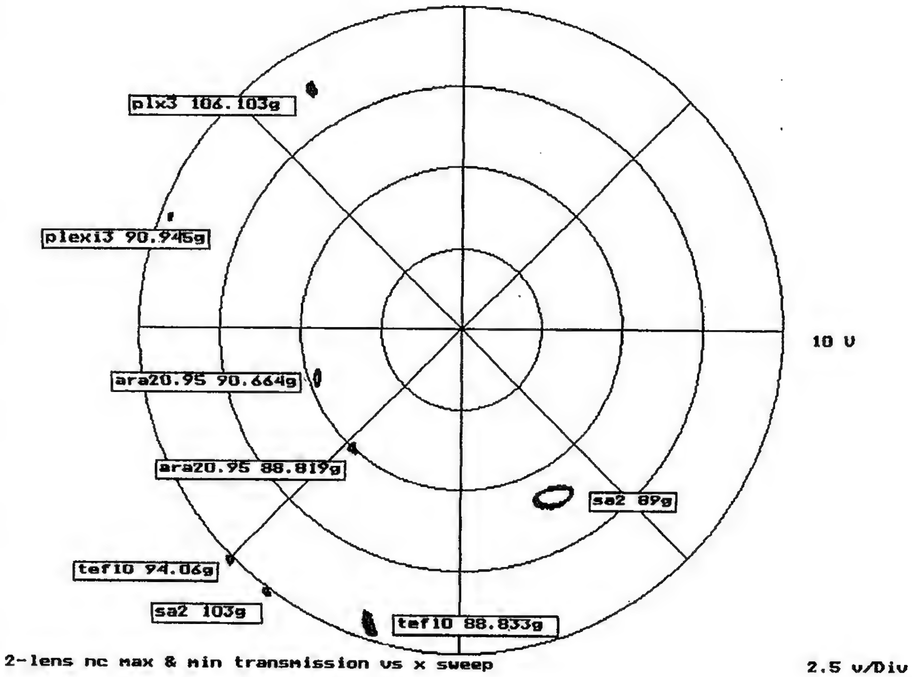

Fig. III. 13.

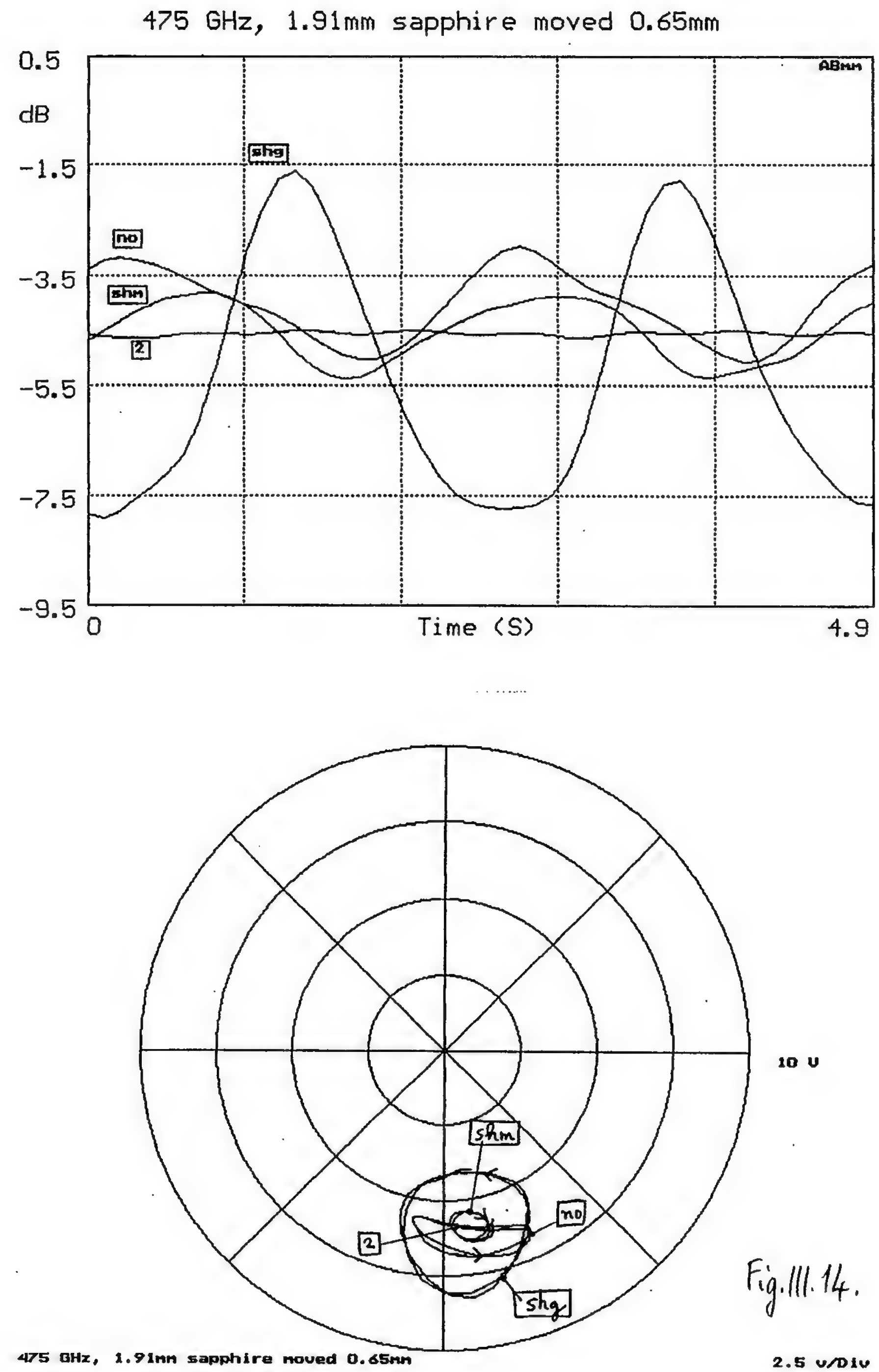

Fig. III. 14.

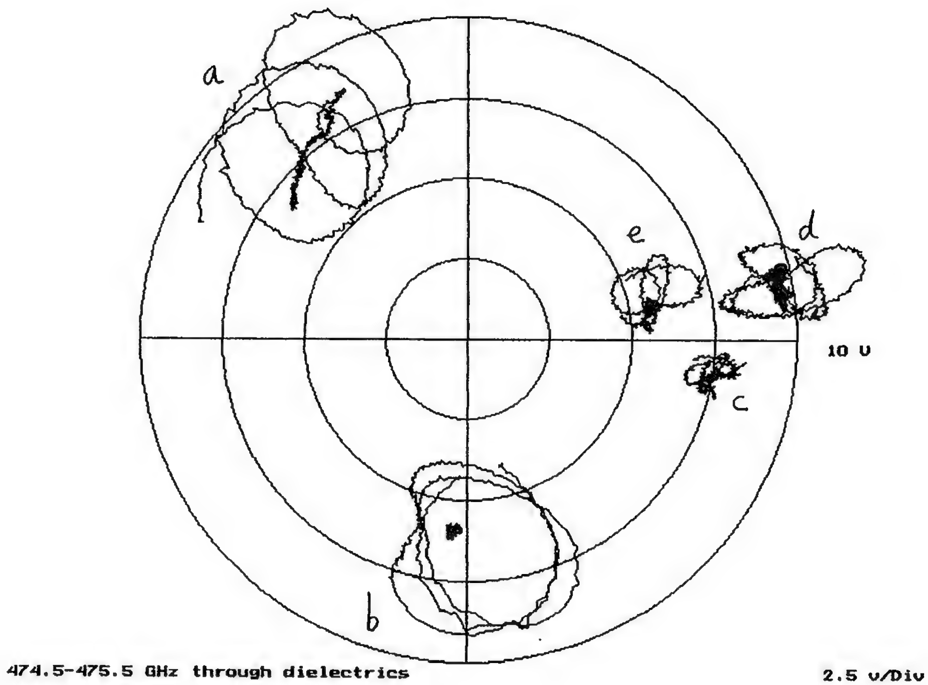

Fig. III.15.

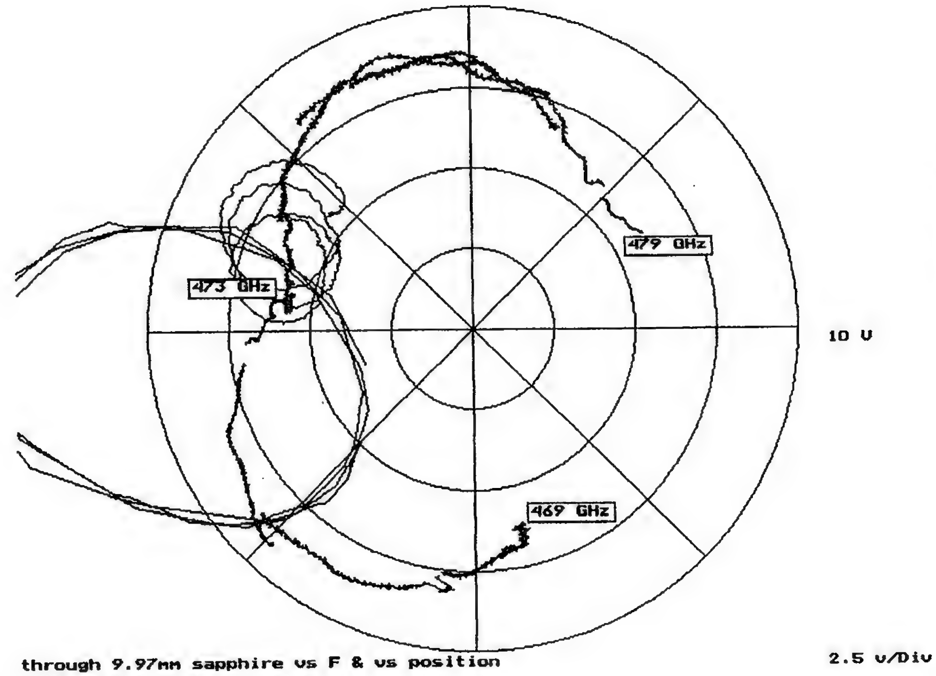

Fig. III.16.

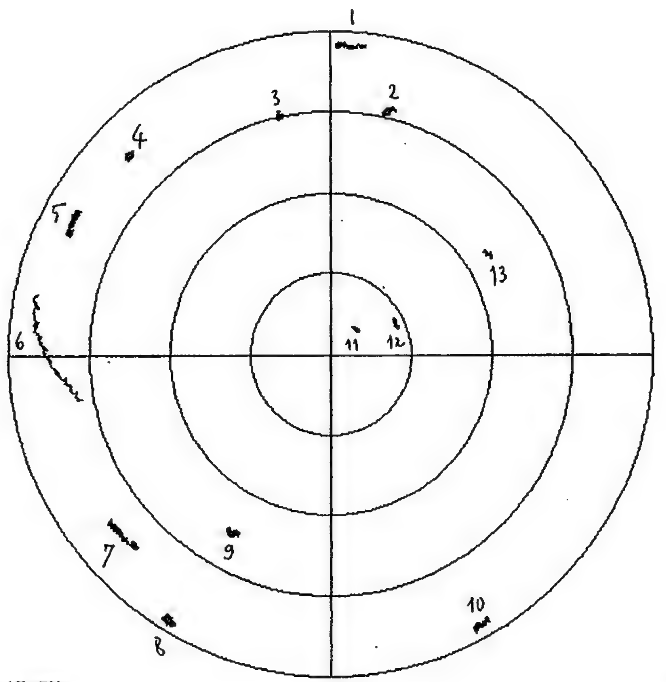

283.55-284.15 GHz 2.5 v/Div

Hard screen copy issued on 01/06/96 at 22:07:16

List of printed registers

					e	ε'
A:\PODI284.MSN	01/05/94 21:14:17	nb aramy/shm	6	SAPPHIRE	9.97mm	9.40
A:\PODI284.MSN	01/05/94 21:18:20	tef10	10	TEFLON	10.mm	2.06
A:\PODI284.MSN	01/05/94 21:20:23	hdpenb	8	HDPE	5.mm	2.29
A:\PODI284.MSN	01/05/94 21:21:44	sa2	1	SAPPHIRE	1.91mm	9.40
A:\PODI284.MSN	01/05/94 21:22:38	plx5.75	9	PLEXIGLAS	5.7mm	2.60
A:\PODI284.MSN	01/05/94 21:23:46	plx3	2	PLEXIGLAS	3 mm	2.60
A:\PODI284.MSN	01/05/94 21:25:02	rex10	5	REXOLITE	10mm	2.53
A:\PODI284.MSN	01/05/94 21:26:11	rex15	7	REXOLITE	15mm	2.53
A:\PODI284.MSN	01/05/94 21:29:02	pvc4.13	13	PVC	4.13mm	2.83
A:\PODI284.MSN	01/05/94 21:31:03	ara0.93	4	ARALDITE	0.93mm	2.90
A:\PODI284.MSN	01/05/94 21:32:01	aral.15	3	ARALDITE	1.15mm	2.90
A:\PODI284.MSN	01/05/94 21:35:12	plx22.43nb	12	PLEXIGLAS	22.43mm	2.60
A:\PODI284.MSN	01/05/94 21:36:51	pvc19.96	11	PVC	19.96mm	2.83

Fig. III.17.

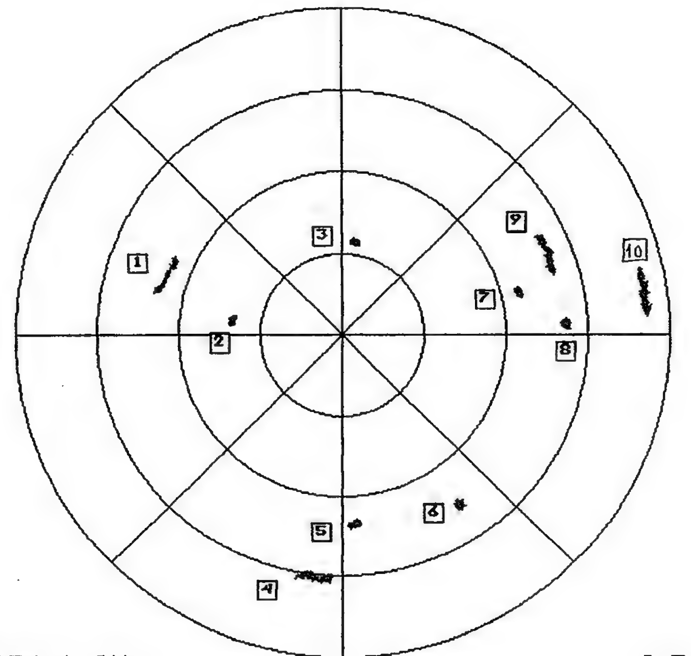

473.4-474.4 GHz 2.5 v/Div

Hard screen copy issued on 01/06/96 at 18:38:08

List of printed registers

A:\NBDI4734.MSN	01/05/94 03:57:39	sa9 2miarave40	1	SAPPHIRE	9.97 mm
A:\NBDI4734.MSN	01/05/94 04:00:17	sa2	5	SAPPHIRE	1.91 mm
A:\NBDI4734.MSN	01/05/94 04:02:43	tef15	10	TEFLON	15 mm
A:\NBDI4734.MSN	01/05/94 04:09:54	pvc4.13	3	PVC	4.13 mm
A:\NBDI4734.MSN	01/05/94 04:10:56	plx3	3	PLEXIGLAS	3 mm
A:\NBDI4734.MSN	01/05/94 04:12:41	plx5.9	2	PLEXIGLAS	5.9mm
A:\NBDI4734.MSN	01/05/94 04:13:37	rex10	4	REXOLITE	10mm
A:\NBDI4734.MSN	01/05/94 04:14:27	rex15	9	REXOLITE	15mm
A:\NBDI4734.MSN	01/05/94 04:15:55	ara0.93	8	ARALDITE	0.93mm
A:\NBDI4734.MSN	01/05/94 04:16:50	aral.15	6	ARALDITE	1.15mm

Fig. III. 18.

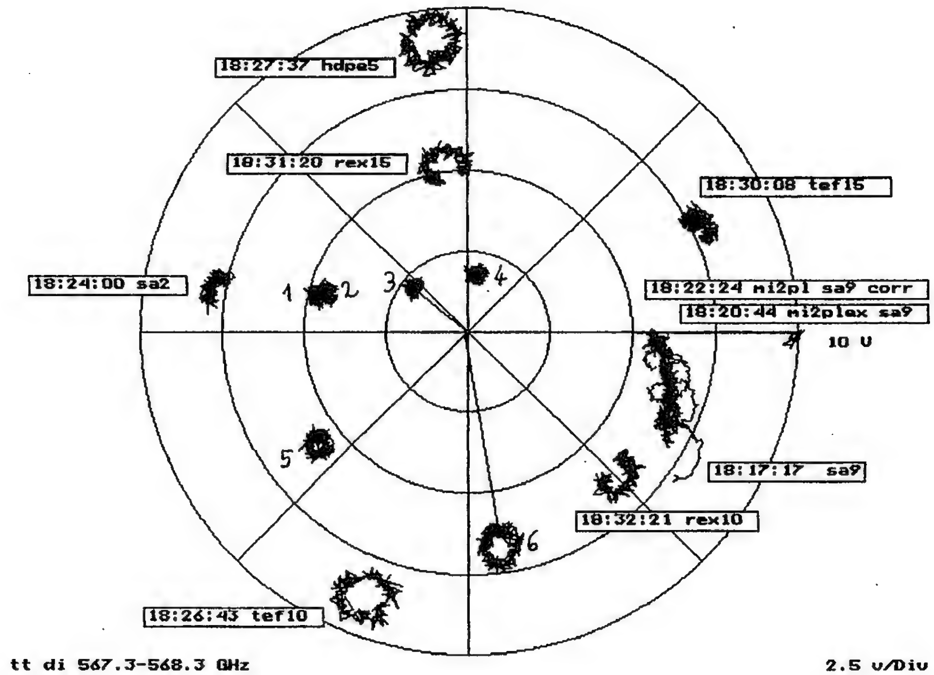

Hard screen copy issued on 01/06/96 at 23:06:41

List of printed registers

A:\PODI567.MSN	01/05/94	18:17:17	sa9	
A:\PODI567.MSN	01/05/94	18:20:44	mi2plex sa9	
A:\PODI567.MSN	01/05/94	18:22:24	mi2pl sa9 corr	
A:\PODI567.MSN	01/05/94	18:24:00	sa2	
A:\PODI567.MSN	01/05/94	18:26:43	tef10	
A:\PODI567.MSN	01/05/94	18:27:37	hdpe5	
A:\PODI567.MSN	01/05/94	18:30:08	tef15	
A:\PODI567.MSN	01/05/94	18:31:20	rex15	
A:\PODI567.MSN	01/05/94	18:32:21	rex10	
A:\PODI567.MSN	01/05/94	18:33:12	ai	
A:\PODI567.MSN	01/05/94	18:33:29	plx5.75	3
A:\PODI567.MSN	01/05/94	18:34:31	plx3	2
A:\PODI567.MSN	01/05/94	18:35:25	pvc4.13	4
A:\PODI567.MSN	01/05/94	18:36:38	noir2	1
A:\PODI567.MSN	01/05/94	18:37:37	ara0.93	6
A:\PODI567.MSN	01/05/94	18:38:30	ara1.15	5

Fig. III. 19.

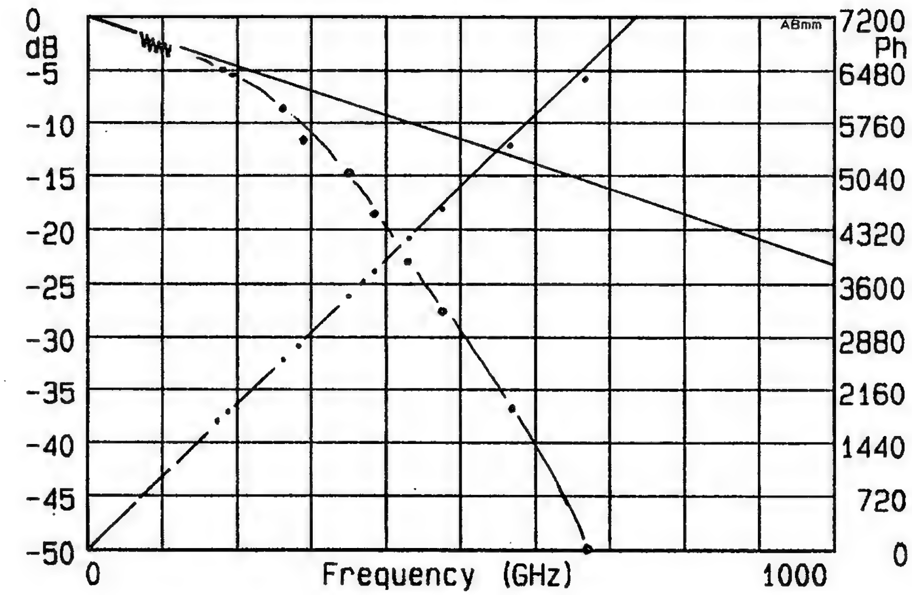

Fig. III.20.

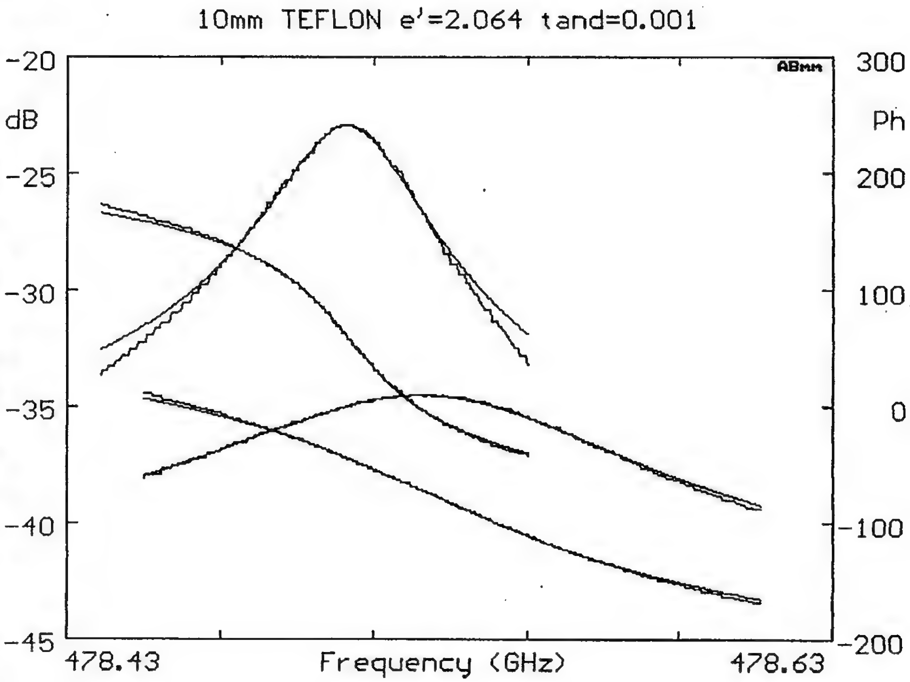

Hard screen copy issued on 01/06/96 at 17:52:05

Fig. III.21.

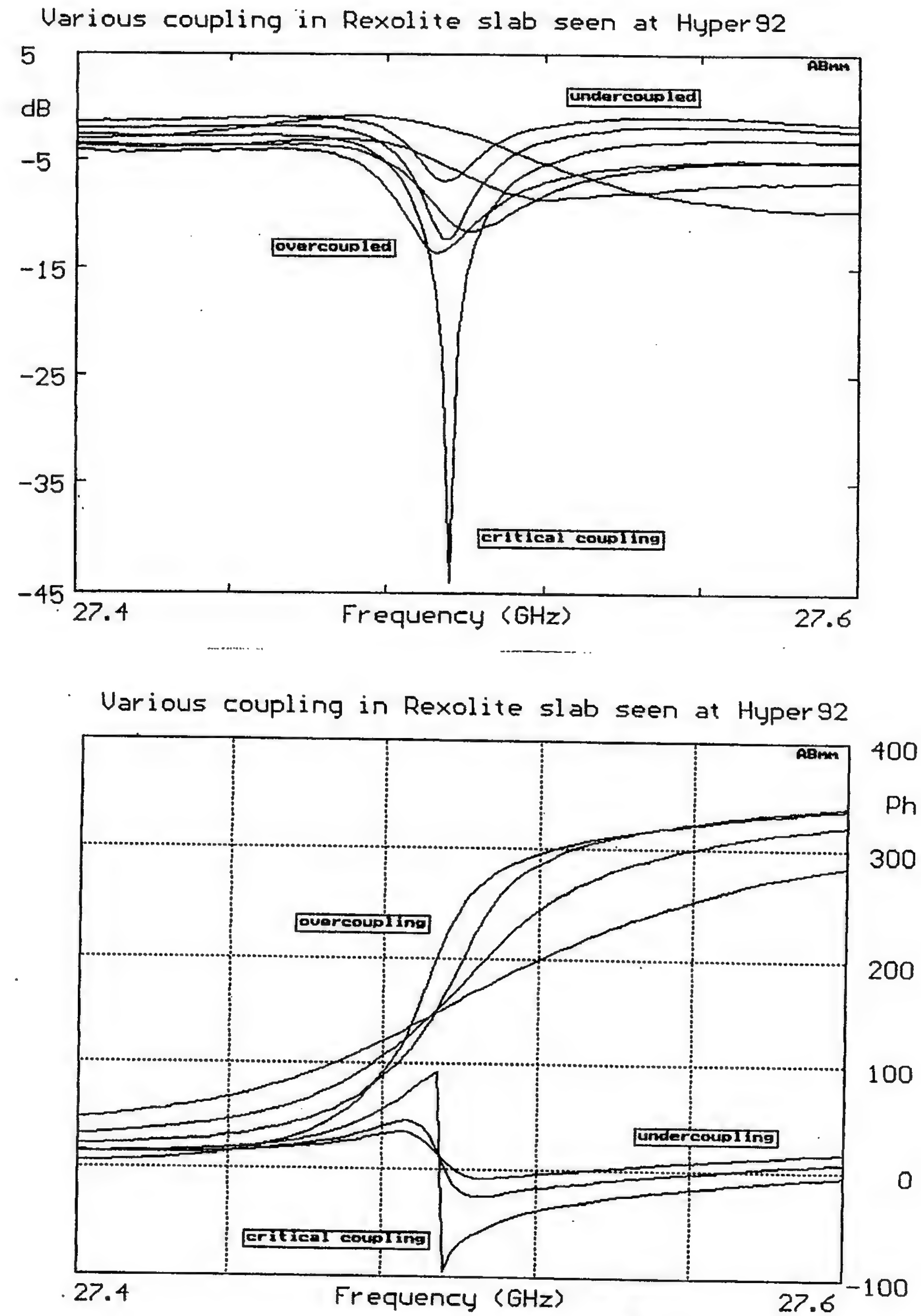

Fig. III.22.

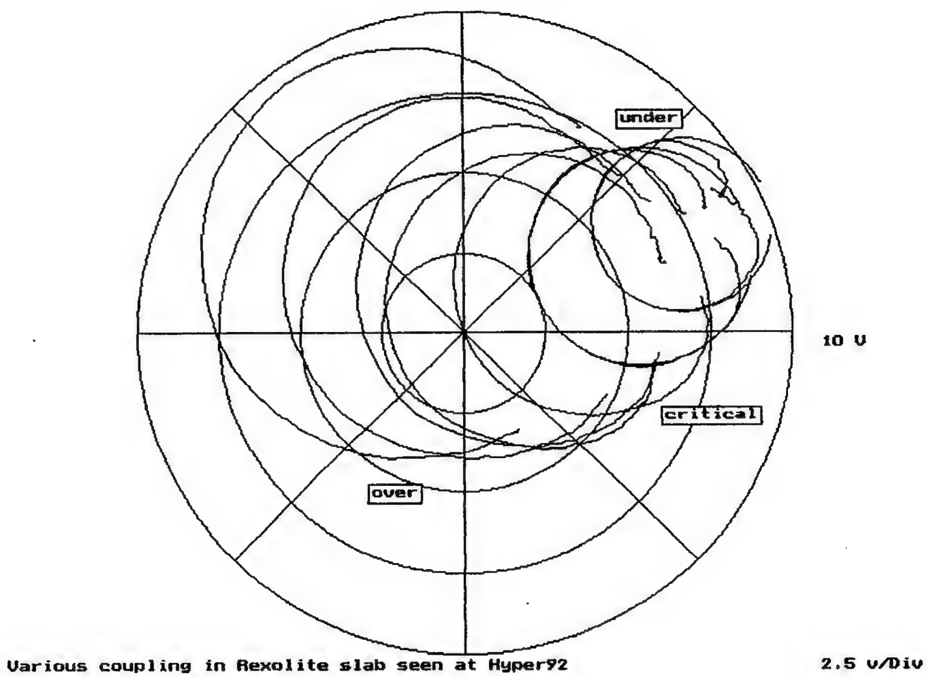
under
critical
over
10 V
Various coupling in Rexolite slab seen at Hyper92
2.5 v/Div

Fig. III. 23.

WEDNESDAY JULY 10

LIGHTWAVE/TERAHERTZ INTERACTION

AN OVERVIEW OF THE FIELD

THEME # 5

NATO ADVANCED STUDY INSTITUTE

July 9, 10

PROFESSOR HAROLD FETTERMAN

UCLA

LIGHTWAVE/TERAHERTZ INTERACTION

* INTRODUCTION
* TESTING USING SWITCHES
* GENERATION USING PICO & FEMTOSECOND SOURCES
* DIFFERENCE FREQUENCY MIXING
* OTHER PROCESSES
* NEW MATERIALS

EXAMPLES OF POTENTIAL TERAHERTZ SYSTEMS USING OPTICAL APPROACHES

* OPTOELECTRONIC OSCILLATORS
* OPTICALLY CONTROLLED PHASED ARRAYS
* OPTICALLY CONTROLLED PHASE CONJUGATION
* CONCLUSION

ADVANTAGES OF USING LIGHT FOR TERAHERTZ SIGNALS

* High Laser Powers
* Natural For Transmission
* Narrow, Stable Laser Lines
* Advanced Optical Components
* Pico & Femto Sources
* Compact Solid State Implementations
* Unique Systems Are Now Feasible

PICOSECOND TESTING

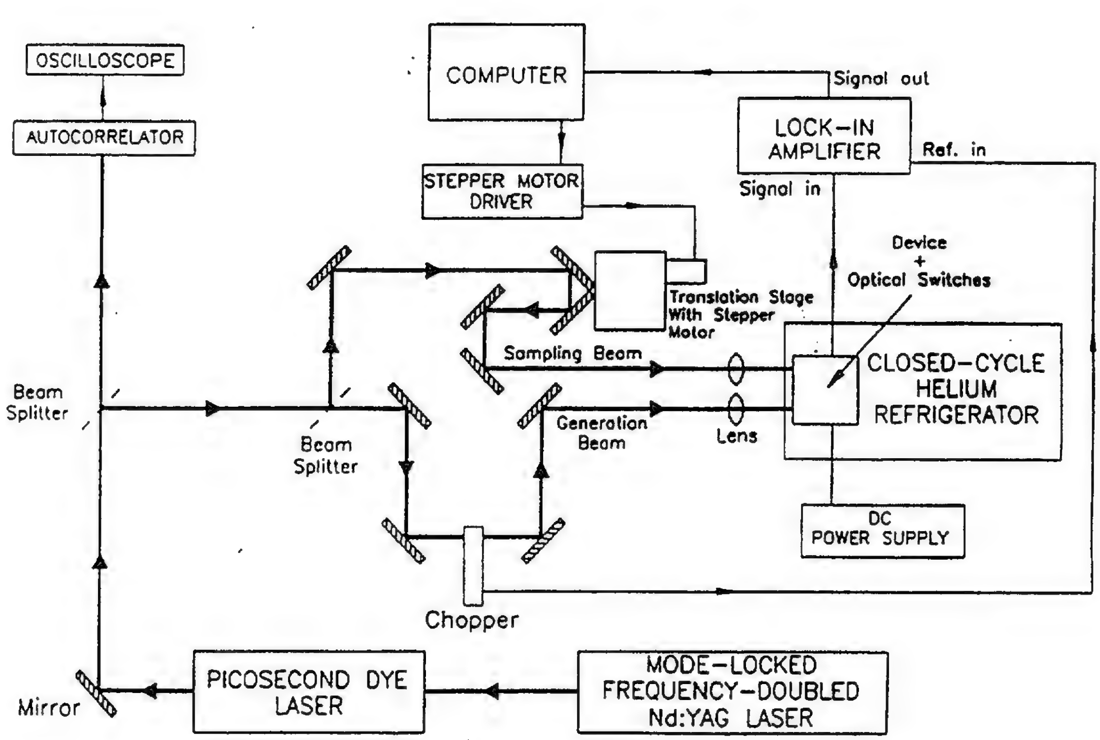

PHOTOCONDUCTING ANTENNA ARRAY

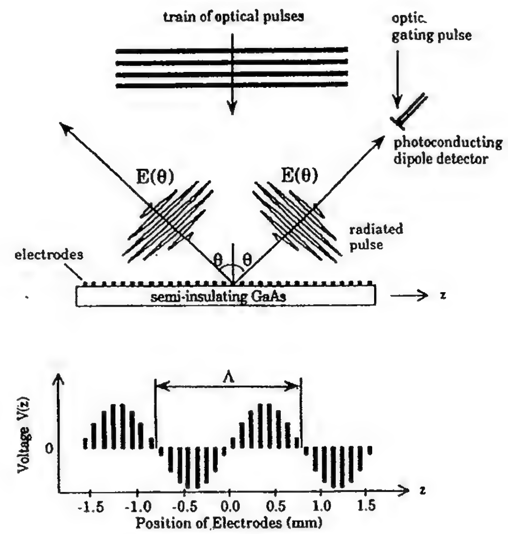

Fig. 1. Setup for the generation of an electrically steerable submillimeter wave beam. The array electrodes are sinusoidally biased with respect to their position, as shown. The array is illuminated with a train of optical pulses in order to generate quasi-sinusoidal radiation.

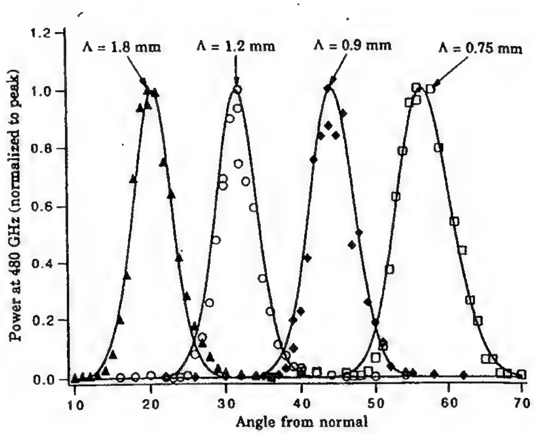

Fig. 8. Power at 480 GHz as a function of detector angle for several bias periods (Λ_{bias}). Measurements were taken in transmission with the fiber-fed detector approximately 4.5 cm from the array. Solid lines show the theoretical fit, assuming an optical beam width of 6 mm (Gaussian).

LOW TEMPERATURE GaAs

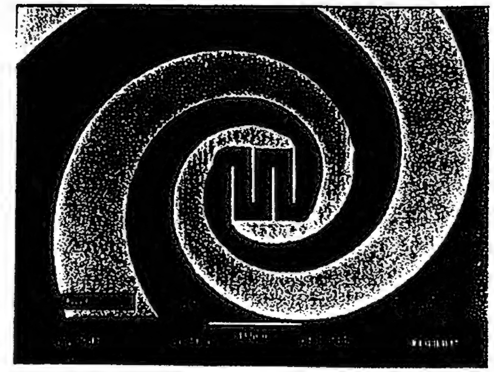

FIG. 1. Scanning electron micrograph of electrode region and first turn of spiral antenna for 8×8 μm photomixer (mixer 2).

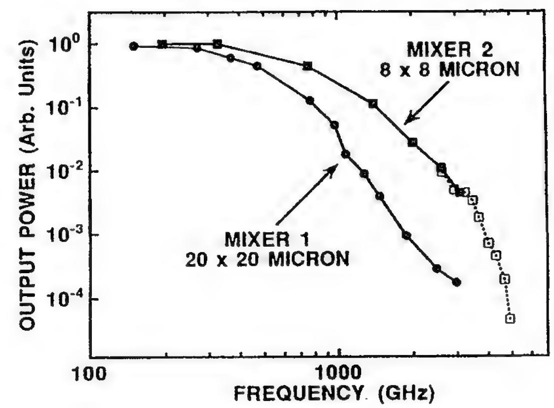

FIG. 2. Comparison of output power from mixer 1 and mixer 2. In both cases the pump lasers are $Ti:Al_2O_3$ lasers operating at λ=780 nm.

HBT PHOTOTRANSISTOR

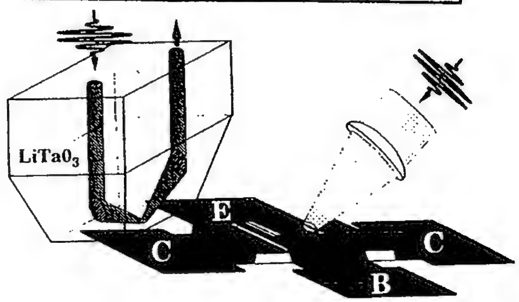

On-wafer electro-optic sampling geometry.

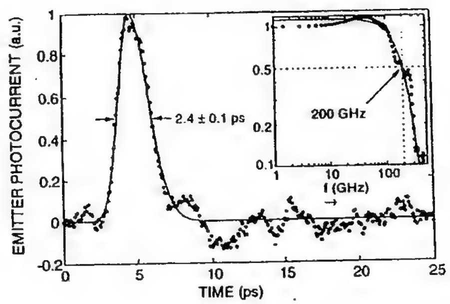

Electrooptic response of covered-base HBT with nulled-out slow component. Symbols—experimental points; solid lines—Gaussian and exponential components numerically fitted to the data.

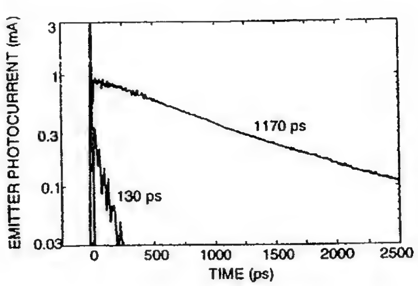

Comparison of slow time constant components with and without 50-Ω-impedance base termination.

OPTICAL RECTIFICATION

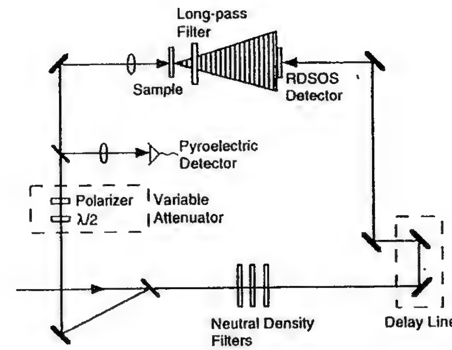

FIG. 1. A schematic of the experimental setup used for the THz optical rectification measurements.

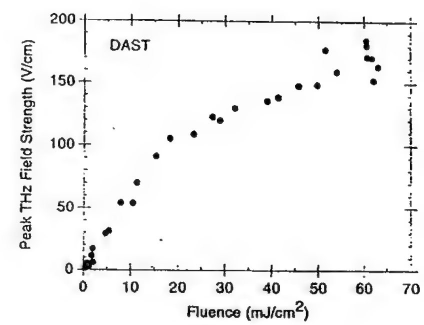

Rectified field strength plotted as a function of incident optical fluence using a 0.6-mm-thick DAST emitter.

THz PULSES FROM THE CREATION OF POLARIZED EXCITONS

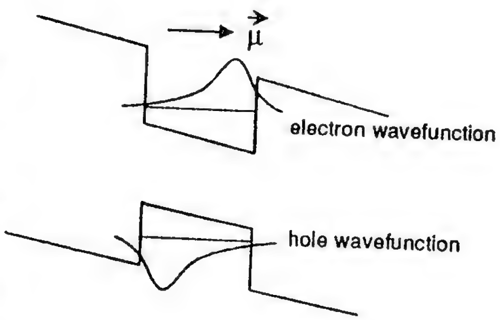

Fig. 1. Diagram of the envelope wavefunctions of the electron and hole in a biased quantum well. The electric field shifts the electron and hole wavefunctions to opposite sides of the well, creating a dipolemoment.

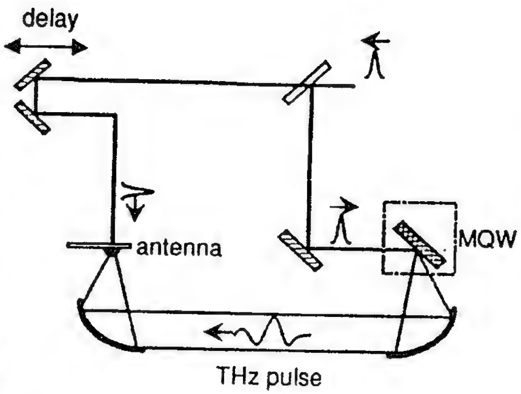

Fig. 2. Experimental configuration. A femtosecond laser pulse strikes the multi quantum well sample MQW. A parabolic mirror collects the generated THz radiation and a second one focuses the radiation onto a 50 μm photoconducting antenna, gated by the second laser pulse.

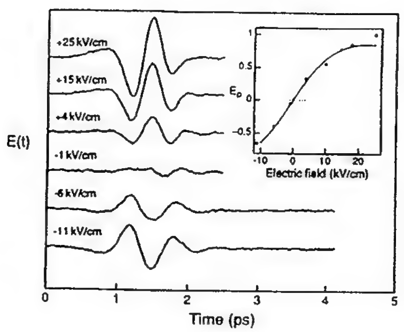

Fig. 3. Measured THz waveforms from the quantum wells at 77 K for several field strengths. The inset shows the peak amplitude of the waveforms (in arb. units) as a function of field strength in the quantum wells. The solid line is a calculation of the field-induced polarization

$$P \propto |\langle\Phi_e|\Phi_h\rangle|^2 [\langle\Phi_h|z|\Phi_h\rangle - \langle\Phi_e|z|\Phi_e\rangle]$$

PARAMETRIC GENERATION

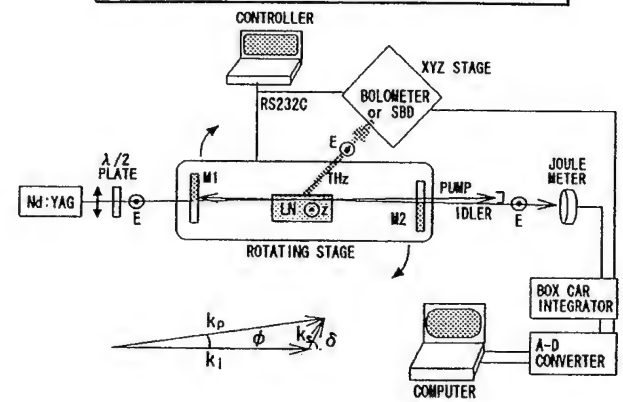

FIG. 1. Experimental setup for the generation of coherent tunable THz wave. The inset shows the momentum conservation relation among the pump, near-infrared idler, and THz signal.

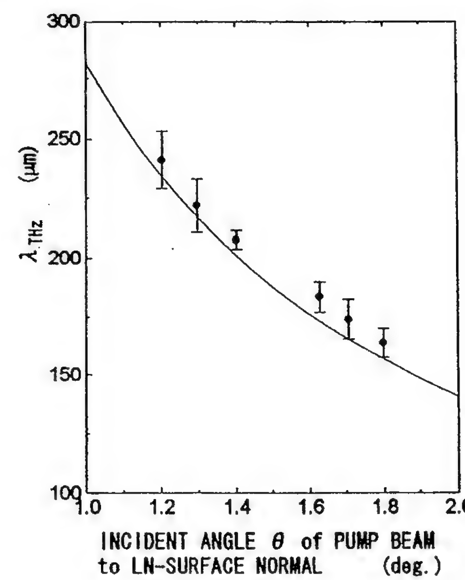

FIG. 2. Characteristic of wavelength tuning of THz wave: (a) shows an example of the wavelength measurement using the etalon, and the result was summarized in (b). Solid curve indicates the calculated tuning curve.

IMAGING WITH TERAHERTZ WAVES

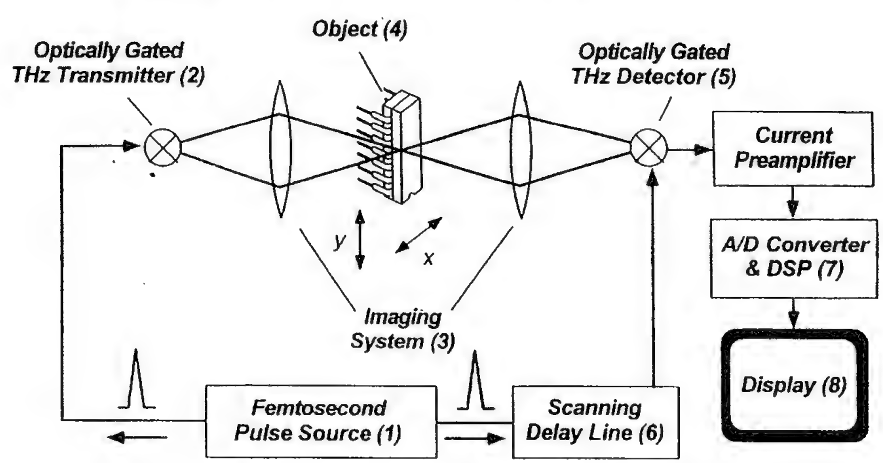

Schematic of the THz imaging system. In our experiments the object is raster scanned

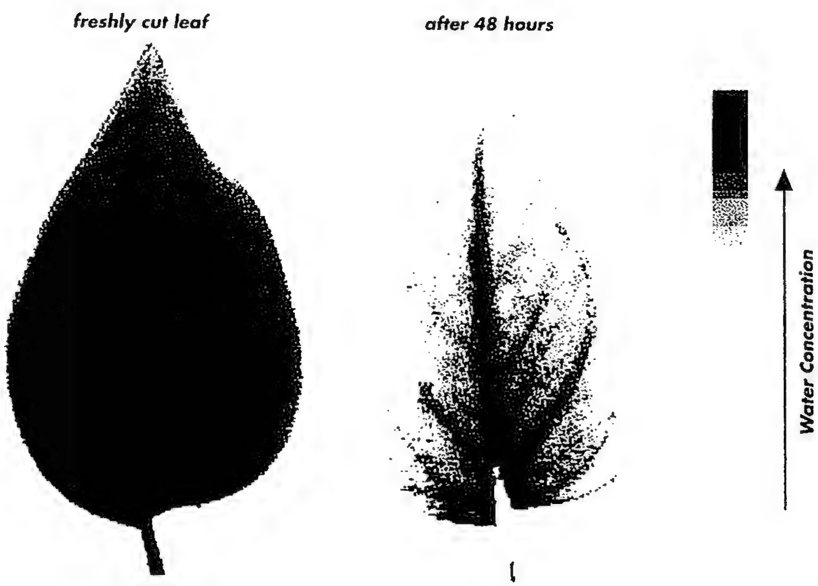

Left: THz image of a fresh leaf. Attenuation of THz radiation through the leaf is largely due to water
Right: THz image of the same leaf after 48 h. Water has clearly evaporated from the leaf

PRINCIPLE OF THE ULTRAFAST PMT

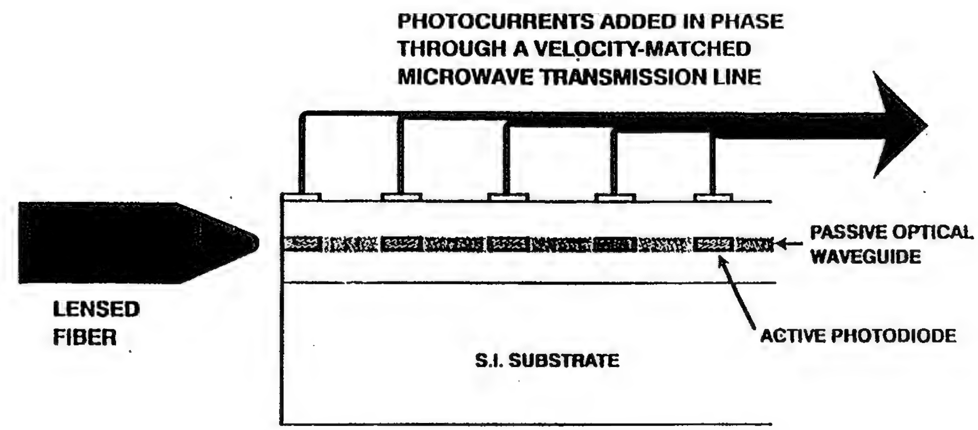

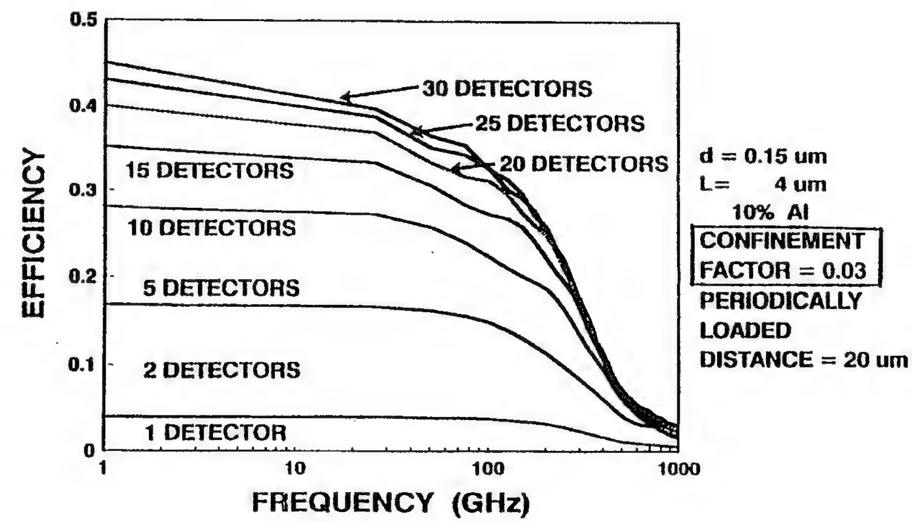

The Traveling Wave HPT Solution

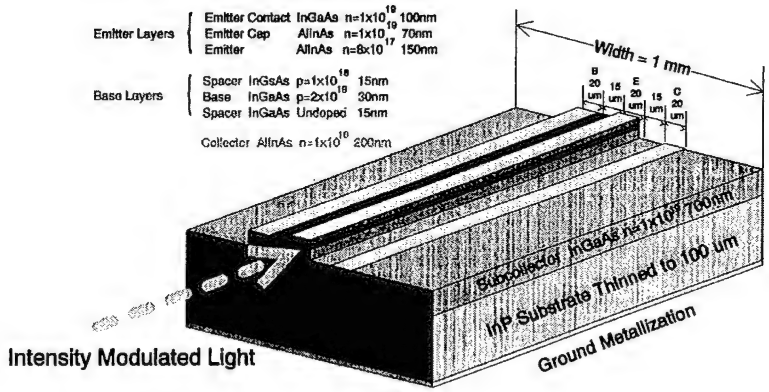

- Supports optical and electrical traveling waves
- Bandwidth limitation based on velocity mismatch
- Separates electrical and optical optimization
- Characteristic impedance designed for 50 Ω
- Long device improves optical coupling and absorption

TW-HPT With Integrated Polyimide Optical Waveguide

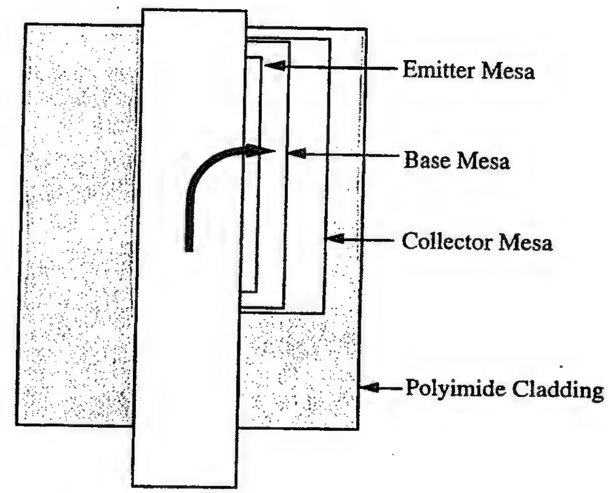

Polyimide Waveguide

- Optical Signal Leaks into Base/Collector Region Via Side Coupling
- Absorption of Intensity Modulated Optical Wave Induces Electrical Traveling Wave Signal
- Use of Polyimide Waveguide Reduces Velocity Mismatch Between Optical Wave and Electrical Wave Resulting in Broadband Operation
- Optical Coupling Efficiency can be maximized
- Electrical Waveguide Characteristic Impedance Designed for 50 Ω Match to External Circuit

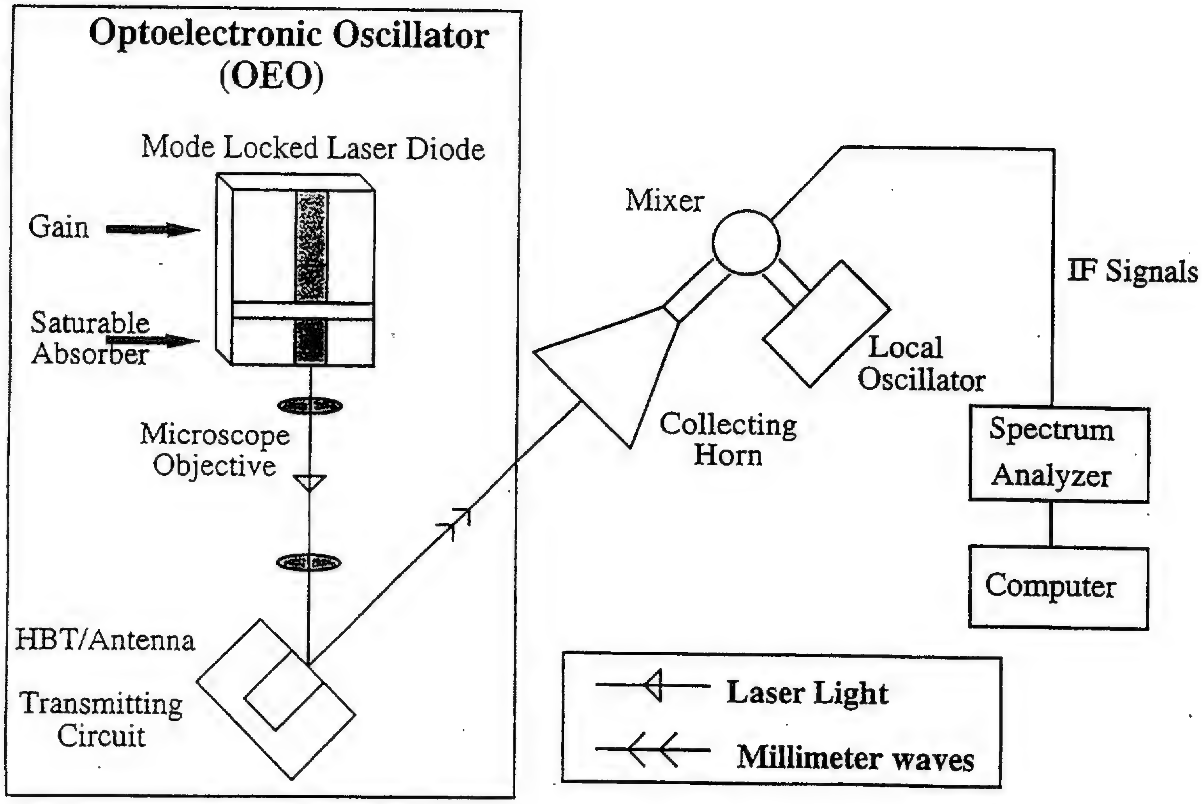

Millimeter Wave Radiation

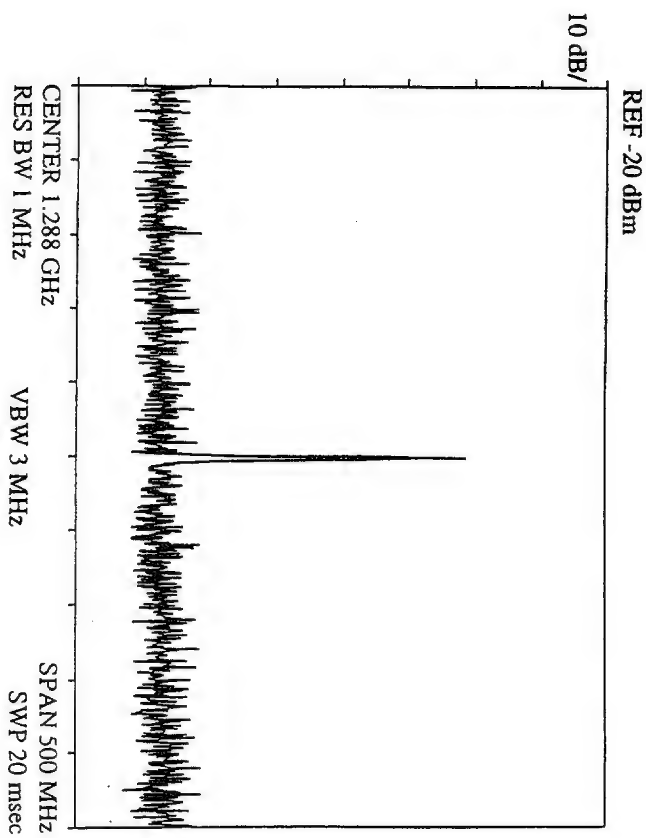

- Center Frequency 59.5 GHz
- SNR 40 dB
- Incident Optical Power .84 mW

Monolithic Colliding Pulse Mode-Locked (CPM) Diode Lasers

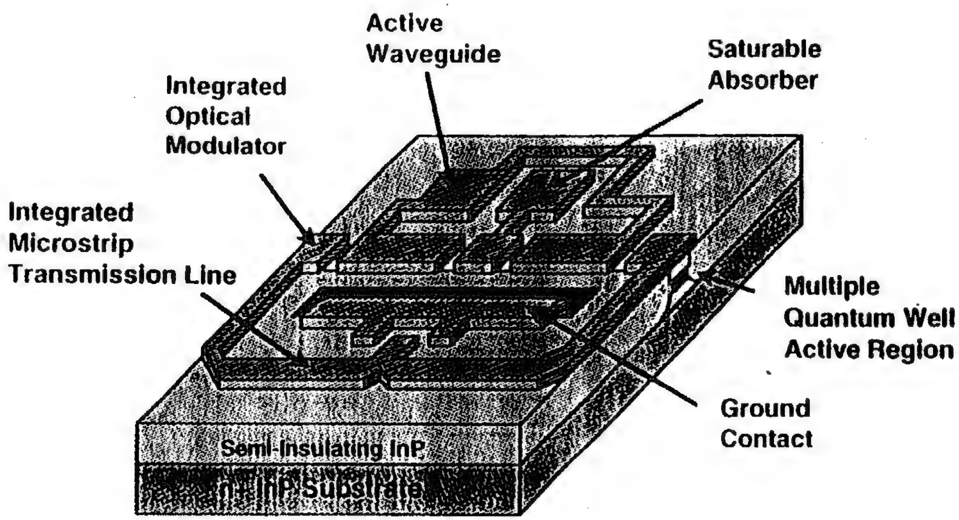

AT 350 GHz

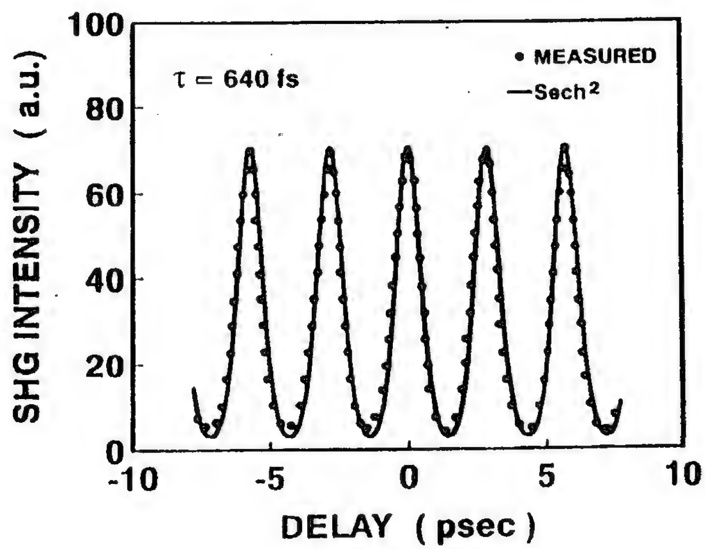

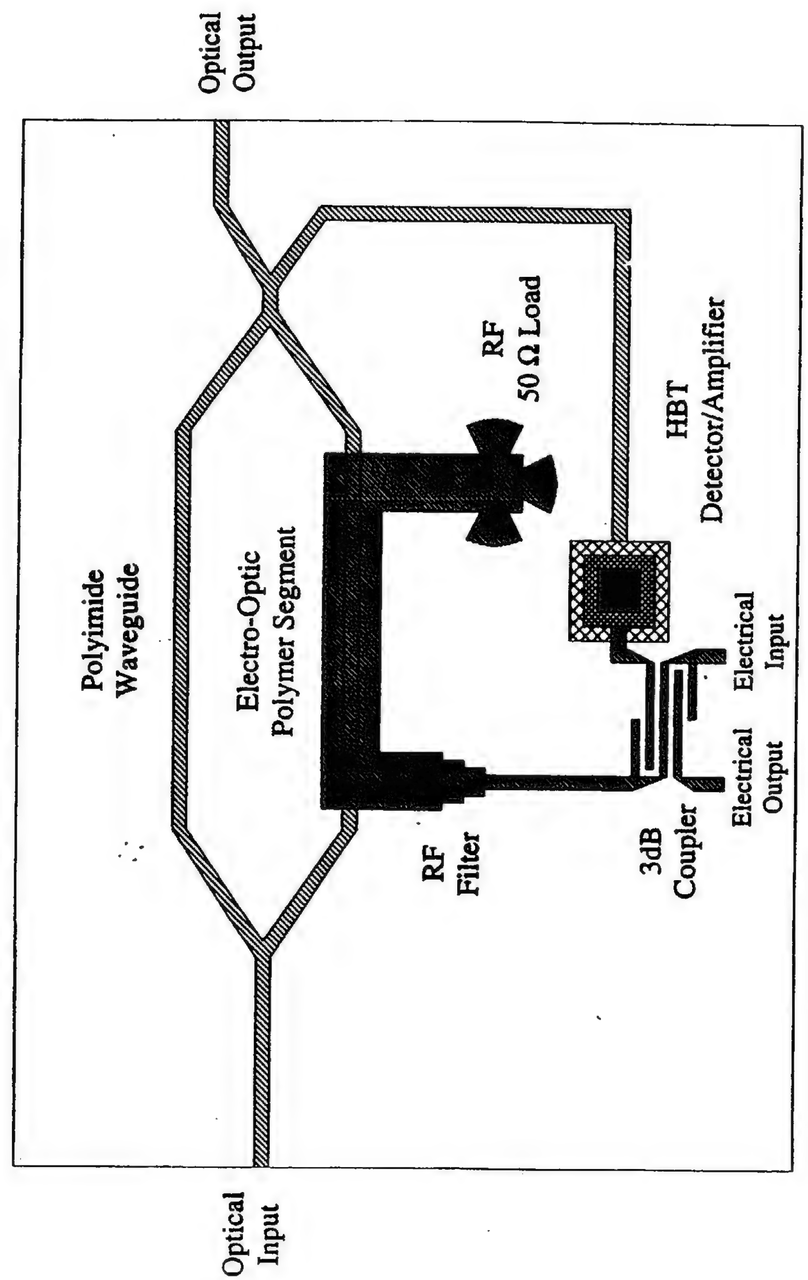

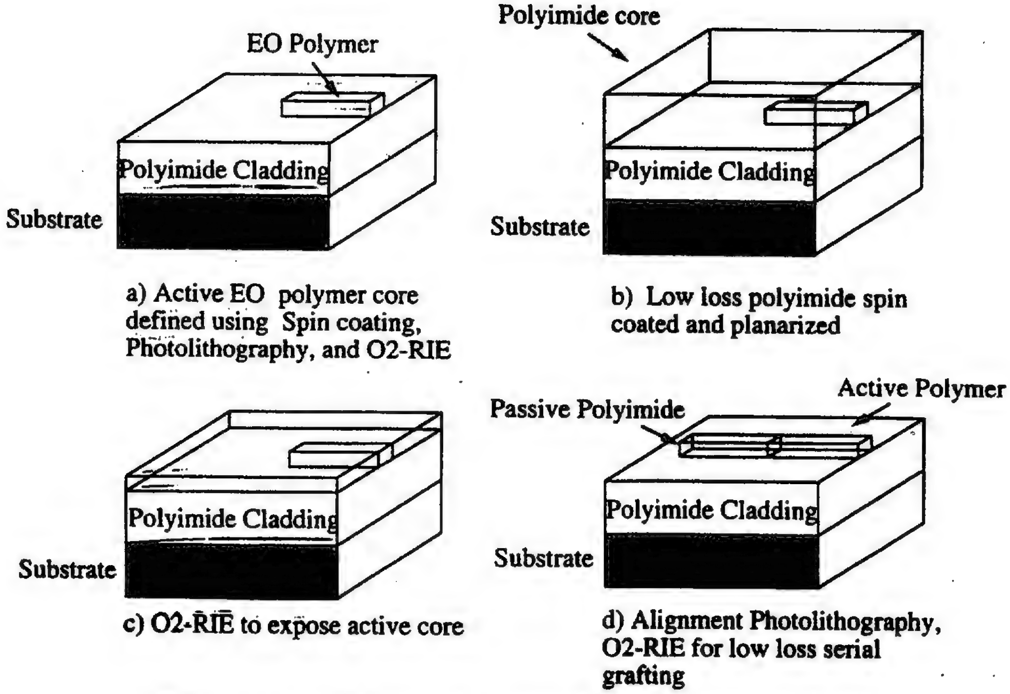

Fabrication of low loss connection between active polymer and low loss polyimide

Self-Oscillation

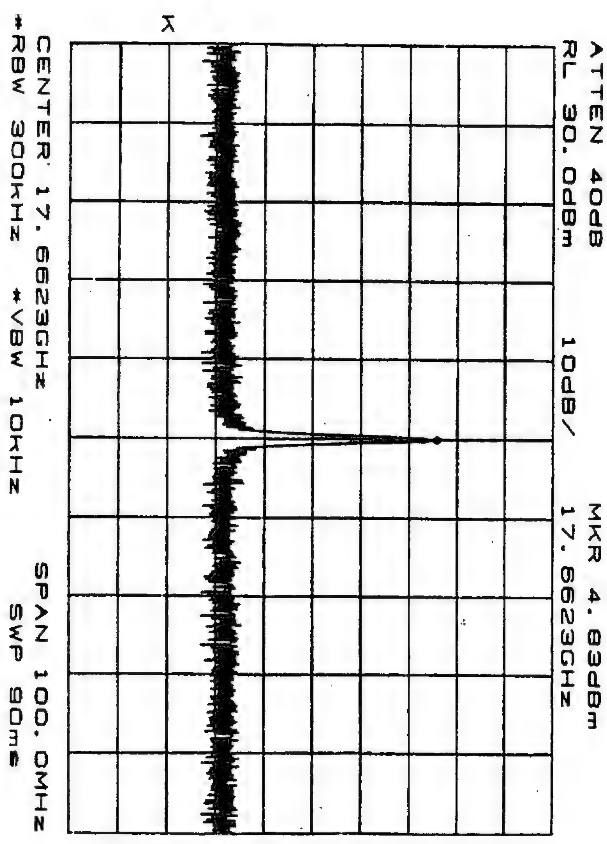

- Center Frequency = 18 GHz
- 3 dB Linewidth = 330 kHz
- SNR = 42 dB

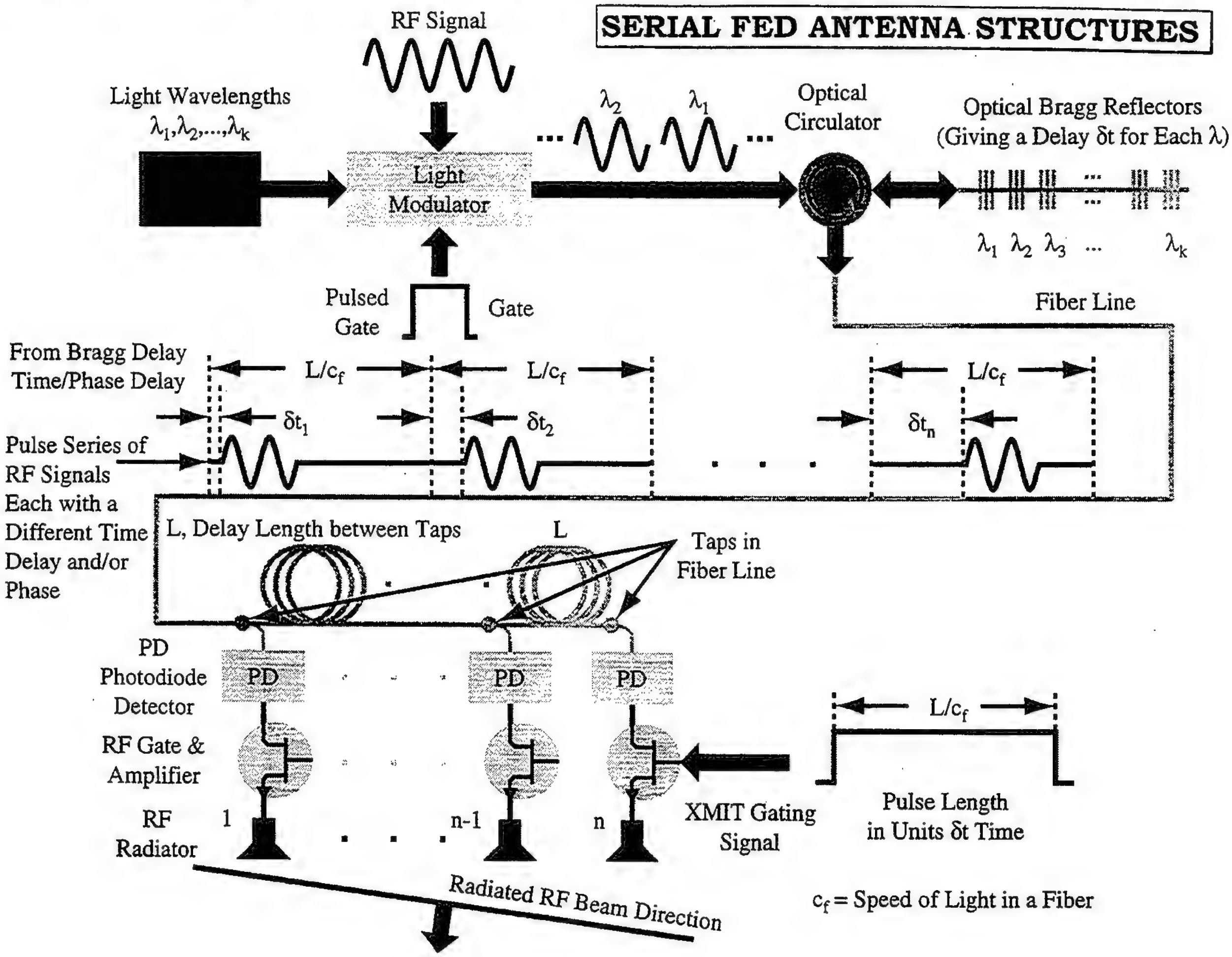

- **Serial Feed Concept:** Experimental results at 9 GHz

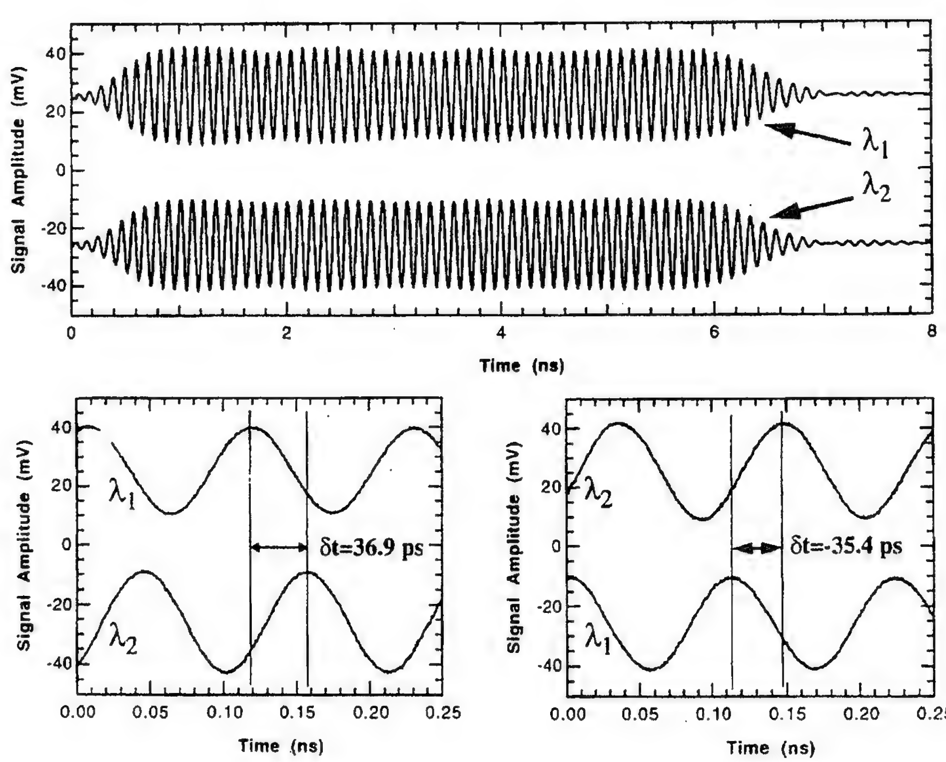

PHASE DELAYS OBTAINED BY CHANGING LASER WAVELENGTHS

3 GHz. 18 degrees 17.5 ps delay

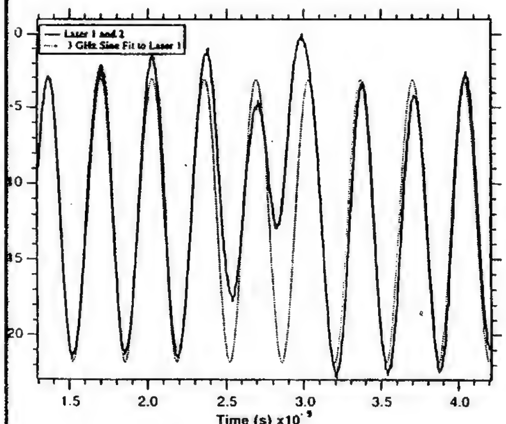

10 GHz. 63 degrees 17.5 ps delay

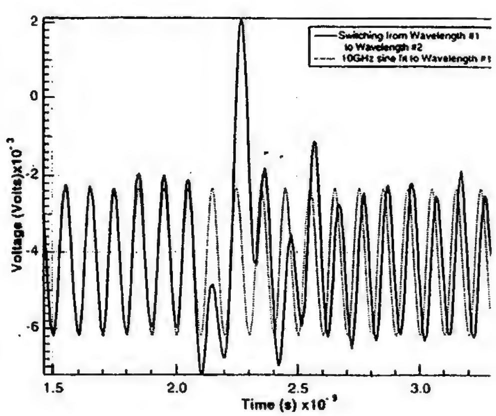

10 GHz. 200 degrees 54.9 ps delay

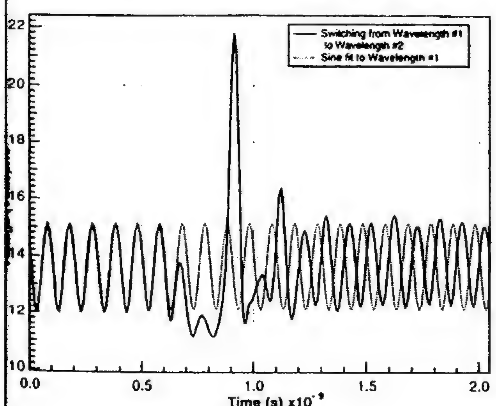

18 GHz. 110 degrees 17.5 ps delay

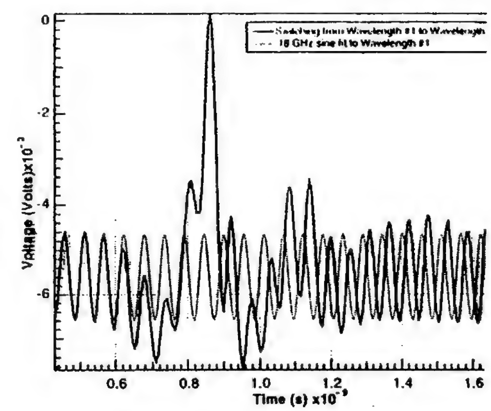

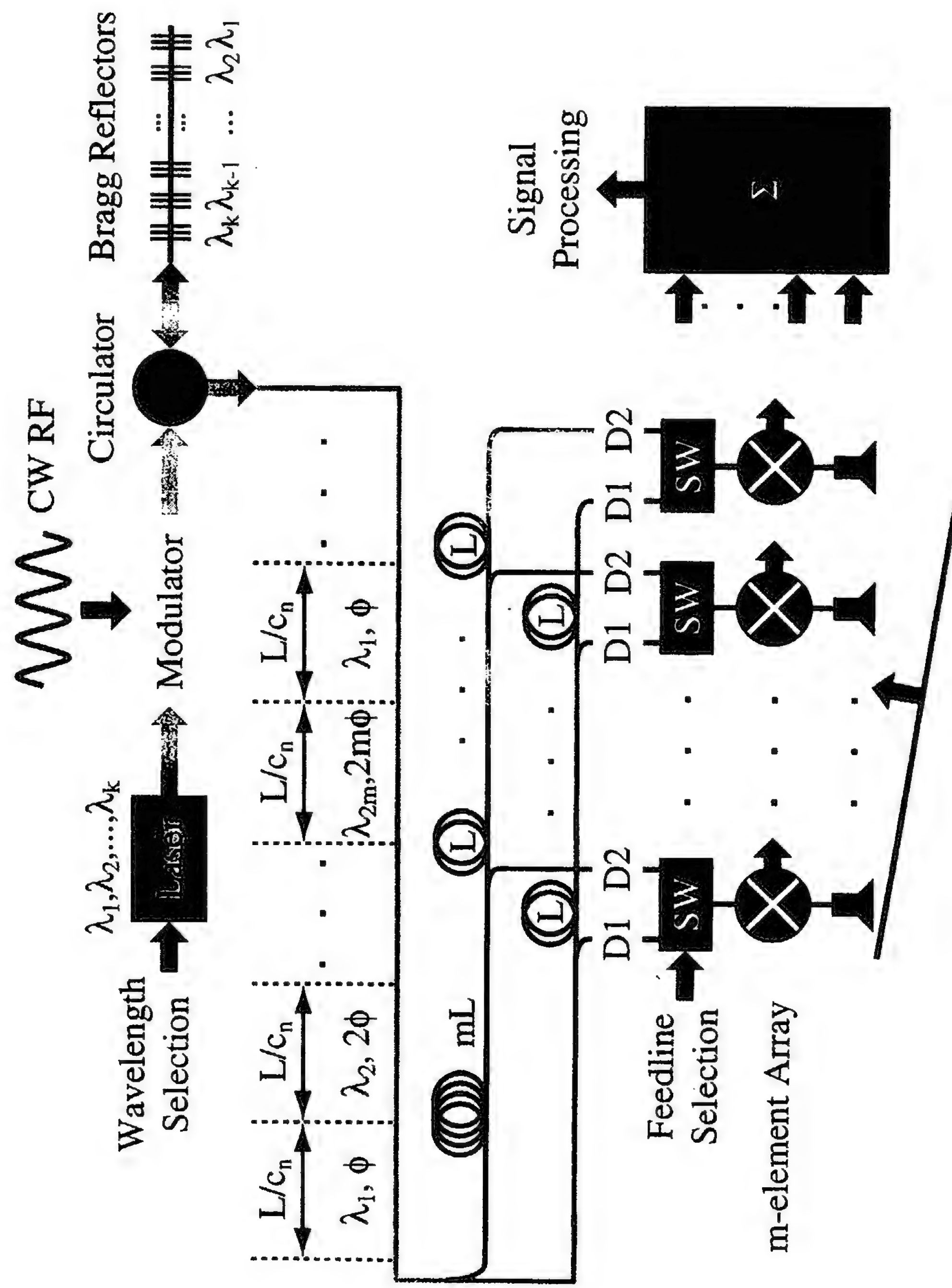

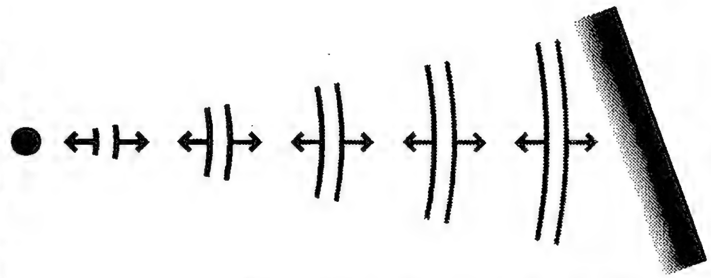

Phase Conjugation

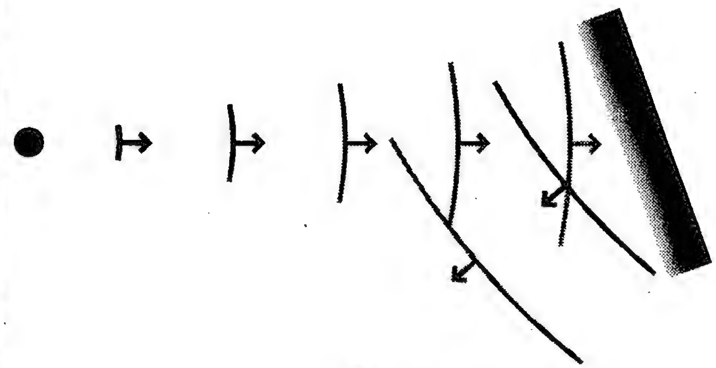

Reflection

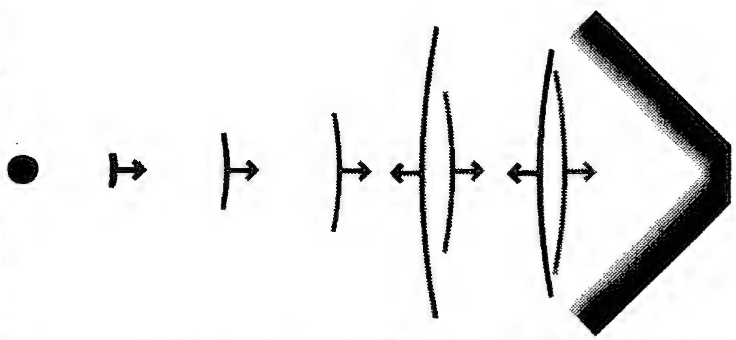

Regular Retrodirectivity

Basic concept:

Instead of using the nonlinearity of materials, we use the nonlinearity of mixers' V-I characteristics

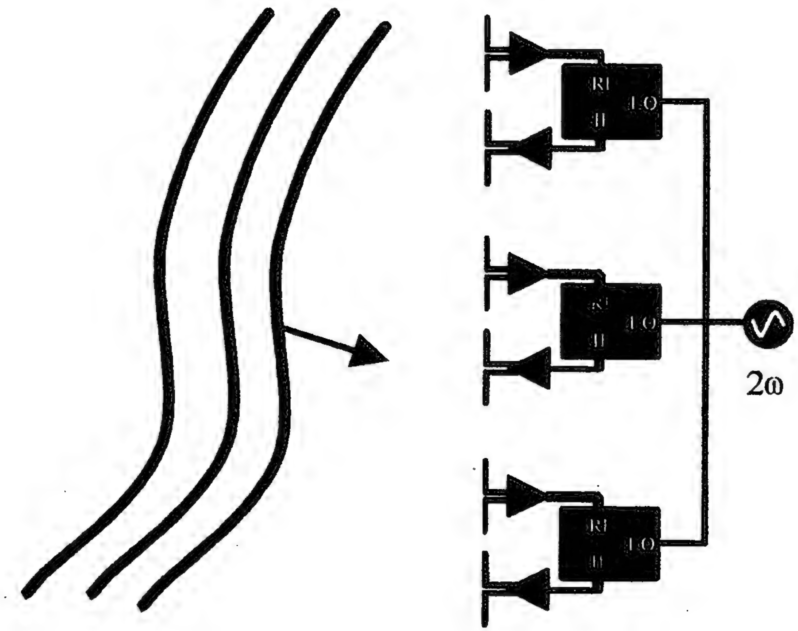

Through the nonlinear response of the mixer, there will be a current component:

$$I_3 = cV_1^* V_2 = cB_1 B_2 e^{i(wt+\phi_j)}$$

This current drives the radiating antenna to generate an *E*-field:

$$\mathbf{E}_C(\mathbf{r}_j) = \mathbf{A}_3 e^{i(wt+\phi_j)}$$

This field is conjugate to the incoming field at $\mathbf{r}_j$

If we can generate $\mathbf{E}_C(z=0)$ for all x,y, we will have $\mathbf{E}_C(\mathbf{r})$ for all $\mathbf{r}$

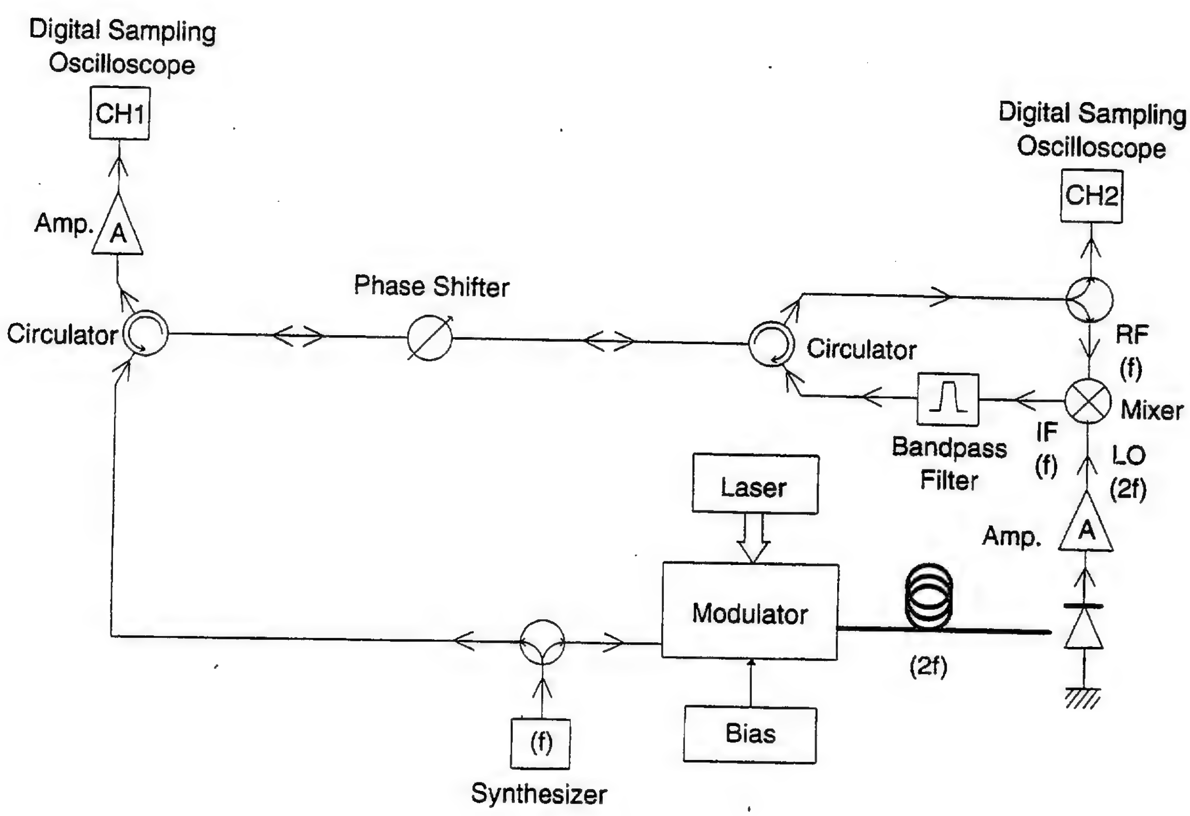

Experimental setup of conjugate phase generation using optically pumped microwave mixers

10-element dipole antenna array, 2/3 λ apart

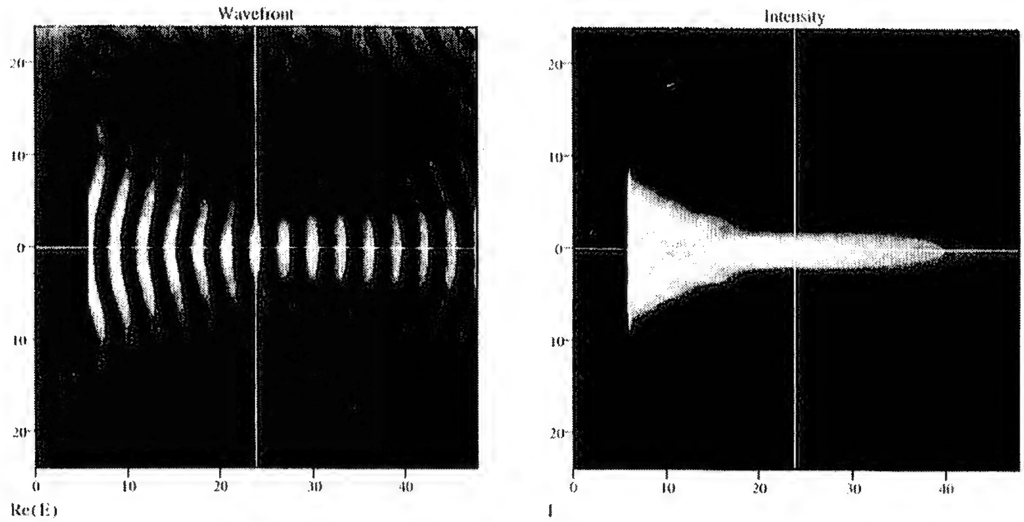

Artificial nonlinear microwave surfaces:

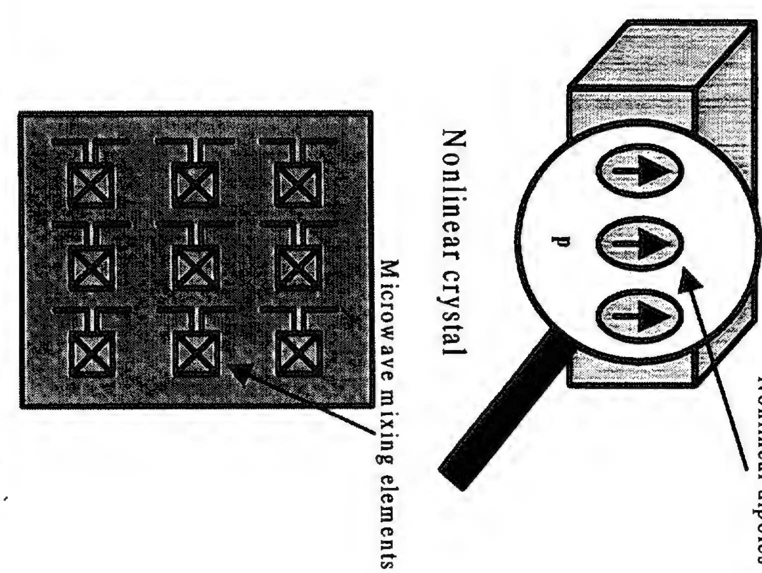

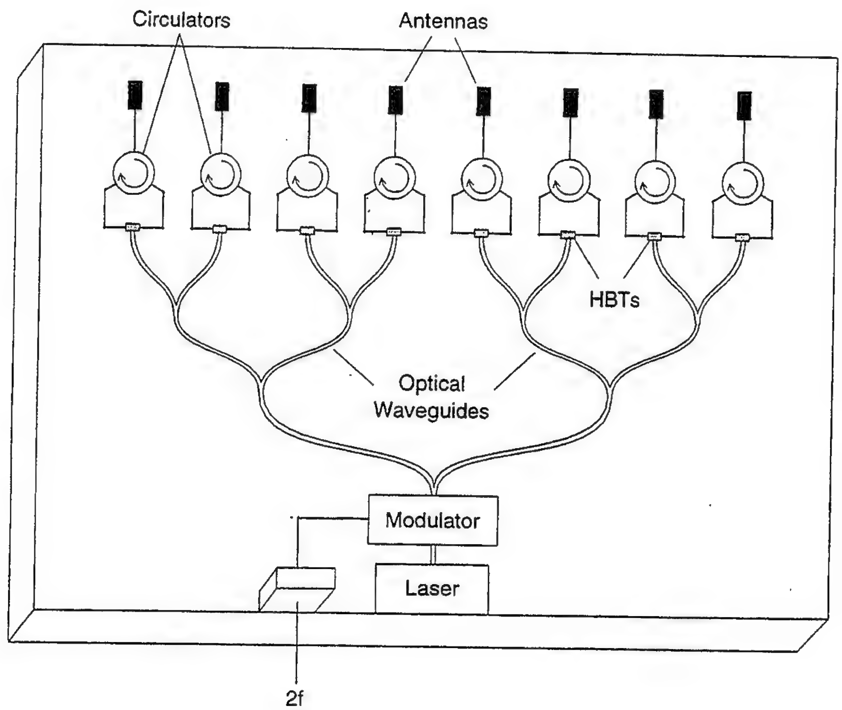

Two dimensional microwave nonlinear optically pumped surfaces

Wafer Scale Integration

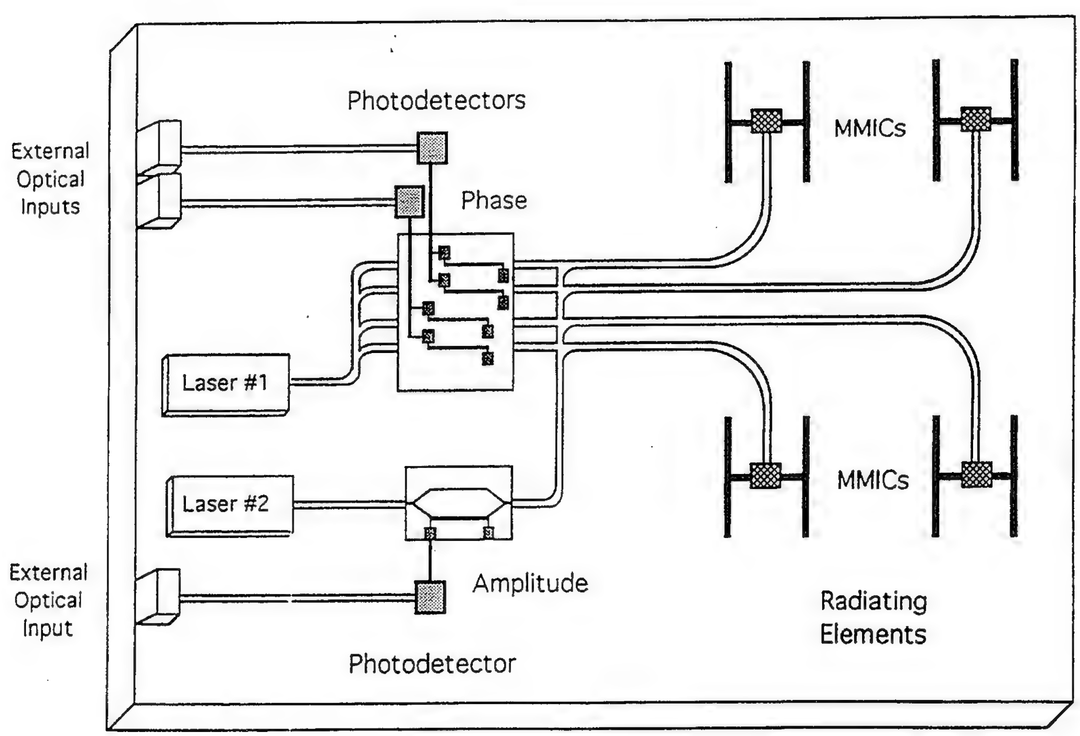

CONCLUSION

* NEW OPTICAL/TERAHERTZ SOURCES

* FIBER TRANSMISSION CAPABILITY

* OPPORTUNITY FOR NOVEL SYSTEMS

* MODE LOCKED SEMICONDUCTOR LASERS

* ELECTROOPTIC POLYMERS

FIELD IS NOW AT AN EXCITING

STAGE

Optical and Electrical Generation of Terahertz Pulses and Imaging Techniques

by

H Roskos

RWTH
Aachen
Germany

Impulsive Characterization
Pump/Probe Measurement Scheme

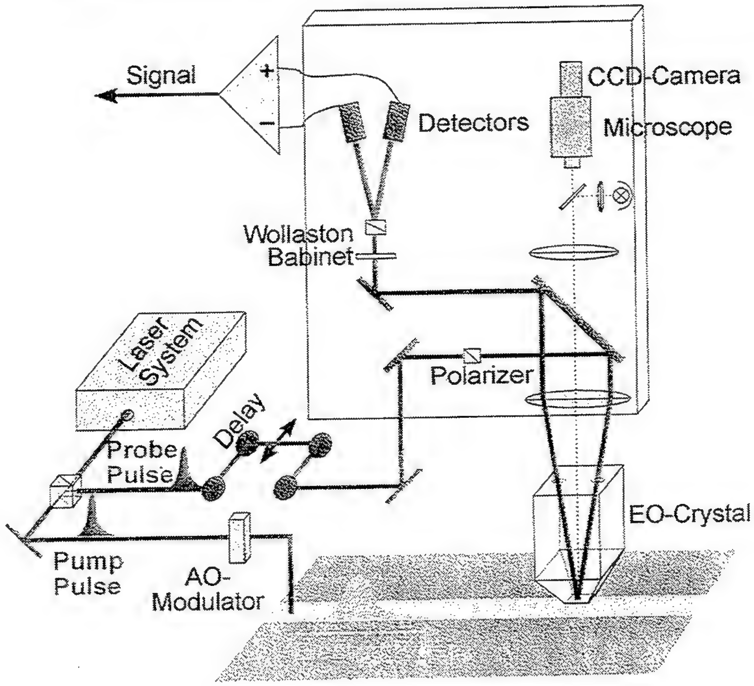

Pump and probe laser pulses originate from the same pulse
=> no jitter
=> very high time resolution

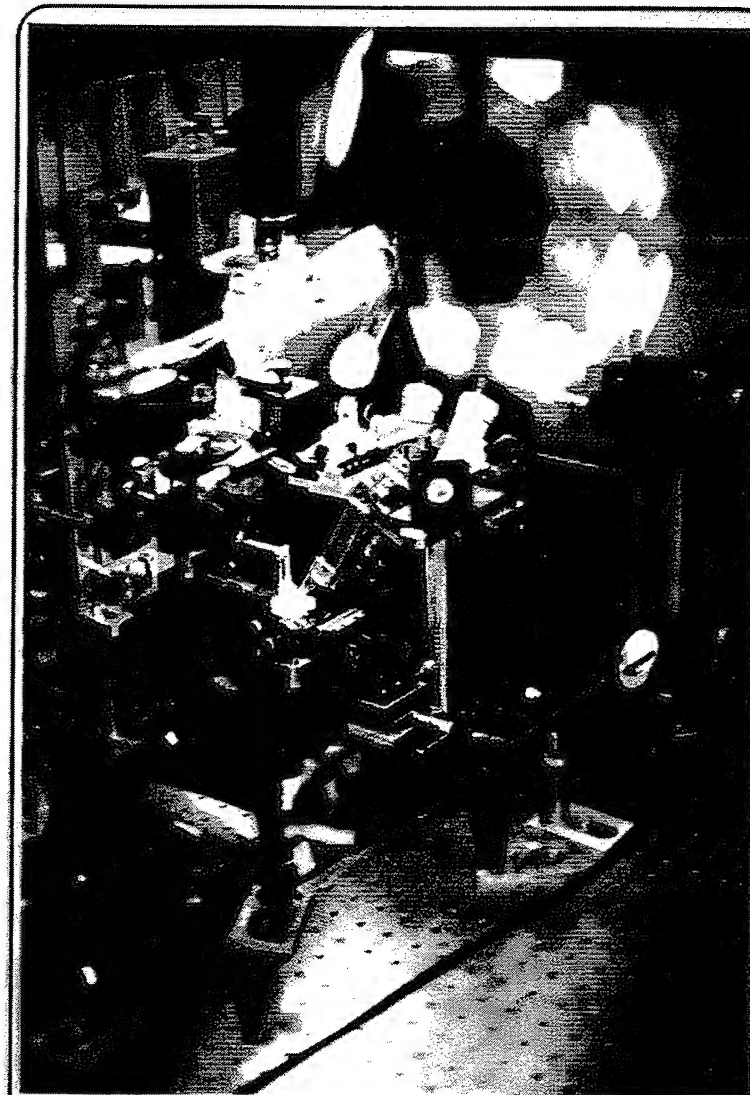

Institut für Halbleitertechnik II, RWTH-Aachen

Generation of Picosecond Electric Pulses

Schematic of a Photoconductive Switch:

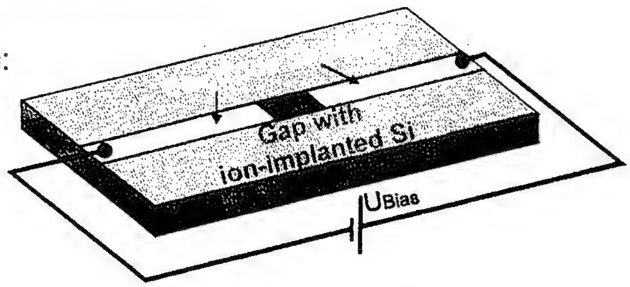

Electric Pulse Stimulation:

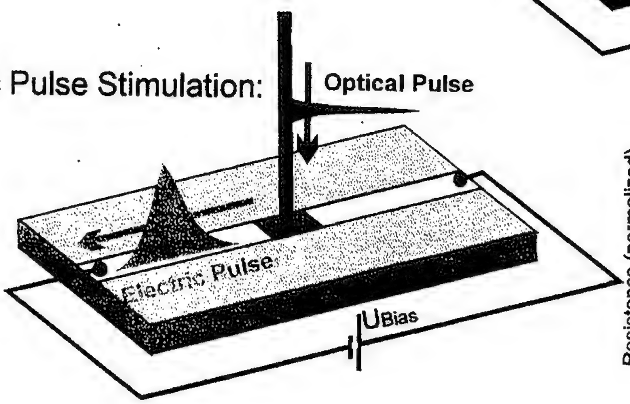

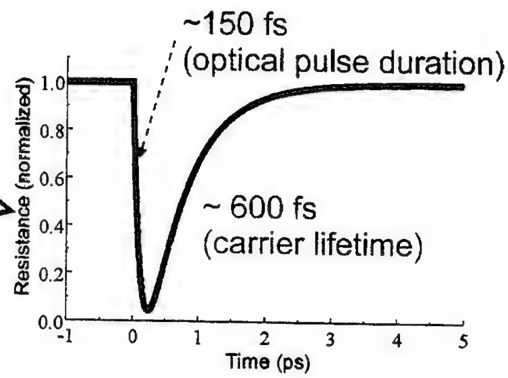

Detection with Freely Positionable Photoconductive Probes

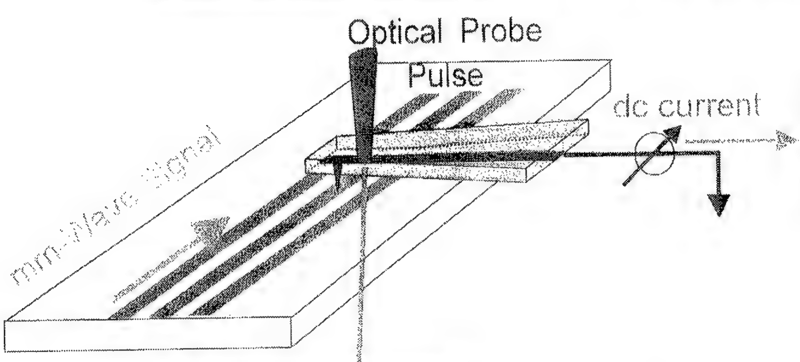

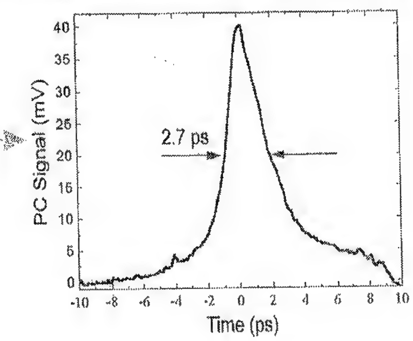

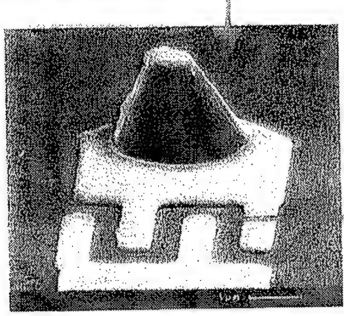

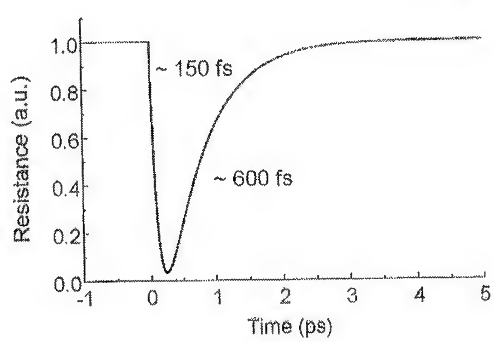

Generation of Picosecond Electric Pulses

Schematic of a Photoconductive Switch:

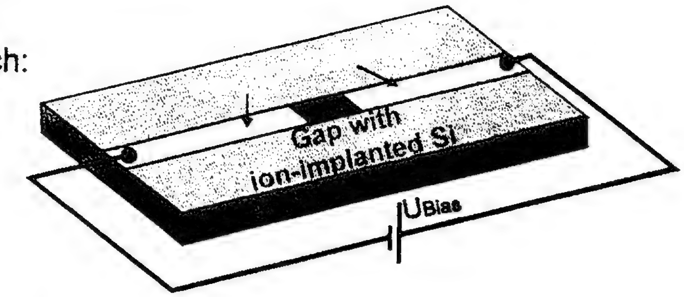

Electric Pulse Stimulation:

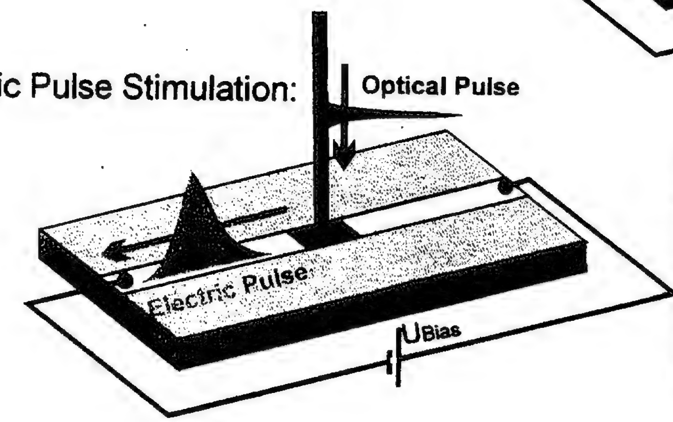

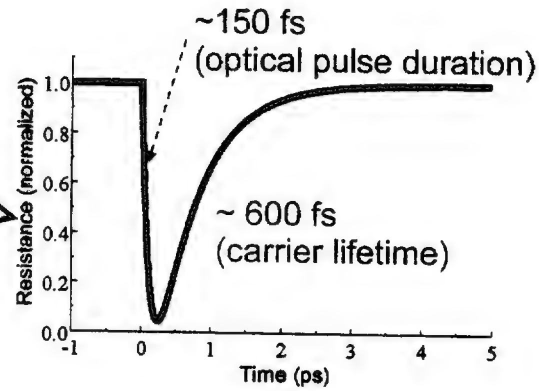

[illegible] Freely Positionable Photoconductive Probe

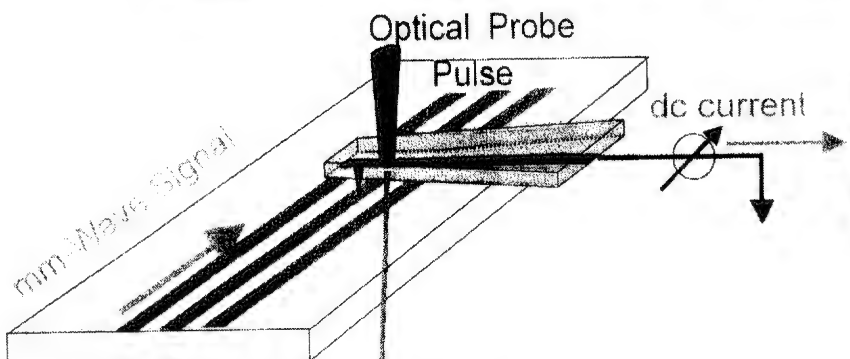

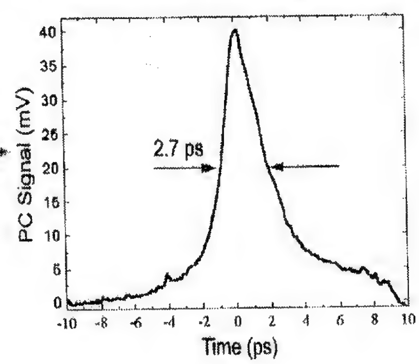

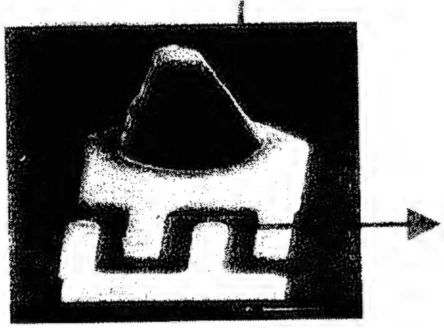

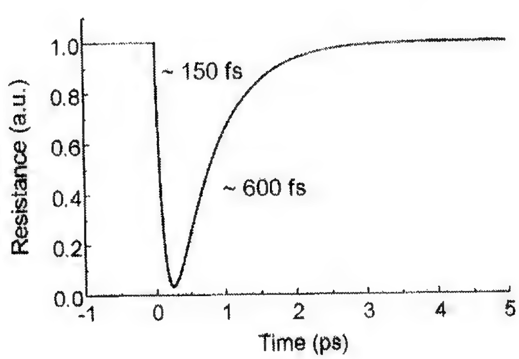

Electro-Optic Detection of Electric Fields

Output: = 0 without Electric Field

$\Delta E \rightarrow \Delta n \rightarrow \Delta\phi \rightarrow \Delta I$

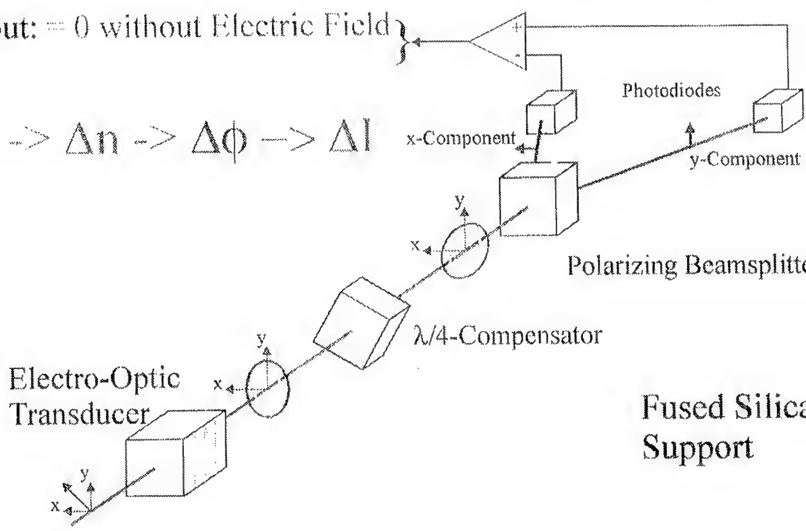

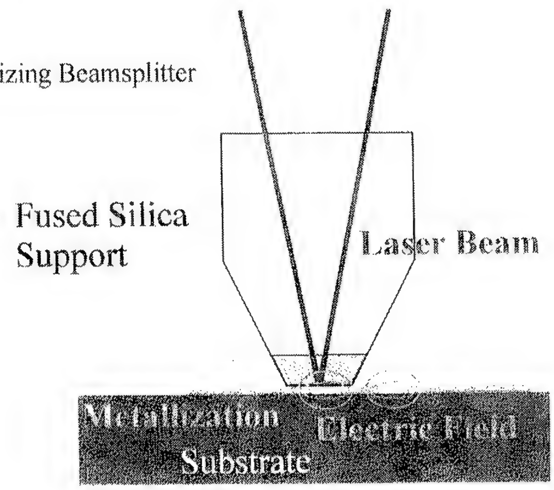

Time Resolution ~ 300 fs
Sensitivity ~ 1 mV

Optoelectronic Characterization

- laser source: Ti:sapphire laser (150 fs, 740 nm, 500 mW)
- pump/probe set up
- ps electric pulse generator: freely positionable photoconductive switch
- ps electric pulse detector: freely positionable electro-optic crystal

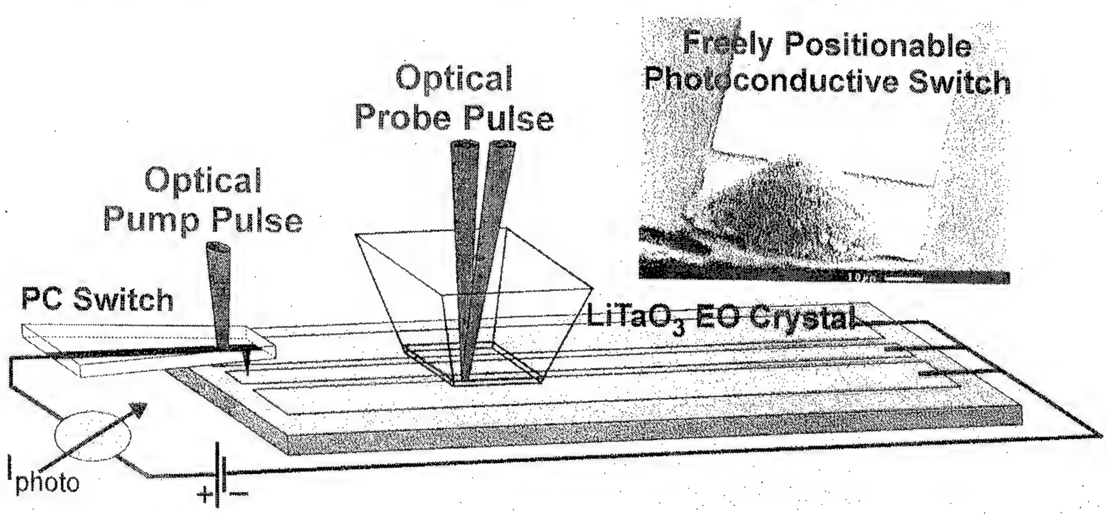

Time Domain Waveforms on a CPW

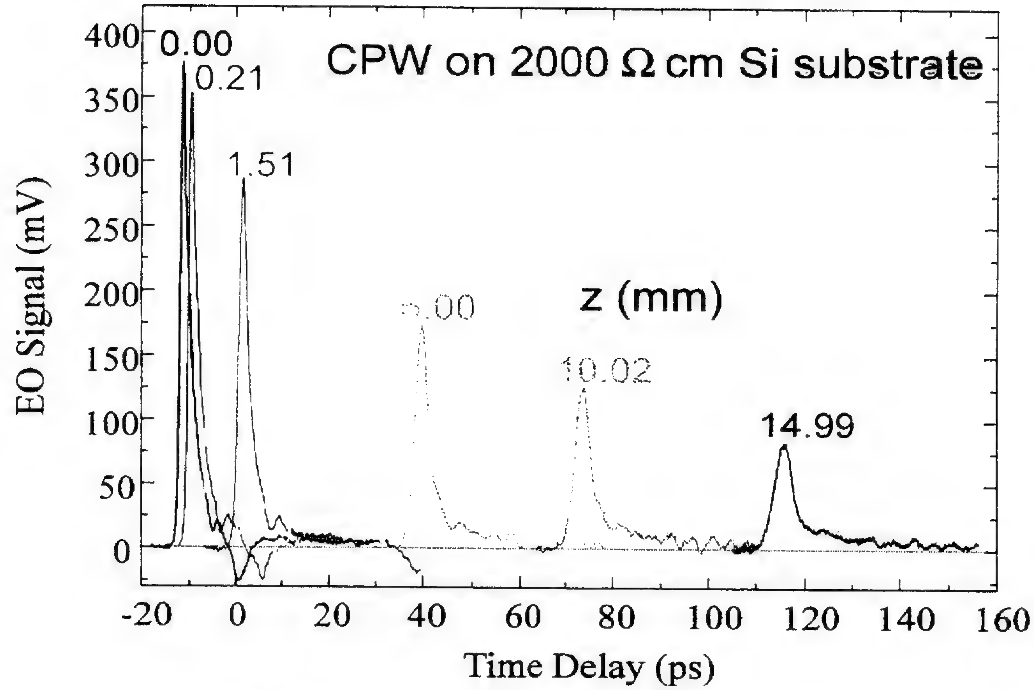

$$V(t,z_2)=\mathcal{F}^{-1}\{\mathcal{F}[(V(t,z_1)]e^{-\gamma(f)(z2-z1)}\}, \quad \gamma(f) = \alpha(f) + i\beta(f)$$

Influence of a SiO_2 Insulation Layer on $\varepsilon_{r,eff}$

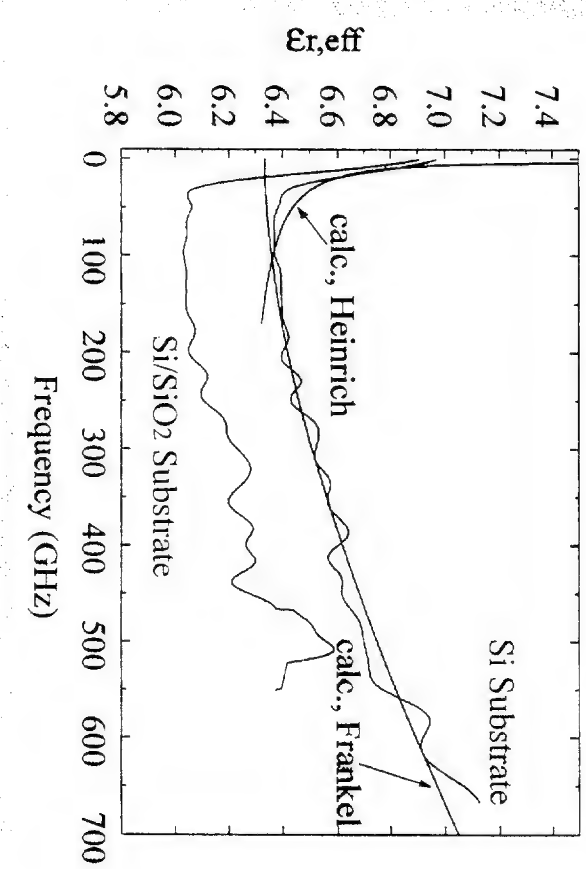

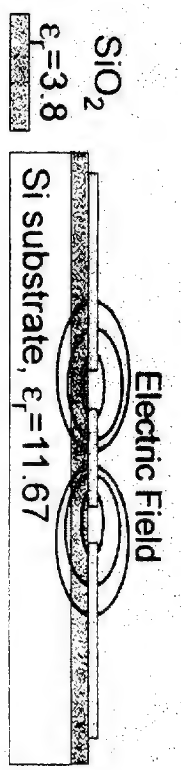

=> with 200 nm SiO_2 insulation interlayer 6.5% decrease of $\varepsilon_{r,eff}$

=> good agreement between experimental data and simulations: 20 GHz - 600 GHz

W. Heinrich, IEEE MTT 4145 (1993)
M.Y. Frankel et al., IEEE MTT 39, 910 (1991)

Synchronisation eines frei laufenden Ti:Saphir-Lasers auf einen freilaufenden GHz-Oszillator

Meßprinzip:
Mischung eines periodischen Millimeterwellensignals (f_{Sig}) mit einer höheren Harmonischen der Laserpulswiederholfrequenz (f_L)

=> Abbildung des Millimeterwellensignals bei einer Zwischenfrequenz f_{Int}

$$f_{Int} = f_{Sig} - n \times f_L$$

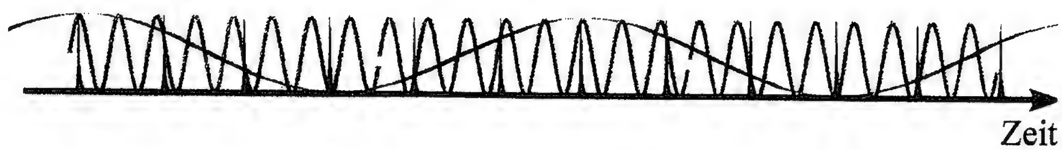

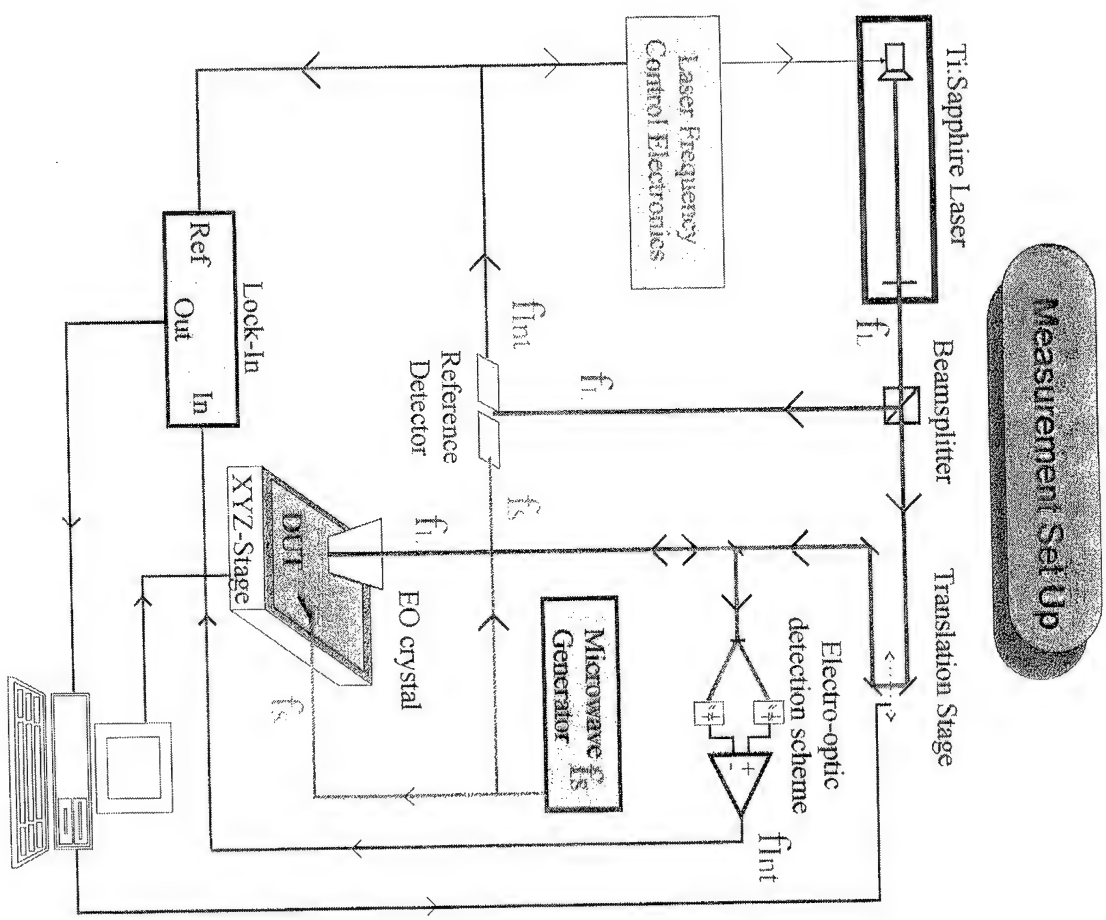

Fast Transients on a Nonlinear Transmission Line (NLTL)

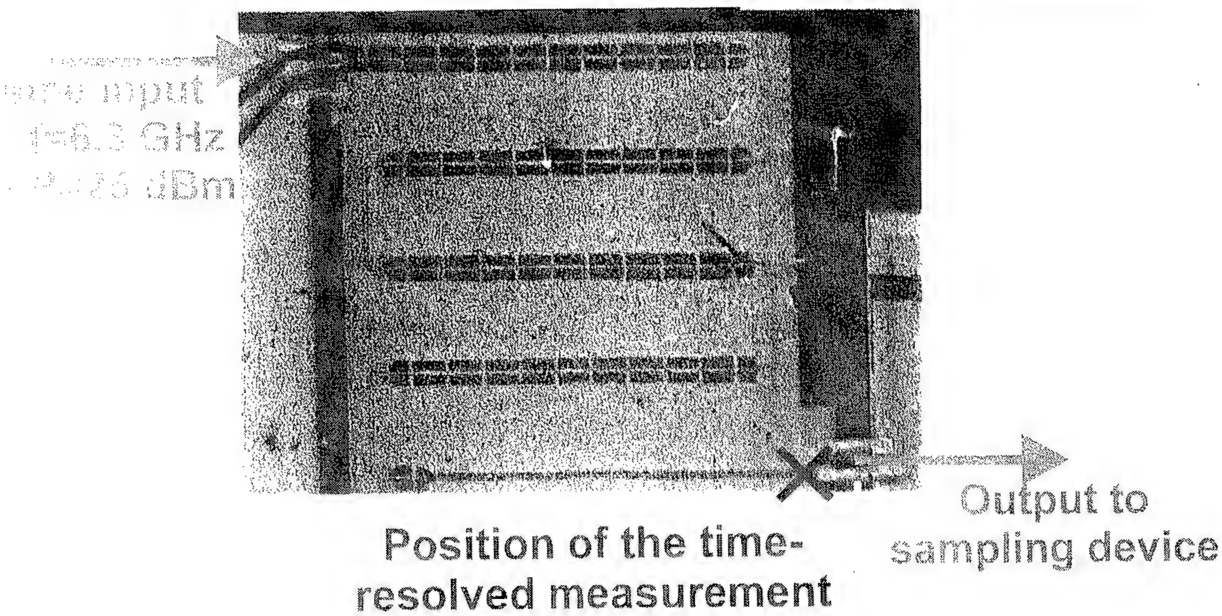

Waveform at the Output of the NLTL

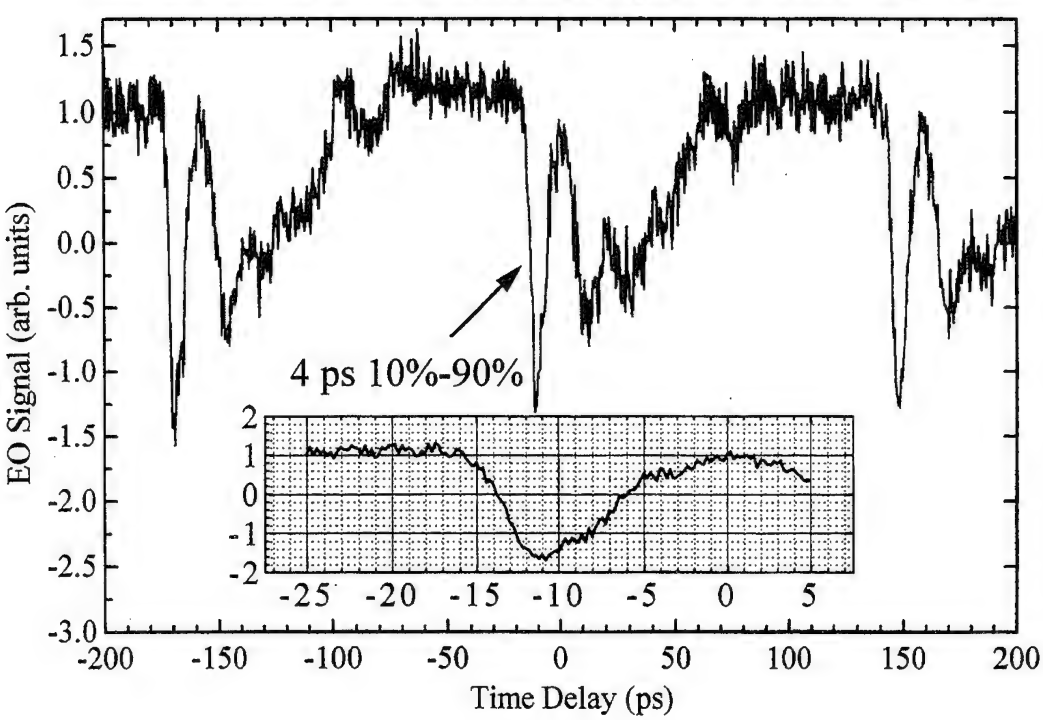

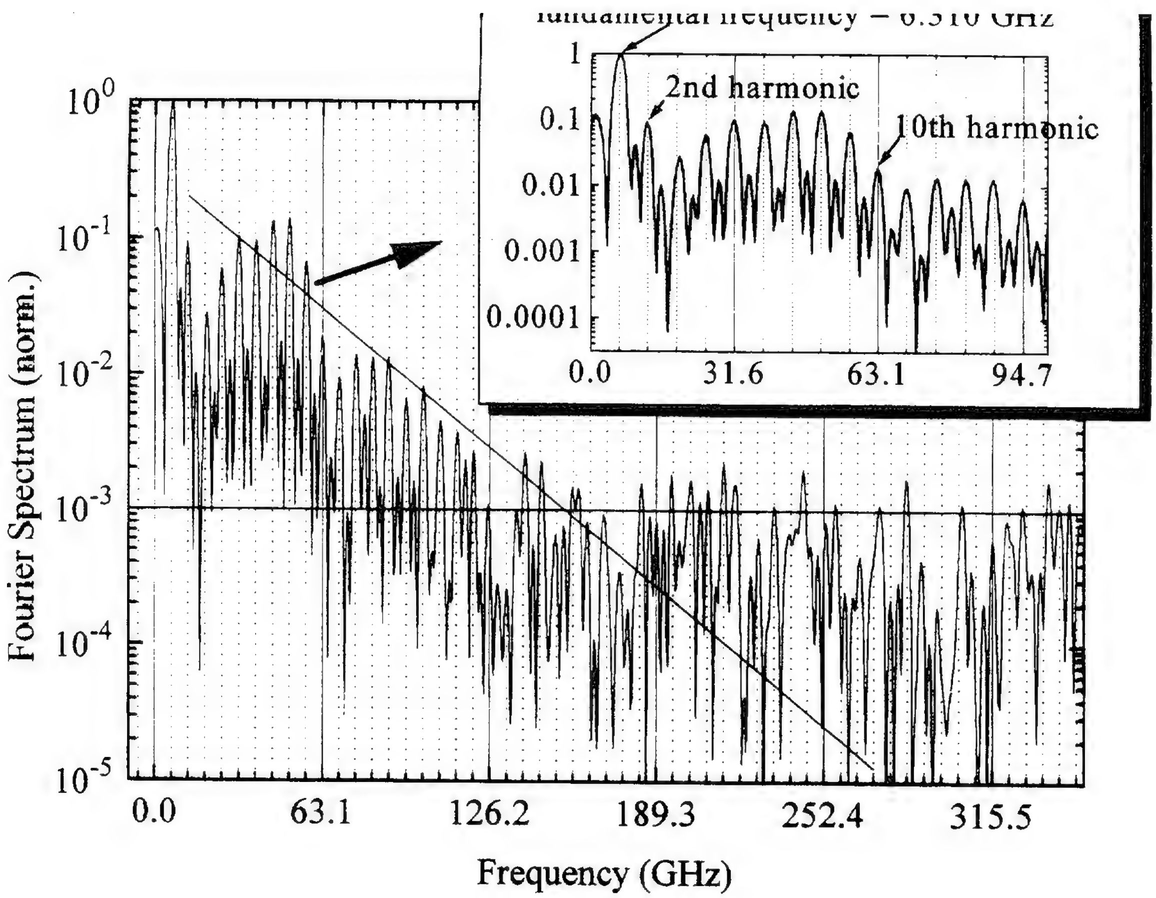

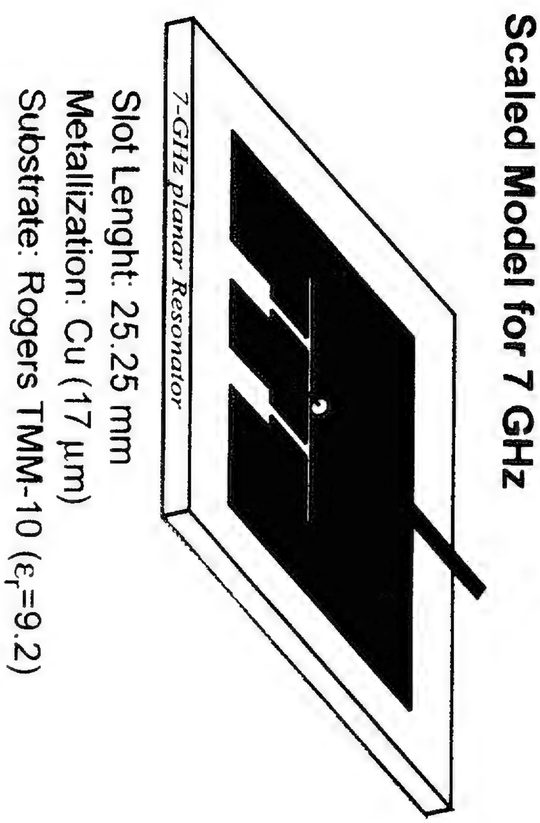

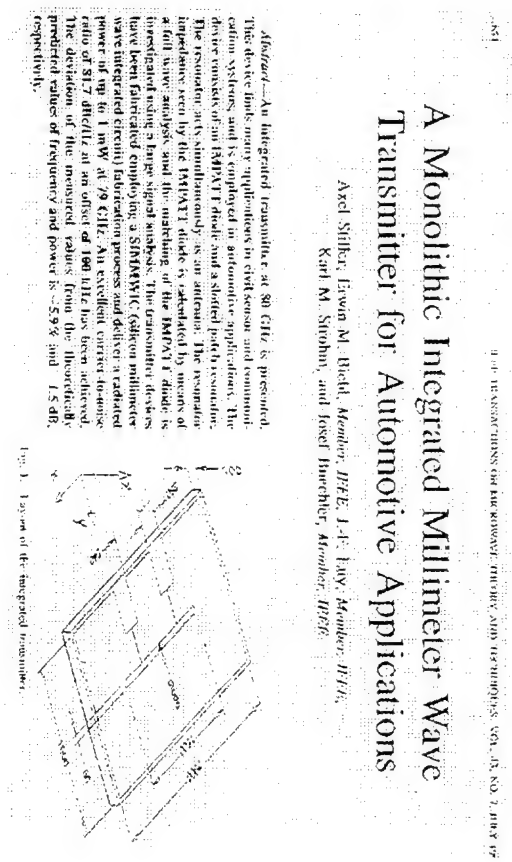

A Monolithic Integrated Millimeter Wave Transmitter for Automotive Applications

Axel Stiller, Erwin M. Biebl, Member, IEEE, J.-F. Luy, Member, IEEE, Karl M. Strohm, and Josef Buechler, Member, IEEE

Electrical Characterization

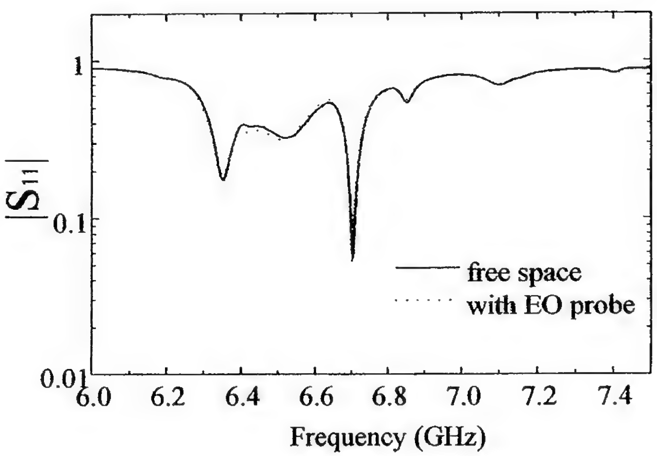

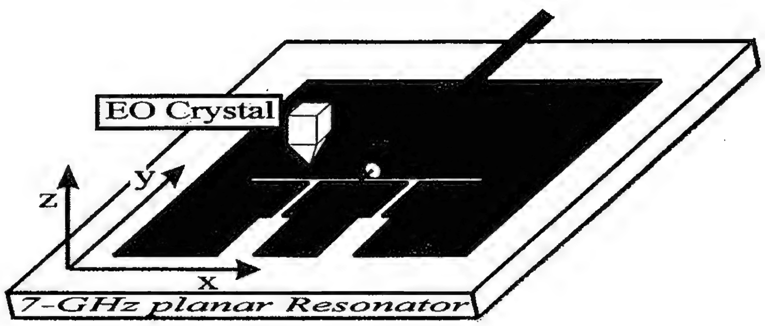

=> noninvasive testing with EO probe

Experimental Set Up For Electric Near Field Mapping

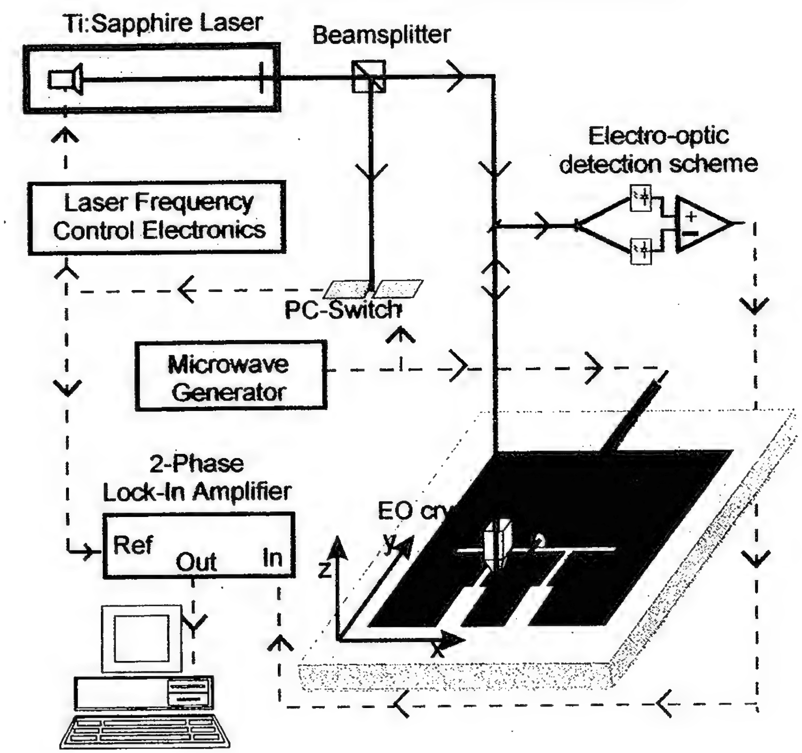

Magnitude of the y-component of the electric field

Probing Distance 1250 μm

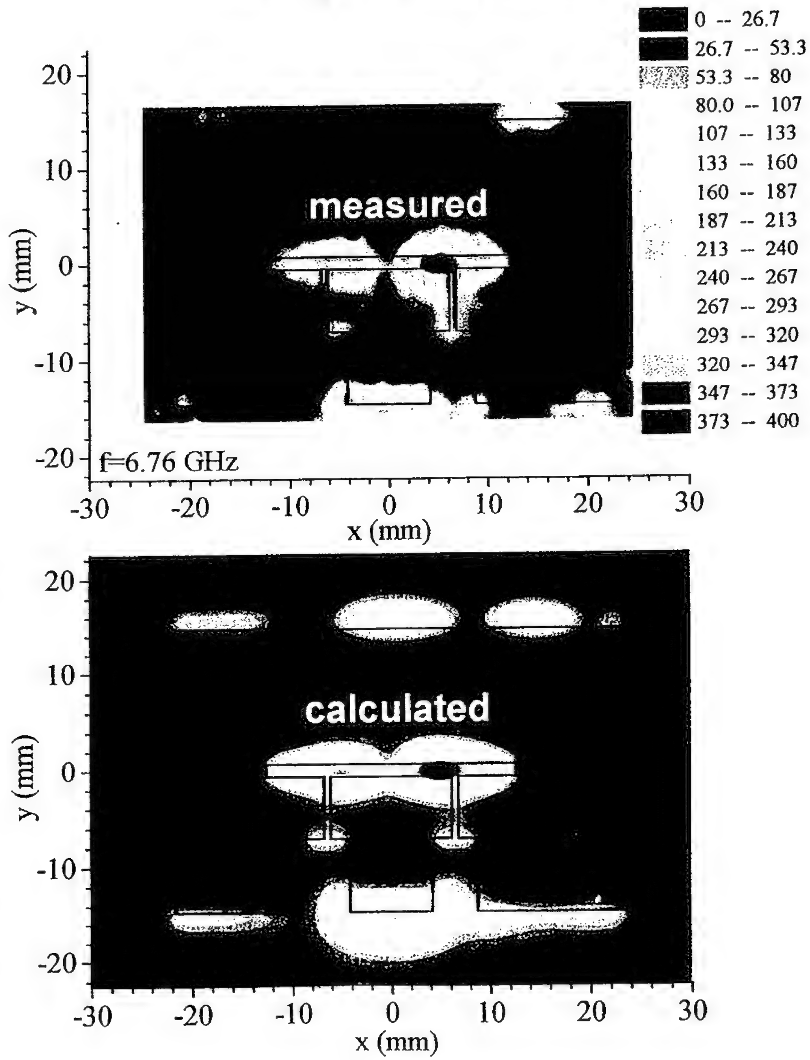

Phase of the y-component of the electric field

Probing Distance 1250 μm

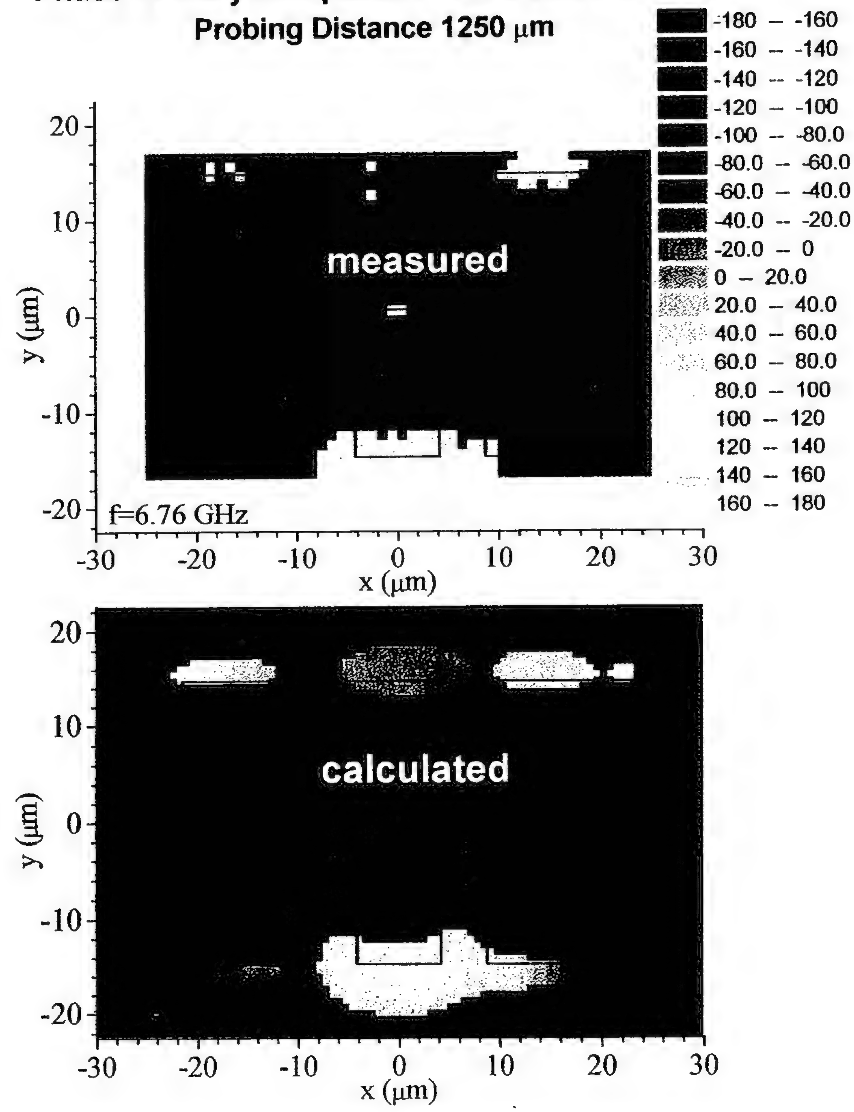

Magnitude of x-component (50 μm height)

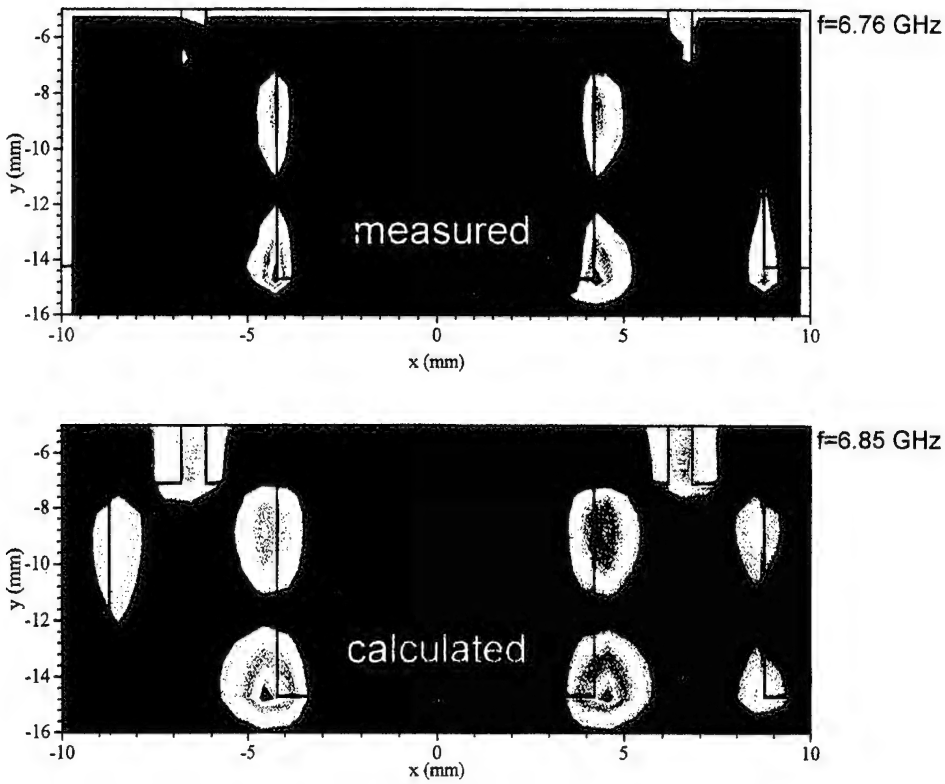

x-Component, Probing Distance 50 μm, Variable Frequency

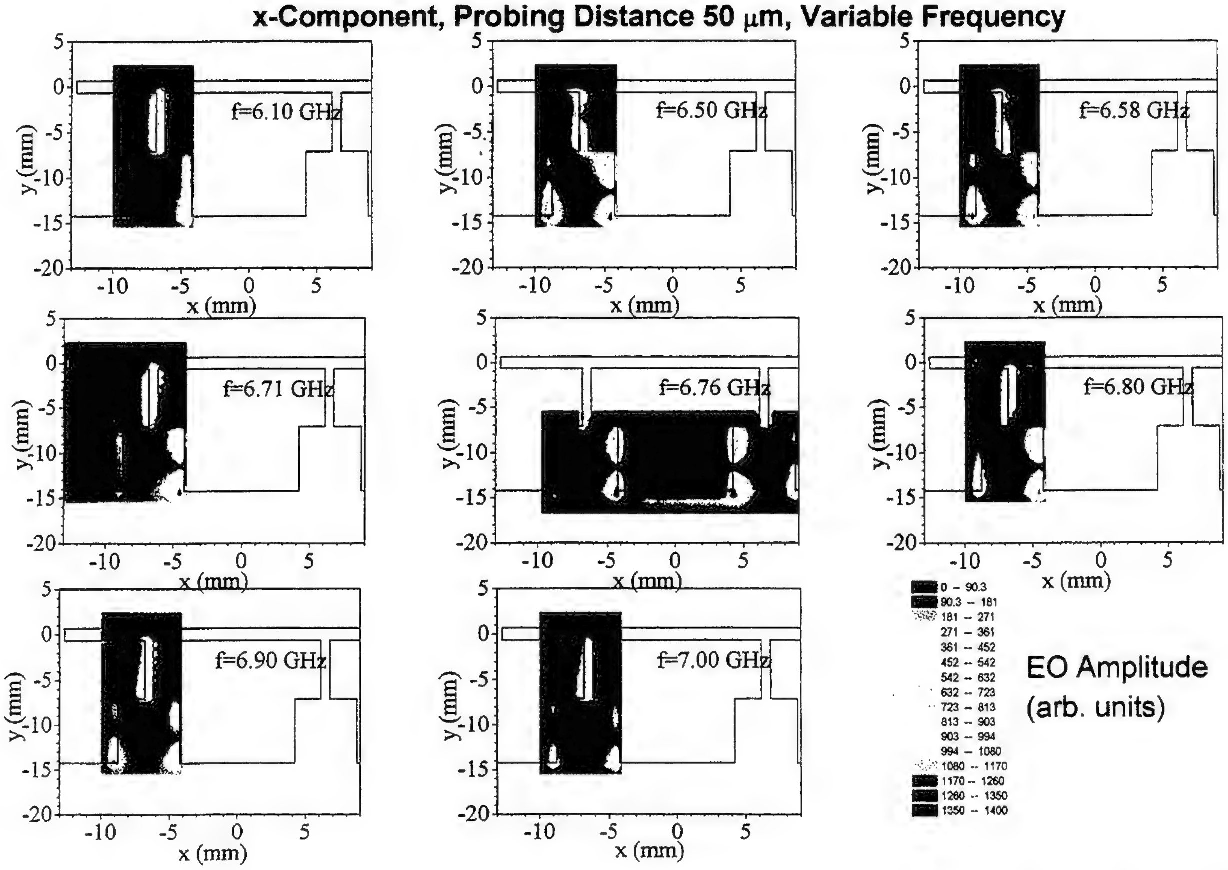

x-Component, f= 6.76 GHz, Variation of the Probing Distance

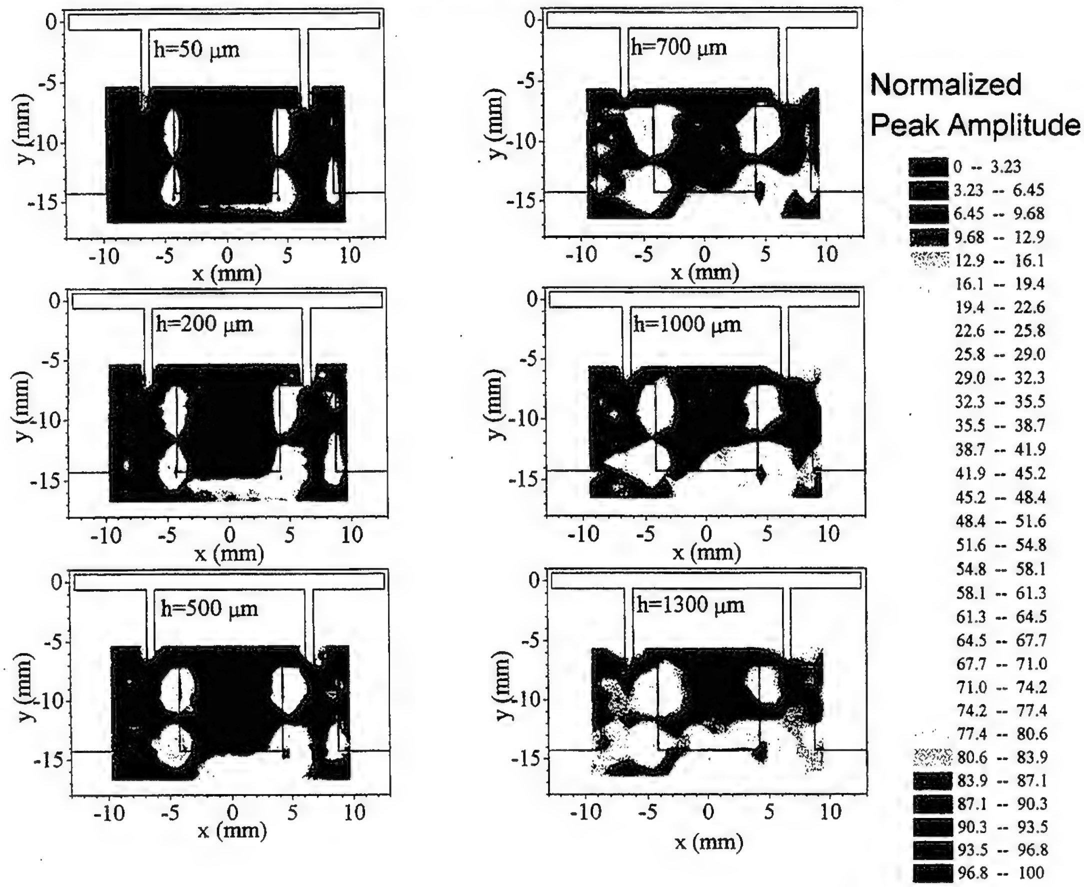

LASER-DRIVEN BLOCH OSCILLATIONS IN SEMICONDUCTOR SUPERLATTICES

Hartmut G. Roskos
R. Martini, F. Wolter, P. Haring Bolivar, C. Waschke,
G. Klose, K. Köhler (Freiburg)

Institut für Halbleitertechnik II, Prof. H. Kurz
RWTH Aachen, Germany

BLOCH OSCILLATIONS IN PERIODIC POTENTIALS

Electronic wave packet in a periodic potential (period: d) superimposed with an homogeneous electric bias field F

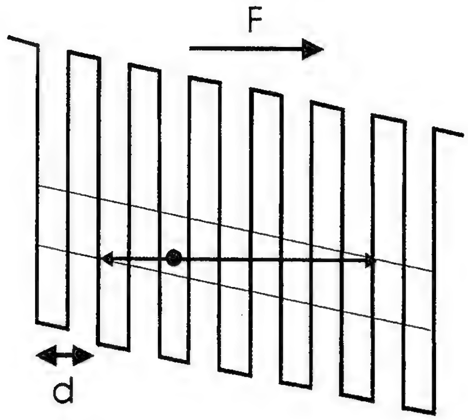

Spatial oscillations of the wave packet because of Bragg reflections

SEMICLASSICAL PICTURE OF BLOCH OSCILLATIONS

Electron wave packet in a periodic potential (period: d) subjected to a uniform electric field F

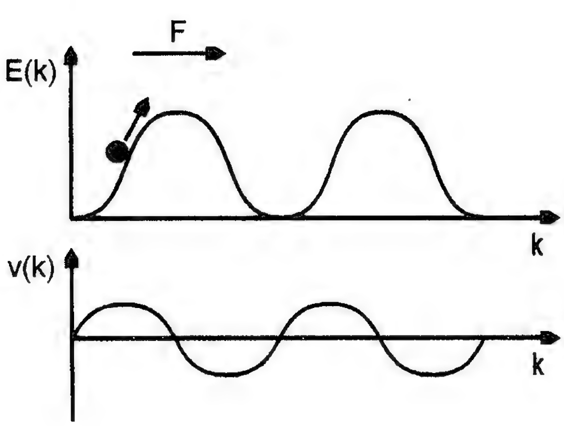

Bloch (1928): Wave packet moves with constant velocity $\hbar d\vec{k}/dt = e\vec{F}$ through k-space

Real-space velocity: $\hbar v(k)=dE/dk$

↓

Zener (1934): Spatial oscillations with Bloch frequency

$\boxed{\nu_B=eFd/h}$

BLOCH OSCILLATIONS

Semi-classical picture (k space)

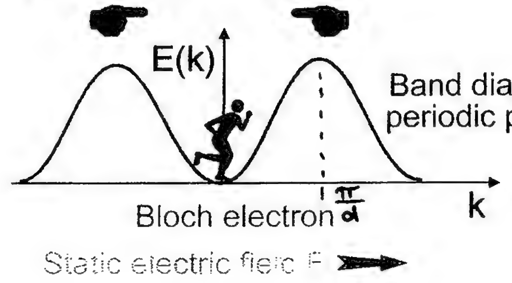

Bloch frequency: $\nu = eFd/h$

Realization: Quantum interference in the Wannier-Stark ladder of a superlattice

Full QM picture (real space)

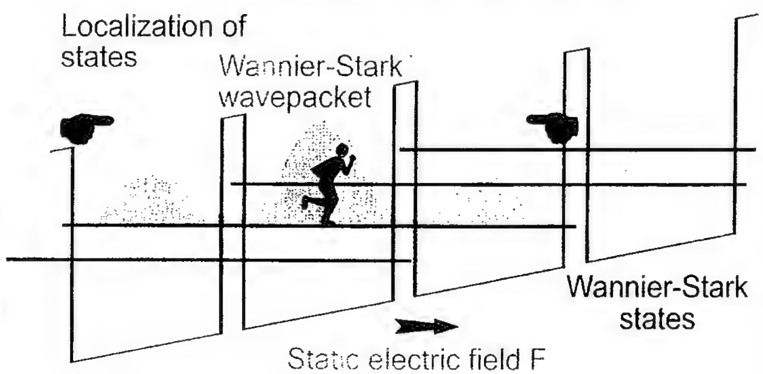

Energy splitting of WS states: $h\nu = eFd$

DETECTION OF BLOCH OSCILLATIONS

Time-resolved detection of Bloch oscillations by three different techniques:

1. Four-wave mixing: **Third-order interband polarization $P^{(3)}(t)$**
2. THz-emission spectroscopy: **Detects emitted coherent electromagnetic transients**
3. Electrooptic probing: **Detects internal electric-field changes**

1. Feldmann et al., PRB 46, 7252 (1992); Leo et al., Sol. State Commun. 84, 493 (1992); Leisching et al., PRB 50,14389 (1994).
2. Waschke et al., PRL 70, 3319 (1993); Roskos, Adv. Sol. Phys. 34, 297 (1994).
3. Dekorsy et al. PRB 50, 8106 (1994) and PRB 51, 17275 (1995)

THz emission:

Emitted electric field: $E_{THz}(t) \sim \frac{\partial j(t)}{\partial t}$

j(t): Quantum-mechanical current density

$j(t) = j^{(2)}(t) = 2\pi e/h \int_k \partial\varepsilon(k)/\partial k \; C_k \, dk,$

$C_k = \langle c_k^+ c_k \rangle$: **Occupation density of electrons or holes**

- Emission efficiency?
- Dephasing times and dephasing mechanisms?
- Properties of excitons or continuum electrons?

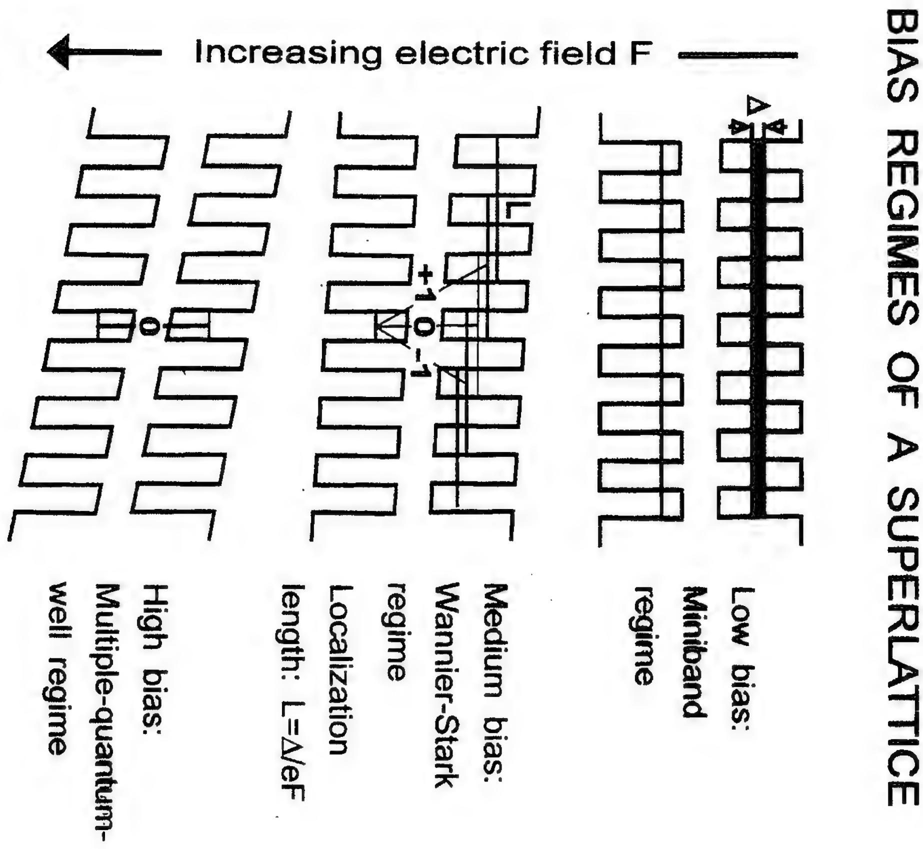

Generation of Bloch oscillations by simultaneous excitation of excitonic and/or continuum Wannier-Stark resonances with an ultrashort laser pulse

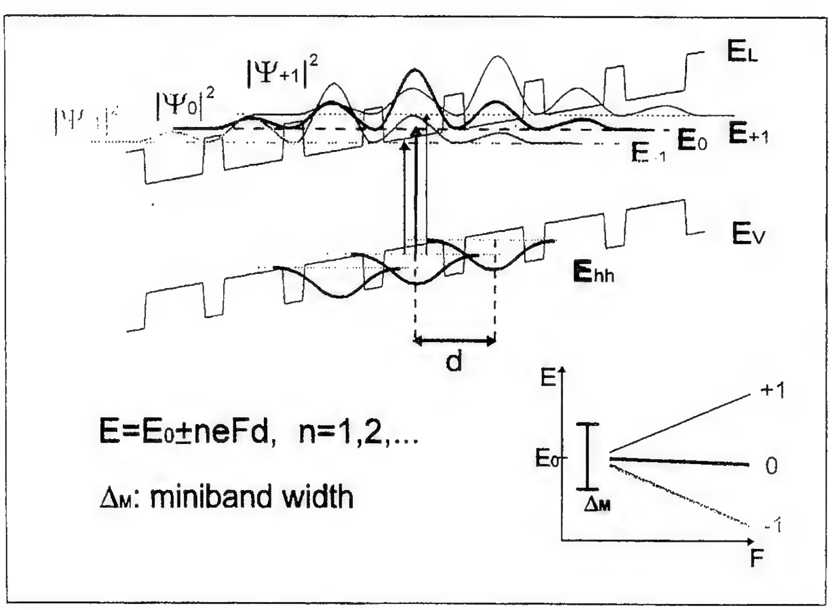

SAMPLE DESIGN

Superlattice structure as the intrinsic region of a pin diode
Sample patterned into 450-µm mesas

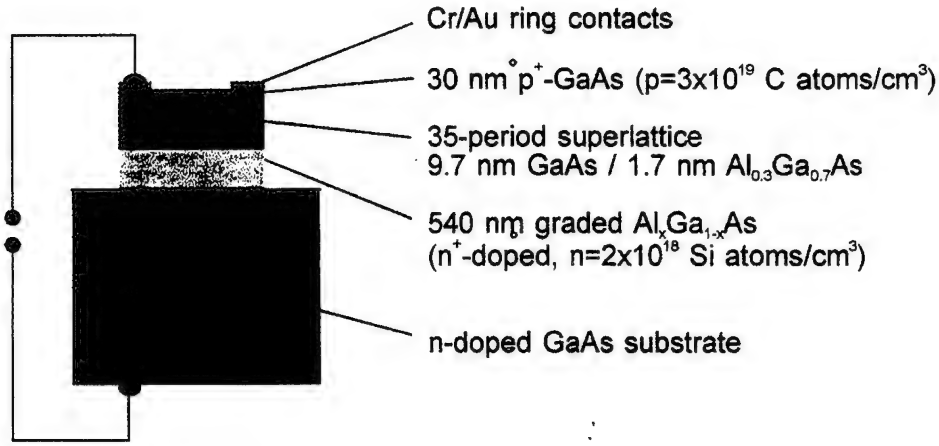

ZEITLICHE ENTWICKLUNG EINES WANNIER-STARK-WELLENPAKETES

$$|\Psi|^2 = |\Psi_0 + \Psi_{-1}|^2$$

$$P(\Delta t) = N_{exc}\, e \langle \Psi^*_{el}(\Delta t) | z | \Psi_{el}(\Delta t) \rangle$$

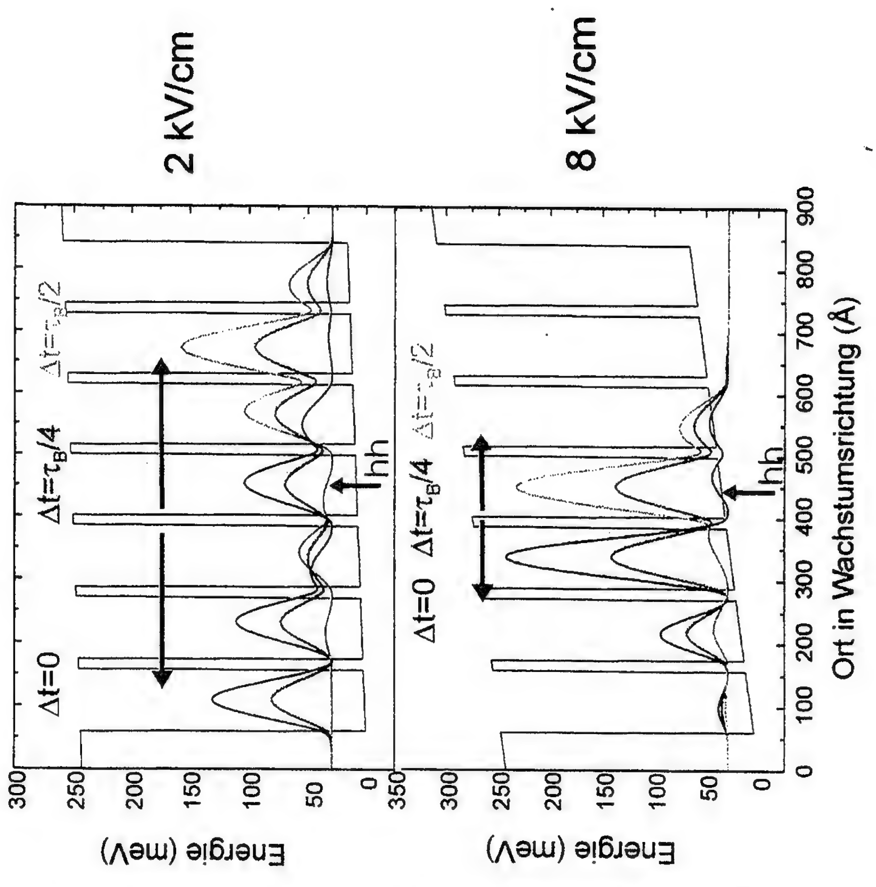

Periode einer Bloch-Oszillation: $\tau_B = \frac{h}{eFd}$

EXPERIMENTAL SETUP FOR THZ-EMISSION SPECTROSCOPY

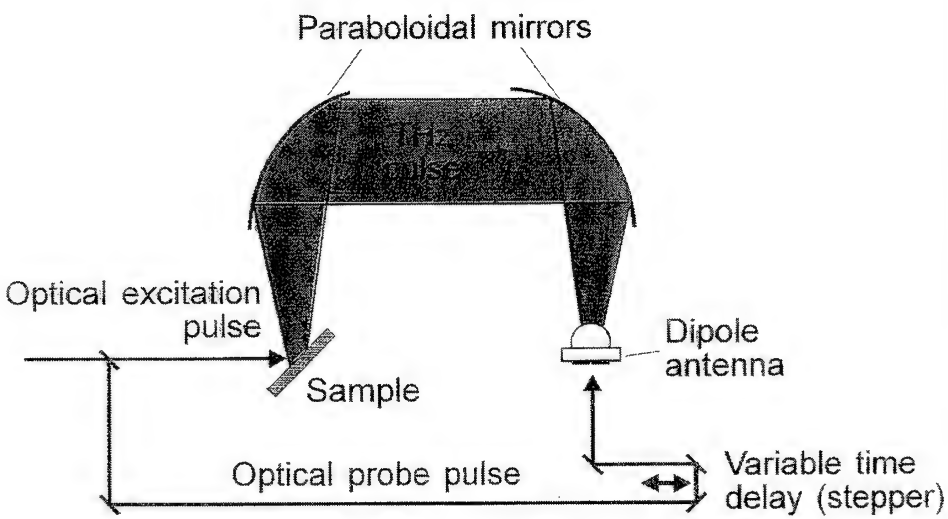

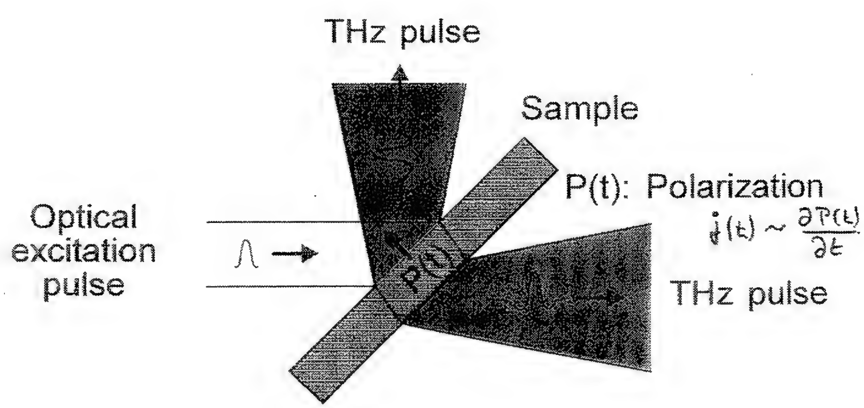

THZ-EMISSION FROM BLOCH OSCILLATIONS

Minibandwidth: 18meV

T=10 K, n = $10^9 cm^{-2}$

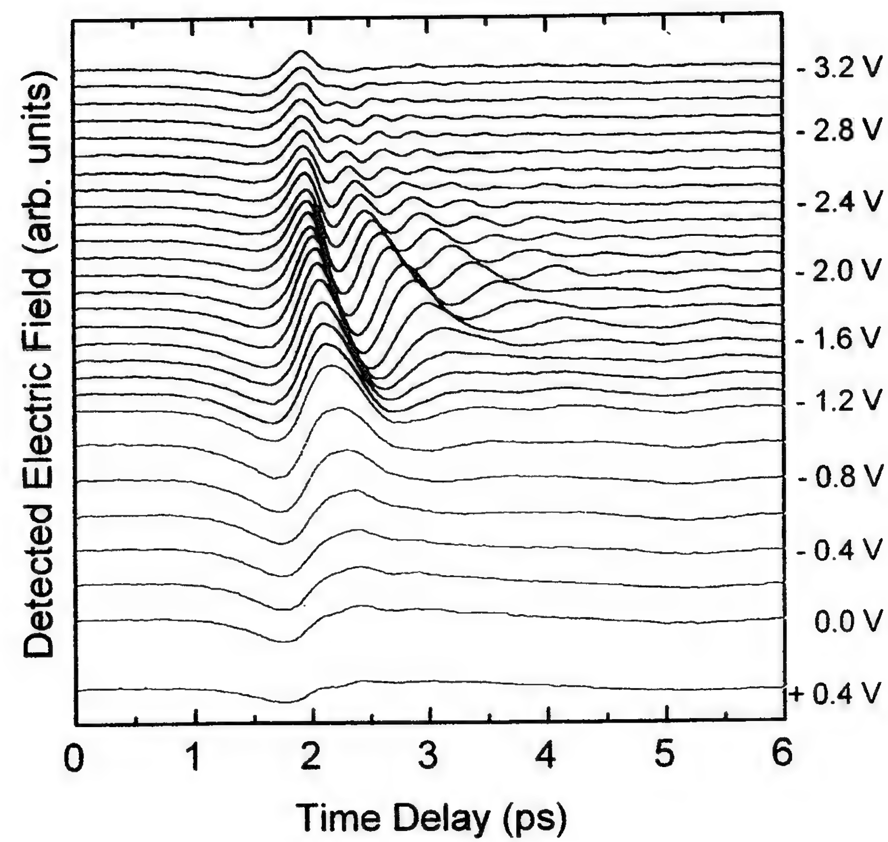

FOURIER TRANSFORM OF THE THZ RADIATION

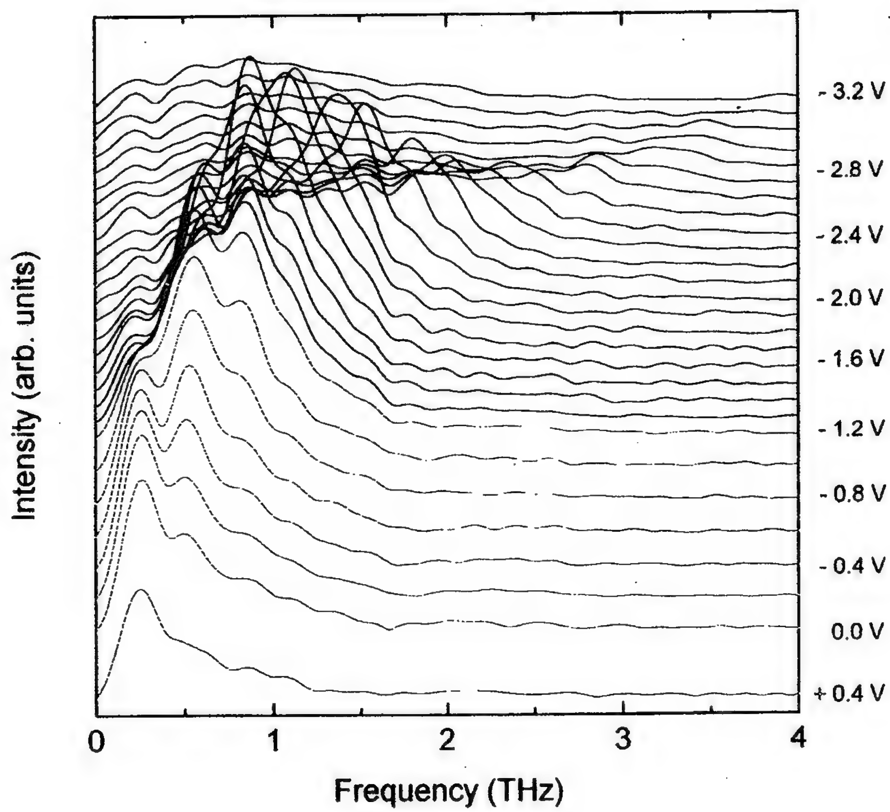

FOURIER TRANSFORM OF TERAHERTZ RADIATION

CORRECTED BY THE SPECTRAL SENSITIVITY
OF THE DETECTION SYSTEM

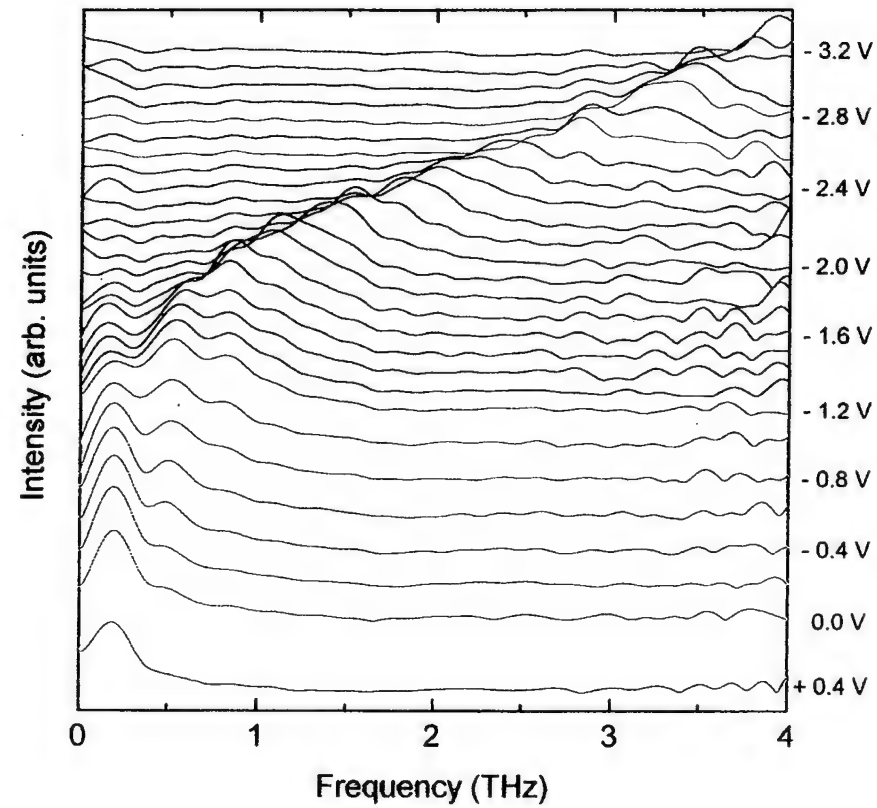

EFFICIENCY OF THZ-WAVE EMISSION

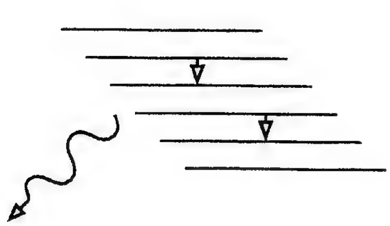

Energy of the emitted coherent radiation is extracted by Wannier-Stark ladder transitions

Questions to be addressed:

- What determines the emitted power?
- How to increase the emission efficiency?

COHERENCE AND EMITTED POWER

Single dipole

$I(t) \sim |E_1(t)|^2$

Two dipoles

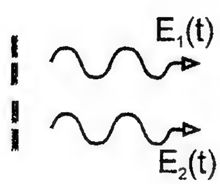

Coherent emission into the same electromagnetic mode:

$I_{coh}(t) \sim |E_1(t)+E_2(t)|^2$

Emission with same phase, same amplitude:

$I_{coh}(t) \sim 4\ |E_1(t)|^2$

Coherent emission into one electromagnetic mode (= SUPERRADIANCE) is more efficient than incoherent emission: $\boxed{I_{coh}(t) = 2\ I_{incoh}(t)}$

SUPERRADIANT THZ EMISSION

$E_{max} = N\,\Delta E$: Interlevel energy available for coherent emission, N: Initial number of electrons

P_{rad} : Power of emitted radiation

$\rightarrow \quad \gamma_{rad} = P_{rad} / E_{max}$: $\boxed{\text{Radiative transition rate}}$

$1 / \gamma_{rad}$: $\boxed{\text{Radiative lifetime}}$

$$\boxed{\gamma_{rad} = \frac{\Delta E^3 e^2 \mu^2}{6\pi\hbar^4 c^3 \varepsilon_0} N^l}$$

Dicke, Phys. Rev. 93, 99 (1953)
Victor et al., JOSA B 11, 2470 (1994)

N_l : Number of cooperatively emitting dipoles

$N^l = 1$: Spontaneous emission rate

An increase of N_l results in an increase of the radiative transition rate. Complete energy extraction, if: $1/\gamma_{rad}$ < dephasing time

COOPERATIVE EMISSION

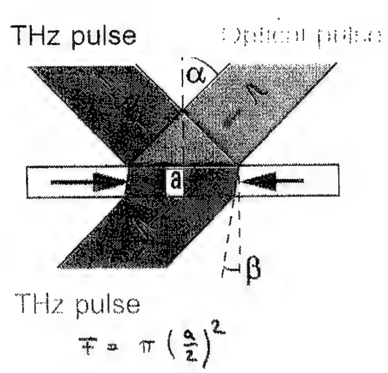

$a \gg \lambda$:

Initial THz radiation power $P(t=0)=P_0$ in each emission cone:

$$\boxed{P_0 = \frac{e^2}{4c\varepsilon_0\, n^l} Z^2_{Bloch}\, \omega^2\, n^2\, F\, \frac{\sin^2(\beta)}{\cos(\beta)}}$$

n^l: index of refraction of semiconductor

n: volume density of carriers

β: internal beam angle

Z_{Bloch}: electron-hole separation matrix

2 Z_{Bloch}: full spatial amplitude of Bloch oscillation

Measurement of $P_0(\omega)$ => amplitude $Z_{Bloch}(\omega)$

DENSITY DEPENDENCE OF THZ AMPLITUDE

Width of first miniband: 18 meV, pin sample, 1.9 THz

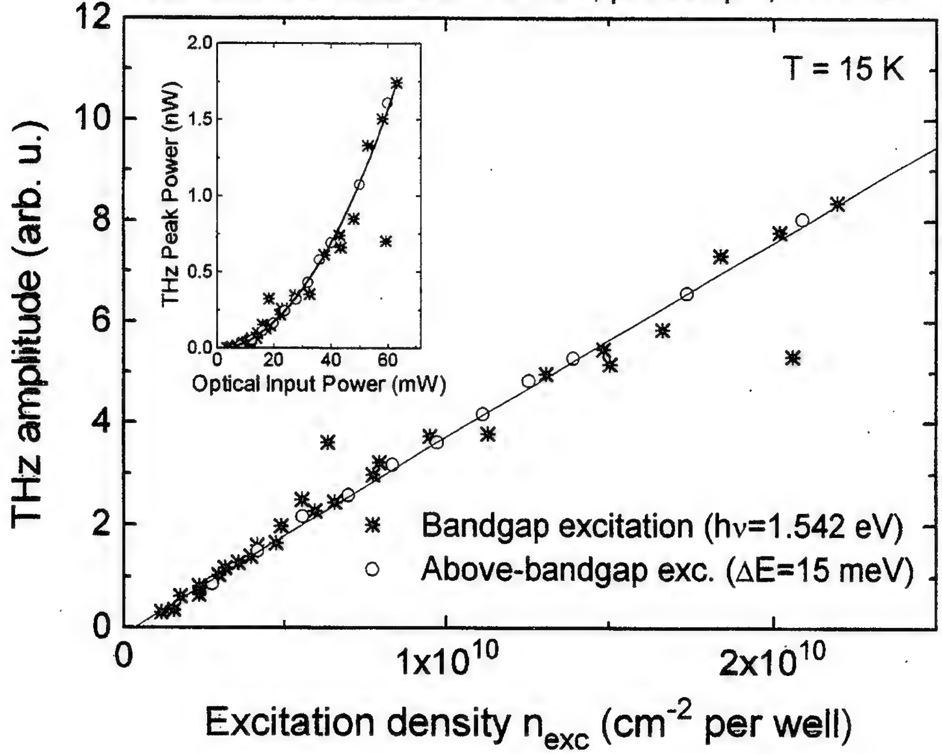

EXCITATION-DENSITY DEPENDENCE OF THz EMISSION

First miniband width: 18 meV, T = 15 K

Red lines: fits with exponentially damped cosine

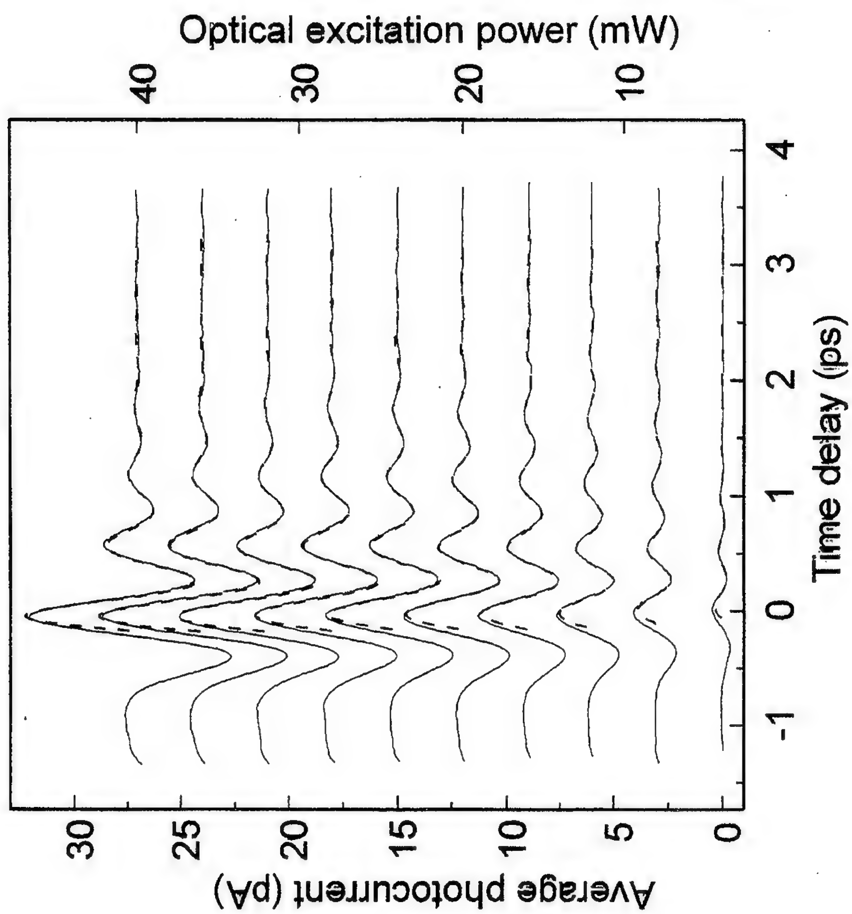

DENSITY DEPENDENCE OF DEPHASING

Width of first miniband: 18 meV, pin sample, ν_{Bloch}=1.9 THz

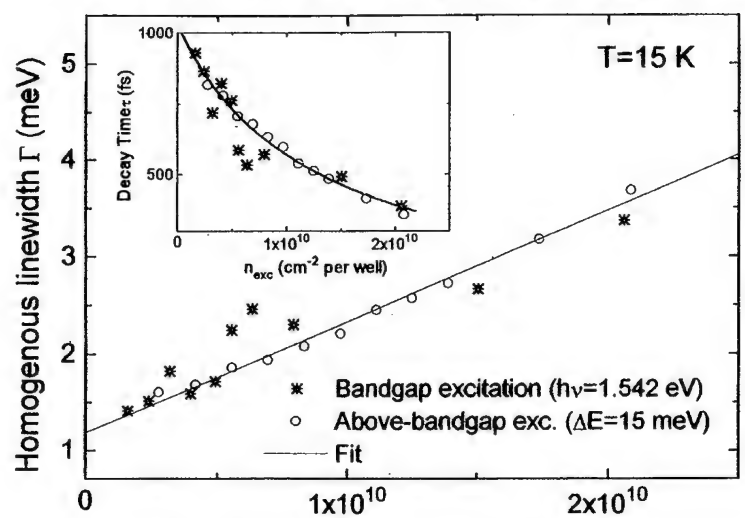

$\Gamma = \frac{2\hbar}{T_2}$

(I) Fit function: $\Gamma(n_{exc}) = 1.18\ \text{meV} + \gamma\, a^2_{Bohr}\, E_{Bohr}\, n_{exc}$

γ=15 for a_{Bohr}=10 nm, E_{Bohr}=6 meV

Corresponds to dephasing measured in four-wave mixing for excitons in quantum wells in the presence of free carriers

(II.) Dephasing for predominant excitation of free carriers (hν=1.557 eV) is not faster than dephasing of excitons alone (hν=1.542 eV)

SPATIAL AMPLITUDE OF BLOCH OSCILLATIONS

Width of first miniband: 18 meV, pin sample

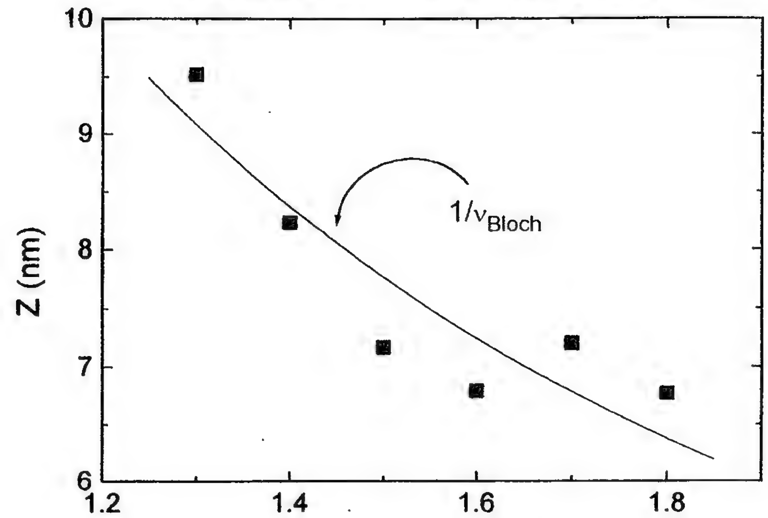

(I) Z determined from detected power of the THz radiation

(II) Semiclassical theory: Amplitude $Z_{sc} = 0.5\, \Delta\, d / (h\, \nu_{Bloch})$

Z_{sc} = 19 nm for ν_{Bloch} = 1.3 THz

Z_{sc} = 14 nm for ν_{Bloch} = 1.8 THz

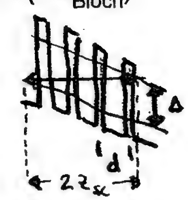

(III) $1/\nu_{Bloch}$ dependence of Z proven.

Factor of two difference between semiclassical prediction and measurement

SUMMARY: COOPERATIVE (SUPERRADIANT) EMISSION

Emitted peak power P_0:

- Quadratic scaling of P_0 with n
- Achieved: 2 nW at 60 mW pump
- 5 % output coupling through 30 nm p^+ top contact (58% Drude absorption, 37 % reflection loss)

Dephasing time τ:

- Decrease with n
- $n=2x10^{10}$ /cm^{2}well: $\tau = 0.4$ ps (radiative lifetime: 10-100 ps)
- Dependence on n like that of interband polarization of ensemble of 2D excitons and free carriers
- But in contrast to interband polarization: same dephasing times for excitons and continuum electrons

Spatial oscillation amplitude Z_{Bloch}:

- Frequency dependence follows roughly the $1/\nu_{Bloch}$ dependence of the semiclassical theory

---

BLOCH OSCILLATIONS OF ELECTRONS EXCITED HIGH INTO THE CONDUCTION BAND

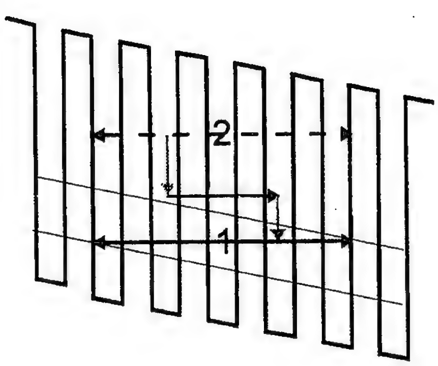

Case 1:
Bloch oscillations of electrons/ excitons at the band edge

Case 2:
Electrons in high-lying continuum states. Expectation:

- No FWM signal => Bloch oscillations not expected
- For excess energy > LO-phonon energy E_{LO}:
  Phase coherence expected to decay within phonon scattering time (~ 200 fs) => Bloch oscillations with ν < 5 THz not expected

EXCITATION HIGH ABOVE THE BANDGAP

(light-hole minibands omitted)

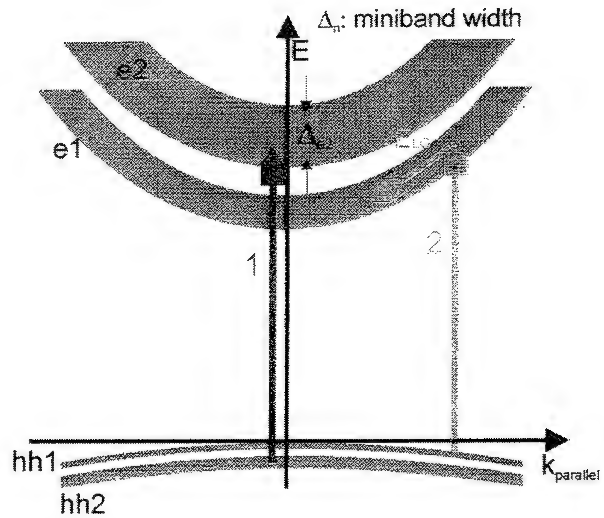

Two explanations for the experimental data:

1. Bloch oscillations of unscattered carriers in high-laying states:
   Implies surprisingly long relaxation times.
2. Bloch oscillations after carrier scattering:
   Implies conservation of intraband coherence during scattering

Variation of excitation photon energy

Width of first electron miniband: 13 meV

Bias voltage: -1.5 V, T = 10 K

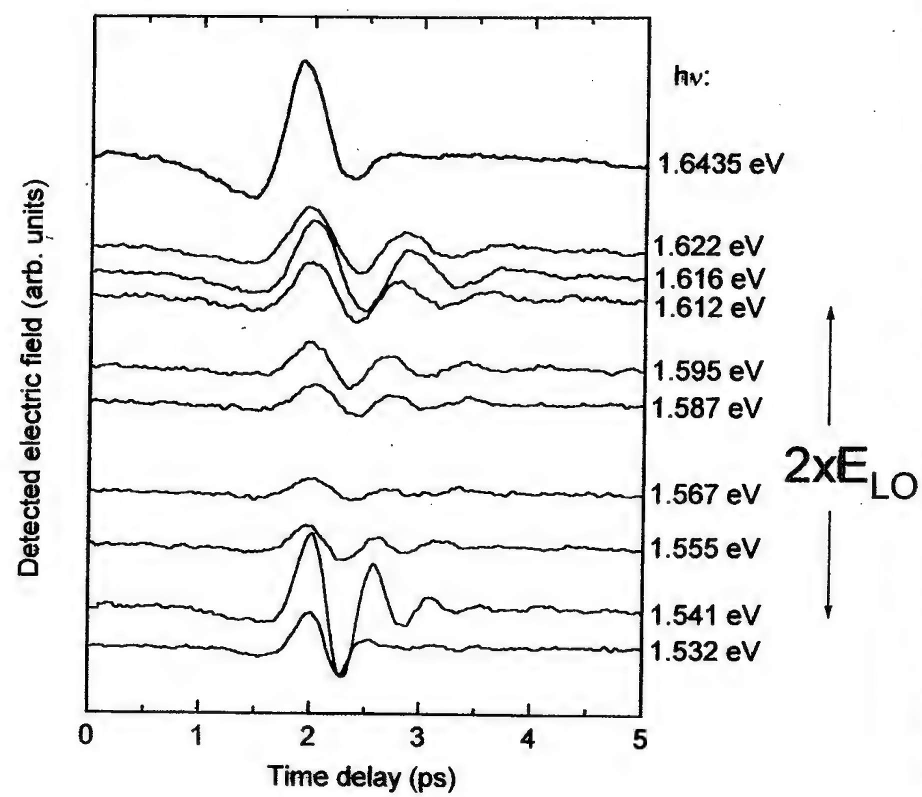

Variation of applied bias field

Width of first electron miniband: 13 meV
T = 10 K, excitation energy: 1.541 eV

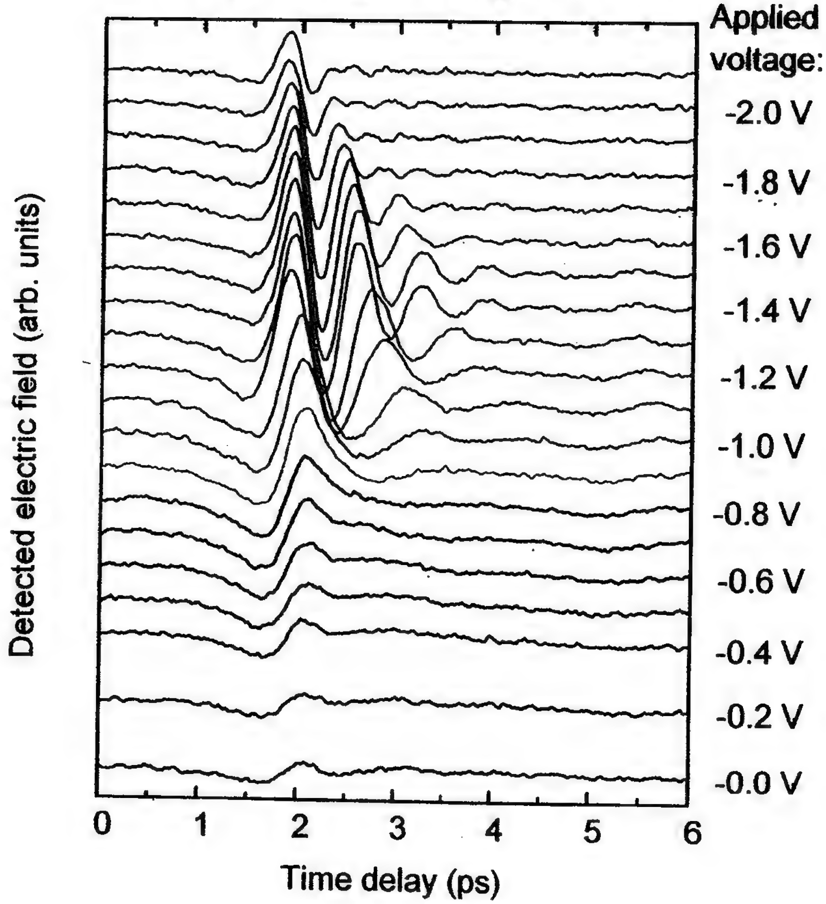

Variation of applied bias field

Width of first electron miniband: 13 meV
T = 10 K, excitation energy: 1.616 eV

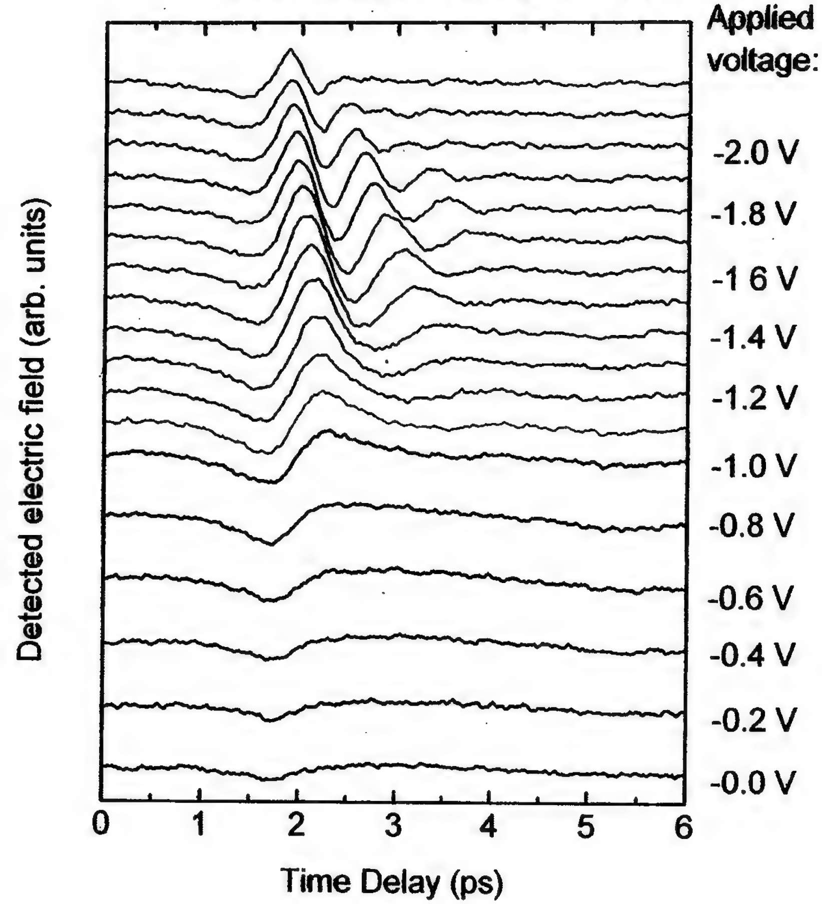

Photocurrent spectrum

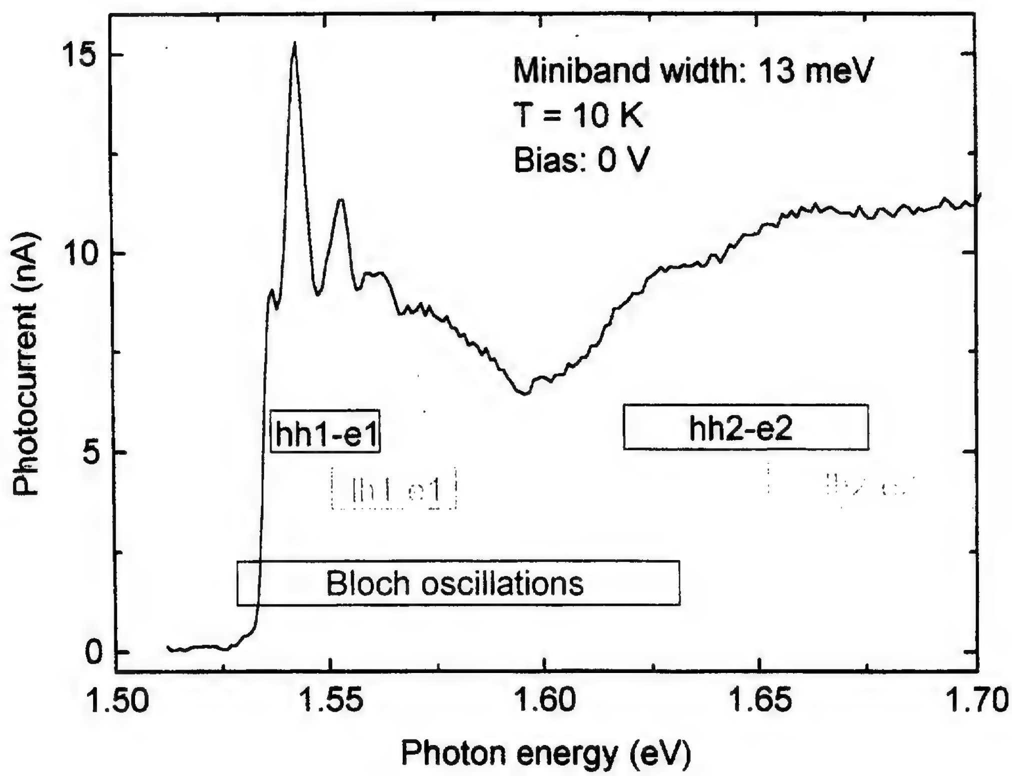

EXPERIMENT: POPULATION DYNAMICS IN THE FIRST ELECTRON MINIBAND AT AND BELOW THE LO-PHONON THRESHOLD

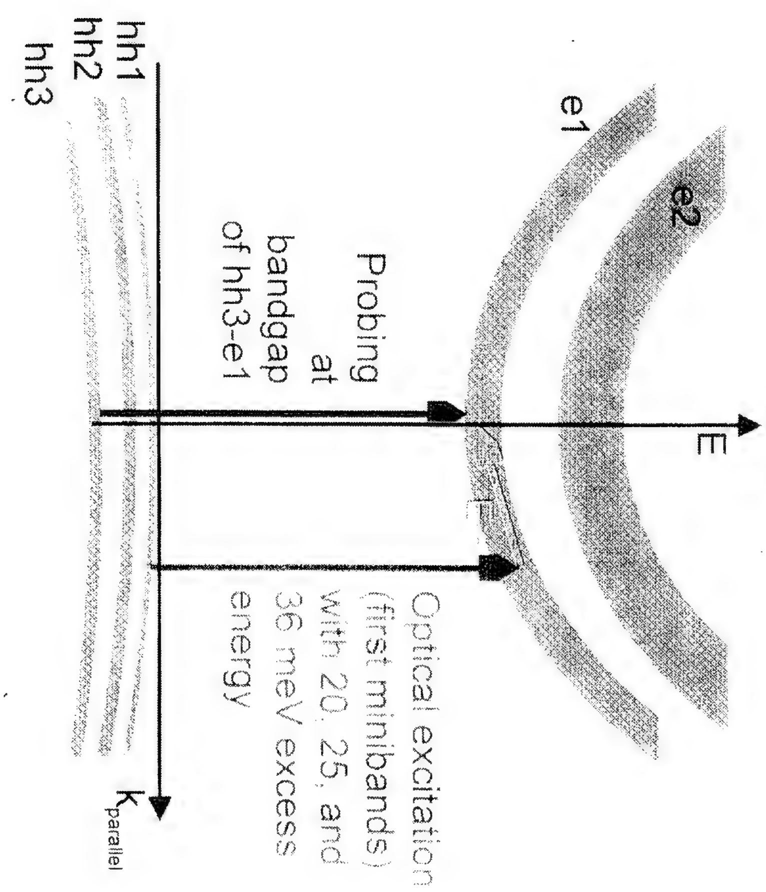

hh3-e1 transition:
only electrons contribute to the signal
(hh3 remains unpopulated, as it is
61 meV above hh1)

ELECTRON RELAXATION VIA LO-PHONON EMISSION

Width of 1st electron miniband: 18 meV, $n_{exc}=10^{10}$ cm^{-2}

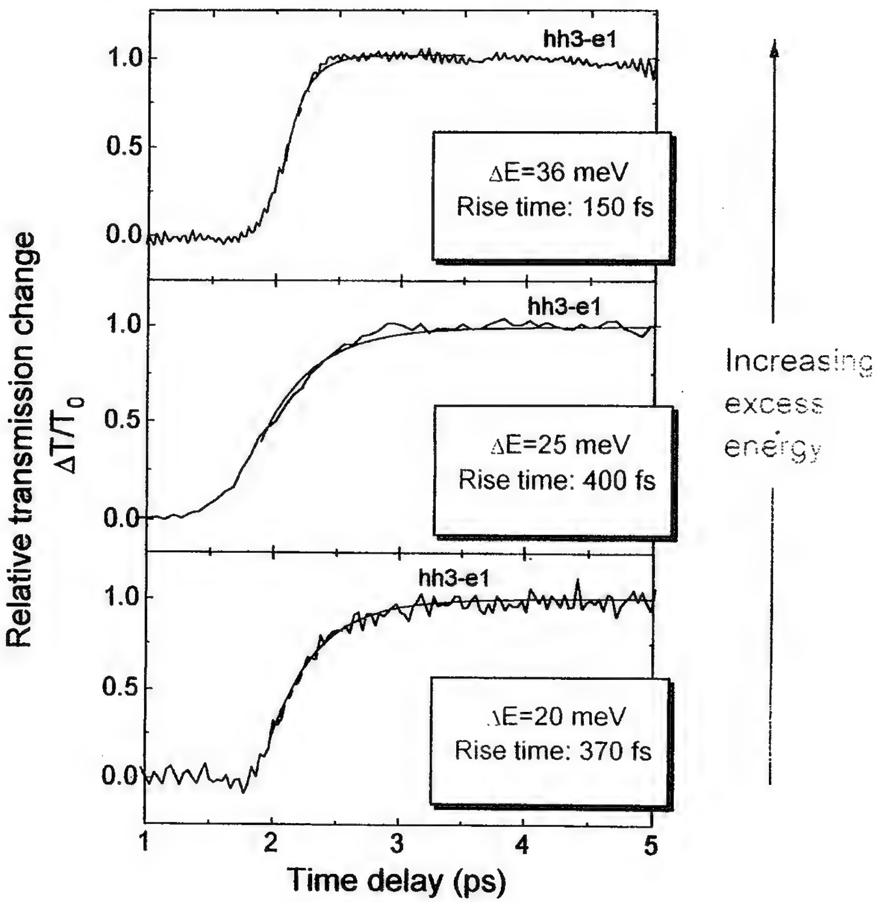

F. Rossi et al., *Phonon-induced suppression of Bloch oscillations in semiconductor superlattices: A Monte Carlo investigation*, ~~WeA3~~ B

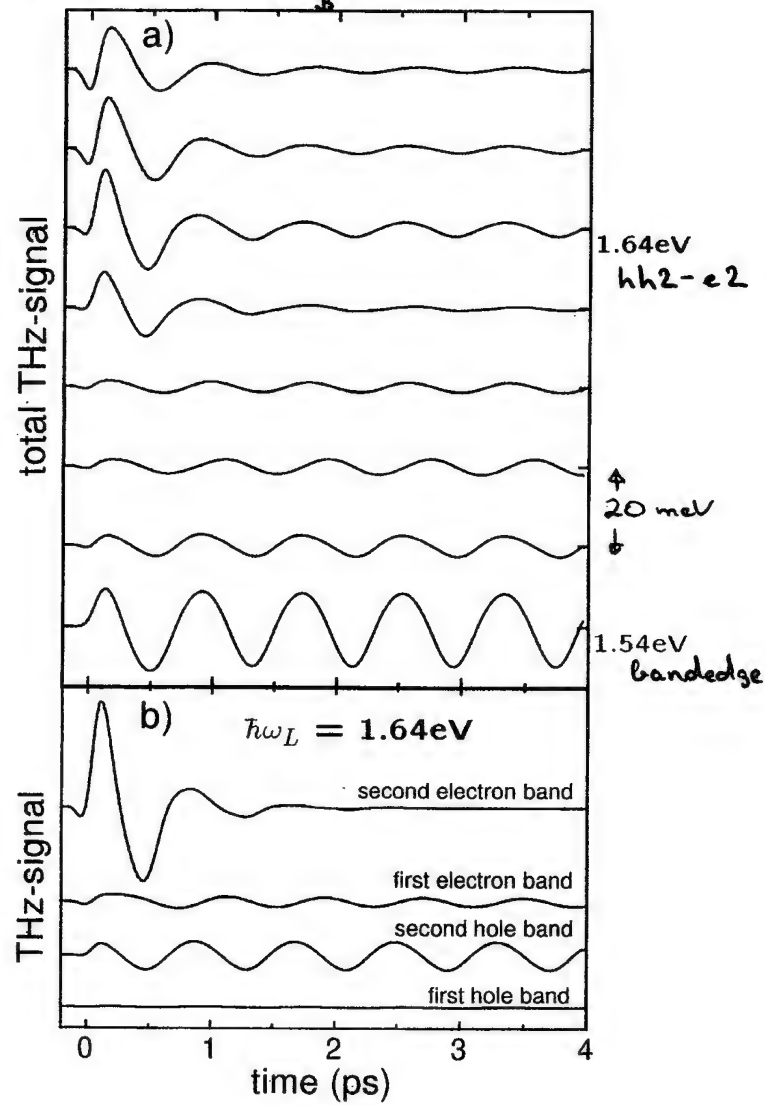

"BUNCHING" EFFECT OF CHARGE CARRIERS IN K-SPACE

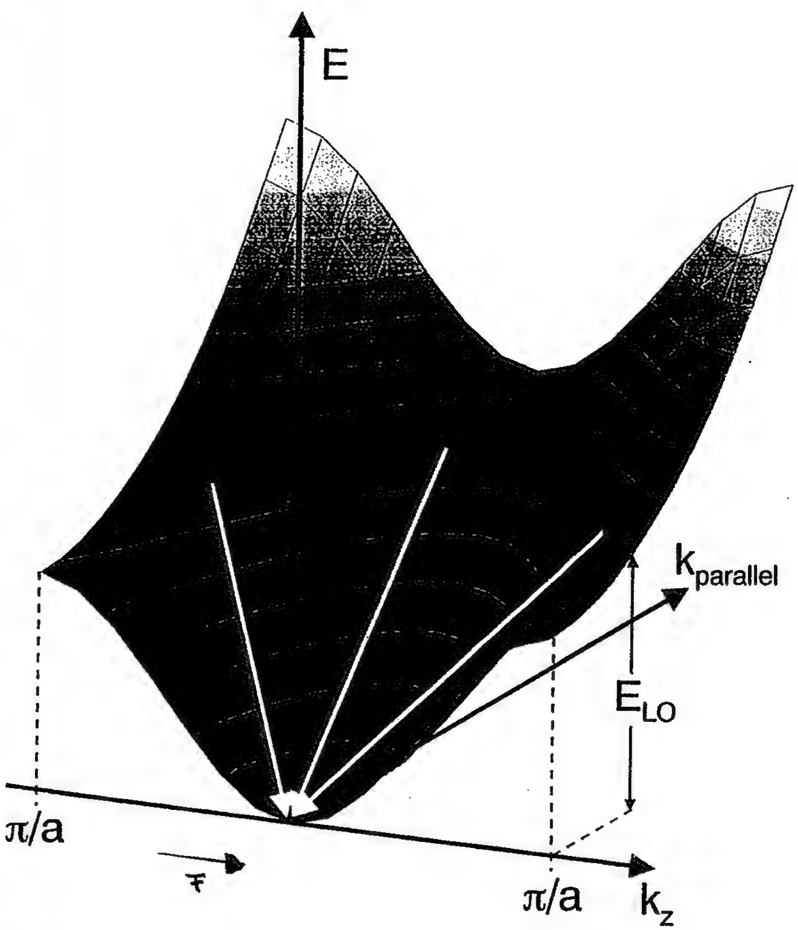

ELECTRONS IN THE FIRST MINIBAND

COMPARISON OF THE COHERENT AND THE INCOHERENT CARRIER DYNAMICS

Measurement of population dynamics:

$E<E_{LO}$: **Relaxation with a time constant of** 400 fs

$E>E_{LO}$: **Relaxation within** $\leq$200 fs

Coherent THz dynamics:

Decay time constant of THz oscillations: 750-1000 fs
(for all excess energies $E<E_{LO}$ and $E>E_{LO}$)

CONCLUSION:
Bloch oscillations are observed in spite of energy relaxation of electrons.
=> Evidence for partial phase conservation during relaxation by LO-phonon emission.

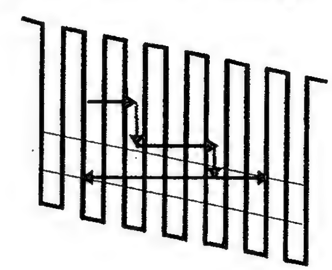

SUMMARY: BLOCH OSCILLATIONS UPON EXCITATION WELL ABOVE THE BANDGAP

Bloch oscillations continue even after emission of 1 or 2 LO phonons

- Indication for intraband phase conservation during LO-phonon emssion
- Phase retardation of the coherent charge oscillations observed.
  Explained by "bunching effect": Uniform and quasi-simultaneous momentum transfer from LO phonons.

DO NOT AFFIX OVERLAYS ALONG THIS SURFACE

FEEDBACK IN A RESONATOR: AN EXAMPLE FOR "LASING WITHOUT INVERSION"

Lu, Opt. Commun. 38 (1990) 1684

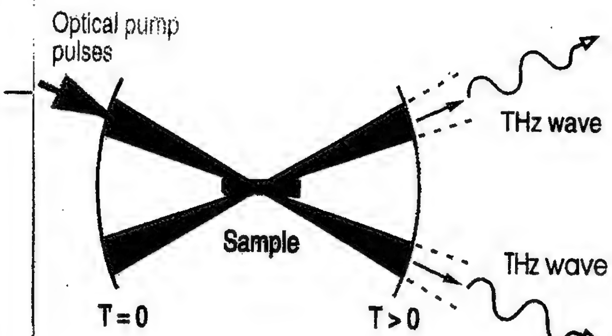

Overall gain with phase-correct feedback consists of:

- Superradiant gain (cooperative emission from the coherent ensemble)
- Lasing gain (with inversion) or absorption loss (higher levels less populated than lower levels)

THURSDAY JULY 11

Multi-Giga-Hertz Optoelectronic Devices

Dr C. N. Ironside
Department of Electronics and Electrical Engineering
University of Glasgow
Glasgow
email Ironside&elec.gla.ac.uk
World Wide Web http://www.elec.gla.ac.uk/~ironside/

Abstract.
Topics from device technology for multi-gighertz integrated optoelectronic systems are covered; monolithic modelocked semiconductor lasers operating at pulse rates up to 375 GHz, and very high speed electroabsorption modulators employing a resonant tunneling diode

Acknowledgements:

Monolithic modelocking :J. F. Martins-Filho ,Unversity of Pernabucco, Recife, Brasil, E. A. Avrutin and S. M. MacDougall, University of Glasgow.

Resonant Tunnelling Diode:
S. G. McMeekin Cardiff School of Engineering, University of Wales Cardiff, PO Box 917, Newport Rd Cardiff, NP2 1XH, United Kingdom.
Jose Figueiredo, Universities of Porto and Glasgow.

Financial Support: EPSRC, UK.

Outline of talk

* Introduction to high speed optoelectronics

*High speed Semiconductor laser -monolithic modelocking

*Resonant Tunneling Diode optoelectronic modulator

Bandwidth of Standard optical fibre

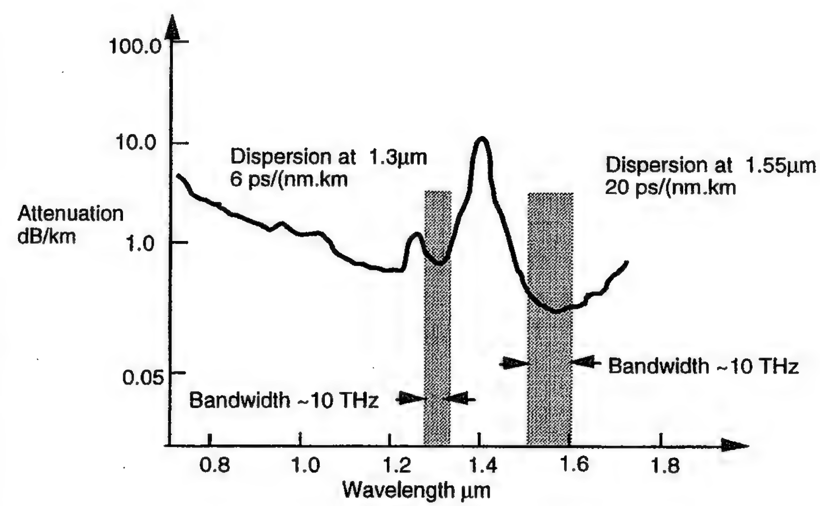

Introduction

* Multi-gigahertz optoelectronic technology is driven by the requirements of optical communication systems

*At Glasgow we are working on integrated devices - usually this means on a semiconductor laser chip. Integration -emulates the success of silicon electronics and increase speed, reliability , functionality and manufacturibility

*Semiconductor lasers are compact (length about 600μm), robust (have operated in extreme environments), reliable (10^6 hours easily), efficient (up to 60% conversion; they are <u>the</u> most efficient means of converting electrical power into optical power); they can produce up to 1W from a single stripe

*They can be directly modulated by a microwave signal up to 30GHz or so. They can operated in a self pulsating manner (either Q-switched up to 100GHz or modelocked up to 1.5THz)

*By integrating saturable sections with a laser diode we have made modelocked laser capable of procducing a plse stream at a repetition rate of up to 375 GHz

*Resonant Tunnelling Diodes have been extensively employed in micorowave generation - although this currently low power

*By integrating a RTD structure with an optical waveguide it is possible to make a optical modualtor which has gain at microwave frequencies

Basics of modelocking

Associated with a laser resonantor of length, l, there are longitudunal modes of separation c/2nl

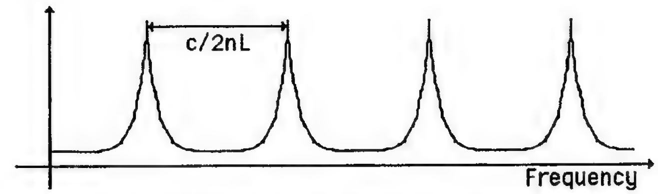

The time dependence of the electric field of the laser is given by:-

$$E(t)=\sum_{n=0}^{n=N} E_n \exp j(\omega_0 + n\omega + \phi)\, t$$

If the laser operates in multimode operation then ϕ is a random phase factor because each mode builds up independently from noise

The Time domain behaviour of a multimode laser is noisy

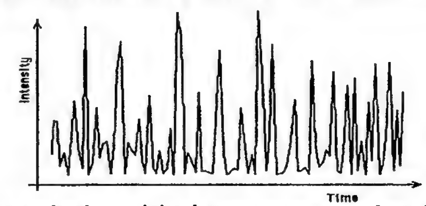

If the phase relationship between modes is fixed , the laser is modelocked and the time behaviour of a modelocked laser is a stream of ultrashort pulses

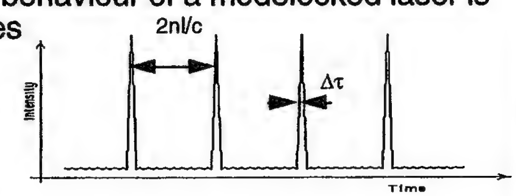

The pulse width is ideally limited by the bandwidth of the laser

Fixed phase fixed amplitude

Colliding pulse modelocking

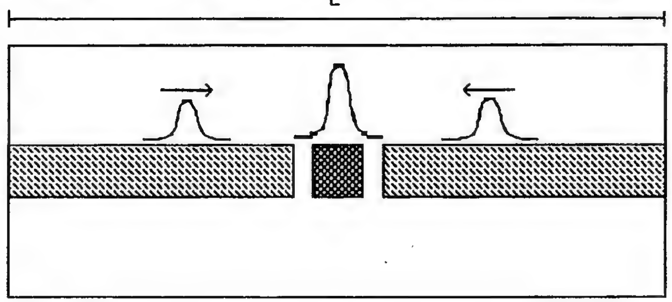

Two pulse buid up from noise the laser operates when both pulses collide in a Saturable Absorber

The Saturable absorber

Absorption in a semiconductor is a function of light intensity; an increase in intensity reduces the absorption. Satruable absoprtion can arise when electrons in the conduction band occupy states and block futher transitions.

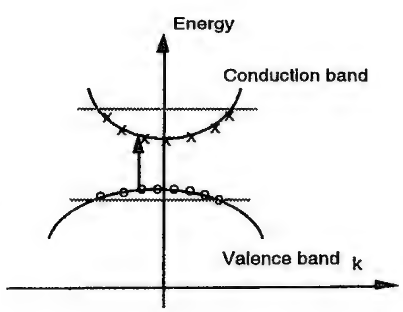

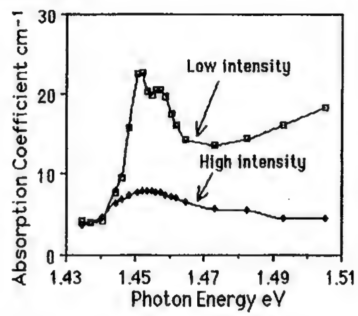

Absorption spectrum of the Quantum welll exciton at low (<20 μW) and high (≈10 mW) input intensities. The waveguide rib width is 3 mm and length is 1 mm. The hh- and lh-excitons are at photon energies 1.451 eV and 1.458 eV respectively.

Device cross-section and chip layout

Device cross-section

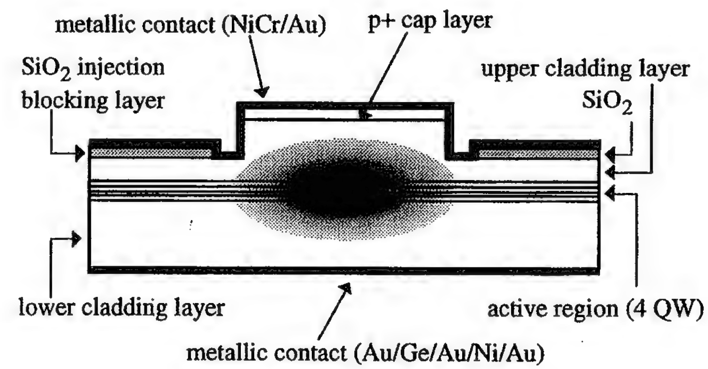

CPM laser chip layout

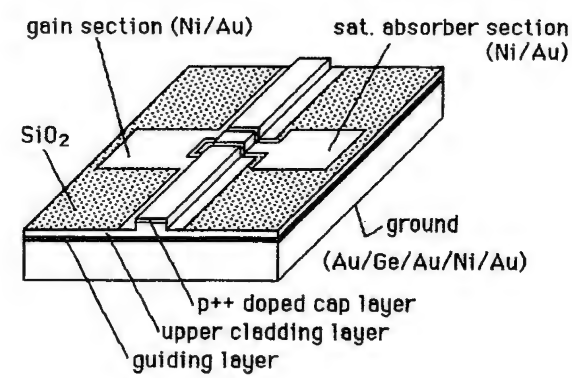

Absorption and Gain spectra of quantum well laser

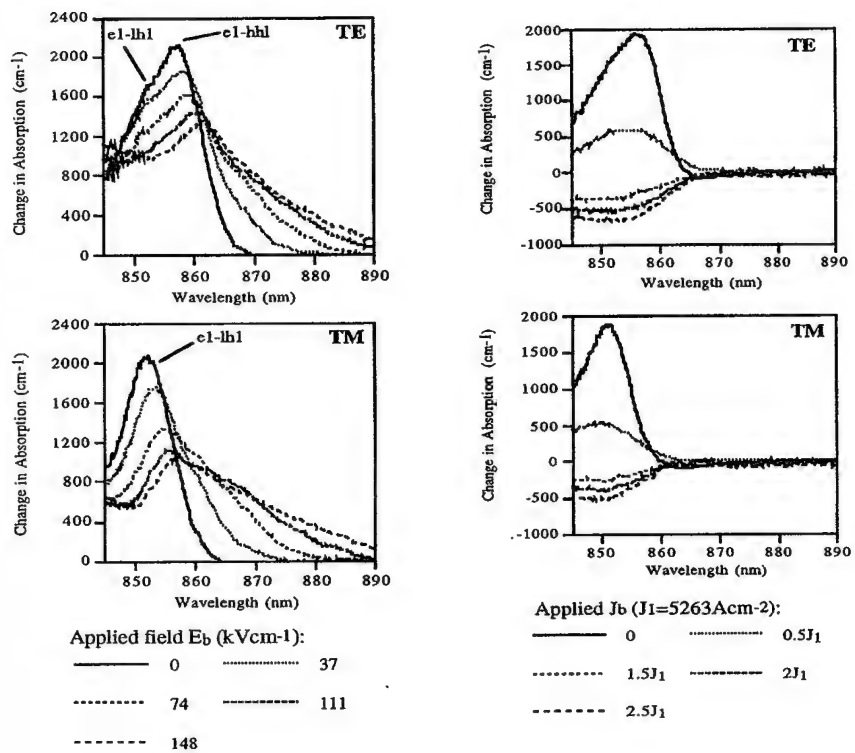

Transform limited pulses from a CPM semiconductor laser

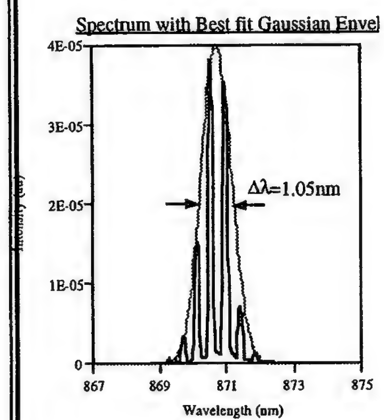

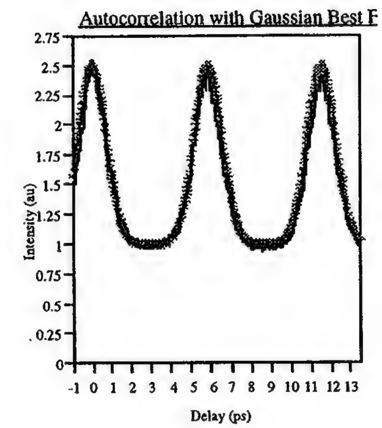

Frequency and time domain measurements of the output from CPM laser show that the pulses are transform limited

The pulse duration is 1ps and the time between pulse is 6 ps repetition rate 166GHz.

The average power is 8mW implies peak powers of 48 mW

The wavelength is around 860 nm and therefore the photon energy is above the band-gap energy of Si .

Multiple colliding pulse semiconductor laser

The idea of the CPM laser can be extended to multiple coliding pulse lasers.

By introducing more Saturable absorbers the laser can be made to operate with more pulses circulating in the laser

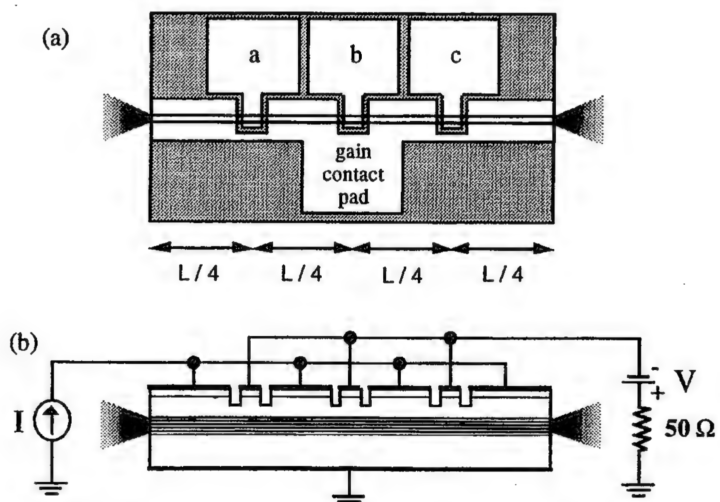

The illustration shows the electrical layout of the chip the three section labelled a,b, c if reversed biased operate as saturable absorbers if forward biased operate as gain sections

Four section MCPM laser Optical Spectra

(MCPM- Multiple Colliding Pulse Modelocking)

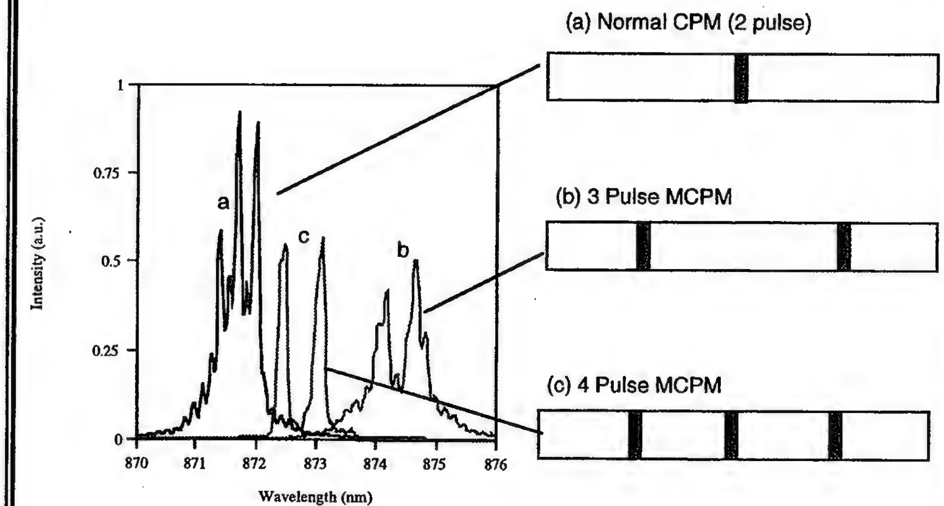

The spectra show the effect of the different biasing conditions

(a) The normal CPM operation with one saturable absorber in the middle at two pulses circulating. The spectrum has the normal mode spacing doubled

(b)Three pulse MCPM operation. The mode spacing increases by a factor of 3

(c)Four pulse MCPM operation. The mode spacing increases by a factor of 4.

MCPM Laser Operation

Four Pulse Operation

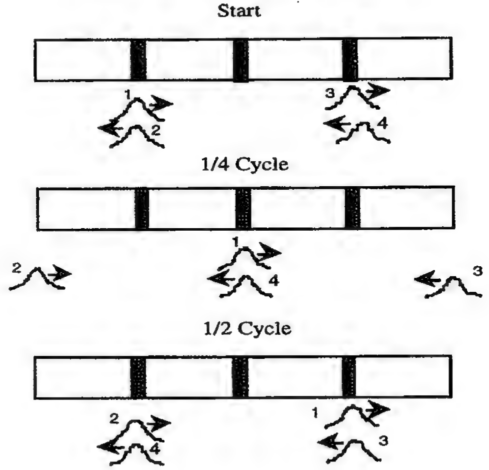

Three Pulse Operation

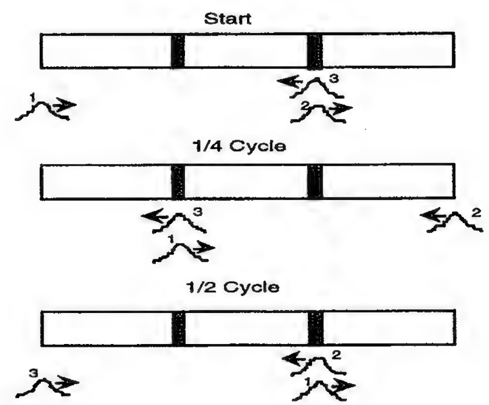

MCPM Rule: Avoid pulse collisions in gain sections

4 sectioned laser operation

Spontaneous emission

Single mode operation

Multimode operation

Modelocked single pulse (55 GHz rep rate)

CPM (2 pulse) operation (110 GHz rep rate)

MCPM (3 pulse) operation (165 GHz rep rate)

MCPM 4 pulse operation (220 GHz rep rate)

MCPM 4 pulse shorter resonator (375 GHz rep rate)

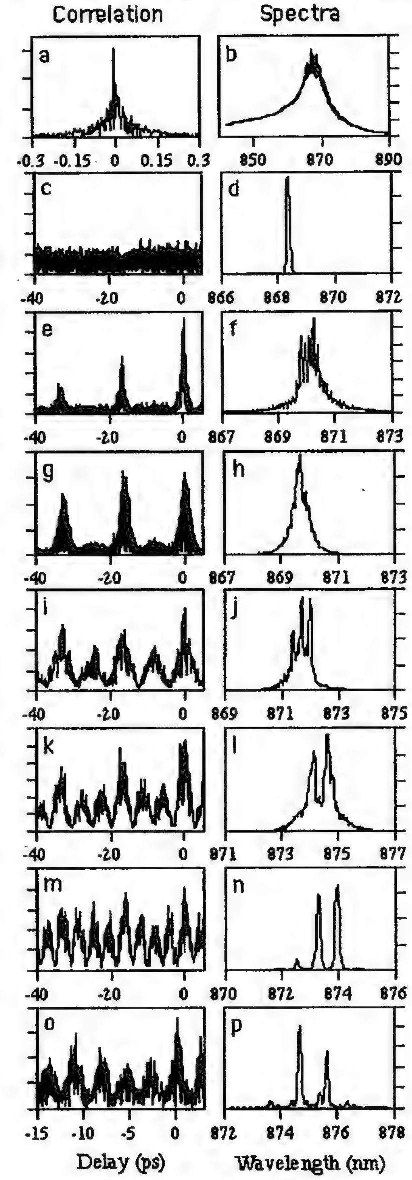

Conclusion to monolithic modelocked lasers section

* Employing simple laser diode fabrication techniques monolithic modelocked semiconductor lasers with high repetition pulses rates can be made

*Monolithic mode-locked semiconductor lasers offer the possibility of very low cost sources of high repetition rate ultrashort pulses which are compact, reliable, robust, efficient and can be mass-produced.

*Possible applications include sources for conversion to microwaves source for electro-optic sampling of MIMICs

Introduction to RTD section

* Since the discovery that the RTD has sufficient negative differential resistance for practical devices most work has concentrated on entirely electronic devices for microwave applications.

* We discuss a simple direct integration scheme to achieve optoelectronic modulation at microwave frequencies from the electric field associated with the RTD by embedding the RTD directly in an optical waveguide.

*With a RTD the electric field distribution across the waveguide is strongly dependent on the bias voltage, this allows small changes in the biasing voltage close to resonance to give a large change in the electric field distribution and the optical characteristics of the guide are field dependent via the **Franz-Kelydsh effect.**

* The RTD can introduce instabilities into the current-voltage characteristics of the guide which can enable the electric field across the waveguide to self-oscillate at microwave frequencies.

*The device has considerable potential as a microwave/optical interface by removing the need for large drive voltages to produce a significant level of modulation.

Resonant Tunneling diode operation

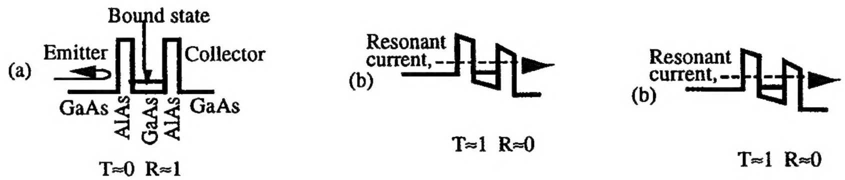

The above diagrams show the lowest energy of the conduction band in a GaAs/AlAs semiconductor heterstructure under various biasing conditions.

The diagram below is a generic I-V curve corresponding to the above description.

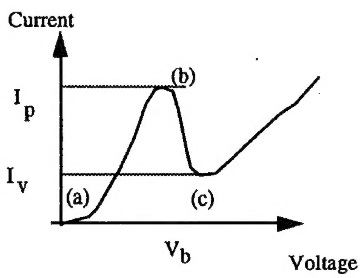

Franz-Keldysh effect with a RTD

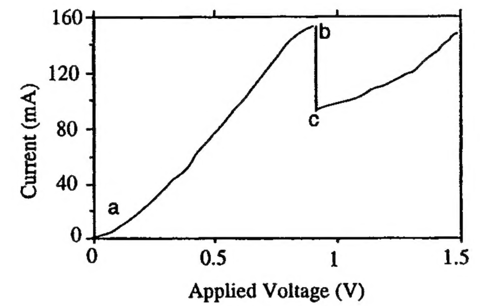

For our devices, in the off- resonance condition corresponding to c in the above diagram the voltage drop,Vd, across the depletion layer is given by:-

$$I_b R_s = V_b = V_c = I_c R_s + V_d \qquad V_d = V_b\left(1 - \frac{I_c}{I_b}\right) \quad = 0.34 \text{ V}$$

The depletion layer thickness in our devices is

$$D = \left(W^2 + 2\frac{\varepsilon}{eN_d}V_d\right)^{\frac{1}{2}} \quad 0.157\mu\text{m}$$

If we assume a uniform field then we have

$$E = \frac{V_d}{D} \quad 2.20 \text{ MV.m-1}$$

The Franz-Kelydsh band-edge shift is given by:-

$$S = -\left(\frac{(eE\hbar)^2}{2m^*}\right)^{1/3}$$

From this the calculated shift in the band-edge should be 9 nm; the observed shift is 14 nm.
We must use waveguide geometry because of thin depletion layer.

RTD Optical Waveguide device

Device Cross-Section

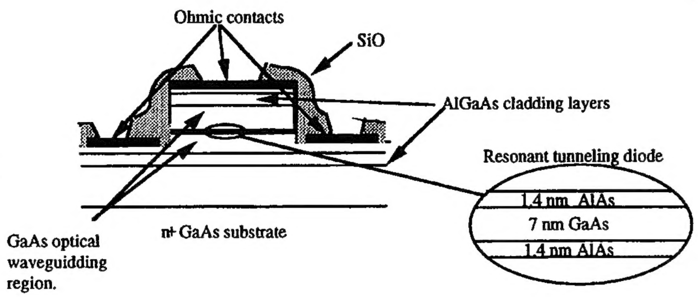

Chip layout

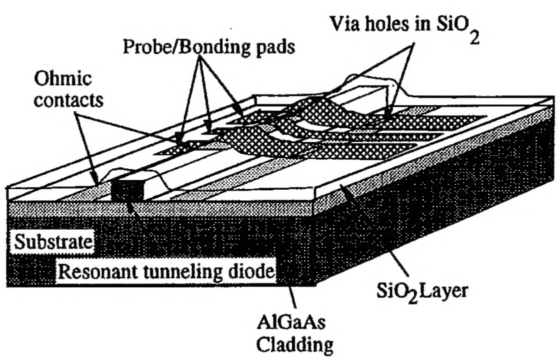

Franz-Keldysh effect in RTD Optical Waveguide device

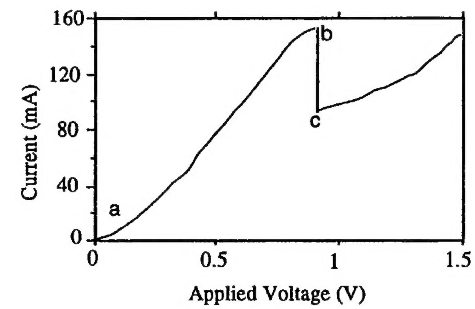

IV curve for a 800 μm^2 RTD electroabsoprtion modulator.

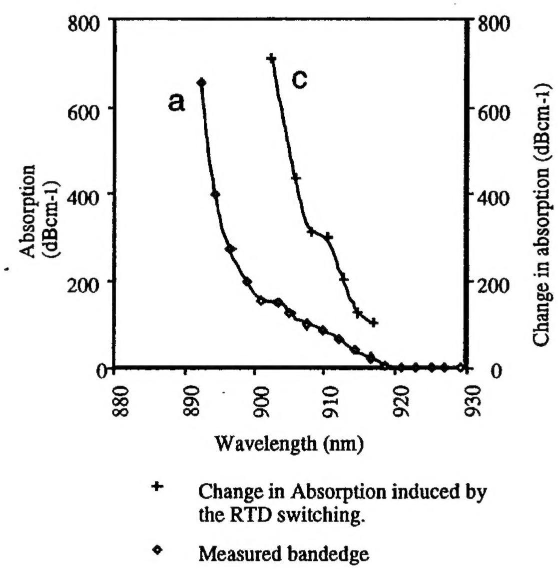

The letters a and c correspond to the letters on the I-V curve.

Resonant Tunneling diode optical modulation results

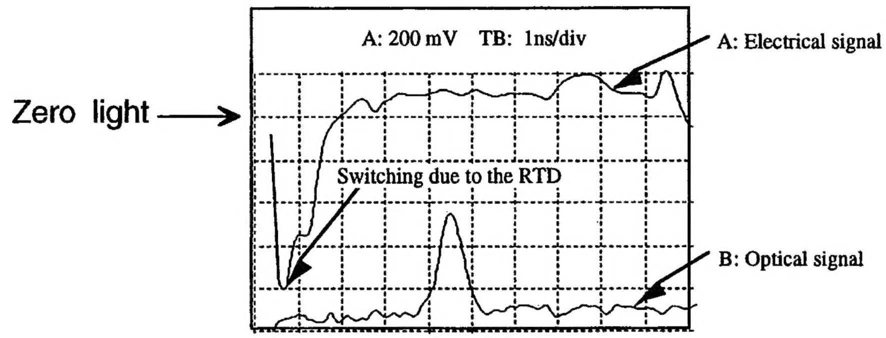

Electro-absorption from a 2 ns electrical pulse. The wavelength of the light is 900 nm. The optical signal is inverted and the change in absorption is characterised of 3 dB modulation in a 100μm long active region. The delay between the optical and electrical pulse is due to propagation delay in free space and electrical cable.

Resonant Tunneling Diode optical modulation limits to speed

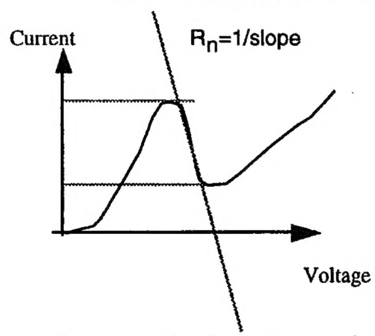

$$\Delta\tau = 5R_nC_w$$

for our device the switching time ~7.5ps, bandwidth ~ 130GHz.

Self - oscillation of the RTD modulator and applied modulation

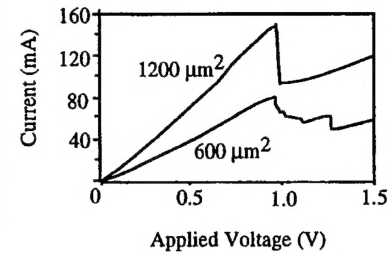

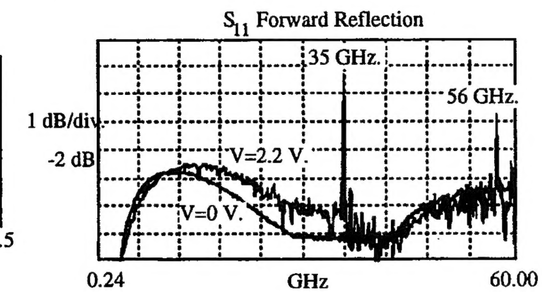

There is some evidence of self osccilation in I-V curves which is confirmed by S parameter measurements.

We have not yet measured optical modulation in a self oscillating device.

Some **direct modulation experiments** have been carried out:-

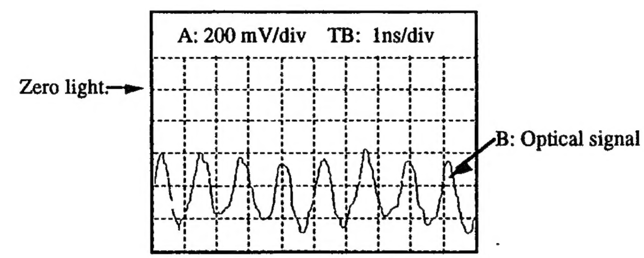

Optical response to a 0.2 V , 900 MHz applied electrical signal.

Conclusions

*Monolithic modelocking of a semconductor laser at repetition rates of up to 375 GHz has been described.

*The four sectioned MCPM laser is programmable and can operate in 1,2,3, or 4 pulse mode.

*An RTD optoelectronic modulator has been described capable of ~10dB of modulation in a 100µm device.

*The device has gain at microwave frequencies and it can operate with low drive powers.

*There some evidence of self oscillation operation.

Future Work

*Synchronisation
We are investigating the synchronisation of both the monolithic modelocked device and the RTD device to optical andelectrical external signals.

*Detectors/ Converters
There is now a requirement for devices which can efficiently convert optical signal to microwave signals. These are now being investigated by several groups using materials with reduced carrier lifetimes either low temperature grown material or material damaged by ion bombardment.

References

Monolithic Modelocking

"Monolithic Multiple Colliding Pulse Mode-locked Quantum-Well lasers:Experiment and Theory" J. F. Martins-Filho, E. A. Avrutin, C. N. Ironside and J. S. Roberts IEEE Journal of Selected Topics in Quantum Electronics 1 539-551 1995.

"Measurements of reverse and forward bias absorption and gain spectra in semiconductor laser material" S. D. Mc Dougall and C. N. Ironside Electronics Letts 31 2179-2181 1995.

"Multiple colliding pulse operation of a semiconductor laser" J. F. Martins-Filho and C. N. Ironside Appl. Phys. Lett. 65 1894-1896 1994.

"Quantum well AlGaAs/GaAs monolithic colliding pulse modelocked laser" J.F. Martins-Filho, C. N. Ironside and J. S. Roberts Electronics Letters, 29 1135-1136 1993.

RTD Modulator

"Franz-Keldysh effect in an optical waveguide containing a resonant tunneling diode" S. G. McMeekin, M. R. S. Taylor, B. Vögele, C. R. Stanley and C. N. Ironside, Appl. Phys. Lett. 65 1076-1078 1994.

"Optical modulation with a resonant tunnelling diode" S. G. Mc Meekin, M. R. S. Taylor and C. N. Ironside IEE Proc. Optoelectronics 143 12-16 1996